UNIVERSITÀ DEGLI STUDI DI PAVIA

SCIENTIFICA ACTA

QUADERNI DEL DOTTORATO

VOLUME XI ANNO XI NUMERO 1

15 MAGGIO 1996

Third
International Workshop on

RESISTIVE PLATE CHAMBERS AND RELATED DETECTORS

Collegio Ghislieri, Pavia Oct 11 - 12 1995

Ed. SERGIO P. RATTI, MARCO MERLO

ISTITUTO NAZIONALE DI FISICA NUCLEARE

CENTRO STAMPA - DIPARTIMENTI FISICI
via Bassi, 6 27100 Pavia

FOREWORD

This Workshop has been sponsored by the University of Pavia, the Istituto Nazionale di Fisica Nucleare and by the Fulbright Foundation, Italian Association of Fulbright Scholars. It has been graciously and elegantly hosted by Collegio Ghislieri. To all these Institutions the organizers are deeply grateful.

The timing of the 1993 RPC Workshop held at the University of Roma Tor Vergata was very appropriate since at that time the Resistive Plate Counters appeared as a very promising detector; this IIIrd Edition is important because now we begin to understand more about the detector: the "detector" as such, in all its components. The RPC's have been employed in a number of important experiments, not only to detect cosmic radiation, but also to detect charged particles -predominantly muons- in fixed target accelerator experiments as well as collider beam experiments. Now, we know "what an RPC really is"; we knew how to make it working, now we begin to understand how to handle it in presence of high ionizing background; how the performances may change depending upon the operation mode (streamer or avalanche); how they change depending upon the gas mixture, upon the material used as electrodes and their surface treatment. We have informations on the limiting performances and on the effects introduced by aging. It is very proper the old detto: "the more we know, the more we wish to know", at this point. We want to know more on radiation damage, we got hold of RPC's operated as early as 1980/81 and stored without any particular precaution for over a decade; we want to know more about working with three component gas mixtures, to mention only very few issues. Indeed there is plenty of room for further experimentations and studies, as well as for future Workshops.

Do we need one? Well, it might be indicative to mention that it has been already proposed at this meeting that in two years from now we might as well meet somewhere near Naples (Italy) for the Workshop number 4 of the serie.

Pavia, january 5th 1996
The Editor Sergio P. Ratti

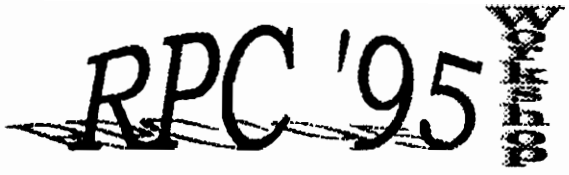

EDITING NOTE

These Proceedings are being printed very late. In our hope, the Proceeding were expected to be distributed during the month of january, being the deadline for the submission of the papers the end of december.

About 10% of the authors submitted their manuscript before the deadline; an additional good 40% submitted their papers by the end of january; the remaining 40% sent in the text by the end of february. However an "hard core" of 10% resisted till the limit of acceptable patience. Unfortunately some of these authors were somewhat "crucial" to the issues discussed at the workshop and could not be simply discarded. This unpleasant situation postponed the possibility of numbering the pages in a logical order.

At the date of may 10th one paper is still missing. I can't wait anymore and I go printing.

I assume full responsability for the delay and I whish to present my apologies. I hope that the shorter delay in providing copies of the transparencies attenuates -at least slightly- the disappointment of the participants who anticipated the printing cost.

I wish at this point to express my personal thanks to Marco Merlo and Germano Bonomi who took care of the assembly of the Proceedings and to Mr. Pietro Cavagnaro and Stefano Bariani who have done the whole job.

Pavia, may 10th, 1996

The Editor, Sergio P. Ratti

INDEX

TOPICS IN RESISTIVE PLATE CHAMBERS

RINALDO SANTONICO
University of Rome " Tor Vergata " and INFN Sezione di Roma 2,
Via della Ricerca Scientifica 1, 00133, Rome, Italy

May 13, 1996

ABSTRACT

The signal pick up in a RPC operating in avalanche mode is analyzed. The ratio between the signal prompt charge and the total charge flowing through the gas is calculated

1. Avalanche growth in RPC's

The basic features of the electric discharge inside the gas of an RPC operating in proportional mode, like the gas amplification and the instantaneous value of the signal current, can be obtained with simple calculations based on the Thownsend theory.

The avalanche growth in a RPC has substantial differences with respect to the case of the wire detectors that are more familiar to the scientific community.

In a wire detector (fig 1) the primary clusters produced by a ionizing particle drift under the action of the radial field and arrive in sequence at the multiplication region near the wire. The signal, if observed with a sufficiently wide frequency band, appears as a series of peaks, one per cluster and can be as long as several hundreds of nanosecond depending on the drift time of the cluster created at the maximum distance from the wire.

On the contrary in a RPC (fig 2) the clusters are all subject to the same field which is strong enough to produce multiplication, so that the corresponding avalanches grow at the same time up to a maximum size depending on the distance of the corresponding primary cluster from the anode plate.The signal is the sum of the simultaneous contributions of all avalanches.

The calculation of the gas amplification in a RPC can be simplified if the number of ionization electrons is treated not as an integer but as a continuous variable uniformly distributed in the depth of the gap. In this way average values but not fluctuations can be evaluated. The primary ionization I can be written in the form:

$$I = eng$$

where e is the electron charge, n is the number of ionization per unit length and g is the gas gap.

Under the action of the field each primary cluster drifts toward the anode plate and originates an avalanche. At the time t, after the gas ionization, the clusters displacement in the direction of the anode is $\Delta x = vt$, v being the electron drift velocity, so that all the avalanches originating at $x > vt$ have the same gas gain $e^{\alpha \Delta x}$ where α is the first Townsend coefficient, and the remaining ones have been absorbed by the anode plate.

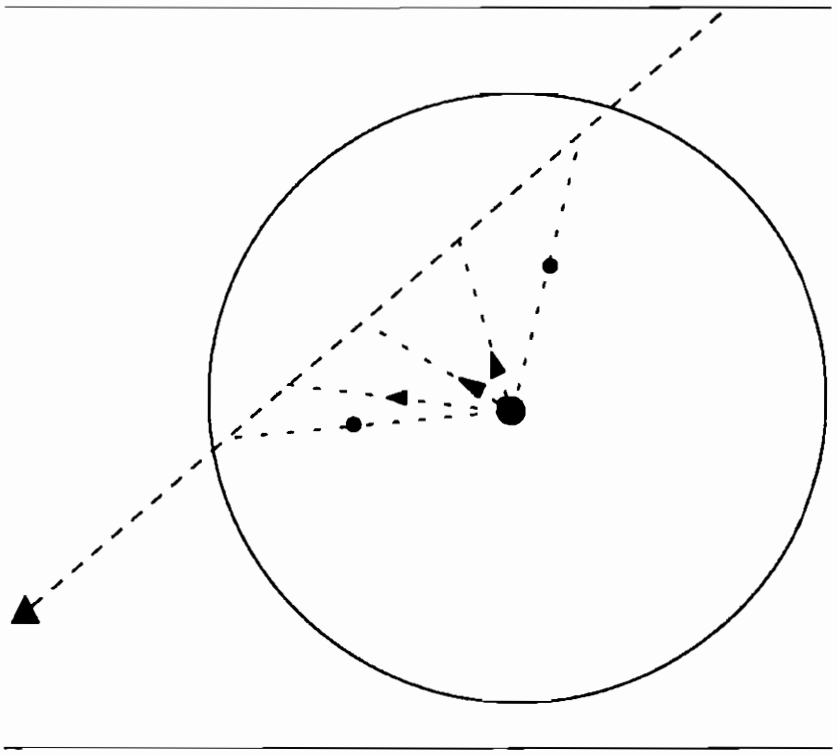

Fig. 1. Sketch of a wire detector. Each primary cluster arrives near the wire at a different time so that the signal is generated by a sequence of avalanches

The total number of electrons is therefore

$$N(t) = n(g - vt)e^{\alpha vt}$$

The current induced on the pick up electrodes is

$$i(t) = eN(t)\frac{v}{g} = evn(1 - \frac{vt}{g})e^{\alpha vt}$$

which reaches its maximum value for $vt = g - 1/\alpha$

$$i_{max} = i(vt = g - \frac{1}{\alpha}) = \frac{evn}{\alpha g}\, e^{\alpha g - 1}$$

The previous relationship is valid under the assumption that only the electron motion contributes to the prompt signal that is detectable

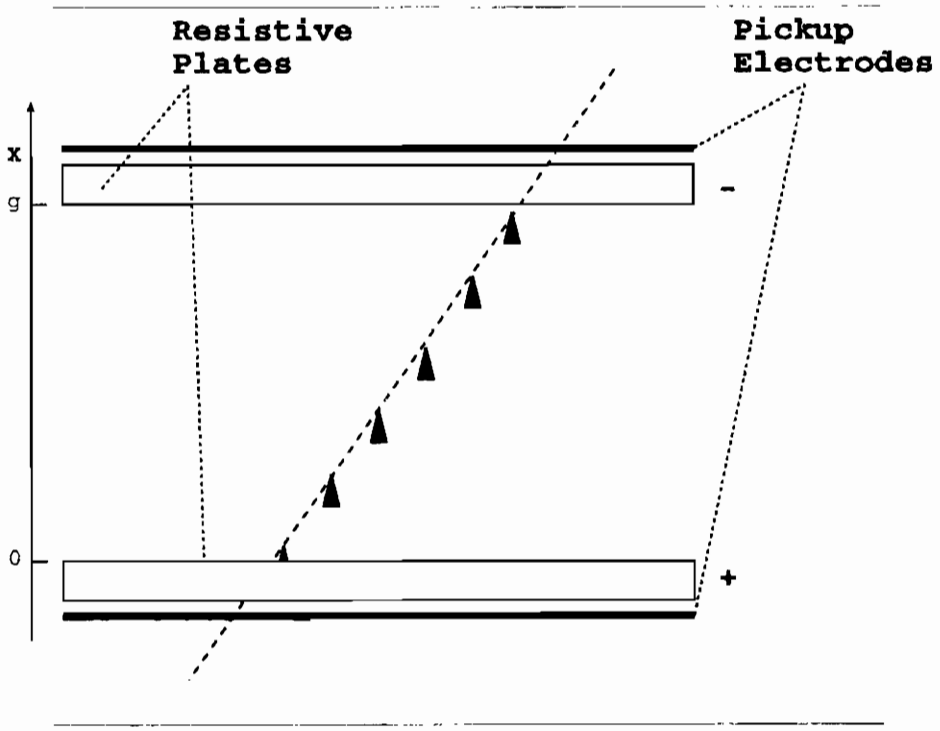

Fig. 2. Sketch of a RPC. The avalanches originated by the primary clusters grow at the same time and the signal is the sum of their simultaneous contributions

on the pick up electrodes. The contribution of the positive ions, due to their low drift velocity, is negligible.

To explain this assumption consider a ionization process that produces a free electron and a positive ion drifting in opposite directions (fig 3). Their displacements at the time t are respectively $\Delta x_e = -vt$ and $\Delta x_I = Vt$ where $V << v$ is the ion drift velocity.

The charge q induced on the pick up electrodes, assuming for the moment a negligible thickness of the resistive plates, is the sum of the contributions due to the electron and ion displacements. According to elementary relationships,

$$q = \frac{-e\Delta x_e + e\Delta x_I}{g}$$

After a time long enough the electron arrives at the anode and the ion at the cathode plate. In this case $-\Delta x_e + \Delta x_I = g$ so that $q = e$.

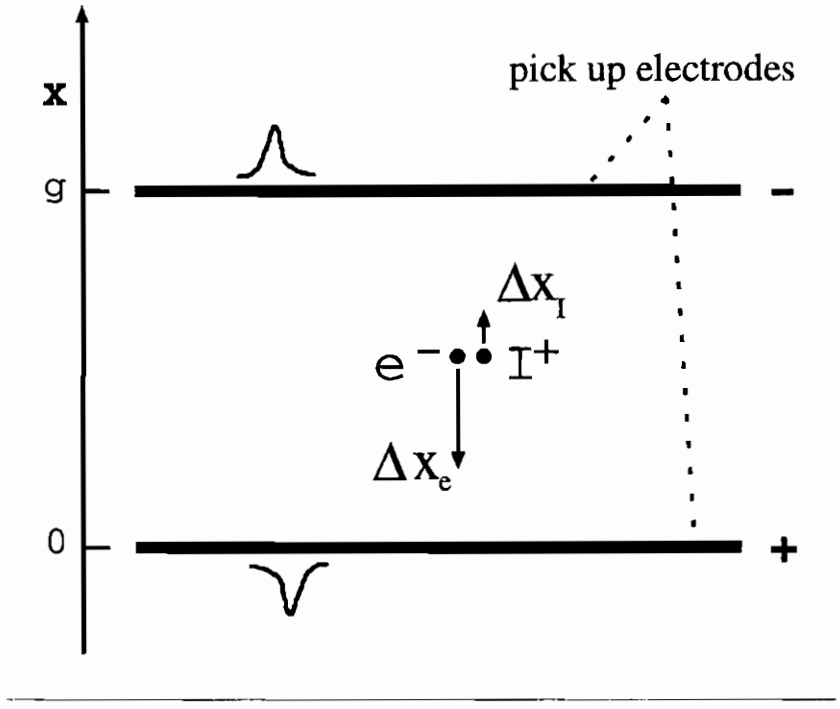

Fig. 3. The motion in opposite direction of the electron and the Ion produces an induced charge on the pickup electrodes

But the prompt signal duration is normally much shorter than the time needed to the ion to arrive at the cathode plate so that in the above relationship only the electron therm is significant. The current induced by a single electron-ion pair is

$$dq/dt = e(v + V)/g \approx ev/g$$

as $V \simeq 10^{-3}v$ and depends only on the electron motion as has been assumed above.

The signal prompt charge q is the integral of the current $i(t)$ up to

the maximum drift time $t_{max} = g/v$

$$q = \int_0^{g/v} i(t)dt \approx \frac{I}{(\alpha g)^2} e^{\alpha g}$$

This is to be compared with the total charge, Q, that is given by

$$Q = en \int_0^{g} e^{\alpha x} dx \approx \frac{I}{\alpha g} e^{\alpha g}$$

The model described above can be checked by measuring the ratio of the prompt to total charge, that according to the above formulas is

$$\frac{q}{Q} = \frac{1}{\alpha g}$$

Here q can be measured with very standard methods based on the use of analog to digital converters and Q=*supply current/rate* can be obtained by simultaneous measurements of the detector counting rate and the current supplied by the high voltage generator.

The maximum value allowed for αg is 20 that corresponds to the limit condition for the transition from avalanche to streamer mode. Near to this limit the prompt charge of an avalanche should be therefore only 5% of the total charge according to the above calculation. This is a consequence of the fact that in the exponential grow of the avalanche most of the electrons are produced very near to the anode plate and can only move through a small fraction of the gas gap.

For an RPC working in avalanche mode, the value of αg should be moderately lower than 20 because, for a much smaller value, the discharge would be too small to be detected. Therefore q/Q should be in the range of 5 - 10 %.

This value is still to be reduced for the following reasons.

In a large area detector the signal is usually picked up by strips that allow the signal to propagate in two opposite directions. The strips behave as transmission lines having one end terminated by the frontend electronics and the other end by a proper resistor. The charge induced on the strip line splits in two equal parts and only one half of the total charge is available at the frontend electronics, the other half being absorbed by the termination resistor.

A further reduction of the prompt charge is caused by the non negligible thickness of the resistive electrode plates that increases the distance of the pick up electrodes from the center of the gas gap. A simple calculation based on a model in which the gas gap and the electrode plates are treated as three serially connected capacitors gives a reduction factor of

$$\left(1+\frac{2d}{\epsilon_r g}\right)^{-1}$$

where d is the resistive plate thickness and ϵ_r is the dielectric constant of the material. For $g{=}d{=}2mm$ and assuming $\epsilon_r \approx 5$, a 30% loss of prompt charge due to the plate thickness can be estimated.

2. Some experimental results

The considerations made in the previous paragraph can be applied to the avalanche working mode of RPCs as it has been experimentally studied in several tests [1].

The proportional and streamer modes in a RPC can be identified in the plot showing the average signal charge, in logarithmic scale, vs the operating voltage. This plot is presented in fig 4 for a gas mixture of $Argon/nC_4H_{10}/C_2H_2F_4 = 10/7/83$ [2]. The low voltage range is characterized by an exponential grow of the charge that is typical of the proportional mode. At higher voltages the avalanche to streamer transition occurs which is characterized by two phenomena: the avalanche saturation at about a 1 pC charge and the appearance of delayed pulses with streamer features. As an example, in the wave form shown in fig. 5 an avalanche signal is followed by a streamer afterpulse [2]. Therefore the avalanche precursor charge and the total charge which includes the delayed streamers, are separately reported in fig 4 for voltages above 9.2 kV.

The plot of fig 4 shows general features of the electrical discharge in the gases. Other gas mixtures [3], show a similar behaviour even if the saturation voltage and charge have specific values for each gas and gap.

According to the Townsend model of the electrical discharge in the gases the exponential grow of the avalanche stops when the space charge field has the same intensity of the external field. This happens when the number of electrons in the avalanche approaches the value of e^{20}.

The calculations made in the previous section give the following ratio between prompt and total charge:

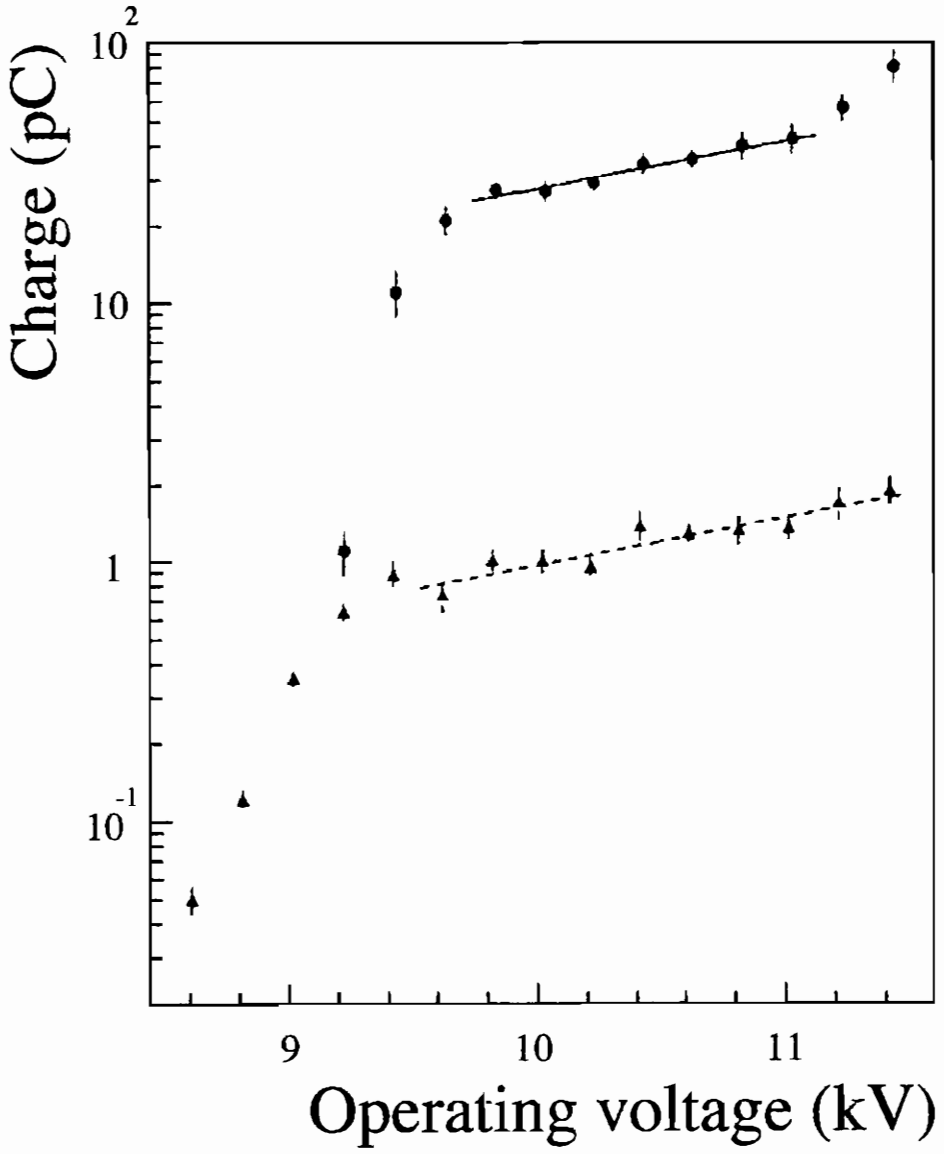

Fig. 4. Average signal charge vs operating voltage for a gas mixture of $Ar/nC_4H_{10}/C_2H_2F_4$ = 10/7/83. Above 9.2 kV streamer-like afterpulses start to appear. The avalanche precursor charge (- -) is therefore plotted separately from the total signal charge (—) which includes eventual streamer afterpulses

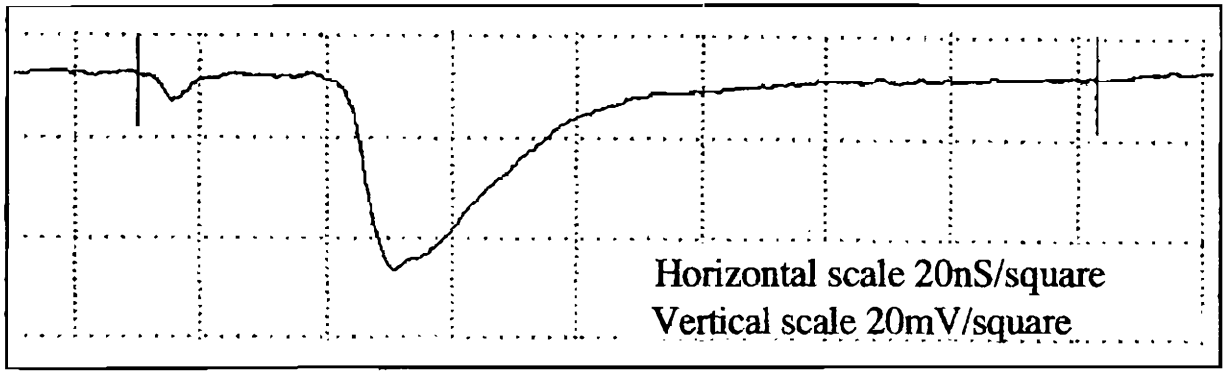

Fig. 5. This waveform [2] , at 9.4 kV, shows an avalanche precursor followed by a streamer afterpulse

$$\frac{q}{Q} = \frac{1}{2\alpha g\left(1 + \frac{2d}{tg}\right)}$$

For the saturated avalanche we take $\alpha g = 20$ and the above formula gives

$$\frac{q}{Q} = \frac{1}{56}$$

so that a prompt charge of 1 pC would indicate a total charge in the gas of 56 pC. This value is not far from

$$q = electron\ charge \times e^{20} = 78pC$$

3. Conclusions

The calculation carried out in this paper shows that in a purely exponential growth of the avalanche the prompt charge is substantially smaller than the total charge. The avalanche saturation has been observed at operating voltage just below the transition to streamer mode.

Based on the calculation shown in this paper the total charge of a saturated avalanche should be not far from *electron charge* $\times e^{20}$.

4. References

1. R. Cardarelli, A. Di Ciaccio and R. Santonico, *Nucl. Instr. and Meth.* **A333** (1993) 399.
   I. Crotty et al, *Nucl. Instr. and Meth.* **A337** (1994) 370.
   I. Crotty et al, *Nucl. Instr. and Meth.* **A346** (1994) 107.
   C. Bacci et al, *Nucl. Instr. and Meth.* **A352** (1995) 552.
   M. Angelone et al, *Nucl. Instr. and Meth.* **A355** (1995) 399.
   K.Abbrescia et al. *Nucl. Phys. B (Proc. Suppl.)* **44** (1995) 218.
   I. Duerdoth et al, *Nucl. Instr. and Meth.* **A348** (1994) 303.
2. V.Makeev, *Contribution to this conference.*
3. A.Di Ciaccio, *Contribution to this conference.*

THE AVALANCHE TO STREAMER TRANSITION IN RPC'S

R.Cardarelli, R.Santonico

Universita' di Roma "Tor Vergata" and INFN Sizione di Roma 2
Via Ricerca Scientifica 1 - 00133 Roma, Italy

V.Makeev

Institute for High Energy Physics Protvino
142284 Protvino, Moscow Region, Russian Federation

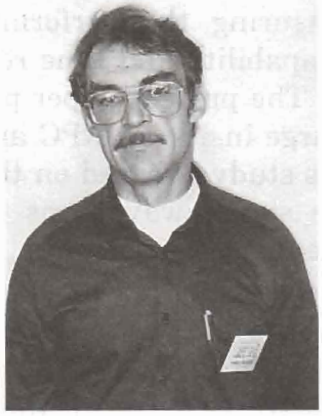

ABSTRACT

The transition region between the avalanche and streamer modes in RPC's working with tetrafluoroetane based gas mixtures was studied in detail. The avalanche amplitude was observed to be strongly dependent on the operating voltage up to a value, where the avalanche saturation occurs and the streamer start to appear. This is normally a late stage of a process initiated by an avalanche precursor pulse. Signal waveforms, charge and timing distributions are reported.

1. Introduction

Resistive plate chambers operating at low gas amplification attracted in the last two years a wide interest in the scientific community because of their capability to efficiently work at particle fluxes at least one order of magnitude larger than in the streamer mode operation /1/. This is of particular interest for the muon physics at hadronic machines like LHC where the muon detectors will operate at rates up to hundreds of Hz/cm^2 induced by low energy backgrounds of neutrons and photons /2/.
The low gas amplification working mode has been already studied by irradiating RPC with muon and pion beams /3/, with gamma and neutron sources /4/ and with beams and sources at the same time /5/. The purpose of these studies was mainly of measuring the performances of RPCs in therms of the rate capability and time resolution in view of their to use at LHC. The present paper purpose is the study of the electric discharge inside an RPC and it's evolution for increasing field. This study is based on the direct inspection and analysis of the signal waveforms produced by RPCs operating at different voltages. This method allowed a modest statistics, of order of 10^2 events per voltage condition, but gave the maximum information per event concerning the amplitude vs time structure of the recorded signals. The gas mixture used in the test was mainly composed of Tetraflouroetane ($C_2H_2F_4$), a component selected in the framework of the search for the environment safe and nonflammable gases that are required by the current safety rules of most laboratories. But, in addition to its positive safety characteristics, this gas exhibits other attractive features. It is cheap, easy to find and it's primary ionization value higher than the same Ar value.

2. The experimental set-up

The present paper describes a cosmic ray test of a RPC of area 50×50 cm^2 that was carried out in Rome.
The set-up shown in Fig. 1 consisted of the test RPC equipped with 1.5 cm wide read out strips and a cosmic ray monitor system consisting of four 50×50 cm^2 RPC's equipped with 3 cm wide read out strips and a thin scintillator finger of size 30×1.8 cm^2, 7 mm thick. Each chamber is composed by two plates of 2 mm thickness bakelite electrodes (a bulk resistivity around 10^{11} Ohm×cm), separated by 2 mm gas gap. The chambers was electrically shielded by a 0.1 mm thick Aluminum foil. A polyurethane rigid foam layer 1 cm thick is inserted between the aluminum foil and the read out strips in order to keep the strip-line impedance around values 50 Ohm. Each strip has one end terminated by a 50 Ohm resistor and the other end connected to the frontend electronics. RPCs M2, M3 and M1, M4 of the monitor system, had strips parallel to the strips of the test chamber and perpendicular respectively as shown in Fig. 1. The RPCs of the monitor system were fluxed with the usual gas mixture of Argon/n-C_4H_{10}/CF_3Br in the ratios 60/37/3 in volume and were operated in streamer mode at 7.4 kV. Gas composition and operating voltage were kept constant all during the test. To select cosmic rays crossing a fixed area of the test RPC, the sensitive areas of the monitor RPCs M2 and M3 , reported in Fig. 1, were limited up to four strips each with respect to the their natural size (16 strips) by excluding the external strips, that eventually were not connected to the frontend electronics board. The scintillator finger was placed possible close to the test chamber so as well to overlap two their read out strips. In consequence, the fifthfold coincidence of the scintillator and the monitor RPCs M1, M2, M3 and M4, selected a cosmic ray beam of intensity about 2/min, crossing the test RPC in narrow fixed region

offered the two read out strips. These two strips were connected to the input of the same voltage amplifier consisting of two identical cascade stages and having a bandwidth of 500 MHz, an amplification factor of 16 and an input impedance of 50 Ohm. As the two strips were connected in parallel to the amplifier input, their impedance was not matched and only 2/3 of the signal charge was fed into amplifier. The amplified signal was delayed on 80 ns by a BNC cable and was sent to a 400 MHz bandwidth oscilloscope triggered by the monitor telescope. The high voltage sensitivity of the scope, up to 2.5 mV/cm, allowed to detect the signals as small as 0.16 mV in spite of the relatively modest amplification factor. The microchannel plate display of the scope produced very bright images even for single random signals. The oscilloscope monitor was watched by a digital camera connected to a PC system which recorded the observed waveforms. The waveforms were recorded in this way and subsequently analyzed by presenting them at the PC monitor. For other waveforms observed at operating voltages below 9.4 kV the recording system was not available and they were directly watched at the scope.

3. Experimental results

The data presented here refer to a gas mixture of Argon/n-$C_4H_{10}/C_2H_2F_4$ in the ratios 10/7/83 in volume. The operating voltage of the test chamber was increased in steps of 200 V from 8.0 to 11.4 kV and for each voltage a number of signal waveforms ranging from 50 to 200 were collected. Typical waveforms are shown in Fig. 2. They exhibit different features in the following voltage ranges:

- Below 9.2 kV the discharge shows a single signal of FWHM= 5.0 ns whose amplitude is strongly dependent on the operating voltage. This operation will be indicated in

the following as "proportional mode" even if the experimental demonstration that the amplitude is proportional to the primary ionization is not given in the present work.

- Around 9.2 kV the "proportional signal" stops to grow with the voltage and behaves like a "saturated avalanche" whose amplitude looks much more weakly dependent on the operating voltage than in previous case. At the same time multiple pulsed signals start appear. The delayed pulses are sometime similar to the first one (i.e. 5.0 ns long) but in some cases much larger signal appear, typically 25 ns FWHM and 0.1 V amplitude, that will be called "streamer signals" in the following. The probability of a streamer afterpulse increases with voltage and is about 95% at 9.8 kV so that the voltage range from 9.2 to 9.8 kV can be characterized as the "avalanche to streamer transition" region.

- In the range from 9.8 to 11.0 kV the signal waveform is normally characterized by two pulses, a single saturated avalanche followed by a single streamer. The time delay of the steamer with respect to the avalanche "precursor" decreases with the operating voltage and around 10.6 kV the two pulses merge in a single one whose leading edge still shows a track of the avalanche phase. This voltage range can be characterized as the "single streamer region".

- The range above 11.0 kV is the "multiple streamer region" being characterized by an high probability of streamer afterpulses.

The arrows on the Fig. 2 points the time position of the avalanche "precursor".

For any recorded waveform the charge signal was obtained by integrating the amplitude profile with respect to the time. The signal charge distribution at 9.4 kV, shown in Fig. 3, exhibits two clearly separated peaks with maximum at 0.8 and 32 pC that we interpret as avalanche and streamer respectively. The plot is in logarithmic scale to

allow for large differences in charge. The average values are 0.87 and 37.5 pC respectively, the difference with respect to the maximum being due to the asymmetry of the distribution around the peak. The relative weight of the peaks is 73% of avalanche and 27% of streamers at 9.4 kV.

The streamer probability, plotted in Fig. 4 as a function of the operating voltage, is zero below 9.2 kV and increases rapidly with the voltage approaching 100% already at 10.0 kV.

The average charge vs the operating voltage is shown in Fig. 5. Above 9.2 kV, were multiple pulses start to appear, the avalanche precursor charge Q_{first} is plotted separately from the total charge Q_{tot}, that include the afterpulses charge. The values, corresponding "proportional" mode and avalanche precursor signals, are signed by triangles, and Q_{tot} by filled circles. The fit results for average charges made in $<Q>= \exp\times(P1+P2\times U(kV))$ form for each charge mode are presented in table below:

Mode	P1	P2	HV range
"Proportional"	-45.32± 1.70	4.92± 0.17	8.6÷ 9.0
Avalanche precursor	4.18± 0.53	0.41± 0.05	9.6÷ 11.4
Streamer	-0.72± 0.91	0.40± 0.09	9.8÷ 11.0

As can see from the data the streamer to avalanche ratio:

$$<Q_{tot}>/<Q_{first}>= 31.8\times\exp((0.01\pm0.1)\times U(kV))$$

is almost independent from voltage.

The mean value of the relative delay between the trigger and the time corresponding to the maximum of the avalanche signal vs the operating voltage is plotted in Fig. 6. The line is the fit to the data:

$$D_A(ns)= (68.8\pm11.84)- (4.51\pm0.18)\times U(kV).$$

The mean value of the relative delay between the avalanche signal and the time corresponding to the maximum of the streamer signal vs operating voltage is plotted in Fig. 7. It is seen that transition area is characterized by the high level streamer delay. The line in Fig. 7 is the fit to the data :
D_{AS}(ns)= (55.81±2.15)- (4.43±0.20)×U(kV). The fit was done for the region where the probability of the streamer is 100% (U≥10.0 kV).

As can see from the fits D_A and D_{AS} the slopes for both curves are almost the same. It is mean that the variation of the high voltage must cause the variation of the streamer time position in two times more then in the avalanche case.

The standard deviation of the relative delay between the trigger signal and of the time corresponding to the maximum of the streamer signal vs operating voltage is shown in Fig. 8. Here we see that transition area characterizes by a high level of the streamer time jitter.

4. Conclusions

We studied the transition region between the avalanche and the streamer modes in detail. The study was based on the direct inspection the signal waveforms produced by RPC. The data shows that the behavior of the relatives times and amplitudes characteristics have the breakdown type dependencies on the operating voltage. We seen that each streamer is accompanied by the "precursor" pulse. It is need to remark that in the range out of the transition area, variation of the high voltage must cause the variation of the streamer time position in two times more then in the avalanche case.

Acknowledgments

Dr. V.Makeev's participation in this work was supported by the "Fondo Afary Internazionali" of the Instituto Nazionale di Fisica Nucleare (Italy).

References

1. R.Cardarelli, A.Di Ciaccio and R.Santonico, *Nucl. Instrum. and Methods* **A333** (1993) 399.
2. A.Ferrari, ATLAS Technical Note **GEN-010**.
3. C.Bacci et al., *Nucl. Instrum. and Methods* **A352** (1995) 552.
4. L. Acitelli et al., Univ. of Rome 'La Sapienza' Preprint **1039** (1994), submitted *Nucl. Instrum. and Methods.*
5. M. Abbrescia et al., Univ. of Rome 'Tor Vergata' Preprint **ROM2F/95/03** (1995), submitted *Nucl. Instrum. and Methods.*

Figure Captions

Fig. 1. Set-up the cosmic ray test.
Fig. 2. Typical waveforms of the signal at different voltage. By the arrays are shown the time position of the avalanche precursor pulses.
Fig. 3. Charge distribution of signals generated by cosmic rays in the test RPC at 9.4 kV.
Fig. 4. Streamer probability versus operating voltage in the events with avalanche signal.
Fig. 5. High voltage dependence of the average charge values. The "proportional" and the avalanche "precursor" signals are signed by triangles, and the total charge by filled circles. The lines are the fit to the data.
Fig. 6. The relative delay between the trigger signal and the

avalanche "precursor" signal versus operating voltage.

Fig. 7. The relative delay between the avalanche "precursor" and the streamer signals versus operating voltage.

Fig. 8. Standard deviation of the relative delay between the trigger signal and the streamer signal versus operating voltage.

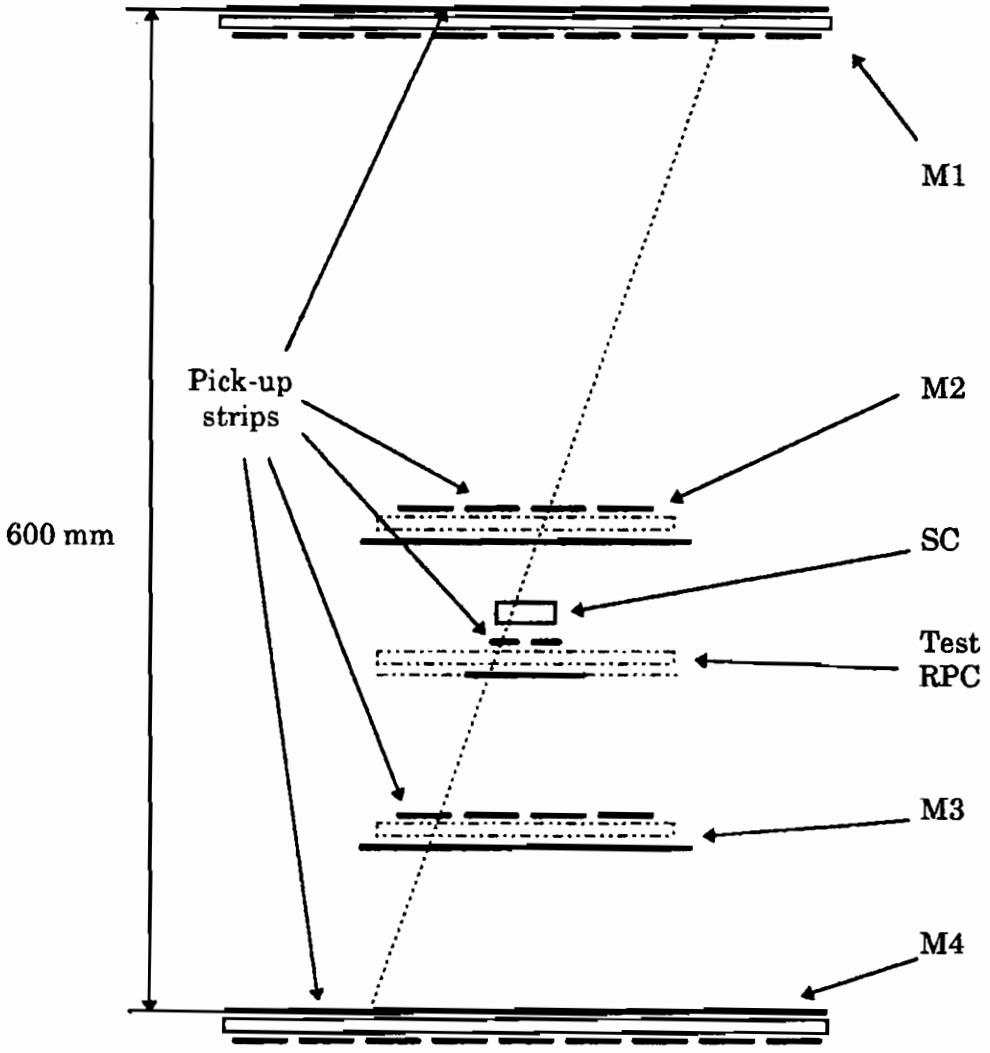

Fig. 1

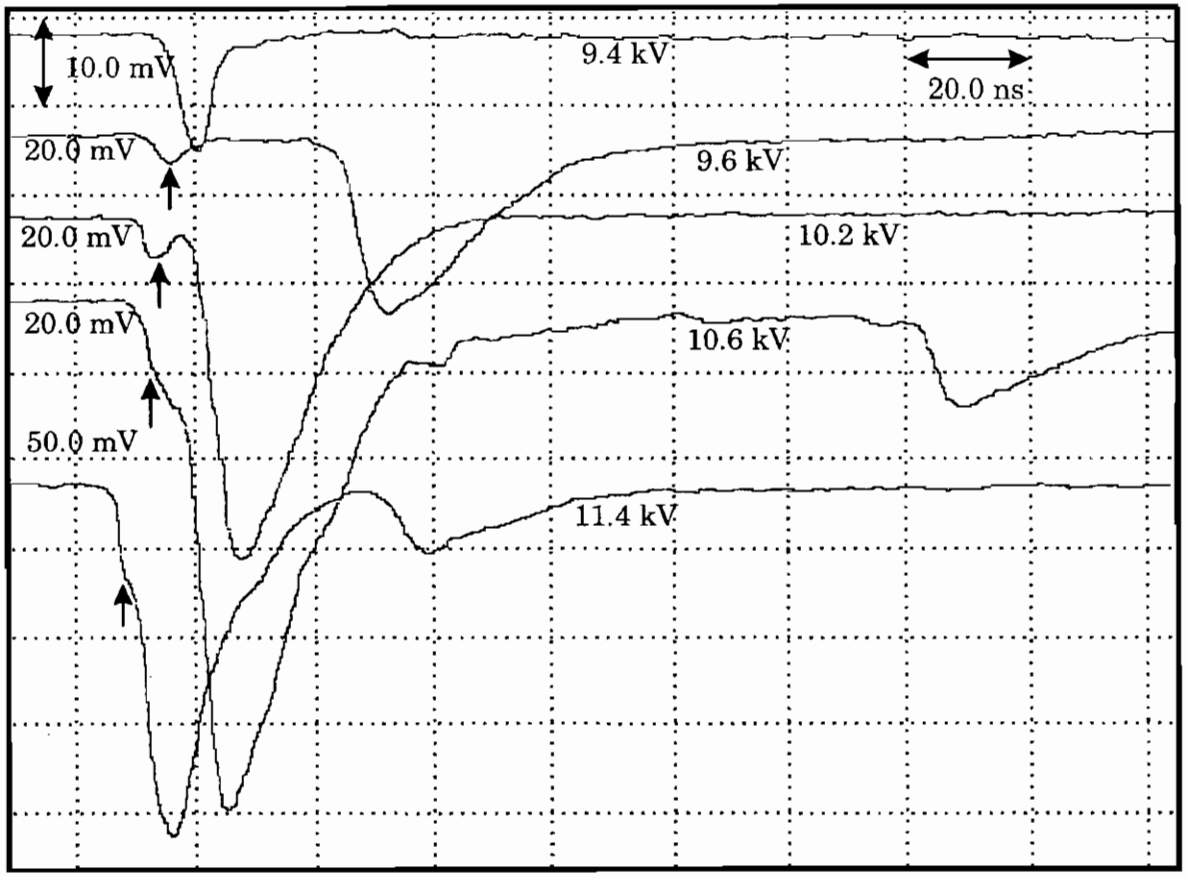
10.0 mV
9.4 kV
20.0 ns
20.0 mV
9.6 kV
20.0 mV
10.2 kV
20.0 mV
10.6 kV
50.0 mV
11.4 kV

Fig. 2

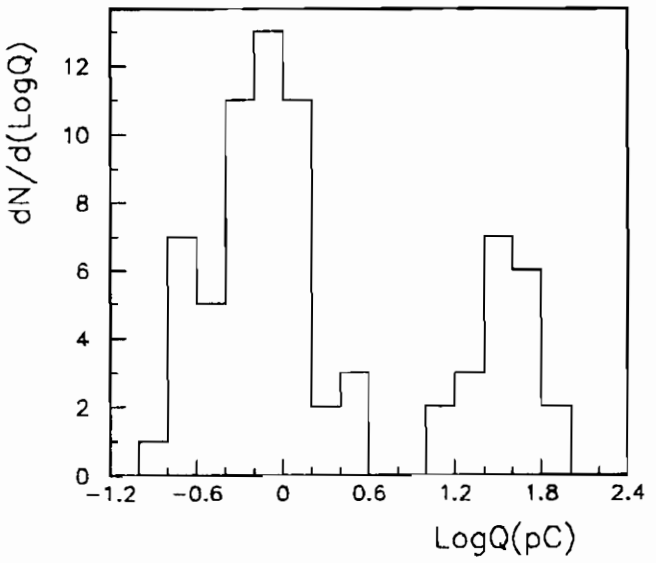
dN/d(LogQ)
12
10
8
6
4
2
0
−1.2
−0.6
0
0.6
1.2
1.8
2.4
LogQ(pC)

Fig. 3

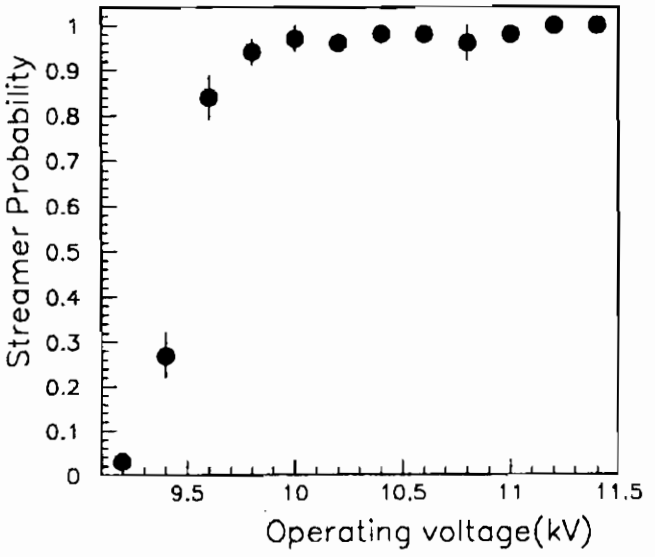
Streamer Probability
1
0.9
0.8
0.7
0.6
0.5
0.4
0.3
0.2
0.1
0
9.5
10
10.5
11
11.5
Operating voltage(kV)

Fig. 4

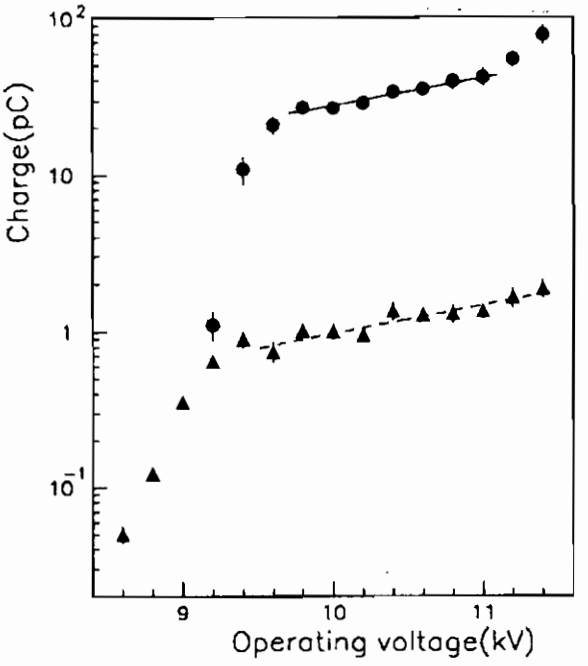
Charge(pC)
10^2
10
1
10^{-1}
9
10
11
Operating voltage(kV)

Fig. 5

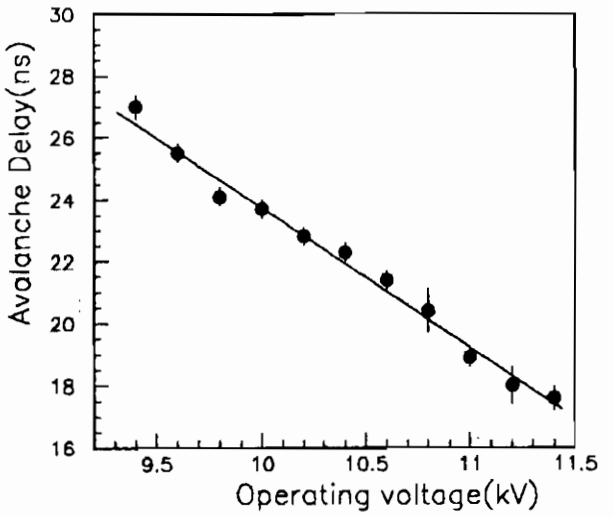
Avalanche Delay(ns)
30
28
26
24
22
20
18
16
9.5
10
10.5
11
11.5
Operating voltage(kV)

Fig. 6

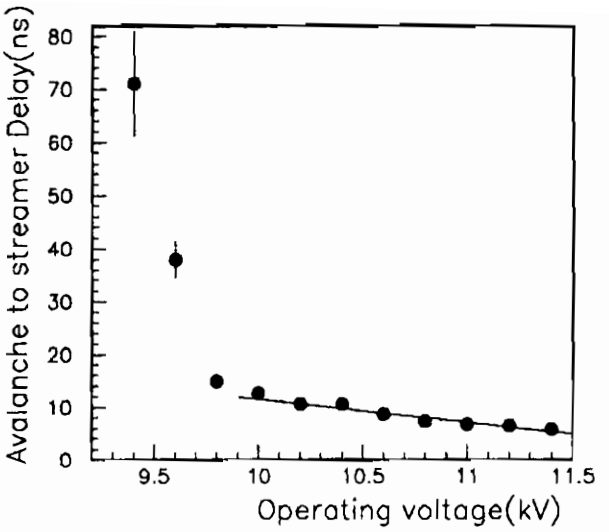
Avalanche to streamer Delay(ns)
80
70
60
50
40
30
20
10
0
9.5
10
10.5
11
11.5
Operating voltage(kV)

Fig. 7

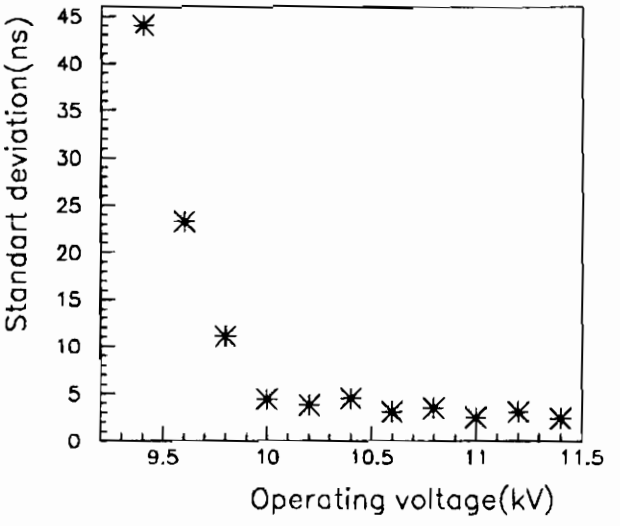
Standart deviation(ns)
45
40
35
30
25
20
15
10
5
0
9.5
10
10.5
11
11.5
Operating voltage(kV)

Fig. 8

A MODEL OF AVALANCHE TO STREAMER TRANSITION IN PPC/RPC DETECTORS

P. FONTE
ISEC-Instituto Superior de Engenharia de Coimbra and
LIP-Laboratório de Instrumentação e Física Experimental de Partículas
Universidade, Departamento de Física,
3000 Coimbra - Portugal.
E-mail: fonte@filip3.fis.uc.pt

ABSTRACT

In the present work we describe a quantitative model of the avalanche to streamer transition phenomenon. The model involves the numerical solution of the electron and ion transport equations in presence of a self-generated photon emission able to photoionise the gas (short range photon feedback) and including the influence of the space-charge generated electric field distortion.

It reproduces well the peculiar behavior of the external current, as observed in PPCs and RPCs and also other known properties as, for instance, the transition threshold and the precursor saturation effect.

1. Introduction

The present work concerns mainly the onset of breakdown in PPCs. However, there are clear indications (precursor, transition threshold) that in RPCs the process is very similar except that the last stage of the breakdown process, the spark, is avoided due to the current limitation provided by the resistive electrodes. In view of this it seems that most of the results obtained in this work for PPCs can be also applied to RPCs.

In a previous paper [1] we have demonstrated experimentally the qualitative compatibility between the breakdown* properties observed in PPCs and the model of streamer breakdown proposed by several authors [2-5].

However the essentially qualitative character of the streamer model doesn't allow a clear comparison between the model predictions and the experimental results. In particular the breakdown properties more evident both in PPCs and RPCs — existence of a signal "precursor" to breakdown [1, 2, 6] and the independence between the breakdown threshold (around 10^8 electrons in PPCs [1, 2]) and the nature of the gases -- cannot be directly interpreted in framework of the model. For these reasons in the present work we developed a quantitative model of the streamer phenomenon, with emphasis on the avalanche-streamer transition region, that will determine the breakdown threshold.

In the literature there are some examples of this type of models; the present work follows essentially the physical model described in [5, 7, 8], which can be considered a "minimum model" of streamer breakdown. It considers the development of an avalanche under the influence of its own space charge field, in presence of a self-generated photon emission able to photoionise the gas. The existence of this radiation in PPCs was experimentally demonstrated [9] for mixtures containing Triethylamine (TEA) vapors.

It is possible to complicate the model by invocating other secondary mechanisms, like the Penning effect (see for example [10]); however, in

*We will use the general expression "breakdown" to refer globally to the complex process that leads to the apearance of a spark in PPCs or to a localised low-current discharge in RPCs.

the present state of knowledge such mechanisms don't seem to be required.

The numeric implementation is different of that described in the above mentioned references. It is aimed to optimize the computational efficiency, owing to the large number of calculations necessary for the quantitative determination of the breakdown threshold as a function of the model parameters.

2. Physical Model

The avalanche evolution and the streamer formation are described by the simultaneous solution of the transport equations for the atomic species involved, together with the Poisson equation, and with functions describing the behavior of several gas swarm parameters as a function of the electric field. The transport equations will include a term describing short distance photoionization: the only secondary mechanism considered.

In presence of space-charge fields larger than about 1% of the applied field, the space-charge effect creates an electron radial velocity that exceeds the effects of diffusion [5]; in view of this the diffusion of electrons was neglected. Since we are considering phenomena that take place in a time scale comparable to the avalanche transit time, the ions were considered as stationary.

For the sake of simplicity and computational efficiency a one-dimensional model of the avalanche was adopted. The charges were considered as being contained inside a cylinder with axis perpendicular to the electrode planes. The charge distribution is considered to be uniform in the radial direction and variable in the longitudinal direction.

The choice (certainly distant from reality) of an uniform charge distribution in the radial direction does not introduce a severe problem because it is possible to show that a gaussian charge distribution in the radial direction (more realistic) would produce a similar axial electric field.

3. Mathematical Formulation

3.1. General Description

The electric field over the axis (x) of a cylinder that contains a linear charge density $\rho(x)$, is given by (see for example [11]):

$$\frac{E(x)}{2\pi} = \int_{-x}^{0} \rho(x+x')\,(-1-g(x'))\,dx' + \int_{0}^{d-x} \rho(x+x')\,(1-g(x'))\,dx';$$

$$g(x') = \frac{x'}{(x'^2 + R_0^2)^{1/2}}\,;\ \rho(x) = e(n_i(x) - n_e(x));$$

where x is the distance along the cylinder axis, R_0 is the cylinder radius, d is anode-cathode gap, $n_i(x)$ and $n_e(x)$ are the numeric linear densities of positive and negative charges, respectively. In an amplifying gap the charges are confined between two conductive electrodes that influence the electric field, forcing the integral of the field along the inter-electrodic space to be equal to the applied voltage. The presence of the electrodes can be taken in consideration by the image-charges method, which in case of two conductive planes are in infinite number. In practice an adequate accuracy can be obtained by considering only the image-charges closest to each electrode. The field integral differs from the applied voltage by some Volt only during the discharge.

The evolution of the electron and ion linear densities is then described by the system of equations:

$$\frac{\partial n_e(x,t)}{\partial t} + W_e \frac{\partial n_e}{\partial x} = S + \left(\alpha\,|W_e| - \frac{\partial W_e}{\partial x}\right) n_e; \qquad 1)$$

$$\frac{\partial n_i(x,t)}{\partial t} = S + \alpha\,|W_e|\,n_e; \qquad (2)$$

$$\frac{\partial n_{ph}(x,t)}{\partial t} = \delta\,|W_e|\,n_e; \qquad (3)$$

$$S(x,t) = \frac{Q}{2\lambda} \int_{-\infty}^{\infty} \frac{\partial n_{ph}(x',t)}{\partial t}\,\Omega(x-x')\,e^{-|x-x'|/\lambda}\,dx'; \qquad (4)$$

$$\frac{E(x,t)}{2\pi} = -\int_{-(d+x)}^{-x} \rho(x+x')\,(-1-g(x'))\,dx' + \int_{-x}^{0} \rho(x+x')\,(-1-g(x'))\,dx' + \int_{0}^{d-x} \rho(x+x')\,(1-g(x'))\,dx' - \int_{d-x}^{2d-x} \rho(x+x')\,(1-g(x'))\,dx'; \quad (5)$$

where the x axis is oriented from cathode to anode. The electrons speed is denoted by W_e, α is the first Townsend coefficient, $n_{ph}(x,t)$ is the numeric linear density of photo-production at a given place and time and δ is a photo-production swarm coefficient similar to the first Townsend coefficient.

Gas self-photoionization is introduced by the term S, defined by Eq.(4), where Q is the gas average quantum efficiency for the relevant emission bands, $\Omega(x-x')$ is the fraction of solid angle (centered in the emission point) spawned by those regions of the amplifying gap susceptible to contribute to the streamer process (essentially the regions upstream and the downstream from the avalanche) and λ is the photon mean free path (for photons in the photoionization band).

The solid angle is given by [7]:

$$\Omega(x-x') = \frac{1}{2}\left(1 - \frac{(x-x')}{\sqrt{R_0^2 + (x-x')^2}}\right) \quad (6)$$

The equations are coupled by photoionization and by the space-charge generated electric field distortions. If those effects are negligible Eq.(1) becomes independent from the others, allowing an analytical solution (see [2] for instance).

The model does not include possible variations of the charge distribution radius along the discharge: the radius existing in the streamer formation region (close to the anode) should be taken.

3.2. Numeric Implementation

The numeric solution of the system (Eqs. (1) to (5)) is based on the repeated application of an approximate analytical solution, valid for stationary electric field and a small time interval. Due to lack of space no details of the derivation will be given. The incremental solution is summarized in the following formulas:

$$n_e(x,t) = P(x,t) + n_e(x_0,0)\, e^{K(x_0,0)t}; \tag{7}$$

$$x_0(x,t) = x - W_e t; \qquad K(x,t) = \alpha\,|W_e| - \frac{\partial W_e}{\partial x}; \tag{8}$$

$$n_i(x,t) = n_i(x,0) + P(x,t) + G(x,t); \tag{9}$$

$$P(x,t) = \frac{M}{2\lambda} \int_{-\infty}^{\infty} G(x',t)\, \Omega(x-x')\, e^{-|x-x'|/\lambda}\, dx'; \tag{10}$$

$$G(x,t) = \left(\frac{\alpha\,|W_e|}{K(x',0)}\, n_e(x',0)\, (e^{Kt}-1) \right)_{x'=x_0(x,t)} \tag{11}$$

valid for

$$t << 1/K(x_0,0). \tag{12}$$

The electric field is calculated before each iteration using Eq.(5). The parameter $M \equiv Q\delta/\alpha$, describes the global efficiency of light emission and absorption in the photoionization band in terms of photoelectrons produced per electron in the avalanche.

3.3. Initial Conditions

The initial conditions correspond to the introduction of N_{e0} electrons in the pre-cathodic region (exterior to the region where the solution is calculated), following a longitudinal spatial distribution approximately gaussian, and the transport of these electrons to the amplifying gap with speed $W_e(E_0)$, being E_0 the applied field.

The numeric linear density of electronic charge at $t=0$ is given by

$$n_e(x,0) = \begin{cases} \dfrac{N_{e0}}{\sigma_0\sqrt{2\pi}}\left(exp\left(-\dfrac{(x-X_0)^2}{2\sigma_0^2}\right) - exp(-9/2)\right) & \text{if } |x-X_0| \le 3\sigma_0 \\ 0 & \text{if } |x-X_0| > 3\sigma_0 \end{cases}$$

The truncation of the distribution at $\pm 3\sigma_0$ introduces an error of 3% in the initial charge deposited. In most cases it was chosen $X_0=-3\sigma_0$, resulting in an amplifying gap void of charges at $t=0$:

$$n_e(x>0,\ 0) = n_i(x,\ 0) = n_{ph}(x,\ 0) = 0.$$

The volume density of charge is given by $n_e/\pi R_0^2$.

When the initial distribution is not truncated, breakdown occurs even in the absence of photoionization because the amplifying gap is continuously fed with charges from the distribution tails.

3.4. Determination of the Model Parameters

The model depends on the physical parameters $\alpha(E)$, $W_e(E)$, $\delta(E)$, λ, and Q.

For the first Townsend coefficient, $\alpha(E)$, we used experimental results obtained for mixtures whose breakdown properties were studied experimentally [1], and whose behavior the present work aims to reproduce. The data can be represented by the formula:

$$\frac{\alpha(E)}{p} = A\ exp\left(\frac{B\,p^k}{E}\right) \qquad (13)$$

where p is the hydrocarbons partial pressure and A, B and k depend on the nature of the gas constituents but not on p.

For the electrons drift speed it was adopted a saturated-speed model. This behavior is qualitatively observed in many mixtures (see [12]) and particularly in the Ar+CH_4 mixture studied in this work. For the Ar+TEA mixture the data existing in the literature are sparse, and the same general behavior was assumed. The model is analytically described as:

$$W_e(E) = W_{max}\left(1 - exp\left(\frac{-E}{E_v}\right)\right) \qquad (14)$$

where W_{max} is the maximum drift speed and E_v is the electric field correspondent to a drift speed of $0.63 \cdot W_{max}$. In most of cases we adopted $W_{max}=5\ cm/\mu s$ and $E_v=300\ V/cm$, values that seem qualitatively adequate for mixtures of argon with CH_4.

There is a considerable difficulty to estimate the parameters describing the emission and absorption of photons ($\delta(E)$, λ, Q). The light emission coefficient, $\delta(E)$, was measured for a narrow band of wavelengths and several gases, being observed for some mixtures a behavior similar to $\alpha(E)$ [1]. It is difficult, however, to determine the importance of the spectral band studied for the photoionization process. Similar difficulties exist in the determination of Q and λ.

It should be noticed that δ, α and Q appear in Eq.(10) combined as $Q\delta/\alpha=M$, this parameter describing the global efficiency of light emission and absorption in the photoionization band. Since for some mixtures and spectral bands $\delta(E)$ seems to follow a law similar to $\alpha(E)$, it will be considered in first approximation δ as proportional to α, with a proportionality constant independent of E. With this simplification M becomes approximately independent of E.

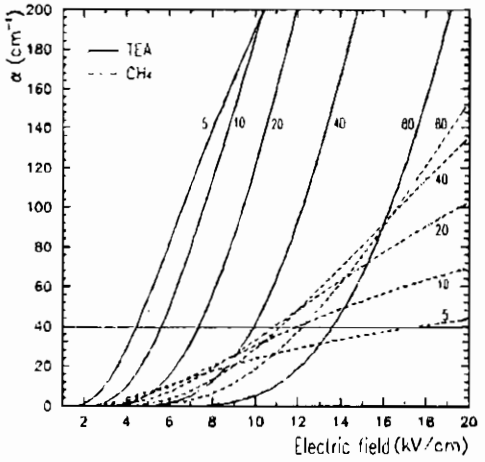

Figure 1 - Model used for the first Townsend coefficient [1]. Mixtures of argon with CH_4 and TEA at several partial pressures of hydrocarbons (indicated in Torr by the figures close to each curve) are represented as a function of the electric field. The horizontal trace at $\alpha=40\ cm^{-1}$ marks the breakdown threshold region (see below): $G_0 \approx 10^7$.

The parameters λ and M are not easily estimated and a distinct strategy must used for their evaluation. Due to space limitations this subject will be discussed elsewhere.

In the initial electron distribution it was chosen $\sigma_0=R_0$, resulting in an approximately spherical charge distribution. The influence of σ_0 in the system is studied for values of 300 μm and 600 μm. The first value corresponds to the typical dimensions of an electron cloud after drifting 1 cm in many mixtures of argon with hydrocarbons (see for example [12]); in presence of space-charge effects the field existing near the avalanche head is repulsive for the electrons, enlarging the avalanche and justifying the second value.

4. Results

According to the present model, along the discharge progression it is possible to distinguish three temporal regions with distinct characteristics: the proportional region, corresponding to the propagation of a Townsend avalanche; the transition region, when the streamer mechanism becomes active; the propagation region, when the streamer advances to the cathode. For each of these regions the global evolution of the electronic and ionic densities and electric field, as a function of time, is represented in figures 2, 3 and 4.

The example shown corresponds to the physical parameters:

p	20 Torr
A, B, k	Corresponding to the mixture Ar+TEA
W_{max}	5 cm/μs
E_v	300 V/cm
M	10^{-6}
λ	500 μm
N_{e0}	100 electrons
R_0	300 μm
σ_0	300 μm
X_0	-900 μm
G_0	4×10^6
d	4 mm

Where G_0 is the nominal gain corresponding to he applied field (E_0): $G_0 = exp(\alpha(E_0)d)$.

4.1. Proportional Region

The proportional region, corresponding to the propagation of a Townsend avalanche, is represented in figure 2. The electronic charge distribution advances in the amplifying gap with speed $W_e(E_0)$ and grows according to an exponential law, keeping a constant shape and leaving a tail of immobile ions (within the framework of the model).

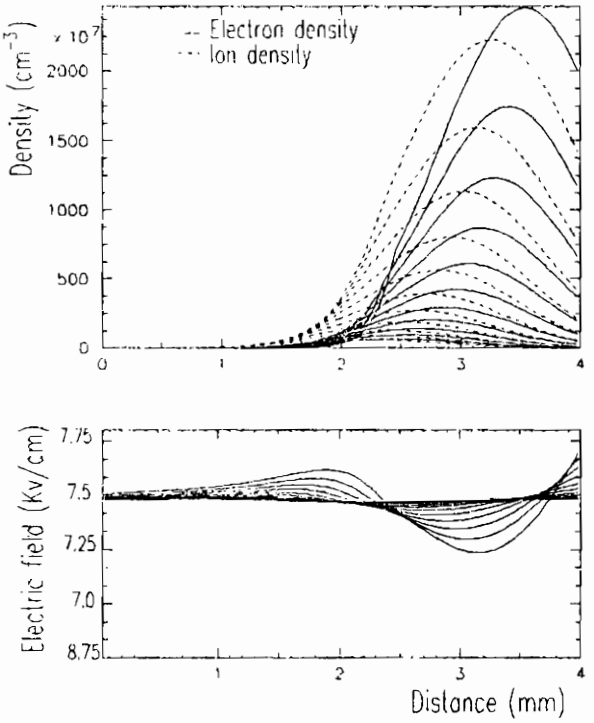

Figure 2 - Electronic and ionic densities and electric field in the proportional region of the discharge, from 56 to 76 ns in steps of 2 ns. The instant $t=0$ corresponds to the arrival at the cathode of the electronic density peak. Cathode and anode are placed, respectively, in the left and right extremes of the horizontal axis.

Although the electronic and ionic densities are almost identical, the slight delay of the ionic distribution relatively to the electronic distribution originates a small electric field distortion. Upstream

(cathode side) from the avalanche the attraction exercised by the ionic cloud (closer than the electronic cloud) causes a reinforcement of the electric field. In the region between the density peaks, the combined effect of ionic attraction (now in the opposite direction) and electronic repulsion originates a field reduction. In the downstream region (anode side) the electric field is again reinforced, due to the repulsion originated by the electronic distribution peak. In the proportional region the net charge density is relatively small, being the electric field distortions unimportant when compared to the applied field.

During the avalanche progression most of the electrons suffer the influence of an electric field inferior to the applied field, resulting in an effective gain smaller than the nominal gain.

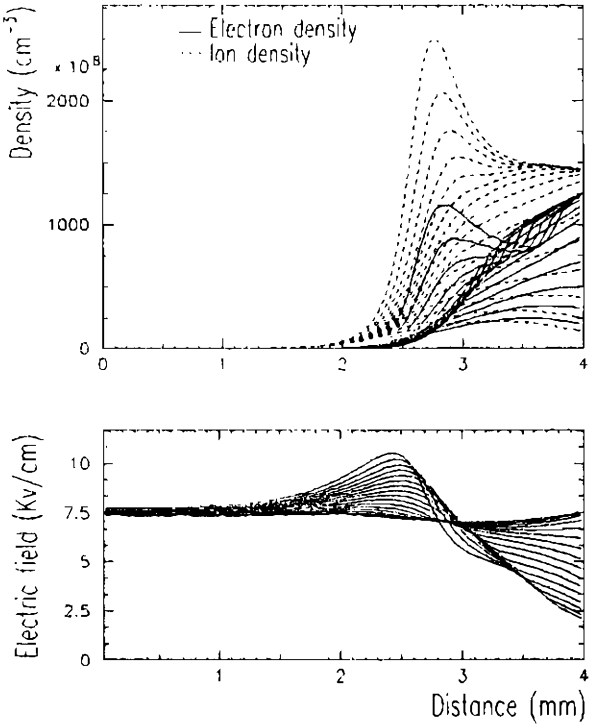

Figure 3 - Electronic and ionic densities and electric field in the transition region, from 76 to 106 ns in steps of 2 ns.

4.2. Transition Region

After being absorbed in the anode, the electrons cease to compensate the ionic charge existing in the gap, considerably increasing the field

distortions arising from ionic influence. The electric field is reduced over the anodic region and reinforced in the region upstream of the ionic distribution, creating there a high-gain region.

In this high-gain region there are some electrons (created by photoionization during the previous discharge stages†) that are strongly multiplied, leading to the growth of the ionic density in the high-gain region. This process becomes self-sustained when photoelectrons released upstream from the high-gain region by ionizing photons emitted from the high-gain region assure a steady current there.

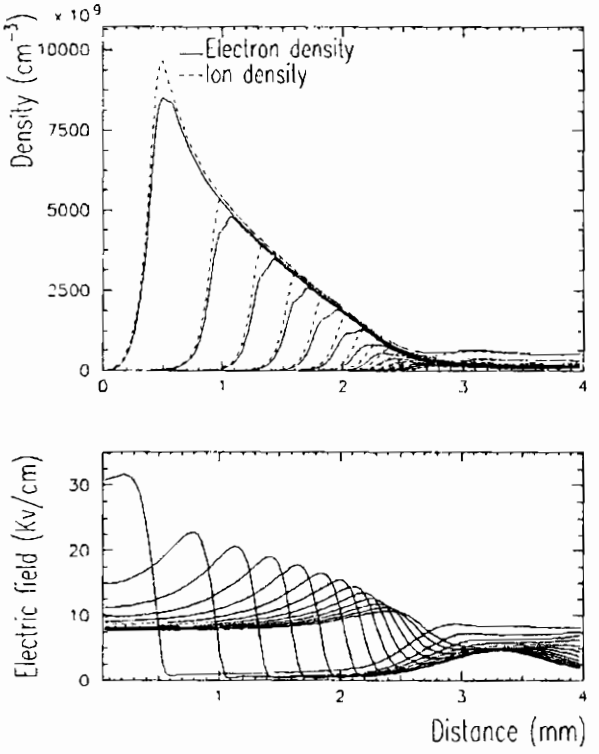

Figure 4 - Electronic and ionic densities and electric field, in the streamer progression region, from 106 to 130 ns in steps of 2 ns.

Although the field reduction in the anodic region may suppress almost completely all charge multiplication, the drift speed in this region remains almost unmodified because the residual field is larger than E_v

† The tail visible in this region is not part of the initial distribution. It is possible to observe in fig. 2, around 2.3 mm, an inflection in the electron density distribution, corresponding to the truncation made in the original quasi-gaussian distribution.

(Eq.(14)). The current reduction observed in the external circuit (see fig. 5) is mainly due to the disappearance of electrons from the amplifying gap, absorbed in the anode.

For avalanches having a charge density larger by a factor of about two, the field near the anode is almost zero, being some of the electrons prevented from penetrating the anode. Close to the anode there is then an immobile region containing similar densities of electrons and ions (about 2×10^{11} cm^{-3}) that in the absence of a streamer remains there indefinitely (in the framework of the model).

4.3. Propagation Region

From the positioning of the high-gain region (upstream from the ionic density peak) it results that the larger ionic yield occurs upstream from the peak, resulting in a displacement of the peak in the cathode direction (figure 4). This effect becomes more important as the local gain becomes larger, "accelerating" the high-gain region in the cathode direction and forming a streamer. This movement does not correspond to a real movement of particles, electrons or ions, but to the displacement of a mathematical point corresponding to the maximum of the density distribution, therefore not obeying the physical laws of movement of the particles in presence.

The ionization wave leaves in its trail a strongly ionized plasma, were the charges are distributed such as to neutralize the electric field.

4.4. External Current

Figure 5 represents the evolution of the external current. It is apparent the existence a "precursor" signal, reproducing the experimental observations [1, 2, 6, 14]. The time interval elapsed between precursor and streamer depends on the initial gain: if the avalanche reaches the anode with a high charge concentration the critical field required for streamer propagation will be reached sooner, reducing the formation interval. In limit cases, close to the breakdown threshold, a formation time up to hundreds of nanoseconds can occur; flowing during this interval a reduced current that eventually originates an accumulation of ions sufficient to initiate the streamer propagation.

The "precursor" signal results from the interaction between an avalanche close to the breakdown threshold and the anode. The same phenomena causing the current reduction between the "precursor" signal and the breakdown pulse (the absorption of electrons in anode) triggers the space-charge mechanism that creates the streamer. The variance of time interval elapsed between the "precursor" and the streamer impulse was also observed by Raether [2].

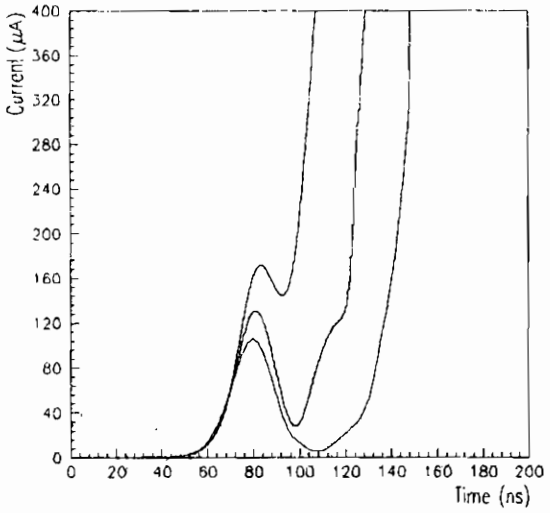

Figure 5 - External current evolution. The first curve corresponds to the same conditions (gain, etc.) represented in the previous figures. The remaining curves are calculated with nominal gain reduced by 25% and 50% respectively.

4.5. Breakdown Threshold

A clearly observed property of streamer breakdown is the independence of the breakdown threshold, around 10^8 electrons, from the nature of the mixtures studied. This property cannot, however, be directly verified by the model because it is not exactly known how the model parameters depend on the gaseous mixture composition.

The gas self-photoionization parameters, λ and M, are particularly difficult to estimate and a lengthy study of this subject was performed, although it cannot be presented here due to space limitations. In the present work we will study the behavior of the breakdown threshold as

a function of the gas composition and avalanche size, corresponding to the (reasonably known) parameters A, B, p, k, R_0 and σ_0, keeping λ and M constant.

A calculation of the breakdown threshold was executed for each set of parameters, scanning G_0 according to the sequence 10^4, 3×10^4, 10^5, 3×10^5... which spans almost equidistant intervals in logarithmic scale.

Generally, there is a value of G_0, G_{0P}, above which not all electrons are gathered in the anode, prevented by the reduction of electric field over the anode surface (due to the ionic attraction); in the framework of the model a stationary plasma is formed. In reality, this situation would be solved by the ion movement away from the anode, increasing the electric field there and restoring the electronic current. Above another value of G_0, G_{0D}, not always coincident with G_{0P}, the streamer is formed, with consequent breakdown. The breakdown threshold was defined as the number of electron-ion pairs created in the amplifying gap for $G_0=G_{0D}$.

The maximum possible value of G_0 is about 3×10^8 (G_{0M}): above this value the extreme field distortion verified during the avalanche advance leads to the formation of an anodic streamer, rendering impossible the continuation of the calculation.

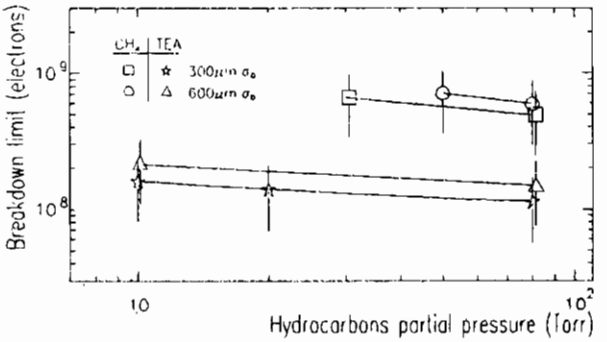

Figure 6 - Breakdown threshold as a function of the gas mixture (parameters A, B, k and p) and avalanche dimensions ($\sigma_0=R_0$), for $M=10^{-6}$ and $\lambda=500\ mm$. The initial charge (N_{e0}) is 100 electrons. Only some discrete values of G_0 were considered (as described above), originating an inaccuracy in the calculated breakdown threshold, represented by the error bars.

The experimental breakdown criteria used in the observations described in [1] does not correspond exactly to the criteria used in the

present calculation and some differences between the experimental and calculated values should be expected.

Figure 6 represents the breakdown threshold as a function of the gas composition (parameters A, B, k and p) and avalanche dimensions (R_0, σ_0), for $M=10^6$ and $\lambda=500\ \mu m$. The threshold occurs between 10^8 and 10^9 electron-ion pairs and is relatively independent of the hydrocarbons partial pressure. The threshold is higher for mixtures containing CH_4, in agreement with the experimental observations.

This effect can be interpreted by analysis of figure 1, where it can be observed that (in the model used) the first Townsend coefficient grows faster with the electric field for mixtures containing TEA than for mixtures containing CH_4. Mixtures containing CH_4 are less influenced by the space-charge field. Additionally, mixtures containing CH_4 require higher applied fields (E_0), so that for an identical percentile variation of total electric field larger charge densities are needed.

In each mixture, to the lower values of $\sigma_0=R_0$ corresponds slightly smaller breakdown thresholds. This effect has a double origin: more concentrated avalanches originate a stronger space-charge effect, that reduces the total charge generated during the avalanche progression and simultaneously increases the field distortion in the streamer formation region, allowing to start of the streamer with a smaller number of ions in the avalanche.

4.6. Precursor Saturation/Space Charge Effect

During the avalanche progression most electrons suffer the influence of an electric field reduced by the space-charge effect (see figure 2). Consequently there is a reduction of the effective gain, being the amount of charge generated smaller than $N_{e0}G_0$. This effect was confirmed experimentally by several authors [2, 13] for some hydrocarbons at low pressure. It does not exist, by the author's knowledge, any observations of this effect in PPCs at atmospheric pressure, but recent experimental results confirm the saturation of the precursor pulse in RPCs [14].

Figure 7 shows a calculation of the space-charge effect in the absence of photoionization. There is a reduction of the effective gain when the avalanche charge becomes larger than 10^7 electrons, approaching a saturation value around 10^9 electrons. The effect is larger for avalanches

of smaller dimensions, and it is larger for mixtures of argon and TEA than for mixtures of argon and CH_4. This result can be attributed to the different behavior of the first Townsend coefficient for each of these mixtures.

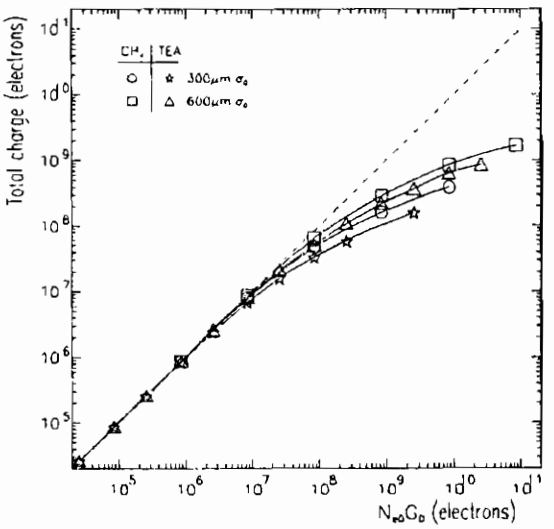

Figure 7 - Reduction of effective gain owing to space-charge effects in absence of photoionization. Mixtures of argon with CH_4 and TEA, at a partial pressure of hydrocarbons of 20 Torr were considered. The initial charge was 100 electrons and the effect was calculated for avalanches of dimensions (σ_0=R_0) of 300 and 600 μm.

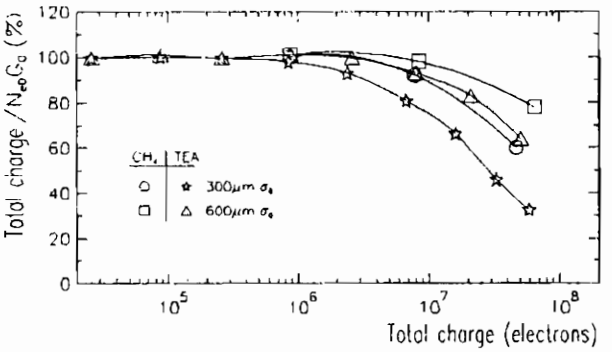

Figure 8 - Deviation from proportional behavior owing to space-charge effects, in absence of photoionization. Experimentally accessible region in PPCs.

It should be noticed that for a total avalanche charge of 10^8 electrons or higher some electrons will not enter the anode due to the electric field reduction over the anodic region.

Figure 8 represents the experimentally accessible region in PPCs. For a total avalanche charge around 10^7 electrons, corresponding to a stable detector operation, the deviation from proportional behavior is not larger than 30% in the worst case.

5. Conclusions

The model described in this work, being a "minimum model" of the streamer breakdown phenomenon in parallel geometry, has the following main characteristics: adopts a cylindrical geometry of fixed radius with the axis perpendicular to the electrodes; allows electronic and ionic density variations only in the axial direction; the electric field distortions are calculated over the cylinder axis; considers short distance gas self-photoionization as the only feedback mechanism; the photon production is proportional to the first Townsend coefficient.

In the present work we considered fixed values for the photon feedback parameters, that are very difficult to estimate. A detailed discussion of this subject, central to the "streamer model", will be presented elsewhere due to space limitations.

Within the framework of the model, streamer breakdown occurs when an ionization wave is formed, progressing in the cathode direction (cathodic streamer) and growing through a feedback mechanism originated by short distance gas photoionization in a region of increased electric field due to the presence of a high charge density. The streamer is formed when the charge in the avalanche is such that its space-charge field becomes comparable to the applied field.

The model also reproduces the anodic streamer observed in high gain conditions, like those found in pulsed discharges (see for example [2]). In the formation of the anodic streamer intervenes the field distortion existing in the frontal region of the avalanche.

The occurrence of a "precursor" signal, observed experimentally by many authors in PPCs ([1, 2] for instance) and RPCs ([6, 14] for instance), is correctly reproduced by the model (figure 5), resulting from the interaction between an avalanche close to the breakdown threshold

and the anode. The time interval elapsed between the "precursor" and the streamer decreases when the applied tension increases, as observed [2, 15].

The model predicts, in agreement with the observations [1, 2], a breakdown threshold between 10^8 and 10^9 electron-ion pairs for a large set of parameters, presumably corresponding to a broad range of gaseous mixtures. The model also predicts correctly a breakdown threshold higher for argon and CH_4 mixtures than for the argon and TEA mixtures. This effect seems to depend on the behavior of the first Townsend coefficient.

It is also qualitatively reproduced the precursor saturation effect found in RPCs [15]. This effect is due to an effective reduction of the electric field over the avalanche volume due to the avalanche's own space-charge.

6. References

[1] P. Fonte et. al., *Nucl. Instrum. and Methods* **A305** (1991) 91.

[2] H.Raether, *Electron Avalanches and Breakdown in Gases* (Butterworths, London, 1964).

[3] L.B. Loeb, *Phys. Rev.* **94** (1954) 227.

[4] J.M. Meek, *Phys. Rev.*, **57** (1940) 722.

[5] E.D. Lozanskii, *Sov. Phys. Usp.* **18** (1975) 893.

[6] D.F. Anderson et. al., *Nucl. Instrum. and Methods* **A348** (1994) 324.

[7] L.E. Kline, *J. Appl. Phys.* **45** (1974) 2046.

[8] A.J. Davies et. al., *Proc. IEE* **124-2** (1964) 179.

[9] P. Fonte et. al., *Nucl. Instrum. and Methods* **A310** (1991) 140.

[10] L.S. Zhang, *Nucl. Instrum. and Methods* **A247** (1985) 343.

[11] A.J. Davies et. al., *Proc. IEE*, **A281** (1964) 164.

[12] A. Peisert and F. Sauli, *Drift and Diffusion of Electrons in Gases - a Compilation* **CERN 84-08** (1984).

[13] J. Sernicki, *Nucl. Instrum. and Methods*, **212**, 195, 1983.

[14] Makeev et. al., this proceedings.

NEW DEVELOPMENTS OF RPC: SECONDARY ELECTRON EMISSION AND MICROSTRIP READOUT

E. Cerron Zeballos[1,4], I. Crotty[1], P. Fonte[2,3], D. Hatzifotiadou[1,4], J. Lamas Valverde[1,4], V. Peskov[2,*], M.C.S. Williams[1], A. Zichichi[5]

[1] *CERN, Geneva, Switzerland*
[2] *LIP, University of Coimbra, Portugal*
[3] *ISEC, Instituto Superior de Engenharia de Coimbra, Portugal*
[4] *World Laboratory, Lausanne, Switzerland*
[5] *INFN and University of Bologna, Italy*
* *present address: Marshall Space Center, Alabama, USA*

ABSTRACT

In this paper we discuss possibilities of broadening the potential capabilities of RPCs. One is the use of secondary electron emitting materials (CsI, diethylferrocenil-mercury) on the cathode; this enhances the efficiency, thus allowing the use of light, non-flammable gases as well as improvement in time resolution. The other is the use of very narrow strips for the readout, where a position resolution of 70 microns was achieved.

1. Introduction

In the last few years resistive plate chambers have been the subject of a great interest since they were considered and later chosen for the muon trigger for both LHC detectors (CMS and Atlas Technical proposals). The main advantages of RPCs are : high gain, good time resolution, simple design and low cost. Of course they are not free from disadvantages. They have low rate capability (several Hz/cm^2 in spark mode)[1,2]; they operate with complicated or flammable gas mixtures; the position resolution in existing devices is poor (around several cm^2).

The main effort of different groups in the last years has focused on improving the rate capability of RPCs and considerable progress has been achieved in this direction [3,4,5].

In the present work we have tried to develop other potential capabilities of RPCs, namely: (a) to enlarge the variety of gases which can be used, including non flammable gases; (b) to get better position resolution.

As a possible approach to solve these problems we have tested the use of secondary electron emitters for the former and microstrip readout for the latter.

2. Secondary electron emission

Charged particles passing through the electrode of a RPC create secondary electrons inside. These electrons have energy of the order ~10 eV and those which are close to the surface can escape through the boundary into the gas, as shown in figure 1a. The escape mechanism for these electrons is similar to the emission of photoelectrons in the photoelectric effect; this is the reason that good photocathodes are also usually good secondary electron emitters. Therefore, to enhance the effect of secondary electron emission, the RPC electrode should be covered by a layer of photoemissive material. It is known that some of

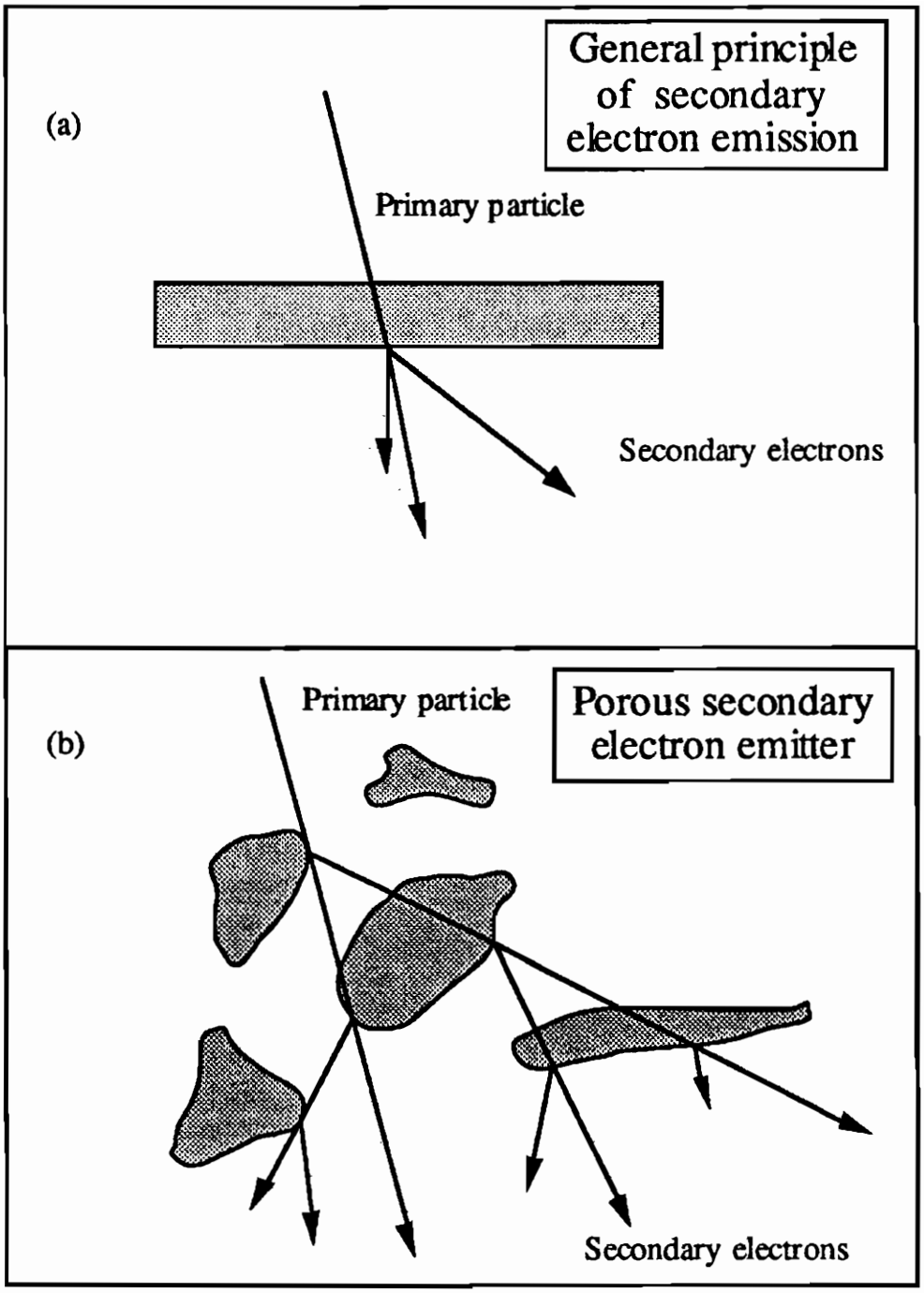

Fig. 1. (a) General principle of secondary electron emission. (b) Schematic representation of enhancement of secondary electron emission with porous surface.

the best secondary electron emitters are alkali-halides, such as CsI, KCl and others.

The other important issue is the structure of the secondary electron emitters. Porous structures, for example, allow a much better yield, because there are many independent surfaces from which the secondary electrons can escape. At very high voltages these electrons may even create more secondary electrons, so multiplication is possible, as shown in figure 1b (see for example [6]).

RPCs with CsI secondary electron emitters are described in ref. [3]. Beta particles passing the RPC create additional 1-2 electrons from the CsI. Since in a parallel-plate geometry the gas gain depends exponentially on the distance of the primary electrons from the anode, the electrons emitted from the cathode obtain a maximum gain. For this reason they have a large contribution to the RPC efficiency and time resolution. As a consequence of this one can use a wider variety of gases; also in some cases this allows an enhanced time resolution [3]. Another important advantage is almost zero parallax.

Since this appears a very promissing approach, we have tried to reproduce the results of [3] and extend our study to other secondary electron emitters. The goal is to find other materials, having a better yield or requiring simpler technology.

2.1 The set up

In order to compare correctly our results with those in [3] we used a similar set up with the anode made from Pestov glass, as shown in figure 2. We used two samples of Pestov glass, one with resistivity 10^{12} Ω cm, the other with resistivity 10^{10} Ω cm. The aluminium cathode was covered by a ~10 μm thick CsI layer evaporated in Argon atmosphere at a pressure of a few Torr. The CsI layer manufactured in such a way had a porous structure. After the installation in the test chamber the aluminium electrode with the CsI layer was heated at 70°C in vacuum for a few hours. This heating is very important to get high yield.

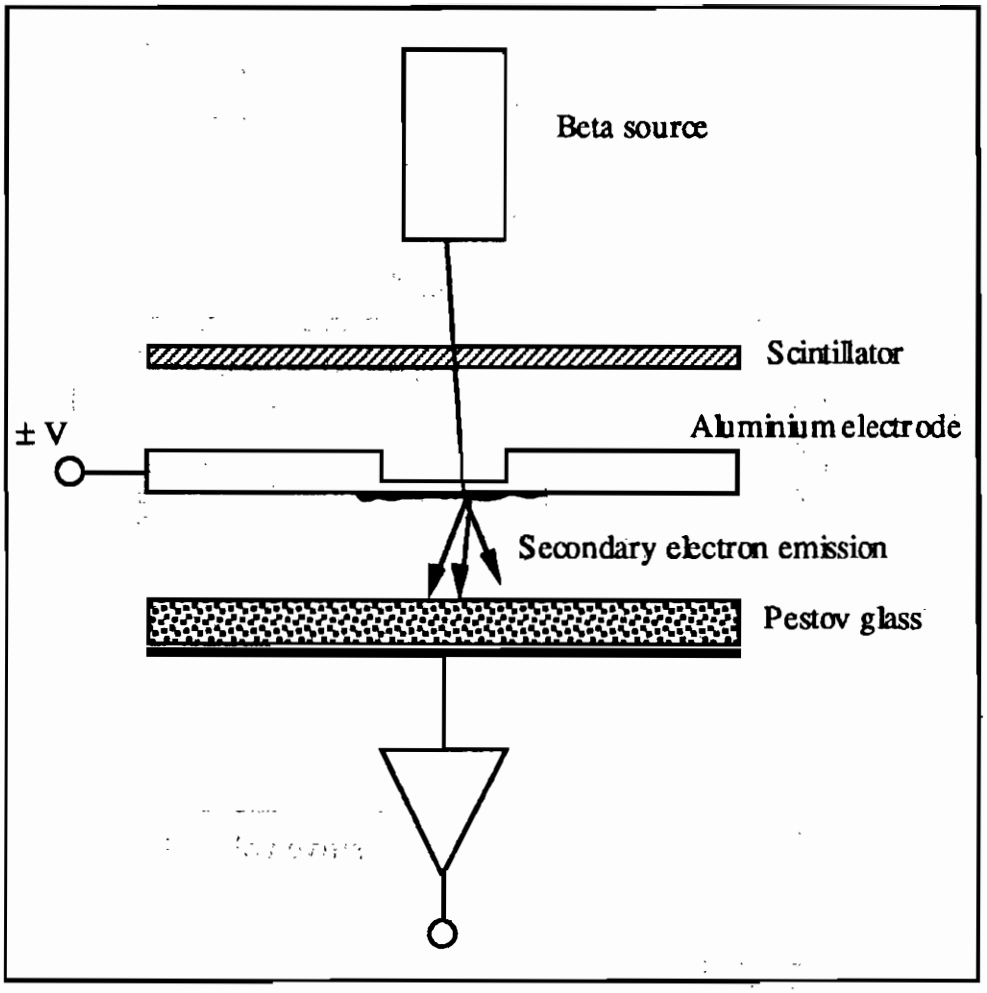

Fig.2. The experimental set up used to measure secondary electron emission.

We also tried other emitters, known to be good photocathodes: TEA and TMAE liquid layers and some metallorganic compounds. In the case of liquid layer the cathode was cooled as described in [7]. Metallorganic layers were obtained as described in [8]. All metallorganic layers were sligthly heated after the installation.

As in [3], we compare pulse-height distributions for two polarities. Without secondary electron emitters they were similar, with they were completely different, as shown below, figures 3 and 4. As in [3] our set-up had a small window allowing to irradiate the electrodes

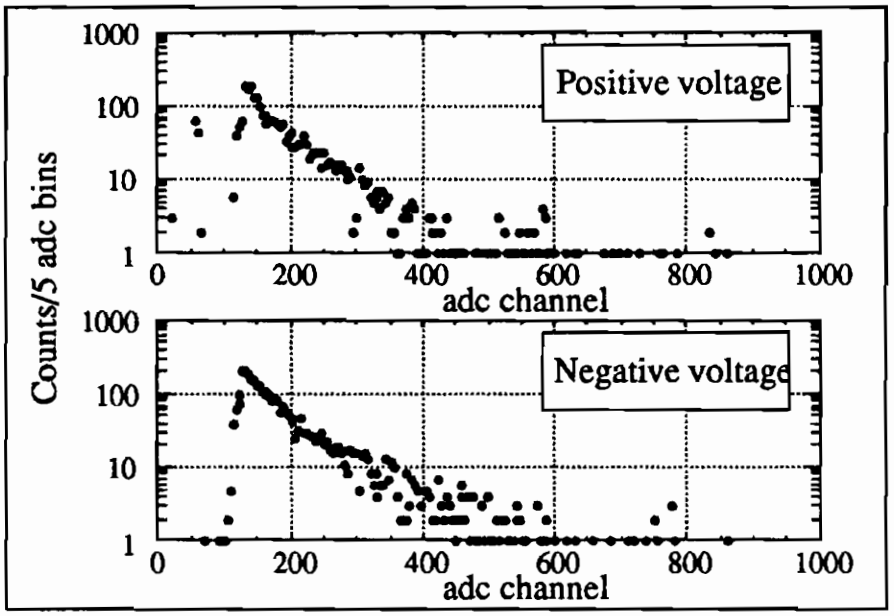

Fig. 3. Pulse height distributions for positive and negative applied voltage to the aluminium electrode when not coated with secondary electron emitter. Pressure was 9.82 Torr isobutane.

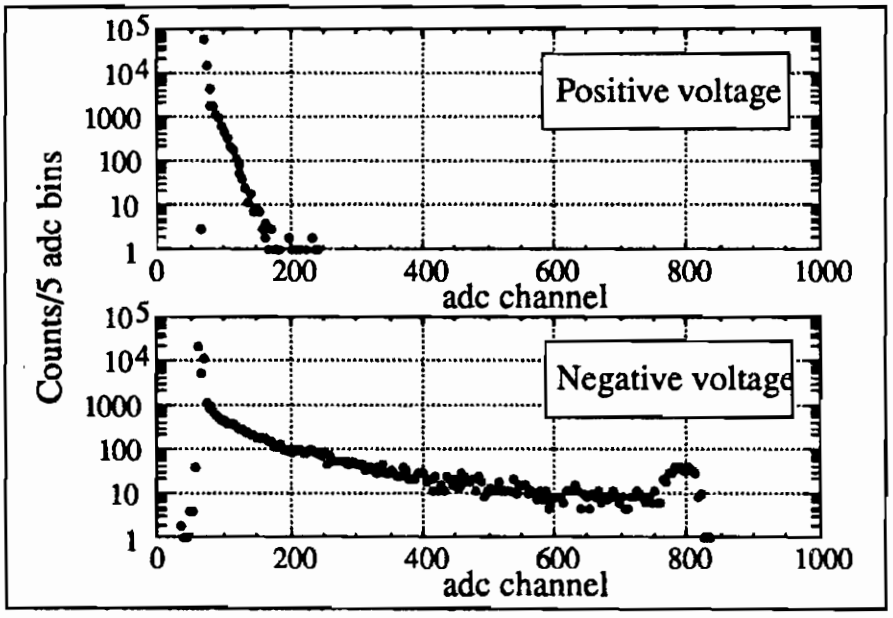

Fig. 4. Pulse height distributions for positive and negative applied voltage to the aluminium electrode when coated with CsI secondary electron emitter. Pressure was 21.5 Torr isobutane.

with UV light from a mercury lamp. This light causes a surface photoelectric effect from the electrodes. This allows us to measure the pulse-height spectrum for single electrons and compare it to the pulse-height spectra obtained with secondary electrons.

2.2 Results for CsI secondary electron emitters

The most pronounced results were obtained at low pressure or with He mixtures containing a low concentration of quencher, for example He+10% ethane. As an illustration, in figures 3 and 4 are presented pulse-height spectra obtained at low pressure. When the Al electrode (see fig. 2) was not covered by a CsI emitter, the pulse-height spectra were identical for positive or negative polarities of the high voltage applied to this electrode - figure 3. When the Al electrode was covered by a CsI emitter, a dramatic difference appeared in the pulse-height spectra, recorded at different polarities (see figure 4). This proves appearance of the secondary electrons from the CsI emitter. The shape of the pulse-height spectra depended on pressure, value of applied voltage and counting rate. Depending on the conditions we estimated that between 1 and 3 secondary electrons were emitted by the CsI layer. This number of electrons was estimated by comparing the mean of the given pulse-height spectrum with the mean of a single electron spectrum. Similar results were obtained in ref. [3]. So the results of ref. [3] were reproduced. The efficiency of detecting β particles from Sr^{90} was measured by comparing the counting rate from the scintillator and from the parallel plate chamber. For our CsI emitters the efficiency of detection of β particles was between 80 and 90% depending on the applied voltage. This efficiency was practically independent of the Pestov glass resistivity up to counting rates of 3-5 x 10^4 particles/cm^2.

In Ar mixtures the pulse-height spectra were almost identical for both polarities (i.e. no observable secondary electron emission). A small difference was observed only in the far tail of the distribution.

We have also studied the feedback and maximum achievable gain with CsI emitters. The results obtained were in good agreement with [9] and demonstrated that a high gas gain can be achieved in many mixtures even when the quencher concentration was low (~10%).

We have also tested a resistive plate chamber with melamine plates (as described by Williams in this workshop [10]) with CsI secondary electron emitter layer on the cathode. However the secondary electron yield obtained was very low. We attribute this low yield to the contamination of the CsI by organic vapours from the glue used in the construction of this chamber.

2.3 Search for other emitters

As mentioned above, the key in the search for good secondary electron emitters is testing good photocathode materials. We have tried a few materials known to be good photocathodes: TMAE, TMP, GaAs, cesiated porous TiO_2 and some metallorganic compounds. The best results were obtained with di(ethylferrocenil)mercury [8]. It has a crystalline structure as shown in figure 5; the surface comprises of many small elongated crystals. Such structure is very favourable for obtaining high secondary electron yield, because each secondary electron has high probability to escape. Indeed, this emitter gives an impressive secondary electron yield, 5-6 electrons per particle at low pressure. However, at high rate ($>10^4$ Hz/cm^2) some drop of the yield with time was observed, as shown in figure 6. When the source was removed for one hour, the yield returned to its initial value, but dropped again with the same time scale when the source was put back. We attribute this loss of efficiency to the charging up effect. The fastest way to recover the emitter was to change the high voltage polarity. In this case the full recovery occurs in 15 minutes.

We also tested this emitter in Helium - ethane mixtures at total pressure 1 atm. With the increase of ethane concentration above 15% the visible difference between the pulse-height spectra measured at two

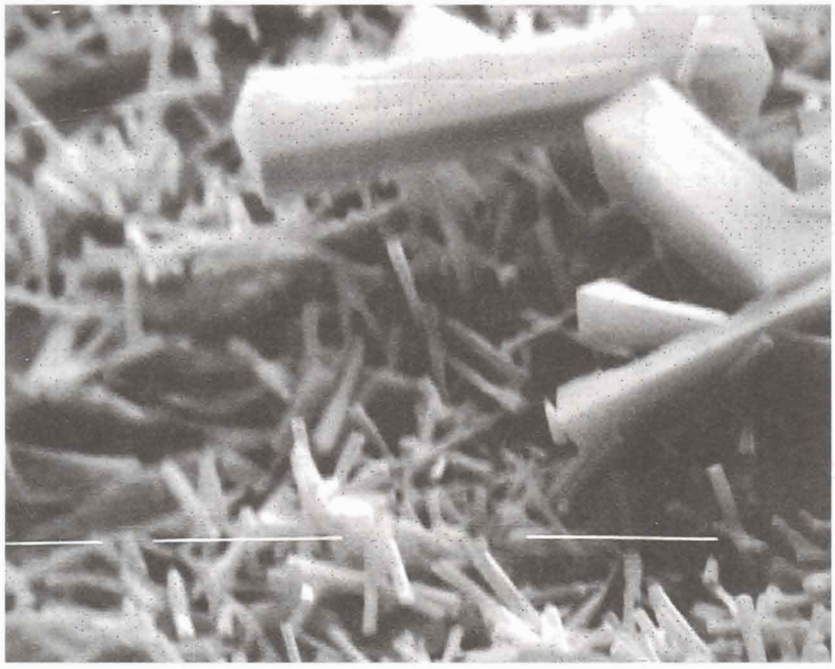

Fig. 5 Photograph of surface of di(ethylferrocenil)mercury with 2500 magnification. The – lines are 10 μm in lenght.

different polarities becomes less and less, and above 20% ethane remains only a difference in the far tail of the distribution.

In He mixtures charging up effect manifested itself at rather low rate, $\geq 10^3$ Hz/cm^2. In the case of di(ethylferrocenil)mercury we were not able to control well the thickness and uniformity of the layer - see figure 5. We do not know, therefore, if the charging up effect is related to the thickness and the quality of the layer.

2.4 Conclusion sfrom the secondary electron emitters study

At least two secondary electron emitters can be used in resistive plate chambers: CsI and di(ethylferrocenil)mercury. The latter gave twice better yield, but the charging up effect was observed at high

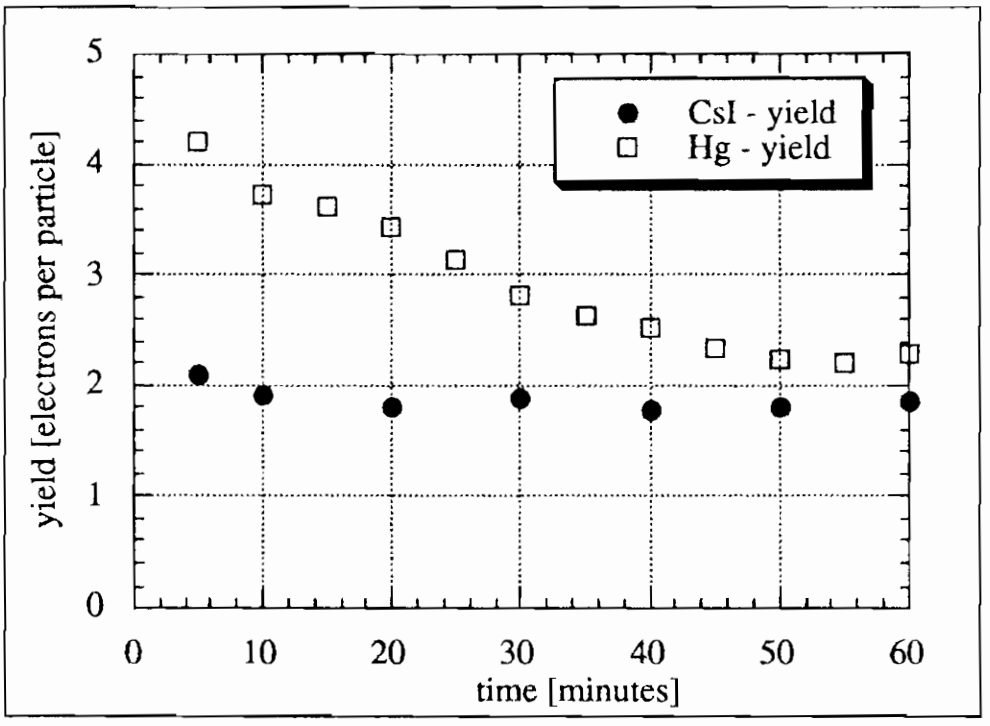

Fig. 6. Yield of secondary electrons with time at high rate (>10^4 particles/cm^2).

pressure (1 atm) and rate ≥10^3 Hz/cm^2. At low pressure (a few tens of Torr) the charging up effect appears at a few times higher rate. Probably at low pressure a surface charge can leak more easily to the uncharged area of the electrode.

It was observed before (for example see [11]) that the charging up of the secondary electron emitters depends on the preparation technique, which affects their composition and structure. For the same secondary electron emitter some have observed charging up, while others have not. It therefore seems that the charging up of these materials depends on the details of the surface structure.

We believe that after some further development and study, ways to fully exploit the high yield of di(ethylferrocenil) mercury will be found. We should not forget, as was demonstrated in [3], that secondary electron emitters allow an improvement of the time resolution of the RPC from a few ns to 1 ns. Secondary electron emitters may

also allow us to reach reasonably high efficiency with many gas mixtures, including non-flammable ones. However, in He mixtures with a high concentration of ethane or in Ar mixtures it is difficult to observe any secondary electron emission.

3. Microstrip readout

In our effort to explore the space resolution of the RPC we constructed an 8 mm gap chamber with read out strips of 280 μm on a 380 μm pitch. The chamber was equipped with 14 of these very thin strips, covering 5.3 mm in one dimension (plus two very broad ones, to cover the rest of the chamber). The resistive plates were made of melamine sheets; their thickness was 0.9 mm. One plate was equipped with pick up strips of the dimensions described; these form the anode. The other plate has a single pad electrode, the cathode, attached via a 1 MΩ resistor to the high voltage power supply. In what follows we present results from (a) measurements in a pion beam and (b) a detailed study in the laboratory with soft X-rays.

3.1 Position resolution with beam

The "microstrip" RPC was tested at the CERN PS East Hall, at the T9 test beam. The beam (8 GeV/c negative particles, mainly pions) was defocused by inverting the polarity of the last quadrapole; thus the whole active area of the chamber was illuminated. One of the trigger scintillators (4x4x0.2 cm^3) was rotated, so that the 2 mm side was covering 5 strips.

The cluster size measured with the "microstrip" RPC is shown in figure 7a. The average cluster size is 2.2 strips, namely ~900 μm. Figure 7b shows the centre of cluster, determined by the following algorithm: if the cluster has one strip, its centre is the strip hit; if two neighbouring strips are hit, its centre is between the two; if it has three strips, it is the middle one, etc. The horizontal axis has bins of 1/2 strip (190 μm). The width of the distribution is ~10 bins, namely 5 strips,

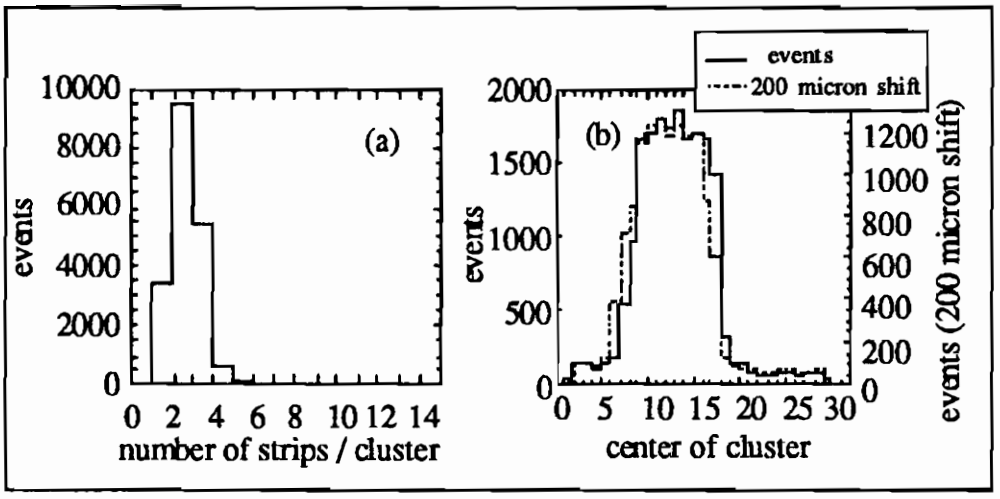

Fig. 7. (a) Cluster size distribution for the "microstrip" RPC; (b) Centre of cluster distribution for the "microstrip" RPC; the dashed line corresponds to relative displacement of the RPC by 200 microns.

as expected from the scintillator width. We moved the chamber by 200 μm and, as shown by the dashed line in figure 7b, the distribution shifted by 1 bin. From the fact that we can see a displacement of 200 μm we conclude that the space resolution is $\sigma \approx 70$ μm (using only digital readout for the strips).

Another interesting feature of the "microstrip" RPC is that, because the electrostatic coupling is enhanced in the case of narrow strips [12], we see a signal above the discriminator threshold for less charge generated in the chamber. The mean value in the charge spectrum was ~0.2 pC.

3.2 Position resolution with soft X-rays

3.2.a Experimental setup

The experimental setup is shown schematically in figure 8. The chamber is illuminated with X-rays from a generator. The voltage applied to the generator was 7.5 kV, but the emitted X-rays were mostly from a fluorescence line of iron at 5.5 keV. The focal spot has

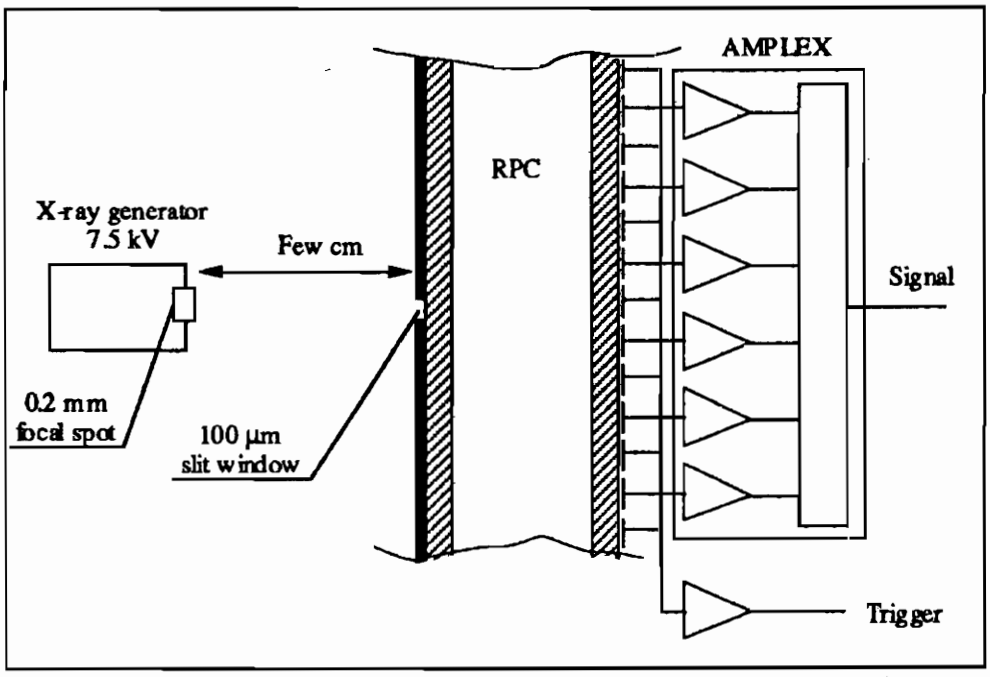

Fig. 8. Set up of experiment to test position resolution with X-ray generator.

a diameter of only 0.2 mm, allowing the beam to be collimated by using simply a slit placed a few cm away. The beam divergence in these conditions is less than 1 %. The collimating slit was cut out of a copper plate 0.8 mm thick, having a width of 100 μm, 1 cm height (in the direction perpendicular to the readout strips) and an area of 1 mm^2. The gas volume was about 2 mm away from the slit, so the increase in beam width from divergence was not larger than 20 μm in the sensitive region near the cathode.

Due to the small slit area and to a local rate limitation of 1 kHz/cm^2, the maximum counting rate from the X-ray beam was only 10 Hz. Under these conditions it was not possible to obtain an efficient trigger from the cathode electrode because the noise rate from the large sensitive area (20×20 cm^2) was much higher. It was also not possible to obtain the trigger from the readout strips because the charge-sensitive electronics used for readout were based on an analogue multiplexer (AMPLEX) and there was no direct access to the individual strip

signals. In order to obtain a reliable trigger we connected only the even-numbered strips (7 out of 14) to the AMPLEX chip and connected the odd-numbered strips together to a fast current amplifier that provided a clean trigger signal.

3.2.b Induced charges profile

Since the profile was sampled every 760 μm, most avalanches gave signals in only 2 strips. If we consider as a guidance the results known for MWPCs [13], then the optimal sampling pitch would be the profile FWHM/1.5 = 0.61 mm.

The profile of the charges induced on the anode side of a RPC is quite narrow (see [14] for a theoretical calculation) when compared to the values observed in MWPCs. In fact we measured a profile FWHM of 0.92 mm, as shown in Figure 9, while in MWPCs the corresponding profile is a few mm wide. The reason for the narrow distribution is that due to the exponential avalanche growth most of the electrons are created very close to the anode.

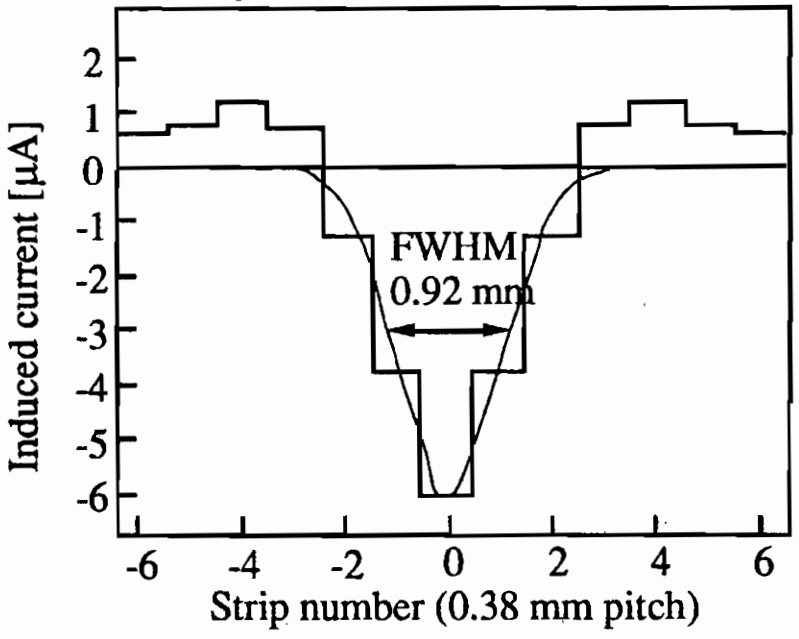

Fig. 9. Profile of induced current using the X-ray generator.

It is well known that by using the centre of gravity method a position resolution of a few percent of the profile width can be routinely achieved, so in the present case one would expect a position resolution of a few tens of μm.

We also measured the contribution of electronic noise (amplifier, pick-up, etc.) to the final result by injecting an electronically generated signal into the flat cable connecting the chamber to the AMPLEX chip (capacitive coupling). Signals were injected at two different locations and with two slightly different pulse heights. The results can be seen in figure 10: the noise contribution to the position spread was 22 μm FWHM.

For avalanches the signal charge was a few hundred fC/strip, corresponding to a gas gain of a few times 10^5.

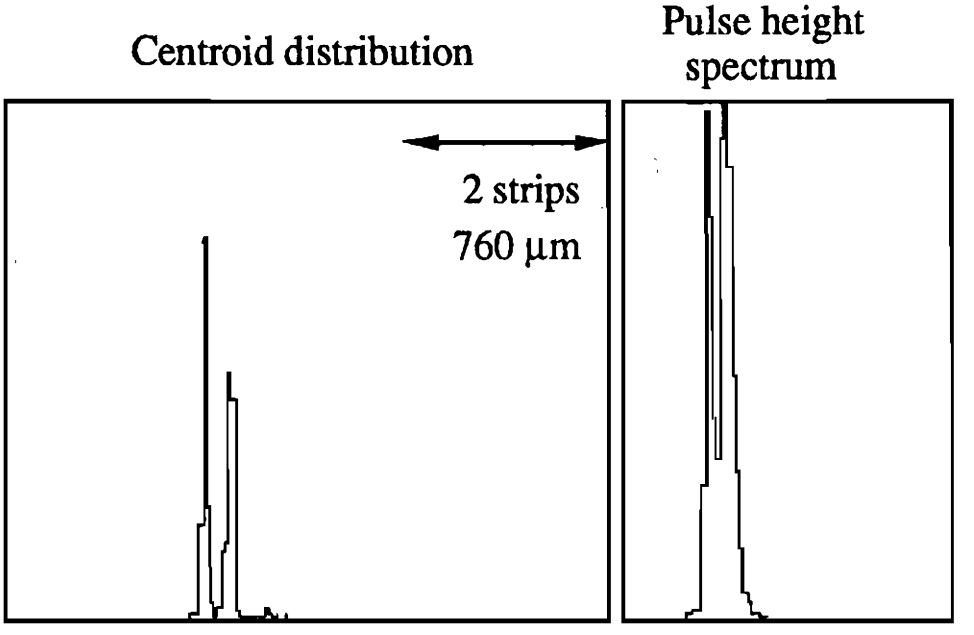

Fig. 10. Centroid distribution and pulse height spectrum when test signals are injected into the electronics.

3.2.c Results

We measure the width of the centroids distribution (figure 11) to be 115 mm. However this width has contributions from the following: the collimator width (100 μm), the beam divergence (20 μm) and electronics noise (22 μm). We subtract these contributions in quadrature and calculate that the chamber and primary electron cloud contribution is 48 μm FWHM. Similar results were obtained by others [15] for PPC.

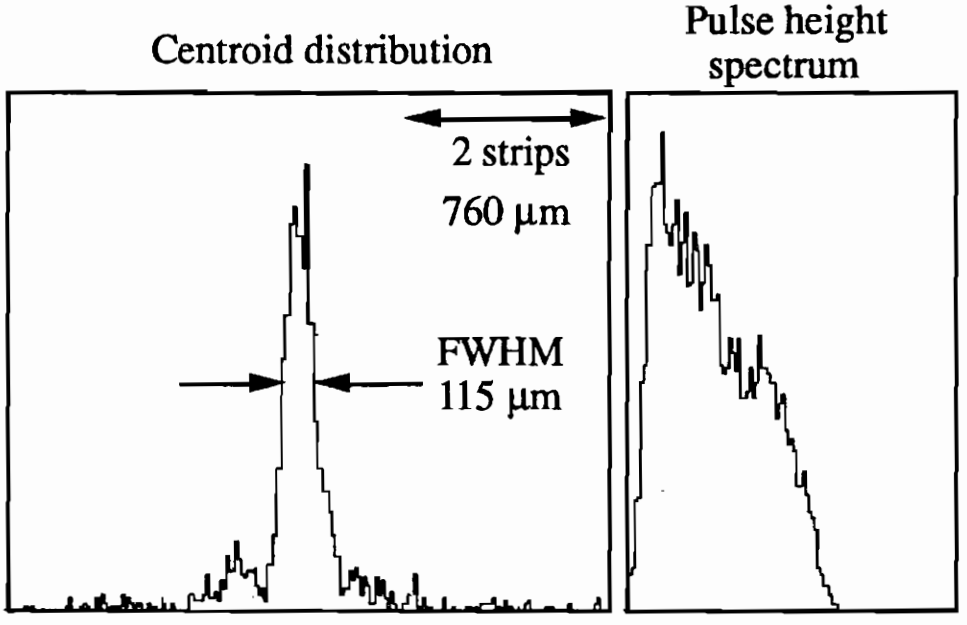

Fig. 11. Measured centroid and pulse height distribution when RPC exposed to X-ray generator.

4. Conclusions

Resistive plate chambers with a layer of secondary electron emitter on the cathode are very promising, since they allow operation with many (including non flammable) gas mixtures. In addition, RPCs with secondary electron emitters have better time resolution. Helium

mixtures or low pressure could be attractive for some applications, for example for tracking (parallax free).

RPCs with "microstrip" readout give good position resolution, allowing them to replace wire chambers in some applications. Their advantages are: they are simpler to construct, cheaper, more robust, less sensitive to magnetic field and they require less stringent mechanical tolerances.

References

1. I. Crotty et al., Nucl. Instr. and Meth. A 337 (1994) 370.
2. M. Iori and F. Massa, Nucl. Instr. and Meth. A 306 (1991) 159.
3. D. F. Anderson et al., Nucl. Instr. and Meth. A 348 (1994) 324.
4. I. Crotty et al., Nucl. Instr. and Meth. A 360 (1995) 512.
5. C. Bacci et al., Nucl. Instr. and Meth. A 352 (1995) 552.
6. V. G. Gavalian et al., Nucl. Instr. and Meth. A 350 (1994) 244.
7. V. Peskov et al., Nucl. Instr. and Meth. A 269 (1988) 149.
8. D. C. Imrie et al., Nucl. Instr. and Meth. A 317 (1992) 92.
9. G. Charpak et al., Nucl. Instr.and Meth. A 307 (1991) 63.
10. E. Cerron-Zeballos et al., "What have we learned from a comparison between the wide gap and narrow gap RPC", these proceedings.
11. C. Chianelli et al., Nucl. Instr. and Meth. A 273 (1988) 245.
12. V. Radeka, Ann. Rev. Nucl. Part. Sci. 38 (1988) 217.
13. F. Piuz, R. Rosen, J. Timmermans, Nucl. Instr. and Meth. 196 (1982) 451.
14. Mathieson et al., Nucl. Instr. and Meth. A 273 (1988) 518.
15. A. Peisert and F. Sauli, Nucl. Instr. and Meth. A 247 (1986) 453.

THE RPC SYSTEM FOR THE CMS EXPERIMENT AT LHC

G. WROCHNA *
CERN PPE, CH-1211 Geneve 23, Switzerland

December 14, 1995

ABSTRACT

The CMS experiment designed for Large Hadron Collider is briefly described. An idea of a muon trigger based on RPC is presented. This talk focuses on the requirements on RPC as the trigger detectors for the CMS. We discuss the required chamber's parformance and segmentation. Current design of the system fulfilling these requirements is presented. Its expected trigger performances are given.

*for the CMS Collaboration

1. CMS Detector

The abbreviation "CMS" stands for Compact Muon Solenoid [1]. It is a general purpose particle detector to be operated at Large Hadron Collider at CERN in Geneva. Its main parts are an inner tracker, calorimeters and a muon system (Fig. 1). The inner tracker consists

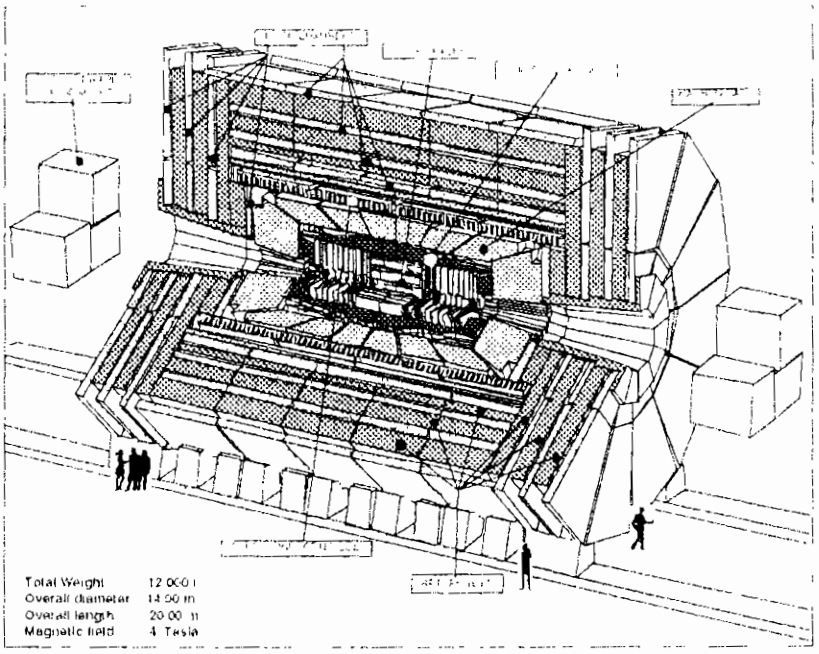

Fig. 1. Layout of the CMS detector.

of silicon pixel, silicon microstrips detectors and microstrip gas chambers (MSGC). The electromagnetic calorimeter is a matrix of $PbWO_4$ crystals. The hadronic calorimeter is a copper/scintillator sandwich up to $|\eta| = 3$. At higher $|\eta|$ it is completed with a very forward calorimeter made of iron with quartz fibers as sensitive elements. The characteristic feature of the CMS detector is that the inner tracker and both calorimeters are contained within the large superconductive solenoid, 6 m in diameter and 13 m long. The coil creates 4 T magnetic field. Outside the coil the magnetic flux is returned by an iron yoke. The yoke is interleaved with 4 muon stations. Each barrel muon station consists of drift tubes (DT) and RPC's. Endcap muon stations are equipped with cathode strip chambers (CSC) and RPC's as well.

2. CMS Muon Trigger

At the highest LHC luminosities about 20-30 pp interaction occure every 25 ns. Basic goal of the CMS first level muon trigger is to reduce this rate (1 GHz) down to a level acceptable for the second level trigger. CMS have chosen a solution where the second and the third level trigger algorithms are performed by a farm of commercial processors. The farm is designed to accept 100 kHz input rate. The output rate of the first level is, however, assumed to be only ~20–30 kHz, leaving a large safety margin. After distributing this bandwidth among various calorimeter and muon triggers, about 6 kHz is left for a first level single muon trigger. In order to achieve this huge rejection factor (1 GHz $\rightarrow$ 6 kHz) it is not enough to recognize a muon. The trigger system should measure the muon momentum quite precisely in order to enable relatively sharp p_t cut.

Another severe requirement is a bunch crossing identification. The recognised muon must be assigned to a given bunch crossing with accuracy better than 25 ns. This must include all possible jitters and time missalignments due to time of flight, detector response, signal propagation, clock distribution, etc.

The task of the muon trigger is especially difficult because of the presence of many kind of backgrounds. Punchthrough from hadronic showers, secondaries radiated by muons, backsplashes from very forward calorimeter and beam collimators, a beam halo and hits due to thermal neutrons may sum up to as much as 1 kHz/cm^2. Therefore the trigger system must be very robust.

In order to fullfill these requirements CMS has chosen to follow experiments running currently on hadronic beams (CDF, D0, H1, and Zeus) and use both precise moun chambers and fast dedicated detectors for the triggering purposes. Drift tubes in the barrel and cathode strip chambers in the endcaps provide track segments in each muon station with spacial and angular precision of 1–2 mm and 10–60 mrad respectively. However, having a long drift time (~160 ns for DT and ~40 ns for CSC), they require rather complicated electronics to make correct bunch crossing assignment. Another drawback of CSC's and DT's is that the two spatial coordinates are given by long strips or wires. This may cause ambiguities in case of several tracks going throught a given

chamber.

These drawbacks should be compensated by superior features of dedicated trigger detectors. They must be characterised by the excellent timing ($\sigma \sim 2$ ns) and high granularity. Current experiments, listed above, use scintillating counters for this purpose. The segmentation required at LHC (see the next section) makes this solution unpracticable because of technical and financial reasons. Therefore both LHC experiments ATLAS and CMS envisage RPC's in this place.

3. RPC Trigger Idea

The idea of the RPC based trigger for CMS is illustrated in Fig. 2. The solenoidal field bends tracks in the $r\phi$ plane. A pattern of hits recorded by RPC's carry the information about the bending, and can be used to determine p_t of the track. This is done by comparison with a predefined set of patterns corresponding to various p_t. Therefore we call this device Pattern Comparator Trigger (PACT) [4]. In this conference it is described in detail in a paper by A. Ranieri [2].

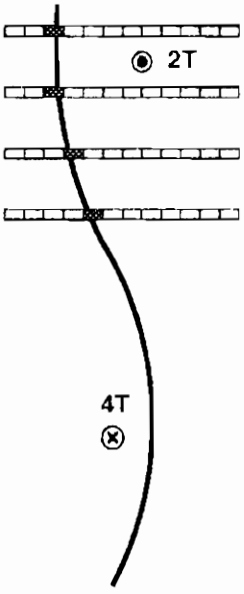

Fig. 2. RPC trigger principle.

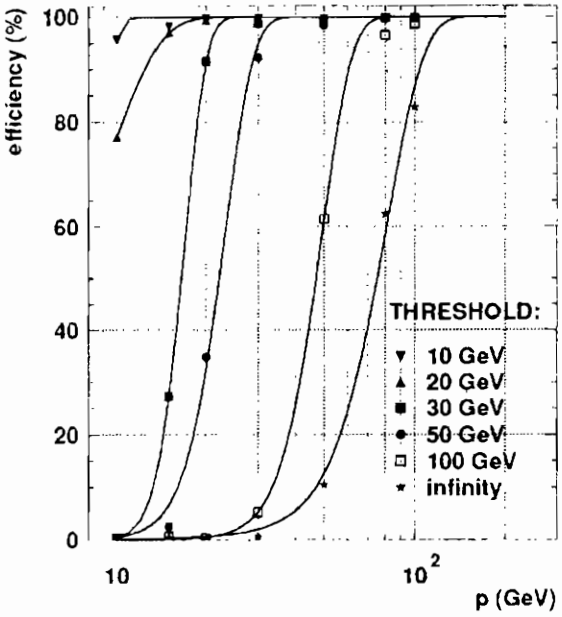

Fig. 3. Results of PACT test in RD5.

This idea has been practically tested in the RD5 experiment [3] especially designed to study various aspects of muon measurement and triggering at LHC detectors. Four RPC planes placed in the magnetic field simulating the CMS configuration (Fig. 4) have been connected to the PACT prototype build with programmable gate arrays ALTERA. Obtained efficiency curves are shown in Fig. 3. Details can be found in Ref. [4].

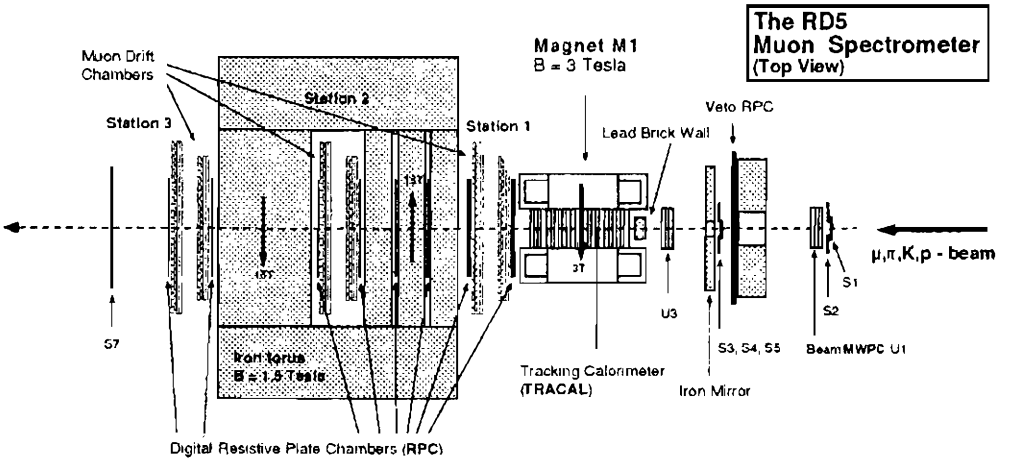

Fig. 4. RPC trigger principle and its test in RD5.

4. Required Detector Granularity

Since the precision in ϕ determines momentum resolution, RPC are equipped with strips running parallel to the beam (along z) in the barrel and radially in the endcaps. The crucial point in the design of the RPC system is the choice of detector granularity. Possible factors to be considered are listed in Tab. 1. Dominant upper and lower limits are marked with $\Downarrow$ and $\Uparrow$ respectively.

Let us discuss the dominant factors one by one.

4.1. Track Bending and Strip Width

In order to maintain the single muon trigger rate at the level of a few kHz for luminosity of $10^{34}\text{cm}^{-2}\text{s}^{-1}$ one should apply $p_t^{cut} \approx$ 20-30 GeV (see Sec. 7). Having in mind necessary safety margin one can require

Table 1. Determination of the RPC granularity

Strip width ($\Delta\phi$)	
track bending (required momentum resolution)	⇓
multiple scattering and energy losses	
cluster size	
Strip length ($\Delta\eta$)	
signal propagation time along the strip (bunch cross. assign.)	⇓ *barrel*
change of the bending with η	⇓ *endcaps*
change of η due to the non-$r\phi$ bending	
Strip area (number of strips)	
number of channels (cost)	
complexity of the trigger processor (feasibility)	⇑
number of interconnections (feasibility)	⇑
capacitance	
occupancy	
probability of random coincidences of background hits	⇓ *endcaps*
mechanics of the chamber	

that the highest possible p_t^{cut} should be somewhere between 50 and 100 GeV. It has been found that this is possible with with strips $\Delta\phi \approx 1/3°$ which corresponds roughly to 2-3 cm in the inner muon stations (MB1 and MB2) of the barrel. This can be seen from the formulas collected in Fig. 5.

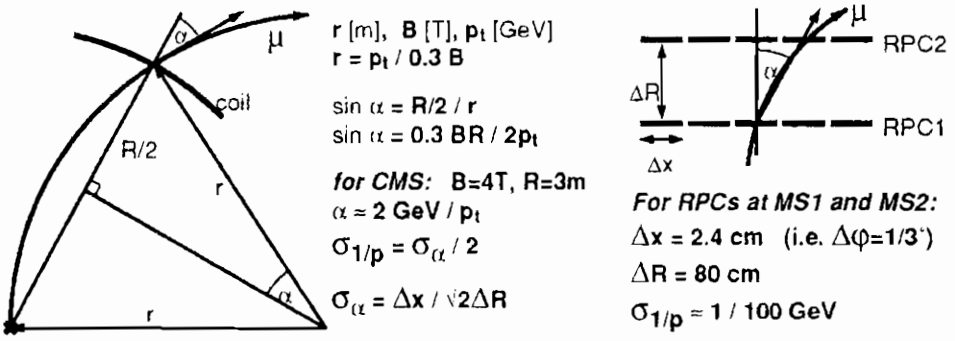

Fig. 5. Momentum measurement in the solenoidal field of CMS.

The obtained $\sigma_{1/p_t} \approx 1/100$ GeV means that a 50 GeV track is measured by two stations with precision $-17/+50$ GeV and a 100 GeV one with $-50/+\infty$. This is confirmed by a detailed GEANT simulation as shown in Fig. 6. It shows the track bending measured by

$\Delta\phi$ expressed in one strip units. It is seen that the 50 GeV track can be easily distinguished from the straight (infinite p_t) tracks, whereas the 100 GeV one can be distinguished neither form 50 GeV nor from infinite p_t tracks. This can be still improved by using more muon stations. One can use the overlap of 50 and 100 GeV distributions as a measure of this improvements. It is plotted in Fig. 7a which shows that it saturates above 5 planes. On the other hand one should watch the complication of the trigger logic. It can be expressed in terms of the number of possible patterns associated with one strip, which is shown in Fig. 7b. This number grows exponentially with the number of measuring planes. The two figures justify the actual choice of 4 RPC planes used for the CMS trigger.

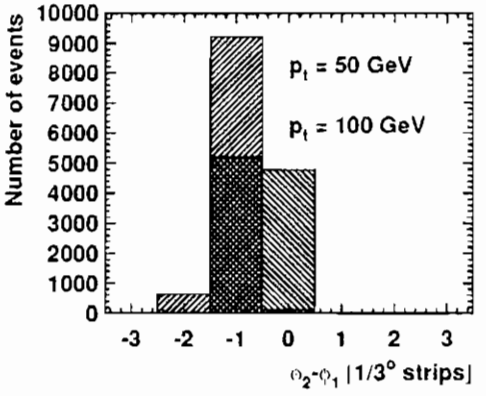

Fig. 6. a) Bending angle measured by the first two muon stations.

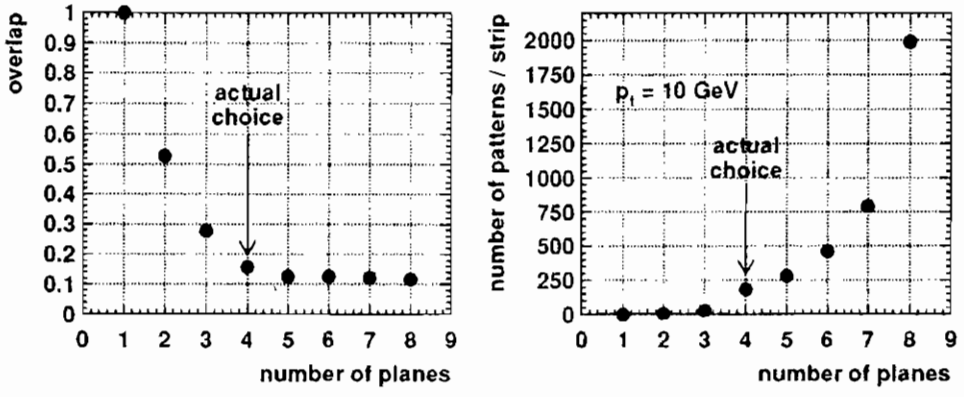

Fig. 7. a) p_t resolution expressed as an overlap of 50 and 100 GeV distributions.
b) Complication of trigger logic presented as a number of patterns per strip.

Another reason for having 4 muon stations is a need for some re-

dundancy. One station can be lost from the measurement because of dead areas, electromagnetic showers caused by radiating muons or punchthrough from hadronic showers. These phenomena have been extensively studied in the RD5 experiment [3]. Two example events are shown in Fig. 8.

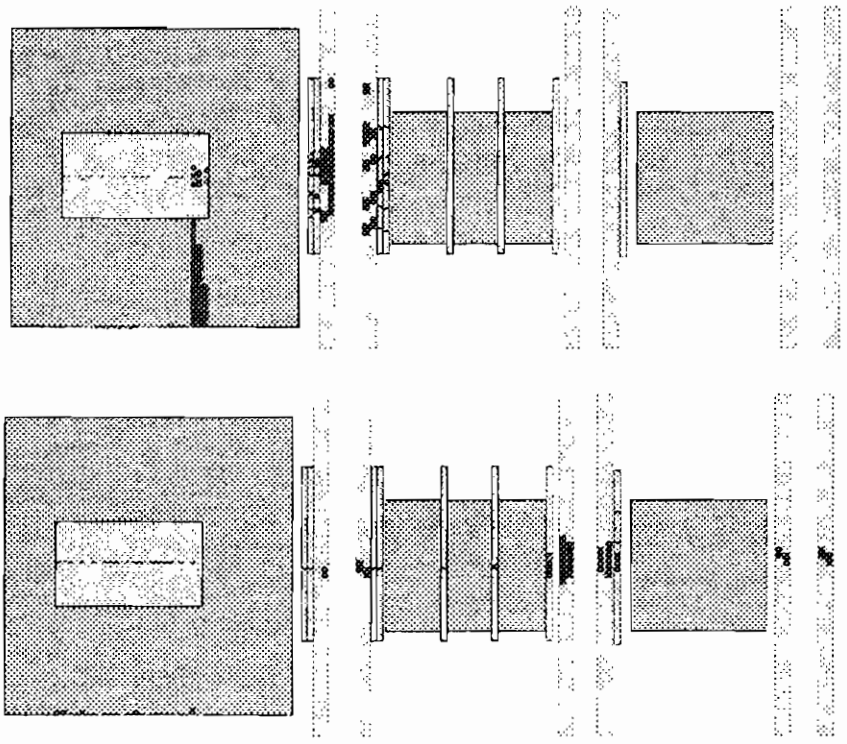

Fig. 8. Events observed in RD5. One station is useless for momentum determination because of large number of hits due to a) punchthrough from a 20 GeV π
b) electromagnetic shower from 300 GeV μ.

Experience gained in RD5 is widely used in the design of the CMS trigger. It will be based on 4 RPC planes requiring a coincidence of 3 out of 4 planes. It has been shown [5] that trigger performance is not afected by dead spaces if the "3 out of 4" acceptance approaches 100% and the "4 out of 4" one is not smaller than 80%.

4.2. Track Bending and Strip Length

The bending power $\int |B \times dl|$ of the CMS magnet in the barrel is

constant and equal 17 Tm. In the endcap however it decrease down to 8 Tm at $|\eta|$=2.0 and to 6 Tm at $|\eta|$=2.4 . Therefore particles of a given p_t are bent differently at different $|\eta|$. This is shown in Fig. 9 where the bending measured by $\Delta\phi$ between the first two stations is expressed in one strip units. The bending angle $\Delta\phi$ significantly depends on $|\eta|$. Thus one has to know $|\eta|$ in order to determine p_t from the $\Delta\phi$ measurement. From Fig. 9 one can see that precision of the order of 0.1 η-unit is needed, which determines the maximal length of the strips.

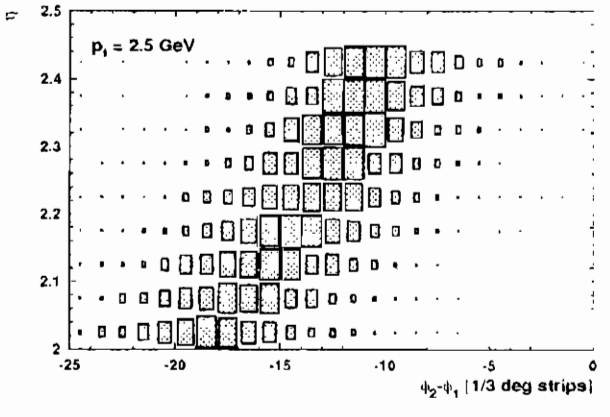

Fig. 9. In the endcaps the track bending $\Delta\phi$ depends on $|\eta|$.

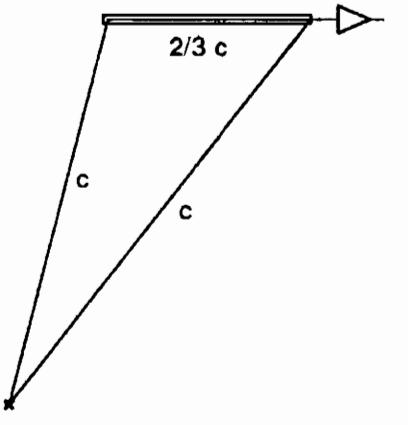

Fig. 10. Uncertainty due to the time of flight and the signal propagation along the strip.

4.3. Time of Flight and Signal Propagation

Muons emitted at different η cross a given RPC strip at different positions. Therefore they have different time of flight and different time is needed for signals to propagate along the strip to an amplifier. Fig. 10 shows two extreme cases. If we require this time spread not to dominate the bunch crossing assignment precision it should not be much longer than 5 ns. This means, that the strip length should be of the order of 1 m or shorter (assuming $\frac{2}{3}c$ for the signal propagation speed).

4.4. Random Coincidences of Background Hits

The single hit rate of RPC in CMS is dominated by random hits due to soft neutrons and photons [6]. In the barrel it stays at the level of 1-10 Hz/cm^2 and it should not cause any problems. In the endcaps it is

quite uniformly distributed if expressed in $\eta\phi$ coordinates [7]. Therefore projective geometry has an advantage that the rate per one RPC strip is roughly constant. For strips of $\Delta\phi = 1/3°$ and $\Delta\eta = 0.1$ it is about 6000 Hz per strip[8]. This corresponds to $\sim$ 30 hits per bunch crossing in the whole detector at high luminosity.

Those hits can affect the trigger rates in two ways. Random coincidence of three such hits in different stations can cause false trigger if they are by chance aligned along a possible muon track. A coincidence of a single background hit with hits of low p_t, curved muon track can look like more straight track and thus increase the apparent muon momentum. These two contributions (denoted as "n" and "μ/n" respectively) are compared with prompt muon rates in Fig. 13c. The "n" rate is proportional to the third power of the number of background hits per strip because the trigger is based on "3 out of 4" coincidences. Therefore increasing the size of the strips by factor e.g. 2 would increase the trigger rate by factor 8 and damage seriously the safety margin.

5. Requirements on the RPC Performance

5.1. Chamber Efficiency

Since the trigger relay on coincidence of several RPC planes, each of them must be very efficient. We set our target at 98%. This can be ensured by use of double gap chambers with staggered spacers.

5.2. Timing

Unambiguous bunch crossing identification requires trigger gates to be open for less then 25 ns. Leaving some margin for electronics set up time etc. one can assume 20 ns for this length. Another 5 ns should be subtracted for the signal propagation discussed above. Thus only 15 ns is left for the intrinsic RPC jitter. The precise requirement may be that: 98% of events should stay within 15 ns wide window. In practice it corresponds roughly to $\sigma \sim 2$ ns, but the tails are important.

5.3. Clusters

A sigle minimum ionising particle often causes signals from several adjacent strips to pass a discriminator threshold. This leads to deterioration of the momentum measurement. Therefore, one should require that the average cluster size is not bigger than 2 strips and that the fraction of events with clusters having more than 4 strips do not exceed 1%.

5.4. Rate Capability

Hit rates expected in CMS have been estimated using three different Monte Carlo programs: Fluka [9], Mars [10], and Gcalor [11]. A sample of results is shown in Tab. 2. One cannot say which program is the best one because they have different advantages and drawbacks. One can only expect that the systematic errors are of the same order as differences between the programs. In order to stay on the safe side we took the most pessimistic estimate and we applied a safety factor of 2. The derived requirements on the rate capability are summarized in Tab. 2.

Table 2. Expected and required RPC hit rates

muon station		expected rate (Hz/cm^2) Fluka	Mars	Gcalor	required rate (Hz/cm^2)
MB1-3		1	–	–	100
MB4		10	20	–	
MF1	$\|\eta\| = 2.1$	200	600	700	1500
MF2-4	$\|\eta\| = 2.1$	20	60	300	
MF1	$\|\eta\| = 2.4$	800	1300	1800	3000
MF2-4	$\|\eta\| = 2.4$	100	300	900	

Assuming uniform technology for the entire endcap one should aim for the most demanding conditions, i.e. those at MF1. However, it should be investigated whether using different technology for MF1/1 and relaxing requirements (by factor 2) for other MF chambers, may result in significant cost savings and/or a more robust design. The limit for $|\eta|$ <2.4 is to remind us that the eventual upgrade requires more performing detectors.

6. Geometrical Layout of the RPC System

As a result of the optimisation process described in Sec. 4 we have chosen approximately projective geometry with strips of width $\Delta\phi \approx 1/3°$ and length $\Delta\eta \approx 0.1$. Precise dimensions of the chambers as well as single strips are given in Fig. 11. The strip width of $\Delta\phi = 1/3°$ would result in having 90 strips per chamber. We have decided to have 96 strip, i.e. $\Delta\phi = 5/16°$ instead, in order to facilitate the design of digital electronics.

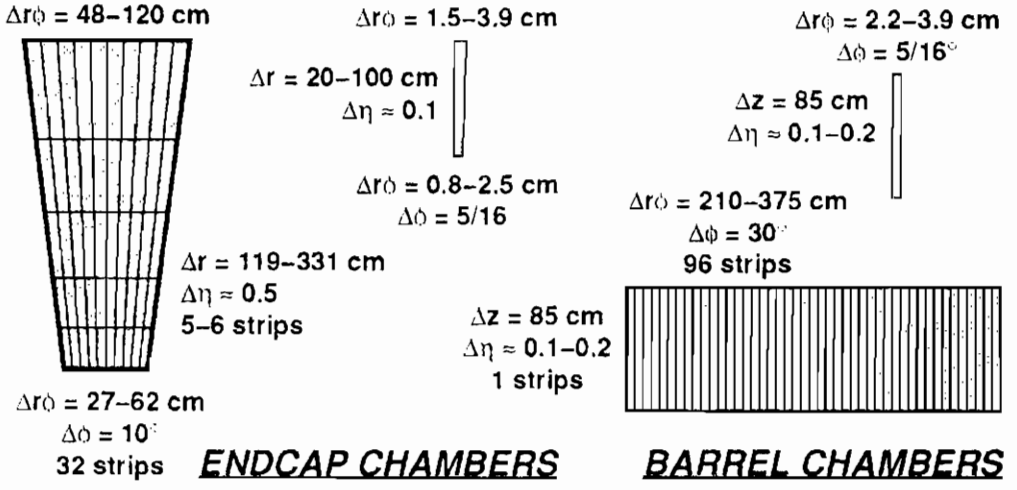

Fig. 11. Dimensions of RPC chambers and strips.

Each muon station will be equipped with one double gap RPC except two innermost barrel stations MB1 and MB2 which will contain two RPC planes. This is because low momentum muons (p_t <6-8 GeV) cannot reach the outer stations, for which a special low p_t trigger is foreseen. This trigger will be again based on 4 planes: 2 in MB1 and 2 in MB2. This is not necessary in the endcaps where the same p_t corresponds to much higher total momentum. Finally, the low p_t reach of the CMS muon trigger will be about 4 GeV in the barrel and 2.5-3.5 GeV in the endcaps.

In total there will be 1656 RPC' in CMS covering the area of 3400 m^2. They will be read out by about 200 000 electronics channels.

7. Summary

The RPC system of the CMS detector is designed to provide an efficient and robust muon trigger. The main advantage of the RPC detector is that all the coordinates ϕ, η and t are given by the same signal so no ambiguities can arise. The superior time resolution of RPC allows us to use adjustable trigger gates shorter than 25 ns, which enables straightforward bunch crossing identification and can largely reduce an "out of time" or random background. Muon momentum measurement is done by a programmable algorithm which can be easily adopted to actual running conditions. In addition, the RPC information can be used offline for solving pattern recognition ambiguities especially in the endcaps, where the CSC strips are 6 times longer than the RPC ones.

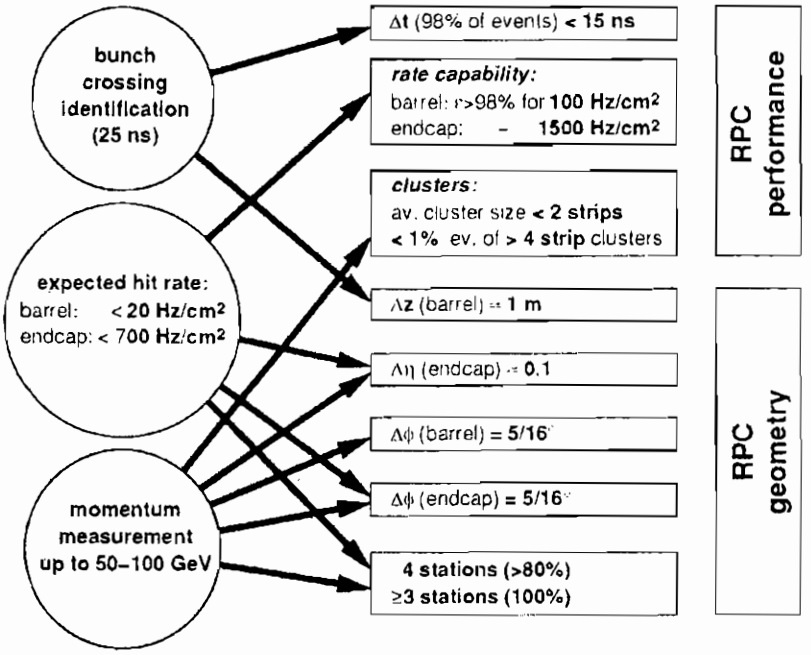

Fig. 12. Driving requirements on the RPC system for CMS.

Main requirements discussed above are summarised in Fig. 12. The final trigger performance in shown in Fig. 13 where various signal and background rates as the functions of the p_t threshold are compared. Fig. 13a shows the rate due to prompt muons. The trigger rate is higher

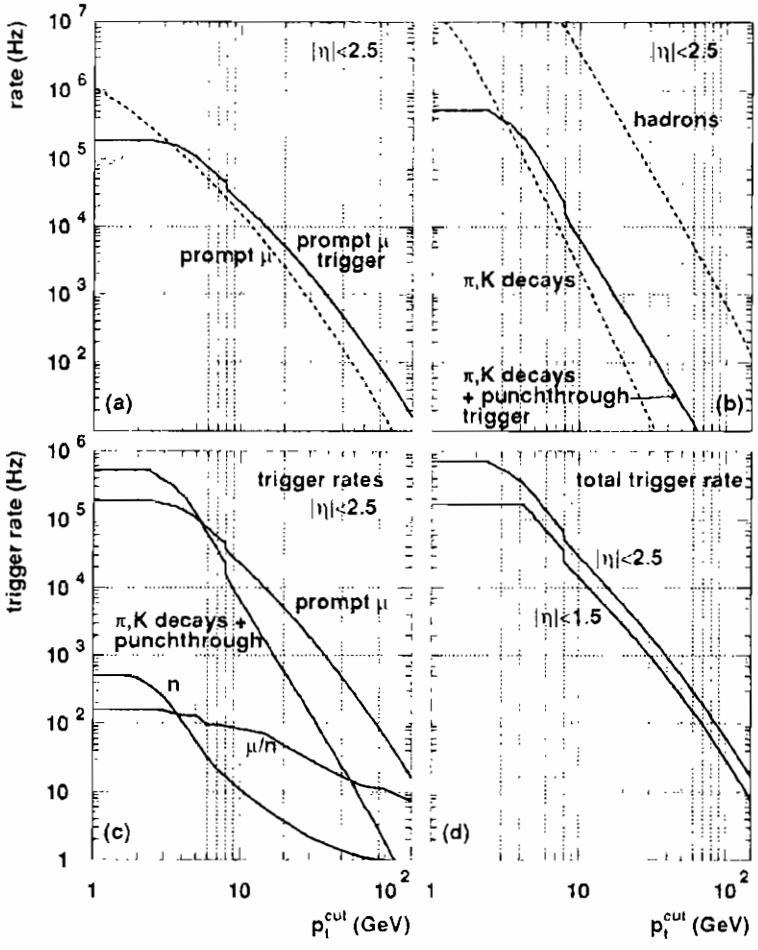

Fig. 13. Single muon trigger rates in CMS.

at high p_t because of its limited momentum resolution. The very low p_t muons are absorbed by the calorimeters and the iron yoke. The top dashed curve at Fig. 13b shows the hadron rate at the vertex. Some of the hadrons decay into muons (lower dashed curve) some others may give punchthrough. Resulting trigger rate is again indicated as a solid line. These two contributions are compared in Fig. 13c with the random coincidences of single hits (denoted as "n" for "neutrons") and mixtures of muon and background hits (denoted as "μ/n"). Finally the total trigger rates at L=10^{33} and 10^{34}cm^{-2}s^{-1} are shown in Fig. 13d.

It should be stressed that the ultimate low p_t reach is determined only by the amount of the absorber, and is as low as 4 GeV in the barrel

and 2.5-3.5 GeV in the endcaps. The actual threshold values will be chosen depending on current running conditions and physics priorities.

8. References

1. *The Compact Muon Solenoid - Technical Proposal*, **CERN/LHCC 94-38**, December 1994.
2. A. Ranieri, *RPC trigger design for the experiment CMS*, this Conference.
3. *Status Report of the RD5 Experiment*, **CERN/DRDC 91-53**, January 13, 1992;
   Status Report of the RD5 Experiment, **CERN/DRDC 93-49**, January 5, 1994;
   M. Aalste et al, *Zeitschrift für Physics* **C 60** (1993) 1;
   C. Albajar et al, *Nucl. Instr. Meth.* **A 364** (1995) 473;
   C. Albajar et al, *Measurement of Momentum and Angular Distributions of Punchthrough Muons at RD5 Experiment*, to be published in *Zeitschrift für Physics*.
4. M. Andlinger et al., *Pattern Comparator Trigger (PACT) for the Muon System of the CMS Experiment*, CERN preprint **CERN-PPE / 94-227**, to be published in *Nucl. Instr. Meth. A*.
5. M. Konecki et al., *RPC geometry and Muon Trigger acceptance*, CMS technical note **CMS TN/95-120**.
6. D. Chrisman and T. Moers, *A Study of Charged Particle Rates and Muon Backgrounds in the CMS Muon Chambers*, CMS technical note **CMS TN/93-106**.
7. M. Huhtinen and G. Wrochna, *Estimation of the RPC Muon Trigger Rates Due to Neutral Particles*, CMS technical note **CMS TN/94-138**.
8. Á. Csilling, M. Konecki, J. Królikowski and G. Wrochna, *Muon Trigger Rates*, CMS technical note **CMS TN/94-282**.
9. M. Huhtinen and P-A. Aarnio, *Neutron and Photon Fluxes and Shielding Alternatives for the CMS Detector at LHC*, CMS technical note **CMS TN/94-241**.
10. I. Azhgirey and A. Uzunian, *CMS Muon system radiation background shielding*, CMS technical note **CMS TN/94-266**.
11. Y. Fisyak et al., *Neutron and gamma backgrounds in GEM and CMS muon systems*, CMS technical note **CMS TN/94-147**.

The RPC Trigger Design for the future experiment CMS

G. De Robertis[d], M. Gorski[a], M. Konecki[b], J. Krolikowski[b], I. M. Kudla[b], M. Lewandowski[b], F. Loddo[d], K. Pozniak[c], A. Ranieri[d], G. Wrochna[e]

[a]Institute of Nuclear Studies, Warsaw, Poland; [b]Warsaw University, Warsaw, Poland; [c]Warsaw University of Technology, Warsaw, Poland; [d]INFN, Bari, Italy; [e]CERN, Geneva, Switzerland.

ABSTRACT

The first level trigger of the RPC based detector muon trigger system for the experiment CMS at CERN is presented here. Its main characteristics and the idea onto which it will be based on are presented. It will be also shown, the Test Bench system which is being in preparation to prove the trigger system main features and capability.

1. Introduction

The first level muon trigger of the CMS will be based on a precise muon chambers (Drift Tubes, CSC) and on a fast dedicated trigger detector (RPC)[1]. Here I describe the RPC based part of the system. Its goals are to identify a muon, estimate its transverse momentum and determine the bunch crossing in which it was originated. One way of selecting interesting events in the 10 /sec interactions of CMS is to look at high transverse momentum muons. The bandwidth allowed for this channel is about 1-10 KHz and thus a reduction factor of about 10^{-6} is required. The trigger should not introduce any dead time and it has to be able to examine every consecutive bunch crossing. The decision about each event should be taken in less than 3 μs. RPC based muon trigger system characterize precise timing, unambiguous position detection and crude momentum measurement.

This talk will show which principle the muon trigger is based on and how this idea is developed, the muon Pattern Comparator trigger system it will be described as well as its principal components.

1. General idea and principle of operation

The RPC will be arranged in four stations interleaved with magnetized iron providing the field up to 2 T. Muon track passing through the four RPC stations will be recorded in form of a pattern of hit strips. In principle knowing the vertex , two measuring planes after the coil giving a local track vector are enough to measure the momentum and apply a p_t cut.

To deal with fluctuations due to multiple scattering and energy losses and to account for the geometrical inefficiencies we take advantage of having four muon stations and make use of 4 measuring planes. This idea is shown in the following figure.

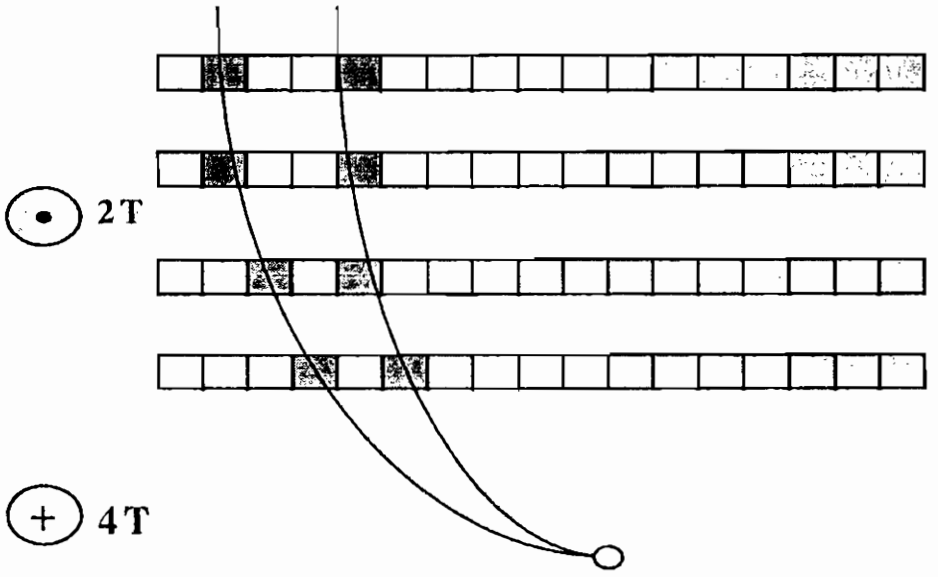

Fig. 1. PAC principle of operation

2. Segmentation

The RPC trigger of CMS is foreseen to cover an area up to η=2.1 upgradable up to η = 2.45 and the smallest logical unit of the trigger system is called a segment, which is 1 strip long and 8 strips wide, covering 2.5 degrees in ϕ and about 0.1 unit in η. These number determine double muon resolution of the trigger, i.e. two muons within the same segment will be seen as one. The information coming from all triggering planes within a given segment of the detector is first processed by the segment trigger processor. The main function of the segment processor is to recognize a muon and measure its momentum. This is performed by the Pattern Comparator, described in the following.

3. Principle of operation of PAC

In the following figure is shown the idea which the principle of operation of PAC (PAttern Comparator) is based on[2]. The pattern of hit strips is compared to predefined patterns corresponding to various p_t. Every AND corresponds to one pattern. One can program which strips are AND'ed together. Then patterns are grouped in several p_t intervals by programmable wired ORs. Finally a code value is assigned to the track with the greatest p_t

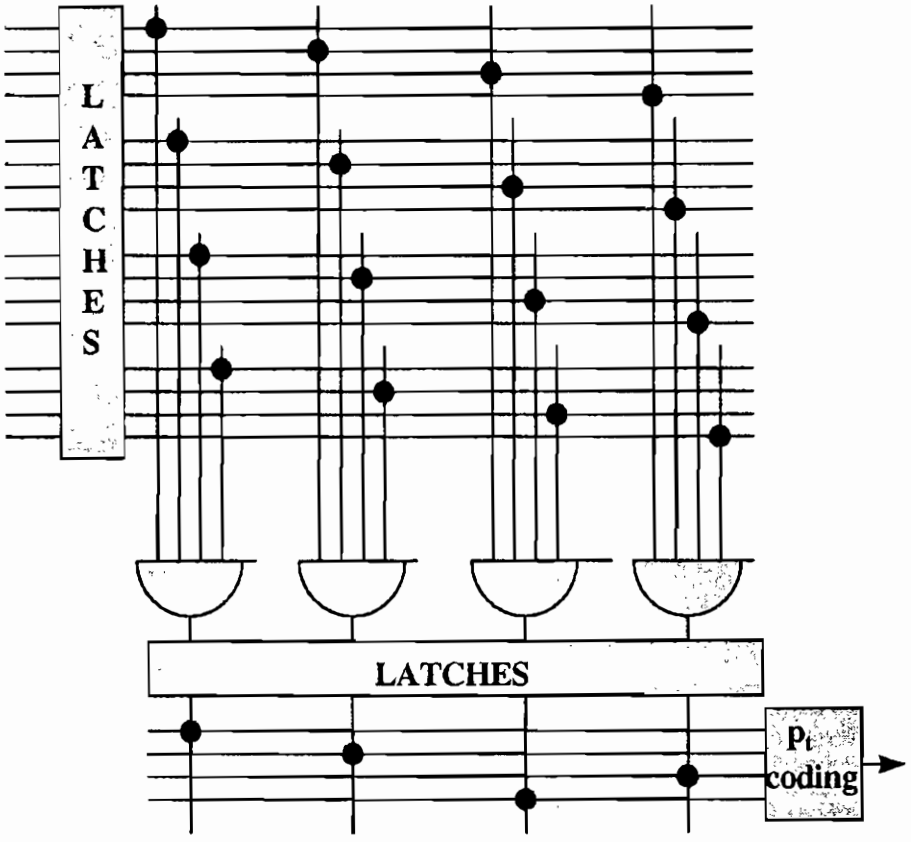

Fig. 2: PAC schematic view

4. PACT - general overview

To make the decision PAC needs of a number of signals coming from several muon stations, most of these signals are used in several PACs. To reduce the length of interconnections we plan to place certain number of PACs with synchronization and pipeline memory ASICs and the first level of sorting ASICs on one Trigger and Readout Board (TRB).

The TRBs will be grouped into the Trigger and Readout Module (TRM) and equipped with the next step of sorting tree ASICs and necessary service circuits, like DAQ interfaces, timing system interface, control system interface, test pulse generator and test processor.

5. PACT - TRB general view

Having 1 PAC per segment, on each TRB will be allocated 12 PACs to process a complete detector sector made by 12 detector segments. To each PAC, after the synchronization phase and in parallel to the pipeline memory which will be seen later, the low jitter digital signals coming from the FEE of each RPC, is sent over a distance of 10 meters into the TRB board without signal quality degradation. We plan to equip our FEE with test facility which will be controlled from the TRM. It is foreseen to use test pulse to check all channels and perform preliminary time calibration. Final time calibration will be done with real muons.

To reduce the number of interconnections between TRBs (and facilitate resynchronization task) part of the chamber signals will be sent to two neighbour TRBs. The output of each PAC, is then sent to a Sorting tree which will furnish to the TRM, the highest momentum muon code out of 12 red on its inputs.

6. Trigger & readout general scheme

Before to analyze in more detail any component of the PACT system, we look how the Trigger and readout scheme is composed, showing at the same time the flow of signals (Fig. 3).

The FE digital signals coming from the 4 RPC planes of one segment, are sent to the Synchronization unit and to the Pipeline Memory and Derandomizer Buffer ASIC. At same time in parallel, the signals output from the Synchronizer are sent to the PAC chip for analysis and as explained before, they are moving toward the Sorting tree.

If the results of sorting compared with a programmed threshold are good, one FLT signal is generated. On this time the event stored in the pipeline are moved to a Zero Suppression circuit first, before to move it to an event buffer for the VME readout.

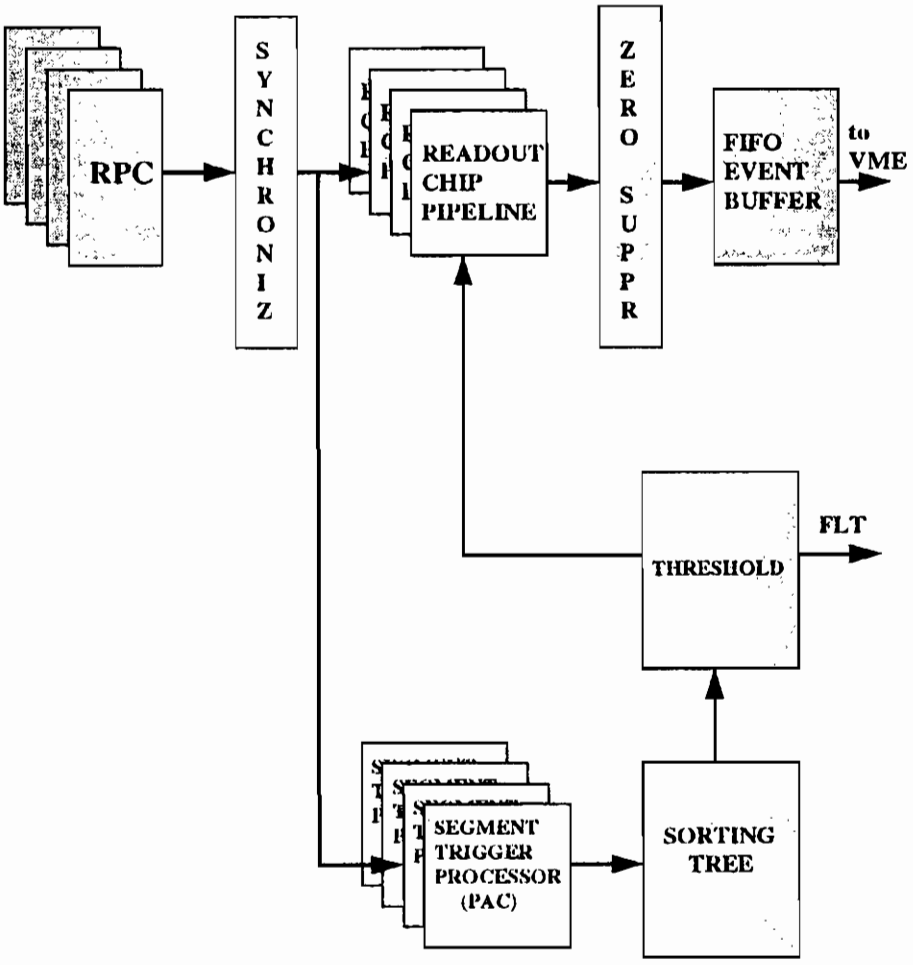

Fig. 3: Trigger and readout scheme of TRB

7. Synchronization and Pipeline Memory

The purpose of the synchronization block is to synchronize the signals coming from 4 different muon stations and to provide signals related to one specific bunch crossing for later PAC trigger processing. Since low momentum muons frequently cross segment boundaries, certain part of the synchronized signals should be sent to the neighbouring TRBs.

The pipeline memory is used for:

- storing data during the time when the FLT decision is elaborated;

- storing data corresponding to the bunch crossing accepted by the FLT and in this case the data are moved toward the Derondomizer.

In the case of CMS the time needed for FLT decision will be of the order of 128*25 ns. Present DAQ simulations shows that the depth of the derondomizer buffer has to be at least 16. The Derondomizer buffer afterward will be accessed by the zero suppression circuit and followed by DAQ interface.

8. Pattern Comparator (PAC)

PAC is the main part of TRB. The PAC chip provides the information about the highest momentum muon crossing the segment volume. The output of the processor will be a 6 bits code of the muon momentum. The most significant bit defines the sign of the muon. Code 'H00' is reserved for situation where was no muon in the segment (or its momentum was below the lowest threshold). PAC uses as its inputs, data from the segment synchronization chip as well as the synchronized data coming into the segment from neighbour TRBs.

The first part of PAC chip increase the quality of the input data, in this way:

- first of all by setting to '0' the noisy strips in case they cause a lot of false trigger;

- second by setting to '1' dead strips in case they cause significant efficiency losses;

- third by replacing the cluster with its center of gravity.

In fact the simulation shows significant increase of trigger quality when simple declustering function replace cluster of 3 hits with its center.

Only the highest momentum muons will be recognized using single strip signals. At low momentum, precision of the measurement is dominated by multiple scattering and full granularity is not needed therefore lower momentum muons will be recognized using the 2-fold, 4-fold or at most an 8-fold Ors of strip signals. This corresponds to increase the strip size. The second part of PAC chip is indeed dedicated to prepare the OR signals needed to recognize muon tracks of lower momentum.

PAC operates in a pipeline mode, which means that each operation which involves more than 25 ns, will be divided into several sub-operation each of which could be made in less than 25 ns. It will allow us to provide the trigger decision for every bunch crossing. Estimated time needed to make the muon momentum identification in the PAC, is 6*25 ns. The PAC ASIC will be equipped with a self test facility and Boundary Scan Test circuit. This circuit will be used to testing of TRB ad also for programming of the PAC.

Patterns will be given first by the simulation of the muon tracks in the detector and of detector response. Later they will be updated using real muon tracks reconstructed with the help of precise muon chambers. Information about dead and noisy strips can also be included in the patterns.

9. Sorting tree

The basic goal of the sorting tree is to reduce the huge amount of data to be sent to the global trigger. This function will be performed by a tree of dedicated VLSI sorter circuits each of which will find the four highest p_t muons out of eight candidates and it will propagate the segment addresses of selected muons as well[3]. We plan for each 15 η ring of RPC

system (the barrel part of the whole detector), to send 4 muon momentum codes (with relevant segment address) to global muon trigger processor.

The basic element of the Sorting Processor is shown in the Fig.4 together with the principle on which it works and this is realized by a simple comparator which performs the comparison between two 6 bits words, followed by a multiplexer which performs an exchange of the input words if necessary.

The Sorting Processor obviously has a more complicated structure and should be realized as a VLSI circuit, composed by the following parts:

a 6 bits two words comparator;

a chain of 4 multiplexers, 2 for data and 2 for addresses;

a 2-fold 4 inputs Sorters;

and an 8 inputs Merger.

These components are connected together to finally form, an 8 Inputs Sorting Network (the Sorting Processor), composed by 2 Sorters plus 1 Merger.

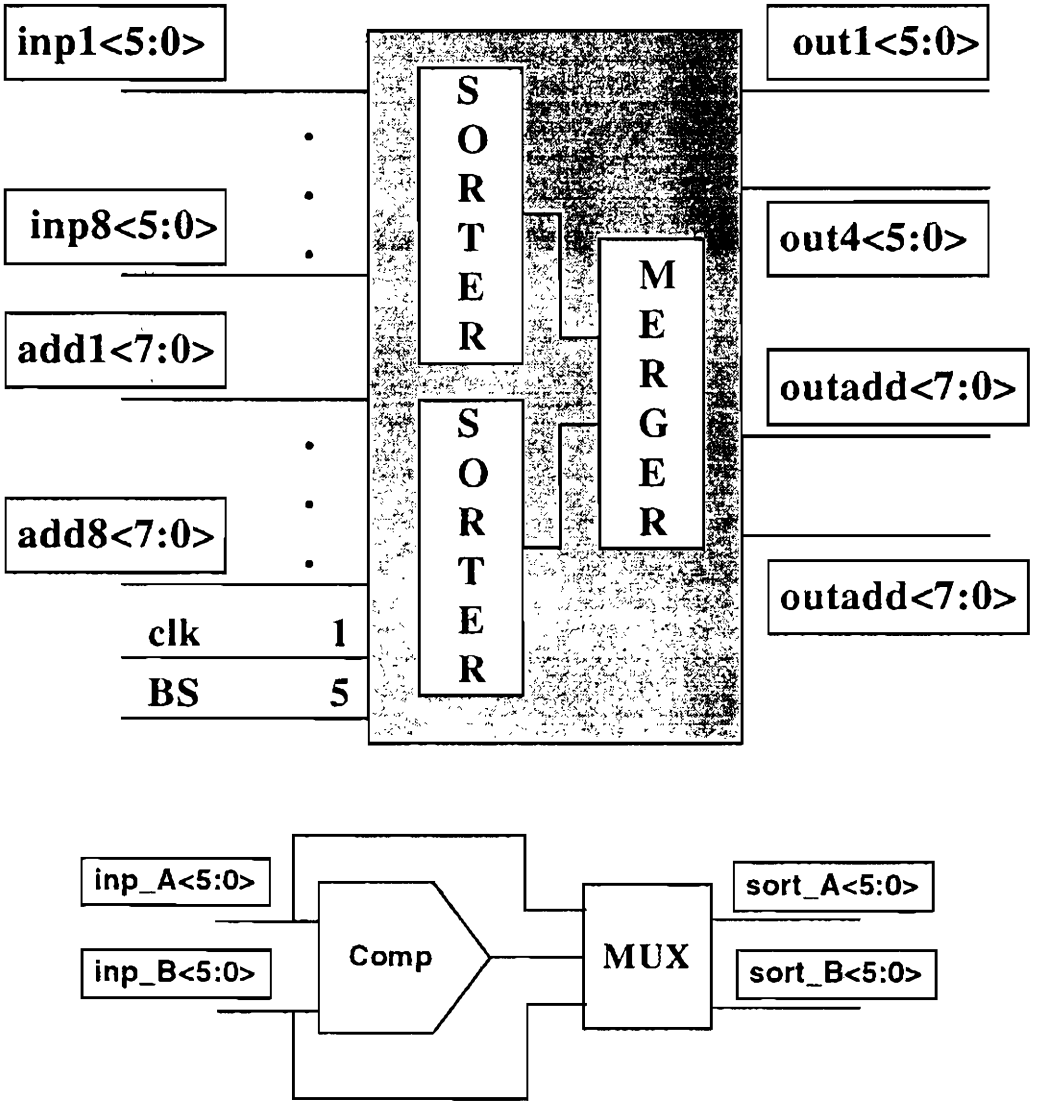

Fig. 4: Scheme of the Sorting Processor and its basic element

10. Test and developments

An ALTERA prototype of the PAC was built and tested with the muon beam in the framework of the RD5 experiment at CERN. Momentum measurement up to 100 Gev was demonstrated[2].

First attempt to put PAC on the silicon done in Mannheim University has shown the possibility to put over 6000 pattern on surface of 1.5 cm^2 using 1.0 μ standard cell technology.

Next ASIC is under design by the Microelectronics group of the Warsaw University of technology. This version will utilize full custom technology in order to take the advantage of a specific architecture of PAC while preserving its flexibility.

The demonstrator chip will be realized in 1.0 μ technology and will contain only a single strip block for 8 bit segment and BST circuit.

Sorter demonstrator ASIC is under design while a XILINX model of the sorter will be used in the PACT test bench device.

11. Conclusions

One modular PACT test bench system for the RPCs detector in CMS, is under construction and for the next year we foresee to test the system in laboratory first and then connecting an RPCs system to it, triggering on real muon tracks.

11. References

1. The Compact Muon Solenoid, Technical Proposal. CMS Collaboration *CERN/LHCC* 94-38.
2. Pattern Comparator Trigger (PACT) for the Muon System of the CMS Experiment. M. Andlinger et al. *CERN-PPE/94-227,* (9 December 1994).
3. The Sorting Processor Project. G.De Robertis et al. *CMS TN/95-028*, (6 March 1995).

The Level-1 Muon Trigger Algorithm of the ATLAS Experiment

Aleandro Nisati
Istituto Nazionale di Fisica Nucleare, Roma, Italy

February 9, 1996

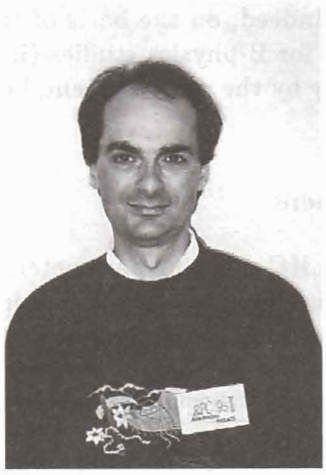

ABSTRACT

The muon trigger is crucial for the experiments proposed at LHC. The wide energy threshold range needed to exploit the physics potential at low and high luminosity, and the high background rate expected in the muon system pose strong requirements to the design and the implentation of the level-1 muon trigger. The algorithm adopted by the ATLAS Collaboration is reported; the relative performances are presented and discussed.

1. Introduction

The muon detection plays an important role to exploit the LHC physics potential [1]. Muons are crucial for the SM and MSSM Higgs boson search through the decay channel $H \rightarrow ZZ^* \rightarrow 4l^{\pm}$ ($l = e, \mu$). In particular the SM Higgs can be identified with this channel in the mass interval 130 GeV/c^2 < m_H <800 GeV/c^2. Also, muons are important for supersymmetric particle searches and for the detection of heavy vector bosons.

Last but not least, muons are essential for the initial low luminosity running of the machine. Indeed, on the basis of the simulation results, the level-1 trigger needed for B-physics studies (in particular CP violation) can be provided only by the muon system, because the low energy threshold required [2].

2. The LHC environment

The more important LHC machine parameters are compared in Table 1 with the ones of existing high energy hadron colliders; the corresponding inelastic cross sections are also reported.

Table 1. Comparison of the Tevatron and SppS collider parameters with LHC

	Energy (GeV)	T (μs)	L ($\mu b^{-1} s^{-1}$)	$\sigma_{inel.}$ (mb)
LHC	14	0.025	10^4	80
Tevatron	2	3.5	10	50
SppS	0.630	3.8	6	40

Two important aspects distinguish LHC:

- the energy "deposited" per time unit in the experimental hall is much higher than the one of previous colliders; in particular this energy is 10^5 times higher than the one of the SppS. This leads to the production of a background particle flux that behaves as a "gas" in the experimental hall. The background is originated mainly from the neutrons produced in the hadronic showers developed in the interaction of p-p hadrons with the beam pipe, the forward calorimeters and the machine elements [4]. Neutrons

(with a wide energy spectrum) are captured by nuclei with subsequent emission of photons with energy of the order of 100 KeV to few MeV. These photons then convert in electrons mainly through the Compton effect and they are detected by the muon chambers. Shielding systems are needed to reduce this background that, otherwise, would make very difficult the muon identification at LHC; from now on the background fluxes and the detector counting rates are referred to p-p detector with shielding system; the nominal LHC luminosity is assumed. The expected counting rate is about 20 Hz/cm^2 in the barrel region of the detector; it increases up to few kHz/cm^2 in the very forward regions.

- The second important conseguence for an experiment at LHC is the need to establish and maintain the syncronization of different regions of the same subsystem and of different detector subsystems. Indeed, at the same time the detector "see" the events of different bunch crossings, depending on the distance of the considered subsystem from the p-p interaction point. Therefore, to trigger and to assembly correctly the complementary measurements of the same event one need to identify the bunch crossing at level-1 trigger for each subdetector.

The consequent main requirements on the muon trigger system are:

- 1 Safe operation in high background conditions;
- 2 Unique bunch crossing identification: resolution time of the muon trigger system $\sigma_t < 4$ ns;
- 3 Sharp p_T threshold over a large range (from 6 to about 40 GeV/c)

3. The ATLAS Muon System

The ATLAS detector [3] is based on an air coir toroid system capable of providing an average magnetic field of about 0.6 T in a large volume system; the external dimensions are 22 m diameter and 26 m length; see fig. 1 and 2.

The barrel spectrometer layout consists of 3 muon stations, one placed at the beginning of the magnetic field, on at the end and the

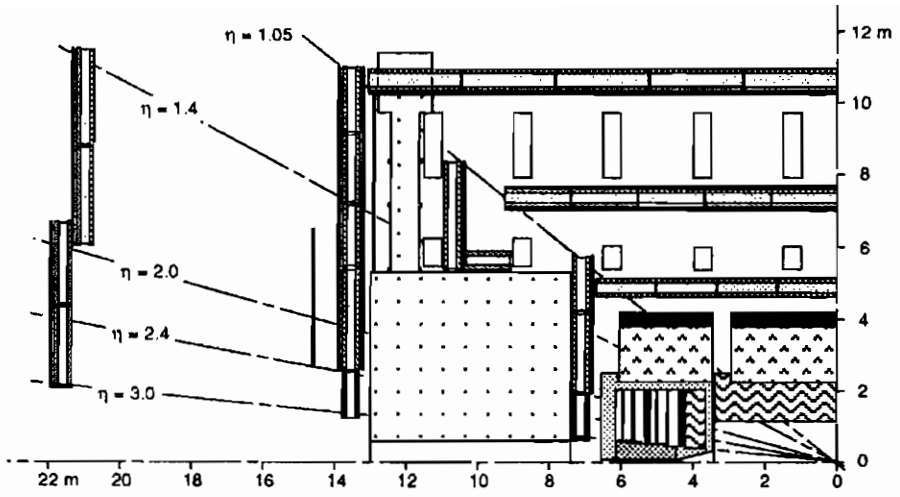

Figure 1: Side view of the ATLAS detector showing the position of the muon chambers. Light shades indicate the precision chamber support structures and the dark shades of grey the precision chamber multilayers. Black lines show the trigger chambers.

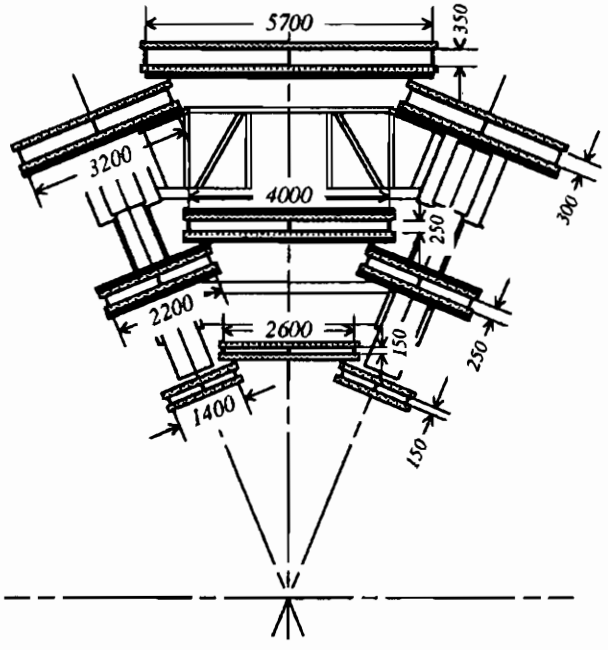

Figure 2: Transverse view of a single barrel sector. Medium shades indicate the precision chambers; the black lines show the RPCs.

last placed in the middle of the magnetic field region, to perform a sagitta measurement. In the forward spectrometer the inner space of the magnet is not available for detector instrumentation and therefore the momentum measurement is based on a direction-point measurement made again with three muon stations, two at the beginning and the end of the magnet, the third far from the detector. This system offers high standalone momentum resolution: $\Delta p/p \simeq 2$ %. The combination with the inner tracker, based on a 2 T solenoid, improves roughly by a factor $\sqrt{2}$ the momentum resolution. The momentum resolution of this spectrometer is coulomb scattering limited for muon transverse momenta up to about 300 GeV/c; the limiting material is located in the muon detectors, in the support frame of the superconducting coils and in the supporting structure of the entire system. For higher momenta the momentum resolution increases and it is dominated by the chamber alignment accuracy, wire positionning and the intrinsic single wire space resolution.

The detector counting rate expected is 20 Hz/cm^2 in the barrel, but two regions around $|\eta| = 0.7$ of the innermost muon station, where the rate is close to 100 Hz/cm^2. This is due to the cracks present in the central calorimeter. The rate in the forward regions increases with $|\eta|$ up to about 1 kHz/cm^2 in the innermost station; on the contrary, the average rate of the outermost muon station is about 20 Hz/cm^2.

4. The Muon Trigger Algorithm

As stated before, the ATLAS muon trigger is carried out by a standalone system based on dedicated detectors, the RPCs in the barrel and the TGCs in the endcaps.

The RPC chamber under development for ATLAS is a single gap RPC read out by two orthogonal strip planes to provide track measurement in the two projections. This is needed to reject fake muon triggers induced by the background present in the experimental hall.

The muon trigger layout is shown in fig 3; it consists of three RPC stations: two made by two RPC layers each and placed one externally ($S2_{out}$) and the second internally ($S2_{in}$) the central muon station; the third trigger station (S3) is made of three RPC layers and is placed internally (externally) the outer large (small) muon station. The low p_T trigger (p_T threshold < 10 GeV/c) is performed by the $S2_{in}$-$S2_{out}$ coincidence in space and time ($\Delta t \simeq 20$ ns).

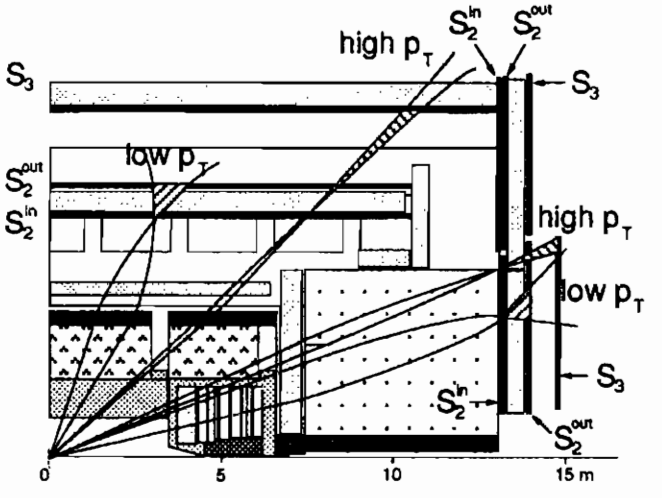

Figure 3: Layout of the muon trigger system in barrel and end-cap.

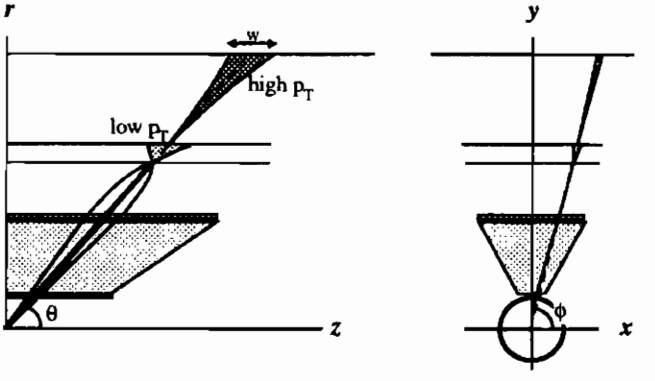

Figure 4: Schematic of the Level-1 muon trigger algorithm in the barrel. The low p_T trigger is based on two groups of RPC layers, while the high-pT trigger uses an additional griup of three layers, as discussed in the text. The shaded area represents the calorimeters and absorbers. Trajectories are indicated for positive and negative-charge muons of low and high-p_T, and for an infinite-momentum muon.

The number of strips of $S2_{in}$ used in the coincidence defines the energy threshold. This coincidence and a 3/4 majority is asked independently for the two projections; see fig. 4. The high-p_T trigger (p_T threshold $\simeq$ 20 GeV/c) is performed by requiring the low-p_T trigger first and therefore making the coincidence of $S2_{out}$ with S3, similarly to the low-p_T trigger logic, with a S3 majority of 2/3, again in the two projections. The coincidence window size are small for low and high p_T-thresholds: about 30 cm at $\eta = 0$ and less than 60 cm at $|\eta| \simeq 1$. The momentum resolution at the threshold is about $\Delta p/p = 0.3$ for p_T-threshold=20 GeV/c and $\Delta p/p$=0.20 for 6 GeV/c transverse momentum threshold. Fig. 5 shows the algorithm efficiency at low and high threshold. The expected trigger rate at $L = 10^{33} cm^{-2} s^{-1}$ with the threshold $p_T^{th.} = 6$ GeV/c is about 10 kHz, while at high luminosity with $p_T^{th.} = 20$ GeV/c the rate is 4 kHz, a factor about 4 larger than an ideal trigger (efficiency=0 for $p_T < p_T^{th.}$; 1 otherwise); the Level-1 trigger efficiency are compared also with the Level-2 muon trigger efficiency [3] as a function of the p_T threshold.

The system total surface is about 800 m^2; If the strip size is fixed to 3 cm in S2 and 4.5 cm in S3, about 300k readout channels are needed.

The expected accidental trigger rate is compared with prompt muon trigger rate in fig. 6 for high threshold. This algorithm allows a margin factor of more than 10 for high threshold. At low threshold this factor is reduced to about 5.

The Muon Trigger Processor for the barrel is described in [5].

In the Forward Muon Trigger system the RPC are replaced by the Thin Gap Chambers, and is is positionned outside the End Cap Toroids, since it is not possible to place detectors inside these magnets.

A trigger algorithm similar to the one above described can be is applied, as shown in fig. 7.

The coincidence window size is now smaller than the one of the barrel both at low and high-p_T; this allow a better background rejection and also prevents triggers induced by the beam-halo. The performances obtained with simulation studies are very similar to the one of the barrel, above described.

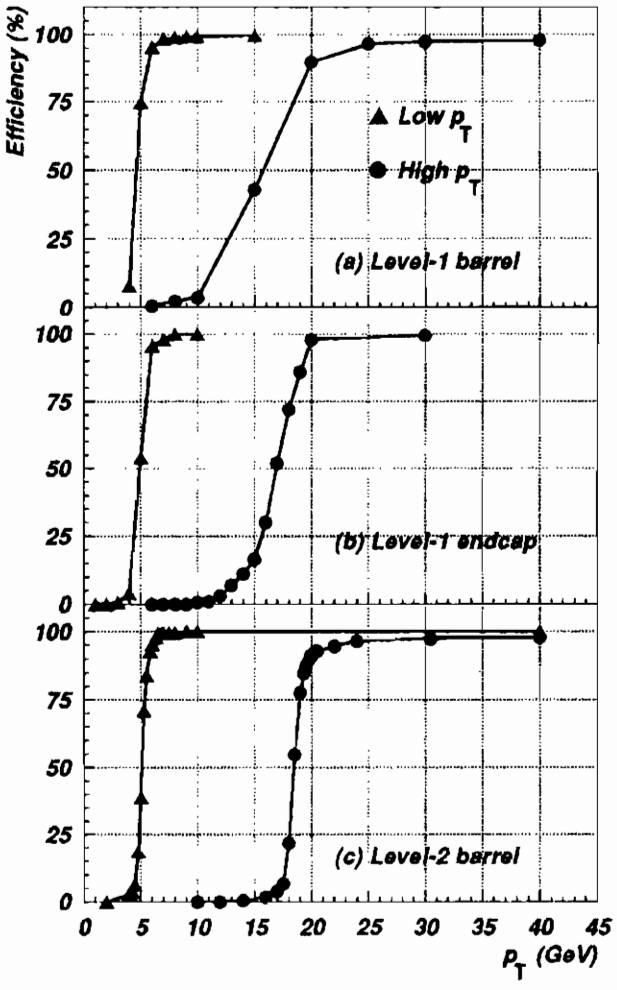

Figure 5: Trigger algorithm efficiency versus muon p_T for (a) the Level-1 muon trigger in the barrel ($|\eta| < 1.1$), (b) the Level-1 muon trigger in the end-cap ($1.1 < |\eta| < 2.2$), (c) the Level-2 muon trigger in the barrel. The curves are shown for trigger thresholds of 6 GeV/c and 20 GeV/c transverse momentum (about 90% efficiency at nominal threshold).

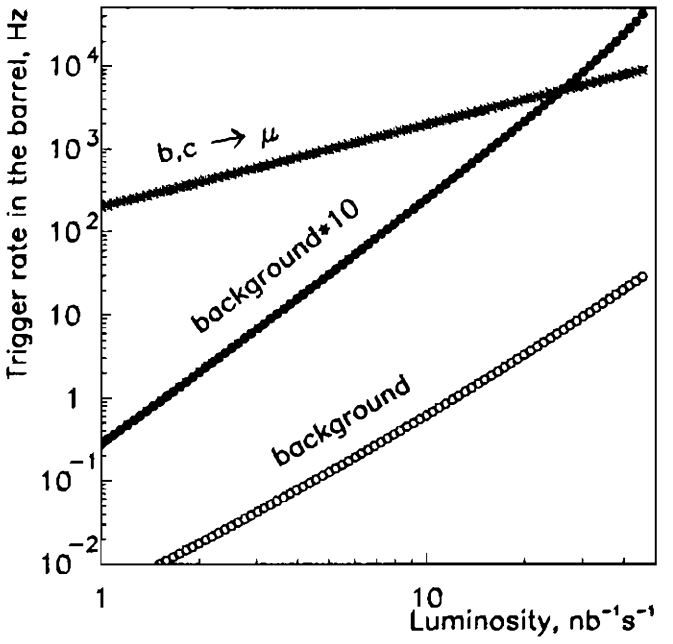

Figure 6: Prompt muon trigger rate in the barrel. The accidental coincidence rate due to low energy particles is shown for the nominal background, and for background rates increased by a factor 10.

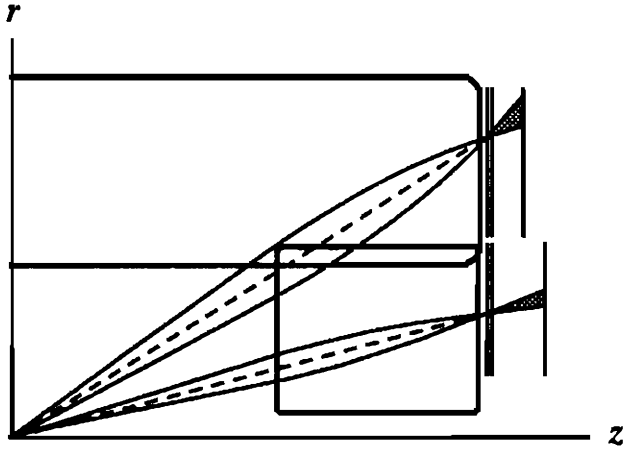

Figure 7: Schematic of Level-1 muon trigger algorithm in the end-cap. Examples of trajectories are indicated for positive- and negative-charge high-pT muons, and for infinite-momentum muons.

5. References

1. Proceedings of the Large Hadron Collider Workshop, Ed. G. Jarlskog and D. Rein, **CERN 90-10 ECFA 90-133** (1990).
2. A. Nisati, B-physics in ATLAS, *Nucl. Instr. and Meth.* **A 368** (1995) 109-114.
3. ATLAS Technical Proposal, **CERN/LHCC/94-43** (1994).
4. A. Ferrari, private communication.
5. S. Veneziano, Proceedings of this Workshop.

Resistive Plate Counters for the BELLE Detector at KEKB

Norman Morgan for the $K_L$muon (KLM) working group of the BELLE collaboration

Virginia Polytechnic Institute and State University, Physics Department, Blacksburg, VA 24061, USA morgan@amy.phys.vt.edu

ABSTRACT

The BELLE detector at the KEK B factory is described. We plan to build glass electrode Resistive Plate Counters (RPC) for muon and K_L detection in the instrumented iron outside of the solenoid. Muons are identified by their greater penetration through the iron. Neutral K_L particles interact with the material in the calorimeter and in the iron and produce charged secondary particles. The performance of prototype counters is described including gas mixture studies and long-term aging tests. A double gap / double readout superlayer design is presented. A total of 2200m^2 of detectors will be built to cover the barrel region.

1. The BELLE Experiment

The BELLE experiment [1] is designed to study the physics associated with the decay of b-quarks. One of the primary goals is to measure the parameters of the Kobayashi-Maskawa (KM) matrix [2] which describes the coupling among the six flavors of quarks in the standard model. Measurement of charge conjugation and parity (CP) violation in b-quark decays will either fit within the standard model or lead to refinements and new knowledge of elementary particle interactions. This knowledge is a key element in our understanding of man-made and extraterrestrial particle production and interactions, as well as in our understanding of the evolution of the early universe.

The experiment will be located at the KEK B factory in Japan. The accelerator provides an asymmetric beam of 8.0 GeV electrons and 3.5 GeV positrons tuned to produce the $\Upsilon(4S)$ resonance which decays to $B^0\overline{B^0}$. Muon identification is vital for this experiment because many of the decay channels of interest involve muons in the final state.

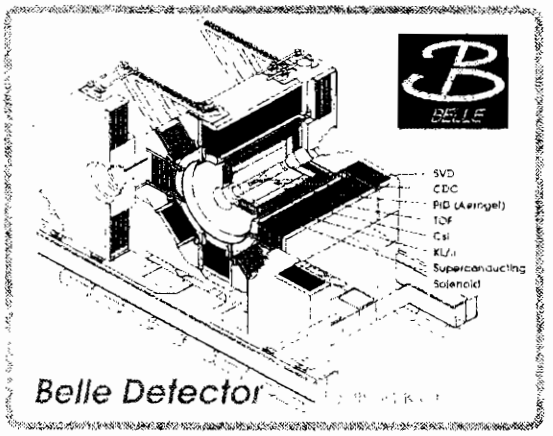

Fig. 1. Schematic of BELLE Detector at KEK B factory.

The detector is shown in Figure 1 and consists of a superconducting solenoidal magnet 4.4 meters long with a radius of 1.7 meters. Inner silicon vertex tracking provides precise B decay coordinates. The central tracking chamber measures particle momentum and an electromagnetic calorimeter of CsI measures photon energy and position. Aerogel Cherenkov counters and Time-of-Flight information from scintillators allow the identification of pions and kaons. Fifteen layers of iron and

RPCs outside of the coil are used to track charged particles for muon tagging and detect the by-products of K_L interactions. K_L detection provides another valuable CP violation measurement through the decay channel $B^\circ \rightarrow J/\psi K_L^\circ$.

2. Freon 116 Studies

In a search for a less environmentally damaging gas mixture we have tested freon 116 as an alternative to freon 13B1. We have tested freon concentrations up to 35%. The RPC was operated with a differential bias of $\pm$HV and streamer pulses were produced. The trigger is defined by a 3-fold coincidence scintillator telescope selecting cosmic rays passing through the RPC. The efficiency is defined as the number of triggered events with RPC signals divided by the number of cosmic ray triggers. Typical streamer pulses are several hundred picocoulombs (pC). A threshold cut of 20pC was applied to define an RPC hit. In Figure 2 the efficiency as a function of voltage is shown for seven different mixtures of freon 116, isobutane, and argon. Within this range of mixtures we found very little difference in performance. Singles rate, current, pulse height, and efficiency were similar. Mixtures with higher concentrations of freon and isobutane operated at higher electric field as expected. At present we have chosen a mixture of 6% freon 116 / 30% isobutane / 64% argon for the long-term tests to be described below.

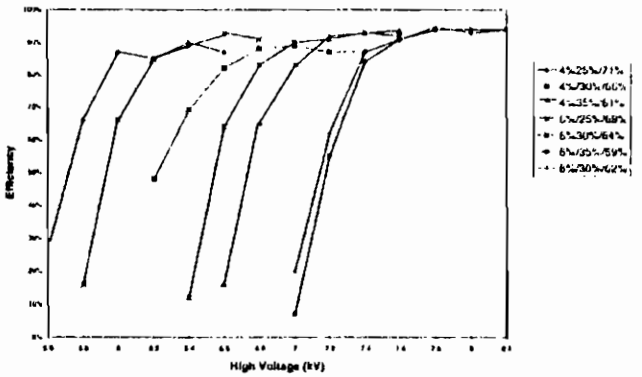

Fig. 2. Efficiency vs. Voltage for various gas mixtures

The desire to operate in streamer mode with the least after-pulsing and current across the gap lead to a second study to determine if higher concentrations of freon are favorable. This study was done at Princeton

University. To quantify the operating point for comparison of various freon concentrations the knee of the efficiency plateau was defined as the voltage at which the extrapolated rising edge of the efficiency curve crosses the 90% level. This definition of the knee is shown in Figure 3.

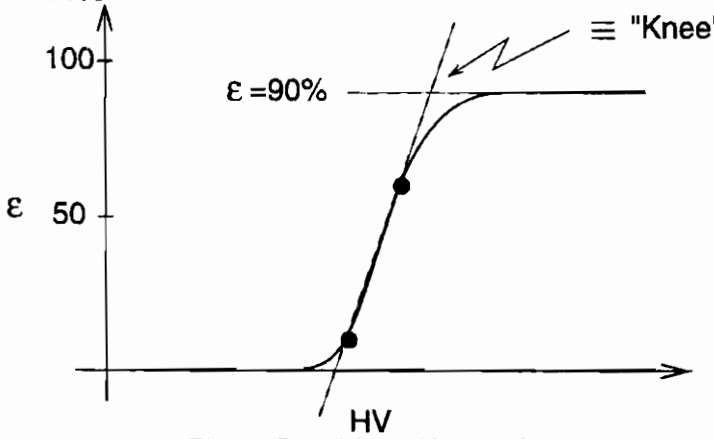

Fig. 3. Definition of knee voltage

In Figure 4 one can see how the operating point defined by the knee voltage increases with increased freon concentration. The knee voltage increases from 6.6kV to 10.5kV as the freon concentraton increases from 0 to 35%. For these tests the ratio of isobutane to argon was kept at 3/7 at a constant flow rate while the freon 116 flow rate was increased to give the quoted percentage.

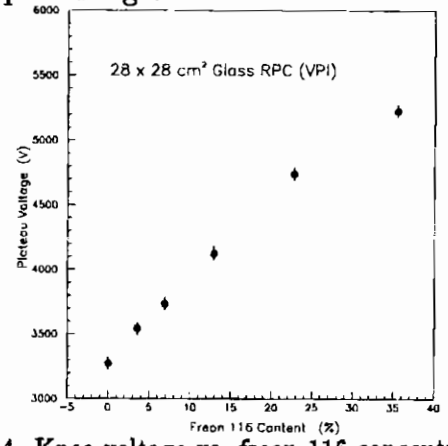

Fig. 4. Knee voltage vs. freon 116 concentration.

As the voltage is applied to an RPC the current increases approximately linearly until discharges begin to occur across the gap. This linear current is attributed to current through the spacers separating

the two sheets of glass. In Figure 5 the current is plotted as a function of the applied voltage. The current through the gap is defined as the difference between the total current and the extrapolated linear current at the knee voltage.

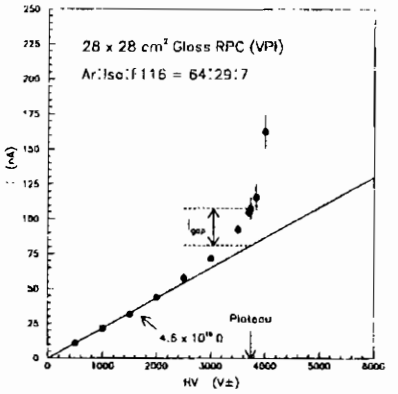

Fig. 5. Definition of the gap current.

This gap current is then plotted as a function of the freon concentration. Figure 6 shows that the gap current is reduced by adding some freon but that it does not decrease with increased freon concentration. Adding some freon reduces the pulse height significantly as shown in Figure 7.

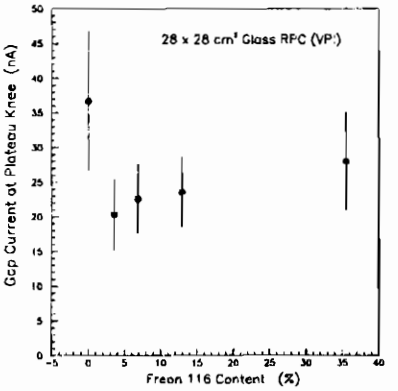

Fig. 6. Gap Current vs. freon 116 concentration.

The conclusion is that the RPC performance is very similar for the freon 116 concentrations that we tested. Increased freon concentration necessitates a higher operating voltage. The hoped for benefit of lower

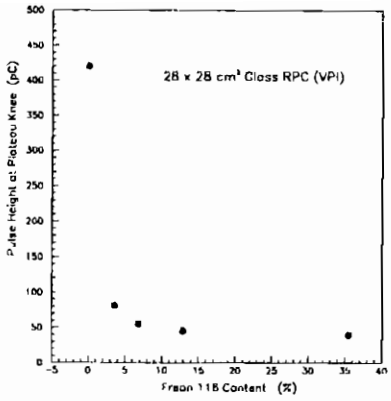

Fig. 7. Pulse height vs. freon 116 concentration.

gap current with additional freon quenching did not materialize.

3. Aging Tests

To date we have built fifteen 1 x 2 m^2 glass electrode RPCs. The electrodes are made of 2.4 mm thick soda-lime float glass with a resistivity of 5 x $10^{12}\Omega$ cm at 20°C and a dielectric constant of 5.7 measured at 1 MHz. The two sheets of glass are separated by 2 mm Noryl spacers attached with 3M 2216 epoxy. The high voltage is distributed on the outer surface of the glass by Koh-i-noor 3080F india ink with a surface resistivity of $10^5\Omega/\Box$. A schematic of the spacer layout is shown in Figure 8. The spacers are separated by approximately 12 cm and provide a channel for the gas to flow from the input near one corner back and forth across the total area of the RPC and then out at the other corner along the same edge. In the superlayer configuration all gas, HV, and signal connections are made at one edge of the superlayer. Two RPCs will be stacked on top of one another with staggered spacers to provide essentially 100% active area. The gas and HV for each RPC in the superlayer are provided independently.

We have chosen a gas mixture of 6% freon 116, 30% isobutane, and 64% argon for the following measurements. For this test the readout strips are 5 cm wide and 2 meters long with a 7 mm separation between the strip and the signal ground plane. Signals travel down 30 meters of 100 Ω twisted pair cable to a differential input discriminator. The output of the discriminator is sent to either a LeCroy 2277 and or 3377 multi-hit TDC. The efficiency, which is defined by a scintillator telescope

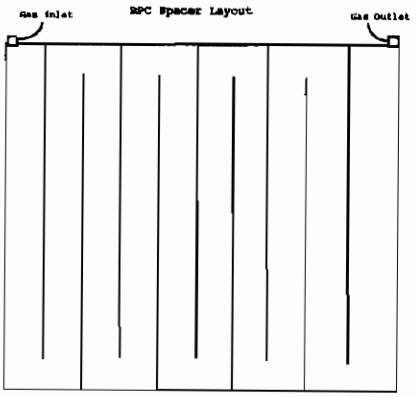

Fig. 8. Schematic of RPC spacer layout.

triggering on cosmic rays, is plotted as a function of the applied voltage in Figure 9. Typical single RPC efficiency is 92% with a wide plateau region.

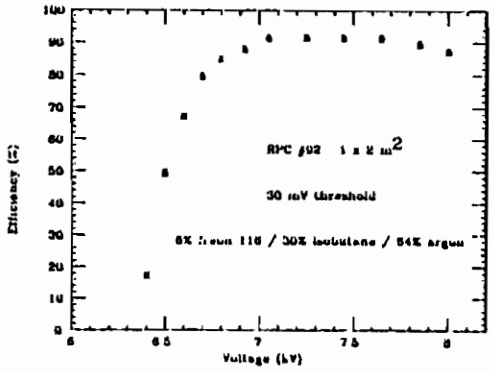

Fig. 9. Efficiency vs. Voltage.

The pulse induced on the external pickup exceeds 100mV. In Figure 10 the efficiency is shown as a function of the discriminator threshold. The efficiency begins to drop for thresholds above 80mV. This of course depends upon the gas mixture, the voltage, and the capacitance of the plates. The signals can be quite large making these counters relatively insensitive to extraneous noise . When operated in streamer mode they require no amplification.

Glass electrode RPCs are typically very quiet. The singles rate is not much more than the cosmic ray rate. Figure 11 shows the singles rate as a function of voltage for one RPC. The discriminator threshold

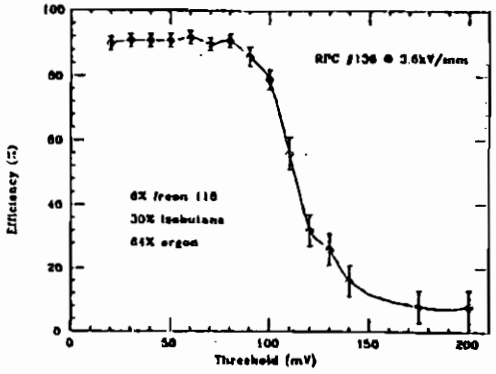

Fig. 10. Efficiency vs. Discriminator Threshold.

was set at 60mV with an output width of 120ns. The rise in singles rate at high voltage is due primarily to multiple pulsing of the initial streamer. In this case the singles rate at full efficiency is less than 250 Hz/m^2.

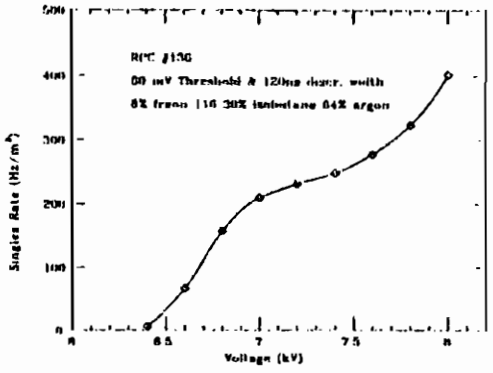

Fig. 11. Singles Rate vs. Voltage.

The current as a function of voltage is shown in Figure 12. As the streamers begin to develop the current increases but is typically of the order of $1\mu Amp/m^2$. The error bars shown indicate the fluctuations seen on a digital ammeter.

As of September 27, 1995 we have thirteen 1 x 2 m^2 glass RPCs which we are operating continuously as a long-term test of glass electrodes. The oldest counter has been operating for 39 weeks with no evidence of deterioration. Table 1 lists the number of weeks of operation, the beginning plateaued efficiency, and the latest efficiency measurement.

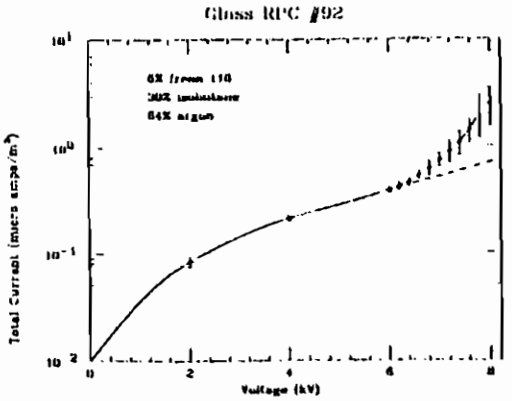

Fig. 12. Current vs. Voltage.

The typical current for each counter is shown, as well as the method of applying the conducting ink to the exterior surface of the glass. The efficiencies generally have improved over the weeks. This is probably attributable to a change of freon concentration from 4 to 6% and the gradual expulsion of residual air from the counters. Gas flow typically exchanges one volume of gas per day. Statistical errors on the efficiencies are 1%.

Table 1. Long-Term Testing of Glass Electrodes as of Sept. 27, 1995

RPC	Weeks	Eff_{begin}	EFF_{end}	Current	Ink
92	39	86%	92%	$1.0\mu A/m^2$	1 cm grid
123	22	85	92	0.9	1 cm grid
124	21	90	96	1.3	1 cm grid
126	21	89	93	1.4	solid
127	20	90	96	1.5	solid
128	18	88	95	0.7	1 cm grid
129	18	89	93	0.7	1 cm grid
130	16	92	95	0.7	solid
131	16	91	94	0.8	solid
134	15	89	94	0.7	0.5 cm grid
135	14	80	93	0.8	0.5 cm grid
136	14	89	96	0.9	solid
137	13	90	89	2.1	solid

Under the assumption that the aging of the RPCs is determined by the integrated charge passing between the plates, we are attempting to accelerate the aging process by irradiating RPCs. This study is being

conducted by Eric Prebys of Princeton University. The two RPCs are oriented vertically and readout front and back. A 70mCi Cobalt^{60} source is raised to irradiate two RPCs. At specified intervals the source is lowered by computer to allow an efficiency measurement using cosmic rays defined by a scintillator telescope.

A computer reads the currents, singles rates, and efficiency scalers. If we assume a baseline current of $2\mu A/m^2$ the increased current due to the source is approximately a factor of five. With this assumption after 45 days of irradiation we have almost 200 equivalent days of aging. Two difficulties in determining the baseline current for extrapolating to an accelerated aging rate are the presence of background radiation in the test area and variations in current due to temperature changes. The two RPCs tested show no deterioration to date. We plan to add twelve more RPCs and continue this accelerated aging test.

4. The Superlayer Design

The superlayer design of the barrel KLM system is shown in Figure 13. It includes two RPCs either of which generates signals on orthogonal pickup strips. These pickup strips act as transmission lines with approximately 50Ω impedance and vary in length from 1.5 to 2.7 meters. The strip width varies from 4.3 to 5.5 cm. The barrel region has 240 superlayer modules varying in size from 2.2 m x 1.5 m to 2.2 m x 2.7 m. The two glass RPCs are covered top and bottom with pickup strips and rigid foam and surrounded by an aluminum frame (see Figure 13). In the barrel region there are a total of 21888 pickup strip channels which will be time multiplexed into 1824 multihit TDCs.

The superlayer efficiency and singles rate as a function of voltage are shown in Figures 14 and 15. The efficiency typically plateaus at better than 99% and the singles rate is less than $600Hz/m^2$ at an operating voltage of 7.2kV with a discriminator threshold of 50mV.

With the RPCs used for the long-term test of glass electrodes we have a stack of four superlayers shown in Figure 16. Scintillators above and below the RPCs provide a cosmic ray trigger. We are presently reading sixteen 5 cm wide strips from each superlayer into LeCroy 2277 and 3377 multihit TDCs. With this setup we are able to track cosmic rays in one dimension. Additional electronics will provide two-dimensional tracking. The pickup strips are two meters long and are read out at one end through 30m of twisted pair cable into a discriminator.

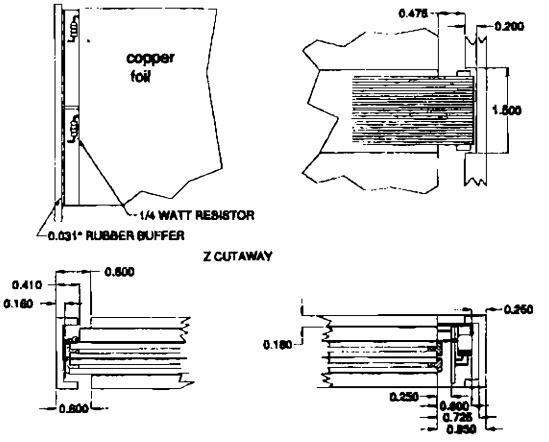

Fig. 13. Superlayer cross section

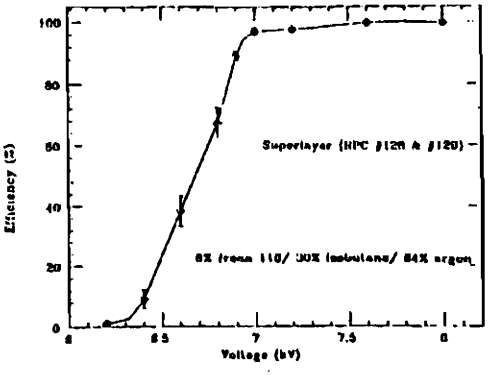

Fig. 14. Superlayer efficiency vs. Voltage

A TDC hit time distribution is shown in Figure 17. A small 10cm wide scintillator localized the triggered events and provided the reference time for the TDC. A gaussian fit to the data has a standard deviation of 2.8ns. This data was taken with the previously mentioned gas mixture, a threshold of 60mV, and an operating voltage of 7.2kV. More precise timing information is not needed for our application. The streamer development timing improves with increased electric field as is well documented elsewhere [3].

By calculating the centroid of the cluster of hits on each plane we are able to fit three planes to a straight line and calculate the difference between the expected location and the measured location at the fourth plane. This was done for each of the planes and a typical residual distribution is shown in Figure 18. The standard deviation of the gaussian fit is shown. Because of the 5 cm wide strips we are limited to a spatial

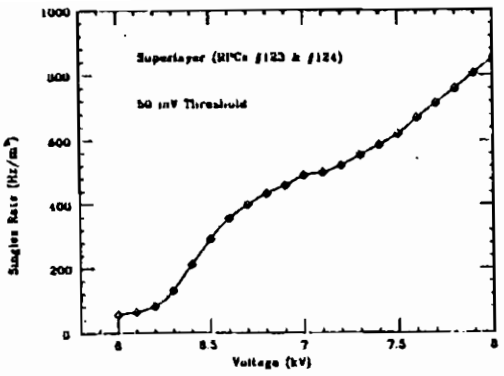

Fig. 15. Superlayer singles rate vs. Voltage.

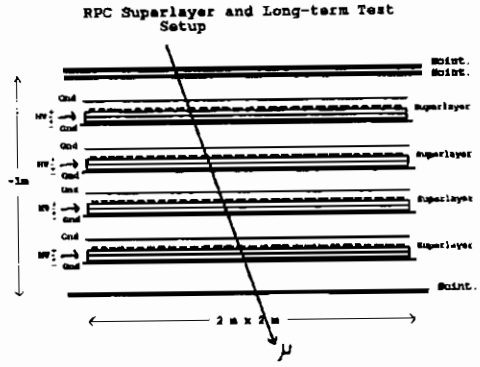

Fig. 16. Superlayer Test Setup

resolution of 2.5 cm which is more than adequate for muon tracking and K_L detection in the BELLE experiment.

5. Conclusions

We have built and tested dozens of glass electrode resistive plate counters with dimensions as large as 1 x 2 m^2. The performance of these counters has been good. They are stable with a wide range of gas mixtures and operating conditions. Double gap superlayers have demonstrated a greater than 99% efficiency for detecting cosmic rays. Long-term tests and accelerated aging tests have shown no deterioration after 1 year of operation. These tests are continuing. The results are encouraging and the technology appears to be well suited for the BELLE

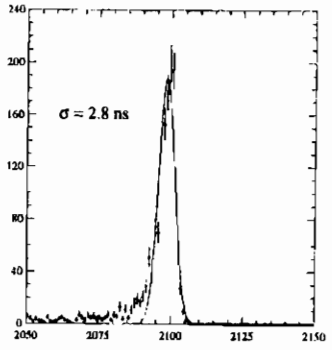

Fig. 17. Hit time distribution.

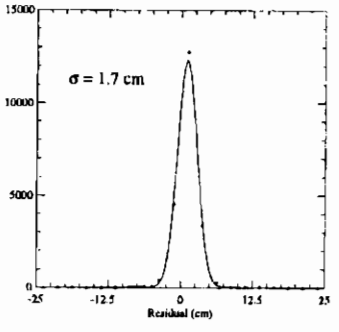

Fig. 18. Reconstructed spatial resolution for each of the four planes.

experiment. Production of the K_LMuon system for BELLE at KEKB is scheduled to begin in 1996.

6. Acknowledgements

This work is supported jointly by the Japanese and United States Governments. The KLM working group consists of physicists from Tohoku University, Tohoku Gakuin University, Osaka City University, Princeton University, and Virginia Polytechnic Institute and State University.

7. References

1. Technical Design Report for the BELLE experiment at KEKB.
2. M. Kobayashi and T. Maskawa, *Prog. Theo. Phys.* **49** (1973) 652.
3. M. Abbrescia et al, *Nuclear Instruments and Methods in Physics Research* **A336** (1993) 322. and N. Morgan et al, *Nuclear Instruments and Methods in Physics Research* **A340** (1994) 341.

Preliminary design of the BaBar detector for muons and neutral hadrons at PEP II

Nicola Cavallo *
INFN, Sezione di Napoli.
Pad. 20 Mostra d' Oltremare
I-80125 Napoli, Italy

February 13, 1996

ABSTRACT

BaBar experiment is aiming to the *CP* violation study in *B* decays. The RPC based system for μ detection and neutral kaons identification is introduced. Motivation and requirements are briefly reviewed and the general layout is described.

*co authors : C.Evangelista, A.Palano (INFN and University of Bari - Italy), R.Baldini, A.Calcaterra, R.De Sangro, M.Piccolo, A.Zallo (INFN LNF - Italy), I.Peruzzi (LNF and University of Perugia), A.Buzzo, R.Contri, G.Crosetti, R.Monge, S.Passaggio, C.Patrignani, M.G.Pia, A.Santroni (INFN and University of Genova - Italy), R.M.Bionta, K.van Bibber, T.J.Wenaus, D.M.Wright (LLNL - USA), G. Carlino, L.Lista, S.Mele, P.Paolucci, P.Parascandolo, D.Piccolo, C.Sciacca, (INFN and University of Napoli - Italy), J.R.Johnson (University of Wisconsin - USA)

1. Introduction

BaBar detector [1] has been designed to study CP violation asymmetries predicted by the Standard Model in B meson decays. It will be installed on PEP II e^+e^- storage ring machine [2], operating at the $\Upsilon(4S)$ resonance energy, providing a luminosity of $3 \times 10^{33} cm^{-2} s^{-1}$. Both the PEP II and BaBar commissioning are scheduled for the fall of 1998. The detector, as shown in fig. 1, consists of a Silicon Vertex Detector, a Drift Chamber, a Particle Identification System, a CsI Electromagnetic Calorimeter and a magnet with an Instrumented Flux Return (IFR) [3], consisting in a large iron structure acting as magnet return joke, with an iron thickness of 65 cm.

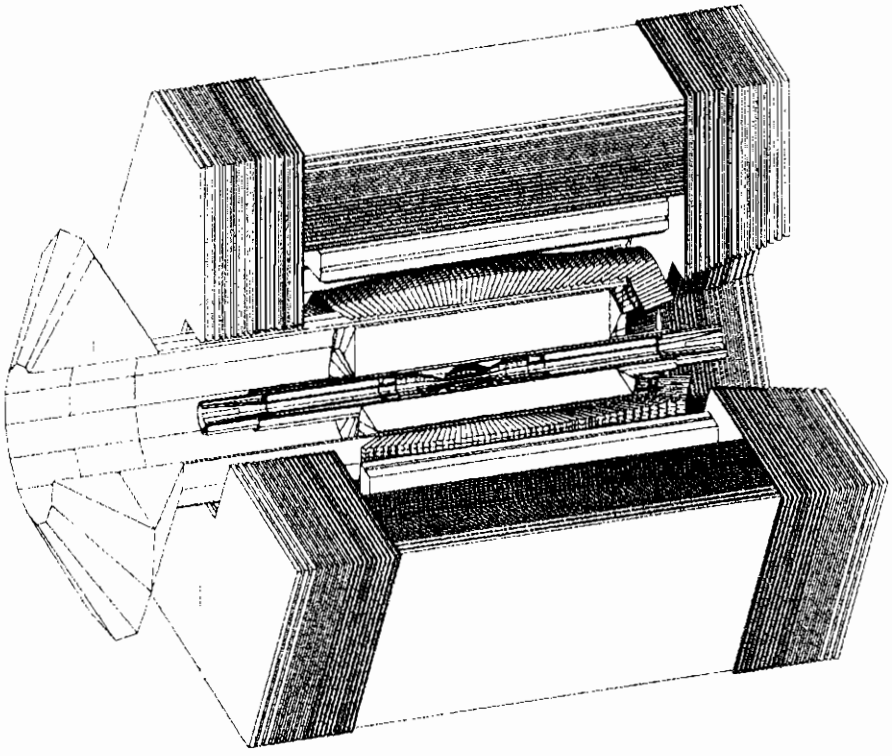

Figure 1: *Three-dimensional view of the BaBar detector.*

The IFR detector is based on Resistive Plane Chamber (RPC) technology whose task is to identify muons and detect neutral hadrons.

Muon are identified by range and hit topology in the IFR and by energy deposition in the central calorimeter detector. IFR also provides neutral hadrons (particularly K_L^o) detection. To achieve sensitivity down to momenta of 0.5 GeV/c, the IFR sub-detector is segmented into several layers of different thickness whose gaps are filled with RPC [4] as the active elements. RPC signals will be read alternatively by one or two planes of strips running in orthogonal directions, so that mono or bi-dimensional informations are provided.

In the following paragraphs a brief review of the physics motivations and requirements for IFR are described. The most important aspects of the design providing the general layout of the detector are then shown with particular emphasis to RPCs. A short description of electronics is given, assembly and installation procedures are illustrated. A preliminary review of R&D activities is also reported.

2. IFR Motivations and Requirements

The primary physics goal of the BaBar experiment is the systematic study of CP asymmetries in decays of the B^o and $\bar{B}^o$ into CP eigenstates. However BaBar will explore the wide range of other B physics, charm and τ physics, two-photon and Υ physics, which will become accessible with the high luminosity of PEP-II.

In order to achieve the required sensitivity for CP measurements it is very important to reconstruct the B^o decaying into a wide range of exclusive final states with high efficiency and low background and to tag the flavor of the other B meson in the event with high efficiency and purity. The most important requirements are solid angle coverage, charged particle momentum resolution, particle identification, photon resolution and detection efficiency.

There are three substantial ingredients of the CP-violating asymmetries measurement: vertex reconstruction, flavor tagging and exclusive state reconstruction. Those requirements affected design criteria and motivates particular choices in individual sub-detectors.

Muon identification and neutral hadron detection is provided by the Instrumented Flux Return, which makes use of the large iron structure needed as the magnet return yoke. At the $\Upsilon(4S)$, muons are produced mostly in semileptonic decays, either directly from the B or from the cascade D's. The sign of their charge determines the "b" or "c" flavor of the parent meson, thus providing a clean tagging for the CP asymmetry

measurements.

Therefore an important goal for the IFR detector is to achieve the highest practical tagging efficiency. Identification as muons or hadrons will result from detailed analysis of the hit patterns in the active detectors. To achieve a high tag efficiency it's necessary to detect low momentum μ's, to reduce hadron contamination and to assign them to "*direct*" or "*cascade*" classes.

Muons reaching the IFR have a momentum range from 500 MeV/c to 3-4 GeV/c and excellent μ identification over the widest possible momentum range is therefore required.

Optimization studies performed by full Montecarlo simulations have dictated a fine iron segmentation and the final design consists of 18 iron layers with graded thickness. In the Barrel region, the system has an additional cylindrical RPC layer inside the solenoid minimum radius.

The ability to detect K_L^o's will allow the study of the *CP* asymmetry in the channel $J/\Psi K_L^o$, thus providing an additional consistency check compared with the $J/\Psi K_S^o$ channel. The K_L^o momentum spectrum is between 1 and 3 GeV/c and it appears quite flat. To benefit of this additional decay channel an efficient identification of K_L^o with a reasonably good angle measurement is imperative. It is worthwhile to note that also in K_L^o detection, efficiency improves as segmentation increases.

3. Detector design and layout

3.1. The Iron Structure

The muon and neutral hadron detector uses as an absorber the flux return iron of the 1.5 Tesla superconducting solenoid.

The iron plates design has taken into account both the requirements dictated by its use as hadron absorber and muon filter and the complex mechanical problems concerning the access to the inner detectors, all subject to the space constraints imposed by the machine components and the experimental hall.

The IFR consists of three main components: the Barrel and the Backward and Forward Endcaps. The Barrel extends radially from 1.82 to 3.04 m and is divided into sextants; the length of each sextant is 3.75 m, and the width varies from 1.90 to 3.35 m. Each Endcap consists of hexagonal plates, divided vertically into two parts to allow opening of

the detector and has a central hole for the beam components and the magnetic shields.

The plates are tied together by side steel plates whose thickness (5 cm) reduces the area available for the active detector. The dead area is concentrated at the joining of the hexagonal blocks and accounts for a small loss in solid angle. The Endcap gaps are divided in three sectors by stiffeners needed to prevent bending due to the magnetic forces and to limit the stress due to mechanical and potential seismic loads. A view of the detector is shown in fig. 1.

As already said, the iron segmentation is dictated by the physics requirements of identifying low-momentum muons and detecting K_L^o's. In the Barrel the plate thickness is graded from 2 cm for the inner plates to 10 cm for the outer ones. The structure consists of nine plates 2 cm thick, followed by four plates 3 cm thick, three plates 5 cm thick and two plates 10 cm thick. The total iron thickness is 65 cm and is the result of a compromise between cost, which scales with the volume, and the need to reduce hadron punchthrough.

In both Endcaps the graded iron structure consists of a sequence of nine 2 cm, four 3 cm, four 5 cm and one 10 cm plates for a total thickness at 60 cm.

3.2. Resistive Plate Chambers as Active Detector

Particular care has been taken in the choice of the active detector. Due to the limited accessibility, a very high reliability is needed. The large area to cover and different shapes to be used imply low costs and a flexible device, with high efficiency and very low noise.

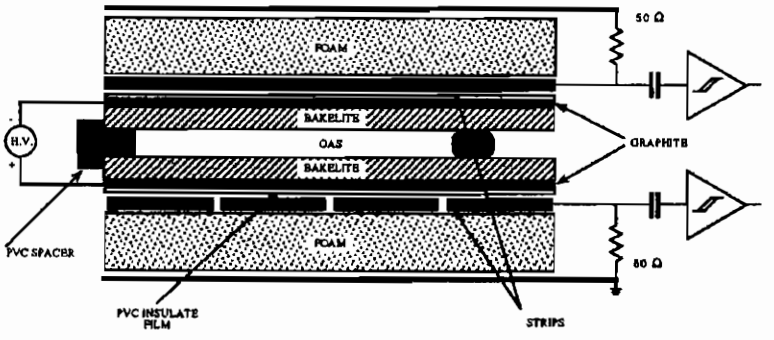

Figure 2: *RPC gap structure.*

Resistive Plate Counters (RPC) (fig.2) have proven to represent a real mature technique providing very high detection efficiency together with great simplicity of construction and operation, at low cost. Further benefits of RPC are fast time response (short pulse risetime), large pulse signals, excellent time resolution (few nsec), good spatial resolution (few millimeters), possibility of large scale industrial production, possibility of easy instrumentation of large areas, maximizing the geometric coverage with various shapes.

The RPC choice has been additionally motivated by the experience that part of the IFR group has gained in the L3 muon trigger implementation, where excellent results have been achieved in reliability and good spatial and time resolution in a 600 m^2 RPC system [5].

4. The Active Detector Coverage

The IFR detectors will cover a surface of approximately 2100 m^2; with 19 RPC layers in the Barrel and 18 in the Endcaps.

Several RPC modules will be joined together to fill each active layer. In the Barrel each gap will be filled by three 1.25 m wide RPC modules with the other dimension ranging between 1.90 and 3.35 m. In the Endcaps, each half door will be filled with 6 modules of trapezoidal shape.

Due to the great interest in RPC production for the new LHC collider experiments, the factory we used for the L3 experiment [6] is approaching a new capability of RPC mass production, increasing the maximum size from 100×200 cm^2 to 130×320 cm^2.

We benefit of this improvement to minimize the total number of modules, reaching a total of to 774 units, 342 for the Barrel and 432 for the Endcaps. Active coverage, test and installation time, improvement in gas and H.V. distribution, as the total cost, obviously will benefit of large module sizes.

Since in the Barrel muon bending measurement is done only using ϕ strips, spatial resolution on z strips it less demanding. In order to reduce the total number of strips, and the corresponding electronic channels to readout, a choice has been taken to alternate planes in which both the coordinate readouts are available (i.e. ϕ and z for the Barrel as long as x and y for the Endcaps) with planes in which only one coordinate is supplied with electronics (i.e. ϕ for the Barrel and x or y in the Endcaps), as shown in fig.3,4.

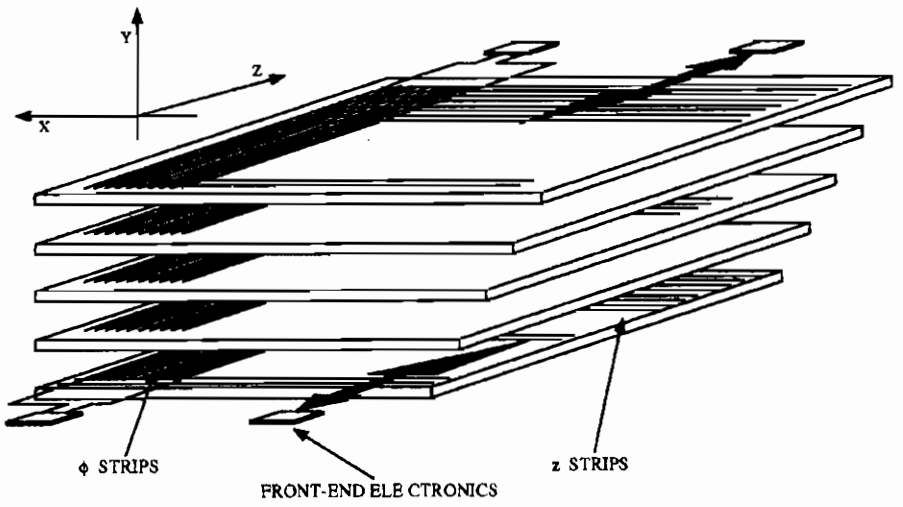

Figure 3: *Barrel strip distribution.*

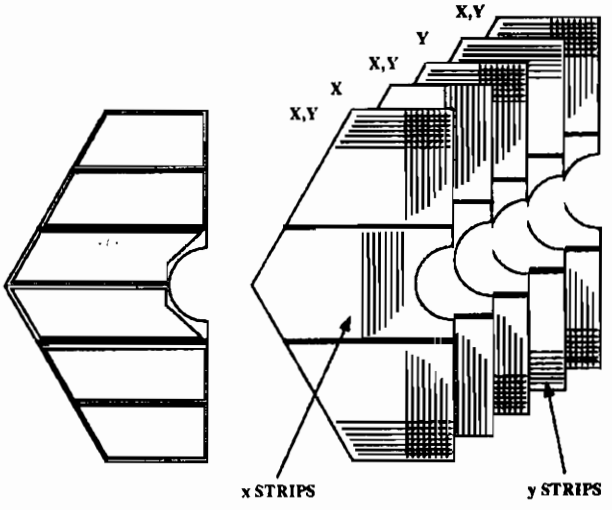

Figure 4: *Endcap strip distribution.*

IFR will have a total number of about ~42,000 strips, ~17,000 for the Barrel and ~12,000 for each Endcap. The first number has been evaluated using a constant number of strips for each Barrel layer, 96 ϕ and 96 z, increasing the ϕ pitch (roughly between 2 and 4 cm) when going from the inner to the outer plane, with a constant z pitch of 3.8 cm. This choice optimizes, at the same time, both the readout performances and the front-end electronics allocation.

5. Electronics and ancillary systems

As the RPC is a noiseless detector, in which the rate is fully dominated by cosmics, and the rate of particles reaching the IFR is relatively low, rejecting unwanted data as soon as possible is not as important as collecting data very rapidly. Buffering during the trigger latency is unnecessary because the probability of having two hits on the same strip during this time is close to zero. Strip signals are thus stored during the latency of the trigger decision ($11.5 \pm 0.5 \mu s$), stretching them and using a fast readout electronics to read the front-end within the proper time.

The electronics system for the IFR must perform the following functions: it must record detected signals during trigger latency; it has to download data on trigger basis from front-end, buffer them, and transfer them to the DAQ modules. In order to do this, IFR Electronics has been conceived in three main part: discriminator cards with serial readout (front-end electronics); FIFO buffer boards on detector and multiplexed readout after trigger.

The first modules (front-end) will operate very close to the detector in the iron gaps; the second module (FIFO Buffering Board) will be on the outside of the detector itself and accessible without opening the Endcaps, while the last one (Read-Out Module) will be on the electronic trailer. A block diagram of the proposed architecture is shown in fig.5. The final design of the front-end cards is available, and the design of the other components is in an advanced stage.

The excellent timing properties of RPCs ($1 \div 2$ ns) could also be exploited. IFR particle detection, in fact, can benefit very much of time measurements in order to improve μ/π separation, noise and beam halo rejection, pattern recognition and cosmic veto together with bunches identification, which are 4.2 ns apart. These kind of measurements could also help to monitor the detector quality both during initial commissioning and data taking phases.

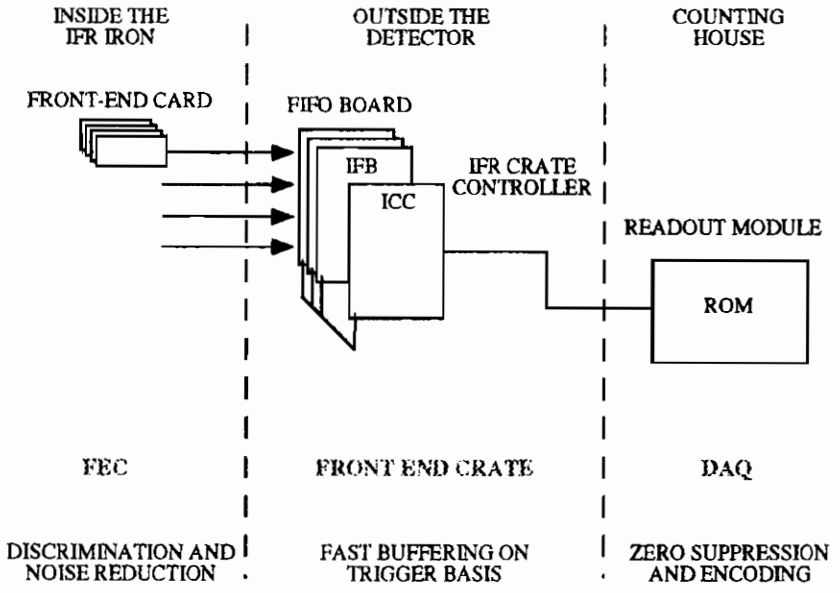

Figure 5: *IFR general electronics scheme.*

High voltage will be individually fed to each RPC module through series resistors (20 MΩ); provision will be made for measuring and recording individual currents drawn from the detectors.

6. Final Assembly, Installation, and Monitoring

The major components of the IFR detectors (RPC modules, readout strips, and the front-end electronics boards) will be manufactured in Italy and shipped to SLAC for final assembly. All modules will be extensively tested with cosmic ray muons using, as pick up electrodes, the final z strips for the Barrel and the horizontal strips for the Endcaps. The shipments will extend over an 8-month period with approximately 200 modules per shipping.

At SLAC, after acceptance tests, the modules corresponding to a given IFR layer will be placed side by side on a pallet, then joined along their frames with plastic film to form a single IFR detector plane. Full-length readout strips, complementary to the ones already in position, will be laminated across the modules of the detector plane.

Front-end electronics cards will be mounted on the edge of the detector, accessible from the open end of the Barrel. For ϕ planes, the

3.75 m-long ϕ readout strips will be soldered through a single wire to the front-end electronics cards laying on top of RPC's, inside the gap between iron plates. On the z planes, the z strips terminate at the edge of the detector plane that is buried inside the IFR, so ribbon cable will be attached to the ends of the strips and folded at right angles to bring the signals out to the front-end electronics cards.

The completed detector plane, on its pallet, will be inserted into a cosmic ray tower for detailed tests of the efficiency of each channel, using components of the BaBar data acquisition system. After final testing, the completed detector plane will be slid off the pallet into the appropriate gap between the IFR plates of each sextant or half door, which will be then moved to the interaction region. During commissioning and data taking, the efficiency of the IFR detector planes will be monitored reconstructing cosmic muons.

7. Conclusions

Active R&D is ongoing to select a nonflammable and environmentally safe gas mixture.

Test with different gas mixtures using Tetra-fluoro-ethane (CF_4), Sulphur Hexafluride (SF_6) and Carbon Dioxide (CO_2) have been carried out. Single rates, dark current, efficiency (absolute and long range stability values), molteplicity, amplitude distribution and time resolution have been studied as a function of operating high voltage.

The final choice has not been taken, but various alternatives have been identified. In the next figures 6 and 7 same results with different gas mixtures are reported.

8. Bibliography

1. D.Boutigny *et al.*, "BaBar Technical Design Report", SLAC-R-95-457 Report, March 1995.
2. PEP II - Conceptual Design Report, Report SLAC-418, June 1993.
3. Chapter 8 in reference ref. [1].
4. R. Santonico et al, Nucl. Instr. Meth. **187** (1981) 377;
   R. Cardarelli et al, Nucl. Instr. Meth. **A 263** (1988) 20.
5. S.Patricelli *et al.*, proceedings of the "International Workshop

on the RPC in Particle Physics and Astrophysic", Rome 1993, Scientifica acta, v.8, n.2 (1993);
A.Aloisio *et al.*, Nucl. Instr. Meth. **A360** (1995) 340;
A.Aloisio *et al.*, Nuclear Phys. B, **44**, (1995) 417;
R.de Asmundis *et al.*, These Proceedings;
P.Paolucci *et al.*, These Proceedings.
6. General Tecnica srl, Colli (Frosinone) - Italy.

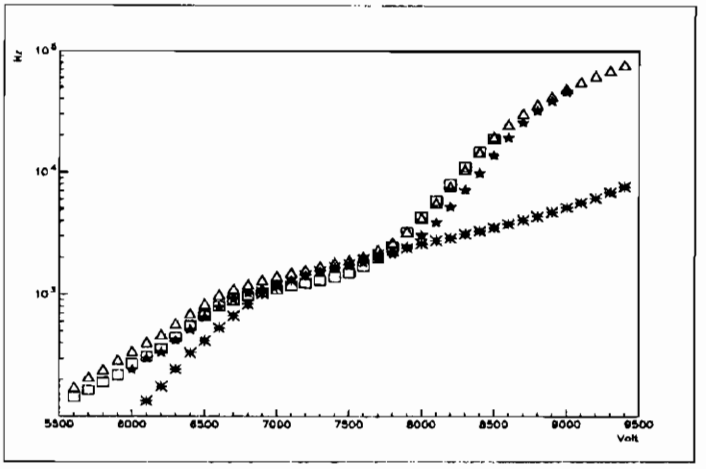

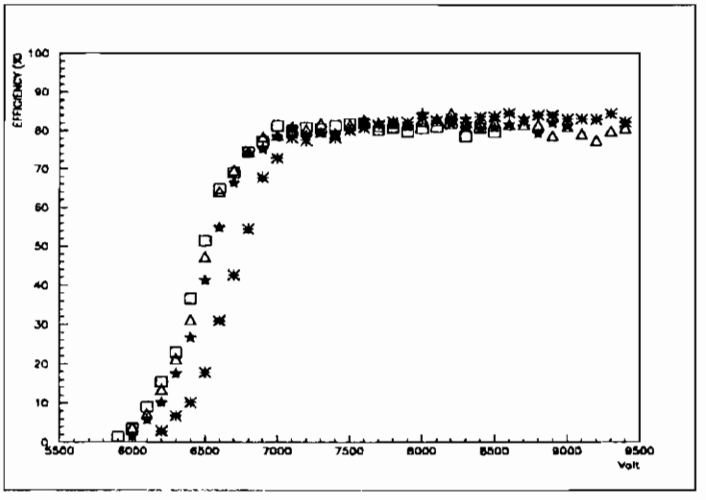

Figure 6: *Single rate and Efficiency .vs. HV:* □ *Argon 58 % + Isob 39 % +* CF_4 *3 %,* △ *Argon 57 % + Isob 38 % +* CF_4 *5 %,* ⋆ *Argon 55 % + Isob 35 % +* CF_4 *10 %,* ∗ *Argon 58 % + Isob 39 % +* $R13B1$ *3 %.*

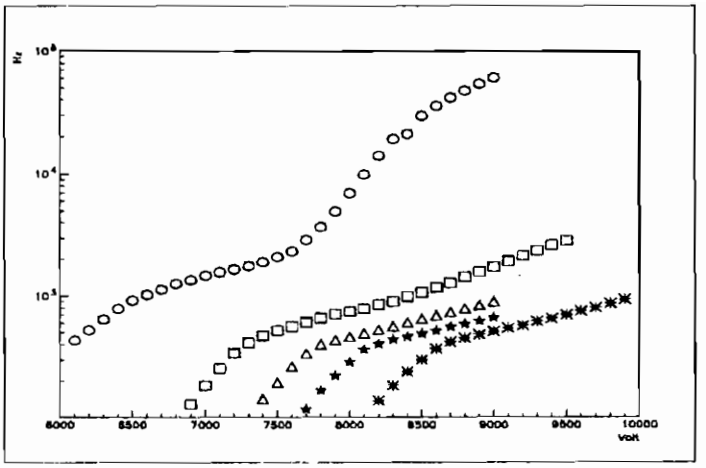

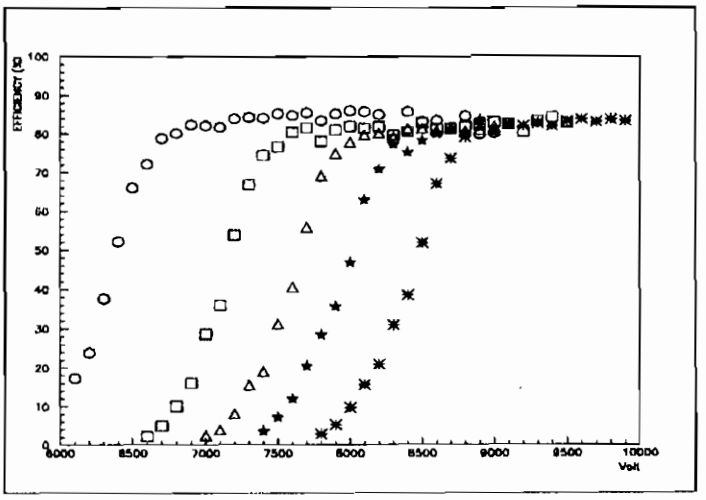

Figure 7: Single Rate and Efficiency .vs. HV: ○ Argon 60 % + Isob 40 %, □ Argon 59 % + Isob 40 % + SF_6 1%, △ Argon 59 % + Isob 39 % + SF_6 2%, ⋆ Argon 58 % + Isob 39 % + SF_6 3%, ∗ Argon 57 % + Isob 38 % + SF_6 5%.

The RPC Forward-Backward trigger system of the L3 experiment

Pierluigi Paolucci *
INFN, Sezione di Napoli.
Pad. 20 Mosta d' Oltremare
I-80125 Napoli, Italy

February 6, 1996

ABSTRACT

In view of LEP200 physics, the L3 detector has been upgraded installing the Forward-Backward muon spectrometer to increase the angular acceptance in muon detection. The trigger system layout is based on 192 Resistive Plate Counters (RPC) covering an area of 300 m^2. We describe the production, test and installation of the whole trigger system.

*co authors : A. Aloisio, M.G. Alviggi, G. Carlino, N. Cavallo, R. de Asmundis, V. Innocente, L. Lista, S. Patricelli, D. Piccolo, C. Sciacca

1. Introduction

Muon detection in the L3 experiment at LEP [1] was achieved by the barrel spectrometer in the polar angular region $44^\circ \leq \theta \leq 136^\circ$. The Forward-Backward (F/B) spectrometer extends the muon detection in the angular regions $22^\circ \leq \theta \leq 44^\circ$ and $136^\circ \leq \theta \leq 158^\circ$ and it is essential for the future analysis at LEP200.

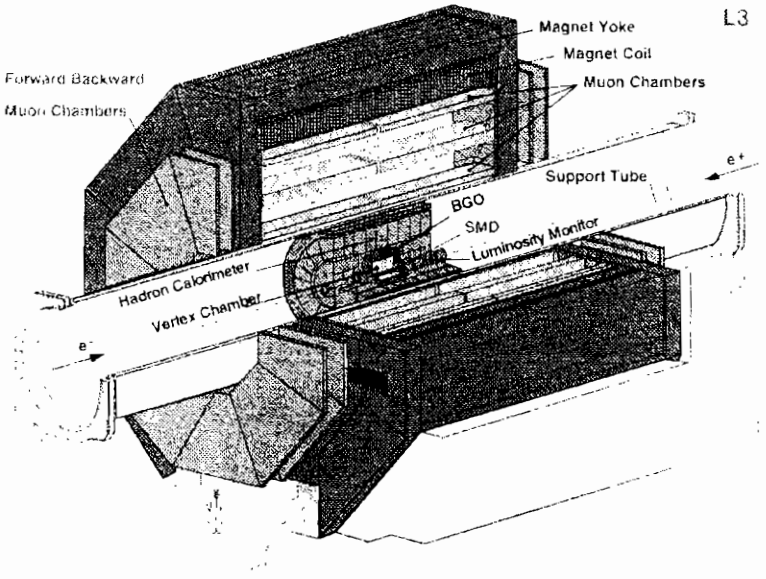

Figure 1: *The L3 detector.*

The F/B detector consists of three layers of precision drift chambers (FI, FM, FO) mounted on each magnet doors which are toroidally magnetized. The whole detector has been installed for the LEP running in 1995. Figure 2 shows the side view of the F/B detector and the definition of the Solenoidal (S region $36^\circ \leq \theta \leq 44^\circ$) and Toroidal region (T region $22^\circ \leq \theta \leq 36^\circ$). In the S region the muon are reconstructed by MI, MM and FI chambers and the trigger is provided adding the information given by the FI chamber to the system already used in the barrel. In the T region muons are deflected by the toroidal magnetic field and the momentum is analyzed by the FI, FM and FO chambers. Trigger is provided by a system of Resistive Plate Counters choosen for

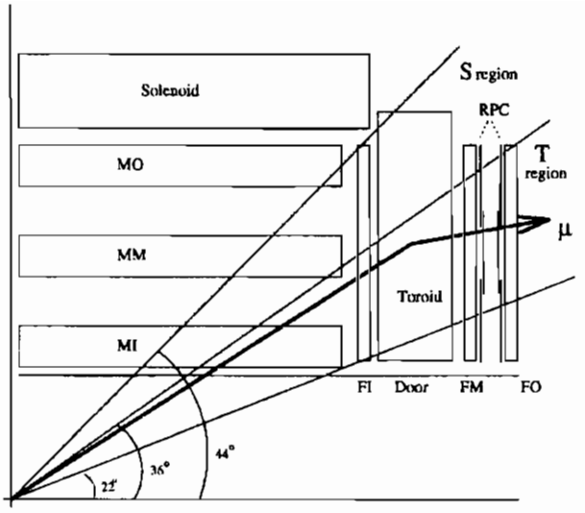

Figure 2: *Cross section of the L3 F/B muon detector.*

their fast time response, high efficiency and the possibility of large scale industrial production.

2. Resistive Plate Counters

An RPC is a particle detector utilizing a constant and uniform electric field produced by two parallel electrode planes made of a material with high bulk resistivity. The RPC used in L3 was developed by Santonico et al. [2], it consist of two indipendent counters superimposed on each other in the same mechanical structure with independent H.V. and single pickup plane (fig. 3). The electrode plates are made of 2mm tick backelite (phenolic polymer) with a volume resistivity of $\simeq 10^{11}\Omega cm$ painted with graphite and covered by two $300\mu m$ PVC insulating planes. The sensitive volume is a 2 mm tick gas gap between the electrodes operating in the limited streamer region under a uniform electric field of about 4 kV/mm. The gas mixture used is: Argon 58 % + Isobutan 38% + Freon 4%.

When a charged particle crosses the detector, the primary electrons by the ionization process in the gas generate a discharge. The discharge is quenched by the following mechanism:

- UV photon absorption by Isobutane

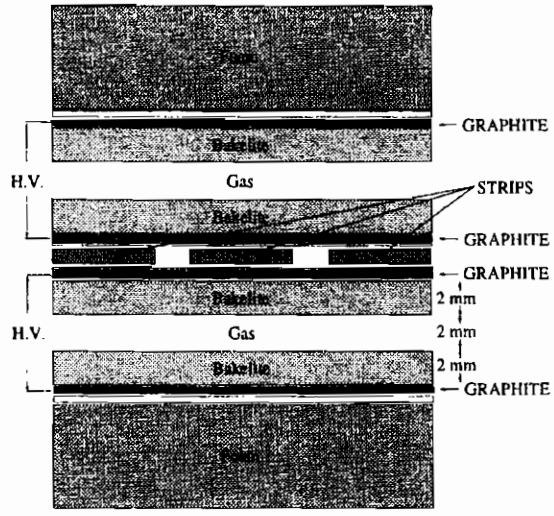

Figure 3: *Cross section of the internal structure of the RPCs.*

- capture of the outer electrons by Freon to reduce the size of the discharge.
- switching off of the electric field around the discharge point, due to the high resistivity of the electrodes.

The duration of the discharge is $\simeq 10ns$ while the relaxation time of the resistive electrodes is $\tau = \rho\epsilon \simeq 10^{-1}sec$, so that during the discharge the electrode plates behave like insulators and a small area around the impact point shows a dead time of the order of τ.

3. System layout

In the L3 F/B muon system [3], each drift chamber of the FM and FO planes is equipped with one layer of RPC. The two drift chambers are joined by a truss structure and the RPCs are located on the inner surfaces of the chambers. Drift chambers, frames and RPCs were prepared as one rigid unit in production and as such mounted on the magnet door (fig. 4). The total number of these sectors (half octant) are 32. Each layer of RPCs is composed of three trapezoidal units: L(large), M(Medium), S(Small). Readout strips are perpendicular to the octant center line; in every octant there are 96 strips per layers. The total RPC counters is 192 for a total of 6144 readout strips.

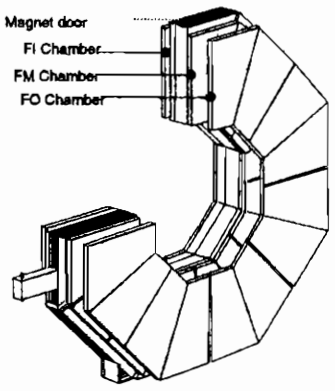

Figure 4: *Expanded view of the F/B muon system. The RPCs are placed between the FM and FO drift chambers.*

4. The RPC trigger system

The RPC system provides the level-1 muon trigger for the Toroidal region of the F/B detector [4]. Muons coming from the interaction vertex hit the two RPC planes after traversing 1m of magnetized iron (fig. 5). The trajectory in the space between the FM and FO planes is a straight line and its slope depends on the polar angle θ, momentum p and charge sign.

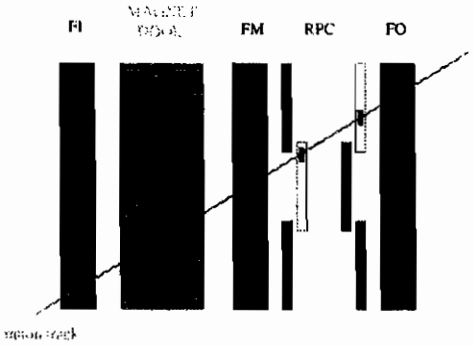

Figure 5: .

If we create a coincidence matrix with 96 FM strips on the X axis and 96 FO strips of the same octant on the Y axis we find that muons populate roads whose width depends on their momentum. Figures 6 and 7 shows the good agreement between data and MonteCarlo trigger matrix.

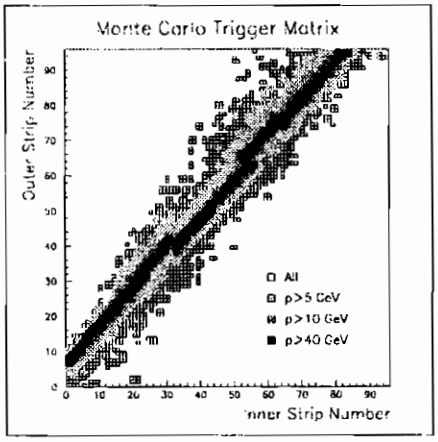

Figure 6: *MonteCarlo simulation of the Trigger matrix for muons with different momenta at the vertex.*

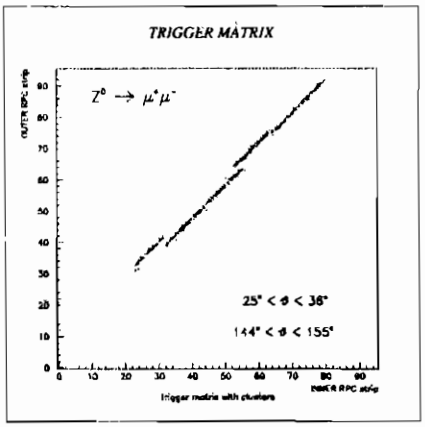

Figure 7: *Trigger Matrix with L3 1994 dimuon data.*

For every octant, the signal of corresponding strips of the same layer are ORed and sended to the *Zero-suppressor and encoder* VME modules

(fig. 8). These modules, strobed by the beam gate, send the address of the fired strips to the *Track-finder and trigger generator.* Each T.F. is responsible for the detection of the coincidences, between the fired strips in the two layers, inside a predetermined road of the Trigger Matrix. The road is programmed, depending on the run condition, using the information from the MonteCarlo simulation. If a coincidence is found, a trigger signal is generated in a typical time of theorder of $1.5\mu s$.

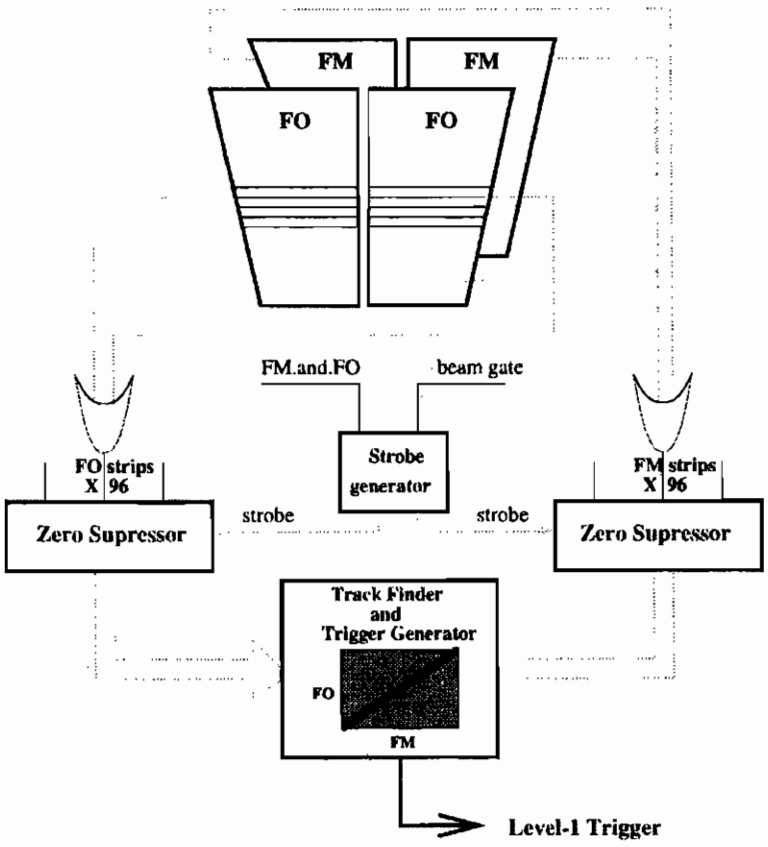

Figure 8: *Trigger schematics for one octant.*

5. RPC test and installation

During the past years, several RPCs of the same type used in the trigger system have been extensively tested in our laboratory in Naples using cosmic rays tracked by a telescope. All the RPCs have been built

at General Tecnica (Italy) with a production rate of about 2.5 RPC/day. These, after a first simple test, were transported periodically to CERN where they were carfully tested in a test station. The test station is formed by two scintillator planes, used to trigger cosmic rays, and 9 slots where are placed the RPC to test. The principal test made are:

- Gas leak
- Single counting rate (strip per strip).
- Single counting rate (Fast-OR).
- Detection efficiency.
- Time and spatial resolutions.

Every module, consisting of 2 layers of RPC (6 RPC) and 2 drift chambers, was built and tested with cosmic rays at CERN. From the efficiency curves (*plateau*) we choose the HV value of the modules. The whole system is working with only four different HV values.

6. Front-End electronics

Induced pulses on readout strips are discriminated and amplified by fast transistors whose outputs drive directly TTL electronics. The front-end electronics is based on the scheme developped by Cardarelli et al. modifed to be mounted on SMD boards. The SMD boards were build by CAEN and tested on RPC in Naples. Each board accepts input from 16 strips and produces shaped outputs (200 ns differential TTL) for fired strips. The board also provides a fast-OR signal of the 16 strips. This signal has a fan-out of three: one output (ECL diff.) is sent directly to an 1875 Le Croy TDC channel for time measurement, another (ECL diff.) is used to generate an early signal for the trigger processor and the last one (NIM) is used for monitoring purposes.

7. Zero-Suppressor and encoder

96 logical OR signals from strips in each plane (FM and FO) in each octant are sent to Zero-Suppressor. A total of 32 modules are needed for the whole system. The strobe to this modules can be chosen between the

beam crossing pickup and the beam crossing pickup in coincidence with the logical AND of the FM and FO planes. Output of this module consist of 8 bits words, one for each strip, containing encoded information of its number and plane, transmitted to the next module via a dedicated bus. The data are encoded and transmitted typically in 800 ns. This module was designed, developped and built in Naples.

8. Track-Finder ad Trigger Generator

The two Zero-suppressor and Encoder Modules for FM and FO planes of the same octant transmit their output data to the Track-Finder module. This module is the responsible for detecting a coincidence between two strips in the two planes that are include in the roads of the Trigger Matrix. Each cell of the Trigger Matrix is mapped into one of the 96 x 96 locations of a 2 bit RAM. Total time of trigger generation is less than $1.5\mu s$.

9. Conclusions

Half F/B system has been installed before the start of the 1994 LEP run and the whole system before the start of the 1995 LEP run. Today, after two years of data tacking and analysis data, we can say that the RPC trigger system operated immediately and the expected performances were reached.

10. Acknowledgments

We wish to express our gratitude to all members of the f/b hardware group and in particular to Prof. U.Becker and Prof. K.Freudenreich

11. Bibliography

1. B.Adeva *et al.*, Nucl. Instr. and Meth. **298** (1990) 35.
2. R. Santonico et al, Nucl. Instr. Meth. **187** (1981) 377;
   R. Cardarelli et al, Nucl. Instr. Meth. **A 263** (1988) 20
3. U.Becker, L3 Forward-Backward Muon Detector, L3 internal note, Dec.3, 1991

4. S.Patricelli *et al.*, proceedings of the "International Workshop on the RPC in Particle Physics and Astrophysic", Rome 1993, Scientifica acta, v.8, n.2 (1993);
G.Carlino *et al.*, proceedings of the "4th International Conference on Advanced Technology and Particle Physics", Como 1994, Nucl. Phys. B. 44 (1995) 417;
D.Piccolo *et al.*, proceedings of the "6th Pisa meeting on Advanced detectors", Isola d'Elba 94, Nucl. Instr. and Meth. A 360 (1995) 340.

Performances of the RPC Trigger System in the L3 experiment

Riccardo de Asmundis *
INFN, Sezione di Napoli.
Pad. 20 Mostra d' Oltremare
I-80125 Napoli, Italy

January 12, 1996

ABSTRACT

We describe the performances of the RPC used as trigger for muon detection in the angular region $22^\circ \leq \theta \leq 36^\circ$ and $144^\circ \leq \theta \leq 158^\circ$. The detector efficiency and both the spatial and time resolutions have been measured. Estimation of trigger efficiency will be reported too. The analysis has been performed on a data sample of about 1000 dimuon events selected in the 1994 LEP runs using the muon tracks reconstructed in the TEC and the information provided by the Forward–Backward drift chambers. In 1994 only half of the system was installed. We will describe run conditions for 1995 runs too and we will discuss some preliminary results about them.

*co authors : A. Aloisio, M.G. Alviggi, G. Carlino, N. Cavallo, V. Innocente, L. Lista, P. Paolucci, S. Patricelli, D. Piccolo, C. Sciacca

1. Introduction

The RPC trigger system of L3 experiment at LEP [1] provides the specific trigger capability for the Forward-Backward (F/B) spectrometer [2]; this spectrometer covers the angular region $22^\circ \leq \theta \leq 36^\circ$ (T region) with respect to the beam axis. The F/B detector consists of three layers of precision drift chambers (FI, FM, FO) mounted on each magnet door which is toroidally magnetized. Two layers of RPCs are assembled outside the magnet door between the FM and FO chambers and apply topological constraints in order to select muon tracks coming from the interaction point.

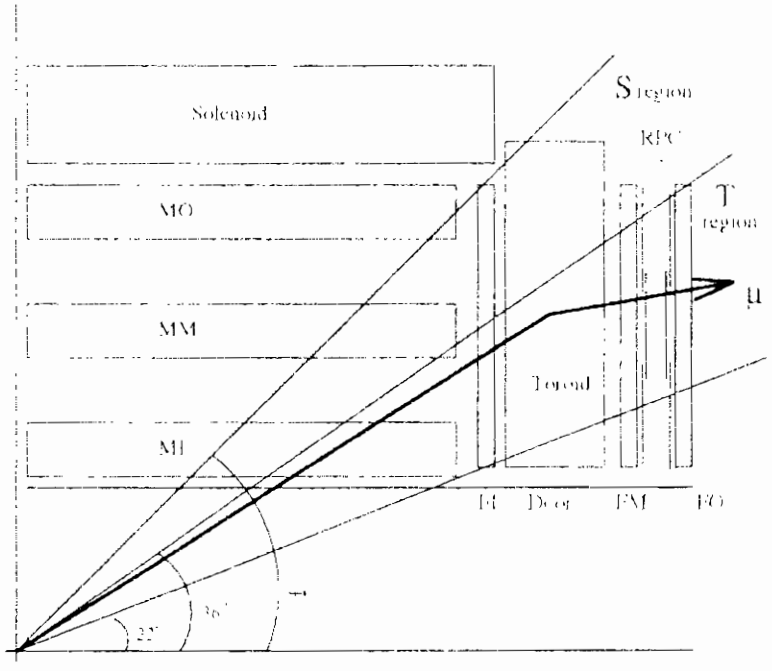

Figure 1: *Cross section of the L3 F/B muon detector.*

Figure 1 shows the side view of the F/B detector and the definition of the Solenoidal (S region, $36^\circ \leq \theta \leq 44^\circ$) and Toroidal regions (T region, $22^\circ \leq \theta \leq 36^\circ$), in which the RPC trigger system is active.

For more details about RPCs used in L3, cfr. [3].

RPCs performances are presented in the following items:

- RPC spatial resolution
- Intrinsic detector efficiency
- Trigger efficiency
- Detector stability
- Time resolution
- Comparison between 1994 and 1995 running conditions
- Bunchlet tagging capabilities

2. RPC Spatial Resolution

To study the spatial resolution of the RPC we group together all the adjacent fired strips in order to define a cluster. The number of strips in the cluster gives the cluster multiplicity.

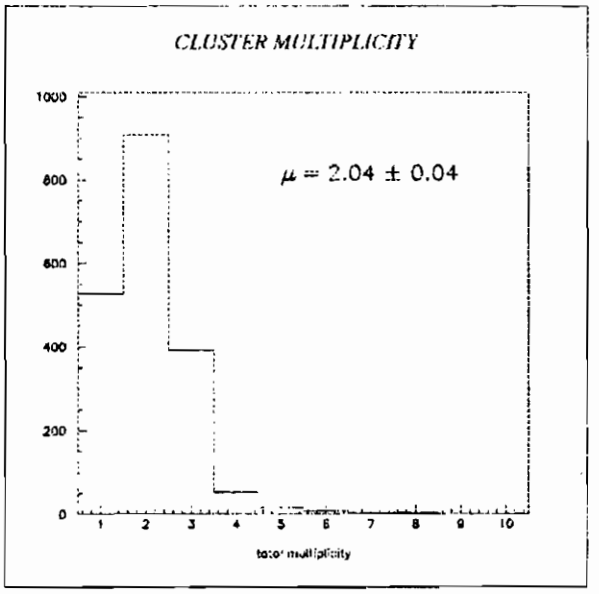

Figure 2: *Multiplicity distribution of the RPC clusters.*

A cluster is associated to a muon track if the distance between its center of gravity and the impact point of the track on the RPC plane is

lower than a given tolerance. This tolerance is chosen according to the cluster multiplicity.

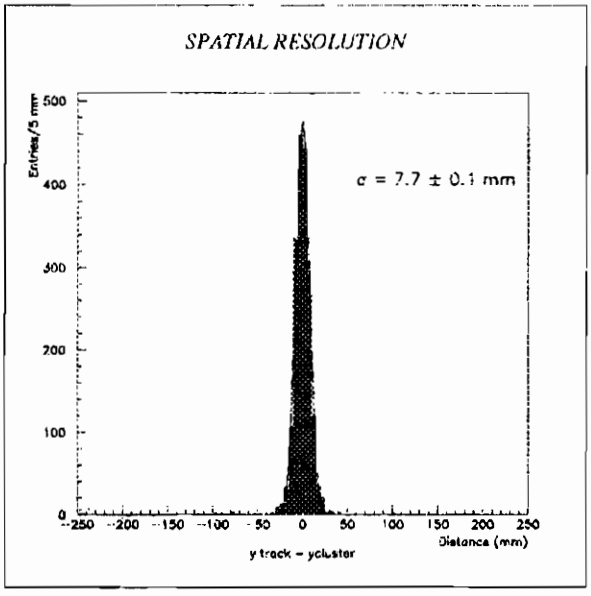

Figure 3: *Distance between the center of the cluster and the track reconstructed with the drift chambers.*

Fig. 2 shows the multiplicity distribution of the clusters associated to the muon tracks. The averaged cluster multiplicity is $\mu = 2.04 \pm 0.04$. In fig. 3 is plotted the distribution of the distance between the center of gravity of the clusters and the impact point of the corresponding muon tracks on the same RPC plane after having corrected the relative position of the RPCs with respect to the drift chambers. The spatial resolution we obtain is $\sigma = \mathbf{7.7 \pm 0.1 mm}$.

The same distributions for events with cluster multiplicity one, two and three are shown in fig. 4. The resolution decreases with the multiplicity: $\sigma(\mu = 1) = 6.1 \pm 0.2$ mm, $\sigma(\mu = 2) = 7.8 \pm 0.2$ mm, $\sigma(\mu = 3) = 8.8 \pm 0.4$ mm.

The cluster multiplicity is correlated to the tracks impact point on the strips. Fig. 5 shows the distribution of these impact points in the local reference frame of the strips taking the origin in their center. As it can be seen, tracks hitting the strips on their edges have an higher

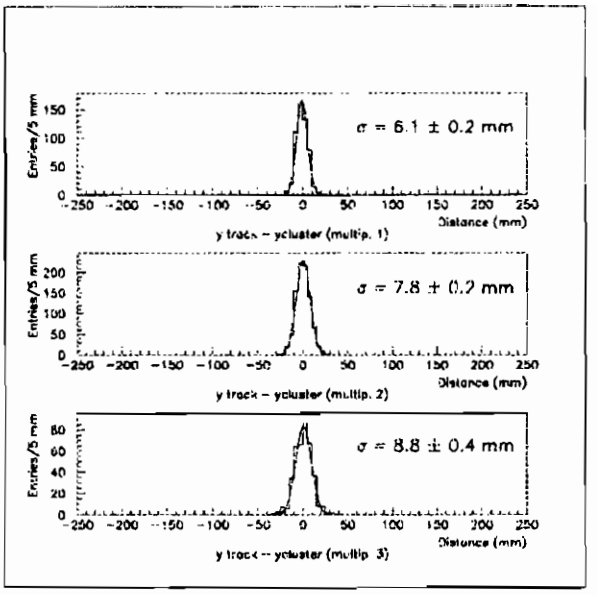

Figure 4: *Distance between the center of the cluster and the track reconstructed by the drift chambers for different cluster multiplicity.*

probability to induce signals on the neighbouring strips.

3. RPC Detector Efficiency

An RPC plane is efficient if, for each muon track, at least one associated cluster is found. More than one cluster can be associated to the track on the same plane because of the overlapping between RPC counters of different sizes.

To measure the detection efficiency we need a sample of well reconstructed muon tracks in order to perform a correct matching between tracks and RPC clusters. We select, for this reason, only the tracks reconstructed using more than 20 hits in the FM-FO segment.

The efficiency is defined as:

$$\epsilon = \frac{N_{FM} + N_{FO}}{2N_t} \tag{1}$$

where N_t is the number of selected tracks and N_{FM} (resp. N_{FO}) is the number of tracks with at least one cluster associated in the FM (resp.

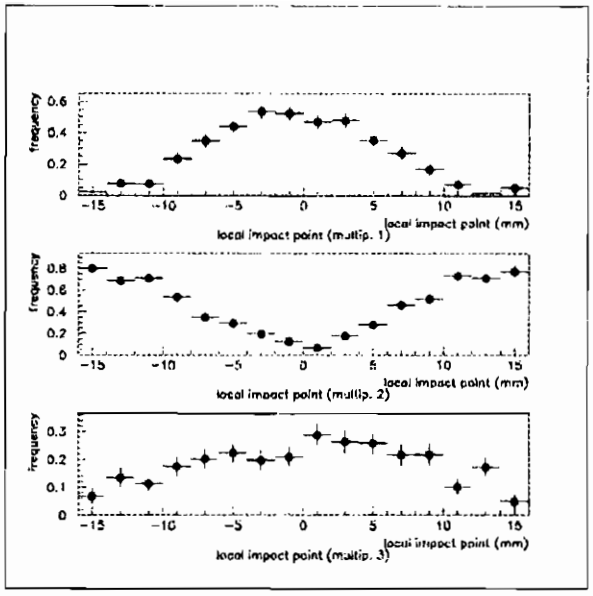

Figure 5: *Distribution of the position of the track in the direction orthogonal to the strips for different cluster multiplicity.*

FO) plane. The detection efficiency we found is $\epsilon = \mathbf{99.50 \pm 0.05\%}$.

4. Trigger Efficiency

Two kinds of global RPC trigger efficiency have been estimated, namely the single track trigger efficiency and the single + dimuon trigger efficiency. In the former, RPC trigger system is efficient if we find a trigger in the correspondig couple of RPC layers hitted by a muon track; single tracks only are taken into account and a double muon event is trated as two single muon tracks. In the latter, RPC trigger is efficient if we find either a single-side (same condition as before) or a "dimuon" trigger fired or both of them fired together. All these three trigger flags come from different logics in the level 1 trigger circuitry, so different algorithms are applied to them. We only watch if one of these way gave a trigger under the expected conditions.

We found for the Single muon trigger $\epsilon = \mathbf{98.3\% \pm 0.4\%}$.

The combined "Dimuon + Single" trigger presents an efficiency of $\epsilon = \mathbf{99.8\% \pm 0.2\%}$.

Trigger efficiency has been stable during 1994 runs as showed in

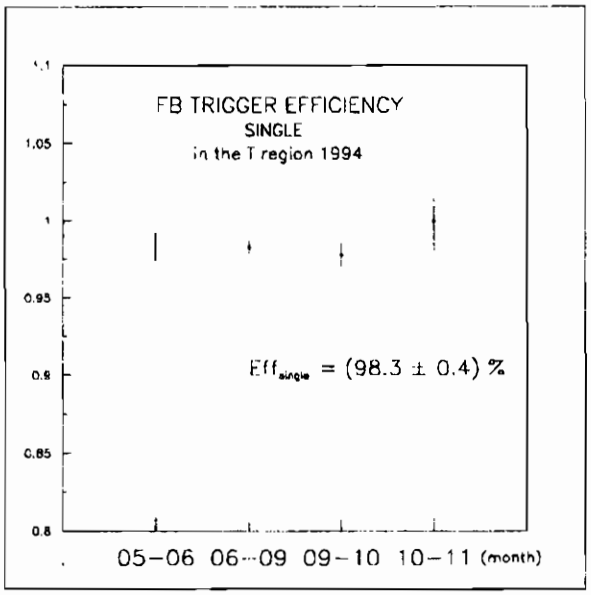

Figure 6: *RPC trigger efficiency all over 1994 runs (single efficiency).*

figures 6 and 7.

5. Detector Stability

Plot of the dark rate averaged on the whole system is shown in figure 8. This sample has been collected over about 16 months of running. Structures present in the plots come essencially from pressure and temperature variations, while we are confident in a gas mixture stability within $\sim$ 1% relative. Spikes are due to beams loosing during LEP operation.

The reduction of dark activity in RPC detector did not infuence the global trigger efficiency as one can see by comparing fig. 8 and 6- 7.

6. Time Distribution

The time distribution, without any correction applied, of the clusters associated to the muon tracks is shown in fig. 9 for the RPCs on the Master and Slave side. Due to the differences in the signal cable lengths, signals coming from different channels show a spread in the time distri-

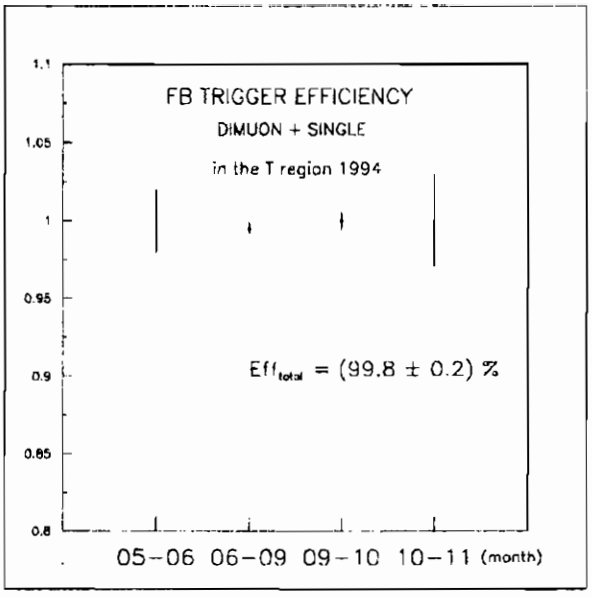

Figure 7: *RPC trigger efficiency all over 1994 runs (single+dimuon efficiency).*

bution. This T_0 offset is fitted channel by channel using the selected dimuon events.

The time distribution has to be corrected also for the propagation time of the signals along the strips. We subtracted to the measured time the interval $\Delta T = \Delta x / v_p$ where Δx is the distance between the impact point of the track and the edge of the strip, and v_p is the propagation velocity of the signals along the strip. The velocity v_p has been measured performing a fit to the data. In fig. 10 is shown the distribution of the times associated to the RPC clusters as a function of the coordinate of the tracks impact points on the strip. The result of the fit is $v_p = \mathbf{20.8}$ **cm/ns.**

The time distribution of the RPC signals after the T_0, the time of propagation and the time of flight corrections is shown in fig. 11. A resolution of **2.16 ns** is achieved.

7. 1995 Running Conditions

On 1995 LEP changed its operational mode by introducing a "bunch

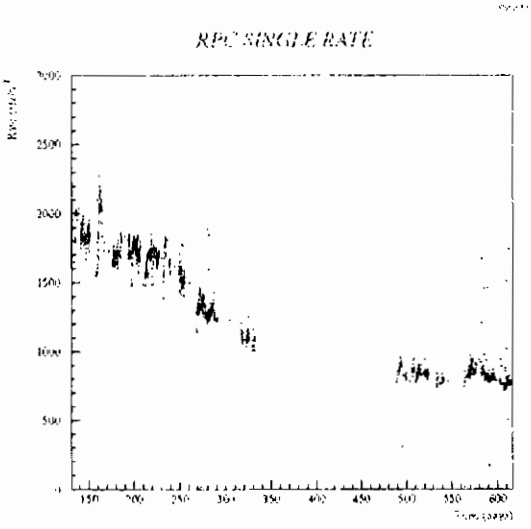

Figure 8: *Averaged value of dark activity of RPCs.*

train" technique. Singles leptons bunches have been substitued with groups of four "bunchlets" (the trains). A total of four trains per beam has been used with an inter-crossing time of 22 μs and 247.5 ns of inter-bunchlet time. Some hardware modification has been necessary on the RPC trigger system in order to accomodate this new mode. A new Programmable Logic Unit (PLU, a VME module) [4] has been designed and assembled.

In the previous year (1994) the beam crossing signal from the machine acted as a reference signal to lock the current situation of fired strips on the system (see fig. 12): strip status (fired/not fired) were strobed into a set of Zero Suppressor boards on the trailing edge of that signal. Zero Suppressors have a dead time of the order of 1 μs that does not allow multiple strobe within the inter-bunchlet time so that a direct application of this procedure whould be not compatible with the new machine running conditions. To overcome this problem we used the fast coincidence signal of an FM-to-FO plane. See fig. 13.

These signals are immediately available to us on some fast NIM electronics and they are affected by circuits propagation time only (typ. of few nanoseconds). The strobe to the whole system is now conditioned by the presence of at least one fast coincidence between corresponding

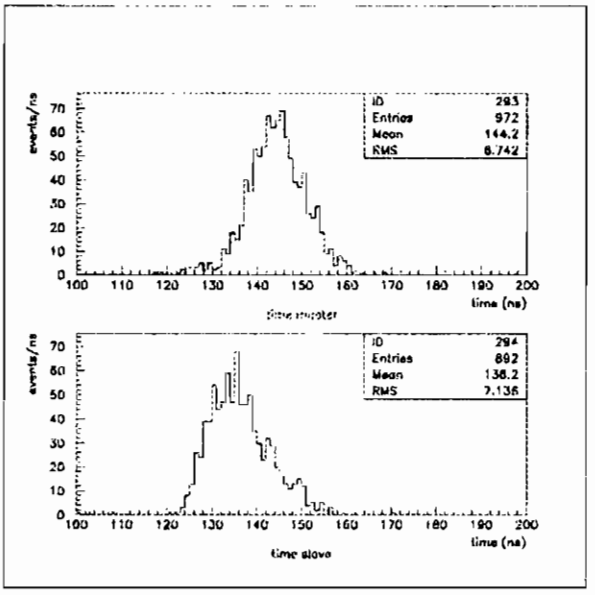

Figure 9: *Time distribution of the RPCs signal on master and slave side.*

FM-FO planes.

The described operation is repeated four times in order to reproduce the timing sequence during the four bunchlet crossing. Figure 14 shows the internal generation of the signal sequence. Obviousely a strobe signal can be generated only one time during a train crossing, i.e. during the 22 μs of interval.

Figure 15 shows a typical time spectrum coming from RPC with LEP in bunch-trains mode.

8. Bunchlet Identification

Bunchlet identification and tagging comes from PLU by encoding the cycle number (from 1 to 4) which gave a strobe. This information is sent to L3 second trigger level and reaches the global data acquisition system. Correlations between this tagging and from some other equivalent but independent source of bunchlet tagging have been studied in order to verify the reliability of the former.

Fig. 16 shows the correlation between PLU tagging and corresponding entry in the total timing RPC spectrum: on vertical scale we enter

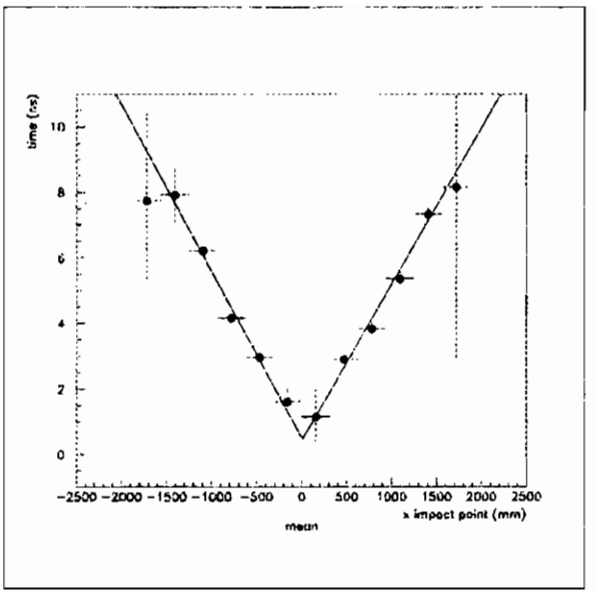

Figure 10: *RPC time versus impact point coordinate of the track along the strip.*

with the index coming from PLU, while on horizontal we represent, in binary code, the peak of fig. 15 on which the corresponding RPC timing is falled. So horizontal values are 1 if the current time falled on the first peak, two on the second, four on the third, eight on the fourth. Box plot shows a quite good correlation between these two sources of bunchlet tagging.

Fig. 17 presents correlation between PLU tagging and level3 final tagging. Level 3 trigger comes from a great numbers of complex algorithmes taking into account informations from several subdetectors. The raw PLU tagging is in perfect agreement with the final level 3 tagging.

9. Conclusions

The RPCs during the first two years of run have shown good performances. For 1994 runs a detection efficiency of 99.5% is achieved; The corresponding trigger efficiency has reached 99.8% on the total FB trigger and 98.3% on the single muon.

Detector performances show no degradation with time, even if RPC dark activity is falling down.

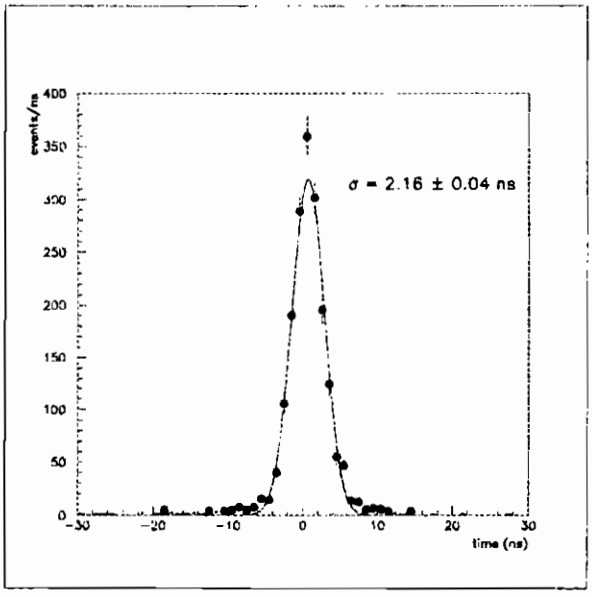

Figure 11: *RPC time distribution.*

Although the width of the strip is 3.1 cm, using the center of gravity of the cluster to measure the muon position on the RPC planes, we got a spatial resolution of 7.7 mm.

A time resolution of 2.16 ns is achieved. The time information can be used to reject cosmic rays by measuring the time of flight of the muons and by comparing time to bunchlet identification coming out from PLU.

Modifications on electronics for 1995 running conditions have been succesfully achieved and bunchlet tagging shows a good reliability.

10. Bibliography

1. B.Adeva *et al.*, Nucl. Instr. and Meth. **298** (1990) 35.
2. U.Becker, L3 Forward-Backward Muon Detector, L3 internal note, Dec.3, 1991
3. S.Patricelli *et al.*, proceedings of the "International Workshop on the RPC in Particle Physics and Astrophysic", Rome 1993, Scientifica acta, v.8, n.2 (1993);
   G.Carlino *et al.*, proceedings of the "4th International Conference on Advanced Technology and Particle Physics", Como 1994;

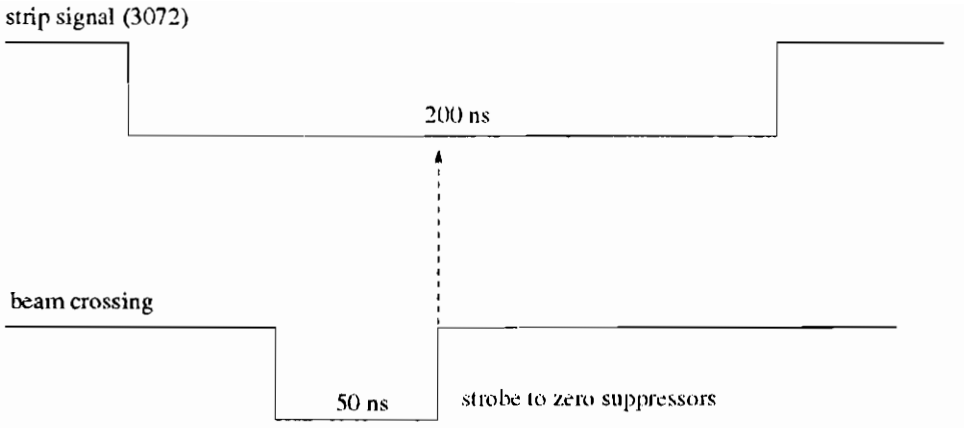

4/8 bunches operation mode

Figure 12: *Timing diagram of 1994 strobing mode.*

Nucl. Phys. B 44 (1995) 417-422;
D.Piccolo *et al.*, proceedings of the "6th Pisa meeting on Advanced detectors", Isola d'Elba 94, Nucl. Instr. and Meth. A360 (1995) 340-344;
G. Carlino *et al.*, "RPC performances at L3 Experiment", L3 internal note n. 1811;
G. Carlino *et al.*, "1994 Forward-Backward trigger efficiency", L3 internal note n. 1867;
P. Paolucci *et al.*: this proceeding;

4. M.G. Alviggi *et al.*, INFN/TC-95/15 (INFN internal note, March 22nd 1995)

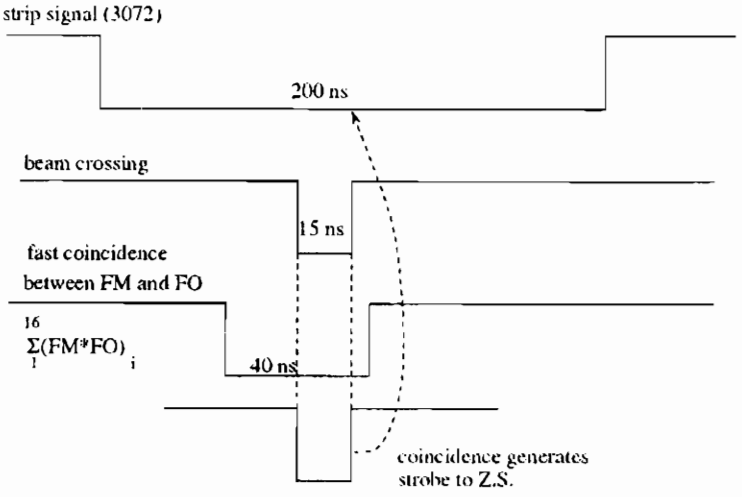

operation mode 1995 runs

Figure 13: *Strobe generation since 1995 runs.*

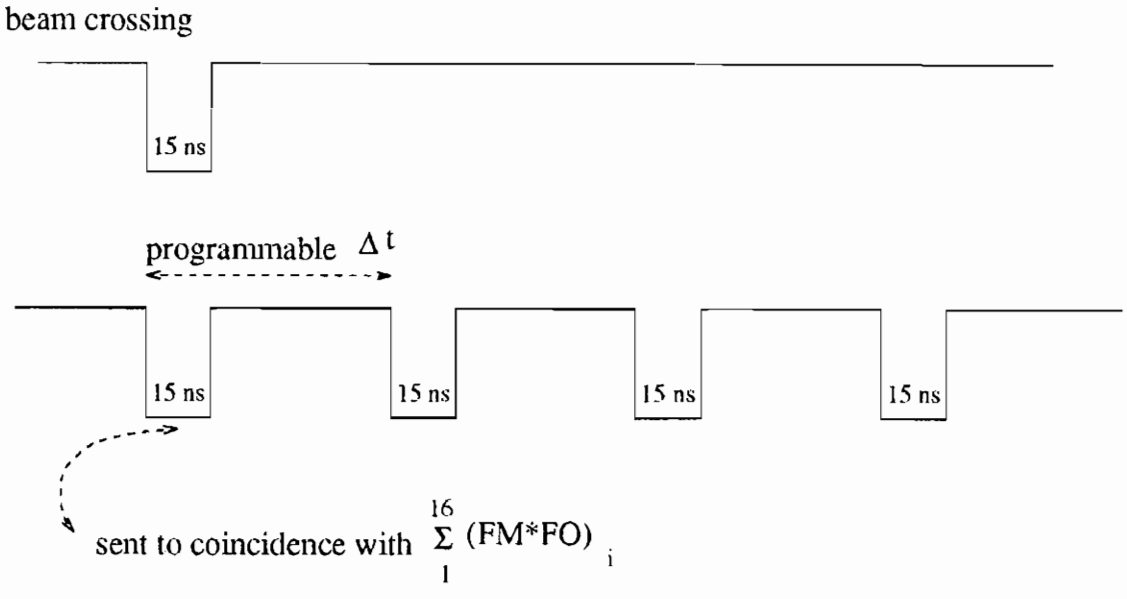

Figure 14: *Cycle of the looking-for-strobe sequence.*

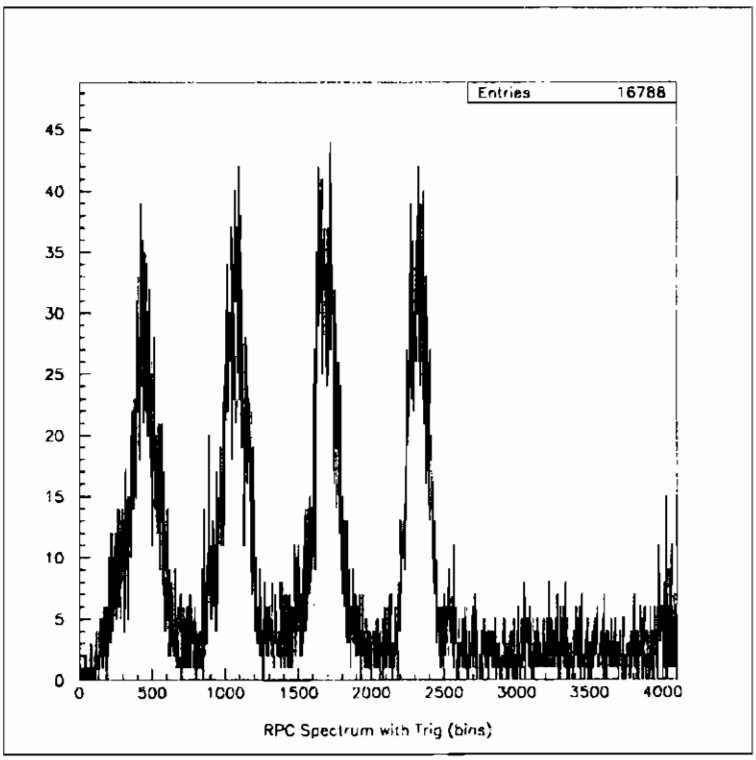

Figure 15: *RPC time spectrum in bunchtrains mode.*

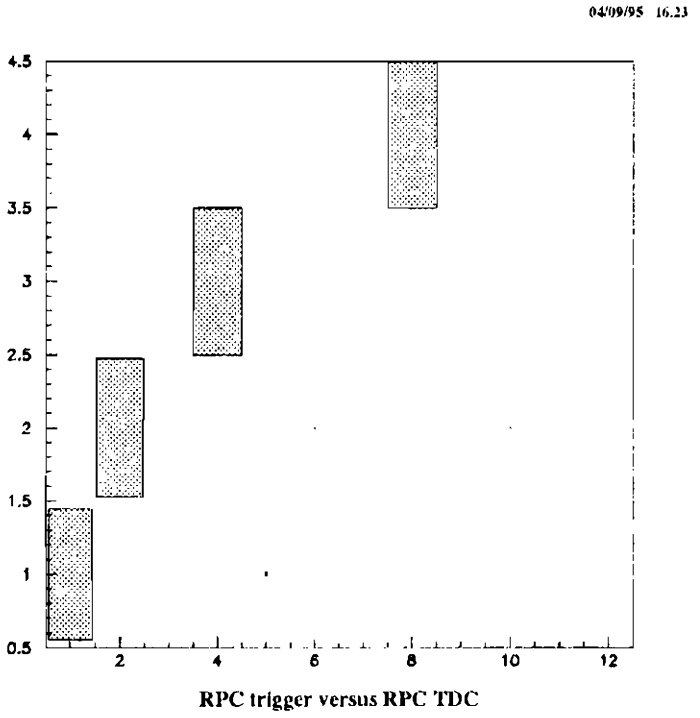

Figure 16: *Correlation between PLU tagging and RPC timing informations.*

USE OF RPC IN THE COVER–PLASTEX EXPERIMENT

G. AGNETTA[1][2], M. AMBROSIO[2], C. ARAMO[2][3], G.C. BARBARINO[2][3], B. BIONDO[1][2], O. CATALANO[1][2], L. COLESANTI[1][2], A. ERLYKIN[2][4], A. LAURO[2], A. MANGANO[1][2]

[1] *Istituto di Fisica Cosmica e Applicazioni dell'Informatica - CNR, Palermo, Italy.*
[2] *Istituto Nazionale di Fisica Nucleare, Naples, Italy.*
[3] *Physics Department - Naples University, Naples, Italy.*
[4] *P. N. Lebedev Physical Institute - Moscow, Russia.*

ABSTRACT

Resistive Plate Counter (RPC) have been used for the first time in Extensive Air Shower (EAS) physics with the COVER_PLASTEX experiment in Haverah Park, near Leeds, U.K., for precise arrival time measurements of particles in the shower front. For this purpose a new front-end electronics has been developed and an accurate investigation on RPC performances and pick-up characteristics has been performed. Measurements of noise, cross talk, after-pulses phenomena and detector saturation have permitted to understand the behaviour of this detector in operational conditions, so allowing detailed investigation of space-time structure of the shower front. Direct comparison with scintillators of the GREX array demonstrates the capability of RPC to measure the lateral distribution of shower disk and emphasizes the advantage of this detector for detailed analysis of EAS front characteristics.

1 Introduction

The RPC capability to measure the arrival time of particles with a ns accuracy, the simplicity of its equipment and the versatility of pick-up readout system gave rise to a big interest in the use of this detector in accelerator physics, where RPC has been mainly used to construct fast muon triggers or cosmic ray veto systems. In the last decade some groups developed various kinds of RPC. Best results were obtained with bakelite RPC [1] and glass RPC [2], but the research is still in progress with the aim to obtain more uniform detectors, easier to be realized and managed.

In non-accelerator physics RPC was first used to build the MINI experiment [3] for the detection of horizontal atmospheric muons and for the measurement of muon backscattering in the rock below the apparatus [4]. MINI was also the first experiment completely based on RPC. In EAS physics RPC has been used in the COVER_PLASTEX experiment to analyze the fine space-time structure of EAS front [5, 6] and to investigate the possibility to depict the longitudinal shower development by tracking and timing techniques [7].

Due to the problem of gas flow, control and stability, RPCs cannot be spread over a large area, but must be concentrated in a few several positions in which conditions can be put under control. This is the approach used to realize the COVER_PLASTEX experiment, inside the GREX array in U.K.. This experiment has measured the temporal and spatial fine structure of EAS disc at PeV energies in a new and original way, using RPC detectors read by a special timing front-end electronics, named T&T [8, 9], for a direct measurement of arrival time of each particle crossing the detector. The advantage of these new detectors for the study of EAS front structure, if compared with the conventional scintillator or water Cherenkov counters, consists on the possibility to obtaine spatial and time measurements with good accuracy on large area simply using a highly segmented pick-up and a relatively cheap readout electronics.

It's obvious that an accurate investigation on RPC characteristics and behaviour has been performed before building the experiment. An analysis of counting rate, efficiency, time resolution and readout electronics performance has been made. Measurements of cross talk, noise, afterpulses and saturation effect have been performed with calibration runs in operational conditions and permitted to characterize each detector used.

2 The COVER_PLASTEX experiment

The COVER_PLASTEX experimental apparatus, shown in figure 1, was located at Haverah Park, near Leeds (U.K.), at 50° 58' N, 1° 38' W and at elevation of 220 m a.s.l.. It is based on a system of limited streamer tube (LST) hodoscope, named PLASTEX, covered by resistive plate counters (RPC). It is embedded into a conventional scintillator array, named GREX [10], which is made up of 36 scintillators, each with 0.84 m^2 area. It was originally planned as a pilot experiment to test the new timing and tracking approach for the study of EAS longitudinal development.

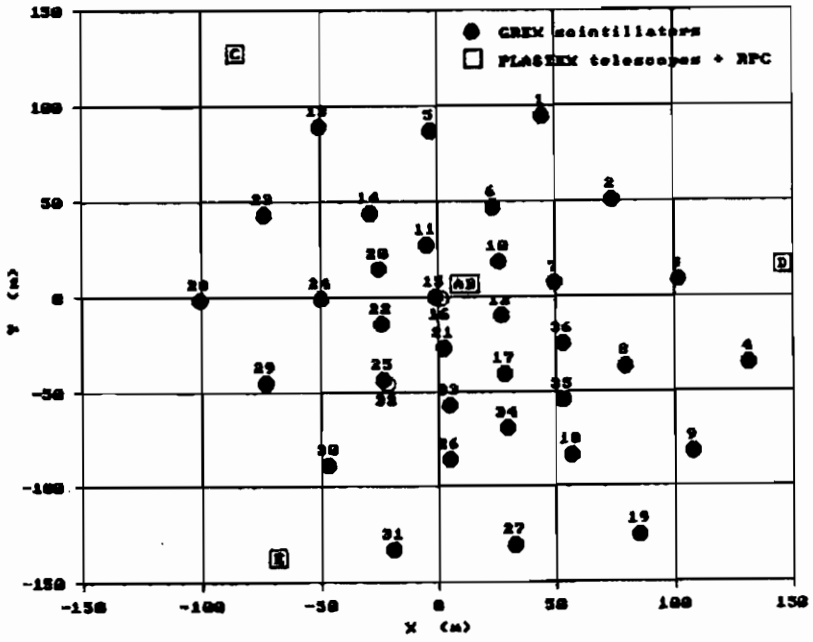

Fig. 1. Layout of the COVER_PLASTEX experimental apparatus.

The PLASTEX sub-array of four tracking telescopes [11] was installed with the aim of identifying and tracking shower particles. A pair of telescopes is placed side by side at about 4 m from the geometric cen-

ter of GREX, while the two other telescopes are located equidistantly at 150 m from the center. Each telescope (figure 2) is a stack of two identical tracking chambers one above the other with a thin layer of high Z absorber between them. Each chamber consists of three nearly square 6 m^2 planes of LST with X and Y readout strips for each plane. The vertical separation of the planes is 0.4 m, the size of single LST is 1 x 1 cm^2, the strip width is 1 cm in X coordinate and 1.2 cm in Y. The purpose of the thin absorber between chambers is to separate and identify electrons, photons and muons in the shower front.

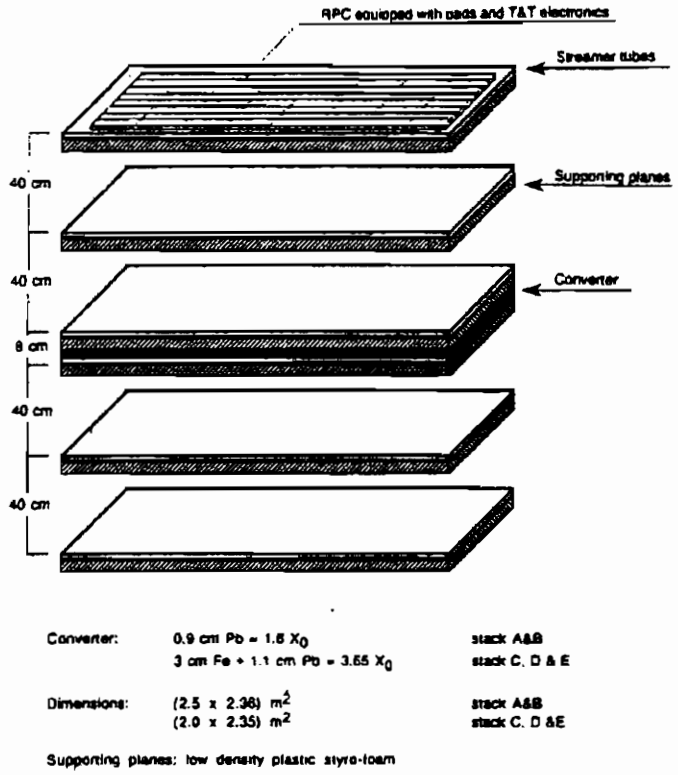

Fig. 2. Layout of COVER_PLASTEX telescopes.

On the top of all telescopes (figure 2) a layer of 4 m^2 RPC was installed [5, 6]. Each layer was equipped by 24 x 24 cm^2 pads, read by a front-end tracking and timing (T&T) electronics able to detect fired

pads and to measure the arrival time and the duration of signals from each of them. By this way 64 timing channels are available in each telescope, which enable the combination of tracking information with timing measurements.

3 Performance of COVER_PLASTEX RPC

Before and during the preparation of COVER_PLASTEX experiment the bakelite single gap RPC performance with the readout electronics has been studied in detail. Time stability, uniformity, temperature and pressure effect have been investigated. The possibility to have a front-end multihits electronics able to detect fired pads, to measure the arrival time and the width over threshold of signals for each pad and to determine an input threshold via computer has been a powerful investigation tool. Best results have been obtained with bakelite single gap RPC, 10^{12} Ωcm resistivity, and a gas mixture of 68 % argon, 28 % isobuthane, 4% freon. According these results working conditions in COVER_PLASTEX experiment have been chosen at 7.2 kV RPC positive voltage and 120 mV input threshold of readout front-end electronics.

3.1 *The T&T front-end electronics*

To use RPCs in EAS physics we need to segment the pick-up in pads of a few cm^2 size. The use of small pads allows direct measurements of the arrival time for each particle in the shower front, but requires a big amount of readout timing channels. For this purpose we developed a cheap and fast timing front-end electronics, named T&T [8, 9], based on the property of a passive delay line to transmit the input signal with a fixed delay. This electronics allows a multihit recording of input signals and measurement of arrival time and width over threshold of each signal with 2 ns accuracy.
The main characteristics of T&T electronics are listed below:
- Front-end electronics, free running mode, multihits;
- 2 ns time resolution;
- Signal width over threshold measurement;
- Double pulse resolution of 4 ns;
- Programmable input threshold in the range 20 - 500 mV;

- Programmable FAST-OR width in the range 20 ns - 5 μs;
- Pattern recognition of fired channels;
- Noise silenting device;
- Parallel bus for data trasmission.

A new version, 1.25 ns time resolution, is now in progress.

3.2 *Single counting rate and time resolution*

Figure 3 shows the single counting rate of 4 RPC. The presence of a wide plateau is evident, and allowed the use of RPC in EAS array, where detectors must be used in a single layer and there is no possibility to make coincidence between superimposed layers to cut the detector noise. Figure 4 shows how the input threshold can determine a single counting rate plateau without a significant efficiency loss. A wide plateau starting at 6500 V is obtained.

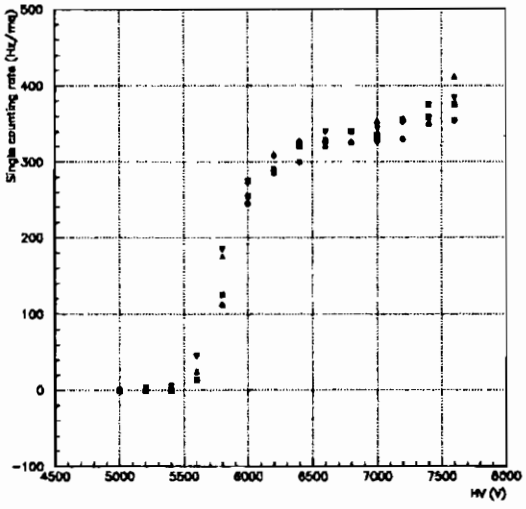

Fig. 3. Single counting rate as a function of HV of 4 bakelite RPC.

The comparison of the time resolution, for 24 x 24 cm^2 pads, measured by ps accuracy Lecroy TDC and 2 ns accuracy T&T electronics is shown in figure 5. A time resolution of RPC better than 1 ns can be easily achieved using pads.

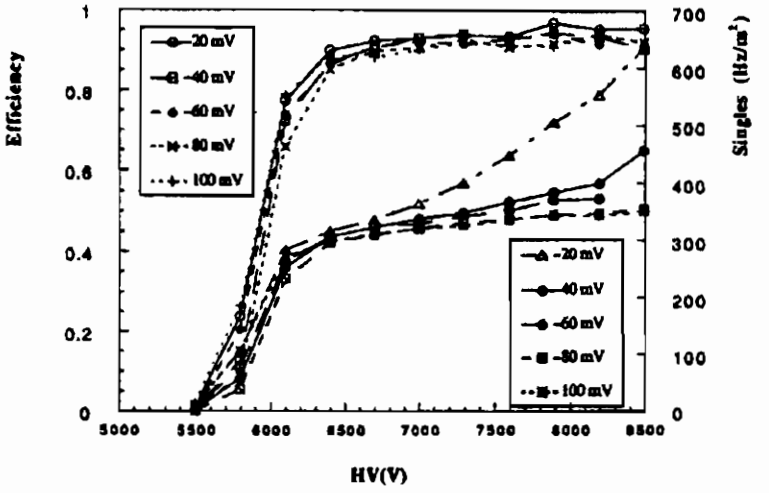

Fig. 4. Plateau and detector efficiency vs electronic threshold.

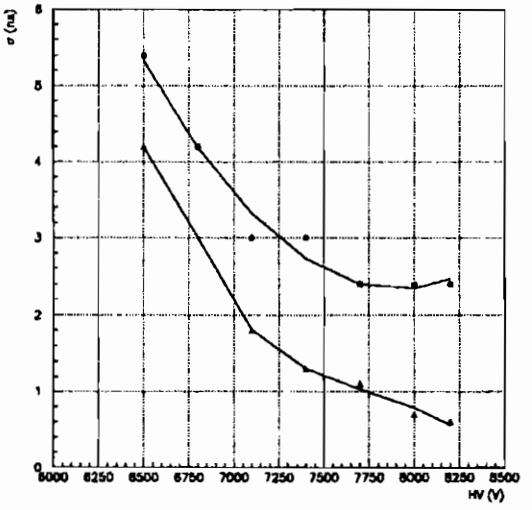

Fig. 5. RPC time resolution measured by Lecroy TDC (250 ps resolution) and T&T front-end (2 ns resolution) electronics.

3.3 *After-pulses*

To investigate the RPCs performance in operational conditions we analyzed their response in calibration runs using PLASTEX tracking telescopes to select atmospheric muons. A trigger requiring a coincidence between the upper and the lower plane of a telescope selects penetrating particles. The data analysis selects events in which a single track crossing the telescope and the RPC layer is present. By this way we can analyze the RPC response to a single penetrating particle.

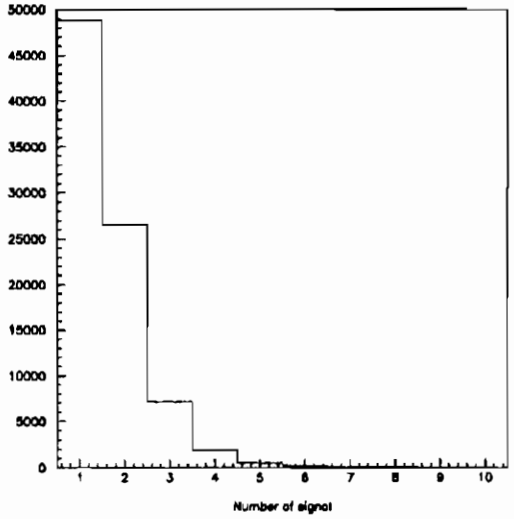

Fig. 6. Number of signals per single pad.

Figure 6 shows the number of successive signals detected by the fired pad. Only in the 57.24 % of events we obtain a single signal: the presence of after-pulses is evident. After-pulses are generated by UV photons produced in the primary discharge generated in the gas; they escape from the avalanche and ionize argon molecules generating secondary discharges. The amount of after-pulses detected depends strongly on HV supply, gas mixture and input electronics threshold, but it is not possible to eliminate them [12]. The only possible action is to mask their presence shaping the input signal or to detect and to discriminate them. Figure 7 shows the first signals and after-pulses detected and reconstructed by the T&T electronics. The width of the first signal is typically 20 ns as well as that of the after-pulses. The typical delay between them is about 30 ns as shown in figure 8, but longer delays, up to hundred ns, are also

detected.

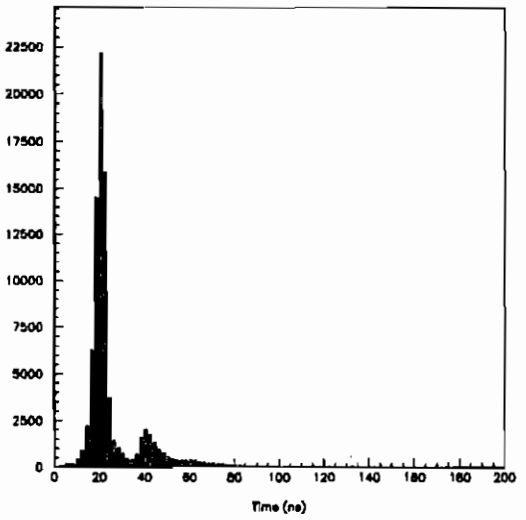

Fig. 7. Width over threshold of the first pulse detected.

To avoid this problem in the COVER_PLASTEX experiment only the first signal on each pad is processed in the analysis.

3.4 *Noise*

The 10^{12} Ωcm resistivity bakelite RPC are very stable in time and have a very low noise level, as expected from the good and stable plateau obtained in the single counting rate (fig. 3). Anyway we measured the noise level in calibration runs, looking at those events in which a single track is present but two RPC pads are fired. Figure 9 shows the time difference between the arrival time of the two first signals detected in each pad. Noise is characterized by a random delay, which clearly appears in figure 9, and is uniformly spread. In a 1.5 μs time window we measured a noise level of 2.2 x 10^{-3} for four square meters, i.e. of 5.5 x 10^{-4} m^{-2}. This correspond to a rate of 366 Hz/m^2, fully compatible with the single counting rate shown in figure 3.

In the COVER_PLASTEX data analysis we subtract statistically the noise level measured according to the counting rate of events. In fact the EAS front is several hundred ns thick [6], and we cannot distin-

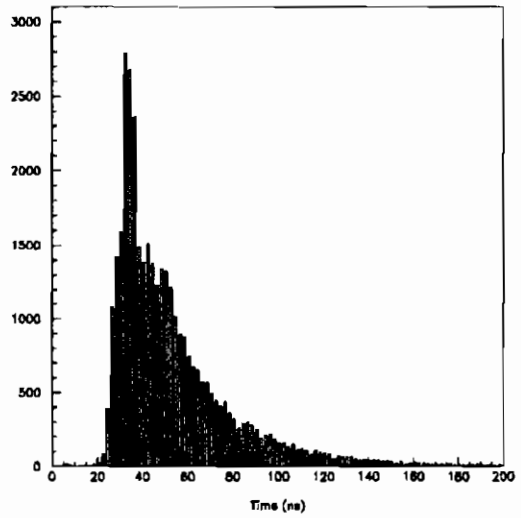

Fig. 8. Delay of the second pulse detected.

guish signals due to an accidental coincidence of uncorrelated particles and within tails of an arrival time distribution of particles in the shower front only by the arrival time.

3.5 *Cross talk*

One of the most unwanted effects in the RPC use is the cross talk between two nearby pick-up elements. Cross talk happens when a particle crosses the area between two pick-up elements inducing a signal on both. To reduce this effect the separation between pick-up elements can be enlarged, but the risk is to introduce a large inefficiency if the gap is too large. Our pick-up layer has a gap between the 24 x 24 cm^2 pads of 3 mm width. In the RPC working conditions we have measured a cross talk level of 3.2 %. This value corresponds to a geometrical area on the pad outline of 1.8 mm wide, that means that we observe cross talk effect when a particle crosses within 1.8 mm from the pad outline.
In the COVER_PLASTEX experiment we can identify cross talk effects by tracking particles. But in the analysis of EAS front thickness, where the amount of incident particles is too big to permit the pattern recognition and tracking, we don't take into account this effect. On the other hand, in this case, the presence of many particles overcomes the importance of cross talk noise.

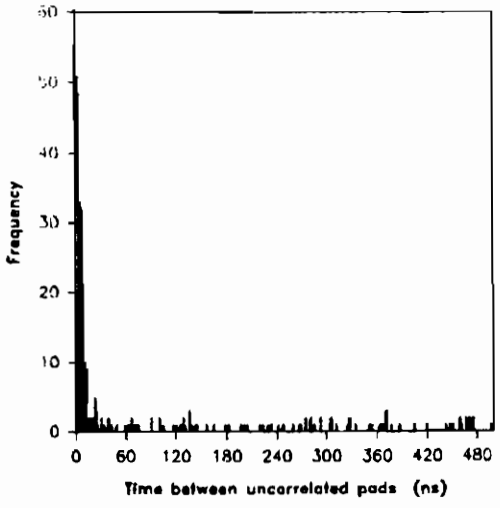

Fig. 9. Uncorrelated noise, characterized by random arrival time.

3.6 *Cross talk induced by after-pulses*

A very dangerous effect has been found in the analysis of calibration runs: the possibility that after-pulses induce delayed signals in neighbouring pads. The UV photons escaping from the main discharge can interact with argon molecules far from the area in which the first ionization has been produced. So the secondary discharge sometimes can happen in the gap between two pick-up elements. In this case the electronics readout detects a first pulse in a pad near the pad which is crossed by a real particle which induced a secondary discharge. This first pulse recorded by electronics readout is delayed with respect to the arrival time of the real particle in the neighbouring pad, but appears at the time of after-pulses generated in the other pad by the primary discharge.

The measured frequency of this effect is very low, 4.3 x 10^{-4}, but it is dangerous for the COVER_PLASTEX physics objectives, based on accurate arrival time measurements of particles in EAS front. To avoid this problem we don't take into account delayed pads if in their neighbouring pads an after-pulse sinchronous with their signal is present.

4 Comparison between RPC and scintillator detectors

An important purpose for COVER_PLASTEX experiment is to test the possibility to use RPCs detectors for a new kind of EAS array. The advantage of this detectors with respect to scintillators is mainly in their cheaper cost and in the possibility to cover large area with a highly segmented pick-up, allowing to get much more detailed information on the shower front space-time structure. The time resolution of RPCs is similar to that available with scintillators, less than 1 ns, and sufficient to estimate the shower axis inclination with a precision better than 1 degree. However there is a substantial difference between RPCs and scintillators: RPCs, with an highly segmented pick-up, permit to count crossing particles, allowing a direct measurement of the particle density, while scintillators, typically of 1 m^2 size, need an accurate calibration and not trivial electronics readout to convert the charge of detected signals to an equivalent density of minimum ionizing particles. It's clearly understandable that the charge released in scintillators by electrons and muons, the most frequently detected particles, can be very different, and energy loss fluctuations can give big errors in charge measurements, that will be immediately reflected in the accuracy of core position and primary energy determination. On the contrary RPC detectors, which count directly the number of crossing particles, provide a direct and better measurement of the particle density, and a more precise core location. So we expect that correlation between two nearby RPC has to be stronger than that between two nearby scintillators.

Figure 10 shows the correlation between number of pads fired in RPC layer covering the telescope A and that covering the telescope B. Each layer has the saturation at 64 pads. The two layer responses are strictly correlated, both for low and high multiplicity, according the fluctuation foreseen in EAS front. Figure 11 shows the correspondent correlation between the particle density detected in two scintillators, S15 and S16, which are close each other and close to telescopes A and B. The plot axes are in the logaritmic scale.
The comparison between the two figures 10 and 11 indicates how a particle density measurement can be performed with a better accuracy by RPC, in spite of the not high segmentation used. In fact the pad pick-up layer has only 16 pads/m^2 while GREX scintillators have a dynamic range of 45 particles per m^2.

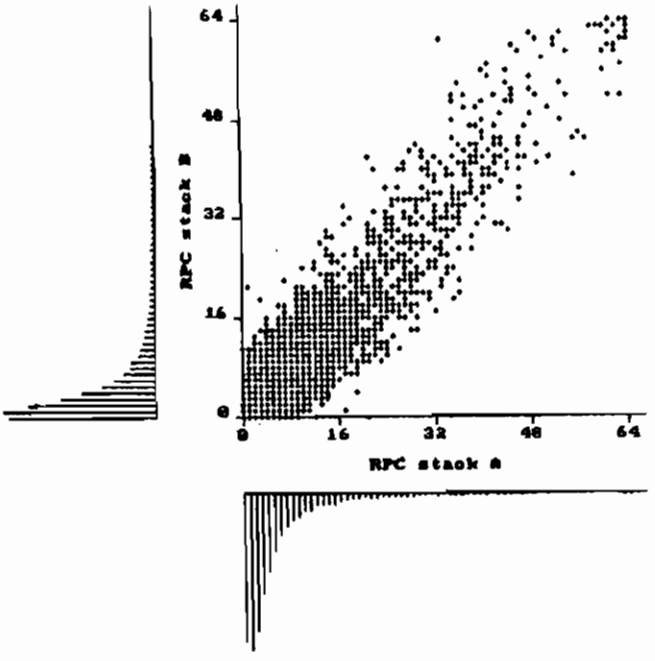

Fig. 10. Correlation between number of pads fired in RPC layer covering the telescope A and that covering the telescope B.

4.1 *EAS lateral distribution measured with RPC*

In spite of the poorer dynamic range of RPCs with respect to scintillators, due to the poor segmentation of the pick-up used, we tried to measure the EAS lateral distribution and to compare results with that obtained by scintillator density mesurements. For this comparison we used the 8 m^2 RPC layer superimposed on telescopes A and B, allowing a maximum density measurement of 16 particles per m^2, and the scintillator S16 (fig. 1) allowing a density measurement up to 45 particles per m^2.
Figure 12 shows the particle density, normalized to the shower size (Ne), as a function of core distance measured by RPCs. The experimental points have been fitted by the NKG function [13]:

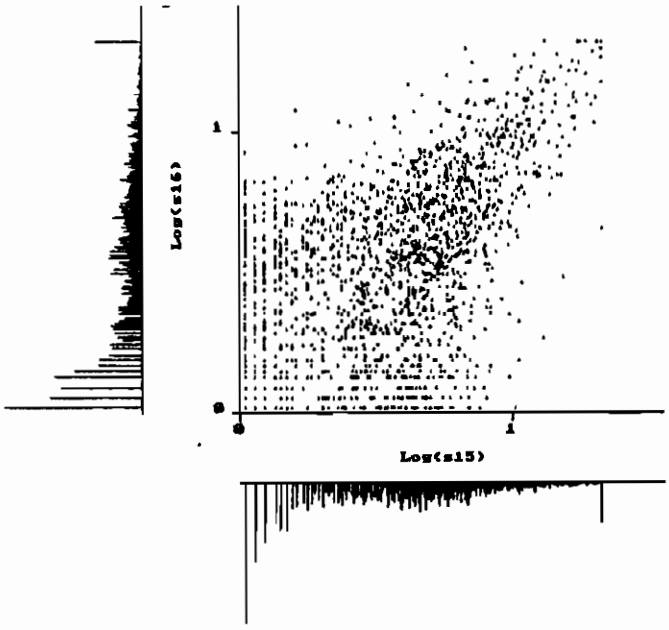

Fig. 11. Correlation between the particle density detected in the two scintillators S15 and S16 of GREX array.

$$\frac{\rho(r)}{Ne} = \frac{c(s)}{R_M^2}\left(\frac{r}{R_M}\right)^{s-2}\left(1+\frac{r}{R_M}\right)^{s-4.5}$$

where R_M is the Moliere radius equal to 79 m for GREX array, r is the core distance, s is the age parameter and c(s) is a constant parameter as a function of s.
The fit gives s = 1.221 ± 0.009 and c(s) = 0.497 ± 0.002.
Figure 13 shows the same measurement on the same events obtained with GREX scintillator S16. In this case the fit gives s = 1.211 ± 0.012 and c(s) = 0.896 ± 0.050.

This comparison demonstrates that, in spite of the poorer range of RPC equipment used with respect to GREX scintillators, the RPCs are able to measure the EAS lateral distribution with the same precision.

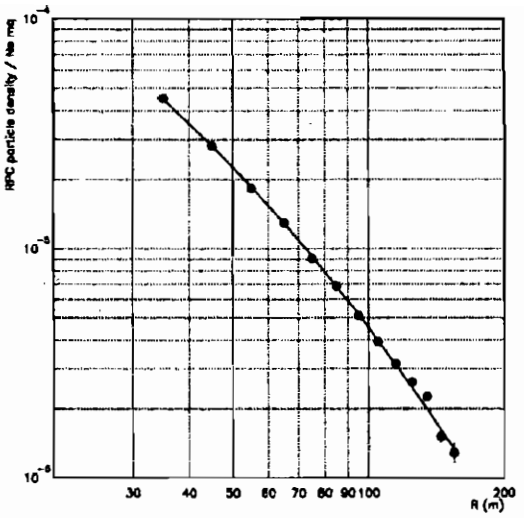

Fig. 12. Lateral distribution of particle density measured by RPC detectors.

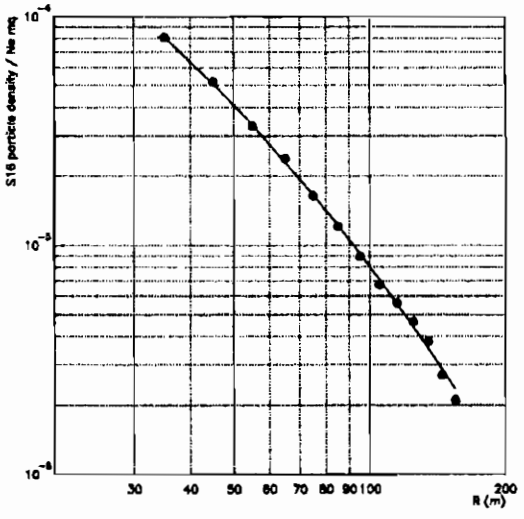

Fig. 13. Lateral distribution of particle density measured by the S16 scintillator of GREX array.

On the other hand, while the dynamic range of scintillators is determinated mainly by the phototubes and the readout electronics, the theoretical linearity for RPC is about 10^5 particles for m^2 and the experimental range depends on pad dimensions. Pads, 6x6 cm^2 sized, can easily ensure a range up to 256 particles for m^2, and RPC with such pick-up can be used to build an array able to detect EAS in an easy and cheap way.
It must be noticed that, the EAS lateral development measured by scintillators is obvious because the core position and EAS size is derived from the GREX array. Instead the RPC measurement is not obvious because RPCs give an independent density measurement with a different detectors and a different electronics. By obtaining the same results we demonstrate that the GREX array works well, and that RPC works at the same level.

4.2 *Average time structure of shower front*

Measurements of noise, cross talk, efficiency and after-pulses made by special calibration runs, and the comparison with scintillators demonstrate that RPCs used in COVER_PLASTEX experiment are very stable and work successfully with GREX array. The possibility to measure in each event the arrival time of particles in the EAS front permitted us to measure the front time structure in the PeV primary energy region. We used only the telescopes A and B placed in the center of the array. Events have been grouped according to core distance intervals of 20 m in the range 0 - 160 m. All measurements were referred to the first arrival time detected, thus avoiding the necessity to make an assumption on the shape of the front curvature, and corrected for the axis inclination. The total number of readout timing channels available is 128, but we limited our analysis to the events in which not less than 5 particles and not more than 80 were present. The first request eliminates events with too low density and energy, while the second request reduces the possibility to have two or more particles in the same pad. In fact due to the after-pulses problem we restrict our analysis only to the first signal detected in each pad fired, despite that our electronics is multihits. The noise has been subtracted statistically from each distribution according to the number of events examined.
Arrival time distributions of charged particles at different core distances

with respect to the first arriving particle are shown in figure 14. All distributions are normalized to their maximum number of particles per a time bin to demonstrate the shape of the distribution. A long tail is clearly visible at any core distance, much longer than that expected simulating the EAS cascade development with the CORSIKA simulation code.
Distributions have been fitted by a Gamma probability distribution function [14] according the relation:

$$d(t) = a\, t^b\, e^{-ct}$$

used in the past by various authors [15] to describe the EAS front development at a fixed core distance. The full lines in figure 14 are Gamma function fit of the distributions.

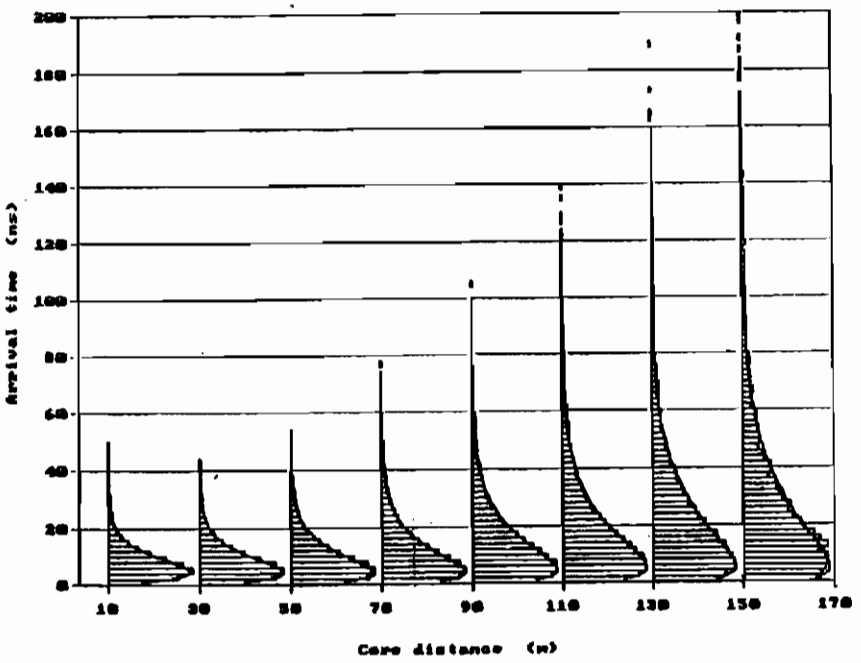

Fig. 14. Arrival time distributions of charged particles at different distances from the shower core. All distributions are normalized to their maximum number of particles per a time bin to demonstrate the shape of the distribution. Full lines are Gamma function fit of the distribution.

The curve fit permits evaluation of the front thickness as a function of core distance. In figures 15 and 16 the EAS profile (<t>) and thickness (σ) are shown as a function of the core distance. It's seen that the EAS disc has, on average, a quasi-parabolic profile in the core distance range up to 160 m, and becomes thicker with increasing distances from the core. The thickness of EAS disc also has the quasi-parabolic dependence on the core distance.

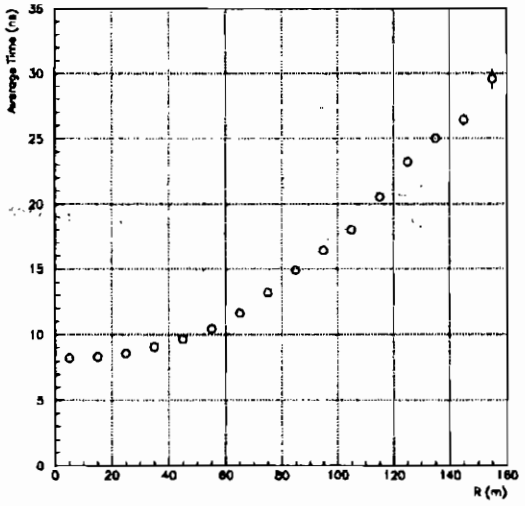

Fig. 15. The EAS profile (<t>) as a function of the core distance.

The RPC time measurements have been permitted to obtain the shower front thickness directely from the arrival time of each detected particle of the front, without any assumption about the courvature of the shower front. Instead analogous measurents maden by scintillators estimated the fluctuations of the arrival time of the first particles crossing in each detectors with respect to the light plane perpendicular to the shower axes.

5 Conclusion

Bakelite RPC with 10^{12} Ωcm resistivity can be used in high energy cosmic ray physics as large area detectors providing accurate time measurements with a good space resolution. The best pick-up to be used is

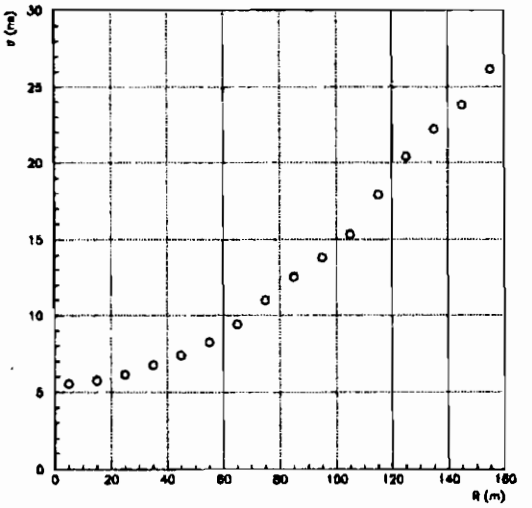

Fig. 16. The EAS thickness (σ) as a function of the core distance.

a pad layer to avoid the problem connected with the signal trasmission along a strip line. Pick-up elements must be sized taking into account the cross talk between nearby elements, while the readout electronics must be able to eliminate or discriminate after-pulses.
The COVER_PLASTEX approach permitted us to obtain for the first time precise data on the average time structure of the shower disc in a wide range of core distance up to 160 m.
It allowed also to demostrate that it's possible to use RPC for particle density measurements in EAS array, instead of scintillators generally used until now.

6 References

1. R. Santonico & R. Cardarelli : *Nucl. Instr. Meth.*, **187**, 1981, p. 377.
   R. Santonico & R. Cardarelli : *Nucl. Instr. Meth.*, **A263**, 1988, p. 20.
2. G. Bencivenni et al. : *Nucl. Instr. Meth.*, **A332**, 1993, p. 368.
3. F. D'Aquino et al. : *Nucl. Instr. Meth.*, **A336**, 1993, p. 322.
4. F. D'Aquino et al. : *Nucl. Instr. Meth.*, **A324**, 1993, p. 330.
5. G. Agnetta et al. : *Proc. XXIII ICRC, Calgary*, **4**, 1993, p. 270.
6. G. Agnetta et al. : *Nucl. Instr. and Meth.*, **A359**, 1995, p. 596.

7. T. V. Danilova et al.: *J. Phys.: Nucl. Part. Phys.*, **20**, 1994, p. 961.
8. G. Agnetta et al. : *Nucl. Instr. and Meth.*, **A315**, 1992, p. 415.
9. G. Agnetta et al. : *Nucl. Instr. and Meth.*, **A337**, 1994, p. 521.
10. G. Brooke et al. : *Proc. XIX ICRC, La Jolla, U.S.A.*, **3**, 1985, P. 426.
11. G. Agnetta et al. : *Il Nuovo Cimento*, **13 C**, 1990, p. 391.
12. M. Ambrosio et al. : *Nucl. Instr. and Meth.*, **A344**, 1994, p. 350.
13. K. Greisen : *Ann. Revs. Nucl. Scie.*, **10**, 1960, p. 63.
14. K. V. Bury: *Statistical models in Applied Science*, J. Wiley & Sons., p. 299.
15. C. P. Woidneck & E. Böhm : *J. Phys. A: Math. gen.*, **8**, 1975, N. 6.

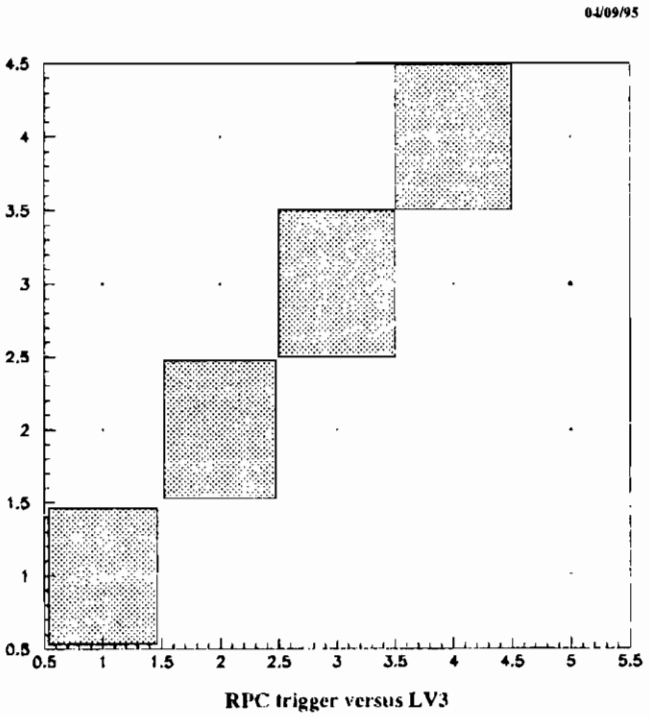

Figure 17: *Correlation between PLU tagging and level-3 trigger.*

A test of the ATLAS First Level Muon Trigger logic

S. Veneziano *

INFN, Dipartimento di Fisica,
Universitá di Roma La Sapienza, Rome, Italy

January 4, 1996

ABSTRACT

We present the design of the first level muon trigger in the central toroid of the ATLAS experiment at the Large Hadron Collider (LHC). The trigger [1] is based on fast, finely segmented gaseous detector, Resistive Plate Chambers (RPC), to unambigously identify the interaction bunch crossing and to provide a sharp threshold over a large interval of transverse momentum. We describe the logic scheme of the trigger and the performance of a circuit prototype tested on a beam.

*co authors : N.Filippini, E.Gennari, A.Nisati, E. Petrolo: *INFN, Dipartimento di Fisica, Universitá di Roma La Sapienza, Rome, Italy*;: R. Cardarelli, R. Santonico: *INFN, Dipartimento di Fisica, Universitá di Roma Tor Vergata, Rome, Italy*;: F.Ceradini: *INFN, Dipartimento di Fisica, Universitá di Roma III, Rome, Italy*; R.Bindra, B.Claxton, J.Dowdell, A.Letchford, S.Quinton: *Rutherford Appleton Laboratory, UK*; N.Ellis: *CERN, Switzerland.*

1. Introduction

Experiments at high energy, high luminosity hadron colliders will need flexible inclusive lepton triggers to select a variety of processes of primary interest for studying the production of Higgs bosons, of supersymmetric particles and the phenomenology of the top quark. The high bunch crossing frequency and the high radiation level at the LHC are the main constraints for the design of the first level trigger.

The proposal of using a fast, finely segmented, detector dedicated to implement the first level muon trigger was first presented in 1990 [2]. This simple trigger scheme exploits the fast response of RPC [3] and their low sensitivity to low energy photon and neutron background [4][5]. Other advantages of RPC are the low cost of mass production and the flexibility in segmentation that makes their use attractive in different spectrometer configurations. In fact this trigger scheme has been adopted by both pp experiments at the LHC [6][7]. Beside the need for a very good time resolution, another requirement for use at the LHC is full efficiency at high rate. Good progress has been made during the last years to achieve the required performance [8] [9] and more recent results have been presented at this conference.

The ATLAS muon spectrometer design emphasises reliable, high-resolution, standalone performance over a p_T range from 5 to about 1000 GeV/c. Precision momentum measurement and triggering are done by two dedicated detectors: Muon Drift Tubes (MDT) and RPC. The trigger chambers also provide the second coordinate measurement and timing information to relate muon tracks to bunch crossings of period $T = 25\ ns$. The low-energy charged and neutral particles flux at the LHC will be fairly high [10]. These backgrounds have a major impact on the trigger rate and pattern recognition efficiency.

2. Trigger system

The transverse momentum selection is done with a fast coincidence between strips on different planes. The number of trigger planes is defined by the need to minimize the rate of accidental coincidences and to optimize the efficiency. To reduce the accidental rate to a level lower than the prompt muon rate, the trigger will operate in two projections,

$r - z$ and $r - \phi$. The trigger detectors will also be used to provide the coordinate in the non-bending plane $(r - \phi)$ to the muon tracking system. The different momentum selection criteria required by the relevant

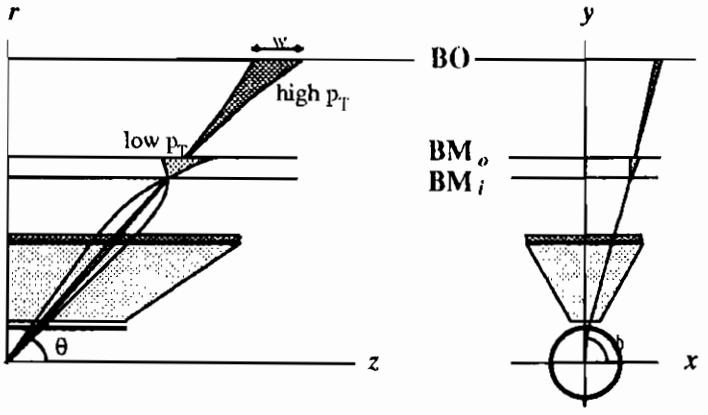

Figure 1: Scheme of the first-level muon trigger in the barrel

physics processes are best met using a *low* and a $high - p_T$ trigger. This is implemented in the barrel as shown in Fig.1. The trigger scheme uses three stations, two middle stations (BM), each made of two RPC planes and the outer station (BO), made of three RPC planes.

Each RPC plane will be equipped with read-out strips on either side of the gas volume: z-strips parallel to the magnetic field and ϕ-strips parallel to the beam.

The size of the trigger window, to select muons with transverse momentum larger than p_T is $w \simeq a/p_T \sin^2\Theta$, where p_T is the value of the transverse momentum after traversing the calorimeter. Fluctuations in the energy loss and multiple scattering in the calorimeter, lenght of the interaction region and non uniformity of the magnetic field are all smearing effects which make the choice of $3-4$ *cm* strip pitch a balanced choice between good selectivity and number of channels.

The $low - p_T$ trigger requires a three-fold majority of the four BM planes while the $high - p_T$ trigger requires a two-fold majority of the three BO planes in coincidence with the $low - p_T$ trigger. The trigger rate in the barrel is shown in Fig.2 as a function of the luminosity for the low-p_T ($p_T > 5\ GeV/c$) and high-p_T ($p_T > 20\ GeV/c$) trigger configurations together with the prompt muon rate.

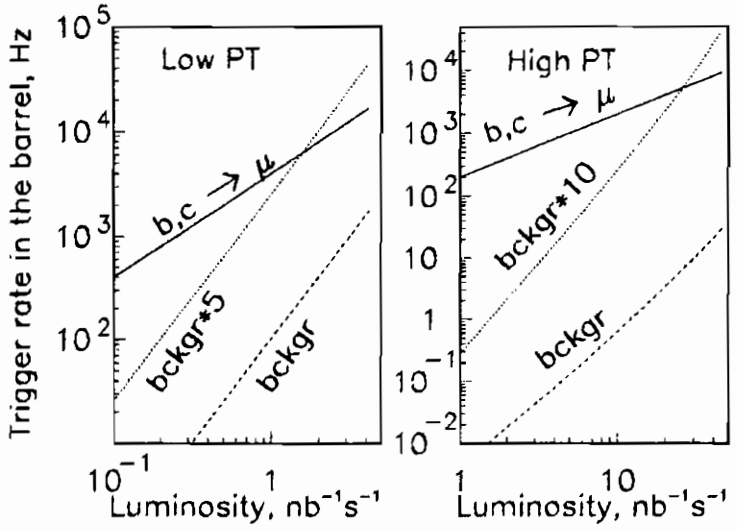

Figure 2: Low and High-p_T trigger rate in $\mid \eta \mid < 1.05$ as a function of the luminosity

2.1. Trigger segmentation, ROI's

The trigger detectors in the barrel are segmented in 24 ϕ sectors: 16 between the coils (large sectors) and 8 close to the coils (small sectors). Along the z axis the segmentation is projective to the interaction vertex. While the segmentation of the detector itself comes mainly from the geometry of the experiment.

The p_T threshold of the first level trigger (L1) will be refined at second level (L2), by using the high precision chambers' information. The L1 will provide Regions Of Interest (ROI), where the L2 processor will search for muon tracks in small sectors of the spectrometer.

The L2 algorithm is initiated by the L1 strip information that has an average occupancy much smaller than the precision drift chamber. A good compromise between layout considerations and L2 needs is a segmentation $\Delta\eta \times \Delta\phi \sim 0.13 \times 0.10$. In this case the barrel will be

equipped with 2304 matrices of 32×64 strips.

3. The Muon trigger processor

To be able to uniquely identify tracks belonging to a bunch crossing, it is not only necessary to have a fast detector, but the trigger electronics itself must have a time resolution comparable to the detector. Moreover the trigger has to be multithreshold, allowing multimuon events to be selected with thresholds lower than the single muon ones. Six thresholds will be programmable in the range $5 - 35$ GeV/c.

All the previous needs are best met by developing an Application Specific Integrated Circuit (ASIC), which will be mounted locally on the detector, close to the frontend electronics. The gathering of data for the local logic will be done by 48 Sector Logic processors (SLP), each reading 24 $r - z$ and 24 $r - \phi$ matrix outputs, covering 24 ROIs.

The main function of the SLP is to concentrate L1 data, cluster together hits from the same track, associate tracks in the two projections and eliminate double counting of tracks giving hits in two or more ROIs. The SLP output will be concentrated to the Global μ trigger through 96 links running at 800 $Mbit/s$. The Global μ Trigger (GMT) will generate total multiplicity for each of the 6 thresholds and send this information to the L1 Main processor at the 40 MHz bunch crossing frequency. In the sector and global μ logic more detailed information will be stored for the ROI builder and sent via the L2 readout links to the L2 buffers.

The total expected data rate does not exceed 10 $Mbyte/s$, while the detector data will be around 70 $Mbyte/s$. The total L1 latency is less than 1.5 μs.

3.1. Synchronization

Due to the large area of the detector, timing is a critical issue; propagation time along different regions of the detector, as well particles time of flight can be longer than 25 ns. The ATLAS Timing Control and Distribution System [11], will be used as the starting point by providing a reference $f_B = 40$ MHz clock and a programmable bunch crossing number. Finer sub-period delays will be implemented using programmable depth micropipelines, for unique assignment of a track to a bunch crossing. A time interpolator running at $4f_B$ or $8f_B$ frequency will be needed

to monitor these delays.

3.2. The coincidence matrix

We have realized a 0.5 μm CMOS $34K$ gate array [12] for the front-end part of the trigger system. The demonstrator circuit contains two

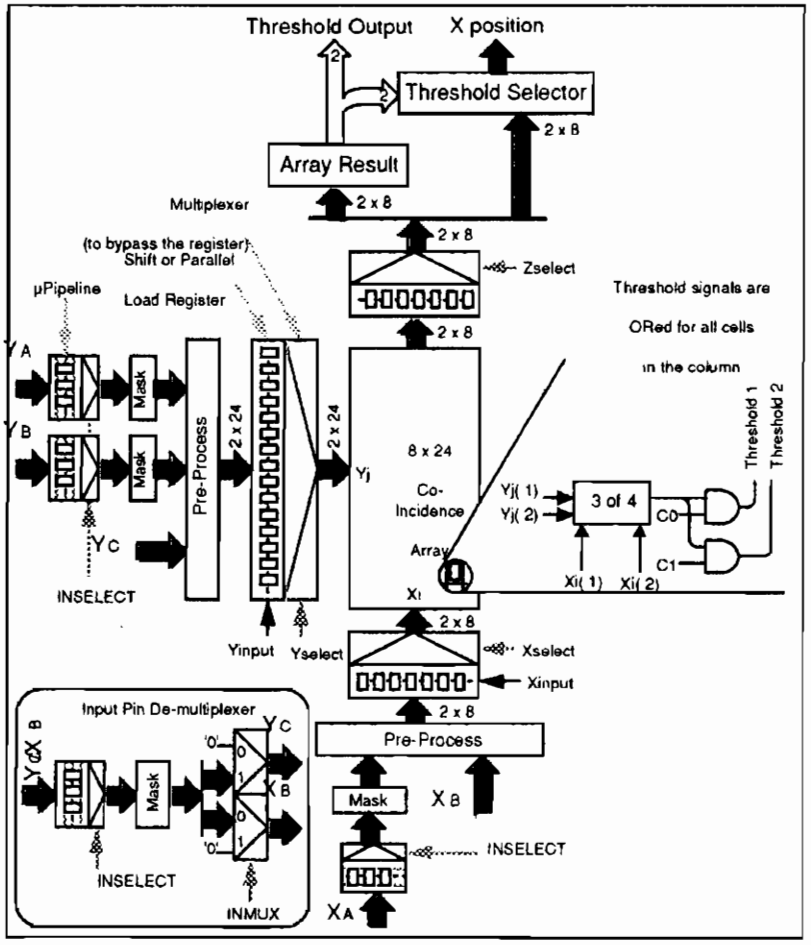

Figure 3: Block diagram of the coincidence matrix ASIC

8×24 coincidence matrices. The $low - p_T$ and $high - p_T$ algorithms can be implemented programming the same circuit for the two modes of operation.

The detector signals, after discrimination, are fed into a micropipeline

running at a frequency multiple of f_B. This is done to compensate for different propagation times from different detector planes. The 3/4 or 2/3 majority algorithm is done in two steps; one part is common to all the columns or rows of the matrix (Pre-Process blocks), while the other has to be done cell by cell. The (most significant) hit pattern of the muon track(s) is fed into an output register, together with the threshold value the track(s) has (have) passed. The logic is distributed over an internal pipeline of maximum 4 steps lenght.

The circuit can operate in fully pipelined mode, fully combinatorial, or any combination of the two. Additional test facilities and the possibility of masking noisy channels or missing planes have been realized within the gate array cell quota. All internal registers are accessed by a dedicated serial input and output lines. The die operates at 3.3 V and is mounted on a 120 pin QFP package.

Laboratory tests have proved that the maximum skew between different inputs to different outputs is below 1.8 ns, maximum operating frequency is above 100 MHz, total processing time in fully combinatorial mode is $\simeq$ 7 ns, the same for the two trigger algorithms.

A dedicated VME board has been designed for testing the ASIC in a test beam. The board is a 6U VME board with 80 differential ECL inputs (four detector planes) and 8 differential ECL outputs (most significant trigger pattern). Two NIM inputs are used for fast clear and for the external clock. Two NIM outputs provide the threshold outputs. The interface between the VMEbus and the ASIC internal registers is realized with a *Field Programmable Gate Array* (FPGA) Xilinx 3042 which converts parallel longwords into variable lenght serial words and vice versa. The ASIC run mode and clock settings can be changed via this FPGA.

3.3. Beam tests

These circuits have been tested in a test beam at CERN with RPCs illuminated by 180 GeV/c muons. The trigger hodoscope used seven chambers with orthogonal strips of 3 cm pitch to identify muons in two projections, and was arranged in two doublets and a triplet, respectively 40 cm and 200 cm apart. The test trigger system is shown in figure 4. The RPC were operated in avalanche mode [13]. The gas was a mixture of Tetrafluor-ethane (0.95) and Isobuthane(0.05) [14]. The RPC signals were amplified with a two-stage bipolar fast amplifier [15] and

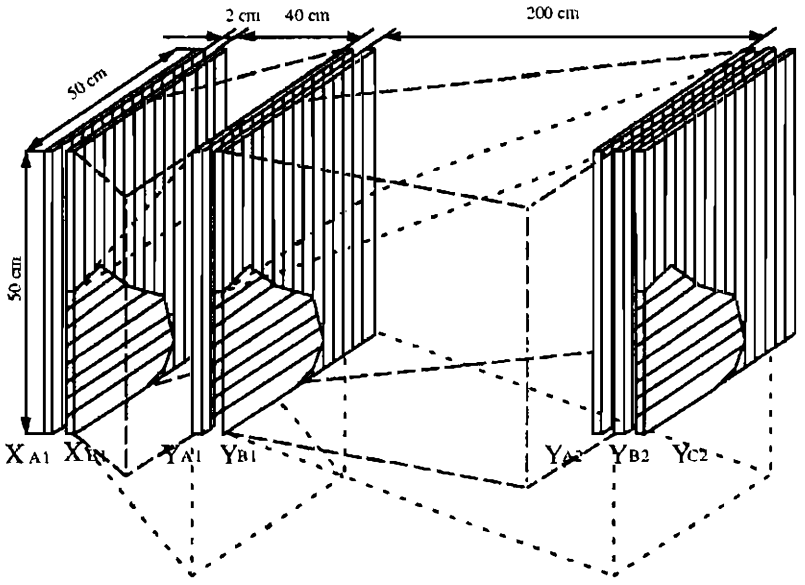

Figure 4: The RPC trigger tower. The dotted lines are regions covered by one matrix

discriminated with standard circuits.

In total eight trigger boards were needed to trigger on both projections and 224 (chambers) + 80 (trigger) channels were digitized by standard 1 ns LSB multihit TDCs. In figure 5 the Time of flight between the two doublets and between the first doublet and the triplets are shown; a $\sigma \simeq 3$ ns is measured. In figure 6 the time response of the low and high p_t coincidence matrices, is shown for both projections. A processing time of the $high - p_t$ algorithm of $\simeq 13$ ns is measured time of flight and interconnecting cables. The integrated detector/electronics time resolution is $\simeq 2$ ns.

4. Conclusions

The ATLAS level 1 muon trigger logic is designed to make unique bunch crossing ID and provide sharp thresholds over a wide range of transverse momenta. The local trigger logic has been succesfully designed and tested, based on a 0.5 μm CMOS circuit ($Fujitsu\ CG51$). The ASIC performed as expected.

This technology is already mature to fulfill our needs of low prop-

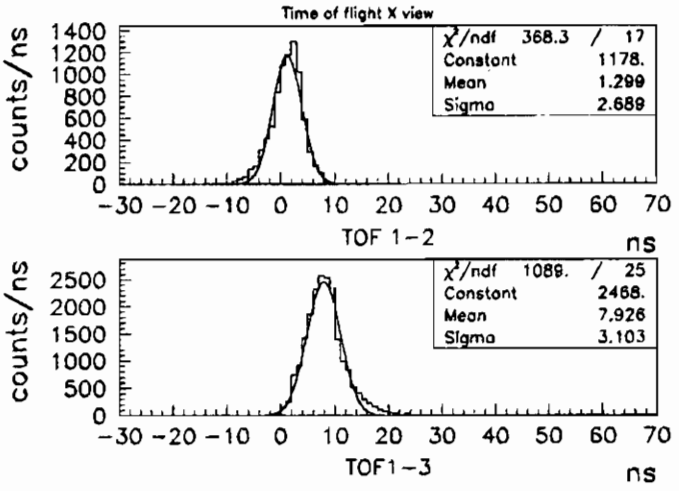

Figure 5: time of flight between the two doublets(top) and the first doublet and the triplet(bottom)

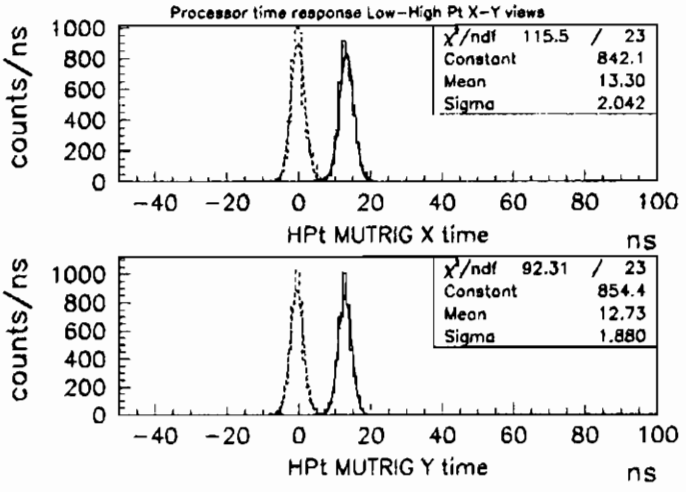

Figure 6: Trigger system time response on the two projections. The dotted line distribution is the $low - p_T$ processor response while the full line distribution is the $high - p_T$ processors response

CAEN ELECTRONICS FOR RESISTIVE PLATE CHAMBERS

A. Bigongiari, G. Franchi, G. Grieco, C.Landi, M. Lippi, F. Vivaldi

C.A.E.N. S.p.A
Via della Vetraia 11, 55049 VIAREGGIO,Italy
Tel. +39 584 388 398; Fax +39 584 388 959
E-Mail/:INFO@CAEN.IT ; URL: http://www.caen.it

ABSTRACT

Resistive Plate Chambers (RPCs) have been extensively used in High Energy Physics in the past few years. In this report we describe the latest electronics developments from CAEN for the RPCs.

1. Introduction

Resistive Plate Chambers (RPC's) have been extensively used in High Energy Physics in the past few years. In this report we describe the latest electronics developments from CAEN for the RPC's.

The description of the latest developments will be preceded by a general overview of the Catalog [1] Modules for RPC's (Front End, Read-out Controllers and High Voltage) already described in previous reports [2,3,4,5].

2. Front End Modules

2.1. A 544 32 Channel RPC Front End

Open Frame board that can be placed near the detector. It allows to read 32 channels either in parallel or in serial mode.

The main features of the unit are the following: 32 input channels; 32 differential TTL outputs; 1 OR of 32 channels; 1 input OR; minimum input width ≈8 ns; double pulse resolution 10 ns (see [2]).

2.2. A 532 8 Channel RPC Front End Board

It is a replica realized in SDM technology, of the front-end hardware developed by INFN-Rome for the FENICE experiment, slightly modified to increase the input sensitivity.

The main features of the unit are the following: 8 channels per board, 1 TEST input, 8 outputs, 1 OR of 8 channels.

The unit can be assembled over a mother board that handles the interface to the remote controller.

3. Readout Controller Modules

3.1. V 533, 50 MHz 32 Bit Pipeline Unit

Used whith the Front-End module A 544, this VME Unit allows to store inside a circular buffer the status of the 32 inputs. The programmed portion of the circular buffer is then transferred to the event memory buffer at the time of the trigger. The exact time reference is achieved via a trigger counter buffer (see [2]).

3.2. C 267 Synchronous Fast STAS

This CAMAC module is designed to be used with Streamer Tubes, but it can be used also with the RPCs via the A 544 Front End module in its serial version.

Each module can control up to 8 chains of front end modules, it supports multi-event operations and can read data from the read-out modules at the maximum speed of 4 MHz. The C267 is interfaced to and drives the SY 480 SPLITTER BOARD.

3.3. A 514 Digital Front End TDC

This unit is an open frame board which includes both front-end and digitizing hardware. The module houses 16 indipendent multi-hit TDC channels with a time resolution of 1 ns. It is interfaced to the host controller via an on board DSP.

4. High Voltage Power Supplies For RPCs

Caen has already developed several High Voltage units for general purpose. Among these, the best suited units for RPCs include the following.

4.1. N 570 2 Channel Programmable High Voltage Power Supply

Double NIM unit which houses 2 indipendent Hight Voltage channels. The output voltage of each channel has two different ranges: from 0 to ±8 KV / 1 mA and from ±8 to ±15 KV / 500 μA.

The output polarity is indipendently selectable.

4.2. SY 127 40 Channel High Voltage Power Supply

The SY 127 features a powerful and friendly software user interface, and sophisticated over-voltage and over-current protections. It can be locally monitored and controlled via an on board alpha-numeric keypad and display. Remote control is also possible via the RS-232-C port and via H.S. CAENET controllers [1].

The series A300-A400 of HV Plug-in Modules for the SY 127 covers the full voltage range from 200 V to 15 KV (positive or negative polarity) with current limits from 200 μA to 3 mA. The A329-A429-A629, 15 KV modules, Have two output channels and HV-LEMO connectors. Each Channel features hardware protection of max output voltage and channel trip detection and switch-off control.

Table 1: SY127 High Voltage Plug-In Modules for RPCs

Model	V	I	ΔV	ΔI
A329P/N	±15 KV	1 mA	4 V	1 μA
A429P/N	±15 KV	200.0 μA	4 V	100 nA
A629P/N	±15 KV	40.0 μA	4 V	10 nA

5. Latest Developments: Front End Modules

5.1. E 657 64 Channel Discriminator Unit

This Unit consist of a VME-like (for its size only, settings performed via serial line) 6U board, that houses 64 Discriminator Channels. The architecture of the System consist of 16 blocks of 4 discriminator each, the latter ORed before translation and available on a back panel connector.

Figure 1 a shows the schematic diagram of a group of 4 channels, while figure 1 b shows the block diagram of the unit. The following are its features:

- 64 updating discriminator input channels;
- 2 global OR outputs for 32 channels each;
- 16 OR outputs for 4 channels each;
- threshold from -6 to -512 mV (2 mV step);
- shaped width from 35 ns to 1 μs;
- threshold and shaped width in common to all channels;
- minimum input width $\approx$5 ns;
- remote setting of threshold and width via serial lines;
- up to 32 modules can be controlled on the same lines.

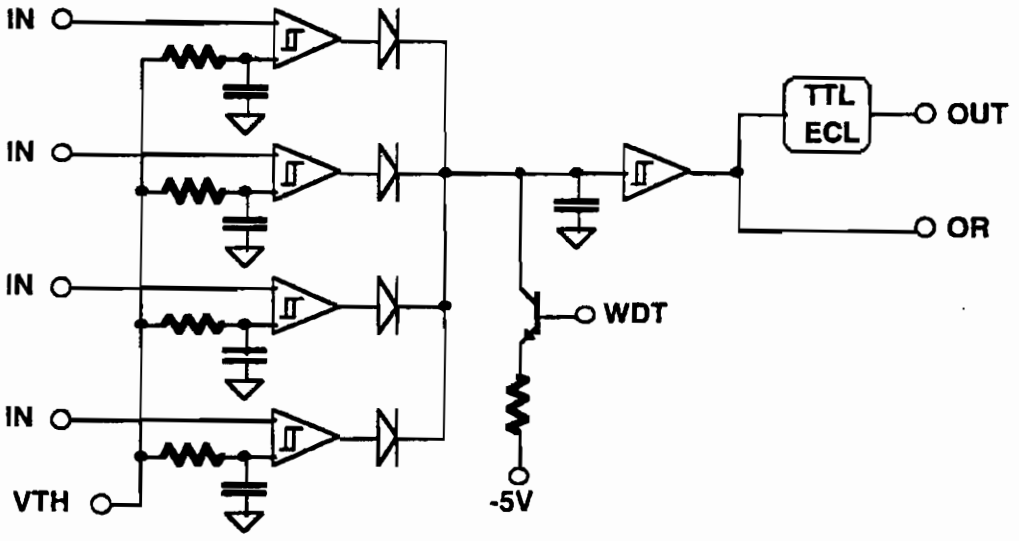

Fig. 1a. Schematic Diagram of a Group of 4 Channels

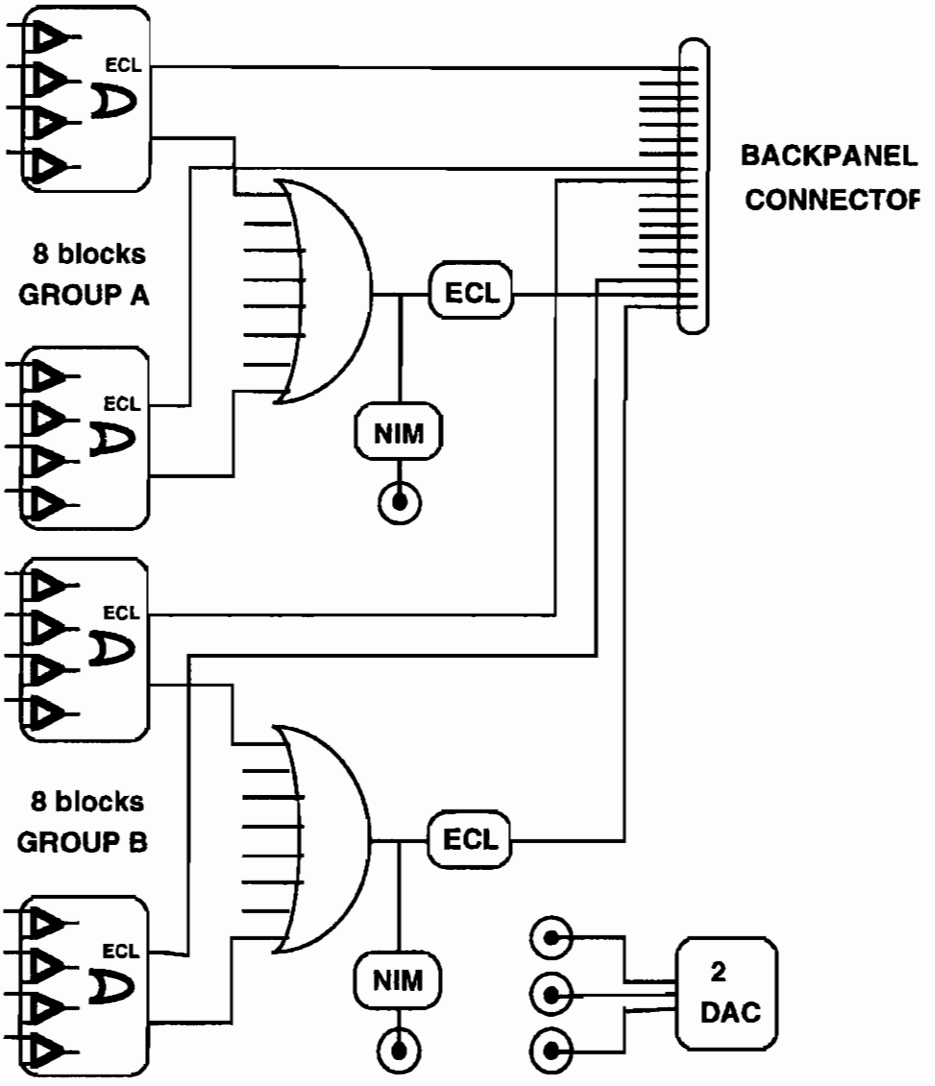

Fig. 1b. Block Diagram of the E657 Unit

6. Latest Developments: ASICs

6.1. PDISC: Programmable Discriminator

The PDISC ia an integrated multichannel discriminator for general purpose in High Energy Physics applications. It houses 8 channels, each channel consisting in a fast comparator, a pulse shaper (monostable) and an output driver. Input polarity and monostable width are programmable in common to all channels. The threshold can be set individually for each channel.

The monostable width has a "coarse" setting done via external capacitors and a "fine" setting via a COMMON WIDTH pin.

It is possible to apply a common VETO and to select Updating or Non-updating operation.

The readout of the channels can be performed either in serial or in parallel way. The serial readout is performed via an internal Shift Register driven by an external Clock. The availability of a serial Input allows to cascade more discriminators. The parallel readout can be either the outputs of the shaper stages or the comparator outputs (after polarity and veto gates). The latter can be useful for test purposes.

The readout techniques are completed by an integrated Digital OR, that receives as input either the outputs of the shaper stages or the direct comparator outputs. A further Digital OR input allows to cascade more discriminators.

The circuit has been realized in BICMOS technology 1.2 μm by AMS (Austria). The size of the Chip is 4.4×4.1 mm$\leq$. The analog and digital sections are supplied separately between -2 V and +3.3 V.

The output drivers have been designed to have null power consumption in standby status, in order to minimize the total power consumption. The channels' input stages incorporate protection diodes to avoid overvoltage problems without limiting the comparators' speed.

Figure 2 shows the block diagram of the Programmable Discriminator. The following are its features:

- 8 Channels per Monolithic (DC Coupled)
- Operating Frequency > 100 MHz
- Indipendent Threshold Voltage from 10 to 500 mV
- Programmable Polarity

- Programmable Shaping Time from 6 ns to 10 μs
- Updating or Non-Updating Mode selection
- Parallel and Serial Readout available
- Common Veto and Digital OR Output
- Time Over Threshold or Shaped Output selectable

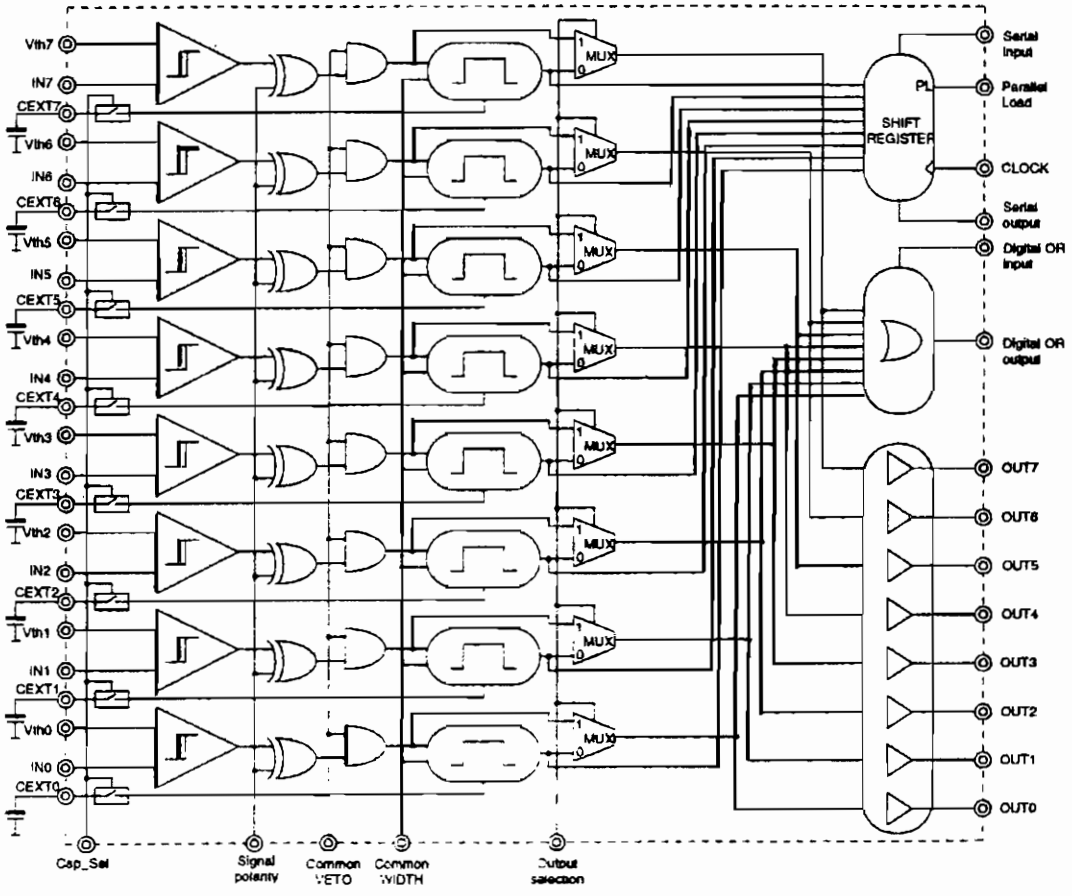

Fig. 2. Programmable Discriminator: Block Diagram

6.2. MHITIC: Multihit Time-To-Digital Integrated Circuit

The MHITIC is an integrated circuit for measurement of timing events with 500 ps time resolution (time to digital converter, TDC).

Its features (see below) include: Common Start or Common Stop operation mode;sensitivity to both the leading and the trailing edge of the pulse; fast output readout; no conversion time or searching for hit; test capability; low power dissipation.

A fully digital approach avoids the operations of trimming and eliminates the typical defects of the analog converters (time-to-amplitude): noise, interferences ,integral and differential non-linearity.

The input signal, sampled at different time bins, is analyzed in real time. If one ore more events are revealed, the value assumed by a digital counter, whose resolution is the maximum achievable with synchronous architectures, is stored in a memory with its encoded high resolution part.

The counter output is distributed to the different measurement channels that are able to store it indipendently under the control of the relevant input pulse. Similarly, a channel is dedicated to store in a suitable register the Common Start or Common Stop time, used for the on-line calculation of the timing intervals.

The MHITIC chip is best suited to be used with wire chambers, but its use for timing applications with RPCs is also appropriate.

The following are its features:

- 8 Channels per Monolithic
- Wide Dynamic Range, >8 ms Full Scale (23 bit)
- 1 ns Least Count, 500 ps R.M.S.
- up to 64 Hits per Channel
- Double Hit Resolution better than 16 ns
- Differential Non Linearity <2%
- Integral Non Linearity <0.2 LSB
- COMMON START or COMMON STOP Selectable
- Leading/Trailing (or both) Edge recorded
- Sparse Read-out of a Multiple Chip System

7. Acknowledgements

The authors would like to thank the following for their collaboration in the development of these systems: R.Cardarelli, R.Santonico (INFN Roma 2); M.Bonori, U.Contino, F.Massa (INFN Roma 1); M.Ambrosio, G.Barbarino (INFN Napoli); A.Lanza, G.Liguori (INFN Pavia); G.Agnetta, O.Catalano (CNR Palermo); R.Roncella, R.Saletti, G.Terreni (Università di Pisa, Dip. Elettronica); S.Brigati, G.Caiulo, F.Maloberti (Università di Pavia, Dip. Elettronica).

8. References

1. CAEN Short Form Catalog 1995, Viareggio, 1995
2. A. Lanza et al.,*Fast Parallel RPC Readout System*, SCIENTIFICA ACTA Vol.VIII, Anno VIII, N.3, University of Pavia, Giugno 1993, p.219.
3. F. Catarsi et al.,*Data Acquisition System Developed at CAEN*, SCIENTIFICA ACTA Vol.VIII, Anno VIII, N.3, University of Pavia, Giugno 1993, p.225.
4. M. Ambrosio et al.,*T&T: A New Design For A Front-End Time Digitizer Electronics*, SCIENTIFICA ACTA Vol.VIII, Anno VIII, N.3, University of Pavia, Giugno 1993, p.123.
5. M. Bonori et al.,*RPC Readout For Particle Astrophysics*, SCIENTIFICA ACTA Vol.VIII, Anno VIII, N.3, University of Pavia, Giugno 1993, p.193.

agation time and integration. The final implementation will simply be scaled to a 32×48 coincidence (100k gates required). Faster IO will be used to provide the necessary $160 - 320\ MHz$ needed in the experiment. The current technology already uses differential PECL to drive signals at frequencies in excess of $350\ MHz$.

1. see A. Nisati contribution to this conference.
2. F. Ceradini et al., "A fast tracking muon trigger for high luminosity colliders using resistive plate chambers", Proceedings of the Large Hadron Collider Workshop, CERN/90-10, ECFA/90-133, eds G.Jarlskog and D.Rein, vol III, page 99.
3. G.L.Bencze et al., Nuclear Instruments and Methods in Physics Research A340,466(1994).
4. M. Angeloni et al., Nuclear Instruments and Methods in Physics Research A355 (1995) 399.
5. L.Acitelli et al., Nuclear Instruments and Methods in Physics Research A360(1995) 42.
6. ATLAS Technichal Proposal, CERN/LHCC/94-43, LHCC/P2, 15 December 1994; A. Nisati, Proceedings of the II International Workshop on Resistive plate Chambers in Particle Physics and Astrophysics, ed. G. Ciapetti, S. ratti and R. Santonico, Scientifica Acta VIII, 3, 1993, p.61.
7. CMS Technichal Proposal, CERN/LHCC/94-38, LHCC/P1, 15 December 1994; G. Wrochna, Proceedings of the II International Workshop on Resistive plate Chambers in Particle Physics and Astrophysics, ed. G. Ciapetti, S. ratti and R. Santonico, Scientifica Acta VIII, 3, 1993, p.73.
8. G.L.Bencze et al, Nuclear Instruments and Methods in Physics Research A352(1995) 552-556.
9. M. Abbrescia et al.,Nuclear Physics B (Proc. Suppl) 44 (1995) 218.
10. G.Battistoni, A.Ferrari and P.R.Sala, "Background calculations for the ATLAS detector and hall", ATLAS note GEN-NO-010, 13.10.1994.
11. B.G. Taylor, IEEE Nucl. Science Symposium, San Francisco, 31/10-6/11 1993.
12. J. Dowdell et al., "A coincidence array demonstrator ASIC for the RD-27 muon trigger", RD-27 Note 30, July 1994.
13. see A. DiCiaccio contribution to this conference.
14. see V. Makeev contribution to this conference.
15. see R. Cardarelli contribution to this conference.

TESTS OF RPC PROTOTYPES IN RD5 DURING 1994 RUNS

H. CZYRKOWSKI, W. DOMINIK, J. KRÓLIKOWSKI,
M. LEWANDOWSKI, Z. MAZUR

Institute of Experimental Physics, Warsaw University, ul. Hoza 69, 00-681 Warsaw, Poland

M. GÓRSKI, M. SZEPTYCKA

Soltan Institute of Nuclear Studies, ul. Hoza 69, 00-681 Warsaw, Poland

ABSTRACT

RPC prototypes were tested in the framework of RD5 experiment to estimate their suitability as triggering devices in the CMS experiment at LHC.

1. Introduction

The CMS is one of the detectors being prepared for the recently approved LHC p-p accelerator at CERN [1]. The purpose of this detector is the detailed study of high energy p-p interactions with special stress being put (among other features) on the precise and efficient reconstruction of muon tracks. Such a detector needs a good muon trigger. It is foreseen that the central part ($|\eta|<1.5$) will be equipped with four muon stations, each of them comprising a high precision muon detector (DTBX drift tubes) and one or two layers of the Resistive Plate Chambers. The RPC trigger detectors will be extended up to ($|\eta|<2$). The purpose of the RPCs is to provide fast muon trigger with bunch crossing identification. They were choosen because of their good timing properties, ease of production, segmentation and low cost.

In order to be able to use the RPC's as the basis of the muon triggering system of the CMS detector we need to study their properties. Since we envisage mass production of the chambers (about 5000 m^2), we need to make sure, that it is as simple and cheap as possible without compromising the chamber performance. The inner surfaces of the classical RPC [2] are treated with linseed oil before chamber assembly. We wanted to investigate the performance of the detector, where such treatment was not used. The main aspects addressed were the chamber efficiency in high incident flux, the timing properties of signal, the multiplicity of responding strips and the noise generated by the chambers.

2. Chamber Construction and Experimental Setup

Extensive and detailed tests of several prototypes were performed in 1994. The chamber inner bakelite surfaces were not treated with oil. Two of them (called A and F chambers), which showed best behaviour were tested in RD5 during May run. Their construction is shown in Figs. 1 and 2.

The chambers were almost identical, the only difference being the resistivity of the graphite layer, which was 800 Ohm in chamber F and 100 kOhm in chamber A. The chambers size was 20×20 cm^2, with 20 1-cm wide strips, 12 of which were read out. At the beginning the chambers were operated as two separate ones, later on they were connected

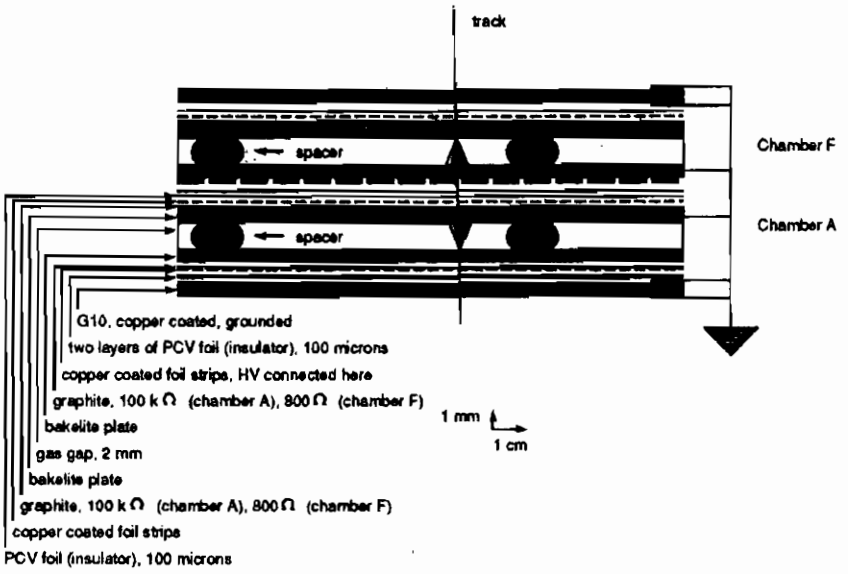

Figure 1: Chambers A and F, side view.

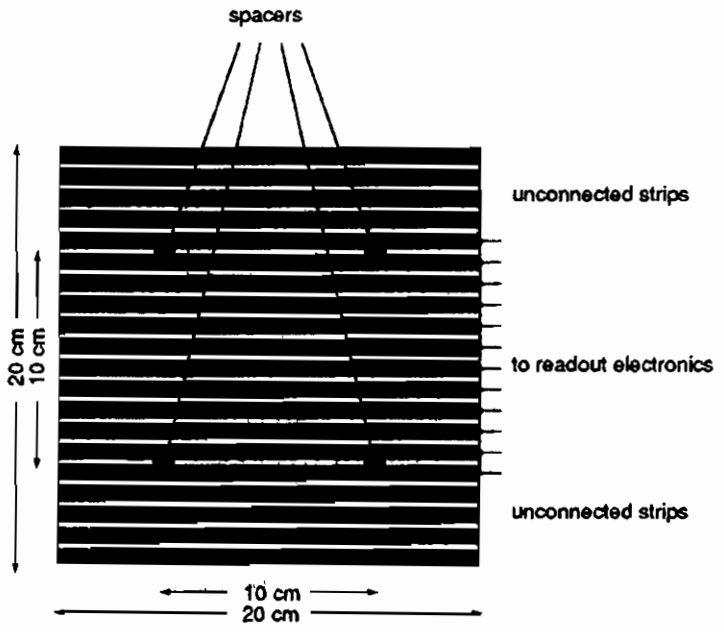

Figure 2: Chambers A and F, top view.

together to form a single double-gap chamber. The specific resistivity of the chamber plates was equal to 1-2$\times 10^{11}$ Ohm$\times$cm.

Twelve strips were read out. During the tests in Warsaw the signals from strips were fed directly into ADC's. During the tests at CERN, where the distance from the chamber to the counting room of the RD5 is about 60 metres, we used line drivers in order to transmit the signals. The cabling scheme used is shown in Fig. 3.

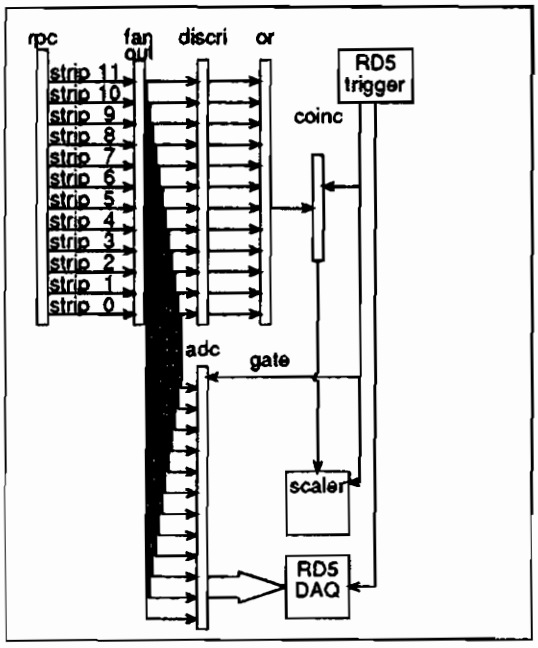

Figure 3: Scheme of cabling for RPC tests in RD5.

It allows us to simultaneously perform the efficiency test using scalers and to record input data with the standard RD5 data acquisition.

During tests in Warsaw we used argon with isobutane and also with DME. At CERN we used following gases:

- standard RPC gas, (3.8% freon CF_3Br + 38.5% n-butane+57.7% Ar)
- argon with DME (various percentages)
- argon + n-butane+freon at various percentages.

The best performance was obtained when running with high percentage of freon.

Two main aspects of the RPC operation were addressed, namely its capability to respond with good efficiency to high incoming rate and its timing properties. We used following types of electronics:

- line drivers mounted directly on the chamber and matching receivers in the counting room;
- linear amplifiers to permit the registration of small pulses;
- amplifiers together with discriminators (kindly provided by C. Williams). Those discriminators were capable of running with very low thresholds down to 5 mV.

3. Chamber Noise Level

In Figs. 4 a to c we show the noise rate for chambers A and F operated as single gap chambers and for the double-gap configuration for different discriminator thresholds and varying high voltage. The amplifiers with discriminators were used in readout.

Following conclusions may be drawn from the figures:

- Two measurements in the same configuration separated by several hours give very similar results (Fig. 4 a)
- The noise comes principally from one chamber (A), chamber F gives much less noise at high voltage - by about an order of magnitude. (Fig. 4 a) The reason for this behaviour is presently not understood.
- The noise depends rather weakly on the discriminator threshold in the range 20 - 80 mV (Fig. 4 b)
- The noise at a given HV value drops with increasing freon concentration (Fig. 4 c)
- At highest HV values studied the combined noise of A+F chambers reaches typically 100-200 Hz/cm^2.

4. Chamber Efficiency vs the High Voltage.

The chamber efficiency as a function of the high voltage was obtained by registering number of events, where at least one strip gave

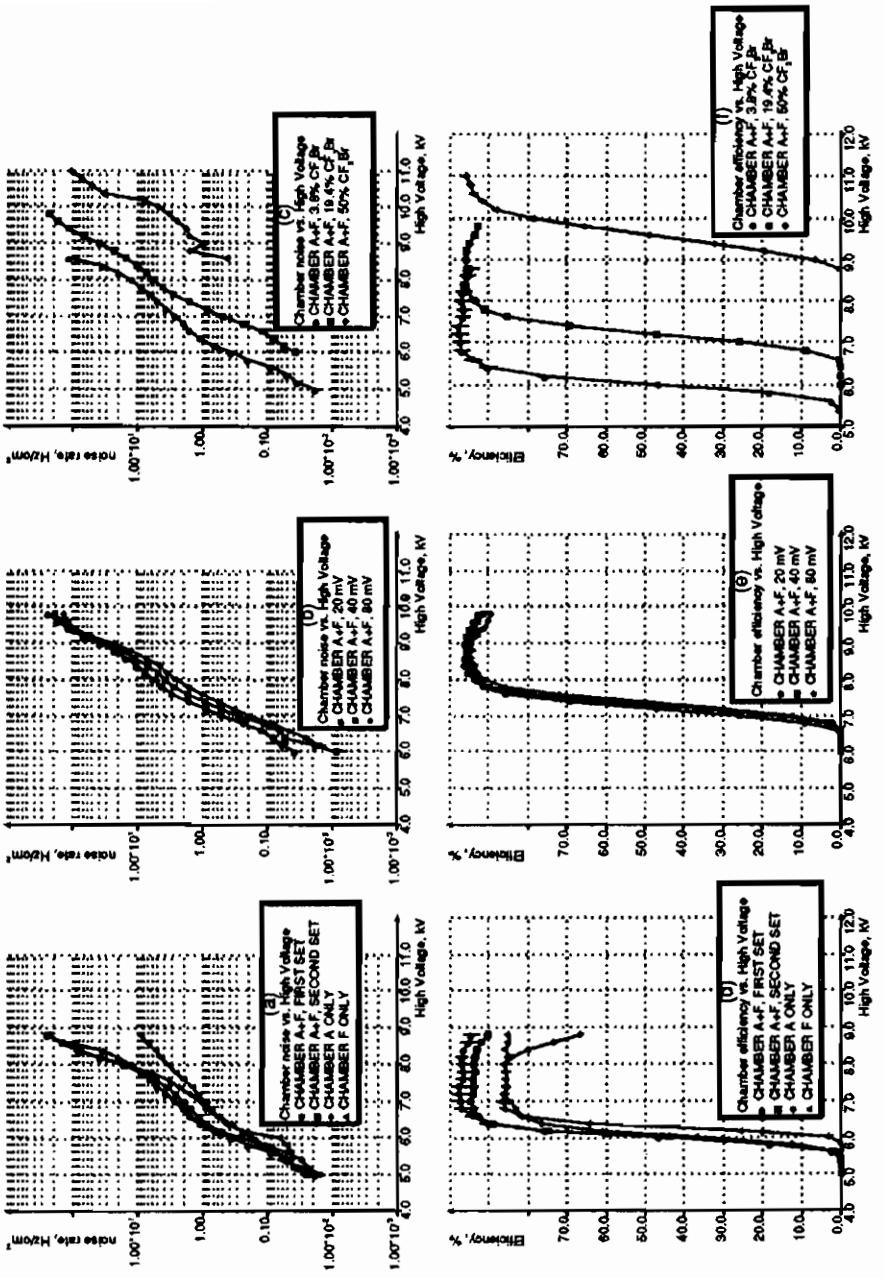

Figure 4: Noise rate and efficiency in the RPC.

signal above a given discriminator threshold. The results are shown in Figs. 4 d to f. It may be seen from them, that:

- The efficiency shows a clear plateau. The HV value, where the plateau starts depends on the freon concentration (Fig. 4 f)
- The chamber A (which gives more noise than chamber F) exhibits a drop of efficiency at highest values of HV (Fig. 4 d)
- The efficiency depends rather weakly on the discriminator threshold, similar effect was observed for noise rate. (Fig. 4 e)
- The double-gap configuration gives better efficiency than a single gap chamber, though less than one would expect from purely statistical behaviour.

5. General Chamber Performance.

The data taken without amplifiers were used to convince ourselves, that the chamber is capable of providing small pulses corresponding to the proportional mode of operation. In Figs. 5 a and b we show the distribution of the ADC spectra obtained. The big discharges form a distinctive peak around 1000 ADC counts (250 pC charge) (Fig. 5a). The peak around zero corresponds to the events, where chamber was inefficient and to small pulses (Fig. 5b). (It is not possible to distinguish the small charge events from events, where the chamber did not respond on the basis of the sum of ADC values only due to the pedestal fluctuations). In further analysis we treat events with ADC counts above 50 as big ones, the remaining being candidates for small pulse events. In order to prove, that the small pulses correspond to real events, we plot in Fig. 6 a, b and c the beam impact position reconstructed from the RD5 beam MWPCs vs the barycentre obtained from the RPC. The Fig. 6 a corresponds to "big pulse" events, 6 b contains "small pulse" events where at least one ADC channel was 2 or more counts above pedestal and 6 c - remaining events. It may be clearly seen from Fig. 6 a that the match between RPC and MWPCs is very good. In Fig. 6 b the agreement is also satisfactory, while in Fig 6 c the background becomes more important.

Fig. 7 shows the dependence of the chamber efficiency for small and big pulses as a function of the high voltage. One sees, that the percentage of big pulses grows with the HV, while that of small pulses drops.

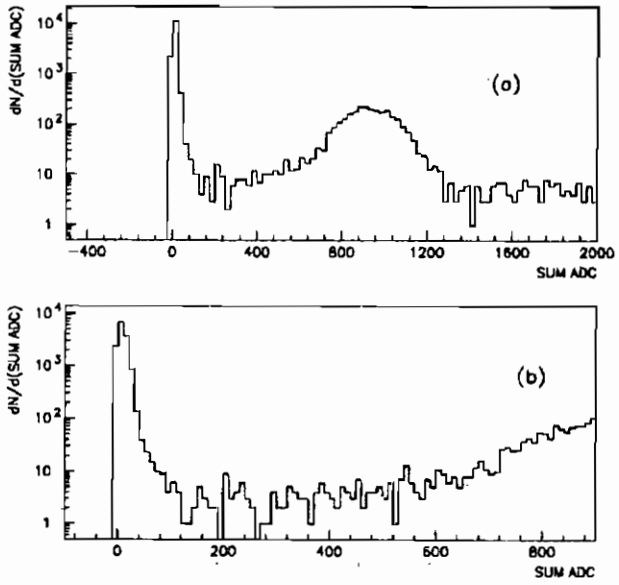

Figure 5: ADC spectra, single gap RPC, rate 100 Hz/cm^2,
- RPC gas,HV = 6.5 kV
- (a): sum (ADC channels), big bins,
- (b): sum (ADC channels), small bins.

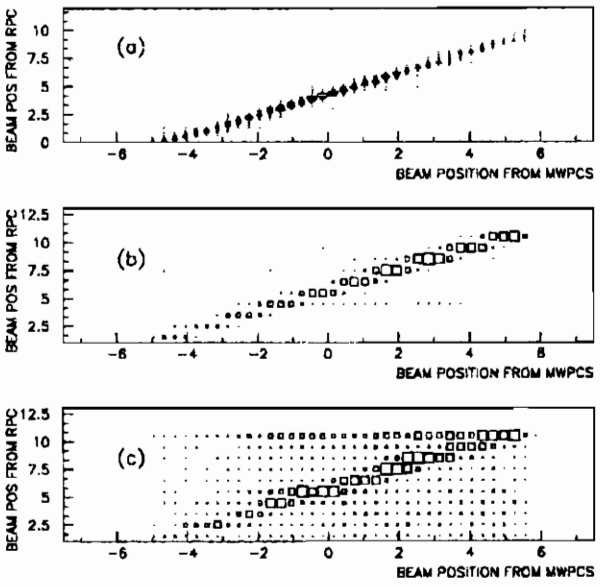

Figure 6: Beam position from RD5 MWPC's vs barycentre from single gap RPC,

- rate 100 Hz/cm^2, RPC gas,
- (a): charge > 12.5 pC,
- (b): 12.5 pC > charge > 0.5 pC,
- (c): 0.5 pC > charge.

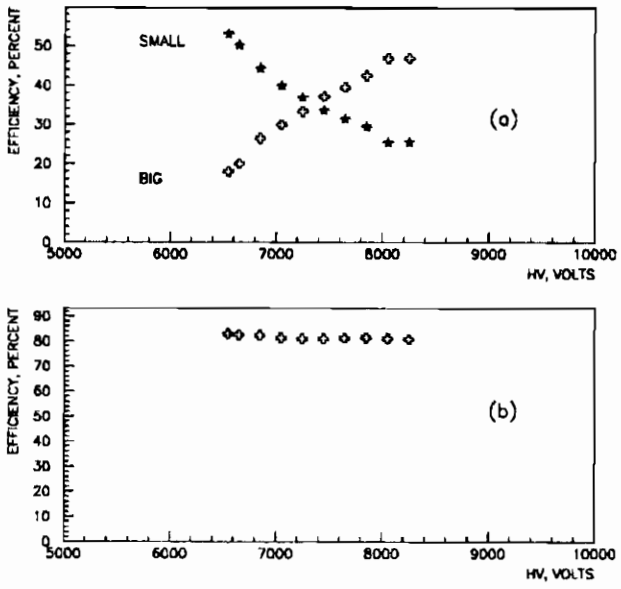

Figure 7: Single gap RPC efficiency vs HV, RPC gas, rate 100 Hz/cm^2,
- (a): small (charge < 12.5 pC) and big (charge > 12.5 pC)
- (b): total efficiency.

6. Efficiency Dependence on Rate.

The chamber efficiency as a function of the beam rate was studied.

The RD5 H2 beam intensity is not constant during spill time. Two examples of this variation and of its influence on the chamber behaviour are shown in Figs. 8 and 9. Figs. 8(9) a show the beam intensity variation during the spill, Figs 8(9) b and c show the partial efficiency for big and small pulses and Figs. 8(9) d - the total efficiency of the chamber. Fig. 8 shows this behaviour for data taken at average beam intensity equal to 400 Hz/cm^2. The intensity varies by almost a factor of two. It may be seen, that the chamber efficiency for small and big discharges follows the beam intensity variation. The situation is much more critical for the average rate about 1 kHz/cm^2, (Fig. 9) where the intensity variation covers almost an order of magnitude. Another important point, which should be made is that if the chamber efficiency is averaged over all the beam spill duration, the obtained value is overestimated, since at the beginning of the spill the chamber is fully charged and responds well, while later on an important drop in the efficiency is observed. The values marked "Average effi" correspond to the efficiency averaged over the beam spill time, while "Saturated" refer to averaging over times from 1 sec till the spill end.

The variation in relative proportions of big and small pulse events may be attributed to the decrease of the electric field during spill. When the field drops, the small events take over, which is consistent with data shown in Fig. 7.

The chamber efficiency as a function of the incoming rate is shown in Fig. 10. The efficiency to register big pulses drops continuouosly with the increasing beam rate, while small pulses efficiency grows up to the rate of about 500 Hz/cm^2. Those two tendencies maintain the overall efficiency at an acceptable level up to the mentioned rate.

This analysis convinces us that in order to profit fully from the chamber capabilities we must be able to register small pulses as well as the big ones. The RPC in order to be able to operate with good

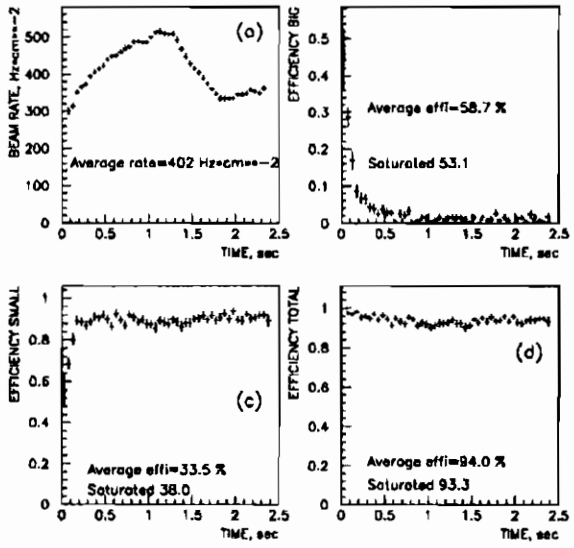

Figure 8: Beam and chamber behaviour during SPS spill.

- Double gap RPC, amplifiers with discriminators, HV=10kV,
- Gas: (37.5% CF_3Br)+(25% n-butane) + (37.5%) Ar).
- Average beam rate 402 Hz/cm^2.
- (a): Beam intensity variation during spill;
- (b): Variation of the efficiency for big pulses during spill;
- (c): Variation of the efficiency for small pulses during spill;
- (d): Variation of the total efficiency during spill.

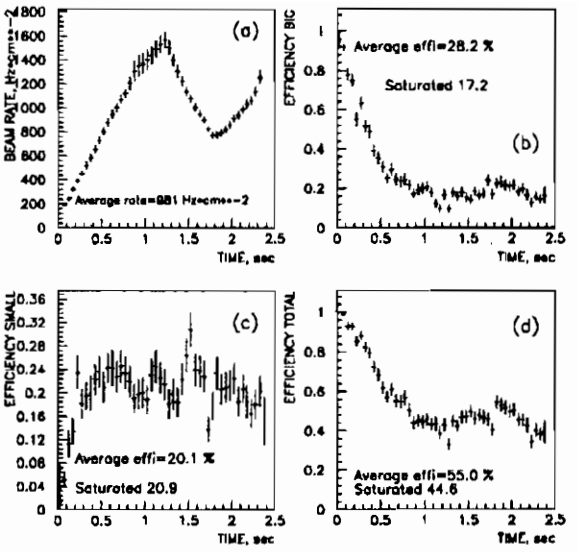

Figure 9: Beam and chamber behaviour during SPS spill.

- Double gap RPC, amplifiers with discriminators, HV=10kV,
- Gas: (37.5% CF_3Br)+(25% n-butane) + (37.5%) Ar).
- Average beam rate 981 Hz/cm^2.
- (a): Beam intensity variation during spill;
- (b): Variation of the efficiency for big pulses during spill;
- (c): Variation of the efficiency for small pulses during spill;
- (d): Variation of the total efficiency during spill.

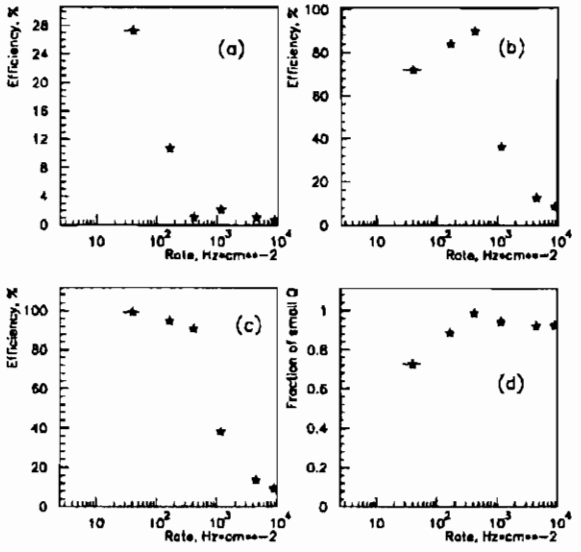

Figure 10: Chamber efficiency vs beam rate averaged over spill end.

- Double gap RPC, amplifiers with discriminators, HV=10kV,
- Gas: (37.5% CF_3Br)+(25% n-butane) + (37.5%) Ar).
- (a): Efficiency for big charge events;
- (b): Efficiency for small charge events;
- (c): Total efficiency;
- (d): Fraction of small charge events.

efficiency must transmit sufficient charge across its plates.

7. Timing Dependence on Rate.

The chamber timing behaviour was measured by a TDC module. The start signal of the TDC was taken from the RD5 trigger, seven stop signals were taken from individual strips, the last - from OR-ed signals of all strips. In Fig. 11 we show the TDC spectra of the OR-ed signal for various beam rates. It is seen, that the peak position shifts with increasing rate, and its width increases. This effect is shown also in Fig. 12, where we plot the average TDC response and its spread as a function of the incoming rate.

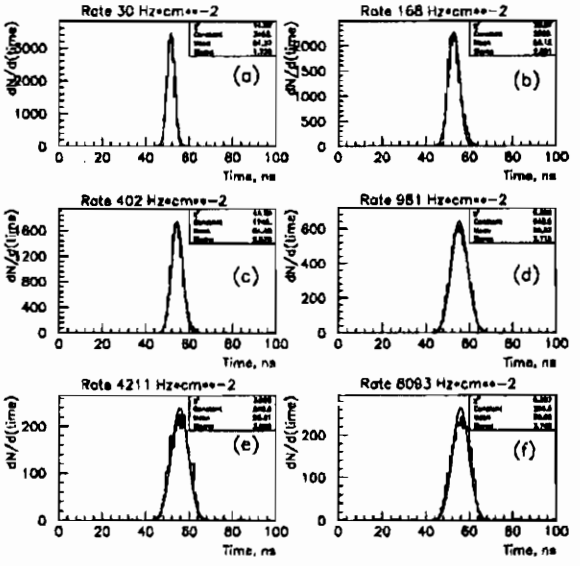

Figure 11: Chamber timing properties for various rates,
- Double gap RPC, amplifiers with discriminators, HV=10kV,
- Gas: (37.5% CF_3Br)+(25% n-butane) + (37.5%) Ar).

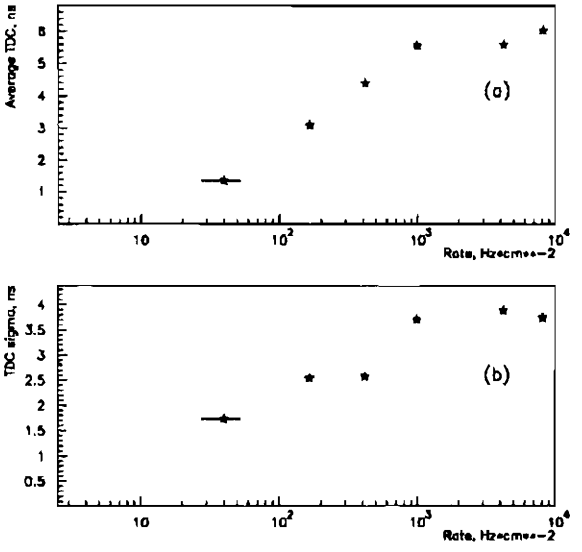

Figure 12: Chamber timing properties vs beam rate,
- Double gap RPC, amplifiers with discriminators, HV=10kV,
- Gas: (37.5% CF_3Br)+(25% n-butane) + (37.5%) Ar).
- (a): Average TDC response;
- (b): RMS of the TDC distribution.

8. Strip Multiplicity

The multiplicity of responding strips is of crucial importance for the performance of the trigger processor. It has been shown in the CMS Technical Note on the PACT (Pattern Comparator Trigger) [3], that in order to obtain good trigger selectivity we need low strip multiplicities. An optimal balance between strip multiplicity and the chamber efficiency must be found in order to have good overall chamber efficiency and good trigger selectivity. The Fig. 13 and show the strip multiplicity distributions taken with a single gap RPC operating with the standard RPC gas at the incoming rate of about 100 Hz/cm^2 without amplifiers for the high voltage values of 7.6 and 7.8 kV. The threshold for big events was taken as 200 ADC counts, equivalent to 50 pC charge. It corresponds to the amplitude value of 125 mV assuming that the pulse lasts about 20 ns. The cut for small events was taken as 2 ADC counts, corresponding to amplitude of 1.25 mV.

The situation becomes more difficult in the realistic case, when we read data after amplification and discrimination, in other words we do not separate small and big events on the basis of pulse height. The multiplicity distributions obtained thus for rates up to 1 kHz/cm^2 are shown in Fig. 14. We have here two types of events: with strip multiplicities below about 8, and with larger multiplicities. We interpret this behaviour as due to the simultaneous presence of small and big discharges. The small ones correspond to low multiplicities, while the big ones (after discrimination at a relatively low level) give high multiplicities.

In order to prevent this situation, a suitable gas mixture must be found, which would prevent the formation of big discharges without destroying the chamber efficiency for the small ones.

9. Summary

Several RPC prototypes were constructed and tested in 1993 and 1994. They showed good timing properties and spatial resolution. The double gap chamber was able to provide efficiency above 90% for incoming fluxes up to 500 Hz/cm^2. It seems, that the lack of oil treatment of the bakelite surfaces does not imperil chamber operation. Following problems are as yet unsolved:

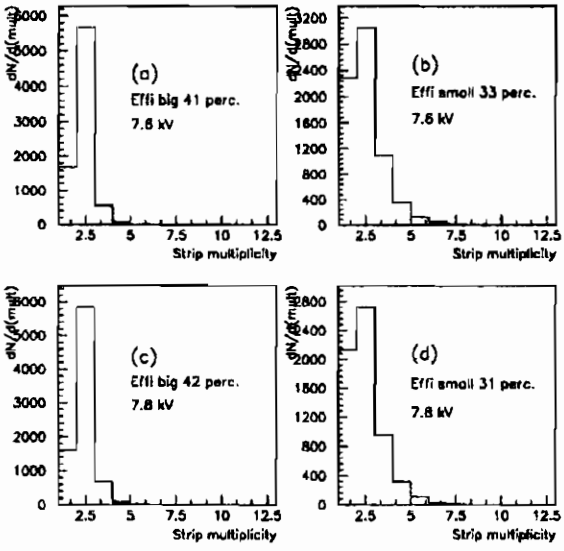

Figure 13: Distribution of the strip multiplicity,
- Single gap RPC, no amplifiers, RPC gas.
- (a): 7.6 kV, big events (charge > 50 pC)
- (b): 7.6 kV, small events (charge < 50 pC)
- (c): 7.8 kV, big events (charge > 50 pC)
- (d): 7.8 kV, small events (charge < 50 pC).

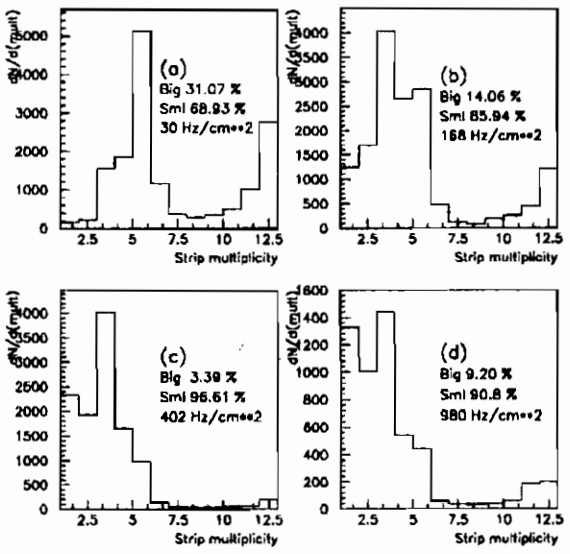

Figure 14: Distribution of the strip multiplicity,

- Double gap RPC, amplifiers with discriminators, HV=10kV,
- Gas: (37.5% CF_3Br)+(25% n-butane) + (37.5%) Ar).
- (a): Beam rate 30 Hz/cm^2
- (b): Beam rate 168 Hz/cm^2
- (c): Beam rate 402 Hz/cm^2
- (d): Beam rate 981 Hz/cm^2

- The strip multiplicity seems too high due to formation of big amplitude events;
- It is necessary to obtain good efficiency for rates up to at least 1 kHz/cm^2;

10. Acknowledgements

The authors would like to acknowledge the support of Polish Committee for Scientific Research under grants KBN-PB-2 0422 91 01 and KBN-SPUB-206/93.

11. References

1. The CMS Technical Proposal, *CERN/LHCC* 94-38.
2. R. Santonico, R. Cardarelli, *Nucl. Instr. Meth.* **187** (1981) 377.
3. Pattern Comparator Trigger (PACT) for the Muon System of the CMS Experiment. M. Anadlinger et al., *CERN PPE* 94-227.

A test on Resistive Plate Chambers with non ozone depleting freon

M. Abbrescia, A. Colaleo, G. Iaselli, M. Maggi, B. Marangelli, S. Natali, S. Nuzzo, A. Ranieri, F. Romano
Dipartimento di Fisica e Sezione INFN, Bari, Italy

G. Gianini, G. Liguori, S. P. Ratti, P. Vitulo
Dipartimento di Fisica Nucleare e Teorica e Sezione INFN, Pavia, Italy

M. Gorski
Soltan Institute for Nuclear Studies, Warsaw, Poland

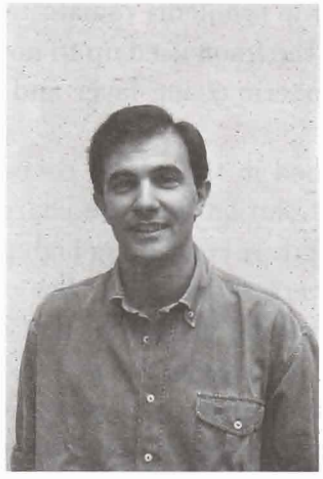

ABSTRACT

Resistive Plate Chambers operating with a gas mixture containing $C_2H_2F_4$, which has a very low ozone depletion power, have been tested in the CMS H2 high intensity muon beam at CERN. The transition from the avalanche mode of operation to the streamer mode has been clearly observed.

1. Introduction

In this paper we present some results obtained by the Bari Pavia Warsaw CMS RPC collaboration during a test beam performed at CERN in July August 1995, the test was intended to investigate the behavior of RPC's operated at low gas gain (10^6 10^7), using gas mixtures containing a high percentage (up to 90%) of freon. Due to the small size of the signals involved, this type of mixture requires, as a consequence, the use of preamplifiers to reveal the signals coming out from the detector. It has been demonstrated by several measurements [1] that an RPC operated in such conditions could safely stand the high trigger rates required in the future LHC experiments ATLAS and CMS.

However, in order to develop a feasible RPC muon system for these experiments, some problems remain to be solved. The most serious has to do with the freon used up to now, which is well known to destroy the atmospheric ozone layer and will be prohibited by the law in the future.

The results described in this paper concern the measure of the efficiency, the time resolution and the charge developed in RPCs operated with a gas mixture containing high percentages of $C_2H_2F_4$, a gas which is characterized by a very low ozone depletion power. We show that the operating voltage of RPCs can be below 10 kV, allowing a substantial decrease in the power dissipation into the detector; moreover the technology and materials (cables, connectors, etc.) necessary to operate with voltages lower than 10 kV is simpler and cheaper than at higher voltages.

At the time of this Workshop the results are only preliminary, and more analysis needs to be performed.

2. Experimental set-up

Double gap type RPCs, made of bakelite plates of dimensions $50 \times 50 \times 0.2$ cm^3 were used; the bakelite resistivity was 0.4×10^{11}

Ωcm. The detector was filled with a gas mixture of 90 % $C_2H_2F_4$ freon and 10 % iso-C_4H_{10}.

The signals were read out by means of aluminum strips, 1.3 cm wide and with a 1.5 cm pitch. The front-end electronics was designed to detect the signals in low gas gain mode and consisted of charge amplifiers; the amplifiers gave an output signal whose pulse height V_{out} was related to the input charge Q_{in} by the relation $V_{out} = AQ_{in}^{\alpha}$ where A = 3.42 V/pC and $\alpha = 1.56$. Only the central 8 strips of each chamber were connected to the preamplifiers. The amplified signals were sent to the counting room by means of 50 Ω RG58 coaxial cables, connected with CAEN mod.96 discriminators with a threshold of 30 mV. The efficiency of the chambers was measured counting the coincidences between the OR of the 8 strip signals and the trigger. The discriminated signals were also sent as independent channel stops to some LeCroy 2228A TDCs, characterized by a 100 ps resolution; the common start was given by the trigger. The data coming out from the TDCs have been used both as an additional independent measure of the efficiency of the detectors, and to measure their time resolution. To measure the charge collected by the pick-up strips the preamplifiers were disconnected, and the signals were sent directly to CAEN C205A ADCs, with a 0.03 pC channel sensitivity.

The chambers were placed immediately upstream of the CMS H2 experimental area (old RD5), at the CERN SPS North Area [2]. A set of scintillation counters was used as trigger system. We used the 220 GeV muon beam, which was defined by the coincidence of three scintillators of dimension 15 × 10, 4 × 4 and 2 × 2 cm^2. The beam profile was measured using two multiwire proportional chambers with 2 mm wire spacing.

3. Experimental results

In Fig. 1a and 1b we present the behavior of the RPC efficiency as a function of the operating voltage HV for two different values

of the flux of incident particles, about 20 Hz/cm^2 and about 150 Hz/cm^2. The chambers worked in double gap mode, meaning that both gaps were on. The fluxes are average values measured with the scintillators inside the beam spot and do not include possible corrections for their inefficiency. While the curve at low value of the beam flux reaches a plateau of about 95 % constant efficiency, the other one is characterized by a marked drop in the efficiency in the range from 8.8 to 9.8 kV. The drop is slightly visible also in the first curve; at the moment the reason of this efficiency drop, which was not present with different gas mixtures and same FE electronics, is not understood.

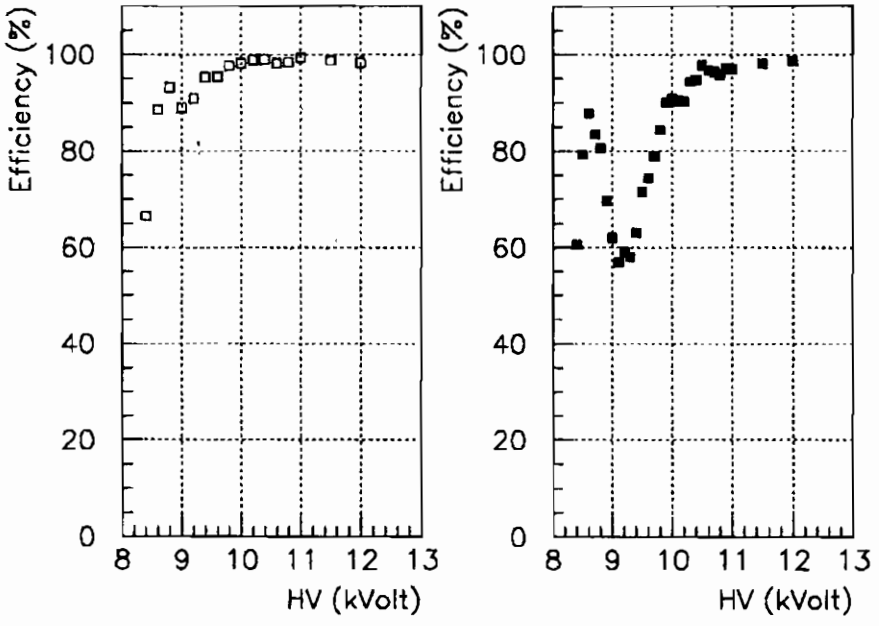

Figure 1: RPC efficiency vs. *HV* for a) 20 Hz/cm^2 and b) 150 Hz/cm^2 of beam flux.

In Fig. 2a and 2b we show the total charge (sum on 8 strips) measured with a 20 Hz/cm^2 beam flux at 9.0 and 9.5 kV; only events with a charge greater than the pedestal plus 2 times its

RMS are included. During these measurements only one gap of the chambers was on. Since the strips were connected to the ADC only at one end, and the other was terminated on a 50 Ω impedance, the measured charge is half of the charge really induced on the strip. The first distribution is characterized by an average charge of the order of 1 pC; in the second distribution it appears also a wide peak centered at about 40 pC. This is the evidence of the two different modes of operation of the RPC: the avalanche mode, characterized by a collected charge 1 pC as order of magnitude, and the streamer mode, with much greater charge values. The distributions related to these two different modes of operation are well separated one from the other; when the operating voltage is increased the streamer mode becomes prevalent, while the avalanche mode, which is the only one present at lower voltages, begins to disappear.

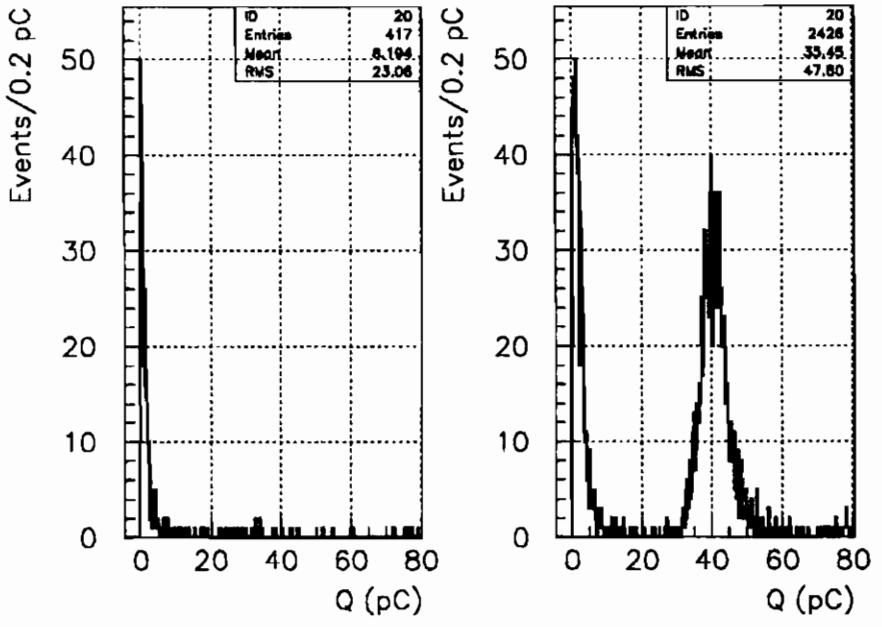

Figure 2: RPC Charge distribution, in single gap mode, at 20 Hz/cm^2, for a) $HV = 9.0$ kV and b) $HV = 9.5$ kV.

The opposite is true when the operating voltage is kept constant and the flux of incident particles on the chambers is raised; in Fig. 3a and 3b we show the charge distributions for one chamber, working in double gap mode, at $HV = 9.5$ kV, and with a beam flux of 20 and 380 Hz/cm^2 respectively. Since there is a reduction of the electric field in the gap due to charge flowing through the resistive plates, a raise of the beam flux causes the streamer mode of operation to begin to disappear, and the avalanche mode to become prevalent.

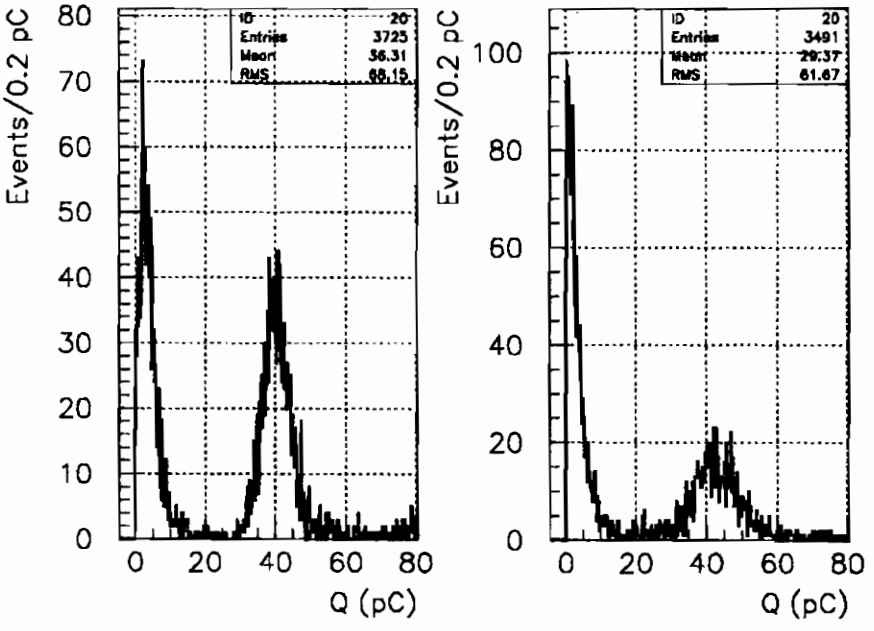

Figure 3: RPC charge distributions, in double gap mode, for $HV = 9.5$ kV and a beam flux of a) 20 Hz/cm^2 and b) 150 Hz/cm^2.

In Fig. 4 we show the average value of the measured charge as a function of the operating voltage, computed separately in the avalanche and streamer regions; this plot is not incompatible with other measures performed in different experimental conditions [3].

In Fig. 5a and 5b we present the distributions of the difference

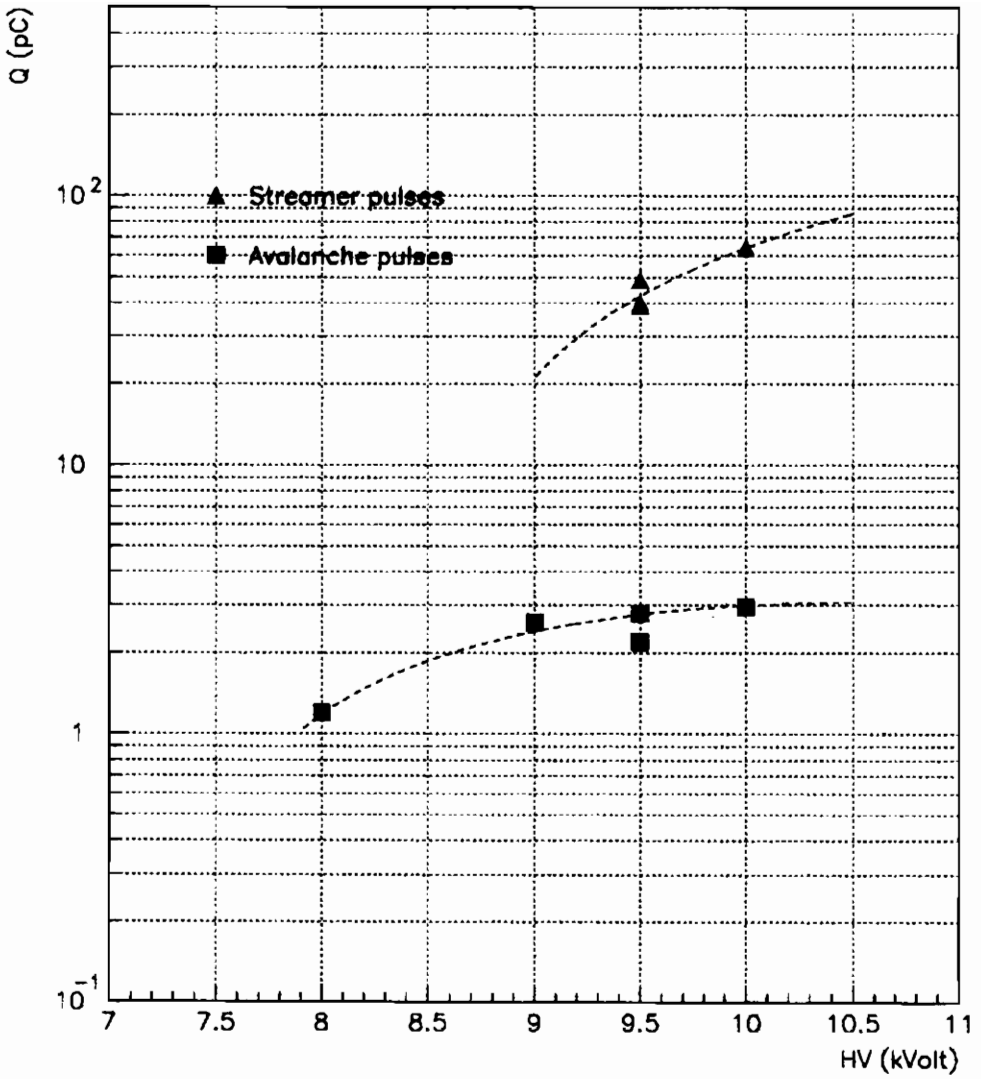

Figure 4: Charge average value vs. HV, computed for the avalanche and the streamer part of the RPC signals; for $HV = 9.5$ kV the values measured for the two RPC gaps are reported.

between the arrival time of the trigger signal and the first of the 8 signals coming from the RPC; this is equivalent to take the OR of these signals. The two figures refer respectively to an operating voltage of 8.6 and 8.8 kV, and a beam flux of about 150 Hz/cm^2. The differences between the intrinsic delay of each channel due to electronic jitter and different cable lengths has been taken into account introducing the relative calibration constants. The two distributions are almost gaussian in shape and have a base of the order of 20 ns; a gaussian fit performed only in the region of the central peak is superimposed to the distribution to put in evidence the little tail due to delayed pulses coming from the chamber.

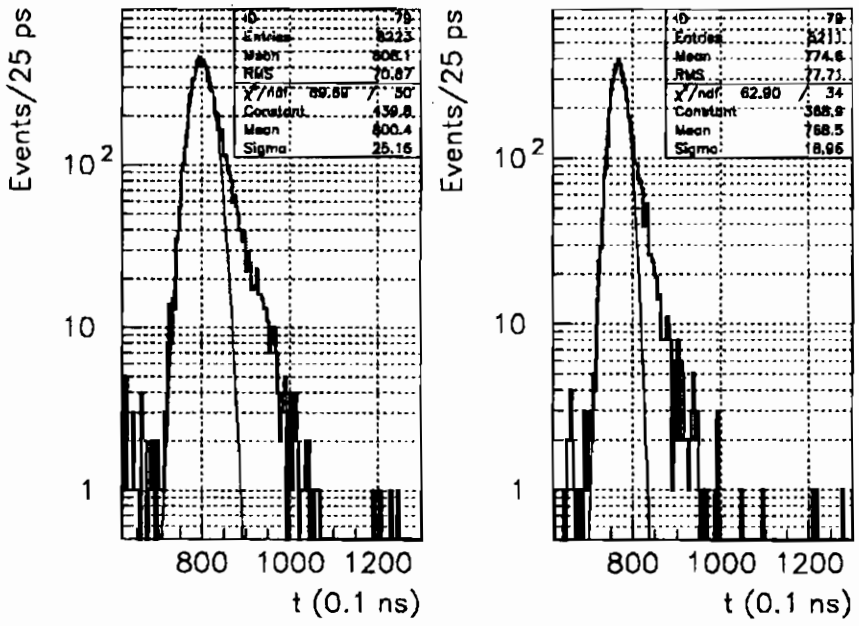

Figure 5: RPC time distributions, at a beam flux of 150 Hz/cm^2 and a) $HV = 8.6$ kV and b) $HV = 8.8$ kV.

In Fig. 6a and 6b there are similar distributions, characterized by a value of the operating voltage of 8.7 and 9.0 kV, and a flux beam of about 380 Hz/cm^2; we conclude that, at least up to this

rate, there is no significant degradation of the time performances of the RPCs.

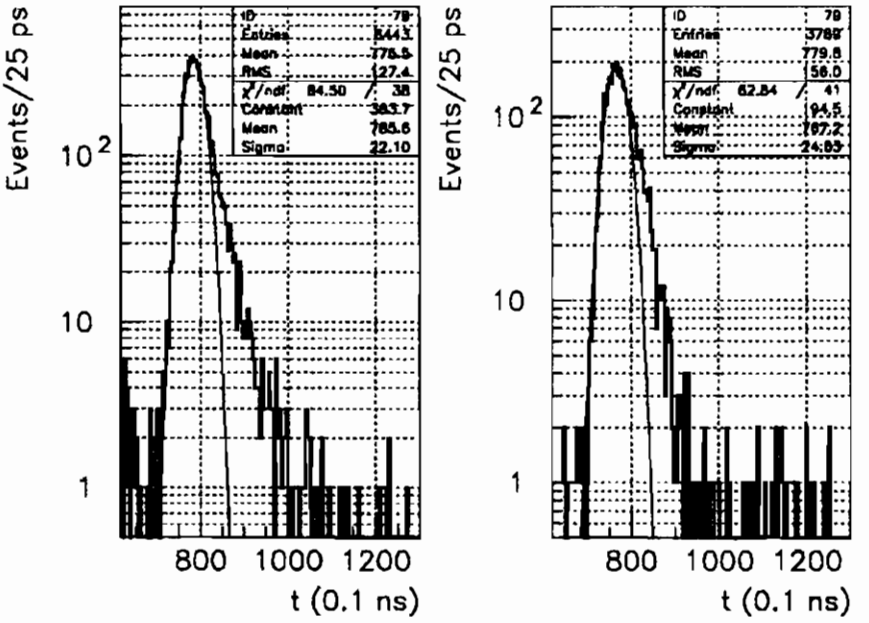

Figure 6: RPC time distributions, at a beam flux of 380 Hz/cm^2, and a) $HV = 8.7$ kV and b) $HV = 9.0$ kV.

In Fig. 7a we report the time resolution as a function of the operating voltage; the squares refer to a beam flux of 150 Hz/cm^2, the triangles to 380 Hz/cm^2. The time resolution is defined as the RMS width of a gaussian fit to the entire distributions of the type shown in Fig. 5; the trigger scintillation jitter has been taken into account. The measured values of the time resolution are contained in the range between 1.7 and 2.8 ns.

The average values of the time delay of the chamber first signal with respect to the trigger as a function of the operating voltage is presented in Fig. 7b, for a beam flux of 150 Hz/cm^2; it decreases of about 8 ns in front of a 2.4 kV voltage rise, from 8.6 kV to 11.0 kV.

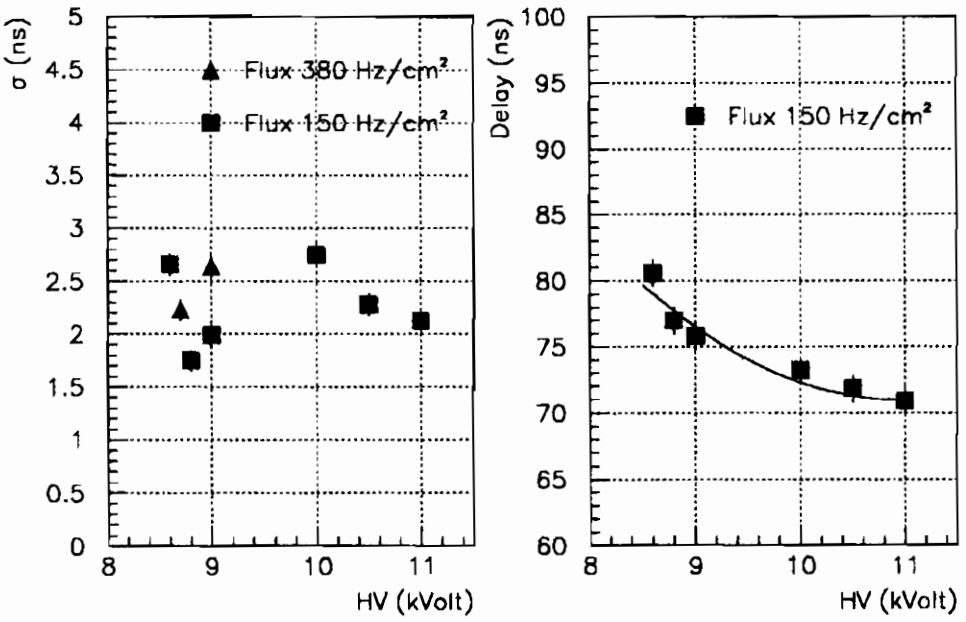

Figure 7: a) RPC time resolution vs. HV, for a beam flux of 150 Hz/cm^2 and 380 Hz/cm^2; b) RPC time delay vs. HV for a beam flux of 150 Hz/cm^2.

In Fig. 8a and 8b we show two cluster multiplicity distributions, defined as the number of strips fired for event, for 8.6 and 10.5 kV operating voltage and 150 Hz/cm^2 of beam flux. At the first voltage value we expect a pure avalanche mode, while the second should be dominated by the streamer mode, as can be deduced from the charge distributions previously presented. The presence of spark events when the signal was observed on all the strips, noticed in other conditions [4], has been greatly reduced.

In Fig. 9 we show the average value of the cluster multiplicity as a function of the operating voltage, in units of 1.5 cm wide strips. It is significant the difference in cluster multiplicity between the range 8.6–9.0 kV, where the avalanche mode is prevalent and the range 10.0–11.0 kV, where the streamer mode is dominant.

4. Conclusions

We have tested double gap, low resistivity bakelite RPCs, using

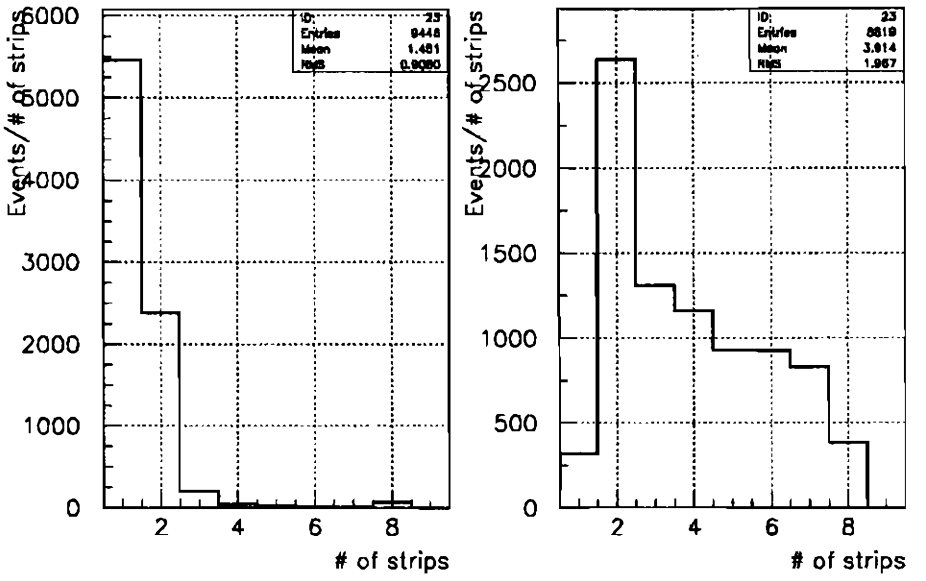

Figure 8: RPC cluster multiplicity distribution at a beam flux of 150 Hz/cm^2 and a) $HV = 8.6$ kV and b) $HV = 10.5$ kV.

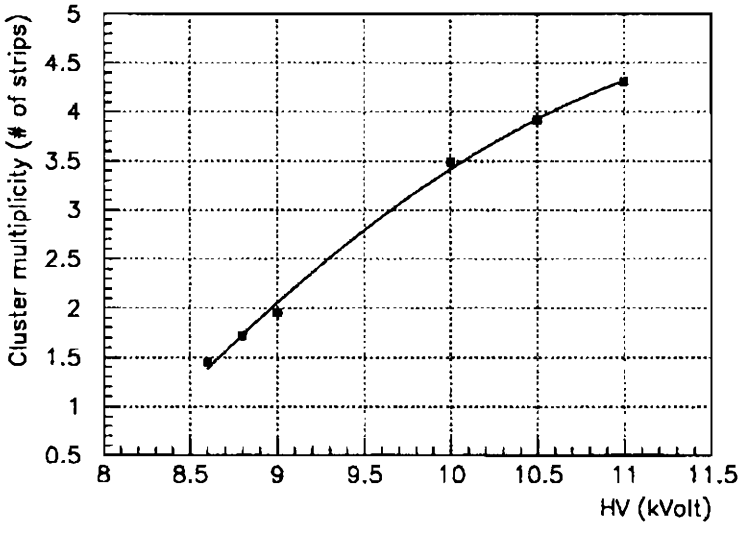

Figure 9: RPC average cluster multiplicity vs. HV at 150 Hz/cm^2.

a non ozone depleting gas mixture with high percentage of $C_2H_2F_4$, which could be used in the future LHC experiments without problems from the ecological point of view. The operating voltage is reduced, lowering, as a consequence, the RPC power consumption and the heat dissipation in the chambers.

The passage from the avalanche mode, with an average charge of the order of 1 pC, to the streamer mode, with a charge in the range between 30 and 50 pC, has been clearly observed.

The measured time resolution is about 2 ns at 150 Hz/cm^2, adequate to the LHC requirements, while the cluster multiplicity, of the order of 1–2 1.5 cm wide strips fired, begins to become compatible with the CMS trigger requests [5].

5. References

1. Bacci et al., *Test of a Resistive Plate Chamber operating at low gas amplification at high intensity beams*, Nucl. Instr. & Meth. **A352** (1995) 552;
   I. Crotty et al., Nucl. Instr. & Meth. **A337** (1994) 370.
2. L. Pontecorvo, *Study of the characteristics of Resistive Plate Chambers in the RD5 experiment*, Proc. of the II Int. Workshop on RPC, Scientifica Acta **8** (1993) 145.
3. R. Santonico, *The physics of the RPC detectors*, this proceedings.
4. M. Abbrescia, *Results of November 1994 Resistive Plate Chambers test beam*, talk given at the CMS Muon Group Meeting at CERN, March 6, 1995.
5. M. Gorski et al., *Clusters in RPC and muon trigger performance*, CMS TN, Draft of July 8, 1995.

STUDY OF ELECTRODE SURFACE TREATMENT EFFECTS ON BAKELITE RPC'S PERFORMANCES

M. ABBRESCIA, A. COLALEO, G. IASELLI, M. MAGGI,
B. MARANGELLI, S. NATALI, S. NUZZO,
A. RANIERI, F. ROMANO

Dipartimento di Fisica and INFN, Bari, Italy

V. ARENA, G. BOCA, G. BONOMI, G. GIANINI, G. LIGUORI,
M. MARCHESOTTI, M. MERLO,
C. RICCARDI, L. VIOLA, P. VITULO

Dipartimento di Fisica Nucl. & Teorica and INFN, via Bassi 6, Pavia, I-27100. ITALY

ABSTRACT

A comparison of the behaviour of several bakelite Resistive Plate Chambers (RPCs) with and without the surface treatment of the internal electrodes will be presented. Currents, single rates as well as charge distributions are compared with a reference oiled RPC and after the surface treatment. Currents and single rate are the quantities most affected by the surface oiling. A factor 4 less in currents and at least a factor 10 less in single rate is achieved using standard oiled RPCs.

1. Introduction

Over the last few years a considerable amount of work has been done in the RPC's field related to the necessity for a good operativity in the LHC environment.

Leading order problems are likely solved: data on high rates capability[1][2][3] [4], green mixtures and front-end electronics[5] are now available and they confirm the good behaviour of these detectors.

Ageing processes are also of extreme importance and are directly related to the internal surface treatment of the RPC's electrodes. So any good behaviour induced by the oiling agents on the RPC's has to be faced to the ageing property of the treatment itself.

In this talk we will point the attention to the first issue by showing how better is the use of the oiled electrodes, the measurement on the ageing properties being still under way. The data presented have been collected in a test on cosmic rays.

2. Experimental Setup

The test has been carried out at the CERN T9b area and consisted of a telescope made of 5 double gap RPC's operated in single gap mode.

The detectors area was 50 by $50\,cm^2$. The bakelite plates (of resistivity $0.4\,x\,10^{13}\,\Omega\,cm$) were $0.2\,cm$ thick.

The aluminum strips ($1.3\,cm$ wide) have been connected at both ends to different electronics for purpose of charge and time measurements; from one side 14 strips signals have been input to independent channels of a CAEN C205A ADC, with a 0.25 pC channel sensitivity.

From the other strips end the same signals have been discriminated and brought to a some LeCroy 2228A TDC's so as to have, event by event, simultaneous information on charge and time behaviour of the detectors.

This scheme permits to double check the efficiency with two independent methods. Three scintillators defined a 10 by $10\,cm^2$ trigger area.

The RPC's were then filled with an argon/isobutane/freon 13B1 (48/48/4) gas mixture. A standard (oiled) RPC has been compared to four not oiled ones and these compared to themselves after the elec-

trodes treatment.

3. Experimental results

In the following the RPCs will be labelled 1 to 4 for the not oiled ones and "R" will be referred to the standard reference detector. For the detectors have been operated in single gap mode the used gaps will be indicated with A and B (i.e. gap 3A means one gap of the RPC 3).

While in some plots only data for a certain gap are shown however all the other gaps have been checked to show the same trend.

3.1. Currents and Single Rate

Fig.1a shows the measured current as a function of the high voltage in the gap 1B for different period of time during almost a month of running. After an initial period corresponding to the conditioning of the chamber itself the current rises to the maximum values.

Some measurements done within the same day showed a sensible variation of these values. Chamber 1 has been chosen because it was nor the worst neither the best of the not oiled RPCs.

For comparison the same type of curves are displayed in fig.1b for the reference gap RA; the gap RA has been chosen because it had the worst behaviour.

As already mentioned the behaviour of the gap 1B is typical of the other not oiled gaps: fig.2a shows the currents of all the gaps as a function of the high voltage: the values correspond to the measured currents on 50 by $50\,cm^2$ area. The two lower curves correspond to the reference gaps.

Single rate has been measured counting the ORed signals coming from 8 strips of each gap; fig.2b shows the single rate as a function of the high voltage for all the gaps; the values have been scaled to a square meter area and have been collected with a discriminating threshold of $-80\,mV$. Also in this case the reference RPC is very quite with respect to the other RPCs of which gaps 4A and 4B have a significant better behaviour.

There is also a sensible local rate effect for the electrodes that are not oiled. Fig.3 displays the strip rate distribution for each gap at an applied voltage of $9\,kV$ and a discriminating threshold of $-80\,mV$; even if the plot scale does not permit to appreciate the locale variation of the

reference gaps there is a substantial effect at least in the absolute values when the electrodes treatment is applied.

The effect of the surface treatment is well shown in the following figures that are equivalent to the ones already presented and regarding the currents and single rate.

Data on RPCs 1, 3 and 4 are now corresponding to the effect of the oiling agent on their electrodes. Fig.4a shows the measured current as a function of the high voltage for all the treated gaps available. The absolute values of RPCs 1,3,4 are at least a factor 4 less than before and even less than the reference gaps.

Fig.4b displays instead the single rate (OR of 8 strips signals) as a function of the high voltage: the effect on the single rate is more noticeable and at least an order of magnitude less than in the previous case of fig.2b. It should be pointed out that in fig.4b the discriminating threshold was $-50\,mV$ instead of $-80\,mV$ as in fig.2b so one should expect a bigger scale factor at the same threshold.

The local rate also has changed significantly as shown in fig.5 where the new oiled RPCs single rate is plotted strip by strip in the same manner of fig.3 and compared to the reference gaps rate. As in that case the voltage is the same ($9\,kV$) but now the threshold is $-50\,mV$ instead of $-80\,mV$.

The new oiled RPCs local behaviour is more homogeneous and better than the reference one. The peaks are probably due to the presence of a spacer.

3.2. Efficiency

Efficiency has been calculated via the ADCs information by requiring a signal to be present after a certain ADC channel (and after pedestal subtraction); in simulating also a threshold at which to calculate the efficiency curve a triangular signal, across a $50\,\Omega$ load, of amplitude equal to the threshold (in this case $50\,mV$) and $20\,ns$ wide at its base has been assumed: the calculated area (divided by the load) then represents the charge above which a signal presence has been used for the efficiency counting.

With this approach we probably overestimate the efficiency at low voltage but the curves plateaux are comparable with those obtained with other methods (via TDCs and scalers).

Fig.6a,6b,6c,6d and 6e show respectively the efficiency of the gaps

1A-B, 2A-B, 3A-B, 4A-B for the not oiled case, and RA-B for the reference oiled gaps. The presence of the surface agent on the electrodes seems to not influence the efficiency of the RPCs. In some cases however (see RPCs 1 and 4) the knee of the plateau is shifted 500 V higher with respect to the reference gaps.

3.3. Charge distributions

The charge distributions have been obtained by integrating for 250 ns any analogic signal inducted on 14 strips in coincidence with a trigger event.

For each channel pedestals have been subtracted from the charge distribution and the rest of the distribution then summed over to obtain the total charge distribution collected over an area subtended by 14 strips.

The results are here presented as integral distributions into so called greater-than-charge histograms that is for each charge value on the abscissa axis the corresponding ordinate value represents the percentage of events with charge above that value.

Fig.7 shows these distributions for the not oiled gaps 1A, 2B, 4A and for the reference gap RA at an applied voltage of 8.5 KV

4. Conclusions

Surface treatment of the internal bakelite electrodes is a necessary step to reduce the noise and the current of RPCs. The overall result seems infact to be the smoothness of the surface itself. However the oiling agent does not influence sensitively other parameters such as efficiency and charge distributions [a]

It is probably true however that the effect of the linseed oil (that is the smoothness of the surface) could be directly obtained inside the industrial process in the bakelite foils production.

Different kind of data have been then obtained by the Bari CMS group on the the linseed oil absorption spectra in the optical range.

Another open question concerns the natural as well as the induced ageing of the linseed oil; several measurements on this aspect are sched-

[a] At the time of this talk the analysis is not complete but the trend is that neither the cluster size is altered as well; data on time resolution are still under study.

uled at the Triga Mark III Nuclear Reactor in Pavia and performed by a Bari-Roma-Pavia collaboration. By the time of the issue of these proceedings results will be available on the induced activity by neutrons on the various components of a standard RPC.

5. References

1. M. Abbrescia et al., *A test on Resistive Plate Chambers with non ozone depleting freon.* These Proceedings.
2. C. Bacci et al., Nucl. Instr. and Meth. **A352** (1995) 552.
3. I. Crotty et al., Nucl. Instr. and Meth. **A337** (1994) 370.
4. A. Di Ciaccio et al., *Performances of RPC's at high rates.* These Proceedings
5. R. Cardarelli et al., *A front-end read-out electronics for Atlas RPC's.* These Proceedings.

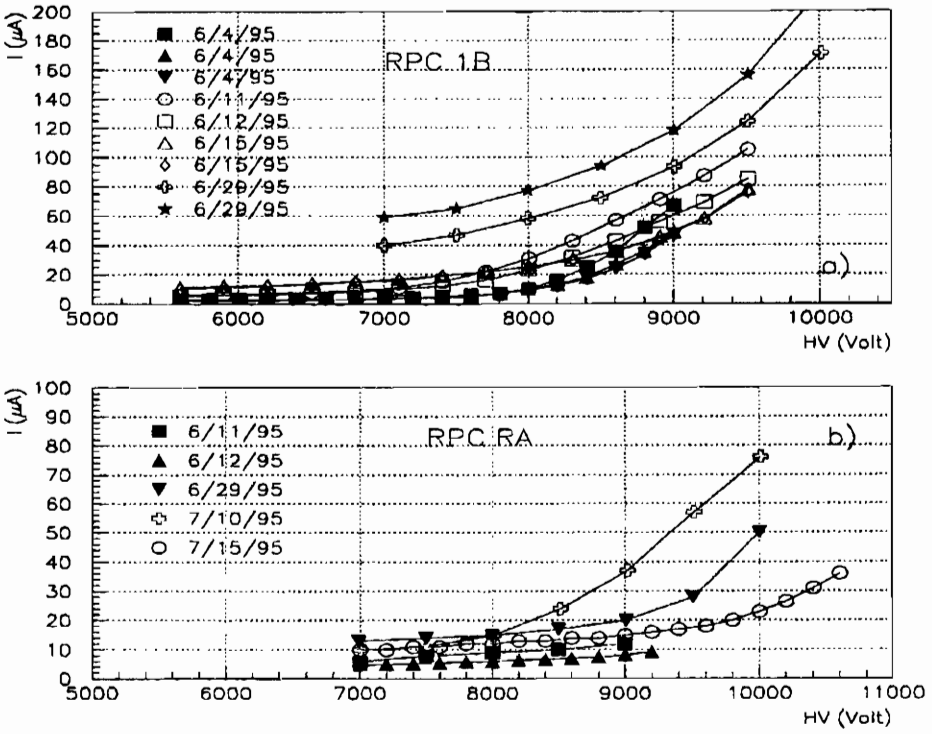

Figure 1: Current vs high voltage for different periods of time: a) Gap 1B; b) Gap RA.

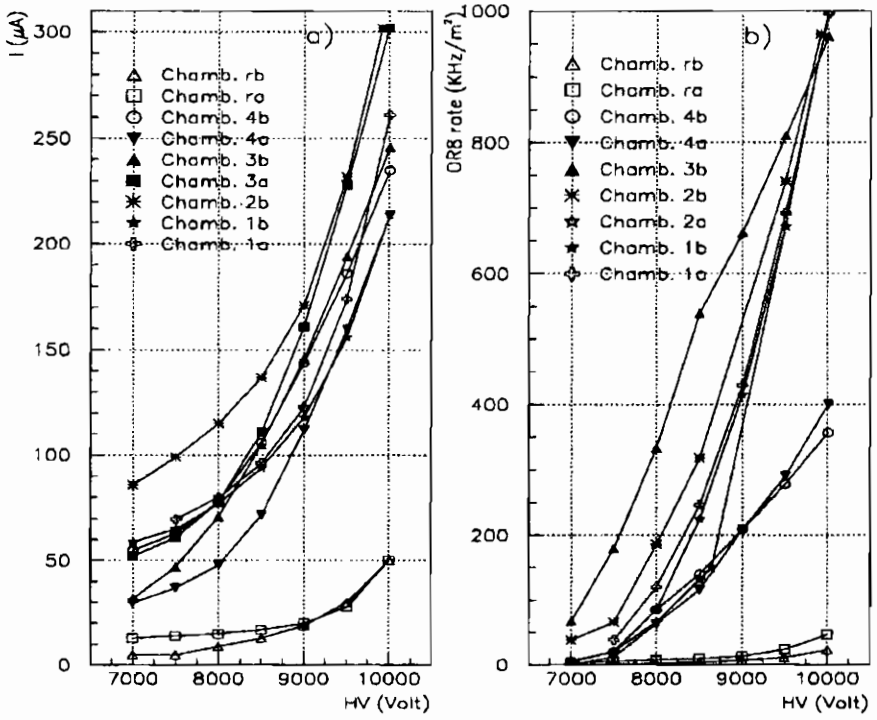

Figure 2: a)Comparison of the currents vs high voltage for all the gaps; b) Single rate vs high voltage for all the gaps. The discriminating threshold was $-80\,mV$.

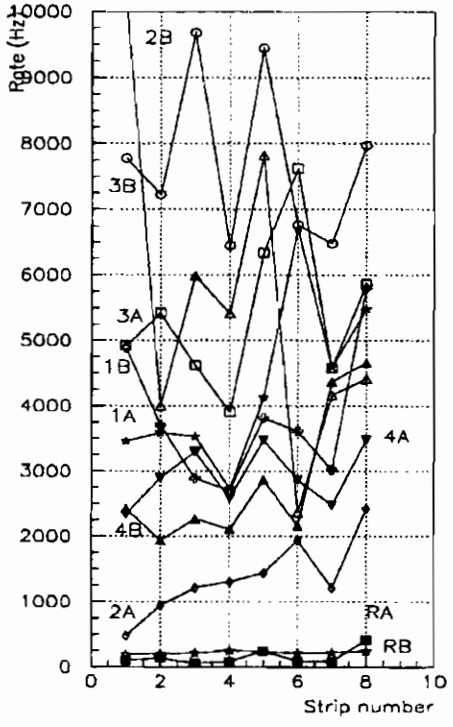

Figure 3: Comparison of the strip rate distribution for the not oiled gaps with respect to the references gaps at an applied voltage of $9\,kV$ and for a discriminating threshold of $-80\,mV$

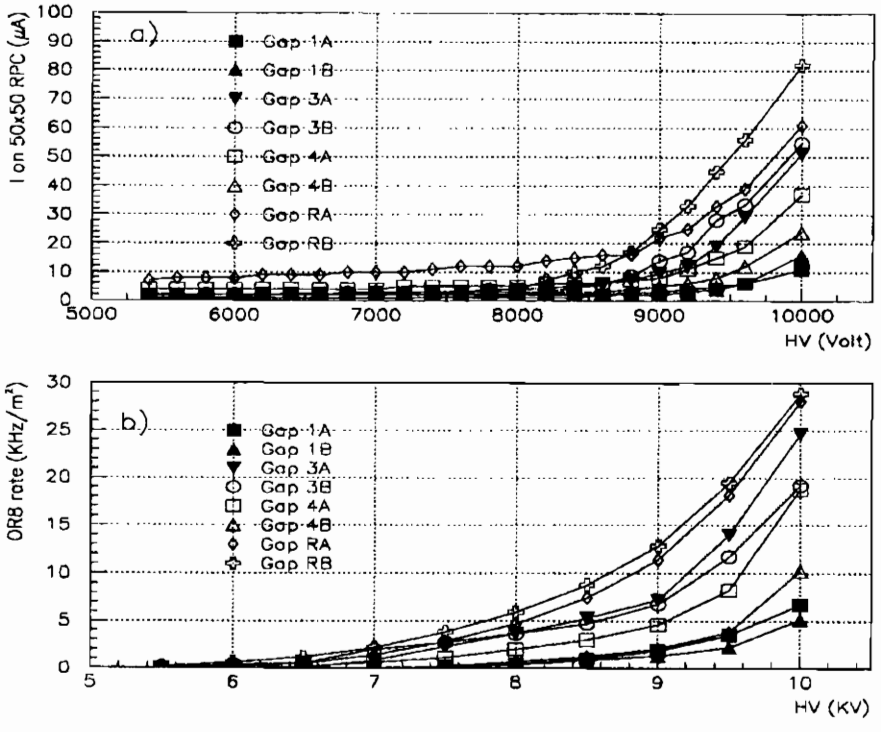

Figure 4: Effect of the internal electrodes treatment on chambers 1,3 and 4: a) Current vs high voltage; b) Single rate (as explained in the text) vs high voltage at a discriminating threshold of $-50\,mV$.

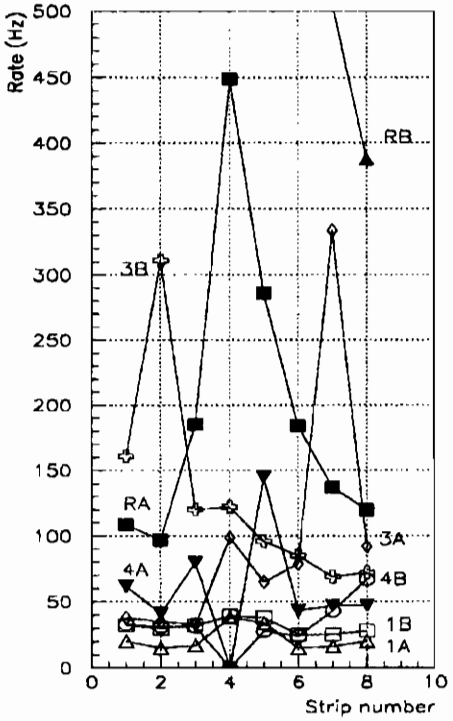

Figure 5: Strip rate distribution for the oiled gaps with respect to the references gaps at an applied voltage of $9\,kV$ and for a discriminating threshold of $-50\,mV$.

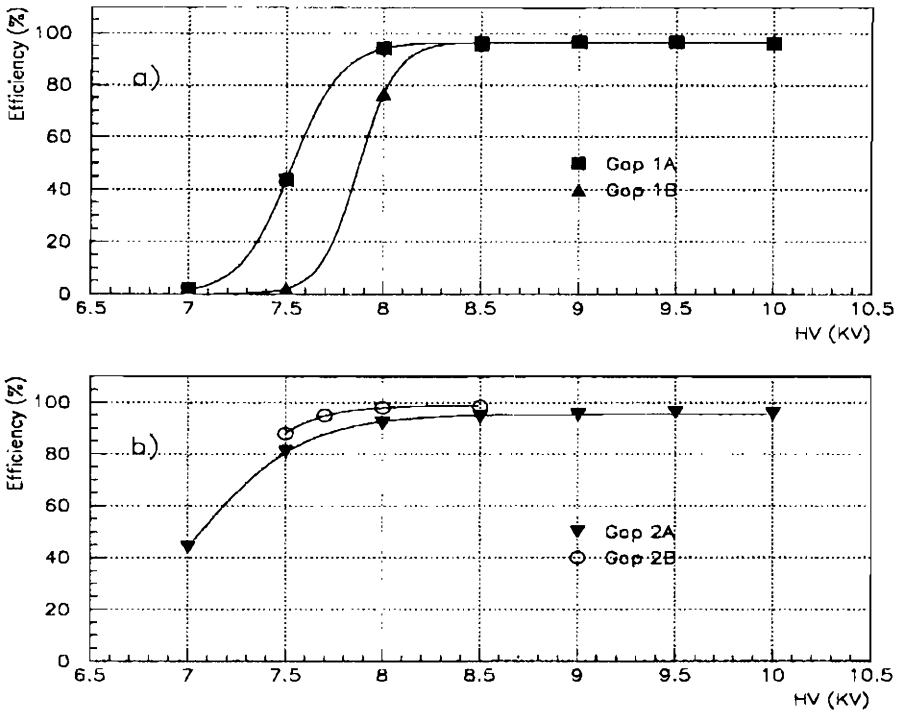

Figure 6: Efficiency curve as a function of the applied voltage for the not oiled gaps (threshold: $-50\,mV$): a) Chamber 1; b) Chamber 2

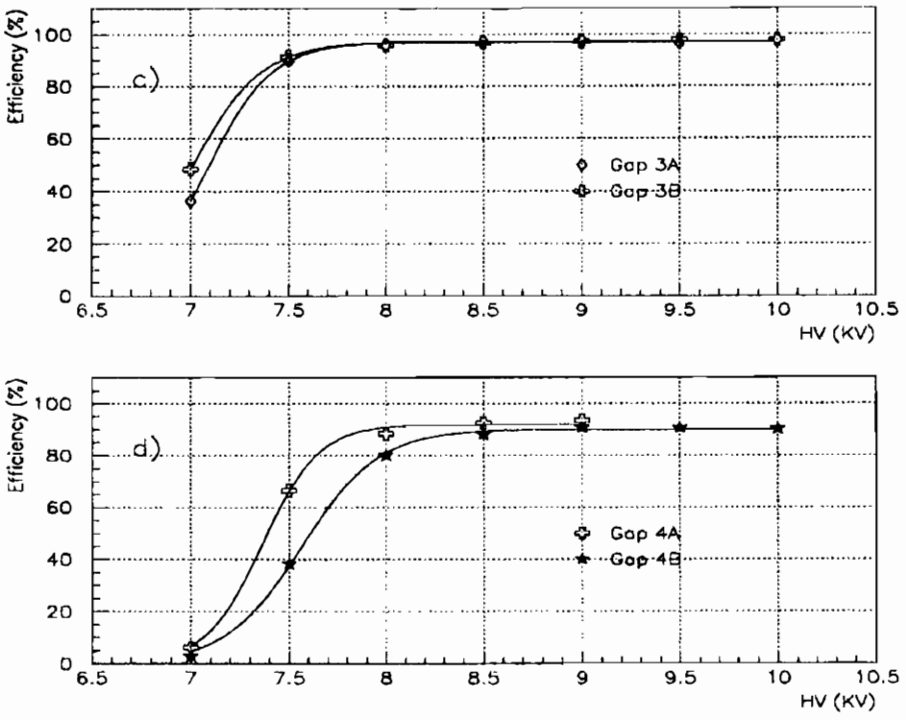

Figure 6: Efficiency curve as a function of the applied voltage for the not oiled gaps (threshold: $-50\,mV$): c) Chamber 3; d) Chamber 4.

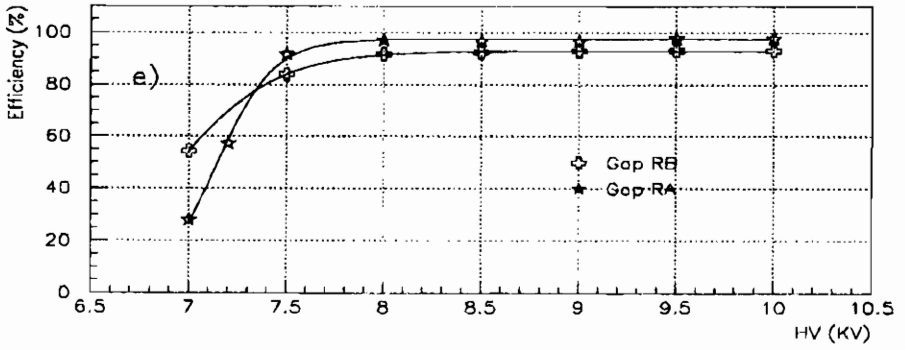

Figure 6: Efficiency curve as a function of the applied voltage for the reference chamber R (threshold: $-50\,mV$).

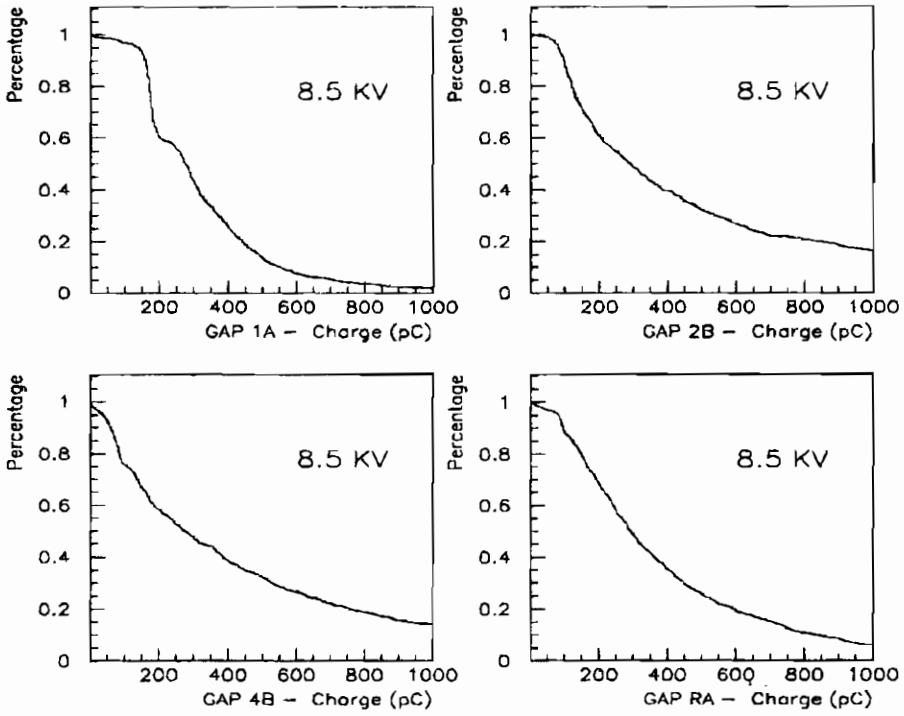

Figure 7: Greater-than-charge distributions. Histograms for gaps 1A, 2B, 4B refer to the not oiled case. For each value on the abscissa the corresponding ordinate represents the percentage of events for which the measured charge was greater than that value.

Resistive Plate Chamber performances at great altitudes

M. Abbrescia, E. Bisceglie, G. Iaselli, S. Natali, F. Romano

Dipartimento di Fisica e Sezione INFN, Bari, Italy

ABSTRACT

The performances at great altitude of 2 mm gap, bakelite RPC detectors operated in streamer mode have been tested. Efficiency, time resolution and cluster size, in a gas mixture of 58% Ar, 40% n-butane and 2% CF_3Br, appear satisfactory up to altitudes of the order of 4000 m a.s.l.

1. General considerations

Resistive Plate Chambers (RPC) detect the avalanche that under fields in the range $10^4 \div 10^5$ V/cm follows the primary ionization produced by a charged particle in few mm of gas [1]. In certain conditions of field and pressure these avalanches give rise to "streamers", a discharge condition where the avalanche is amplified into the gas itself, under the action of the field. In this paper we will refer only to RPC run in streamer mode.

The gas where the streamer is produced flows between two parallel plates made of resistive material (bakelite in our case) in general of large area (order of square meters) and small thickness (2 mm). The gap between the resistive plates where the gas flows is controlled by a dense network of spacers glued to both plates.

With such mechanical structure, to prevent RPC from being blown up, care must be taken that the pressure of the gas circulating inside the gap be very close to the pressure outside. It follows that running RPCs at high altitudes, where the atmospheric pressure can be much smaller than at sea level, requires an equivalent decrease in pressure (and density) for the gas inside. The consequent decrease in primary and secondary ionization could therefore limit the use of RPCs at high altitudes. Our tests were made to ascertain these limits.

2. Apparatus

The tests were made at sea level, on bakelite RPCs with 2 mm gap, a size that insures a time resolution better then ± 2 ns. A large vacuum tank (see Fig. 1) was used to simulate the low pressure environment. In the tank, two 2×2 m^2 RPC chambers were operated, front-end electronics included. The gas (a mixture of 50% Argon, 40% n-butane, 2% CF_3Br), after slowly circulating in the

RPCs (four volumes changes per day), flowed eventually into the tank; in this way we made sure that the RPC inside pressure was greater than the pressure in the tank by only a few mm of water, measured in a U manometer. The tank was pumped out while air was continuosly let in from a variable leak; with this air we could easily pump out the vapours entering the tank with the gas mixture and keep stable the wanted pressure. Pressures of 800, 600 and 400 mbar were created and the RPC behaviour compared to the behaviour at the atmospheric pressure.

For the tests, the large area of the two chambers, mounted vertically, was covered with horizontal cosmic muons selected and reconstructed with a muon telescope (MINI) laying downstream (Fig. 2). The telescope could predict the crossing point of a reconstructed muon in the test chambers within few cm and the precise (± 2 ns) time of flight of the same muon to any of the 12 RPC of the telescope, 11 m long. All together, this system allowed precise measurements of efficiency, time resolution, cluster size, etc. at various pressures. Details on this system are given elsewhere [2].

3. Results

Efficiency curves are shown in Fig. 3. They show a plateau of 95% efficiency at atmospheric pressure. The plateau efficiency decreases more and more rapidly to 82% at 400 mbar.

First of all it should be remembered that 95% efficiency for our 2×2 m^2 test chambers, made each of two 2×1 m^2 single gap RPC, not overlapping, is equivalent to about 100% efficiency on the sensitive area of each chamber, which corresponds to 95% of the chamber itself [3].

The fact that, at plateau, increasing the voltage the efficiency does not increase, can be interpreted as if all the primary ion pairs, even when a single one was produced, gave rise to a streamer.

The number of primary ion pairs expected in this mixture, at atmoshperic pressure, is about 7 [4], so at 400 mbar we expect 2.8

ion pairs, which implies, assuming Poisson statistics, a probability of having 0 ion pair of 6%; therefore the Poisson-expected value of efficiency at 400 mbar is 95% − 6% = 89%. Our experimental value (84%) can be considered in good agreament with the expectation, given the systematics due to temperature and casual pressure oscillations, that we can estimate of the order of 2%.

Fig. 4 shows the same curves plotted as a function of E/p. In theory the curves should overlap, while the curve corresponding to $p = 400$ mbar clearly does not. The effect is due to the gap size, too small to allow the streamer mode to be reached at $HV/p < 10000$ V/Atm, as it does at higher pressures.

Time resolution is plotted in Fig. 5 and cluster size in Fig. 6. In both cases the results at low pressure are compatible with those at sea level.

4. Conclusions

Compared to its well known sea level performances in streamer mode, the 2 mm gap, with a mixture of the type studied here, can be used up to 4000 m, corresponding to 600 mbar, without sensible lossed of efficiency, time resolution and cluster size. A small increase in the density of Argon-like gases is nevertheless desiderable.

5. References

1. R. Santonico and R. Cardarelli, *Development of Resistive Plate Counters*, Nucl. Instr. & Meth. **A187** (1981) 377-380
2. M. Abbrescia et al., *A horizontal muon telescope implemented with resistive plate chambers*, Nucl. Instr. & Meth., **A336** (1993) pg. 322-329
3. M. Abbrescia et al., *Resistive Plate Counters performances at cosmic ray fluxes*, Nucl. Instr. & Meth., **A359** (1995) pg. 603-609

4. F. Sauli, *Principles of operation of multiwire proportional and drift chambers*, CERN 77-09, 3 May 1977

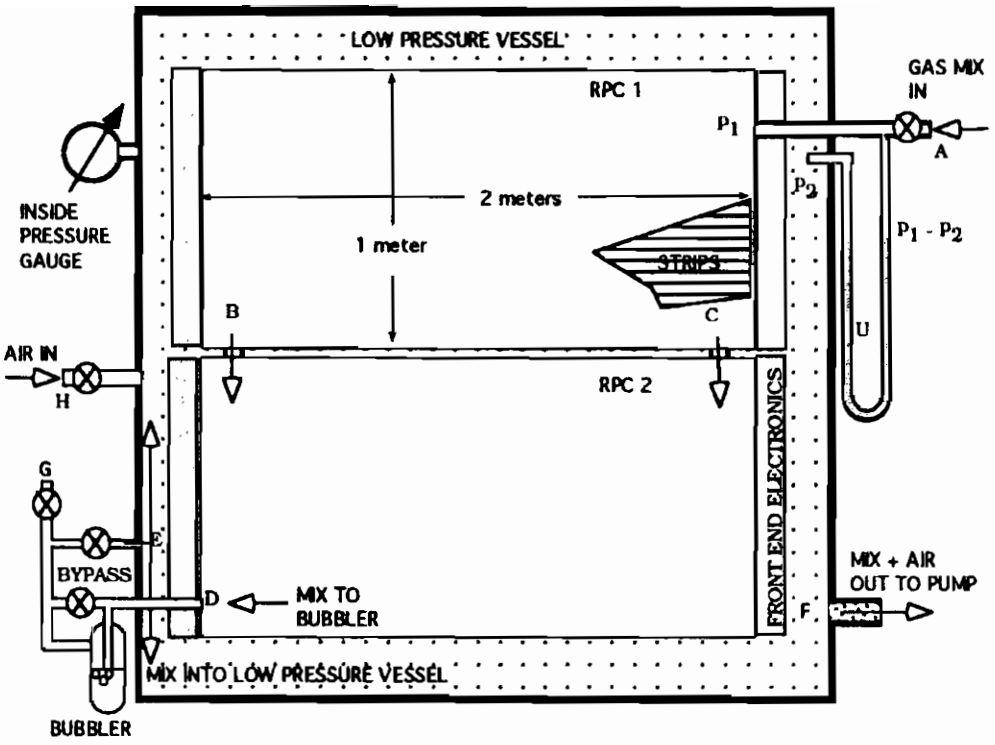

Figure 1: Layout of the vacuum tank used to create the low pressure.

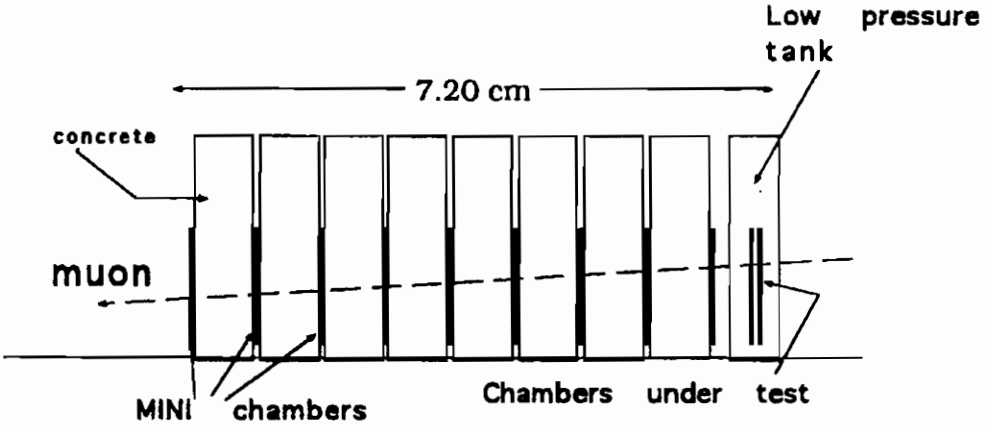

Figure 2: Layout of test chambers with MINI telescope downstream

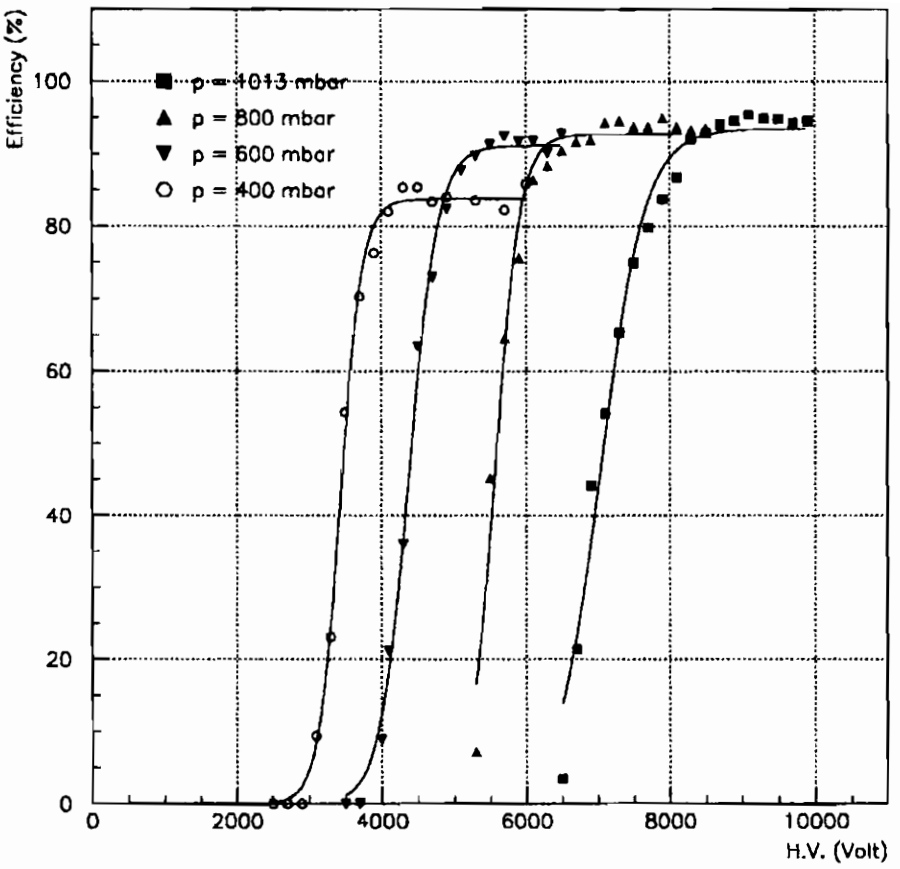

Figure 3: RPC efficiency vs. HV for p = 1013, 800, 600 and 400 mbar

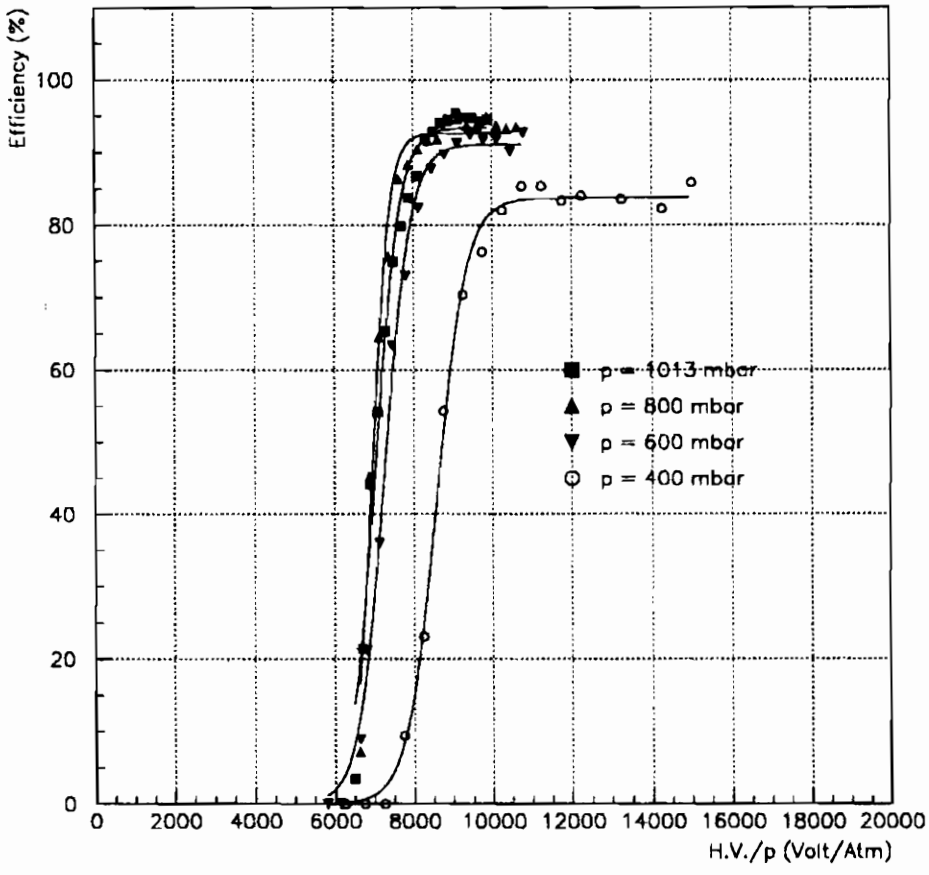

Figure 4: RPC efficiency vs. HV/p for $p = 1013$, 800, 600 and 400 mbar

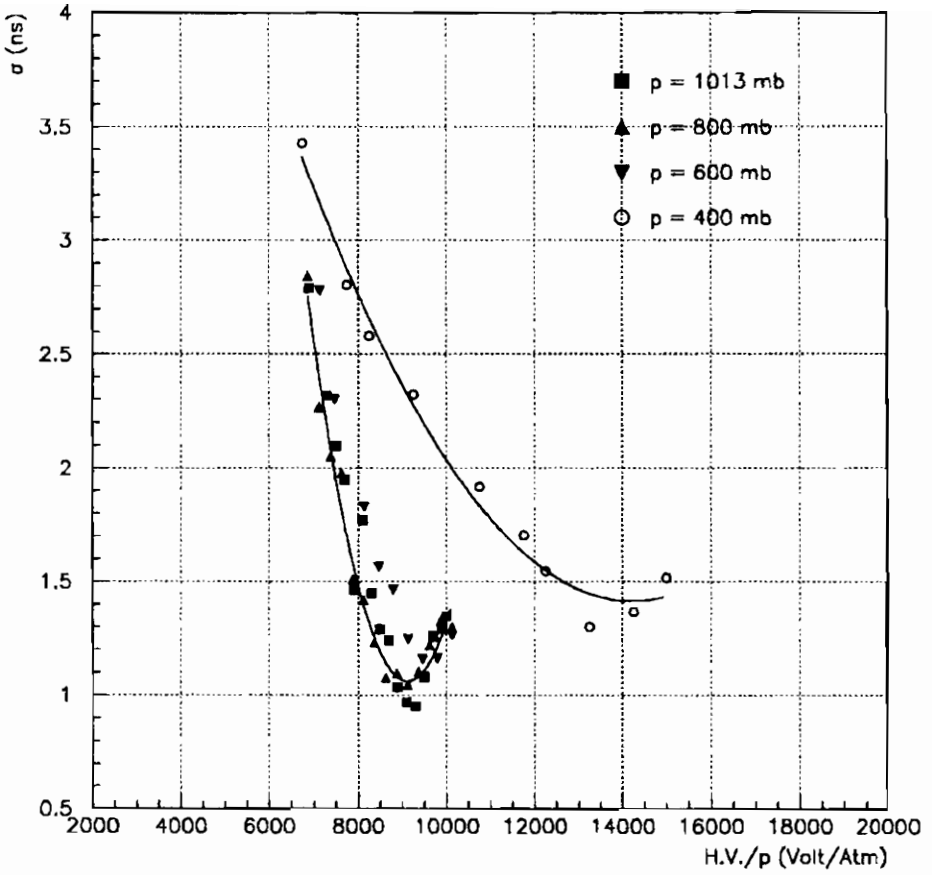

Figure 5: RPC time resolution vs. HV/p for p = 1013, 800, 600 and 400 mbar

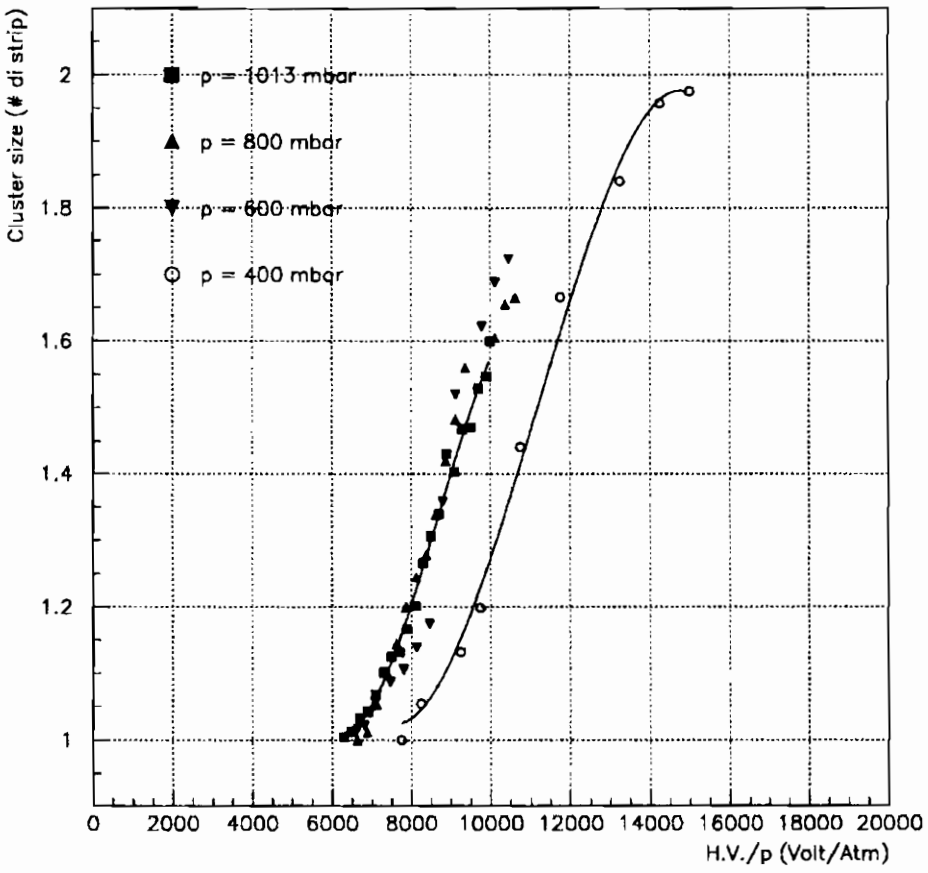

Figure 6: RPC cluster size vs. HV/p for $p = 1013$, 800, 600 and 400 mbar

EFFECTS INDUCED BY DIFFERENT KINDS OF FREON ON THE RPC CHARGE ACCUMULATION

V. Arena, G. Boca, G. Bonomi, G. Gianini,
G. Liguori, C. Riccardi, P. Vitulo, L. Viola

Dipartimento di Fisica Nucleare e Teorica dell'Universita' di Pavia and INFN, Sezione di Pavia

ABSTRACT

The performances of Resistive Plates Counters (RPCs) fluxed with mixtures containing allowed freon have been studied. In particular the charge collected by single strips have been compared with that obtained fluxing the RPCs with the freon *R13B1* no longer allowed. Preliminary results show that *R134A*, mixed in larger percentage with *argon* and *isobutane*, seems a good replacement. Additional work is needed in order to study the RPCs performances using other kinds of freon and to check thoroughly all the work parameters.

Introduction

New laws concerning the environment preservation forbid the freon *R13B1*, that in mixture with *isobutane* and *argon* has been so far used to fill the Resistive Plate Counters (RPC) [1]. The main effect of freon in gas mixture is to capture the electrons spreading away from the discharge axis. In order to look for a substitute, we assembled a simple apparatus in our lab to test the behaviour of RPCs using different kinds of freon. In these preliminary tests we used *R134A*, a freon utilized today in domestic refrigerators, and*R116* used in low temperature machines.
One of the main problems of the RPCs to tackle in accelerator experiments, is the rate of the incoming particles. If this is too high, the charge released by particles crossing the gas gap could limit the performances of RPCs because of the drop of the high voltage on the electrodes. For these reasons in the current study we focused our attention on the charge released by the particles crossing the detector as a function of the gas mixture. Because with the mixtures used so far (namely 2/3 argon, 1/3 isobutane and few per cent of freon) the charge involved has a value for which the RPCs can sustain a rate up to 100 Hz/cm^2 [2] without performances degradation, the goal of this analysis is to find a mixture, containing one of the allowed freon, in which there is a similar charge release: in this way the possibility to operate the RPCs up to the same rate can be guaranteed.

Apparatus for the test

This study was carried out using the layout sketched in fig.1. A coincidence among a sandwich of scintillation counters allows the detection of cosmic rays in the solid angle viewed by the RPC of 50*200 cm^2 size, located inside. The RPC strip size is 3*50 cm^2. In order to measure the RPC parameters, the signals go to discriminators and logic modules [3] allocated in a VME crate read out by a personal computer Quadra MacIntosh equipped with LabView software package. The system allows to perform a remote control by computer: it is possible to set and check the threshold of the front-end discriminators, both for the signals coming from the photomultipliers and from the RPCs. It is also possible to arrange different kind of triggers. To measure the charge, the RPCs signals go directly into an Analog Digital Converte (ADC) module.

Test conditions

To make a comparison among the charge collected by the RPCs fluxed by different gas mixtures, it is necessary to establish an operative procedure.

Actually it is important to note that the working points change in correlation with the different gas mixtures. Just to fix a reasonable working point, we decided to measure and compare the charge at a voltage in which the efficiency of a single gap counter was about 95%, with threshold fixed at 50 *mV* in all tests. Each of the eight strips were connected to an ADC channel. The three-fold coincidence among the scintillator counters shown in fig. 1 generated the gate for the ADC's (100 *ns* width) as well as the trigger for the RPC's data acquisition.

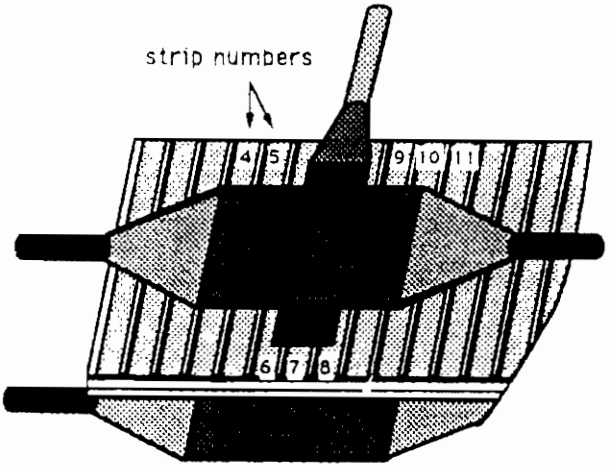

fig 1 sketch of the charge measurement apparatus (not in scale)

Preliminary results

Taking into account that in past experiments the RPC's were filled with mixtures containing argon, butane and freon in a range of different percentages [4], as a first step we fluxed the counter with two gas mixtures at the edges of the range: *Argon* 65%, *Isobutane* 30% and 5% *Freon R13B1* and *Argon* 18%, *Isobutane* 18% and *R13B1* 4%. The single gap efficiencies as a function of the high voltage (HV) are shown in fig. 2a) and 2b). To measure the charge collected by the strips, we fixed the HV at the value at which the efficiency was 95%, according to the working procedure described above: 7.4 *kV* for the first mixture and 8.4 *kV* for the second one. The pie plots of fig. 3 show the

charge distribution of the eight strips under test for the first mixture after the electronics pedestal subtraction. As you can see, only three strips collected a significant amount of charge, namely those involved by the trigger. Strip 7, located just in the middle of the scintillator counter 4, is the most fired strip and collects more charge than the adjacent ones.

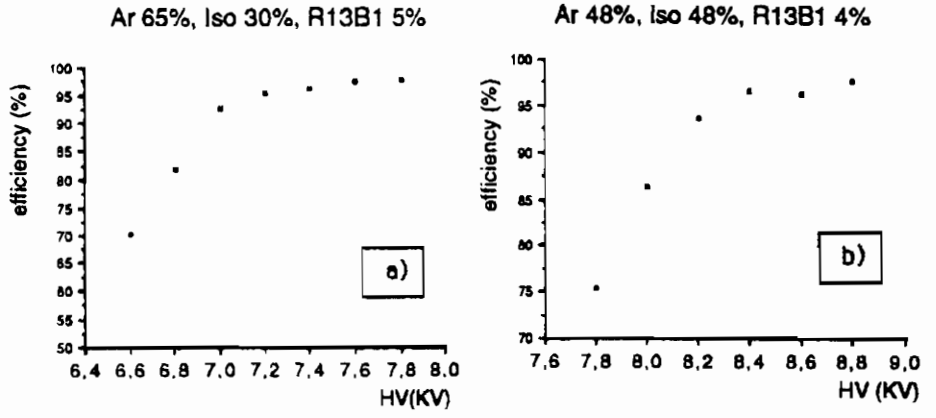

fig. 2: **RPC efficiency with two mixtures containing R13B1**

The pie plots of fig. 4a) and 4b) show the charge collected by the strip 7 for both mixtures. They are almost the same, the main difference being that the working point is 1 KV higher for the second mixture enriched by isobutane.

The charge distribution of strip 7 showed in fig. 4a) was used as a reference for the next measurements.

Operating the RPCs with mixture containing 5% of *R134A* or 5% of *R116* instead of *R13B1*, the charge collected by the strip 7 in the working conditions fixed as before (95% efficiency), was higher, as it is showed in fig. 5a) and 5b). Comparing these figures with the one in reference (fig.4a) it becomes apparent that both the new tested freon are less electronegative then the *R13B1*. As a consequence the charge involved in the process is larger and the strips collect more charge, although the full efficiency is reached at a lower voltage. In order to obtain the same charge distribution as the reference one the new freon percentage has to be increased at the expenses of the percentage of argon. As an example, using the following gas mixture: *Argon* 20%, *Isobutane* 20%, *R134A* 60%, the charge distribution of strip 7 (fig.6) is quite similar to the reference one, indicating that the RPCs could be operated, in principle, at the same rate than with the so far used mixtures.

Ar 65%, Iso 30%, R13B1 5%

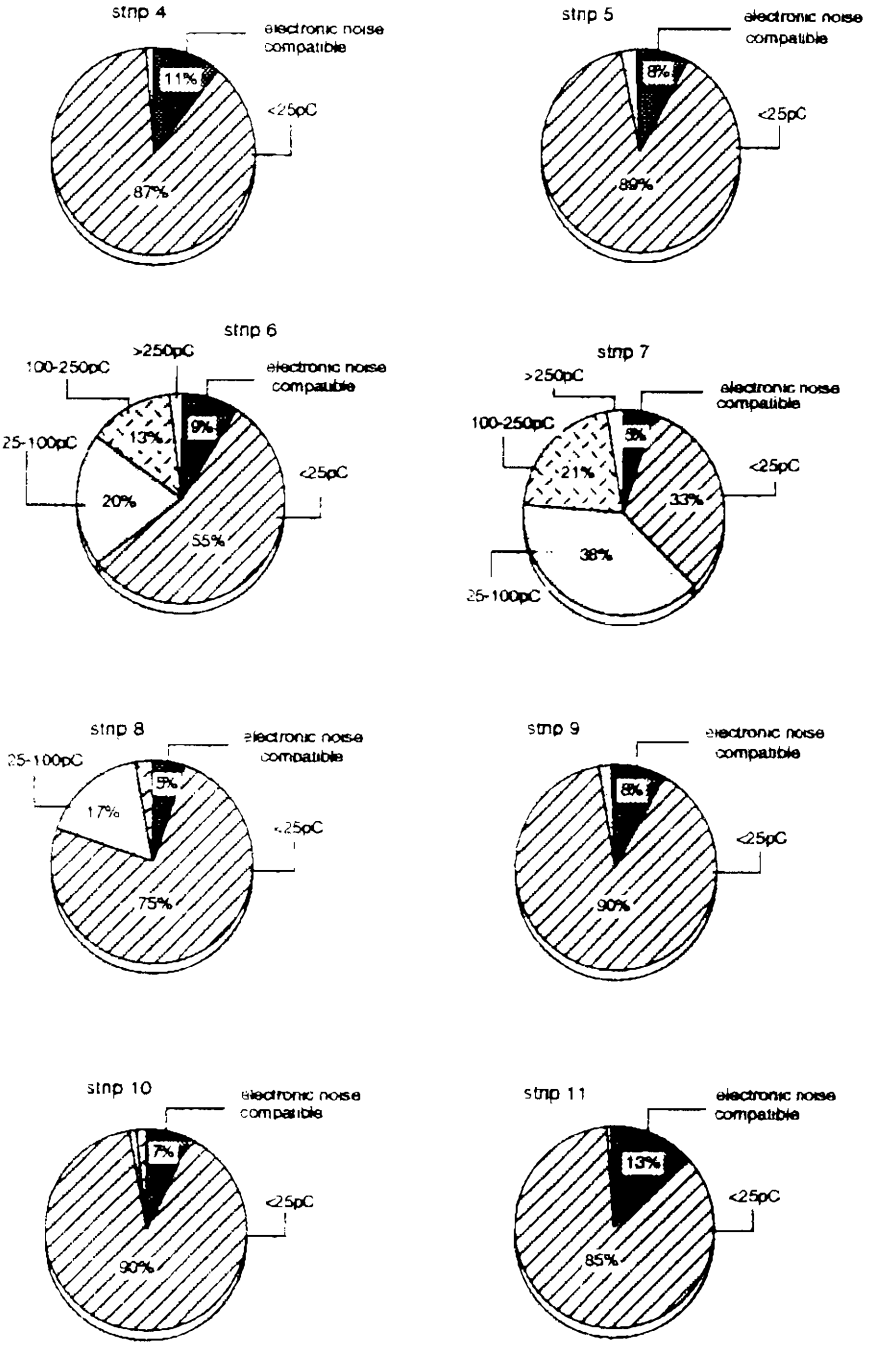

fig 3. single strips charge distribution

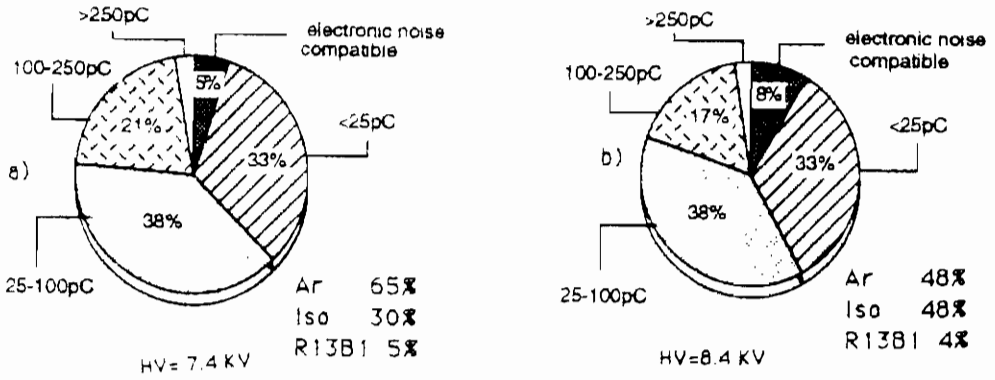

fig. 4: strip 7 charge distribution for mixtures containing R13B1

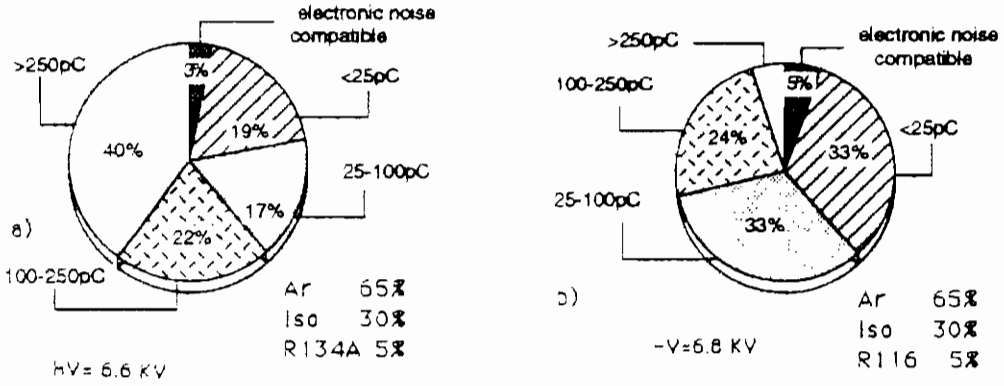

fig. 5: strip 7 charge distribution for mixtures containing R134A and R116

Ar 20%, Iso 20%, 134A 60%

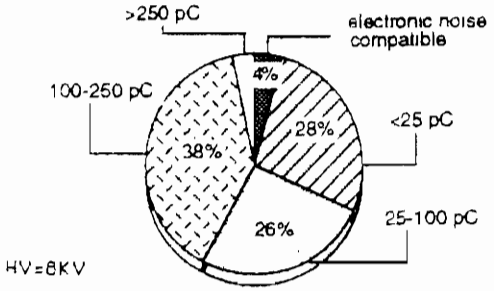

fig. 6: strip 7 charge distribution for mixture containing high percentage of R134A

Conclusions

Using gas mixtures containing low percentage of *Freon R13B1*, RPCs were operated in the past at a local rate up to 100 Hz/cm^2, without significant loss in performances. Because it is not possible to use the *R13B1* any longer, due to environment problems, we tested the behavior of RPCs fluxed with different kind of allowed freon. In order to sustain a local rate of incoming particles similar to one obtained with the old freon, we looked for mixtures giving the same charge distribution. Preliminary results show that *Argon* 20%, *Isobutane* 20% and *R134A* 60% give a similar charge, although we have not yet checked all the RPC parameters. To complete the work, it is necessary to test RPCs further with other kinds of freon more electronegative, measuring at the same time all the RPCs parameters very carefully.

References

[1] R.Santonico and R.Cardarelli, *Nucl. Instr. and Meth.* A187, 337 (1981).
R.Cardarelli et al., *Nucl. Instr. and Meth.* A263, 20 (1988).
[2] C.Bacci et al., *Nucl. Instr. and Meth.* A345, 474 (1994).
[3] V.Arena et al., *Nucl. Instr. and Meth.* A349, 237 (1994).
[4] G.Cataldi et al., *Nucl. Instr. and Meth.* A337, 350 (1993).
M.Abbrescia et al., *Nucl. Instr. and Meth.* A336, 322 (1993).
A.Antonelli et al., *Nucl. Instr. and Meth.* A337, 34 (1993).
C.Bacci et al., *Nucl. Instr. and Meth.* A324, 83 (1993).

Test of Low Gas Gain RPCs with ozone and non ozone depleting gas mixtures

Anna Di Ciaccio *
University of "Tor Vergata" and INFN Sezione di Roma II,
via della Ricerca Scientifica, 1, Roma, 00133, Italy

February 6, 1996

ABSTRACT

Resistive plate chambers operating at low gas amplification have been tested with particle beams and in presence of high intensity low energy photon flux from a radioactive source at the RD5 and H8 test area at CERN. Measurement of rate capability and time resolution in view of their use at LHC were performed. The study of the charge as a function of the applied voltage has allowed the observation of the transition between the avalanche and streamer mode. A new gas mixture, mainly composed of Tetrafluoretane, a gas environment safe and widely industrially employed, has succesfully been tested.

*co authors : M.G.Alviggi, P.Camarri, R.Cardarelli, F.Ceradini, P.Creti, R.de Asmundis, V.Gapienko, E.Gorini, F.Grancagnolo, L.Pontecorvo, S.Rosati, R.Santonico, Y.Sviridov, S.Veneziano, V.Zaet.

1. Introduction

Since 1993 resistive plate chambers are operated at a lower gas amplification to cope with the demand of a higher rate capability to performe an efficient muon trigger at LHC [1]. Several tests have already shown the capability of RPCs to work in such a regime [2], [3], [4]. The choice of low gas amplification requires no modification to the detector structure but has a major impact on the read-out electronics that must amplify signals a factor 100 smaller.

More recently we began a search for a gas mixture non flammable and environment safe. In fact the usual mixture was containing a polluting Freon, CF_3Br, that is no more commercially available. In this paper we present studies showing the feasibility to operate RPCs at low voltage, in a pure avalanche regime, using a new gas, $C_2H_2F_4$, ecological and non flammable.

2. RD5 experimental lay-out

The RPCs tested are three single gap chambers built with bakelite plates of 50 x 50 cm^2 area, 2 mm thick, with 2 mm gas gap. The signals are read-out from two sets of orthogonal pickup strips of 17 mm pitch. The strips are signal trasmission lines of 50 Ω impedence, connected to the electronics on one side and terminated on 50 Ω on the opposite end. The frontend electronics, specially conceived to read the signals in the low gas amplification, consists of a two stage voltage amplifier of 500 MHz bandwidth, a total amplification of a few hundred and an input impedence of 50 Ω.

They were placed immediatly upstream the RD5 experimental area in the H2 SPS beam line [5].

The chambers have been fluxed with a gas mixture of Freon CF_3Br and n-Butane C_4H_{10} in several ratio(from 50 % up to 85 % Freon).

The measurements were done using 200 GeV/c muon and pions up to 10 KHz/cm^2 flux. A 14mCi Co^{60} source was used to illuminate the detector with a roughly uniform flux of 1.2 MeV photons, producing on

the first RPCs an average rate of 150 Hz/cm^2.[a]

2.1. Experimental results

In Fig. 1 the RPC efficiency is presented as a function of the beam flux. The chamber shows a good efficiency (>98%) up to beam fluxes of 1 KHz/cm^2. The detector rate capability has increased of more than one order of magnitude respect to the previous operation mode. The quoted beam fluxes do not include the additional photon flux induced by the Cobalt source.

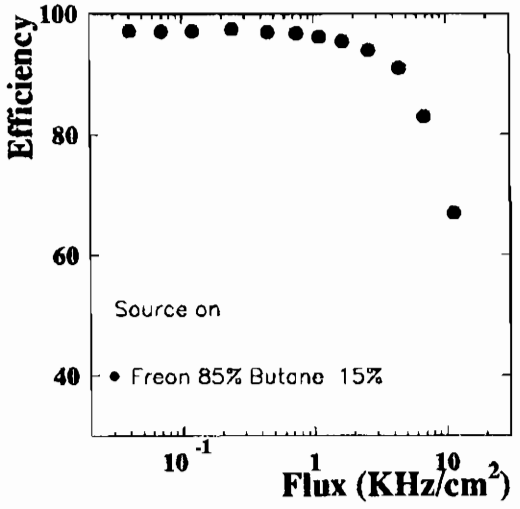

Fig. 1. Efficiency versus beam flux.

In Fig. 2 and Fig. 3 the time resolution and the delay time are shown as a function of the beam flux. The time resolution is about 1 ns and the response delay is flat within 2 ns up to fluxes of 1 KHz/cm^2, a considerable improvement respect to the previous regime. The quoted time resolutions and delay times are obtained from the sigmas and the means of the gaussian fit to the time distributions.

To study the discharge mechanism inside the RPCs and its behavior

[a]The RPCs sensitivity to 1 MeV photons is around 10^{-2}.

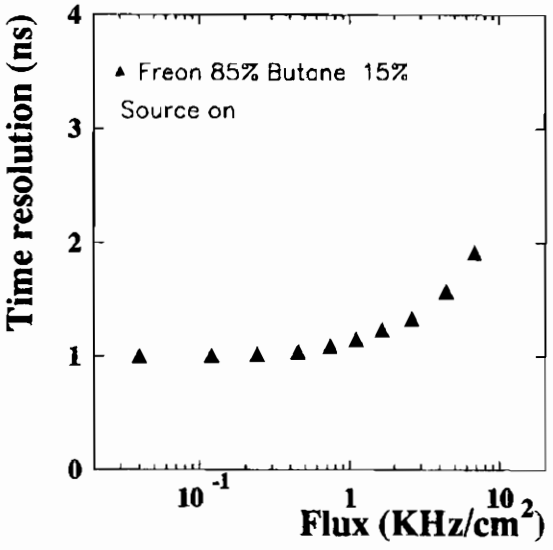

Fig. 2. Time resolution versus beam flux.

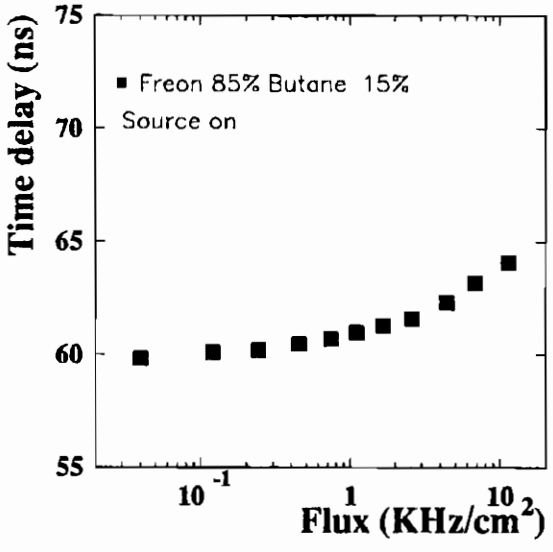

Fig. 3. Delay time versus beam flux.
The zero for the time scale is arbitrary.

for increasing electric field we have operated the chambers at different voltage over a few kilovolt range. The strip signals were directly sent into a Lecroy 2249 ADC module, with a 0.25 pC sensitivity.

In Fig. 4 the total charge collected on the pickup strips of a chamber is shown for two different gas mixtures, at a beam flux of 450 Hz/cm^2.

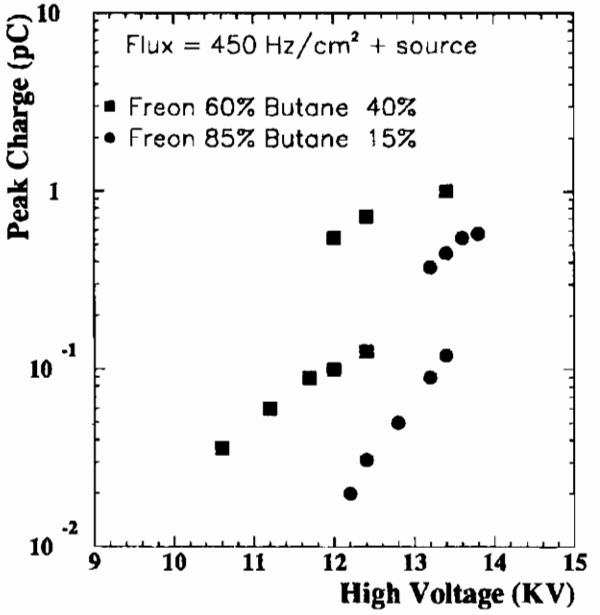

Fig. 4. Total charge versus high voltage. For the charge an electronics amplification of 500 was assumed.

The signal from a strip is contributing to the total charge only if it is greater than three times the r.m.s. of its pedestal. The plotted values are the peak values of the charge distributions. The collected charge is clearly voltage dependent and at first follows a nearly exponential behavior typical of a proportional mode and then suddenly jumps to the limited streamer mode where the charge multiplication is almost a order of magnitude larger. Between 12 and 13.5 KV(depending from the gas mixture) the charge distributions show a double peak because both regimes are present.

The total charge seen by the detector is < 1 pC and it is clearly gas

mixture dependent.

3. H8 experimental set-up

In summer 1995 a trigger hodoscope, consisting of seven single gap RPC chambers of 50 x 50 cm^2 area with orthogonal(X, Y) strip read-out, has been tested on the H8 ATLAS test area at CERN. The hodoscope was supposed to reproduce a small sector of the ATLAS trigger chamber lay-out.

The purpose of the test was to study the performance of the ATLAS level 1 muon trigger processor prototype [6] and at the same time to see the chamber behavior with new gas mixtures, enviroment safe and non flammable.

A schematic of the set-up is shown in Fig. 5.

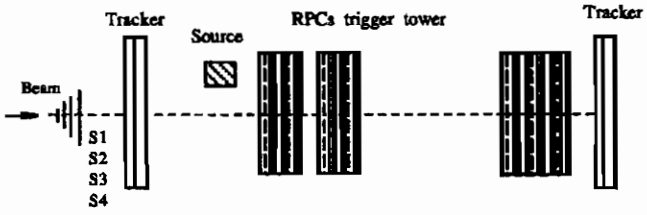

Fig. 5. Schematic view of the H8 set-up.

In front of the RPCs system a set of four scintillator counters of various dimensions was installed to trigger on beam particles. Two trackers, consisting of a 4 x 4 matrix of 3 cm diameter drift tubes, were put just before and after the RPCs to measure the beam spot along the vertical coordinate. The triggered area(10 x 10 cm^2) was illuminated with 180 Gev/c muons and with a continuous flux of low energy photons produced by a 14mCi Co^{60} radiactive source.

The RPCs trigger system was arranged in two doublets and a triplet of chambers, respectively 40 cm and 200 cm apart. A doublet(triplet)

was consisting of two(three) X and two(three) Y read-out planes. Each plane was made of 16 aluminum strips of 3 cm width. The read-out electronics consisted of two stage amplifier(10 and 30) with a bypolar output signal [7].

The 224 strip signals were send first to the input of the 4022 Lecroy discriminators with adjustable threshold between 15 and 300 mV and then to the 2277 TDC Lecroy modules with 1 ns resolution.

3.1. Experimental results

The need to find a replacement for the usual Freon with a non ozone depleting gas induced us to select a new gas, Tetraflouretane, $C_2F_2H_4$ [8], cheap and largely industrially employed. This gas is also caracterized by a high density that insures an high primary ionization.

The chambers have been fluxed with Tetraflouretane together with a small amount of iso(n)-Butane(from 5 to 9%).

In Fig. 6 the time difference between two RPCs of a doublet is shown. From a gaussian fit of this distribution we extract a $\sigma = 1.8$ ns that corresponds to the chamber time resolution.

The chamber efficiency is presented in Fig. 7 as a function of the applied high voltage. The RPCs are already 98% efficient at 8.4 KV, a much lower voltage respect to the gas mixture with the Freon CF_3Br.

4. Conclusions

We have successfully tested RPCs chambers at low gas amplification with different gas mixtures at the RD5 and H8 test-beam at CERN.

The chamber efficiency and time resolution look adequate to the LHC requirements.

We have found a new gas mixture, ecological safe and non flammable, that allows to operate RPCs at a voltage less than 9 KV, in avalanche mode, with 98% efficiency.

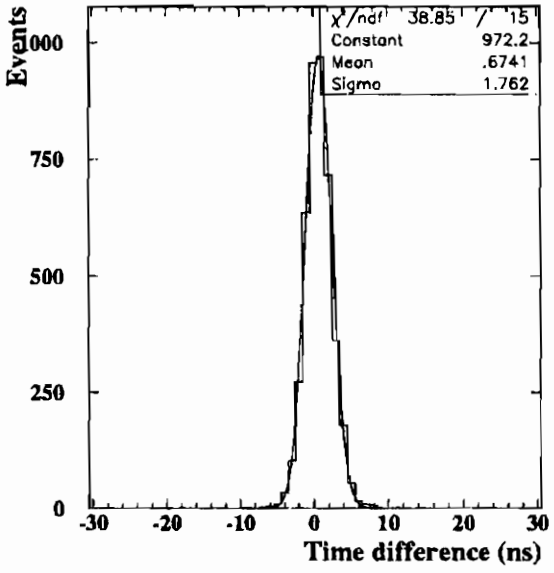

Fig. 6. Time of fligth between two RPCs.

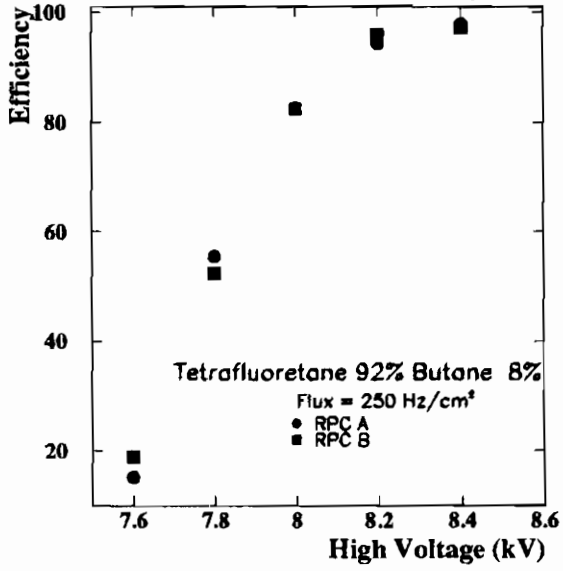

Fig. 7. Efficiency versus high voltage.

5. References

1. The Atlas Collaboration , Technical proposal, CERN/LHC/94-43, LHC/P2 , 15 December 1995.
2. R.Cardarelli, A.Di Ciaccio and R.Santonico, *Nucl. Instr. and Meth.* **A 333** (1993) 399.
3. C. Bacci et al., *Nucl. Instr. and Meth* **A 352** (1995) 552.
4. M. Angelone et al., *Nucl. Instr. and Meth.* **A 355** (1995) 359.
5. M. Abbrescia et al., *Nucl. Phys.* **B 44** (1995) 218.
6. S. Veneziano, contribution to this Workshop(Pavia, october 1995).
7. R. Cardarelli, contribution to this Workshop(Pavia, october 1995).
8. R. Santonico, contribution to this Workshop(Pavia ,october 1995).

POSITION MEASUREMENT IN RPCs BY TOF

GEOFFREY H. GRAYER
Rutherford Appleton Laboratory,
Chilton, OX11 0QX, England
E-mail: GRAYER@V2.RL.AC.UK

ABSTRACT

A resolution of $\sigma \approx 5$ mm was obtained for the position along a strip of an RPC by using time-of-flight (TOF) information. By taking the difference in arrival time of the pulse at each end of the strip, time jitter originating from the development of the discharge is removed. Although the test was made with a chamber 1m long, it is argued that similar resolution should be possible for much longer lengths.

1. Introduction

RPC signals are fast; Fig. 1 shows the 90% rise time to be a few ns.

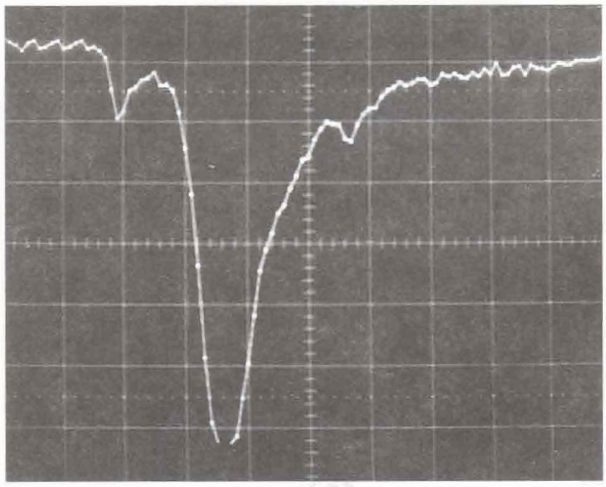

Fig. 1. A typical RPC signal as seen by the amplifier. The scales are 10 ns/division horizontally, and 5 mV/division vertically. The proportional mode precursor to the streamer discharge is clearly seen. An LRS 7200 oscilloscope was used, with a sampling rate of 1 $GS.s^{-1}$ and a bandwidth of 500 MHz.

The use of readout strips configured as correctly-terminated constant-impedance trasmission lines ensures that these signals travel at constant velocity while retaining their shape, and are free from reflections. The strips are usually wide, giving them a large surface area, thus reducing the skin effect and hence the series resistance. This, together with the use of a low-loss dielectric, reduces the dispersion and high frequency attenuation to a very small value. Use of a backing plane obviates radiation loss. It seems probable that the fast leading edge would be retained over the lenght of any practicable chamber.

However, there is a substantial variation in the time between a particle traversing the RPC and the detected signal. Because relatively few ion-pairs are produced in a few mm of gas, statistical variations occur in the time taken to develop a discharge. However, this jitter is correlated at both ends of the strip line, and can be removed by taking the difference in the measured arrival time at the each end, this being

proportional to the distance of the origin from the middle of the chamber. This procedure also contains the possibility of making a consistency check of the data, since the sum of the two times measured from a trigger pulse should give a value corresponding to the length of the transmission line, within errors. This could be used as a filter to remove doubtful data.

2. Experimental Measurement of Precision

The measurements were made on an RPC with one metre long strips, 10 mm wide, with an earthed backing plane separated by expanded polystyrene. The characteristic impedance was close to 50 ohms. This chamber was mounted in a cosmic ray telescope formed by several large horizontal scintillation counters and a small position defining counter, with an energy filter consisting of a layer of lead bricks above the lowest counter. A schematic diagram of the electronic trigger and readout logic, formed from NIM units, is shown in Fig. 2.

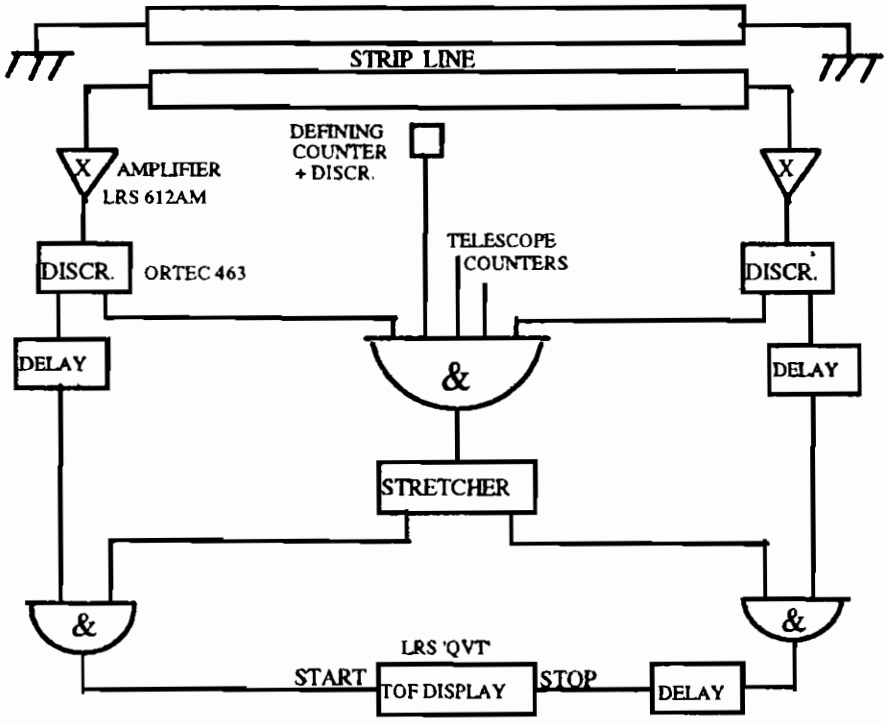

Fig. 2 TOF and trigger logic.

The important units from the timing point of view are the pre-amplifiers (LRS 612AM) set at a level of x10, and the Ortec 463 discriminators, used in their 'constant-fraction' mode. Because it is not possible to measure negative times, a delay is added to one side to ensure that the difference is always positive. The final display utilised an LRS 'QVT' analyser in its 'T' (time) mode, on its fine range (100 ps /channel). Although this arrangement represents 'off-the-shelf' electronics some tens of years old, the results obtained were surprisingly good, as will be described.

First a check was made on the timing of the gates controlling the signal passed to the QVT. It is essential that the stretched gate pulse, derived from the counters in coincidence with signals from each end of the strip, is early and long enough to pass the delayed signal pulses, regardless of the position of the defining counter. Then this counter was moved along the chamber while observing the proportional movement of the peak observed on the QVT (Fig. 3). The peak (FWHM $\approx$ 4 bins) was observed to move 64 channels, i.e. 6.4 ns, as a result of moving the defining counter 730 mm, giving the velocity in the strip to be 1.14×10^8 m.s $^{-1}$ or 0.38*c*. Applied to the 400 ps width of the observed peak, this gives a FWHM corresponding to 45.6 mm. From this value must be unfolded the length subtended by the defining counter, projected on to the chamber. The counter measured 25 mm in the strip direction, but was not in contact with the chamber. The combination of this counter and the lower telescope counters defined the accepted angle, and by projection on to the chamber it was estimated that the tracks passing through the defining counter would extend over about 30 mm in the RPC. The square distribution which would result from the counter trigger can be subtracted directly from the observed width of the distribution, suggesting an intrinsic resolution of 15.6 mm, or *sigma* (assuming a Gaussian distribution) of about 5 mm.

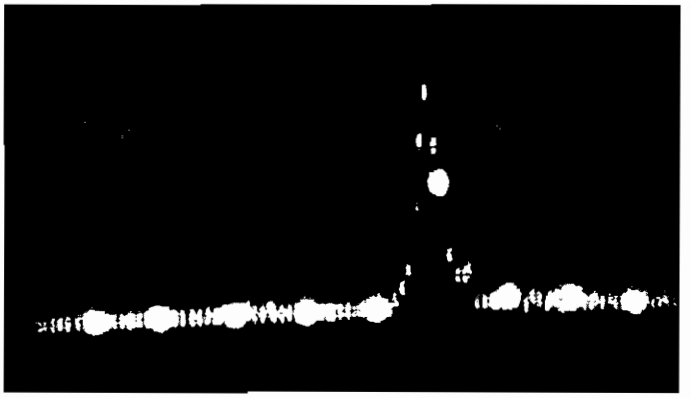

Fig. 3 The peak observed on the QVT. Each point represents 100 ps, the brighter points being 1 ns apart.

3. Conclusion

As far as we are aware, no one has exploited the fast rise time of the RPC for position determination orthogonal to the strip lines, but in view of the high accuracy observed with conventional electronics, it would seem to offer advantages in certain circumstances. Thus position readout with similar accuracy in all three co-ordinates is now possible from one RPC, giving essentially space points. This could well be an advantage where the maximum possible number of position measurements were required in a limited space, and certainly considerably simplifies fitting. The disadvantages are the necessity for readout at both ends of the strips, and the relatively high cost of sufficiently accurate timing electronics; 100 ps resolution implies (naïvely) using a scalar counting at 10 GHz!

The chamber used for this test was only 1m long; can one expect the same resolution over a much longer length? Probably yes, for the reasons given in the Introduction: a well built transmission line will introduce very little distortion over the dimensions of even a large RPC.

4. Acknowledgements

I wish to thank my colleagues at RAL who assembled the test rig, Dr. R. Cotton and Mr. J. Alner, for their support and interest in this work. This investigation was carried out during 1995 as part of the development for the MINOS experiment, led by Dr. P. Litchfield.

POSSIBLE USE OF RPCs IN THE MINOS EXPERIMENT

GEOFFREY H. GRAYER
Rutherford Appleton Laboratory,
Chilton, OX11 0QX, England
E-mail: grayer@v2.rl.ac.uk

ABSTRACT

RPC's are being considered for inclusion in the proposed MINOS experiment located at Fermilab (IL, USA) and Soudan mine (MN, USA). The particular requirements and difficulties for this application are considered, particularly with regard to their use for calorimetry. Some possible modifications to the standard structures are proposed.

1. Introduction

MINOS stands for Main Injector Neutrino Oscillation Search. It is an experiment in which it is proposed to produce a collimated beam of neutrinos at Fermilab and detect them at the bottom of the Soudan Mine situated near Tower, Minnesota [1]. The proposal is to build a magnetised-iron tracking calorimeter with good spatial resolution, so all interactions will be well determined. This 'Far Detector' is planned to contain some 10 ktons of iron absorber. To minimise systematic errors, a similar but much smaller detector will be built at Fermilab to monitor the composition of the beam.

2. Spatial Detector Requirements

The requirements of the spatial detectors are exacting:

i) Position resolution sufficient to give tracks fitted over several planes a sigma of a few mm: [1] p.81;
ii) Energy resolution sufficient for use as the calorimetry sampling element;
iii) Time resolution sufficient to use the beam gate to reject background;

iv) Tolerance to stray magnetic field;
v) The materials used for the chambers (including gas) must not present an unacceptable fire hazard at the bottom of Soudan Mine;
vi) The detectors must be easy (and hence cheap) to fabricate in very large quantities; final assembly of the detector will be below ground;
vii) Reliability must be extremely high. Because of the extremely high cost of excavating at the bottom of a mine, it will be impossible to remove chambers after installation in the experiment;
viii) The cost must be affordable (i.e. extremely low).

Candidate detectors being considered are:
i) Limited Streamer (Iorocci) Tubes (LSTs) - the base solution;
ii) RPCs;
iii) Tubes of liquid scintillator with a coaxial light fibre doped with wavelength shifter.

3. Critical Test of RPCs

The decision on the type of position detector which will finally be chosen is scheduled for mid 1997. One major question remains to be answered about RPC performance: this is how the integrated pulse height will relate to the energy density of a shower, which is vital to their use for calorimetry. It is expected that some saturation will take place at high particle densities, due to the limiting effect of the resistive plates, but as long as complete saturation does not take place, a correction factor (which will be a function of the observed energy) could be applied. The most demanding situation is at the peak of an electromagnetic shower caused by a high energy electron or gamma. This question also exists for the LST option, whereas scintillators are known to be extremely linear up to very high levels of radiation.

It is intended to answer this question in a test beam at SLAC in Spring 1996. It is not necessary to build a complete calorimeter to ascertain the response of the chambers (although this will eventually be done). Instead a scintillator and an RPC will be set up one behind the other, and the pulse height from each detector compared with varying

amounts of material placed in front, to simulate the varying position in a calorimeter. (Material will also be placed behind, to simulate the albedo of the downstream calorimeter.) A plot of the pulse height from the RPC against that from the scintillator (assumed linear) will show directly the amount of saturation.

4. Prototype RPCs at RAL

The RPC possibility is being investigated by (in alphabetical order):

i) Caltech;
ii) Livermore;
iii) RAL.

Some results of the work done at RAL will be described.

Prototype RPCs have been constructed at RAL for tests in the SLAC beam. The chambers have been quite small - up to 1 m in length - whereas the chambers planned for the experiment will be 8 m in length. In the transverse direction they will be quite narrow; in this way it is hoped that the necessary mechanical tolerances can be maintained over this length, aided by the fact that the chambers will be mounted in a vertical plane. RAL is proposing that the gas envelope and support structure be formed from the plastic NORYL, which has the advantages of being resistant to fire, and when subjected to high temperatures does not release toxic gases. These safety properties, important though they may be in a surface experiment, are even more important when deep underground. (The group is also very interested in the non-flammable gases discussed at the RPC'95 Workshop.) NORYL also has the advantages of being thermally stable, possessing a very high electrical resistivity [2], can be extruded within a (claimed) tolerance of $\pm$ 0.1 mm, and although is significantly more expensive than very cheap plastics like PVC, is still not cost prohibitive. NORYL has been used successfully for the construction at RAL of LSTs used for the OPAL experiment end-cap muon chambers [3], hence there is experience within the collaboration on the properties and techniques involved, and existing connections with industry.

For the resistive electrode material, glass has been adopted because:

i) It is cheap;

ii) It is easily available;
iii) Commonly available glass has suitable resistivity;
iv) It has a naturally smooth surface, no treatment being required, and therefore reportedly the noise count is less;
v) With careful control and selection, we believe that glass can be obtained with the mechanical tolerance required from standard industrial production;
vi) Apart from its fragility, its mechanical properties are suitable, with good medium term stability;
vii) It does not burn.

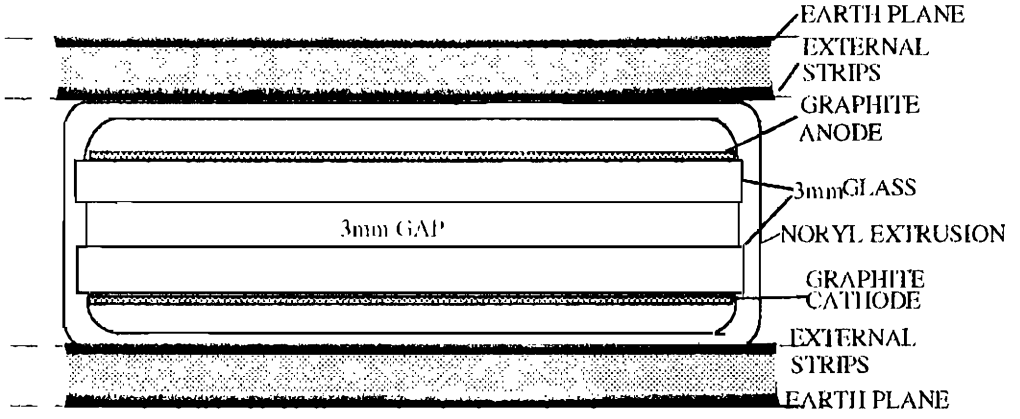

Fig. 1. A cross-section of the RAL RPC construction (not to scale).

A cross-section of one prototype is shown in Fig. 1. The NORYL extrusion will act as gas envelope and support the glass electrodes in slots, thus obviating the need for separate spacers. Two read-out possibilities are being considered:
i) Single co-ordinate readout from strips contained in the chamber, coupled through a semi-transparent graphite deposit on the anode; the cathode would consist of a foil-backed glass sheet;
ii) Read-out of orthogonal co-ordinates. In this case the internal strips running along the chamber are on the cathode side; the anode conductor is again a semi-transparent graphite layer, but the read-out strips will be placed external to the chamber, running perpendicular to its long dimension across the assembly of chambers. A back plane will provide

the transmission line characteristics and screening. Fig. 1 shows this second configuration.

5. Some new proposals

Several ideas have emerged during work on these chambers:
i) The possibility of reading out both co-ordinates from one strip by using TOF along the strips. It has been demonstrated that this gives surprisingly high accuracy, as was reported elsewhere at RPC'95 [4]. However, the cost of timing electronics for the number of channels in MINOS, even if multiplexed, would seem to be prohibitive.
ii) It seems that the majority of problems in fabricating RPCs of conventional design is in obtaining an even semi-resistive layer of suitable resistivity. Feedback is delayed as the measured resistance of the layer deposited changes significantly over many hours as it dries. This is particularly important where the RPCs are used for calorimetry, as an uneven layer would lead to variations in pulse height which would compromise the energy resolution. To control this in large scale production, as will be necessary for MINOS, will clearly be difficult and therefore expensive.

An alternative design is therefore being considered, in which this layer is replaced by conductive anode strips (Fig. 2). Capacitively coupled through an insulating layer is an identical pattern of strips lying on top, which form the other element of a transmission line. Charge injected on the anode strip from a gas discharge will attract an image charge on this second strip, and this pulse will travel to the ends of the line. Here the anode strip is capacitively decoupled to ground, while the insulated strip feeds the amplifier at one end, while at the other it is terminated by a resistor to prevent reflections.

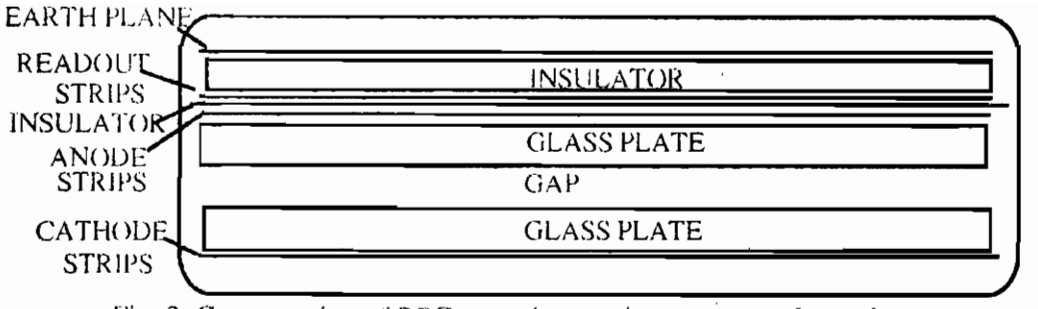

Fig. 2 Cross-section of RPC not using semi-transparent electrodes.

A small chamber of this design has been built and proved, although in the absence of terminating resistors, significant reflections were observed. There seems no reason why the orthogonal co-ordinate cannot be simultaneously read out from the cathode side.

iii) Another possible modification is the use of glass for one electrode only, this being sufficient to limit the discharge. This benefits by reducing the weight, thickness, and cost of the chambers produced.

6. Conclusion

RPCs appear well suited to the MINOS experiment, with the reservation that their suitability as calorimetric detectors has still to be established. In the course of planning this experiment, a number of possibly new ideas regarding the construction and readout of RPCs have emerged, and some have been presented here.

7. Acknowledgements

The work at RAL on RPCs was carried out in collaboration with J. Alner and R. Cotton, within the MINOS group led by P. Litchfield.

8. References

1] MINOS Collaboration, "P-875: A Long-baseline Neutrino Oscillation Experiment at Fermilab", *Fermilab Proposal* (February 1995).

2] G.H. Grayer, "Resistivity Measurements on RPC Materials", *RPC'95*.

3] G.A. Arnison et al., *N.I.M.* **A294** (1990) 431-8.

4] G.H. Grayer, "Position Measurement in RPCs by TOF", *RPC'95*.

RESISTIVITY MEASUREMENTS ON RPC MATERIALS

GEOFFREY H. GRAYER
Rutherford Appleton Laboratory,
Chilton, OX11 0QX, England
E-mail: grayer@v2.rl.ac.uk

ABSTRACT

One of the factors controlling the operation of RPCs is the resistivity of the plates, which although not particularly critical, should be monitored when a large number of similar chambers are to be produced. The high values of resistance possessed by these materials (technically classified as insulators) are difficult to measure in a reproducible way, tending to change with applied voltage and time, as well as depending on surface contaminants and humidity. Surface and volume resistivity are generally distinct. A system of measurement is described, together with some results.

1. Introduction

RPCs are one solution being considered for instrumenting the MINOS experiment [1]. This will require a very large area of chambers, which once installed will be inaccessible. In order to produce reliable and predictable chambers, it will be necessary to characterise and control the materials used in their construction. It is accepted that the resistivity for RPC electrodes must exceed a few times 10^{10} ohm.cm for current limiting, but too high a resistance would extend the time for recovery and result in poor rate dependence.

The materials used for the electrodes are classified as insulators. Small chemical changes can significantly change their resistance; hence their surface resistance is often different from what would be expected from a homogeneous material through contamination, even if this is just from absorption of atmospheric gases and water vapour. Furthermore, at the voltages applied (possibly 10 kV or more), many materials exhibit time dependent effects (due to the slow movement of ions in the material), and do not necessarily obey Ohm's Law (i.e. the electric current does not necessarily vary linearly with voltage). At

RAL[a] we have been building RPCs with glass electrodes. Glass resistivity can vary over six orders of magnitude [2], though the glasses from the upper end of this range are special types one would not consider for RPC construction. Because of these complications, and the exacting requirements of the MINOS experiment, a program of fully characterising the materials to be used is under way.

2. Resistance and Resistivity

Insulators (defined arbitrarily as having $\rho_V > 10^6$ ohm.cm) are characterised by both a volume resistivity ρ_V and surface resistivity ρ_S. At these very high values of resistivity, the properties of the surface may be different due to contamination, especially from water condensed out of the air, and may be dependent on surface treatment and finish. If, conversely, the material is homogeneous and the surface free from contaminants, then $R_S = \infty$.

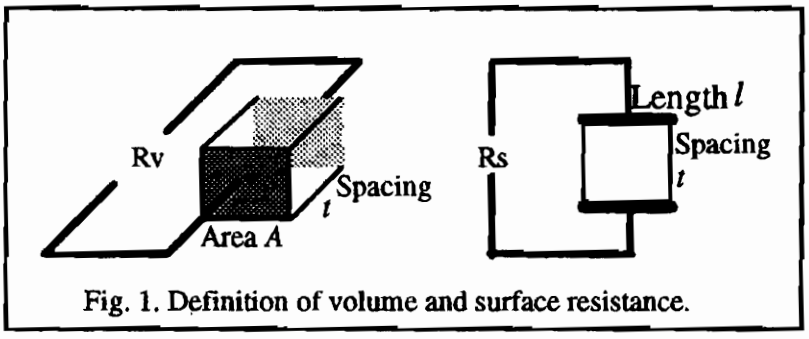

Fig. 1. Definition of volume and surface resistance.

The volume resistance R_V (ignoring surface effects) varies as the thickness t between the electrodes, and inversely as the area A of the surfaces between which the resistance is measured:

$$R_V = \rho_V \, . \, t/A \, , \quad \text{or} \quad \rho_V = R_V . A/t \, .$$

Although not an S.I. unit, ρ_V is often specified in ohm.cm.

---

[a] Rutherford Appleton Laboratory, see paper heading.

When defining the surface resistance R_S, the surface is considered as two-dimensional, i.e. the thickness is not considered. Thus it varies as the distance t between the electrodes, and inversely as their width l:

$$R_S = \rho_S \cdot t/l, \quad \text{or} \quad \rho_S = R_S \cdot l/t.$$

ρ_S is measured in ohms (per square).

The measured resistance R is the sum of the two values in parallel:

$$1/R = 1/R_V + 1/R_S.$$

3. Determination of ρ_V and ρ_S

In order to separate the surface and volume components of resistivity, two measurements were made, the first measuring almost exclusively R_V. The second was biased towards R_S, but still containing a contribution from R_V, which can be calculated and subtracted.

To isolate ρ_V, copper electrodes with conducting glue were stuck on each side of the sample plate almost covering the plane surface, separated by a small gap from an isolated metal strip stuck round the edge of the plate, and returned directly to earth, by-passing the electrometer (Fig. 2). By having a large surface area and small thickness, most of the current flowing would tend to be through the glass. At the edge, current flowing across the surface from the live electrode would be passed to ground without being measured, while on the reverse side both the electrode and shield are at the same potential, therefore no current will flow. Measurement of the surface area of the electrodes, the thickness of the material, and the resistance allows ρ_V to be calculated directly.

To evaluate ρ_S, the effect of volume conductivity is minimised by sticking electrodes along two opposing edges of the sample (Fig. 2). In this case the volume flow cannot be prevented, but it can be calculated from the result of the previous measurement. The measured resistivity is then treated as the result of this volume resistance in parallel with two equal resistances representing the two surfaces plus edge. The surface resistivity ρ_S can then be calculated from the dimensions of the sample.

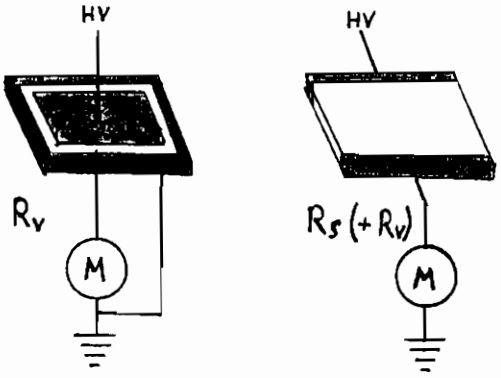

Fig. 2. Measurement of the volume and surface resistance.

4. Experimental details

The measurements were carried out in a clean room environment. The two measurements were carried out in the reverse order to that described above, i.e. measure R_S and then R_V, as the measurement of R_S uses much smaller electrodes, which can be incorporated into the other measurement. This avoids the need to clean the plates between measurements.

The glass samples were typically 2 - 3 mm thick and 100 mm square. After cleaning (see below), they were handled by the edges using surgical gloves. Copper foil tape backed with conducting glue was used for the electrodes, and a short length of flexible wire soldered to this tape to allow connection. Care was taken not to contaminate the glass while soldering, only a small area of tape being exposed, and the operation carried out in a laminar flow cabinet. The sample was then placed inside a glass container containing desiccator and allowed to reach equilibrium. The plate was supported on ridged PTFE pillars with pointed top and concave base, designed to have minimum contact area with the plates and the base.

A model PAR-135 electrometer was used to make the resistance measurements. At this very high impedance, electrostatic changes due

to movements of the operator can affect the readings; this effect was cured by placing the enclosure on a metal sheet, grounded to the electrometer. The electrometer was first checked by measuring a number of glass-encapsulated resistors measuring between 10^8 and 2.10^{10} ohms.

5. Cleaning the samples

The value of any high value resistance is dependant on surface contaminants. In an attempt to remove impurities, the samples were first treated as follows:

i) swabbed by a solution of industrial detergent in de-ionised water;
ii) rinsed in de-ionised water;
iii) rinsed in analytic grade Ethanol (ethyl alcohol);
iv) finally the plates were dried in a filtered air stream.

During and after this treatment the samples were handled with surgical gloves. However, despite the utmost care, it was difficult to get reproducible results with this procedure. Therefore a number of samples were cleaned in the Balzer process[b] , used by the EBL[c] group at RAL for cleaning material used for lithographic masks. In retrospect, it is probable that the problems were due to residual water on the surfaces.

6. Float Glass - Are the Two Sides Different?

Before addressing the measurement of resistivity, the results of a simple comparison between the resistance on the two sides of a piece of float glass will be considered. Some groups claim that there is a significant difference in conductivity between the two surfaces of float glass, due to the production process during which the glass is floated on molten tin. The sample used was standard window glass 3 mm thick

---

[b] The Balzer cleaning process consists of 7 minute exposures to the following: Sulphuric Chromic Acid at 50°C, de-ionised water spray, an ultra-sonic bath containing 4% Decanex, again a water spray, immersion in agitated alcohol, finishing with an alcohol vapour bath at 80°C.

[c] EBL = Electron Beam Lithography.

and approximately 100 mm square, which had been through the special cleaning process. Two pairs of electrodes were stuck on opposite sides of the glass near opposite edges. The current between electrodes on the same side was measured as a function of applied voltage (Fig. 3). It can be seen that the resistance closely follows Ohm's law, and that the surfaces differ only by about 30% - certainly insignificant for chamber behaviour. Neither could any difference in optical properties of the two surfaces could be detected, even under illumination by UV light, as is supposed to be the case. It is considered unlikely that the cleaning

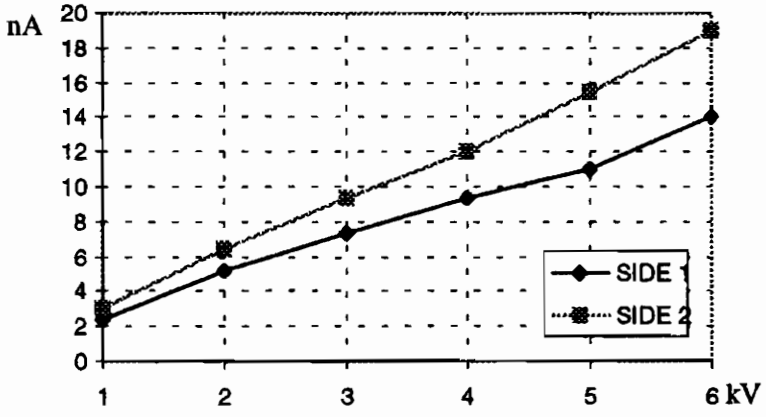

Fig. 3. Comparison of current vs. voltage for two sides of glass.

process could have removed these tin atoms, which are assumed to be diffused into the surface. There remains the possibility that the surface resistivity was actually being dominated by residual water on the surface which had not been removed by the desiccator.

7. Other Results

A large number of measurements have been taken, so only the more significant results will be presented. In particular, the results from the super-clean glass and from NORYL will be given.

7.1 Resistivity of Local Glass

A sample of locally-obtained window glass measuring 100 x 100 x 3 mm^3, which had been cleaned by the Balzer process, was measured as described in Sections 3 and 4. The bulk resistivity was found to decrease with applied voltage (Fig. 4), seeming to imply that more carriers become available. The second effect is the increase inresistivity with time, about 30% over 4 hr. This can perhaps be explained by gradual polarisation of the sample as former carriers get trapped.

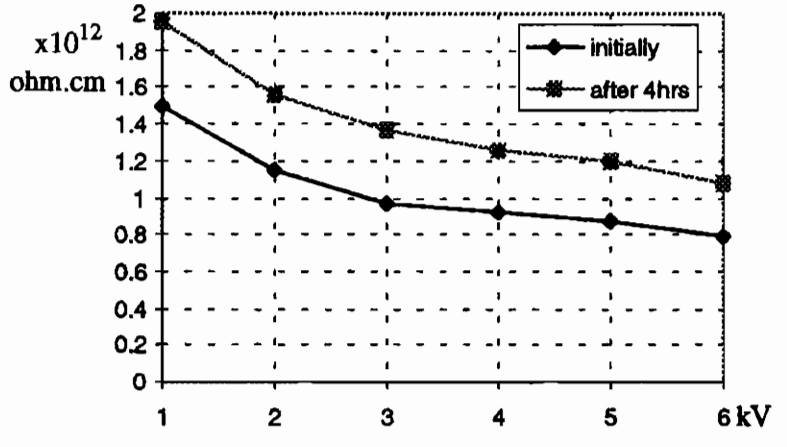

Fig. 4. Volume resistivity of "super-clean" window glass.

The surface resistance (Fig. 5) shows an even greater reduction with time - about 5 times in 3 hr - but this could be due to the surface drying out in the desiccated enclosure.

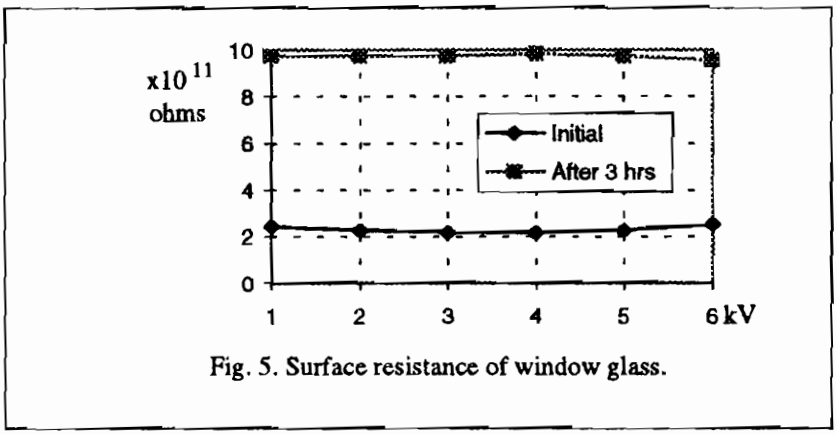

Fig. 5. Surface resistance of window glass.

7.2 Resistivity of Italian Glass

As a comparison, a sample of glass (here referred to as "Italian" glass) used in successful RPCs produced for a Gran Sasso experiment was cleaned in the Balzer Process and measured in the same way. This new sample was left under high tension for some hours before the measurement was made, so that it would be comparable with the previous sample. The volume resistivity of this Italian glass is almost ten times higher (Fig.6).

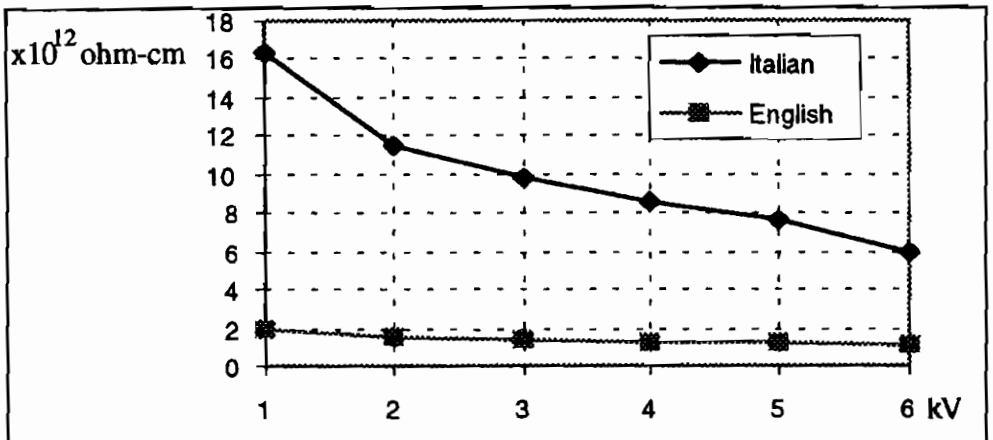

Fig. 6. Comparison of Engish and Italian Glass: Volume Resistivity.

7.3 Behaviour of the plastic "NORYL"

The plastic "NORYL" is of interest to us for RPC fabrication because of its resistance to burning and its lack of noxious gases when subject to heat. It has been successfully used for the fabrication of limited streamer chambers [3]. A sample measuring approximately 77 x 71 x 0.94 mm was cut from an unused extrusion made for these chambers, and was cleaned by hand as described in section 5. When the volume resistance was measured, the current was initially high, but fell rapidly, attaining a value after some hours corresponding to a volume resistivity of 4.8×10^{14} ohm-cm, some two orders of magnitude greater than the Italian glass. However, when the applied potential was reduced, the current was observed to reverse, showing that the material was acting as a storage battery, presumably through polarisation effects. This stuation remained for about half an hour.

8. Conclusion

A method of measuring the volume and surface resistivities of materials such as glass has been described. In general, the resistivities fall as the potential applied is increased, but increase considerably with time. It has been shown that the locally available window glass differs by an order of magnitude in volume resistivity from a sample of Italian glass, and that the two sides of the glass differed by only about 30%. The plastic NORYL has been shown to reach resistivities some two orders of magnitude greater than the highest value glass measured, but shows charge storage properties.

9. Acknowledgements

This work was done in 1995 during the development work for MINOS in the RAL group lead by Dr. P. Litchfield.

10. References

[1] MINOS Collaboration, "P-875: A Long-baseline Neutrino Oscillation Experiment at Fermilab", Fermilab Proposal (February 1995). See also G. H. Grayer, "Possible use of RPCs in the MINOS Experiment", RPC'95 Workshop.

[2] "Handbook of Tables for Applied Engineering Science", p. 166.

[3] G. A. Arnison et al., *N.I.M.* **A294** (1990) 431-438.

WHAT HAVE WE LEARNED FROM A COMPARISON BETWEEN THE WIDE GAP AND NARROW GAP RESISTIVE PLATE CHAMBER?

E. Cerron Zeballos[1,2], I. Crotty[1], D. Hatzifotiadou[1,2], J. Lamas Valverde[1,2], S. Neupane[1,2], V. Peskov[3], S. Singh[1,2], M.C.S. Williams[1] and A. Zichichi[4]

1) LAA project, CERN, Geneva, Switzerland
2) World Laboratory, Lausanne, Switzerland
3) L.I.P.-Coimbra, Portugal
4) University of Bologna and INFN, Bologna, Italy

ABSTRACT

In this paper we study the performance of a wide gap RPC and compare it with that of a narrow gap RPC, both operated in avalanche mode. We have studied the total charge produced in the avalanche. We have measured the dependence of the performance with rate. In addition we have considered the effect of the tolerance of gas gap and calculated the power dissipated in these two types of RPC. We find that the narrow gap RPC has better timing ability; however the wide gap has superior rate capability, lower power dissipation in the gas volume and can be constructed with less stringent mechanical tolerances.

1. Introduction

The Resistive Plate Chamber using bakelite plates was developed some years ago by Santonico et al. [1]. Basically it is a very simple detector; a gas volume, 2 mm thick, is contained between two resistive plates. An electric field is generated across this gap by applying a voltage to electrodes on the outer surface of the plates. A through-going charged particle creates electron and positive ion pairs. The electrons multiply by avalanching in the high electric field. Depending on the applied voltage, either the avalanche signal can be detected (avalanche mode operation) or the avalanche initiates a spark break-down (spark mode operation; some authors refer to this mode as streamer mode). The resistance of the plates limits the intensity of the spark. At this moment, experiments using RPCs operate in spark mode; however in spark mode operation, the efficiency of the RPC drops quickly with rate [2,3] since the surface of the resistive plates becomes charged and reduces the electric field across the gas gap. The full electric field is restored by current flowing through the resistive plates.

A possible route to high rate operation is to reduce the amount of charge produced by the gas-gain process initiated by the through-going particles; thus one attempts to operate the RPC in avalanche mode rather than spark mode. The problem with avalanche mode operation is that there is a certain probability that a spark also occurs; this spark generates a very large signal. In avalanche mode operation the RPC is equipped with many sensitive preamplifiers, thus any spark will affect a large area of the RPC. There are two methods to reduce the effect of sparks. The first is to quench the spark by using a high fraction of u.v.-absorbing gas, such as freon [4,5]. The second method is to increase the size of the gas gap[6], which decreases the probability of a spark. Here we will look at the results of these techniques; we have made a detailed comparison of a narrow gap (2 mm) RPC operated with a gas mixture containing 85% freon and a wide gap (8 mm) RPC operated with a freon-free gas mixture.

In discussions regarding the operation of RPCs, the magnitude of the fast signal generated by the movement of electrons is often quoted. However, we are concerned with the total charge produced inside the gas gap, since it is this charge in its totality that has to be neutralised by a current flow through the resistive plates; this current flow causes a voltage drop across the resistive plates and thus limits the operation at high rates. We discuss the fast signal and the expected total amount of charge produced in the RPC. We show measurements from the two types of RPC mentioned above. We find that operating the chamber with the same threshold, the average charge of the fast signal is much lower for the 8 mm than for the 2 mm gap RPC; this gives the wide gap RPC a superior rate capability; in addition less power will be dissipated in the gas volume.

2. The Fast Signal and Total Charge

The fast signal produced by a gaseous avalanche is due to the movement of the electrons towards the anode. The ratio of the fast signal (due to the movement of electrons in the avalanche) to the total signal is $1/\alpha D$; where α is the first Townsend coefficient and D the gap width. This has been discussed previously [7], where we calculated that the integrated charge of the fast signal is 7% of the total electron charge produced in the avalanche. The reason for this is clear, to obtain the full signal one has to wait for all the positive ions to drift to the cathode. Thus for an avalanche that produces 1.5 pC of electrons, the fast signal will be 100 fC; additionally there exists 1.5 pC of positive ions, which will be attracted to the cathode.

Freon is an electronegative gas, and thus there is a certain probability that an electron, instead of having an ionising collision and participating in the avalanche process, is captured by the freon molecule and forms a negative ion. The number of electrons in an avalanche is given by: $N = N_0 e^{\alpha x}$, where x is the distance, N_0 is the original number of electrons and α is the first Townsend coefficient. In the presence of an electronegative gas the Townsend coefficient is replaced by the

effective Townsend coefficient $\alpha' = \alpha - \eta$, where η is the attachment coefficient. This has two consequences; the first is that commonly α' increases linearly with electric field as discussed by Qiu et al.[8]; the second is that negative ions are created. These negative ions do not participate in the production of the fast signal; however depending on the actual values of these coefficients (α and η) a large number of negative ions can be produced, in some cases more than the number of free electrons arriving at the anode. Thus, with freon one may expect an increase in total charge without a corresponding increase in the magnitude of the fast signal.

3. Experimental Procedure and Cosmic Tests

The RPCs that we tested were of simple construction. The 2 mm gas gap chamber was constructed with 1.2 mm thick melamine-phenolic-melamine* resistive plates. Pad electrodes of dimension 24 x 24 cm^2 (which defined the active area) were mounted on the outer surfaces of the plates. The resistive plates were held flat by two sheets of 2 cm thick Plexiglas. The cathode was attached via a 1 MΩ resistor to a negative high voltage power supply and the signal read out via a 1 nF high voltage capacitor. The other electrode, the anode, was held at ground potential either by the 50 Ω input impedance of an amplifier or the 1 MΩ input impedance of the oscilloscope. The cathode was coupled to a fast current amplifier followed by an ORTEC shaping amplifier; this signal fed a discriminator, the output of which we associated with gas avalanches. The anode signal was either amplified by a factor 2 and then passed to a discriminator with a threshold of 150 mV (i.e. detection of sparks) or fed directly to a digital oscilloscope with 1 MΩ input impedance for the charge measurement (described below). The movement of charge between the anode and cathode induce opposite going signals on these two electrodes. There is a large capacitive coupling between the anode and cathode. Therefore

---

* The Melamine laminate was produced by Argolite, S.A.

the induced signal on the anode, for example, is reduced by the induced cathode signal transmitted to the anode via this capacitance; similarly the cathode signal is also reduced. This effect depends on the impedance between the electrode and ground. In our measurements we find a reduction factor of 2.5 when the anode is connected via the 1 MΩ to ground. For the beam test (discussed later) the pickup-strips (i.e. the anode) were connected to ground via the low impedance of the pre-amplifiers, thus the cathode signal was unaffected.

Using cosmic ray muons we have made various measurements in the laboratory. We have measured the efficiency plateau for both spark mode and avalanche mode operation. The "avalanche" discriminator would fire on signals above 100 fC, while the "spark" discriminator would fire on signals greater than 10 pC. Figure 1 shows two plateau curves for freon content of 35% (a) and 85% (b); in addition we show the dark current. The balance of the gas mixture was Argon/isobutane in a 6:4 ratio. Additionally in all our tests we bubble the gas through water at 10°C to add 1% water vapour to the mixture; this was to keep the resistivity of the electrodes constant in time[9]. As discussed by Duerdoth et al.[5] the magnitude of the fast signal generated by sparks is reduced with increasing freon concentration. Extrapolating the results of Duerdoth, one predicts that at ~80% freon concentration, the magnitude of the spark signal is similar to that of the avalanche signal. For the 85% freon data, the curve labelled sparks in the plateau curve can in reality be considered as "extra large" avalanches.

We measure the total charge produced in the RPC at various voltages along the plateau curve. For this measurement the anode is directly connected to a digital oscilloscope; a typical display is shown in figure 2. The fast step is due to the electrons; the slow ramp is due to the positive ions drifting towards the cathode, and flattens out when the ions arrive at the cathode. The total capacitance has been previously measured, thus the total voltage swing can be equated to a charge. For

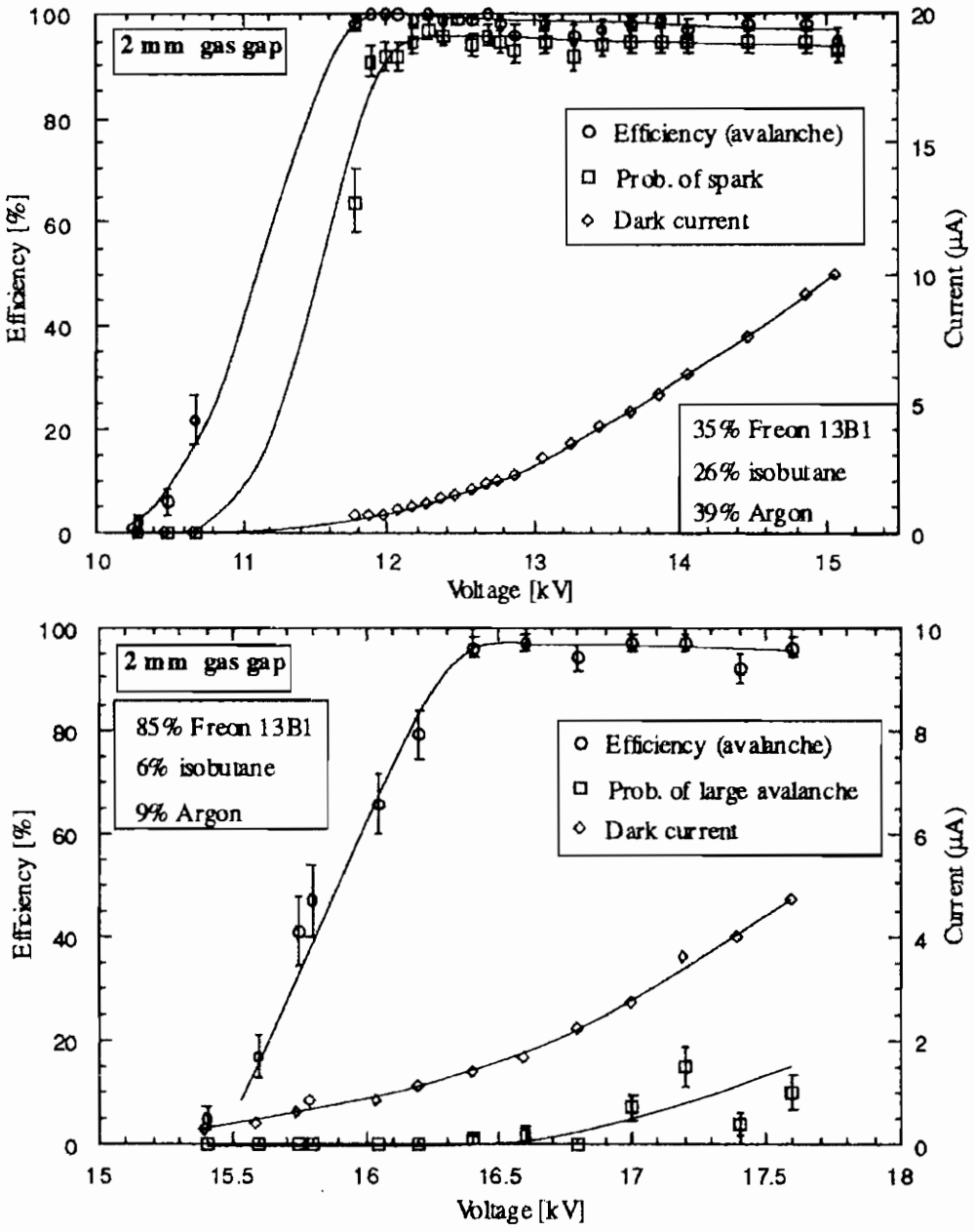

Fig. 1. Efficiency plateau of a 2 mm gap RPC measured with cosmic ray muons for 34% Freon (upper plots) and 85% Freon (lower plots). The balance of the gas was Argon:Isobutane in a ratio of 6:4, additionally the gas was bubbled through water at 10°C to add 1 % water vapour. We also show the probability for sparks and the dark current. The lines are added to guide the eye.

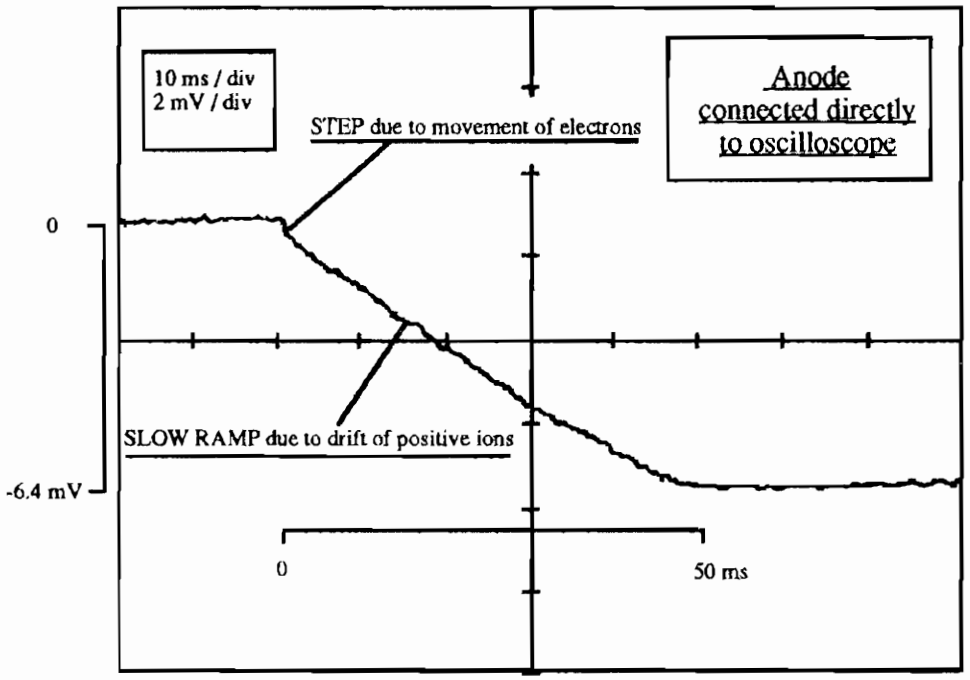

Fig. 2 Typical anode signal from the 8 mm RPC as measured by a digital oscilloscope (used for the measurement of the total charge).

each coincidence from the cosmic ray telescope, we record the magnitude of the fast signal (as observed by the fast current amplifier attached to the cathode) and the total voltage swing on the anode. Events where the fast amplifier produces a large saturated pulse we label as 'sparks'. We plot the average of the total charge produced by avalanches and sparks versus voltage in figure 3, for the two freon mixtures shown in figure 1. Figure 4 shows the voltage that corresponds to the knee of the efficiency plateau as a function of freon concentration. The chamber that we tested in the test beam had a slightly larger gas gap and needed an increased high voltage. We also show the data from Duerdoth et al.[5] and Bacci et al.[10]; the results of Bacci et al. appear to be inconsistent with our data and the data of Duerdoth et al.

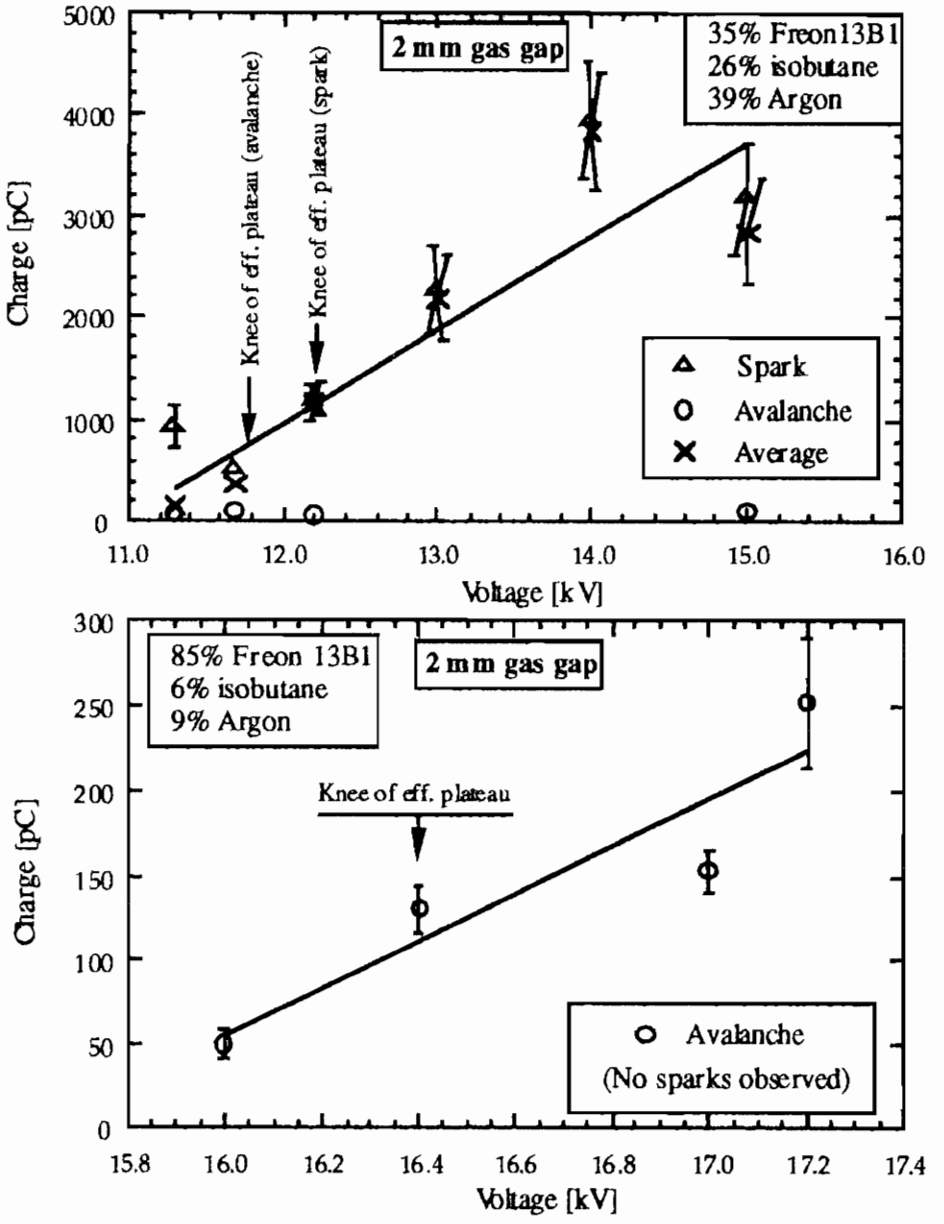

Fig 3. Mean value of the total charge of avalanches and sparks as a function of the high voltage for 34% Freon (upper plots) and 85% Freon (lower plots) for a 2 mm gap RPC. Error bars (only shown when larger than the plot symbol) are statistical. The data for 'spark' and 'avalanche' is only for cases where the signal is classified as one or the other, the average includes zero when we observed no signal at all. The line is a linear fit to the average.

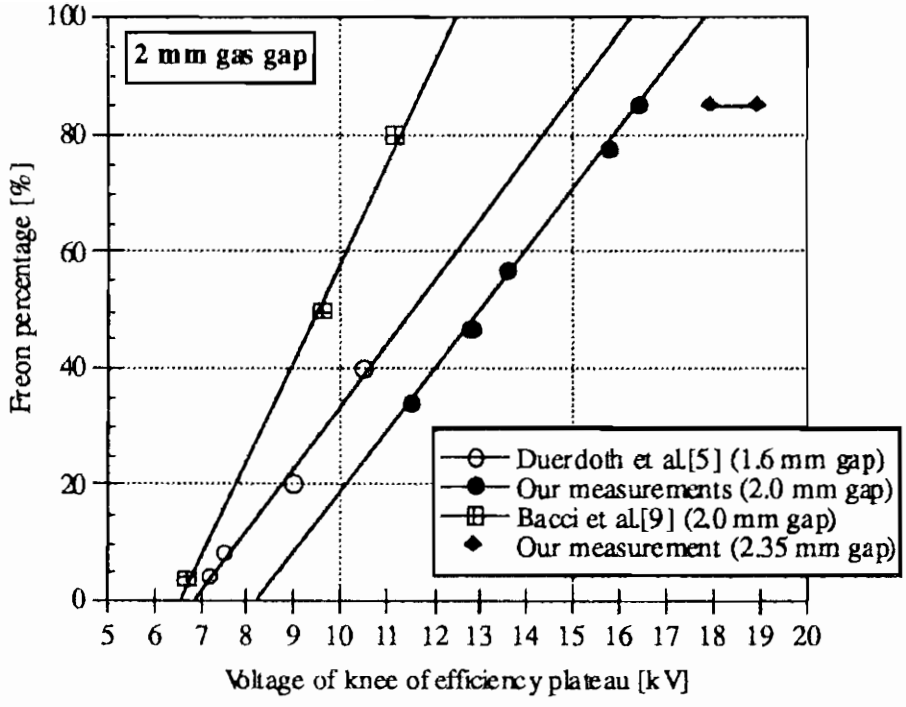

Fig 4. The voltage corresponding to the 'knee' of the efficiency plateau as a function of freon concentration for a 2 mm gap chamber. We compare our measurements with Duerdoth et al.[5] and Bacci et al. [10]. We show a range of values for our 2.35 mm gap chamber corresponding to various values measured over a several month period in a test beam. The lines are linear fits to the data.

We have constructed and tested a chamber with a similar construction to the above 2 mm gap chamber, but with an 8 mm gas gap. The remainder of this paper is concerned with comparative tests on these two chambers. In figure 5 we show the plateau curve with a gas mixture of 42% Argon, 39% CO_2 and 19% DME. Figure 6 shows the average charge per avalanche as a function of voltage.

We have also measured the ratio of charge contained in the fast signal to the total charge, using the technique above. As stated above this ratio is simply $1/\alpha D$; this gives 8.6% for a gas gain of 10^5 reducing to 6.2 % for a gas gain of 10^7 (the gas gain is defined as $e^{\alpha D}$). In

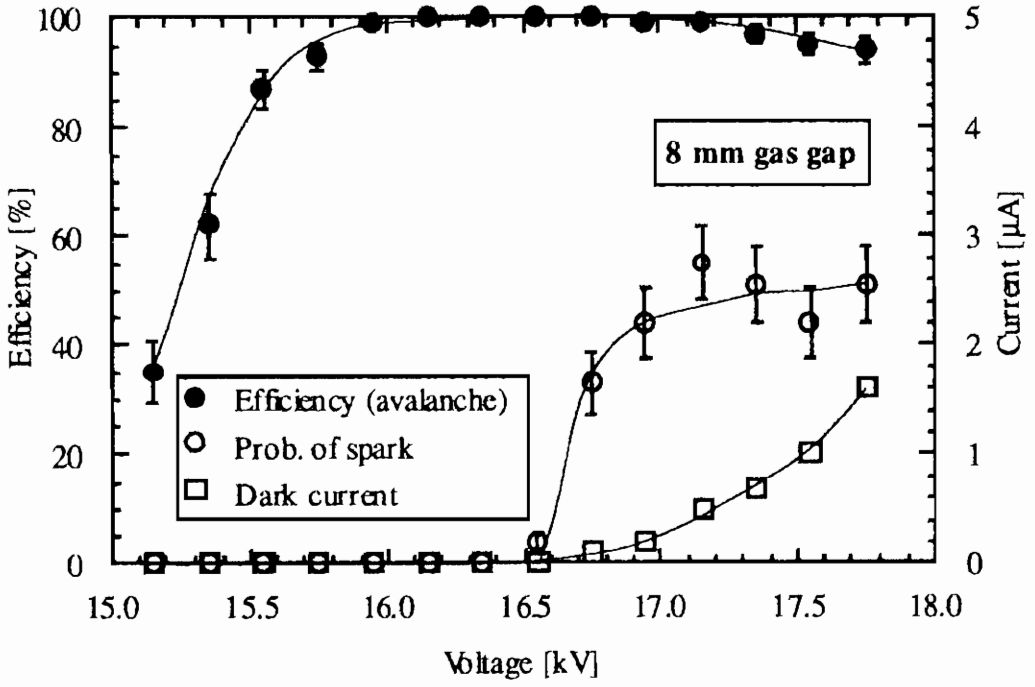

Fig. 5. Efficiency plateau measured with cosmics for an 8 mm gap RPC (gas composition : Ar 42%, CO_2 39%, DME 19% bubbled through water at 10°C). In addition to the total efficiency, the probability for sparks and the dark current are shown. The lines are to guide the eye.

figure 7 we plot our measurement of this ratio as a function of the fast signal charge for the 8 mm chamber; the shown errors are statistical. In figure 8 we show the ratio for the 2 mm gap chamber for two freon mixtures (other intermediate freon mixtures give very similar results). Since there is a production of negative ions due the freon, we would expect that this ratio should be smaller than the calculated 7-10%. For small avalanches the ratio is indeed smaller (~2%), but as can be seen this ratio increases for large avalanches.

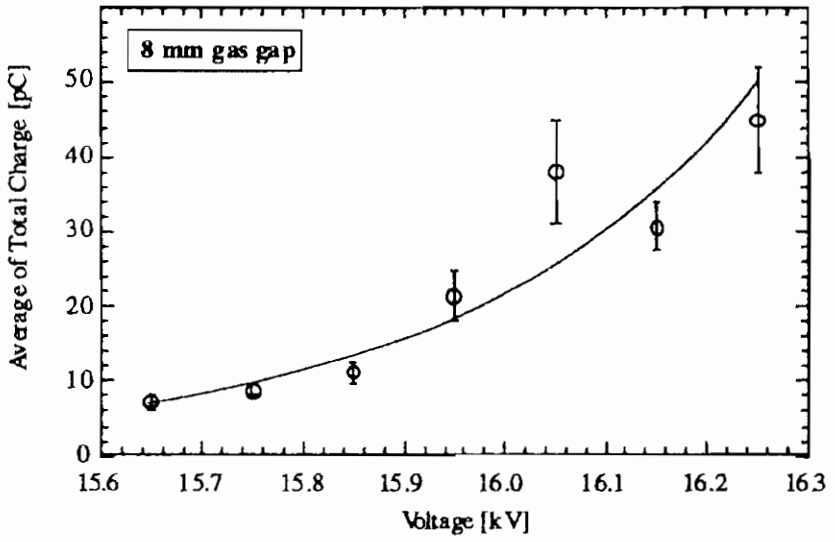

Fig. 6. Average charge as a function of the high voltage for the 8 mm RPC. The range of voltage was chosen to be around the knee of the plateau curve shown in figure 5. The line is an exponential fit.

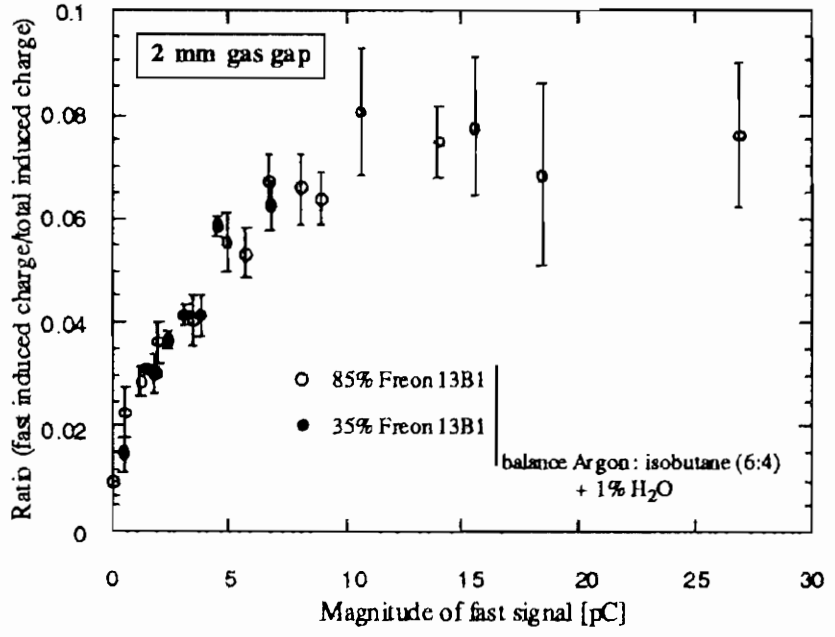

Fig. 7. Ratio of fast to total charge as a function of the charge of the fast signal for the 2 mm RPC, the gas mixture contains freon. The error bars are statistical only.

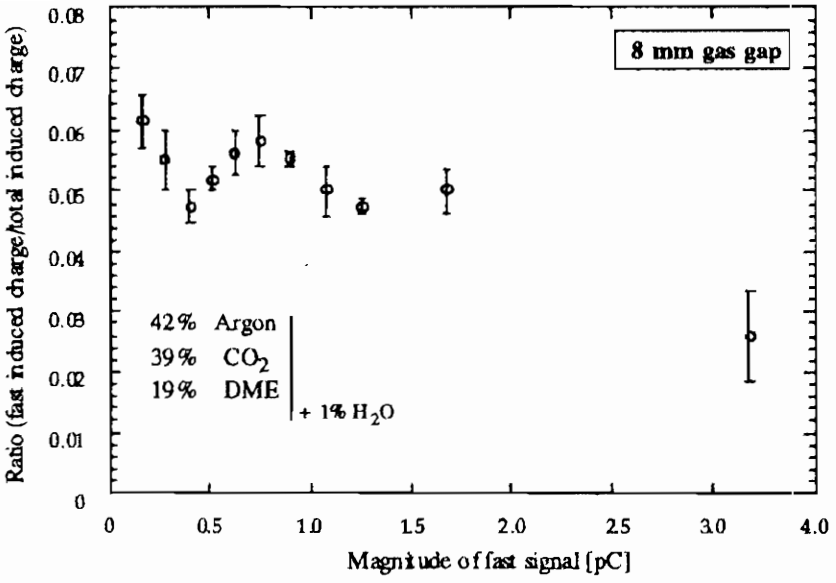

Fig. 8. Ratio of fast to total charge as a function of the charge of the fast signal for the 8 mm RPC, the gas mixture is freon-free. The error bars are statistical only.

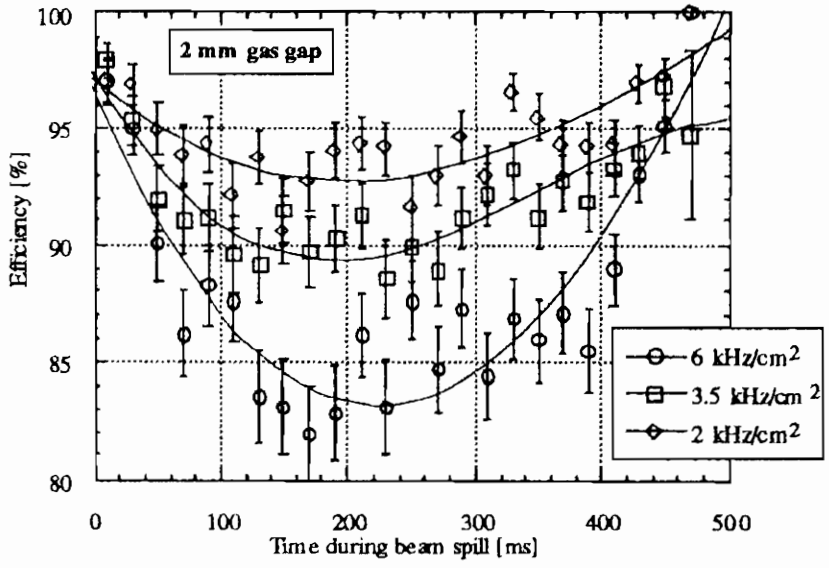

Fig. 9. Efficiency during spill for 3 different rates for the 2 mm RPC. The curves are 2nd order polynomial fits to guide the eye. The flux of particles was constant between 100 and 350 ms; we defined a time slice between 200 and 300 ms for the efficiency measurements presented in figures 10 and 11.

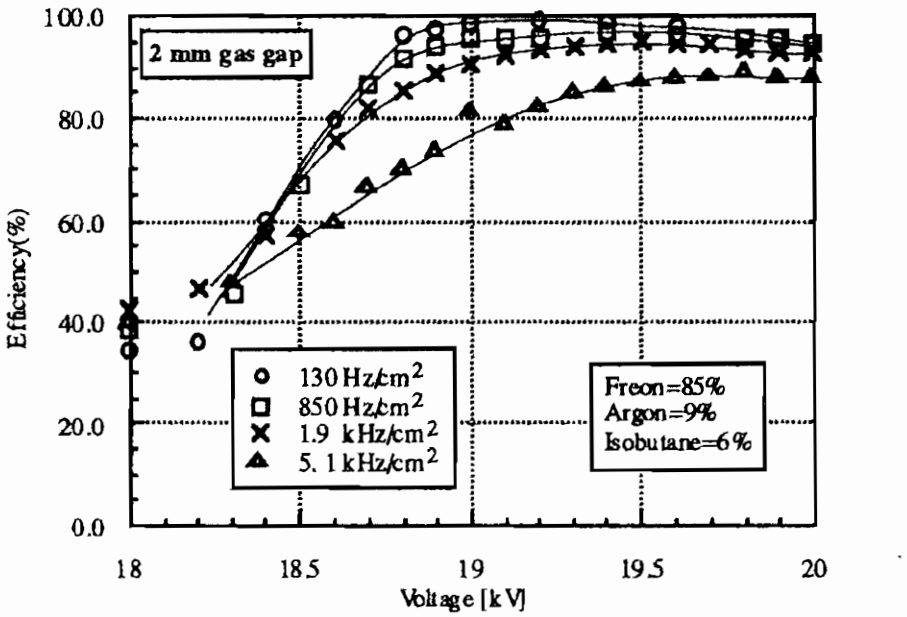

Fig. 10. Efficiency plateau for the 2 mm RPC for 4 different rates. The lines are to guide the eye

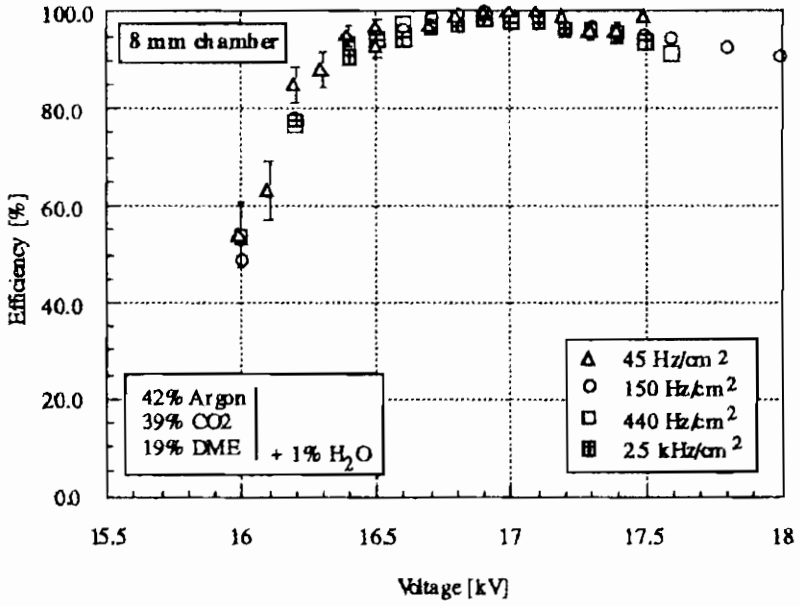

Fig. 11. Efficiency plateau for the 8 mm RPC for 4 different rates.

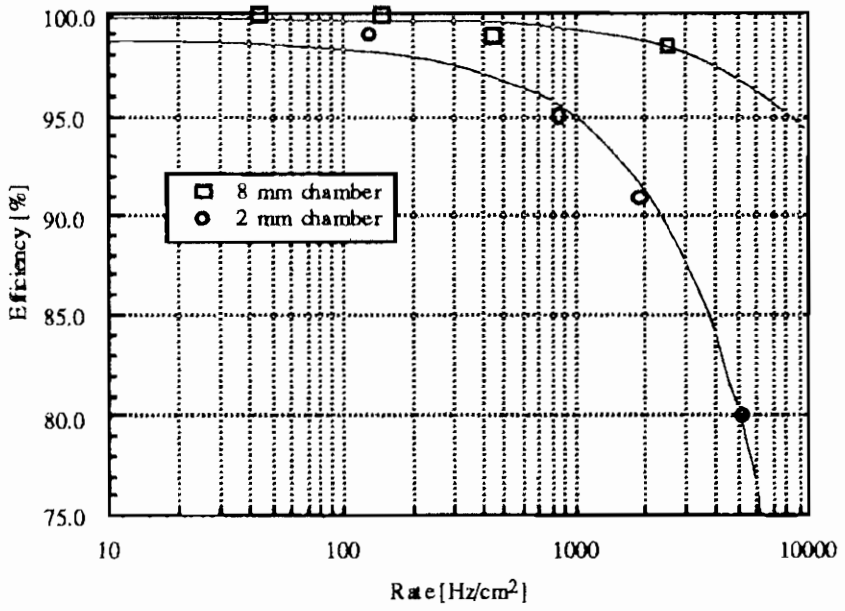

Fig 12. Efficiency versus rate for the 2 mm and the 8 mm RPC. The data points were extracted from figures 10 and 11 for a fixed applied voltage to the chamber. The lines are linear fits to the data.

4. Measurements with the Test Beam

We tested the RPCs in the T9 test beam in the CERN East Hall. The 2 mm gas gap RPC was constructed with resistive plates of 1.2 mm thick melamine-phenolic-melamine laminate. This chamber was a different chamber than the one used for the cosmic ray tests; it had a gas gap of 2.35 mm; however for brevity we will still refer to it as the 2 mm gap chamber. We tested this chamber with the 85% freon mixture in avalanche mode. The 8 mm gas gap chamber had resistive plates of melamine-phenolic 0.9 mm thick. For both chambers we added 1% water vapour to the gas mixture by bubbling the gas through water at 10°C; the bulk resistivity of the melamine laminate (in presence of this water vapour) was between 10^{10} and 10^{11} Ω cm. One resistive

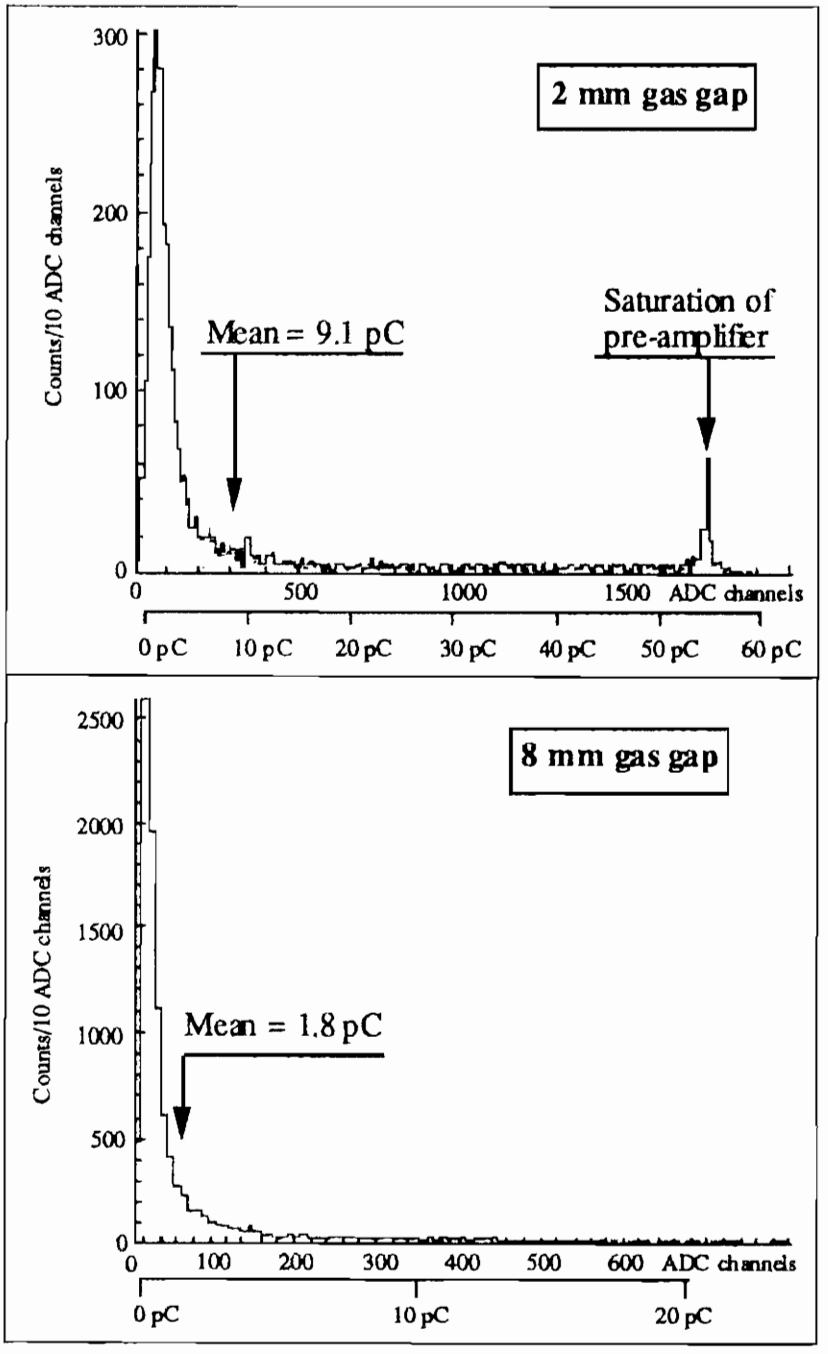

Fig. 13. Distributions of the charge magnitude of the fast signal for the 2 mm RPC and the 8 mm RPC, exposed at 100 Hz/cm^2.

plate was equipped with pick up strips on a 15 mm pitch, while the other plate was a single pad electrode attached via a 1 MΩ resistor (in later tests this was reduced to 15 kΩ) to the high voltage power supply. The strips form the anode plane; initially we had a gap of 2.5 mm between strips, however this led to reduction in efficiency. We reduced this gap to 250 μm and recovered the lost efficiency. We used a defocused beam covering the whole active area. A 4 x 4 cm^2 scintillator selected the central region of the chamber under test. We used this counter for the rate measurements. A larger 12.5 x 12.5 cm^2 scintillator measured a flux about a factor 2 less than the central 4 x 4 cm^2. In figure 9 we show the variation of efficiency of the 2 mm RPC during the spill for three rates with a chamber voltage of 19.3 kV. The curves are 2nd order polynomial fits to guide the eye. For the efficiency versus rate measurements, we gated the spill to the time interval 200 to 300 ms. Figure 10 shows the efficiency plateaux for the 2 mm chamber for various particle fluxes; Figure 11 shows the efficiency plateaux for the 8 mm chamber. Note that a higher voltage was required for this chamber than that shown in figure 1 since the gap is slightly larger. In figure 12 we show the efficiency of both the 8 mm and 2 mm RPC as a function of rate. The efficiency plateau is practically unchanged for the 8 mm chamber for rates up to 2.5 kHz/cm^2. However, for the 2 mm chamber not only does the efficiency decrease with rate, but also the efficiency plateau changes shape. Thus for high rates the maximum of efficiency occurs at a higher applied voltage.

In figure 13 we show the charge spectra of the 2 mm and the 8 mm RPC; the data have been taken at 100 Hz/cm^2. The electronics (fast current preamplifiers followed by time-over-threshold discriminators) attached to the chamber were the same in each case; we operated at a threshold of ~50 fC. In both cases one can see that the most probable value is lower than the mean value, due to the long tail. The 2 mm chamber has a far larger average charge (9.1 pC) than the 8 mm chamber (1.8 pC). This is due to the increased dynamic range of

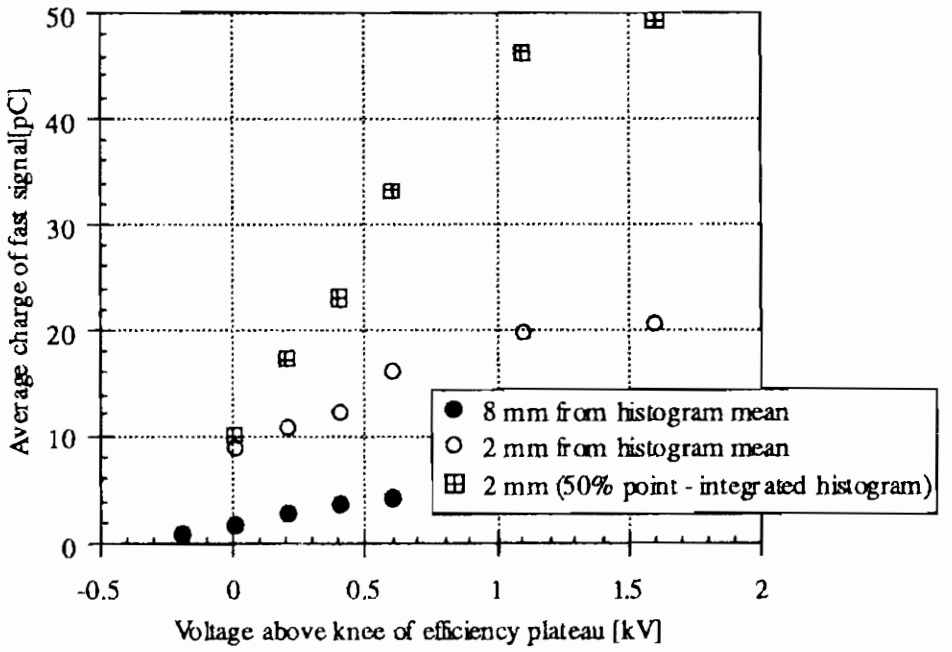

Figure 14. Average charge of the fast signal as a function of the high voltage for the 2 mm RPC and the 8 mm RPC. Two values are shown for the 2 mm chamber. The lower value corresponds to the mean of histograms similar to that shown in figure 13. This is an underestimate, the higher points are obtained from the 50% value of the integrated histogram. The 8 mm chamber did not produce signals large enough to saturate the pre-amplifier, and thus the mean value is not an underestimate.

gain that one has with a 2 mm gas gap [6]. In figure 14 we show the average charge (fast signal) as a function of the applied voltage for the 2 mm chamber and the 8 mm chamber, exposed to a rate of 100 Hz/cm^2. For the 2 mm chamber we show two curves. The lower curve is obtained from the average value of the histograms similar to that shown in figure 13; however this is an underestimate due to the saturation of the preamplifier. The upper curve is calculated by using the 50% point of the integrated histogram and normalising to 10 pC at the knee voltage; this is insensitive to the saturation of the preamplifier, but does assume that the charge spectrum has the same shape for increasing applied voltage.

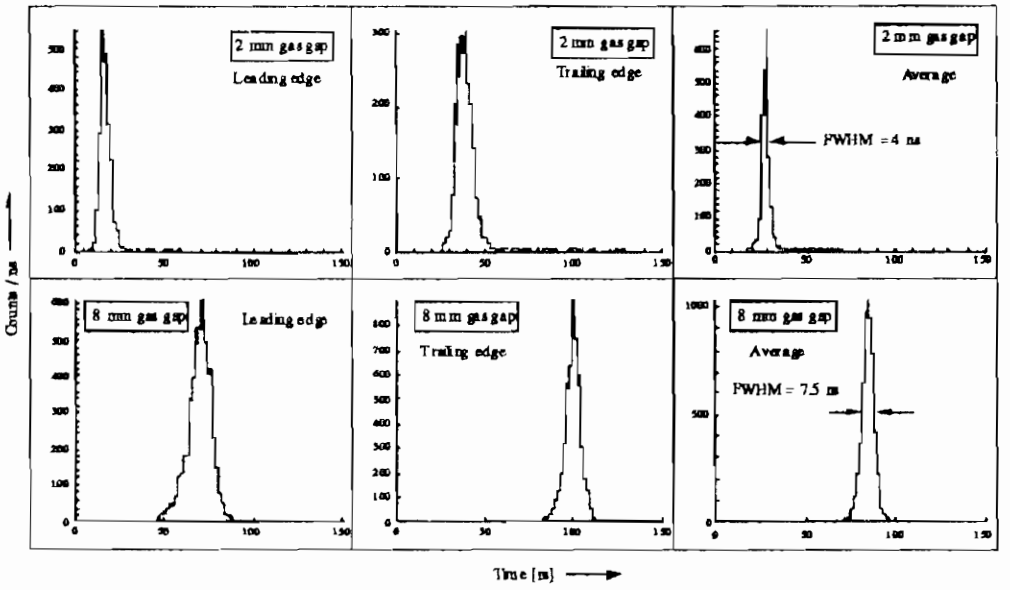

Fig. 15. Time distributions corresponding to the time of the leading-edge, trailing-edge and the average of the leading and trailing-edges. The upper three histograms refer to the 2 mm RPC; the lower histograms to the 8 mm RPC. This data was taken at the knee of the efficiency plateau, at 100 Hz/cm^2.

Time-over-threshold discriminators are attached to each strip on the chamber; the read out is with a LeCroy CAMAC TDC 2277, which records the time of both the leading and trailing edge of the pulse. The rise time of the pulse depends on the time needed for avalanche formation; the fall time depends on the capacitance of the pick up strips and electronics. The upper histograms in figure 15 show the time distribution the leading-edge, the trailing-edge and the average of these for the 2 mm chamber; the lower histograms show the distributions for the 8 mm chamber. These measurements correspond to 100 Hz/cm^2. The absolute value of the timing depends on the drift speed of the electrons in the gas and the gap width; the signal from the 2 mm chamber occurs ~60 ns earlier than the 8 mm chamber. However what is significant, for example for triggering at LHC, is the width of the distribution. As expected, the narrow gap RPC gives better timing. The average of the leading-edge and trailing-edge timing, which

corresponds to a slewing correction, gives the best result and should be used, with the appropriate electronics (for example, constant fraction discriminators).

5. Discussion

From the previous results it is clear that the narrow gap RPC has superior timing compared to the wide gap RPC; however the 8 mm RPC has superior rate capability. It should be noted that the 2 mm and 8 mm gas gap are the extremes. Recently we have started to test 5 and 6 mm gas gap; these chamber appear to have both excellent time resolution and rate capability. This is discussed in detail in another paper presented at this conference.

Besides these straightforward results, two other factors must also be taken into account: these are the precision of the gas gap and the power dissipated in the gas volume. The tolerance in the distance between the parallel plates (exact width of the gas gap) will depend on the size of the chambers and the number of spacers used. The RPCs that we use for our tests are small (30x30 cm^2) and the tolerance of the gap is tight (~$\pm$25 μm). For large area detectors, as will be used for LHC, the allowed limits for this tolerance must be relaxed, and $\pm$100 μm is a realistic lower limit. However, the gap variation results in a variation of the electric field inside the chamber, since the voltage applied on the plates is constant. For example, for the 8 mm chamber operating at 17 kV (21.25 kV/cm), a variation of $\pm$100 μm translates into a change of the field by $\pm$250 V/cm. The knee of the efficiency plateau (fig. 10) is at 16.7 kV. To allow for a gap variation of $\pm$100 μm, the chamber should have stable operation in the range of 16.7 to 17.3 kV. From figure 11 this seems to be the case.

For the 2 mm RPC operating at 19 kV (95 kV/cm), a variation of $\pm$100 μm translates into a change of the field of $\pm$4500 V/cm. The knee of the efficiency is at 18.8 kV; therefore, in order to allow for $\pm$100 μm variations in the gap width, the chamber should be operated at 19.8 kV, and should be stable in the 19 to 21 kV range. From fig. 10

one can see that the plateau for the 2 mm RPC is extended; however, as one can see from figure 14, inevitably the signals have a higher average charge.

Another factor which has to be considered is the power drawn by the detector from the high voltage supply. For the 2 mm gap RPC in order to compensate for variations in the exact gap width, one has to operate at 1000 V above the knee of the plateau. From fig 14 one finds that the average induced fast charge is 20 pC. This is only 7% of the total induced charge (or less, see figure 8), thus the total induced charge per avalanche (due to one detected particle) is 300-600 pC. For a rate of 1 kHz/cm^2, this means the total charge per second and per m^2 is equal to 3-6 mC [11] i.e. a current of 3-6 mA/m^2. The power drawn per m^2 (with 20 kV applied) is calculated to be in the range 60-120 W/m^2. We have measured the current drawn by the chamber during our test runs and find it consistent with the above calculation.

Following the same logic, if we operate the 8 mm gap RPC at 200 V above the knee of the plateau, namely at 17 kV, the average fast charge (from fig. 14) will be 2 pC. Therefore the average total induced charge will be 30 pC. For a rate of 1 kHz/cm^2 the current will now be 0.3 mA/m^2. The power drawn per m^2 therefore will be 17 kV x 0.3 mA/m^2 = 5 W/m^2; i.e. a factor of 10 less than the 2 mm gap RPC.

From the above calculations it is clear that the current and therefore the power drawn by the RPC for the kHz/cm^2 range has to be given serious consideration. The problem of power limitation could be solved by using more powerful power supplies; however this does increase the expense of the system; also, for such values of power one has to start considering the amount of heat generated in the gas volume. In addition, ageing effects are often related to the amount of deposited charge; if this is so, then clearly the lower charge observed with the wide gap RPC would be an advantage. Are there any easy solutions to this problem of power? One obvious way would be to have more sensitive pre-amplifiers and work at lower gas gain. We are investigating this possibility, however we find the RPC is somewhat a

noisy device; at the thresholds we are using (~ 50 fC) we believe that the principal cause is the flow of current through the resistive plate itself, and thus different resistive plate materials may generate less noise, allowing a lower threshold to be used. Assuming that one can reduce the threshold, it is not clear that one makes any significant gain with the 2 mm gap chamber. The reasons are: first, one has to sit well above the knee of the plateau to allow for variations of the gas gap (discussed above); the second reason is that when one works with an electronegative gas mixture, the effective Townsend coefficient, α', which defines the avalanche gain, is the difference between the Townsend coefficient, α, and attachment coefficient, η. Thus at low gas gains (low $\alpha' = \alpha - \eta$) the Townsend coefficient and attachment coefficient become close in value. Any small decrease in electric field (due to variation of gas gap, surface imperfections, deposited charge, etc.) will result in an increase of the attachment coefficient and a decrease of the Townsend coefficient; thus α' becomes negative and no avalanche is produced at all. Since the wide gap RPC operates without the use of an electronegative gas, lower electric fields result in smaller avalanches; in this case a lower threshold would help. Another possibility would be to reduce the dynamic range of the charge spectrum; a heavy gas which has a high number of primary ionisation clusters per mm would help achieve this.

6. Conclusion

From the results presented above, it is clear that the narrow gap RPC has better timing compared to the wide gap RPC; however the wide gap RPC has superior rate capability. This is due to a lower dynamic range of avalanche charge, and thus a lower average charge being produced. Thus the power dissipated in the gas gap in the wide gap RPC is also a factor 10 lower than the narrow gap RPC. This problem of power dissipation may be a deciding criterion for LHC operation. In addition, the wide gap RPC can tolerate a ± 100 μm gap variation - whereas the performance of the 2 mm chamber is

compromised. Recently we have started to test wide gap RPCs with 5 and 6 mm gas gap. Initial results (also presented at this conference) are very promising, indicating excellent timing and rate capability.

Acknowledgements

The availability of test beams at CERN is vital for this type of R&D. This is enhanced by the excellent services of the PS division that makes the use of the CERN East Hall test beams a pleasure. We thank everyone involved that makes this possible. Also, we thank the organisers of this conference that has made possible this vast exchange of information in a simulating and friendly atmosphere.

References

1. R. Santonico and R. Cardarelli, Nucl. Instr. and Meth. **187**(1981)377.
2. M. Iori and F. Massa, Nucl. Instr. and Meth **A306**(1991)159.
3. I. Crotty, J. Lamas Valverde, G. Laurenti, M.C.S. Williams and A. Zichichi, Nucl.Instr. and Meth. **A329**(1993)133.
4. R. Cardarelli, A. Di Ciaccio, R. Santonico, Nucl. Instr. and Meth. **A333**(1993)399
5. I. Duerdoth et al., Nucl. Instr. and Meth. **A348**(1994)303.
6. I. Crotty et al., Nucl. Instr. and Meth. **A337**(1994)370.
7. E. Cerron Zeballos et al., High rate resistive plate chambers, CERN PPE 95-93 and submitted to Nucl. Instr. and Meth.
8. Y. Qiu, X. Ren, Z.Y. Liu and M.C. Zhang. J.Phys. **D22**(1989)420.
9. I. Crotty et al., Nucl. Instr. and Meth. **A360**(1995)512
10. C. Bacci et al. Nucl. Instr. and Meth **A352**(1995)552.
11. A.J. Walton Am. J. Phys. **45**(1977)1117.

LATEST RESULTS ON THE PERFORMANCE OF THE WIDE GAP RPC

E. Cerron Zeballos[1,2], I. Crotty[1], D. Hatzifotiadou[1,2], J. Lamas Valverde[1,2], S. Neupane[1,2], V. Peskov[3], S. Singh[1,2], M.C.S. Williams[1] and A. Zichichi[4]

1) LAA project, CERN, Geneva, Switzerland
2) World Laboratory, Lausanne, Switzerland
3) L.I.P.-Coimbra, Portugal
4) University of Bologna and INFN, Bologna, Italy

ABSTRACT

In order improve the timing of the wide gap Resistive Plate Chambers, we constructed RPCs with gap widths of 5 mm and 6 mm. Here, we present results with various gas mixtures. An efficiency of 98% up to some kHz/cm^2 was achieved; the mean value of the fast charge is 1-4 pC for the full plateau range; the FWHM of the time distribution is 5-6 ns and the full width at the base 18 ns. In addition, noise measurements are shown, and the variation of timing, average charge and cluster size with particle flux.

1. Introduction

The conventional design of resistive plate chambers is with a gas gap of 2 mm [1]. However, for pure avalanche mode of operation one has to suppress sparks. In our effort to achieve this we have studied extensively the performance and characteristics of resistive plate chambers with narrow and wide gas gap [2,3]. Our comparison was for gas gaps of 2 mm and 8 mm. The summary of our experience is the following:

(a) RPCs with a narrow gap have a large dynamic range of pulse height, which results in large charge and therefore limited rate capability; also the power consumption from the high voltage supply is large. They need good mechanical tolerance; they require a large proportion of an electronegative gas in the gas mixture. However the timing resolution is good.

(b) RPCs with a wide gap have smaller dynamic range of pulse height, which results in smaller charge and therefore excellent rate capability; also the power consumption from the high voltage supply is lower. The mechanical tolerance is less critical; they operate with freon free gas mixtures. The obvious disadvantage is the timing resolution, which needs improvement.

In order to improve the timing, we constructed resistive plate chambers with 5 mm and 6 mm gas gap. Our aim was to imrove the time resolution, since it is crucial for the use of RPCs for the LHC muon trigger, but also to keep the good performance of the wide gap (rate capability, small charge etc). In section 2 we present results of the performance of the 5 mm and 6 mm RPCs for various gas mixtures; in section 3 we show noise measurements; in section 4 we show results for a non flammable gas.

2. Performance of 5 and 6 mm gap RPC for various gas mixtures

Both RPCs are constructed with melamine plates; the plate thickness is 0.9 mm. One plate is equipped with pick up strips on a

15 mm pitch; these form the anode. The other plate has a single pad electrode, the cathode, attached via a 1 MΩ resistor to the high voltage power supply. The chambers were tested at the CERN PS East Hall, at the T9 test beam. The beam (8 GeV/c negative particles, mainly pions) was defocused by inverting the polarity of the last quadrapole; thus the whole active area of the chamber was illuminated.

Search for a good gas showed that Argon - CO_2 mixtures are not suitable as they gave a maximum efficiency of only 90%. It was therefore judged necessary to add some hydrocarbon quencher. With addition of methane to the Argon - CO_2 mixture the efficiency reached a maximum of 94%. However, addition of isobutane, ethane and DME (dimethylether) to the Argon - CO_2 mixture gave good results, which are presented below. In all cases, the gas is bubbled through water at 10°C to add 1% water vapour, in order to prevent change of the plate resistivity [2].

Figure 1 shows the efficiency, the dark current and the average fast charge as a function of the high voltage, for the 5 mm RPC (white squares) and for the 6 mm RPC (black circles) obtained with a gas mixture consisting of 14% DME, 42% CO_2 and 44% Argon. The measurements were taken with a flux of 100 Hz/cm^2. We see that the efficiency reaches 98% and the plateau is long (800 V for the 5 mm RPC; 700 V for the 6 mm RPC). The average charge obviously increases with increasing high voltage and has values between 1-6 pC for the 5 mm RPC and 1.5-4 pC for the 6 mm RPC in the plateau area. The dark current (in μA, corresponding to a 24x24 cm^2 area) rises faster for the 5 mm than for the 6 mm RPC.

Figure 2 shows the efficiency, the average fast charge and the dark current obtained with a gas mixture consisting of 10% isobutane, 45% CO_2 and 45% Argon. The measurements were taken with a flux of 100 Hz/cm^2. Figure 3 shows the same quantities as a function of the high voltage for a gas mixture consisting of 10% Ethane, 44% CO_2 and 46% Argon. Comparison of figures 1, 2 and 3 shows quite similar behaviour for all three gas mixtures.

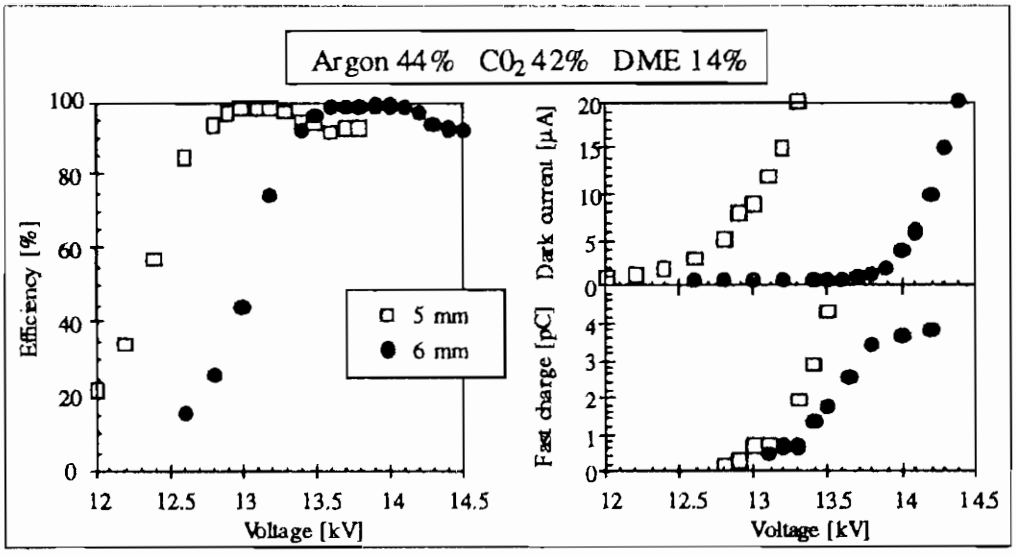

Fig 1 Efficiency, dark current and average fast charge for a gas mixture of 44% Ar, 42% CO_2 and 14% DME. In addition the gas is bubbled through water at 10°C.

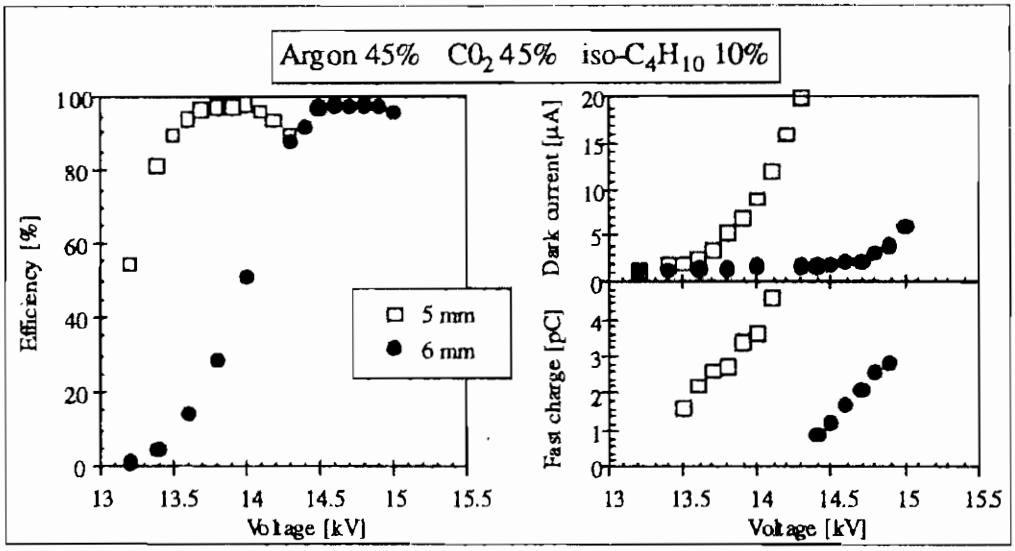

Fig 2. Efficiency, dark current and average fast charge for a gas mixture of 45% Ar, 45% CO_2 and 10%iso-C_4H_{10}. In addition the gas is bubbled through water at 10°C.

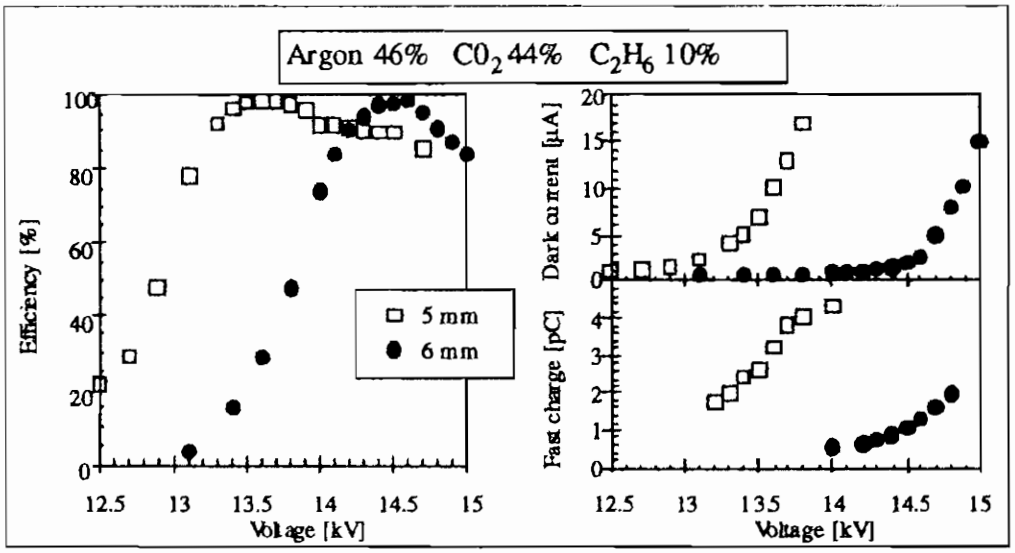

Fig 3. Efficiency, dark current and average fast charge for a gas mixture of 46% Ar, 44% CO_2 and 10% C_2H_6. In addition the gas is bubbled through water at 10°C.

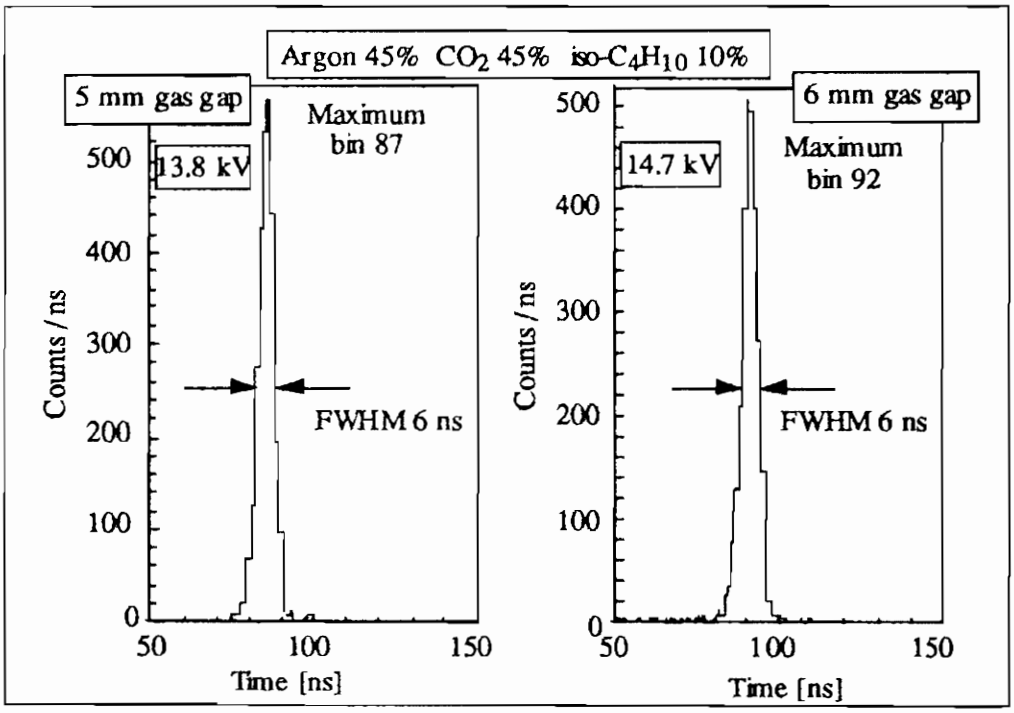

Fig 4. Timing spectra of a 5 mm and a 6 mm gas gap RPC. The gas mixture was 45% Argon, 45% CO_2 and 10% iso-C_4H_{10}. The gas was bubbled through water at 10°C.

Figure 4 shows the timing spectra obtained with a gas mixture consisting of 10% isobutane, 45% CO_2 and 45% Argon (efficiency plateau etc in figure 2). The left-hand plot is for the 5 mm RPC and the right-hand for the 6 mm RPC; they were both operated at 200 V above the knee of the efficiency plateau and the flux was 100 Hz/cm^2. The distributions show the average of the measured time of the leading edge and time of the trailing edge of the pulse; this average time corresponds to a slewing correction and has been found to give the narrowest distribution [2,3]. We expect similar time resolution if we used a constant fraction discriminator. In both plots, the FWHM is 6 ns. Similar results have been obtained with the other gases.

One of the problems of all parallel plate chambers is the tolerance of the gap width; previously we have assumed that a tolerance of 100 μm is reasonable [3]. From figure 1 we see that in this particular case there is an overlap of the efficiency plateau of the 5 mm and 6 mm RPCs. Based on this, one could naively conclude that we could build a RPC with a gas gap of 5.5 mm and allow a tolerance of 500 microns. However the variation of gap width also has an effect on the timing. Figure 5 shows the timing for the 5 mm RPC (left-hand plot) and the 6 mm RPC (right-hand plot), obtained with a gas mixture consisting of 14% DME, 42% CO_2 and 44% Argon, both operated at 13.6 kV where the efficiency plateaus of figure 1 overlap. There is a shift of the peak of 8 ns. This is expected since : a) for the same applied voltage (13.5 kV) the electric field is lower for the 6 mm RPC (22.7 kV/cm) than for the 5 mm RPC (27 kV/cm); b) the avalanche forms over 6 mm (compared with 5 mm), therefore the signal comes later. In figure 6 we show the time walk of both 5 and 6 mm RPCs versus the high voltage. The time of the peak comes earlier as the voltage increases and then stabilises. The time difference between the 5 mm and 6 mm chamber at a given voltage is 8 ns. Thus Δt = 8 ns corresponds to Δ(gap) = 1 mm; therefore we have Δt = 0.8 ns for a realistic tolerance of 100 microns; this is a negligible contribution compared to the FWHM of 5-6 ns.

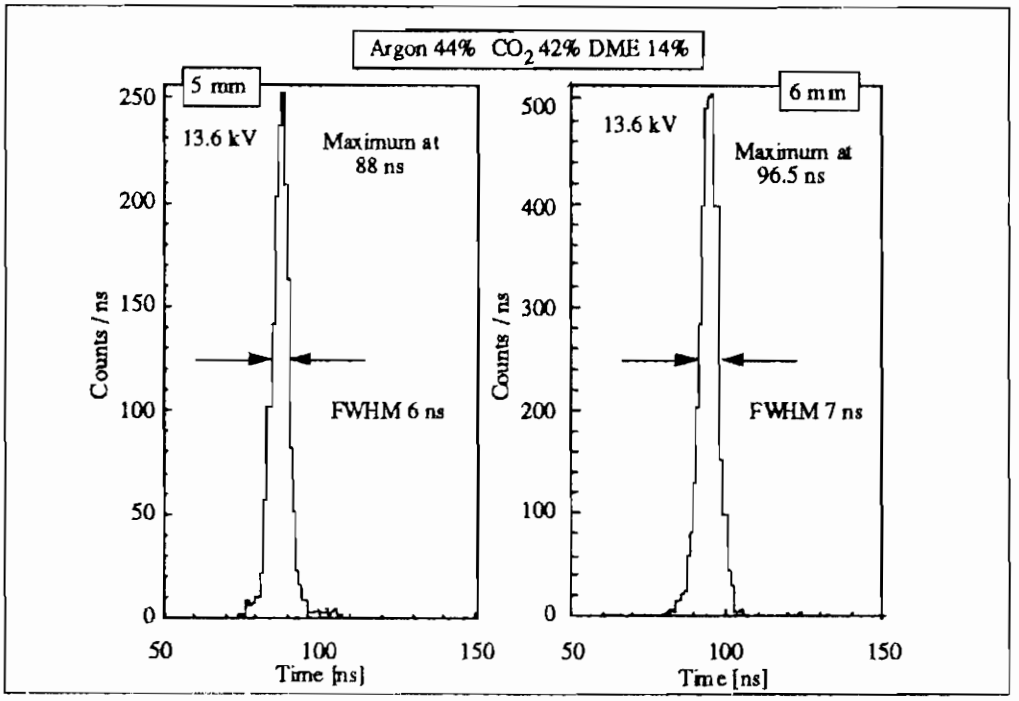

Fig 5. Time spectra of a 5 and 6 mm gas gap RPC, with the same applied voltage of 13.6 kV. The gas mixture was Argon 44%, CO_2 42% and DME 14%, bubbled through water at 10°C.

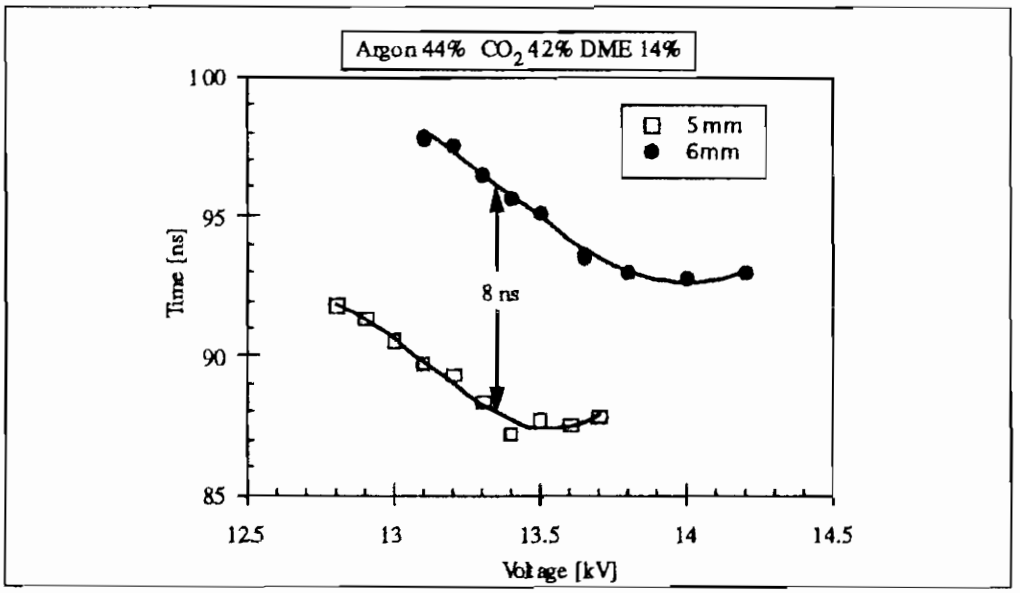

Fig. 6. Plot showing the time of the avalanche signal for the 5 and 6 mm chamber. At a given voltage the difference is 8 ns.

3. Noise of the RPC

Noise can be generated by the electronics, the detector itself and other sources. Considering first the electronics as a source of noise, one can distinguish: the noise due to the capacitance of the read out strips ($\sim C/\sqrt{T_p}$); the noise due to the biasing resistor ($\sim\sqrt{T_p}/\sqrt{R}$); the noise due to the dark current which, if the resistive plate behaves like an amorphous semiconductor, is proportional to $\sqrt{(I.T_p)}$ (I : diode leakage current). In addition there is cross talk and after pulsing in the electronics and oscillations of the amplifiers at low threshold.

The noise from the actual detector is mainly due to field emission of electrons from the cathode; in addition there could be spontaneous ionisation of the gas due to the electric field (a small effect) and real afterpulses.

Miscellaneous other sources of noise can be : breakdown across spacers and around the edges; also switching spikes from the high voltage power supply (these can be current dependant).

The circuit diagram of the electronics is shown in figure 7

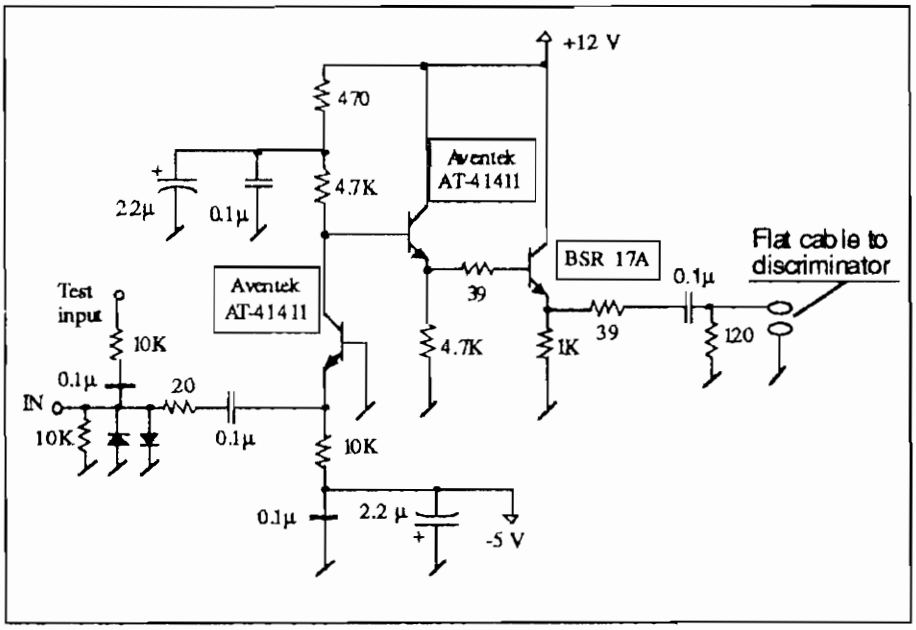

Fig. 7. Circuit diagram of fast current amplifier attached to the pick-up strips.

(described also in [2]). In our current set up there is a preamplifier attached to each pick up strip on the chamber; the signals from the 16 strips are sent (via twisted pair flat cables of 1 m length) to a unit containing an additional preamplifier and a time-over-threshold discriminator for each channel.

In figure 8 we show (a) the efficiency versus high voltage and (b) the dark current for the 5 mm RPC (gas mixture consisting of 14% DME, 42% CO_2 and 44% Argon). In figure 9 (a) we show the noise in Hz/cm^2. The threshold voltage corresponds to 1V≅ 50 fC. The noise is zero for zero applied voltage, which indicates that noise due to the capacitance of the pick up strips is not significant. The noise apparently plateaus below the knee of the efficiency plateau (for minimum ionising particles); this may be due to electrons emitted from the cathode which avalanche over the full 5 mm and give signals above the threshold even at this "low" field. "Real" signals from minimum ionising particles are smaller. In the high voltage range where the RPC has full efficiency the noise level is 5 Hz/cm^2; at higher values of voltage (corresponding to the end of the efficiency plateau) the noise starts to rise substantially.

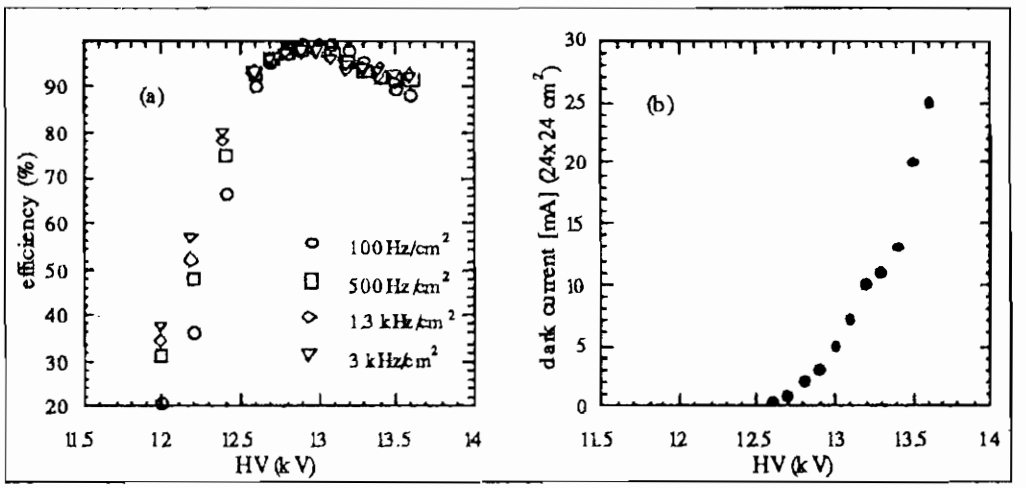

Fig. 8. (a) Efficiency versus high voltage and (b) dark current for the 5 mm RPC (gas mixture consisting of 14% DME, 42% CO_2 and 44% Argon)

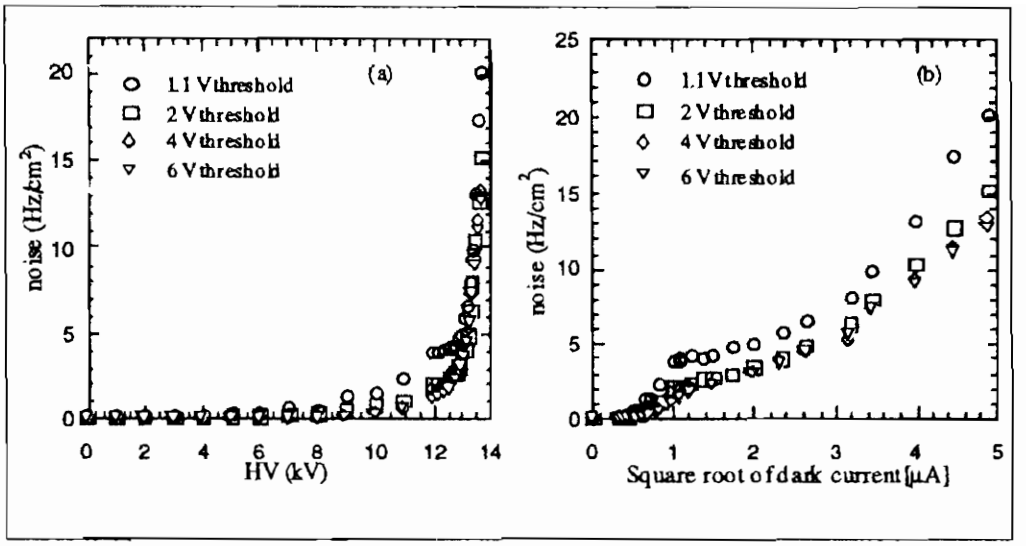

Fig. 9. (a) Noise versus applied voltage and (b) noise versus the square root of the dark current.

Figure 9 (b) shows the noise as a function of the square root of the dark current. After the plateau, one can observe a linear rise with square root of dark current. This could indicate that the resistive plates are behaving like a semiconductor.

4. Performance of the 5 mm RPC with a non flammable gas

An important property of any gas used at LHC is that it should be non flammable. In this section we show results obtained with the 5 mm RPC filled with a gas mixture of 15% Argon, 80% CO_2 and 5% DME; this gas is non flammable [4].

In figure 10 (a) we show the efficiency versus high voltage for the 5 mm RPC, measured for 4 particle fluxes (flood illumination); in figure 10 (b) we show the dark current. The efficiency reaches 98% and is unchanged up to a flux of 3 kHz/cm^2; however, the knee of the efficiency plateau occurs at 2 kV higher voltage than for the gas mixtures discussed in Section 2.

Figure 11 shows the charge spectrum for the 5 mm RPC obtained at 200 V above the knee of the plateau, with a flux of 100 Hz/cm^2. The mean values is 2.8 pC; the long tail is due to the

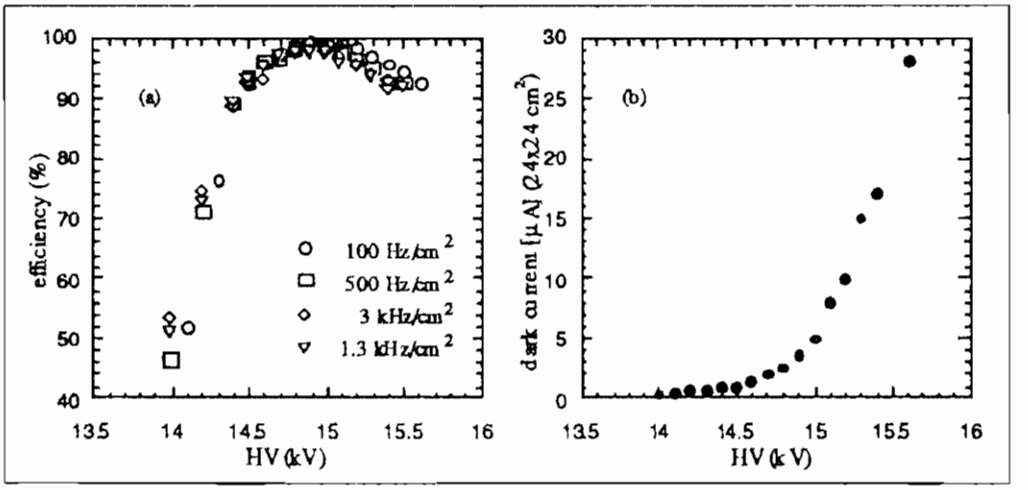

Fig. 10. 5 mm gap RPC with a gas mixture of 15% Argon, 80% CO_2 and 5% DME. (a) Efficiency versus applied voltage for 4 fluxes (flood illumination). (b) dark current versus high voltage.

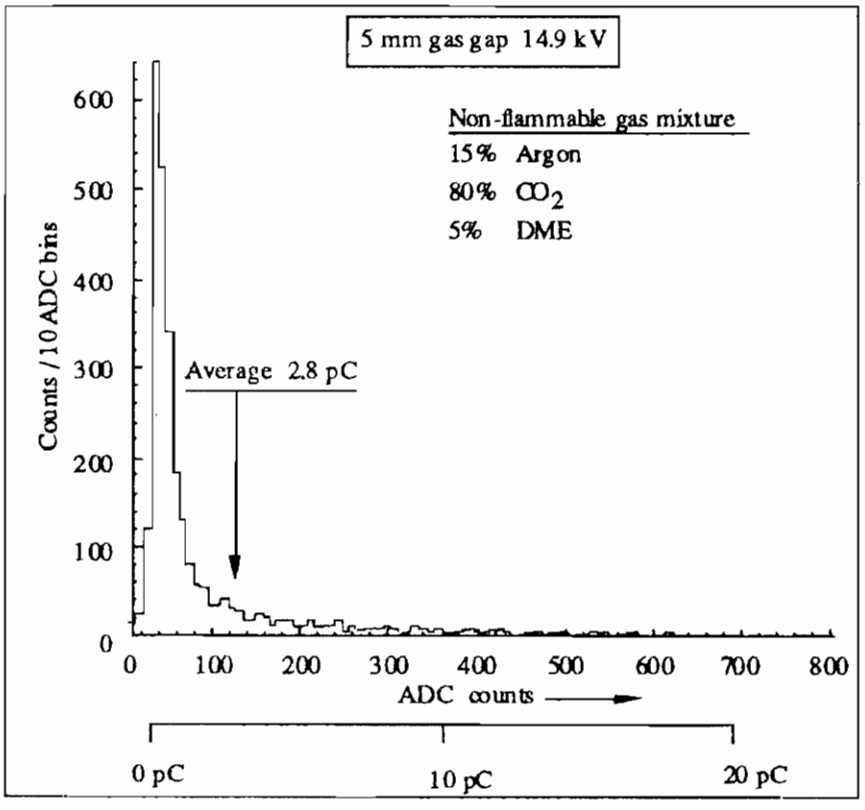

Fig. 11. Charge spectrum of 5 mm chamber with non-flammable gas mixture at 14.9 kV (200 V above knee of efficiency plateau).

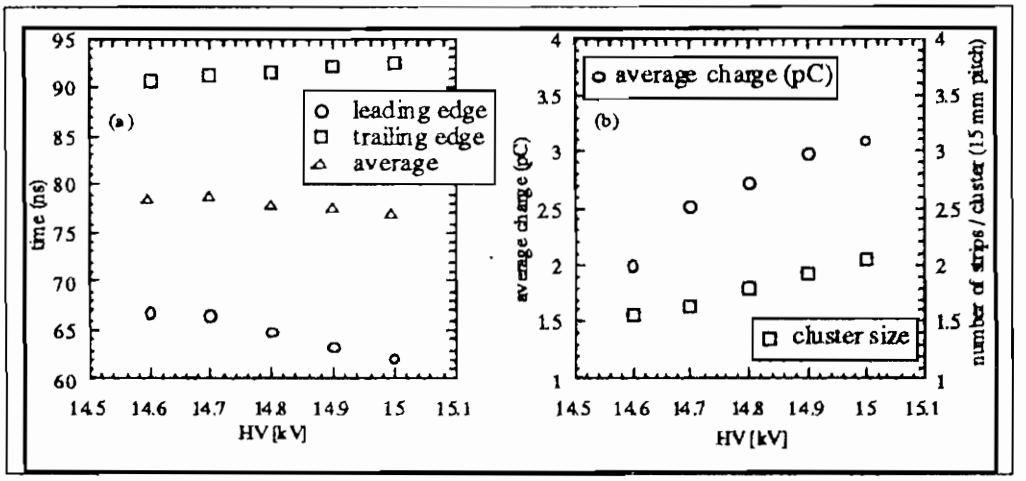

Fig. 12. Variation of (a) time, (b) average charge and cluster size with high voltage for 5 mm chamber with non-flammable gas mixture.

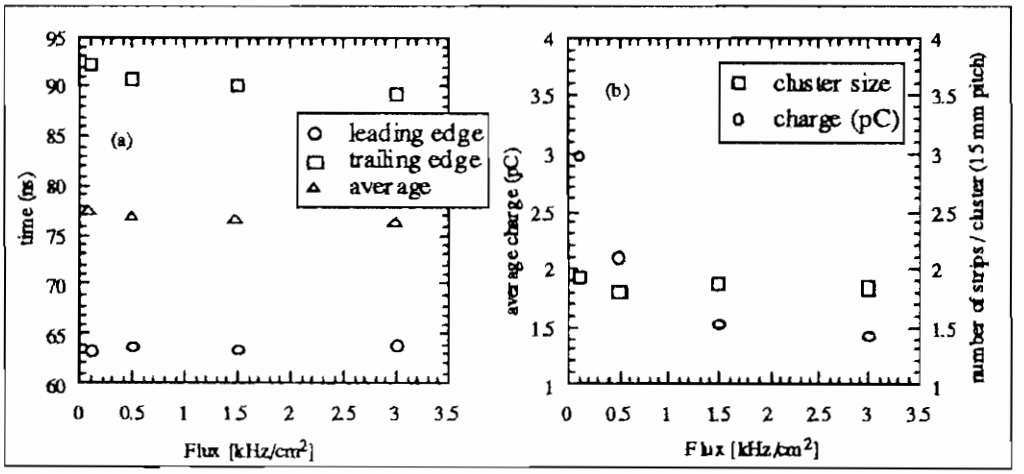

Fig. 13. Variation of (a) time, (b) average charge and cluster size versus flux; the data was taken at 14.9 kV.

statistics of primary ionisation. The timing distribution for the same conditions has FWHM = 5 ns and the width at the base is 15 ns.

Figure 12 shows the variation of (a) time, (b) average charge and cluster size with high voltage. The leading edge of the signal comes earlier as the voltage increases; the trailing edge comes later, due to the increased magnitude of the pulse; the average of these two changes by 1.5 ns for 400 V. The cluster size changes between 1.5

and 2 strips per cluster. This is a little bit wider than it used to be [2]; some increase of the cluster width could be due to an increase in cross talk between the preamplifier channels and is being investigated.

Figure 13 shows the variation of the same quantities versus flux; the data was taken at 14.9 kV. The average charge decreases with rate; the timing and the cluster size remain practically unchanged.

5. Summary

As a summary of our results, we make a comparison with the required performance of the RPCs for the endcap muon trigger of CMS, as presented in this Workshop by G. Wrochna [5].

(a) Timing: it is required that 98% of the events are within 15 ns (for two planes in OR). We have obtained full width at the base of the time distribution 18 ns (for single gas gap).

(b) Rate capability : efficiency > 98% is required up to 1.5 kHz/cm^2 (for two planes in OR). We have obtained 98% up to 3 kHz/cm^2 and 95% at 8 kHz/cm^2 (for single gas gap).

(c) Noise and induced charge : The noise level was measured to be 5 Hz/cm^2 and the average charge 2 - 4 pC for the plateau range of voltage.

(d) Cluster size : The average cluster size is required to be less than 2 strips per cluster. We obtained < 2 strips per cluster (for a single plane).

(e) Power dissipated : The heat dissipation from the high voltage power supply, based on our measurements, is estimated to be 1 W/m^2 at 200 Hz/cm^2 (for the single gas gap).

6. Conclusions

We have shown that an RPC with a 5 & 6 mm gas gap can give the required performance even with a flux corresponding to the

endcap of CMS. In addition we have a candidate gas mixture that is non-flammable.

Acknowledgements

We thank the organizers of RPC95 for making possible the exchange of a vast amount of information among RPC developers in a stimulating and friendly atmosphere.

References

1. R. Santonico and R. Cardarelli, Nucl. Instr. Meth. 187 (1981) 377.
2. I. Crotty et al., Nucl. Instr. and Meth. A 360 (1995) 512.
3. E. Cerron-Zeballos et al., "What have we learned from a comparison between the wide gap and narrow gap RPC", these proceedings.
4. R. Magnier, private communication.
5. G. Wrochna, "The RPC system for the CMS experiment at LHC", these proceedings.

DEVELOPMENT OF RESISTIVE PLATE COUNTERS FOR THE PIERRE AUGER COSMIC RAY OBSERVATORY

PETER O. MAZUR
Fermi National Accelerator Laboratory
P.O. Box 500, Batavia, Illinois 60510, USA

February 5, 1996

ABSTRACT

The Pierre Auger Cosmic Ray Observatory will study the highest energy cosmic rays by observing extensive air showers using a large array of surface detectors, spaced on a triangular grid of 1.5 km on each side. Resistive plate counters were studied as a possible candidate for the surface detectors to be used. Several RPC's were built using soda-lime float glass resistive plates with spacers of PVC and polystyrene plastic, glass, and aluminum. These were tested using gas mixtures which included halocarbon 13B1, 116, or which were halocarbon free. Gas flow rates were reduced or stopped to study aging effects of the gas. Operation at temperatures as low as - 10°C was studied as was operation with a non-flammable gas mixture.

1. Introduction

Following their discovery in 1912 by Victor Hess, cosmic rays have been extensively studied and their composition, energy spectrum, and direction recorded in an effort to determine what they are and where they come from. In the last 30 years or so, a handful of cosmic rays with energies above 10^{20} eV have been observed. These events are remarkable because cosmic rays of this energy are expected to interact with the cosmic microwave background radiation and lose energy[1]. As a result, the energy of a proton in this energy range traveling through space is degraded with a characteristic length of about 150 million light years. Consequently, if protons are observed on Earth with such high energies they would be expected to have been produced relatively nearby (in cosmological terms), but there are no credible sources of these high energy events within this distance. Cosmic rays of these high energies are likely to have sufficient magnetic rigidity to point back to their sources, so observation of a reasonable number of cosmic rays with energies above 10^{20} eV should tell us not only what these remarkable cosmic rays are but where they come from.

The Pierre Auger Cosmic Ray Observatory[2] will study the highest energy cosmic rays by observing extensive air showers initiated by these cosmic rays as they strike the upper atmosphere. The technique consists of sampling the air shower as it reaches the surface of the earth with a large number of particle detectors spaced on a 1.5 km triangular grid. A total of approximately 1600 surface detector stations at each of two sites, one in the northern hemisphere and one in the southern hemisphere, will be required for a total area coverage of 6000 km^2. The very large area requirement stems from the low rate at which cosmic rays above 10^{20} eV strike the earth: 0.5/sr km^2 century. Each surface detector station will consist of a solar power system, a radio communications link, a GPS satellite receiver for recording precise time signals, and a particle detector with a sensitive area of 10 square meters. Resistive plate counters (RPC's) were studied as a possible candidate for the surface detector technology. RPC planes would be used in pairs as a "sandwich detector" with an electromagnetic converter such as lead, steel, or even concrete between the two planes to identify the muonic and electromagnetic components of the air shower. The muon/electron-

photon separation is performed by correlating tracks in the counter plane above the converter with those below the converter: Muons will tend to produce correlated tracks in both counter planes, whereas electrons will count in the upper counter only and photons will count in the lower counter only. The direction from which the cosmic ray which initiated the shower came is determined by the angle of the shower as reconstructed from the time of arrival of the shower front at each detector station. Counters for the sandwich detectors have these requirements:

1. A reasonable efficiency is required, at least 95%.
2. The detectors must be able to operate continuously at cosmic ray rates, about 200-300 Hz/m^2.
3. The detectors must be able to record at least 10 tracks per square meter in a 20 μs period, the typical time-of-arrival spread of a large shower.
4. A time resolution of 20-30 ns or better is required.
5. The detectors must be able to operate from -5°C to +45°C with both daily and seasonal temperature cycles.
6. The detectors must be able to operate in remote locations where scheduled visits can be no more often than annual. This sets particularly stringent requirements on the choice of gas, and on its consumption rate.
7. Construction and operating costs over the 20 year life of the experiment must be minimized.

2. Description of the RPC's

2.1. The Resistive Plates

Eight 30 × 30 cm^2 test RPC's have been built using 2.1 mm soda lime float glass plates separated by 2.1 mm spacers. The counters were assembled without regard to whether the residual tin contamination from the glass manufacturing process was on the inside or outside of the counter and no characteristic of performance has yet been identified as being correlated with which side of the glass has the tin contamination. (The side of the glass which had the tin contamination was determined by observing the fluorescence induced by a short-wavelength (254 nm) ultraviolet lamp.) The glass was cleaned using several techniques: washing with detergents and water, followed by washing with ethyl alcohol, and scrubbing with these cleaning agents using paper wipers, stainless

steel wool, or Scotchbrite pads. The stainless steel wool and Scotchbrite pads both produced fine scratches visible on the glass, and the RPC's that resulted tended to have higher noise levels than the others, so these abrasive cleaning methods were abandoned. None of the cleaning methods resulted in a flawless surface as tested by forming a water condensate and looking for patterns such as streaks which indicate surface contamination. A simplified cross section of the RPC is shown in Figure 1.

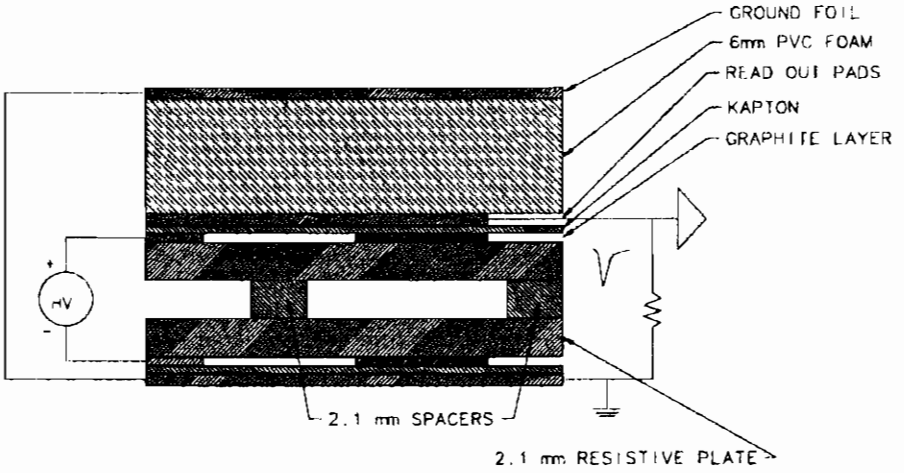

Figure 1: Simplified cross section of the test RPC's.

RPC's have been demonstrated[3] [4] [5] [6] successfully in the past which used glass electrodes, although some of the experiments used specially doped glasses to lower the resistivity in order to operate at high rates. Because of the low counting rate requirements of the Pierre Auger Project, low resistivity glass was not required and ordinary commercial glass was used. The resistivity of the glass plates was measured by attaching copper electrodes to the surfaces on opposite sides of the glass and applying a high voltage while monitoring the current. The resistivity measured this way appears to have a voltage dependence causing variations of a factor of 2-3 over a range of 1000-7000 V as shown in Figure 2. The temperature dependence of the resistivity was also measured and found to increase by a factor of 44.2 as the temperature was reduced from 23.2°C to -15.0°C. That surface resistivity was not large enough to affect these measurements was verified by varying the size of the copper electrodes and observing that the value of the resistivity was not affected.

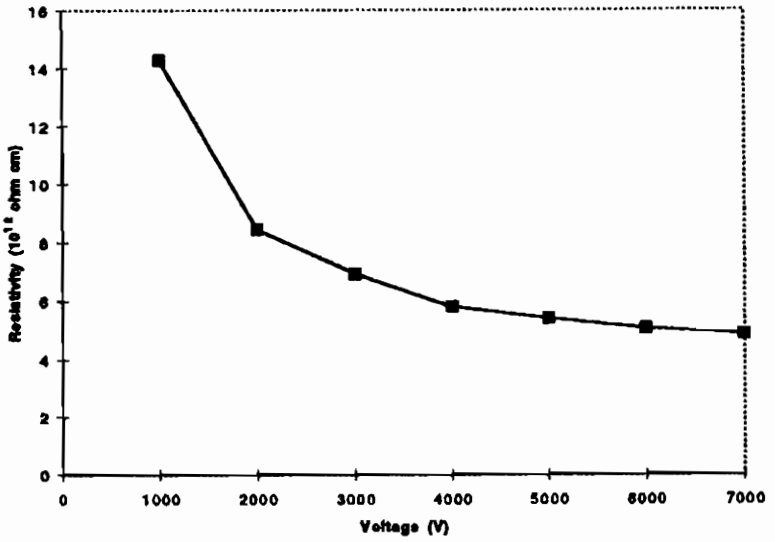

Figure 2: Resistivity vs. voltage for a 2.1 mm thick glass plate at 23.2° C.

2.2. Spacer Construction

RPC1, the first RPC tested, had nine PVC button spacers of 9.5 mm diameter installed on a 102 mm grid and polystyrene edge spacers at the perimeter. The conducting graphite layer was removed from a 25 mm diameter circular area around each button spacer and from a 12.7 mm wide strip along the edge spacers. RPC2 was constructed with four aluminum button spacers of 7.9 mm diameter installed on a 152 mm grid and aluminum edge spacers at the perimeter. The graphite layer was removed from a 38.1 mm diameter circular area around the button spacers and from a 19 mm strip along the edge spacers. All subsequent RPC's were built with the same geometry as RPC2. RPC8 employed 10 mm square glass spacer buttons and glass edge spacers. Other RPC's used either aluminum spacers or glass spacers in which the buttons were round. The plastic spacers of RPC1 had rounded edges to reduce the possibility of edge sparking; all the other spacers had straight edges.

2.3. Why Glass Conductors and Aluminum Insulators?

The electric field along the edge of an insulating spacer is typically 4000V/mm in these RPC's leading to concern about electrical breakdown along these surfaces and consequent increased noise as the breakdown occurs. If a conducting spacer is used, the field along the surface of the spacer is zero, and the electric field along the surface of the resistive plates can be reduced as much as desired by removing the graphite high voltage distribution planes near the spacers. For the simple case of a cylindrical conducting spacer of radius r_1 between two resistive plates of thickness t and resistivity ρ, with conducting sheets outside with a clear radius r_2, the resistance R is

$$R = \frac{\rho}{\pi t} ln \frac{r_2}{r_1} \tag{1}$$

The maximum electric field is

$$E_{max} = \frac{V}{r_1 ln \frac{r_2}{r_1}} \tag{2}$$

where V is the RPC operating voltage. For example, an RPC of this geometry operating at 8000 V with a conducting button spacer of radius r_1 of 5 mm and a graphite clearance radius of 15 mm would have a peak electric field of 0.73 kV/mm instead of the 4.0 kV/mm that would occur at a 2 mm thick insulating spacer.

2.4. Voltage Distribution and Signal Readout

The high voltage was distributed by a graphite film formed by spraying five light coats of ink[a] which resulted, after drying and polymerization, in a durable coating of 300-400 kΩ/square resistivity. The early RPC's were built with this ink very successfully. Later RPC's used ink that was manufactured later and the formula used by the manufacturer apparently had been changed. As a result, the resistivity became highly variable and the durability of the film and its adhesion to the glass were

[a]Higgens Black Magic Waterproof Drawing Ink 4465, manufactured by Eberhard-Castell, Inc., Lewisberg, TN 37091, USA.

Table 1. Differences between various test RPC's

RPC1	9 PVC button spacers, polystyrene edge spacers
RPC2	4 aluminum button spacers aluminum edge spacers
RPC3-7	4 buttons of either aluminum or (ground) glass, with aluminum or glass edge spacers
RPC8	4 square (cut) glass button spacers glass edge spacers

greatly reduced. (This unexpected change illustrates the risk of using a proprietary product in ways not intended by the manufacturer.) The readout plane consisted of an aluminum foil pad taped to one of the 6 mm plastic sheets that formed the structural backing of the RPC. The readout pad on one side of the RPC and the ground pad on the other side were separated from the graphite coating by 0.13 mm sheets of Kapton insulation. The 240 mm square readout pad was connected to a 50 Ω cable and read by a discriminator. The discriminator threshold was typically 80 mV, although studies are also described below in which the threshold was between 30 mV and 150 mV.

RPC8 is the closest example to the ideal RPC for the Pierre Auger Project for several reasons.

1. It performs well.

2. Because the edge spacers and the button spacers are glass cut by the traditional score-and-fracture method, manufacture of these parts is very inexpensive.

3. Because the spacers and the resistive plates are made of identical material, the coefficient of thermal expansion will be identical and thermally generated stresses resulting from diurnal and seasonal temperature variations will be minimized.

4. Because the construction is all glass, the use of adhesives cured by ultraviolet light is possible, although the test RPC's were all assembled using conventional epoxy.[b]

RPC2 is shown in Figure 3 and RPC8 is shown in Figure 4.

[b]Scotch-Weld DP-190 Epoxy Adhesive, manufctured by 3M, St. Paul MN 55144 USA.

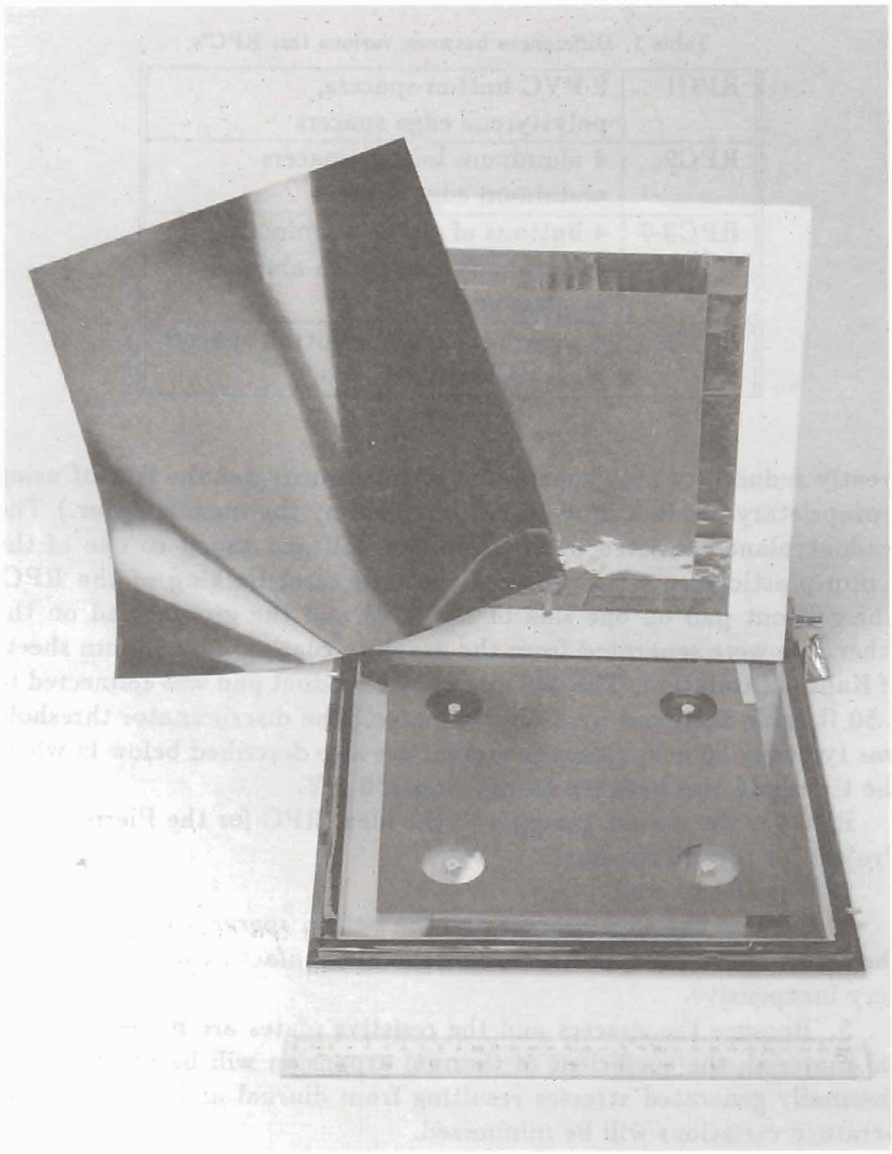

Figure 3: RPC2 was made with glass resistive plates and aluminum button and edge spacers. Photo: Fermilab Visual Media Services.

3. Performance of the RPC's

3.1. Tests with Various Gas Mixtures

All testing was done using cosmic rays selected by a scintillation counter plus RPC telescope. Because of the fragile nature of the electromagnetic part of the cosmic ray flux, efficiency tends to be underestimated. The standard gas mixture used consisted of 30% isobutane, 4% halocarbon 13B1, and 66% argon. For comparison, a mixture consisting of 40% isobutane, 4% halocarbon 13B1 and 56% argon was tested as well. As shown in Figure 5, performance with the two gas mixtures was very similar, with a very broad plateau at 98-99% efficiency and noise rates after subtraction of the cosmic ray background of much less than 100 Hz/m^2. The performance difference observed is mainly the shift of the efficiency plateau and the singles rate curves higher by 1000 V in operating voltage for the 40% isobutane mixture.

Halocarbon 13B1 is becoming very expensive and difficult to obtain because it is being phased out of use due to its ozone layer-damaging properties. The results of the Tohoku Group[7] suggested that halocarbon 116, C2F6, which is not restricted by the Montreal agreement and therefore should remain relatively inexpensive and available, might become a practical substitute. Therefore, tests were performed using a mixture of 30% isobutane, 4% halocarbon 116, and 66% argon, and compared with the standard gas mixture (30% isobutane, 4% halocarbon 13B1, 66% argon) as well as with a halocarbon-free mixture of 31% isobutane and 59% argon. As shown in Figure 6, the voltage plateau using halocarbon 116 is 600-800 V wide, compared with about 2000 V for the halocarbon 13B1. The maximum efficiency observed with halocarbon 116 was 97.4%, compared with 98.9% for halocarbon 13B1. Operation with no halocarbon resulted in a maximum efficiency of 93.8% with a narrow plateau of less than 600 V. Clearly, operation with halocarbon 13B1 will be much more forgiving than with halocarbon 116, or with no halocarbon.

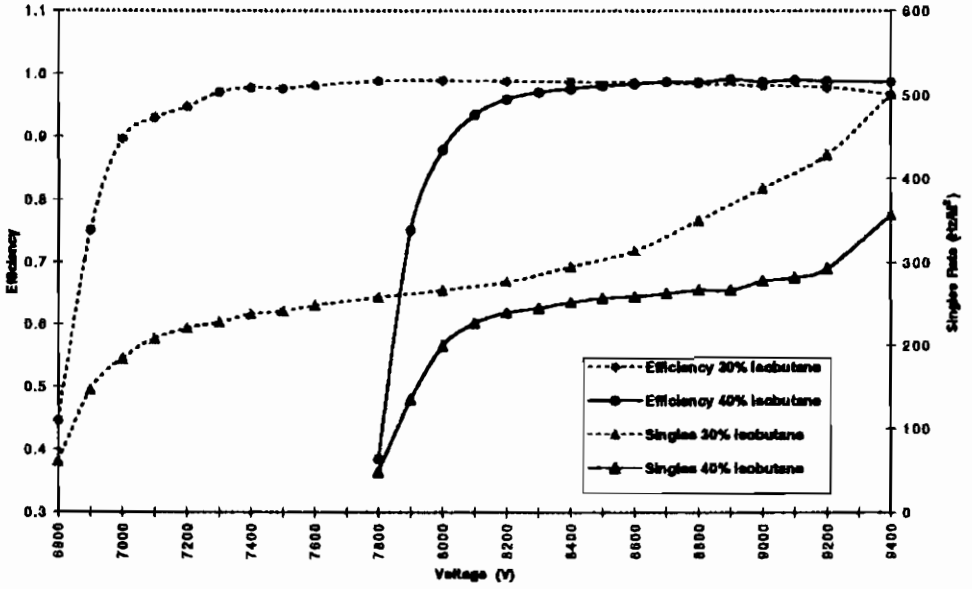

Figure 5: Comparison of RPC operation using gas mixtures consisting of 30% isobutane, 4% R13B1, 66% argon with 40% isobutane, 4% R13B1, 56% argon.

3.2. Low Temperature Operation

The Pierre Auger Project requires that the detectors operate outdoors. RPC's were therefore tested briefly outdoors in winter using the standard gas. The RPC's performed satisfactorily at the lowest temperature tested, -10°C, at which it had an efficiency of just over 95%. As can be seen from Figure 7, the plateau is shifted toward higher voltages at lower temperatures. The power supply used was limited to 9.4 kV. At that voltage at 4°C the efficiency was still increasing with increasing voltage, so higher efficiencies than that shown might have been possible. The resistivity of the glass increases by about a factor of 40 as the temperature is reduced from 21°C to -4°C so a shift of the efficiency plateau toward higher voltages might be expected on that basis. However, the fact that the singles rate changed remarkably little with temperature is more surprising. As seen in Figure 7, the shape of the efficiency curve

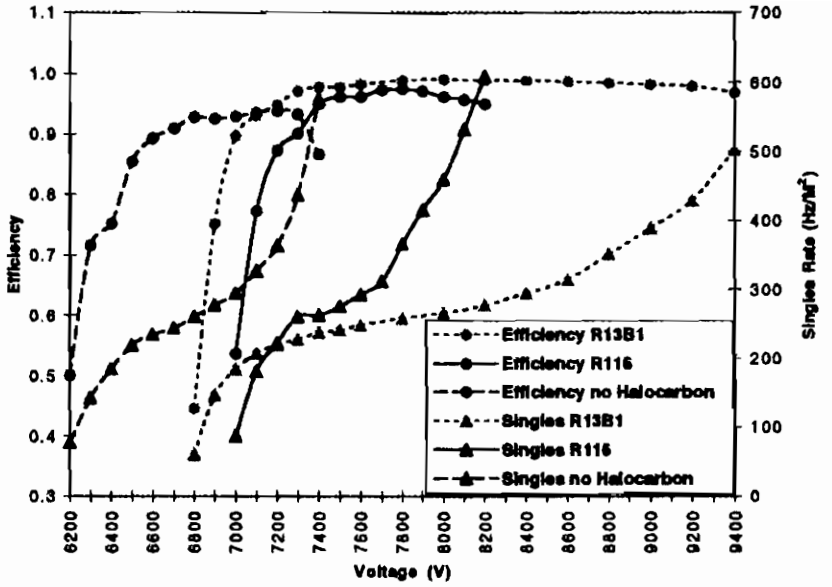

Figure 6: Comparison of RPC performance with 30% isobutane, 4% R13B1, 66% argon; 30% isobutane, 4% R116, 66% argon; and 31% isobutane, 69% argon.

changes somewhat with temperature so it is difficult to determine a temperature coefficient of the plateau voltage: At the 50% efficiency level, the temperature coefficient would be about -40V/°C whereas if the maximum efficiency were considered, the temperature coefficient would be about - 64V/°C.

Concerns about low temperature operation of the detector stations for the Pierre Auger Project are not limited to the detectors alone. The requirement for a gas supply which will last as long as possible between refilling and which will not be affected by low temperatures, i.e., none of the components may be allowed to condense because that would alter the composition of the gas mixture, suggests a reduction in the amount of isobutane in the mixture. At -10°C, the vapor pressure of isobutane is 707 Torr. Since that is less than one atmosphere, a local gas mixing system would not work. Storage of a 30% isobutane mixture would be limited to a maximum pressure of 3.1 atmospheres, severely limiting the amount of gas that could be stored at each detector station, whereas a mixture with only 8% isobutane would not condense below 11.6 atmospheres. At a pressure of 11.6 atmospheres the amount of gas

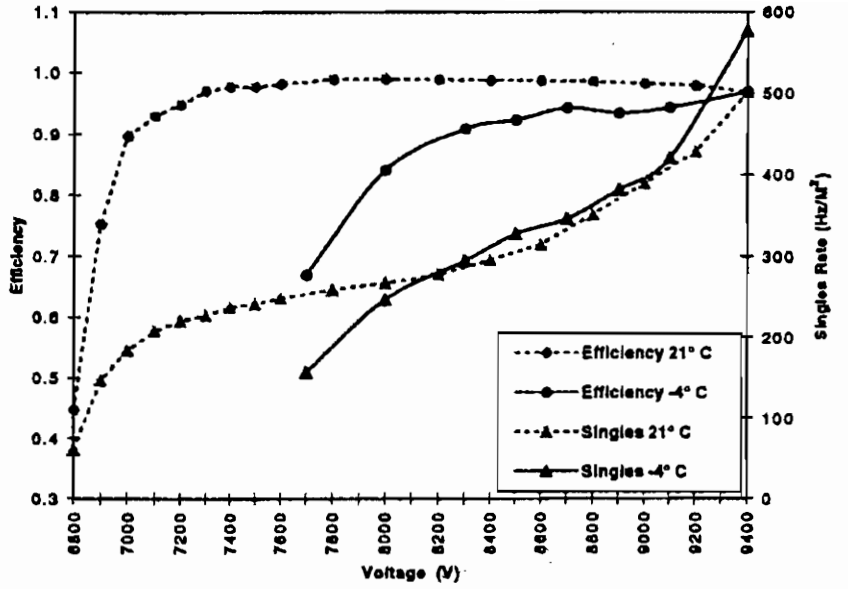

Figure 7: RPC operation at 21°C and at -4°C using 30% isobutane, 4% R13B1, 66% argon.

contained in a (USA) standard 1000 gallon (3785 l) storage tank could provide one gas change per day in the 44 l RPC volume at each station for a period of over 900 days before refilling is required. Therefore a non-flammable gas mixture which has been tested by others[8], consisting of 8% isobutane, 16% carbon dioxide, 5% halocarbon 13B1, and 53% argon was tested. As shown in Figure 8, the efficiency, with a maximum at 98.9%, and singles rate curves are similar to those obtained with the standard gas mixture but are slightly compressed in voltage and appear at a voltage about 1100 V lower.

3.3. Gas Lifetime Tests

It will be advantageous to the Pierre Auger Project to minimize the required gas flow to the RPC's in order to minimize both gas costs and the costs associated with delivering the gas to detector stations distributed over two 3000 km^2 sites. One method with which to determine the minimum gas flow required for proper operation is to stop all gas flow and observe the RPC performance. The time at which operation first becomes unacceptable indicates the maximum possible time per

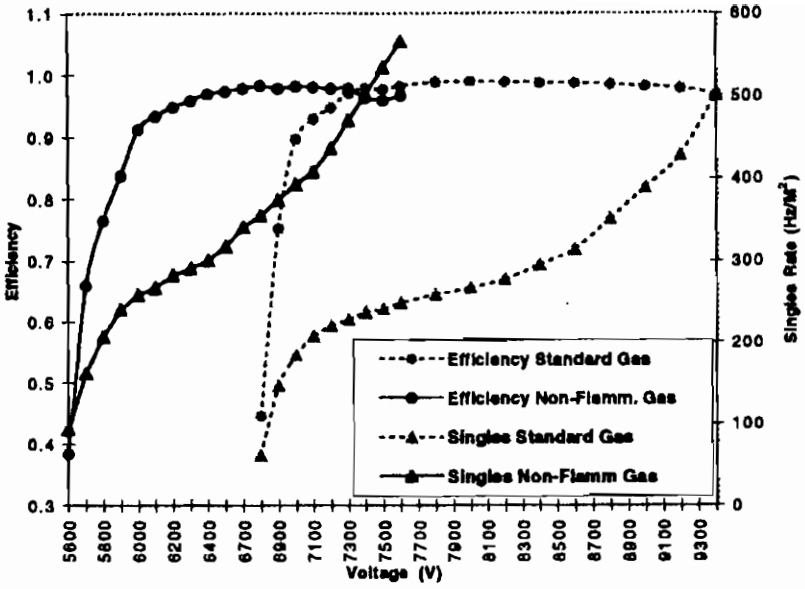

Figure 8: Comparison of RPC operation with the standard gas mixture consisting of 30% isobutane, 4% R13B1, 66% argon with a non-flammable mixture consisting of 16% CO^2 8% isobutane, 5% R13B1, 61% argon.

gas change. For these RPC's the first indication of gas contamination is an increase in the singles rate. The efficiency does not change significantly. Figure 9 shows the results of a test of RPC1 with no gas flow with three different values for the discriminator threshold using the standard gas mixture. The results do not appear to have an important threshold dependence. The singles rate increases very rapidly with time for this RPC, much more so than other RPC's tested. The difference between this RPC and the others is that the spacers were made of PVC and polystyrene plastics in RPC1 whereas they were either glass or aluminum in the other RPC's. Figure 10 shows a similar curve for RPC2 which had aluminum spacers. The gas lifetime was more than three times as long: three days as compared to one. One suspects that the plastic components may be outgassing chemicals which tend to strongly poison the gas. RPC2 was tested with a mixture of 40% isobutane, 4% halocarbon 13B1, and 56% argon and the results of this test with no gas flow are shown in Figure 11. RPC2 was operated with no gas flow for 104 hours during which time the singles rate gradually increased to

550 Hz/m^2. The RPC was flushed and the test repeated. This time the singles rate began the test at a slightly higher level and continued to increase at about the same rate as before, ending at 100 hours with 610 Hz/m^2. These tests (and others) suggest that it is possible to induce permanent noise increases on RPC's by operating them with contaminated gas for even short periods of time.

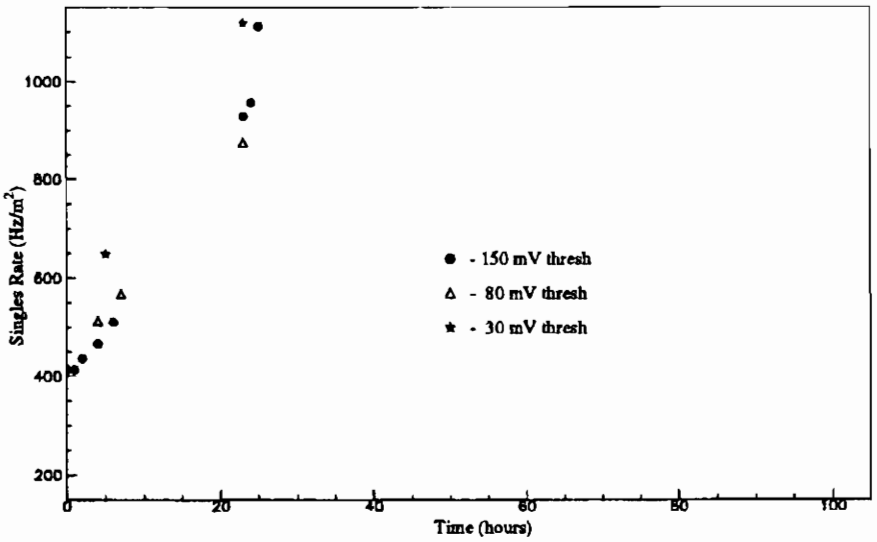

Figure 9: Singles rate with zero gas flow vs. time: RPC1 (plastic spacers 30% isobutane, 4% R13B1, 66% argon 7.5 kV.

4. Conclusions

The Pierre Auger Project will study cosmic rays with energies above 10^{20} eV by observing the particle showers initiated by these cosmic rays when they strike the upper atmosphere. The showers will be detected by an array of particle detectors on the ground distributed in a triangular grid 1.5km on a side over an area of 3000 km^2 at two sites, one in the northern hemisphere and one in the southern hemisphere. RPC's were considered as a potential detector for these arrays and a test program was undertaken to determine their suitability. RPC's made with ordinary soda-lime float glass resistive plates were built with plastic, aluminum, and glass spacers. Those with aluminum and glass spacers performed well, with efficiency above 95% under all expected operating conditions,

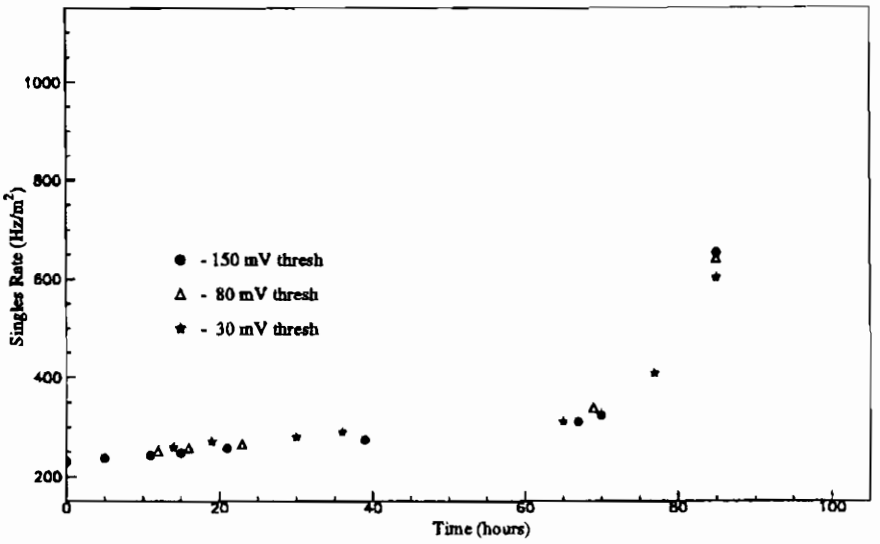

Figure 10: Singles rate with zero gas flow vs. time: RPC2 (aluminum spacers) 30% isobutane, 4% R13B1, 66% argon, 7.5 kV.

noise rates well below 100 Hz/m^2, and reasonable gas lifetimes due to the non-outgassing nature of the materials of their manufacture. The RPC's perform acceptably at temperatures as low as -10°C and with fewer than one gas change per day. A non-flammable gas was tested which has the virtue that the components of the gas mixture will not condense at the low temperatures expected in operation up to a pressure of 11.6 atmospheres allowing sufficient gas storage at each detector station to require delivery of gas no more often than every 2-3 years. Although the reference design for the Pierre Auger Cosmic Ray Observatory calls for water Cerenkov counters, the RPC detectors may be considered for a supplemental array to increase sensitivity to lower energy cosmic ray showers. Further studies of long term aging effects will be required before a decision to do that can be made.

5. Acknowledgments

The author wishes to thank the technical staff at Fermilab's Magnet Test Facility, particularly D. Validis and A. J. Bianchi, for their help in fabrication of the RPC's and N. Theis for the preparation of the manuscript.

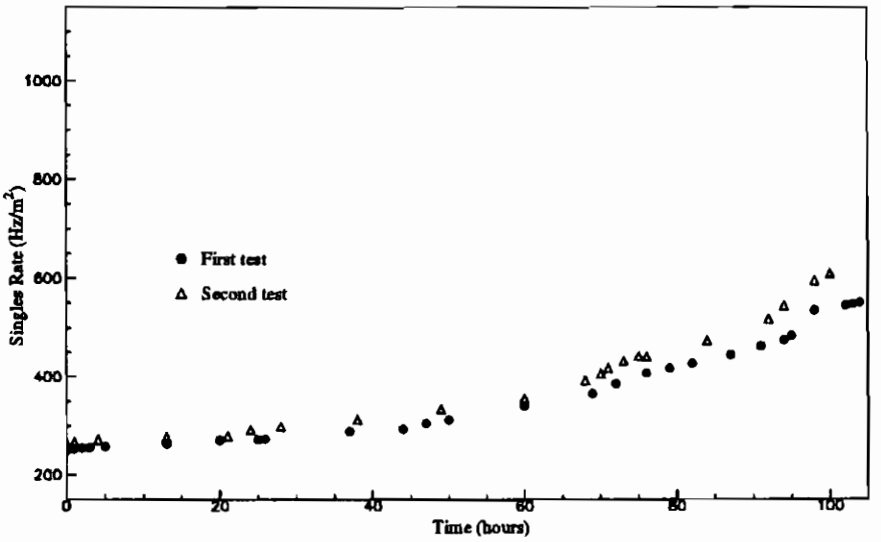

Figure 11: Singles rate with zero gas flow vs. time: RPC2 40% isobutane 4% R13B1 56% argon. The test was performed twice, with flushing between the two tests. The second test indicates a higher noise rate than the first.

1. K. Greisen, *Phys. Rev. Lett.* **16** (1966); G. T. Zatsepin and V. A. Kuz'min, *JETP Lett.* **4**,)1966) 78.
2. *The Pierre Auger Project Design Report.* Fermilab-Pub-96/024 (1965).
3. M. Anelli, et al., *Nucl. Inst. and Meth.* **A300** (1991) 572.
4. G. Bencivenni, et al., *Nucl. Inst. and Meth.* **A315** (1992) 507.
5. G. Bencivenni, et al., *Nucl. Inst. and Meth.* **332** (1993) 368.
6. G. Bencivenni, et al., *Nucl. Inst. and Meth.* **A345** (1994) 456.
7. A. Yamaguchi, et. al., Tohoku-HEP-94-01.
8. Y. H. Chang, et. al., *Nucl. Inst. and Meth.* **A349** (1994) 47.

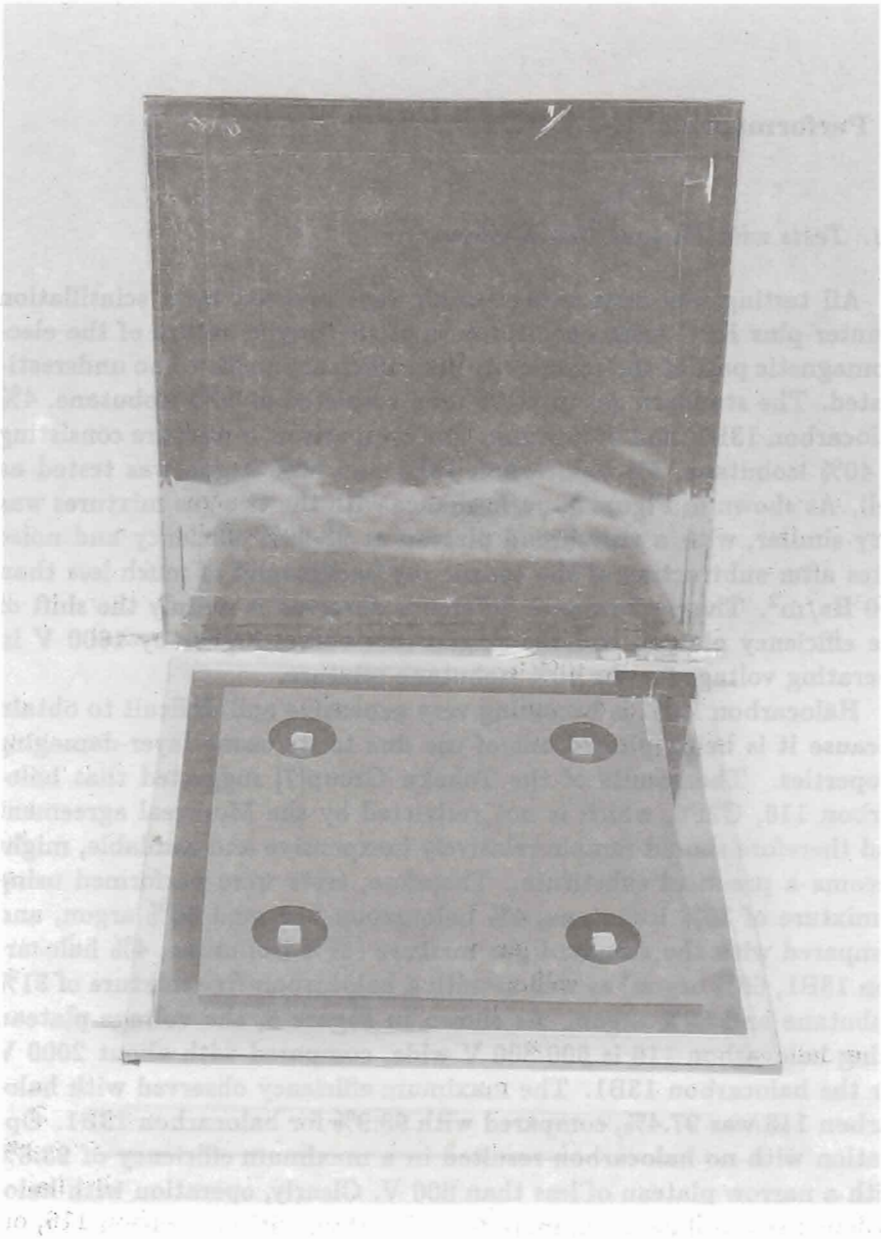

Figure 4: RPC8 was made with glass resistive plates, edge spacers, and square button spacers. Photo: Fermilab Visual Media Services.

THIN GAP CHAMBER: PERFORMANCE AS A TIME AND POSITION MEASURING DEVICE

Y.ARI[a], E.BARBERIO[b], T.EMURA[c], J.GOLDBERG[d], K.HOMMA[e], M.IKENO[a], M.IMORI[f], K.ISHII[e], H.ISHIWAKI[e], T.KAWAMOTO[f], T.KOBAYASHI[f], D.LELLOCH[b], L.LEVINSON[b], N.LUPU[d], G.MIKENBERG[b], M.MIYAKE[f], K.NAGAI[b], T.NAGANO[e], I.NAKAMURA[e], M.NOMACHI[c], M.NOZAKI[e], S.ODAKA[a], T.K.OHSKA[a], O.SASAKI[a], H.SHIRASU[c], H.TAKEDA[e], T.TAKESHIDA[g], S.TANAKA[e], C.YOKOYAMA[e]

[c] *National Laboratory for High Energy Physics, Tsukuba, Japan*
[b] *Weizmann Institute of Science, Rehovot, Israel*
[c] *Tokyo University of Agricolture and Technology, Tokyo, Japan*
[d] *Technion Institute of Technology, Haifa, Israel*
[e] *Kobe University, Kobe, Japan,* [f] *University of Tokyo, Tokyo, Japan*
[g] *Shinshu University, Matsumoto, Japan*

ABSTRACT

Thin Gap Chambers are a mass production device with good time resolution for trigger purposes ($\sim$ 3.6 ns) and a good rate capabilities (operation up to 200 KHz/cm ^{2}). They have no strong sensitivity to mechanical deformation and they offer a reasonable position resolution (150 μm) and two particle separation(2 mm).

1. Introduction

Thin multi-wire chambers (Thin Gap Chamber) were first developed by S.Majewski et al [1] and then optimised by Israeli institutions for the use in sampling counter calorimeters [2,3,4]. Thin Gap Chambers operate in a high gain mode using strong quenching gases, hence they provides large saturated signals. The saturation is essential to obtain a good energy resolution in a calorimeter. In addition, it makes the amplification relatively insensitive to mechanical variations which is an advantage in the construction of large chambers. The 'pole-tip' hadron calorimeter and the endcap presampler in the OPAL experiment at LEP were constructed using 384 Thin Gap Chambers which are still operating successfully.

Due to its operational characteristics Thin Gap Chambers provide a timing signal with a small jitter. In fact, for CO_2-based gases the drift velocity of electrons does not reach the saturation at high electric field, therefore for this chamber the drift time is short. Thin Gap Chamber has been chosen as the first level muon trigger system in the ATLAS experiment for LHC to cover the endcap region [5]. The first level muon trigger system is required to identify the bunch crossing, which occurs every 25 ns. Furthermore, the rate of low energy photons, low energy neutrons and hadrons in the ATLAS endcap region has been estimated to be about 1 kHz/cm^2 [5]. Hence, the high rate capability of the chamber under such a high background is essential for an efficient trigger system.

The Thin Gap Chamber performance as a time and position measuring device has also been measured. The chamber shows a reasonable position and a good two particles separation.

2. Chamber Structure and general characteristics

The general structure of the Thin Gap Chamber is shown in figure 1. It consists of 50 μm gold-plated tungsten wires spaced every 2 mm. The wires are strung with a tension of 350 g and soldered at both end to copper strips on a G10 frame along the sides of the chamber. The wires are supported with spacers of 7 mm width located 20 cm apart to provide mechanical strength for the chamber itself.

The cathode planes are thin (200 μm) G10 sheets coated with resis-

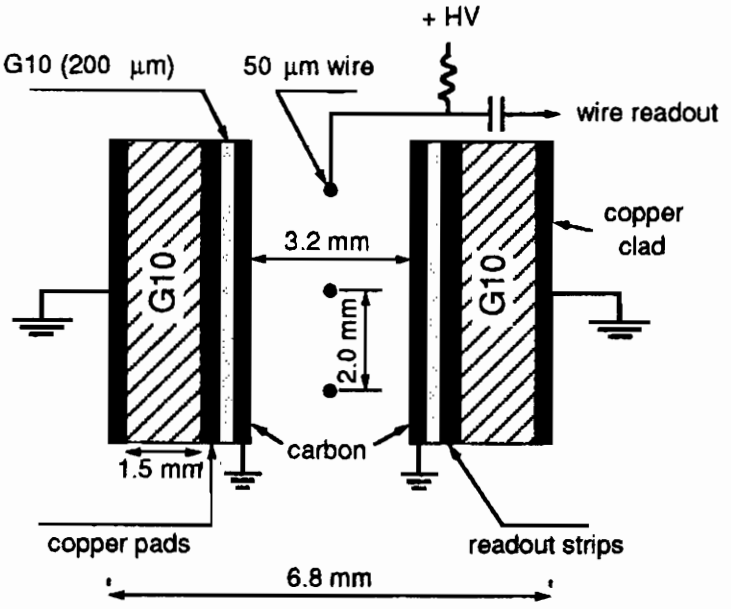

Fig. 1. Schematic view of the cross-section of the Thin Gap detector (OPAL design).

tive (about 1 MΩ/square) carbon paint on the inner side and bonded on 1.5 mm thick G10 plates which provide the mechanical rigidity. The outer copper coating of the G10 plates is left on the outer surfaces for electrical shielding. The inner surface is etched to form pads, strips or any desired geometrical pattern,according to the specific needs, with small dead areas. Hence, the mechanical accuracy of the chamber is limited only by the quality of the printed circuit readout board. Thus the Thin Gap Chamber can provide three sources of readout, one from the anode and a capacitively induced readout from each of the cathodes.

The Thin Gap Chamber operates with a gas mixture of CO_2(55%) flowing through liquid n-pentane(45%) at a temperature of 17 ^{0}C. The behaviour of the ratio between the signal obtained for a ^{55}Fe source to a minimum ionising electron form a ^{90}Sr source as function of the high voltage for CO_2-n-pentane gas mixture is shown in figure 2. It can be seen that in order to operate in a saturate mode the voltage on the detector must be above 4 kV. For large surfaces, the chamber is operated at a voltage between 3.2 kV and 3.7 kV, where saturation is not fully

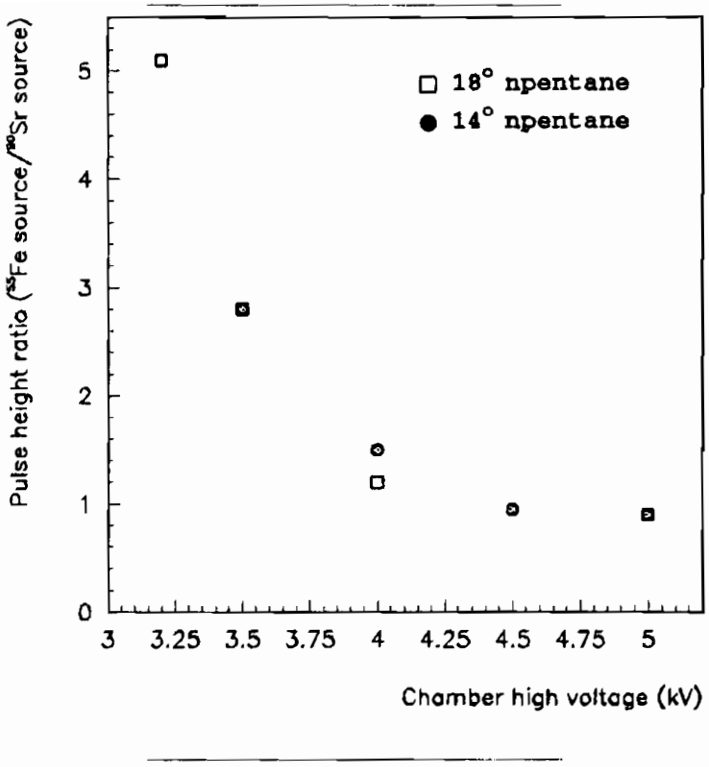

Fig. 2. Pulse height ratio between ^{55}Fe and ^{90}Sr source as a function of the operating voltage.

reached.

General characteristics of the Thin Gap Chamber are [2,3]:

- a) they show no parallax up to 45^0 angles (figure 3a);
- b) low sensitivity to mechanical deformations, i.e to a local change of the anode-cathode distance (figure 3b);
- c) the pulse height spectrum from a single ionising particles has a small Landau tail (less than 2%);
- d) a signal raise time of less than 5 ns.

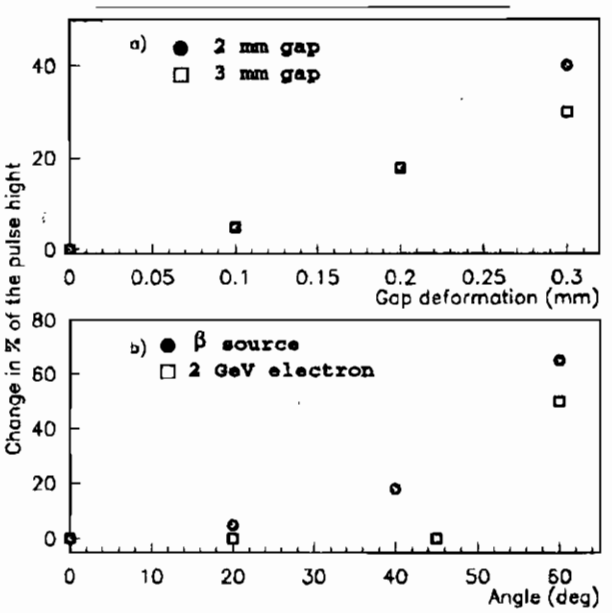

Fig. 3. Change in the signal height (in %) a) as a function of the gap deformation and b) of the relative angle between beam and detector plane.

3. Timing Properties and Time Resolution

The timing properties of the chamber has been studied in a test beam held at KEK using a 3 GeV/c pion beam [6]. Two gas mixtures have been employed: the standard CO_2+n-pentane and CF_4+isobutane (20:80).

For CO_2 n-pentane more than 99% of the events fall into 25 ns time interval for both anode and cathode (figure 4a). The non-Gaussian tail comes from particles hitting in the middle of two neighbouring wires where the electric field is weak and the electron drift velocity is slow. The time resolution has been defined as the r.m.s. of the data within 25 ns interval. At 3.4 kV a time resolution of 4.5 ns has been reached.

Since the slow drift velocity in the middle region gives rise to the late arrival tail of the time distribution, an operation with fast gas is expected

to improve the time resolution. For this reason the CF_4+isobutane mixture has been tested. The timing distribution of the anode signal at 3.1 kV is shown in figure 4b. The tail disappears as expected and 99.7% of the events fell within 20 ns time interval. The time resolution has been found to be 3.7 ns. The overall efficiency was measured to be higher than 99% for CO_2 n-pentane gas mixture operating at 3.4 kV and 97.5% for CF_4 isobutane at 3.1 kV [6].

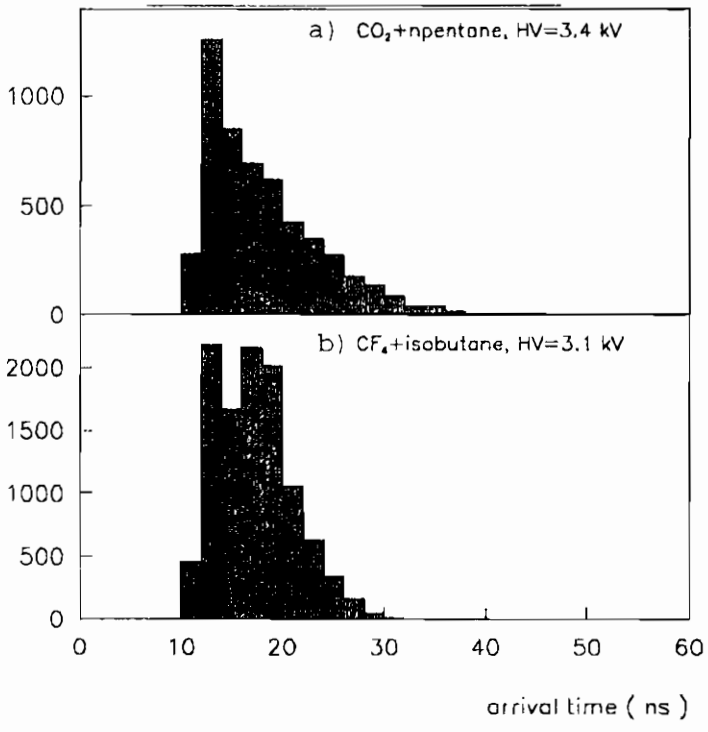

Fig. 4. Timing distributions a) with CO_2-n-pentane at 3.4 kV and b) with CF_4+isobutane at 3.1 kV.

The tails in the timing distribution for the CO_2+n-pentane mixture, which are due to late arrival electrons can be also cured by modifying the chamber geometry. For this reason a new chamber with a wire distance of 1.8 mm and a cathode-anode gap of 1.35 mm has been built. This chamber has been tested using a ^{106}Ru source and found to contain 99% of the events within a 20 ns interval with an efficiency higher than 99%.

With this new configuration a time resolution of 3.5 ns was reached for a CO_2+n-pentane mixture.

3.1. Operation with High Background and Long Term Stability

The high background conditions in which Thin Gap Chamber will operate in ATLAS was simulated placing a radiative source (^{90}Sr= 1mC) close to the Thin Gap Chamber surface. The particle rate was modified by adjusting the distance of the source from the chamber. Figure 5 shows the rate dependence of the signal obtained for a minimum ionising particles for different background fluxes and high voltage conditions.

No signal deterioration has been seen for rates up to 200 kHz/cm^2 at 3.3 kV.

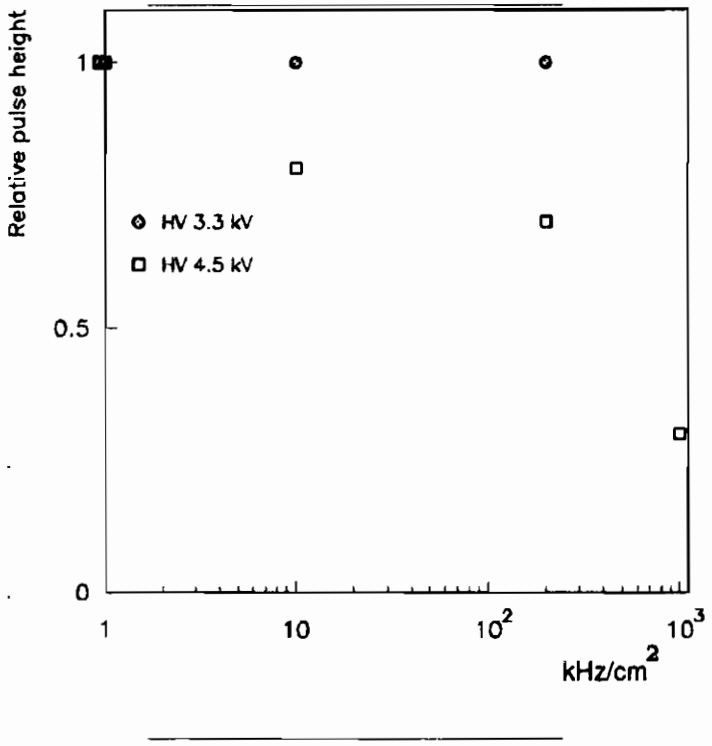

Fig. 5. Relative pulse height as a function of the incident rate.

The reliability of the Thin Gap Chamber over many years in a high radiation environment has also been tested. The chamber has been op-

erated while being irradiated with a collimated ^{90}Sr source. The setup was operated continuously for a period of 14 days and with some interruptions for a period of over a month. The total irradiated density correspond to 10^{11} particles/cm^2 equivalent to 3 years of LHC at high luminosity. The response of the counter to minimum ionising electrons as a function of time is constant within 10% [2].

4. The Thin Gap Chamber as Position Measuring Device

The performances of the Thin Gap Chamber as position measuring device has been tested on the H2 π/e beam line of the SPS at CERN. The setup of the test bean is shown in figure 6: two chambers with strip and wire readout were positioned perpendicular to the beam line with a 10 cm of distance between them. Strips and wires were perpendicular to each other and the strips had a pitch of 2 mm. A converter of half of a radiation length was placed in front of the chambers.

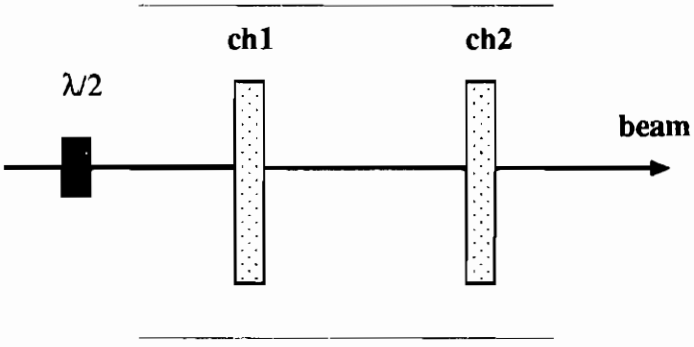

Fig. 6. Layout of the test beam held on the H2 π/e beam line of the SPS at CERN.

The spatial resolution of the chambers has been measured using the strips. In each chamber the cluster was reconstructed starting from the strip with the highest pulse height and taking the three contiguous strips on both side. The difference of the baricenter of the clusters for the same electron in the two chambers had a r.m.s. of 150 μm. This value is quoted as spatial resolution of the chamber. It must be notice that the cluster size on the strip is of the order of 6 mm.

To measure the two particles resolution, single particle events overlayed have been used. Because of the small Landau tails of the signal, two particle were considered resolved when their overalyed signals could

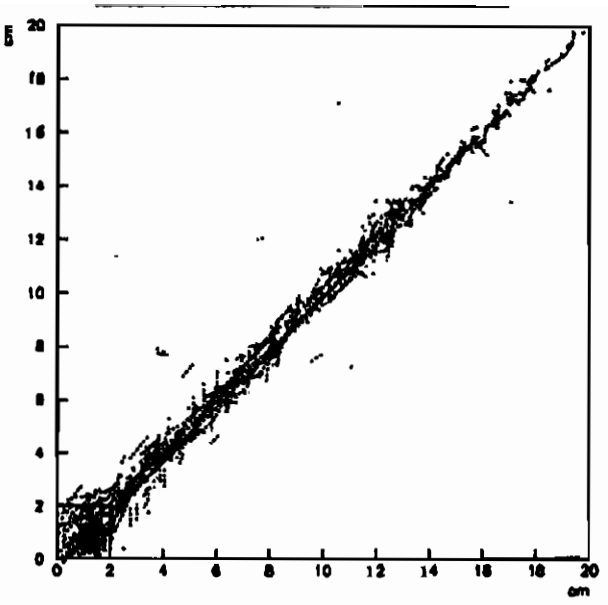

Fig. 7. Two particles resolution: the measured centre of the cluster in the single particle events is compared with the one obtained with the Gaussian fit

fit by two different Gaussian. The measured centre of the cluster (calculated as explained above) in the single particle events compared with the one obtained with the Gaussian fit is shown in figure 7. It can be seen that two particles can be separated down to the 2 mm of the strip pitch.

5. Conclusions

Thin Gap Chambers are a mass production device with very good time resolution for trigger purposes ($\sim$ 3.6 ns) and good rate capabilities (operation up to 200 KHz/cm ^{2}). They have no strong sensitivity to mechanical deformation. Furthermore they offer a reasonable position

resolution (150 μm) and two particle separation(2 mm).

6. Acknowledgments

We would like to thank Mr. M.Shoa for his contribution throughout construction, testing and installation of the detectors.

7. References

1. S. Majewski et al., *Nucl. Instr. and Meth.* **271** (1983) 265.
2. G.Bella et al., *Nucl. Instr. and Meth.* **A252** (1986) 503.
3. S.Dado et al., *Nucl. Instr. and Meth.* **A252** (1986) 511.
4. G.Mikenberg, *Nucl. Instr. and Meth.* **A265** (1988) 223.
5. ATLAS Collaboration, *CERN/LHCC/94-43*
6. Y.Arai et al. *submitted to Nucl. Instr. and Meth.*

RECENT STUDIES OF PARALLEL PLATE CHAMBERS FOR LHC EXPERIMENTS

A.AREFIEV[1], GY.L.BENCZE[2,3], A.BIZZETI[4], E.CHOUMILOV[1], C.CIVININI[4], G.DAJKÓ[5], R.D'ALESSANDRO[4], A.FENYVESI[5], A.FERRANDO[6], M.C.FOUZ[2,6], A.IGLESIAS[2], V.IVOCHKIN[7], M.I.JOSA[6], A.MALININ[1], M.MESCHINI[4], J.MOLNÁR[5], V.POJIDAEV[4], J.M.SALICIO[6], F.SIKLÉR[3] G.VESZTERGOMBI[3]

[1] *ITEP, Moscow, Russia.* [2] *CERN, Geneva, Switzerland.*
[3] *KFKI-RMKI, Budapest, Hungary (under OTKA Grant T 016823).*
[4] *Università and Sezione INFN di Firenze, Firenze, Italy.*
[5] *ATOMKI, Debrecen, Hungary (under OTKA Grant T 016823).*
[6] *CIEMAT, Madrid, Spain (under CICYT Grant: AEN95-1335-E).*
[7] *PNPI, St. Petersburg, Russia*

ABSTRACT

The Parallel Plate Chamber (PPC) has been investigated from the point of view of its applicability for LHC experiments. Basic properties of the PPC are presented and questions of applications are discussed.

1. Introduction

In the working conditions of LHC with luminosity of $10^{34}\mathrm{cm}^{-2}\mathrm{s}^{-1}$, bunch crossing every 25 ns, energies up to $\sqrt{s} \simeq 14$ TeV) the main detector requirements are fast response, high rate capability and radiation resistance. During the past years an R&D work has been carried out by a group of institutions forming the "PPC Collaboration" in order to develop PPCs capable to satisfy these requirements. Some of the main results of this work are summarized in this paper.

The construction and working principle of PPCs are discussed briefly in section 2. Results of studies of the basic parameters (efficiency, timing properties, spark probability, rate capability) as well as the comparison with Monte Carlo are presented in section 3. In section 4 results of investigations of some practical questions, namely spatial uniformity, spark resistance and radiation hardness are described. In section 5 trigger and calorimetry applications are discussed.

2. The PPC: construction and working principle

The PPC is a single gap gaseous detector with planar electrodes working in avalanche mode. The construction of PPCs used during the tests is shown in fig. 1.

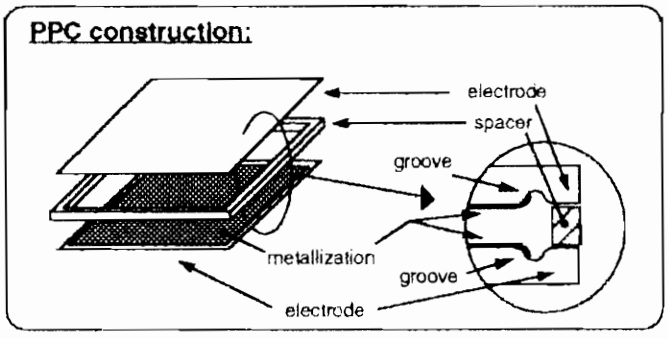

Figure 1: The PPC construction.

Chamber units (referred to as PPC pixels) are made of two electrodes separated by a ceramic frame, which determines the size of the

gas gap (typically 1-2 mm wide). The electrodes are built from 1 mm thick ceramic substrate, polished to a flatness accuracy of 5 μm. The PPC pixels have typically 50x50 mm^2 transverse dimensions. Grooves made in the ceramics serve to avoid edge effects on the electric fields. Particular care is taken to eliminate sharp corners. The electrode is metallized by deposition of chromium vapour, obtaining a conductive layer of 0.5 μm thickness. The metal covers the central 47x47 mm^2 area up to half the grooves width plus a hole drilled in one of the corners for electrical connection: a gold plated pin is inserted and glued with conductive paste into the hole from the back side of the electrode plane. The PPC pixels are then placed in a gas-tight box.

The working principle of the PPC is shown in fig. 2.

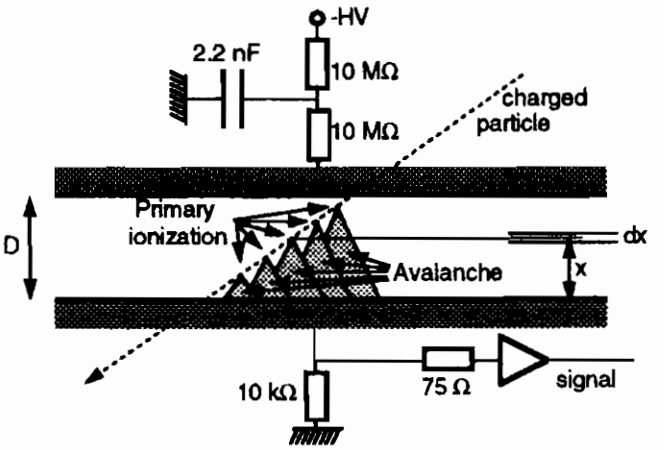

Figure 2: The PPC working principle.

A charged particle passing through the PPC produces a series of centers of primary ionization. The number of primary electrons produced in the dx subvolume at the distance of x from the anode is $n(x) = \Delta E(x)dx/W$, where ΔE(x) is the energy deposited in the subvolume dx, W is the ionization energy for the given gas (e.g. 33 eV for CO_2 and 37.8 eV for the CF_4/CO_2 80%/20% mixture used in our tests). The number of primary electrons is typically 10-15 for the full gas gap (1.5 mm). The number of electrons collected from this subvolume is $N(x)dx = n(x)e^{\alpha x}dx$, where α is the first Townsend coefficient. Its value depends on the electric field, the gas type and density and is typically in the range of 50-80 cm^{-1} at normal working conditions [1]. The

total number of collected electrons is $N_{tot} = \int_0^D N(x)dx$. Finally, the average gas gain $G = \frac{N_{tot}}{\int_0^D N(x)dx} = \frac{e^{\alpha D}}{\alpha D}$ is in the range of 5x10^2-2x10^4.

A typical charge spectrum for MIPs is shown in fig. 3.

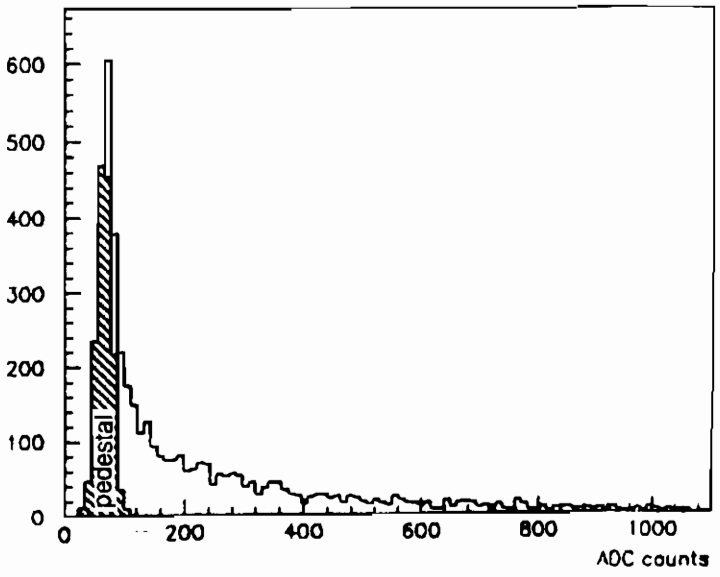

Fig. 3. Typical charge spectrum for MIPs.

The typical deposited charge (Q) is in the order of 10 fC for $\sim 10^3$ gain. The spectrum is 1/Q-like. For analysis the treshold is set to $3\sigma_{noise}$ above the pedestal.

3. Study of the basic properties

Tests described in this section were made at the CERN SPS accelerator (part of the spark probability test was measured at Serpukhov, Russia). All the tests described in this paper are made at atmospheric gas pressure.

3.1. Efficiency

As the number of primary electrons and the gas gain is small (the gain has to be below the "spark" range, it is difficult to reach high (close

to 100%) efficiency.

Efficiency measurements have been made for various gases at two different gas gaps: 1mm (fig. 4 a) and 1.5mm (fig. 4 b). All the curves

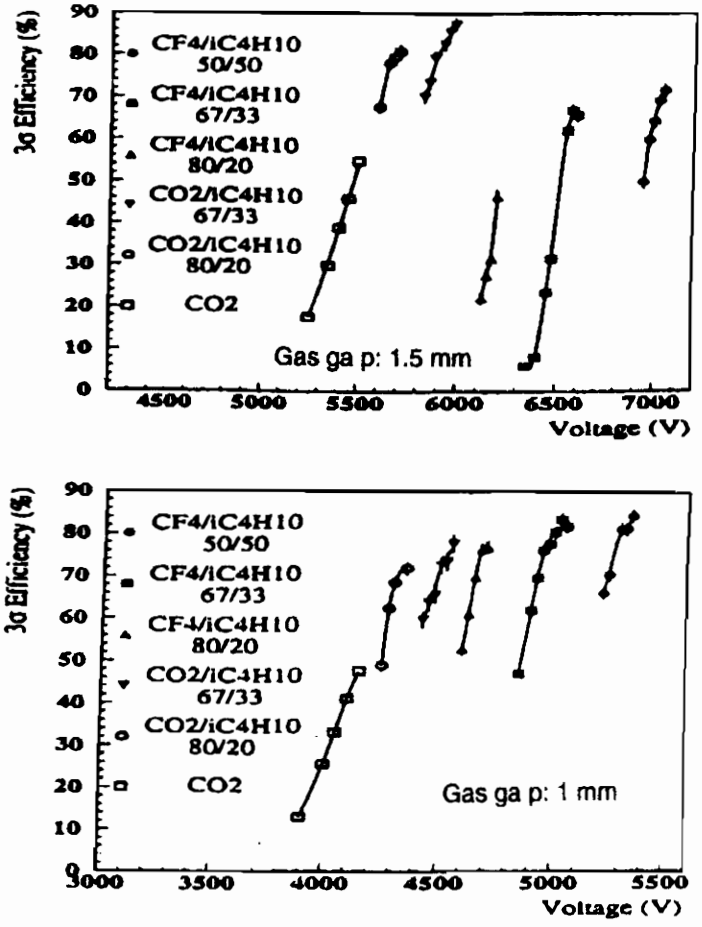

Fig. 4. Measured efficiency for various gases at two different gas gaps (a: 1mm; b: 1.5mm)

stop below the region of spark discharge (approximately at the same gas gain). As it can be expected, the efficiency is higher for wider gap, however, there is no improvement for gases containing CF_4. This can be explained by the following fact: The maximum achievable gain corresponds to lower field in the case of wide gap. The CF_4 gas, however, has a stronger electron attachment at lower fields.

The "record" efficiency of $\sim$ 90% for a single PPC pixel is observed in pure i-buthane [2].

3.2. Timing properties

A typical output signal is shown in fig. 5.

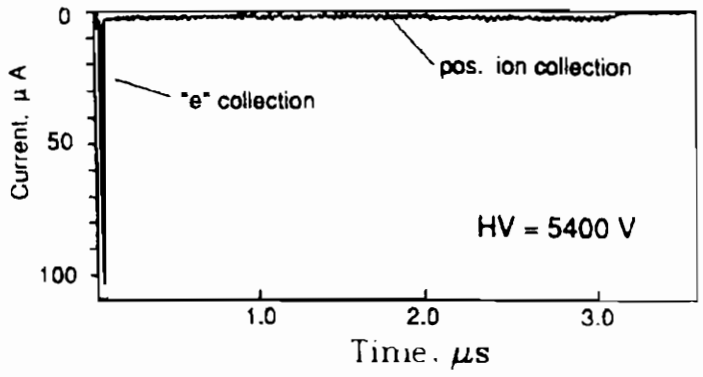

Fig. 5. Typical PPC output signal.

The electron component is very fast (several ns) due to the high electric field and the narrow gas gap. An upper limit of 470 ns for the time resolution measured by comparison of two identical pixels and using preamplifiers with 7 ns rise time is shown in fig. 6.

3.3. Spark probability

The probability of spark discharge has been tested for two gases (CO_2 and CF_4/CO_2 80%/20% mixture) at different gas gain values. As the expected probability is very low, high beam rate is required to measure the probability, especially at low gas gain. Three subsequent measurements (10^6 particles/spill at CERN SPS H2, $7.5x10^8$ particles/spill at Serpukhov, $3.5x10^9$ at CERN SPS H4) were made to cover the full gain range from 10^2 to 10^5. The measurements have confirmed the expected exponential dependence of the spark probability (P_s) on average gain (G_e) giving

$$P_s = 3.1x10^{-27}xG_e^{4.89} \quad \text{for} \quad CO_2 \textit{ and}$$
$$P_s = 4.2x10^{-26}xG_e^{4.23} \quad \text{for} \quad CF_4/CO_2.$$

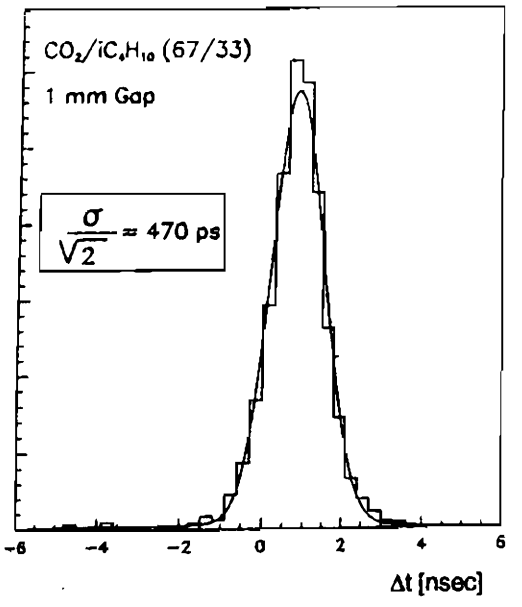

Fig. 6. Measured time resolution.

Using these results the influence of sparks for different applications can be estimated.

3.4. Rate capability

The rate capability is limited by the space charge effect and the spark probability (discussed above). As the charge is distributed over a large surface the charge density is low. Therefore the space charge effect is expected to be small. Direct measurements have shown no efficiency degradation at least up to 10^6 Hz/cm at a gas gain of 10^4. The rate capability (presently) is limited by the preamplifier.

3.5. Comparison with Monte Carlo

The behaviour of PPC has also been simulated by Monte Carlo. As an example, comparison of efficiency curves predicted by simulation and measured experimentally are presented in fig. 7.

The very good agreement shows that the simulation correctly de-

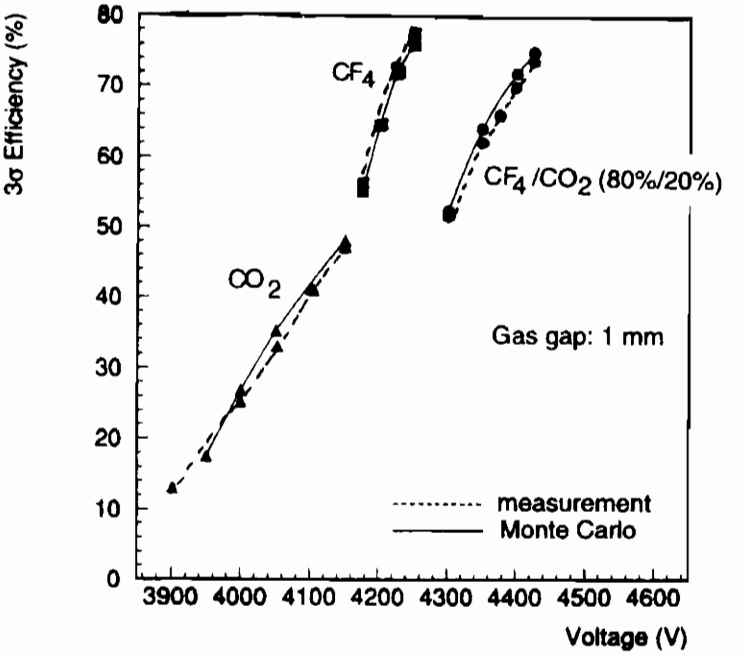

Fig. 7. Comparison of the PPC efficiency predicted by Monte Carlo and measured experimentally.

scribes the relevant processes in PPC.

4. Practical studies

Besides the studies of basic parameters practical questions important from the point of view of applications have also been investigated.

4.1. Spatial uniformity

As the chamber response strongly depends on the electric field, the spatial uniformity of the gas gap is very essential. It has been shown by measuring the local efficiency along the surface of a PPC pixel and comparing several pixels that the present technology including the assembly

enables us to achieve a planarity and uniformity better than $\pm 4\mu m$.

4.2. Spark resistance

Even if the spark probability is low it is important to know whether the spark can couse any degradation in the chamber performance. A direct test has shown that after 37 million forced sparks (which can be achieved by operating a PPC at high voltages above the spark limit) no degradation could be observed. In general, no aging effects are expected due to the fact that the anode surface is at least two order of magnitude larger for the same area than that of the wire chambers.

4.3. Radiation hardness

The PPC has been tested also for radiation hardness using the fast neutron source based on the MGC-20 cyclotron and the ^{60}Co gamma irradiation facility available at ATOMKI (Debrecen, Hungary). In both cases two PPC pixels have been irradiated. One was put on high voltage and the output current was permanently monitored, the other was grounded. In this way effects due to the presence of high voltage could be separated.

During the gamma test both PPC pixels were irradiated, for 60 days, supplying a daily dose of 1 Mrad. The monitored current is shown in fig. 8. The current remained constant during all the time.

The current monitored during the neutron test is shown in fig. 9. The total neutron fluence was 0.5×10^{16} neutrons/cm^2. The small increase of the current can be explained by the activation of the container of the PPC pixels.

The irradiated pixels were tested and compared with non-irradiated ones. No degradation in the performance could be observed.

5. Applications

Based on the characteristics described above the PPC can successfully be used for time-of-flight, triggering and calorimetry purposes. The

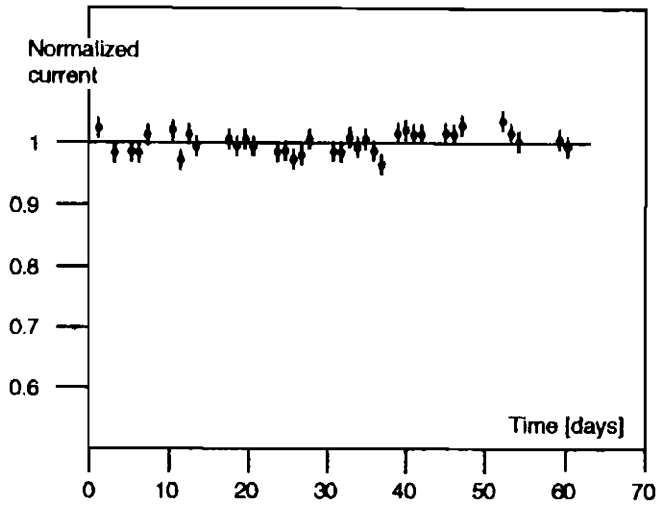

Figure 8: PPC current as a function of the exposition time during gamma-irradiation (1 Mrad/day).

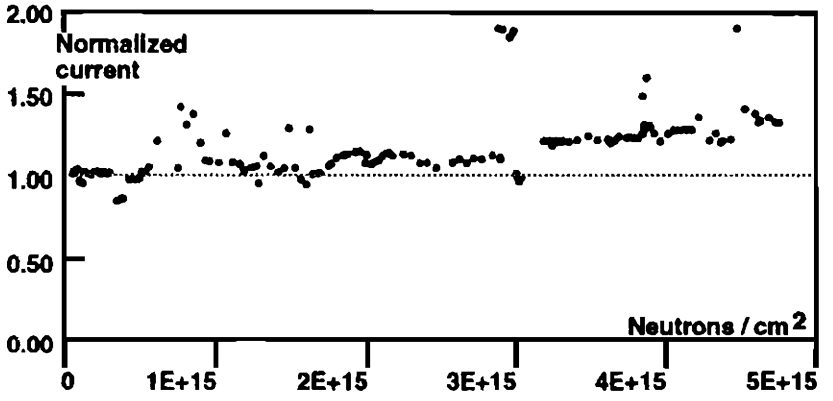

Figure 9: PPC current as a function of the fluence during neutron-irradiation.

two latter applications have been studied by the PPC collaboration.

5.1. Muon Trigger

In the case of muon trigger applications an important question (besides the efficiency and the timing properties) is the segmentation possibility. Naturally, a PPC with segmented anode could be a prototype of a larger muon trigger chamber made of PPCs.

In order to study the crosstalk between the anode segments a test PPC with 16 separate anode strips (fig. 10) has been built and tested with a ^{106}Ru source in self-triggering mode.

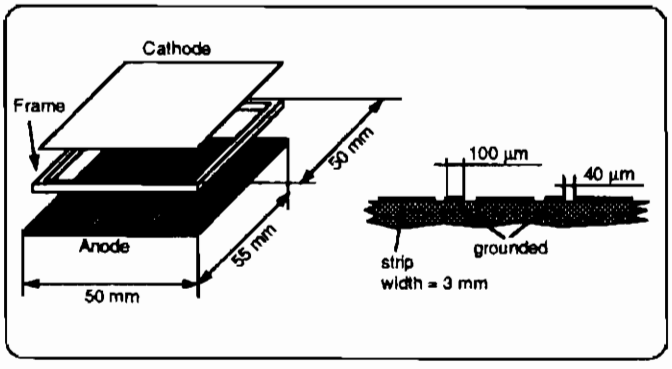

Figure 10: Construction of the PPSC.

The relationship of the collected charge between the triggered ("middle") strip and the adjacent ("left" and "right") strips (fig. 11) show that the level of the crosstalk is rather low.

5.2. Calorimetry

A Very Forward hadron calorimeter to be used at the CMS experiment ([4]) has been put forward by the PPC Collaboration. Starting from 1993, More and more complete prototypes have been and going to be built to achieve the required performance. In the autumn of 1994 a calorimeter containing 13 layers made of PPCs were tested at CERN at the X5 beam of the SPS accelerator. Each layer contained 3x3 PPC pixels with 1.5mm gas gap (covering 150x150 cm^2 surface). The layers were interleaved with 30 mm thick iron absorbers forming a 23 X_0 long

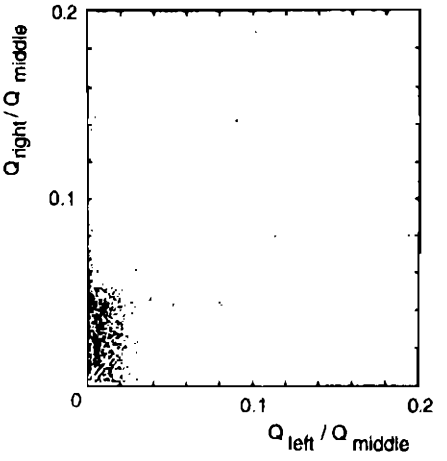

Fig. 11. Measured crosstalk in PPSC (see text).

calorimeter (fig. 12).

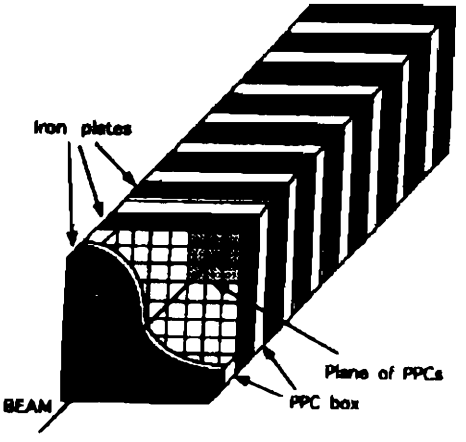

Fig. 12. PPC calorimeter prototype.

The size of the prototype allowed us to study its behaviour in electron beam. As an example, measured resolution is shown in fig. 13 for the case of CF_4/CO_2 80/20 gas mixture at 5600 V.

The measured resolution is $82.3/\sqrt{E}+3.1$. Monte Carlo simulations calculated for infinite depth predict $84.1/\sqrt{E}+1.4$.

ABS Plastic RPCs

Elden Ables, Richard Bionta, Harlan Olson, Linda Ott, Eric Parker, Douglas Wright,* Craig Wuest

Lawrence Livermore National Laboratory, PO Box 808, Livermore, CA 94551, USA

**E-mail: wright20@llnl.gov, tel: (510) 423-2347, Mail Stop: L-291*

ABSTRACT

After investigating a number of materials, we discovered that an ABS plastic doped with a conducting polymer performs well as the resistive electrode in a narrow gap RPC. Operating in the streamer mode we find efficiencies of 90-96% with low noise and low strip multiplicities. We have also studied a variety of operating gases and found that a mixture containing SF_6, a non-ozone depleting gas, argon and isobutane gives good streamer mode performance, even with isobutane concentrations of 20% or less.

1. Introduction

Our group at Lawrence Livermore National Laboratory (LLNL) became interested in RPC technology in early 1992 as a triggering system for the GEM muon detector at the SSC. Such a system would operate in a high rate environment (particle fluxes of $\sim$ 1kHz/cm^2). To construct an RPC that could operate at such incident particle fluxes, we began a search for an electrode material with a low resistivity and a correspondingly fast recharge time. As a result of this search we discovered that a commercially available plastic blend of ABS and a conducting polymer performed well in a narrow gap RPC.

Since the demise of the SSC, we have applied our RPC experience to other experiments. We are developing a multi-layer curved RPC and conducting gas studies for the BaBar experiment at SLAC, pursuing an RPC option for the MINOS experiment at Fermilab/Soudan, and are involved in the RPC effort for the forward-muon detector of the CMS experiment at LHC.

2. Electrode Materials

The plastic RPC, first developed at the University of Rome [1], and its commercially available descendant from General Technica Corporation employ resistive electrodes made from bakelite plastic coated with linseed oil. Bakelite is formulated for its physical, not electrical, properties, and its composition is by no means unique. Bakelites are made by many manufacturers with paper, cloth, glass, fiberglass and other core materials.

In order to avoid the variability associated with the bakelite/linseed oil construction, we decided to look for resistive materials that had a well-defined formulation and that did not need a surface treatment. In addition, we were interested in materials with resistivities lower than the standard bakelite bulk resistivity of 10^{10}-$10^{11}\Omega$ cm. Since the resistivity affects the recharge time, lower resistivity materials should perform well at higher incident particle rates.

We made resistivity measurements and small RPC chambers (nominally 12 cm x 12 cm) from many candidate materials including a variety of glasses, bakelites and other plastics.

Glasses, except for extremely expensive specialty glass, tended to have high resistivities and were difficult to handle, at least compared to plastics, in small thicknesses (< 1 mm). We were interested in thin electrodes to keep the total resistance low and for keeping the pick-up strips close to the gas gap.

Many of the plastic materials, while they had low resistivity, also had low dielectric strengths. Some materials heated up and melted under high voltage. Two materials made by MiTech Corporation looked promising: M411 and M310. Both materials are manufactured for their electrical properties. They are used in large quantities for static-dispersive packaging for electronics components. M411 is an alloy of PVC and Polytron^{TM} conducting polymer, while M310 is a combination of ABS and Stat-Rite^{TM} conducting polymer.

M411 exhibited lower resistivity than M310 and chambers constructed from both materials attained greater than 90% efficiency. However, we found that after prolonged operation in streamer mode, the M411 material eventually broke down, causing permanent failure. Furthermore, because of the toxic fumes that it emits when burned, PVC poses an ES&H hazard. In contrast, the ABS M310 material has a much higher dielectric strength, did not break down under operation and does not pose an environmental or safety hazard.

The ABS M310 material is easy to handle, can be cut with regular scissors, is extrudable and can be made in a variety of thicknesses. Sheets less than 1 mm thick are flexible enough to be wound on a roll, which makes for easy chamber assembly to arbitrary length and has the potential of industrial production with reel-to-reel techniques. For these reasons ABS M310 became our electrode material of choice.

We have previously reported on these and other materials prior to the demise of the SSC [2], and other groups have experimented with M411 and M310 achieving similar results [3][4].

3. ABS M310 Resistivity

ABS M310 is not an ohmic material. The resistance of the material changes as a function of the applied voltage. For example, the initial bulk resistivity of M310 is about 5×10^9 Ω cm for an applied field of 40V/mm. The resistivity increases to $5 \times 10^{11} \Omega$ cm for an applied field of 1000V/mm. These resistivity values are valid only for measurements made within the first few minutes of applying the high voltage.

Prolonged high voltage results in an increase in the resistivity. The resistivity is also observed to change with respect to humidity, temperature, and orientation of the applied electric field.

We determined the bulk resistivity of a sample by measuring the current passing through a known area of the material kept at a constant voltage. Initially we made our measurements with the sample exposed to the room environment. We observed large fluctuations in the resistivity that had multi-day time scales. These fluctuations were subsequently eliminated by placing the sample in an enclosure that is slowly flushed with dry nitrogen gas. The system remained in thermal equilibrium with the room and the only temperature control was the room thermostat.

After turning on the high voltage the resistivity steadily climbs until it reaches a plateau value of about 10^{13} Ω cm after many hundreds of hours, as shown in Figure 1. The final plateau value depends on the room

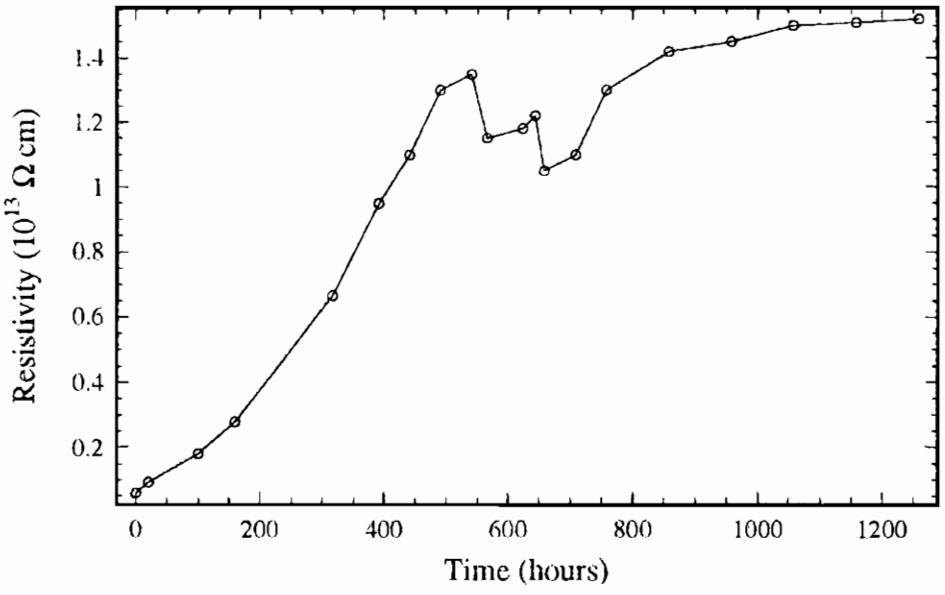

Fig. 1. Bulk resistivity of 0.5 mm thick sample of ABS M310 at 1000 Volts.

temperature and the flow rate of the nitrogen gas. We suspect that the latter effect is due to convection removing the ohmic heat produced by the sample itself. The fluctuations at around 600 hours were due to unintentional changes in the room temperature.

Figure 2 shows the fluctuation of the resistivity from changes in the temperature (set crudely via the wall thermostat). The resistivity can

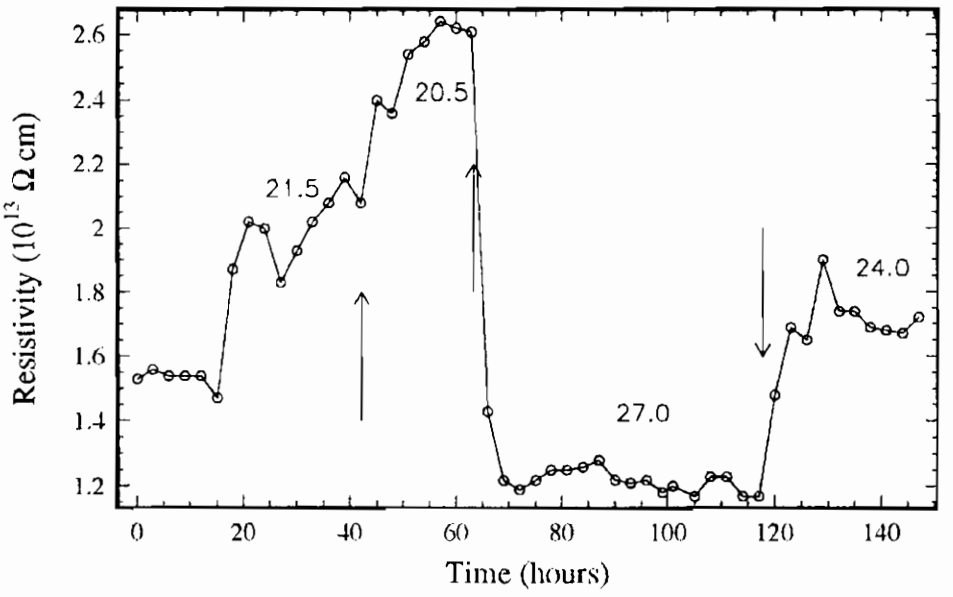

Fig. 2. Effect of temperature change on ABS M310 resistivity. Arrows indicate beginning of temperature change. Numbers indicate equilibrium temperature in Celsius.

change rapidly by a factor of two for a 7 degree difference in temperature. The fluctuations at around 20 hours were again due to unintentional (and unrecorded) temperature changes.

The ABS material also appears to be polarizable. If the polarity of the applied voltage is reversed (in this case from 1000V to -1000V), the resistivity of the sample will decrease for approximately 24 hours and then begin to increase again until it reaches the same plateau as before, as shown in Figure 3. The sample had reached a plateau of 1.6×10^{13} Ω cm before the polarity switch. The minimum resistivity after the switch was was 2.5×10^{12} Ω cm which occured at about 24 hours after the polarity change.

It is not yet clear how these measurements relate to the conditions the ABS experiences in an operating RPC. Once the ABS charges up, there should be no electric field across the material and little change in its resistance. In a localized region near a streamer discharge, an electric field is produced for a short amount of time while the region charges up again. We estimate that the instantaneous electric field across a region of uncharged ABS in an operating RPC is about 1000V/mm. The data in Figures 1-3 were taken with a higher field, 2000V/mm, in order to exaggerate the effects. We plan to investigate ways of verifying the

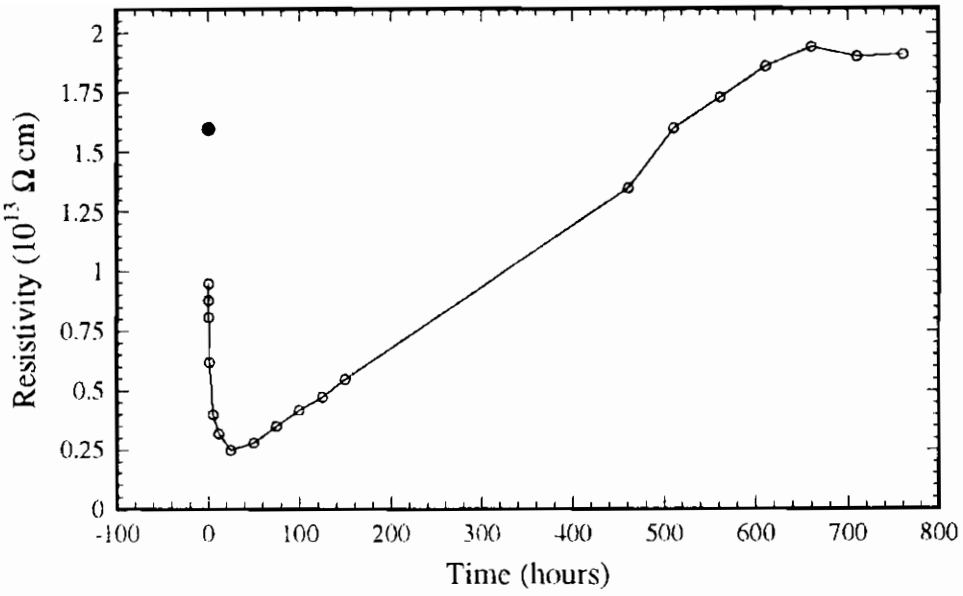

Fig. 3. Effect on ABS M310 resistivity from switching the polarity of the applied high voltage. Data between 150 and 500 hours are missing due to a power failure. The solid circle indicates the resistivity before the polarity switch.

resistivity of the ABS in a functioning RPC.

4. RPC Test Facilities at LLNL

Throughout the RPC R&D program at LLNL, we have developed a number of RPC test facilities. For measuring chamber performance we constructed a large cosmic-ray tower. RPCs are placed on shelves in a 1.5 m × 1.5 m test rack and are connected directly to LeCroy 4413 discriminators. The discriminator thresholds can be set as low as 15 mV. The discriminators are connected to LeCroy 2229 TDCs which are read-out to a Sun workstation via CAMAC. The total system contains 128 channels. The trigger is provided by the coincidence of a number scintillator paddles (nominally 20 cm by 40 cm).

We are now bringing on-line two additional read-out systems: a Fastbus based system with 480 channels of LeCroy TDCs and ADCs, and a second cosmic-ray tower dedicated to chamber longevity studies. The second system has a separate test stand and electronics similar to the original cosmic-tower.

For precision mixing of RPC gas, we have constructed a four component gas mixing system. The system utilizes mass flow controllers to select the gas mix. The mixture is fed to the RPCs from a buffer bottle that is automatically filled by the mixing system.

5. Chamber Construction

We constructed more than 20 chambers with a 2 mm gas gap (see Figure 4). Chamber size varied from 0.5 m $\times$ 0.5 m, up to 1.2 m $\times$ 2.4 m. We typically used 0.5 mm thicknesses of ABS M310 resistive electrodes. The gap between the electrodes is maintained by 1 cm diameter lucite

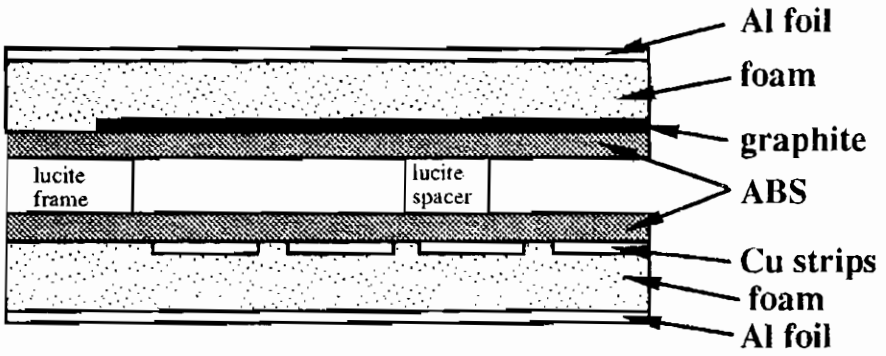

Fig. 4. Standard RPC construction.

buttons. The buttons are arranged with a 10 cm spacing.

One electrode is coated with a graphite paint and connected to a high voltage power supply. Copper read-out strips backed by conducting adhesive are placed on the other electrode. The copper strips provide both the ground plane and read-out. The typical strip pitch is approximately 1.5 cm. The M310 electrodes are glued to foam sheets that provide stiffness and electrical insulation. An aluminum foil backing is attached to the foam, which electrically shields the RPC and forms a transmission line on the side with read-out strips. On the anode side, the copper strips are attached to this foil through terminating resistors at one end of the chamber. The other of the strips is connected to the read-out electronics. The resistors are chosen to match the impedance of the transmission line formed between the strips and the Al ground

plane. The strip impedance is also matched to the impedance of the cables attached to the strips. In most cases, 50 Ω lemo cables were used for the read-out.

6. Chamber Performance

We have focused mainly on the streamer mode of operation. Using standard 15 mV threshold discriminators on 50 Ω cables, without the use of amplifiers, we obtain efficiencies between 90-96% averaged over a region of approximately 30 cm × 30 cm for a variety of chambers. The noise rate for our chambers is around 1-10kHz/m^2.

The efficiency plateau and noise rate, measured with cosmic rays, for one of our standard chambers is displayed in Figure 5. The gas used was a freon-less mixture of 78% argon, 20% isobutane 20%, and 2% SF_6. The plateau is wide and the singles rate does not rise rapidly.

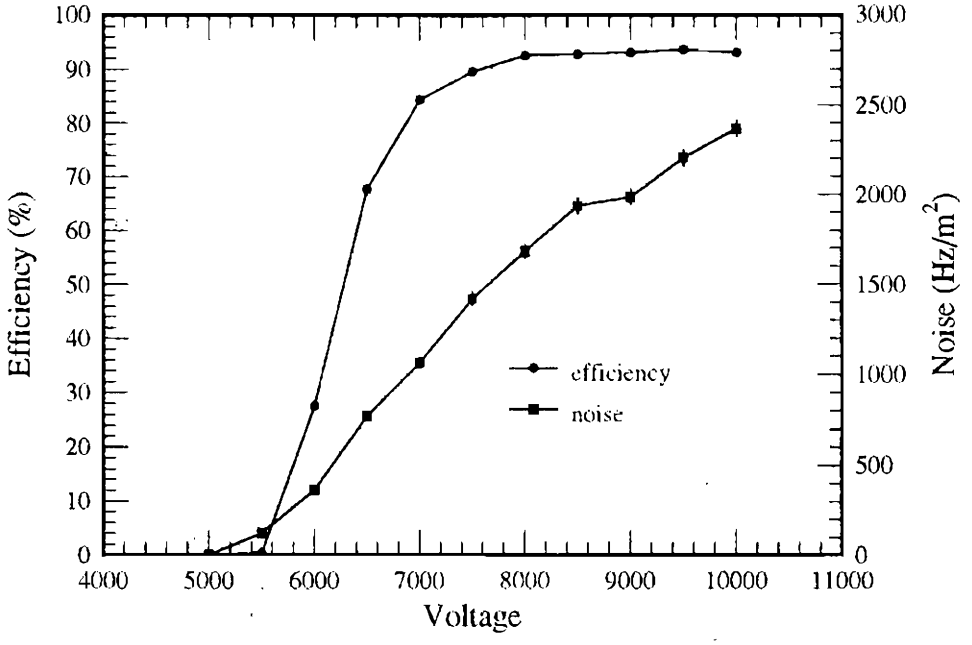

Fig. 5. Efficiency plateau and noise curve for standard ABS RPC.

The details of the chamber's performance at 8 kV are displayed in Figure 6. The timing data, in Figure 6a, is summed over a number of uncalibrated TDC channels and the timing jitter of the trigger has not yet been well characterized, yet the measured timing resolution is better than 3 ns RMS.

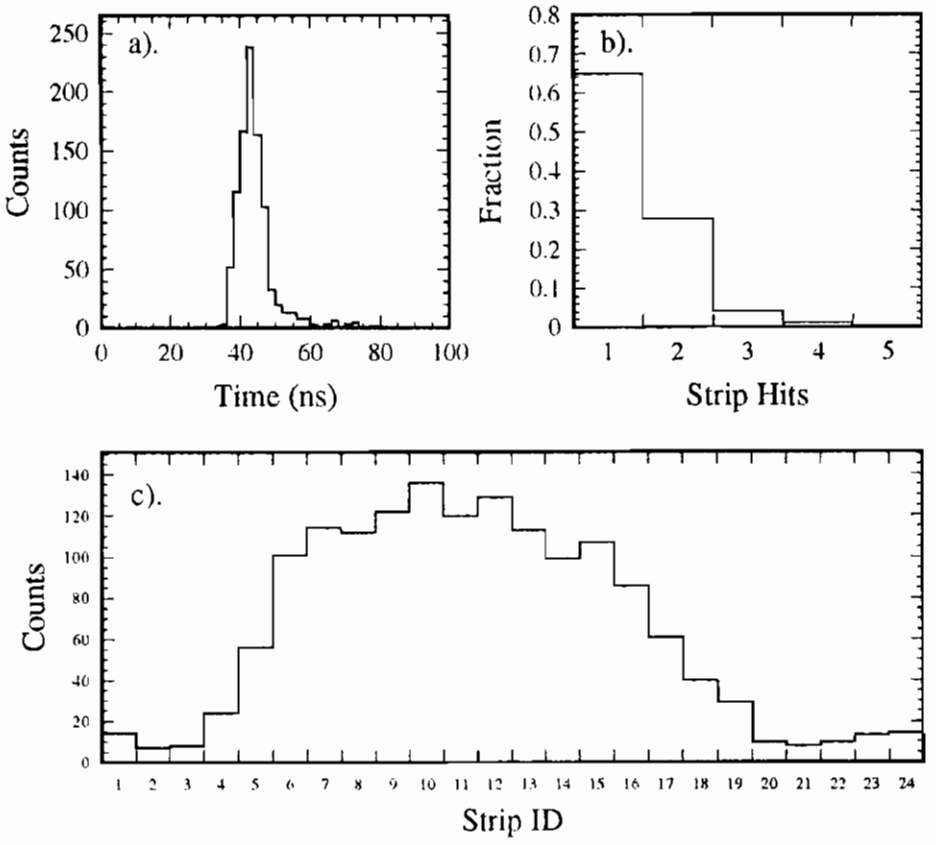

Fig. 6. Standard RPC performance, a) time of first strip hit; b) fraction of events with N strip hits; c) hit population for all read out strips. Data from same RPC as in Figure 5.

Figure 6b shows the hit multiplicity, sometimes called cluster size. Even at our low discriminator threshold of 15 mV, we observe low multiplicities. The average number of strips firing in an event is 1.6, where 92% of triggers had only one or two strips. We have no external tracking to exclude particle trajectories that pass between two strips.

Figure 6c shows the hit distribution for every strip that was readout, summed over all triggers. The trigger covers a fairly wide region of the chamber, about 18 strips (at a strip pitch of 1.6 cm).

We have been running various chambers for up to 10 months continuously. Throughout that time, however, we varied the gas (different components and different concentrations) and the high voltage. We noted that from two chambers that are of similar construction and were

operated nearly simultaneously, one showed a change in performance after many months of running and the other did not. We do not yet know if this was due to an intrinsic property of the RPC or represents damage induced by external sources.

Long term performance is essential and we have begun to make long term tests. Already, we have discovered that Epon 815, an epoxy adhesive that we had been using to join the M310 to an insulating backing, degrades the graphite coating on the high voltage plane.

7. Cylindrical RPC

Because the M310 material is thin and flexible, we developed a concept for a multi-gap, curved RPC for the BaBar [5] experiment. By placing an RPC between the electromagnetic calorimeter and the superconducting solenoid cryostat, the charged particle detection efficiency improves. This improves the detection capability for neutral kaons and hadronic punch-through from the calorimeter.

We constructed a 1 m prototype with the appropriate inner radius of 1.4 m. The prototype achieved an efficiency of 90%, but had excess noise concentrated in a few strips. We disassembled the prototype to study this effect.

8. Gas Studies

The standard RPC operating gas for streamer mode contains a large fraction of flammable isobutane (~40%) and Freon 13B1 which is an ozone-depleting compound. Reducing the flammability and eliminating the freon are important goals for producing a gas that meets current ES&H requirements. All of the studies mentioned below use a 2mm gap RPC operated in streamer mode with 15 mV discriminators and no amplifiers.

We have conducted a number of tests with isobutane concentrations as low as 5%. We find that we can operate our chambers with good efficiency plateaus at concentrations of about 20% with 2% F13B1. The timing distribution is significantly worse than with standard gas (by a factor of two).

For F13B1 substitutes we investigated Freon 116, Freon 23, Freon 14, and SF_6. SF_6 is often used in Van de Graaff and high power transformers to reduce the spark probability. Of these, only mixtures with

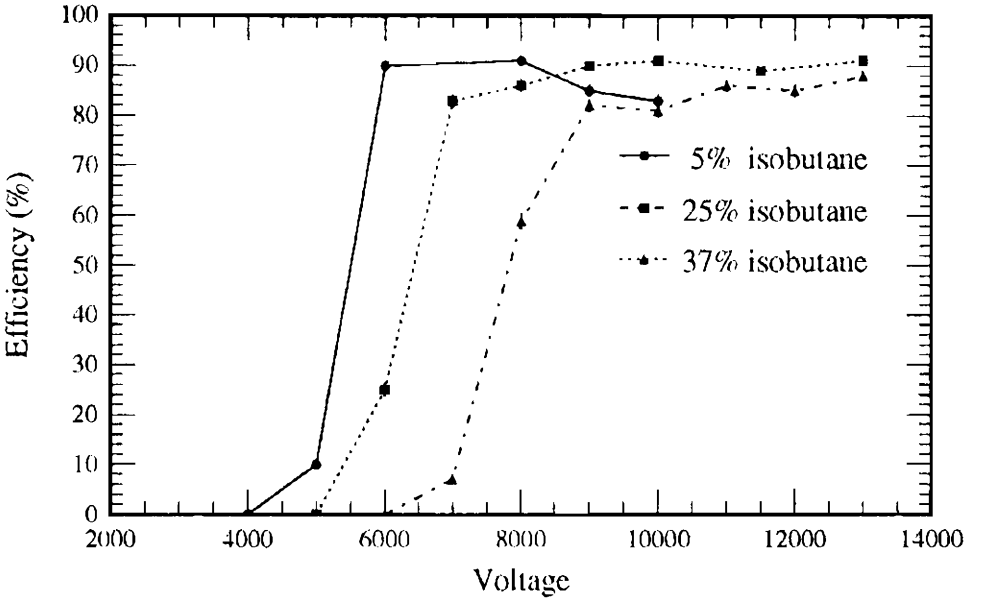

Fig. 7. Efficiency plateaus for gas mixtures with 2% F13B1, various isobutane concentrations and the balance argon.

SF_6 resulted in full efficiency, although F116 and F14 showed some positive effect. Figure 8 shows the performance of various gas mixtures with 20% isobutane, various F13B1 replacements and the balance argon. The mixture with 2% SF_6 is half as flammable as the "standard" streamer gas mix (which contains 37% isobutane) and is ozone-safe.

9. Work In Progress

Our program in RPC R&D is progressing in a number of ways. We are now testing bakelite chambers from General Technica for direct comparison with our ABS chambers. We are studying alternative gases (for flammability and ES&H compliance) that can be used for BaBar. We are building ABS chambers with double-sided graphite to investigate potential performance and construction trade-offs. We are making long-term tests of both bakelite and M310 chambers to study the intrinsic stability and potential harm from gas breakdown. Using our new multi-channel Fastbus ADC system, we are looking at the charge response of RPCs. We are preparing for a test of the shower response of our RPCs

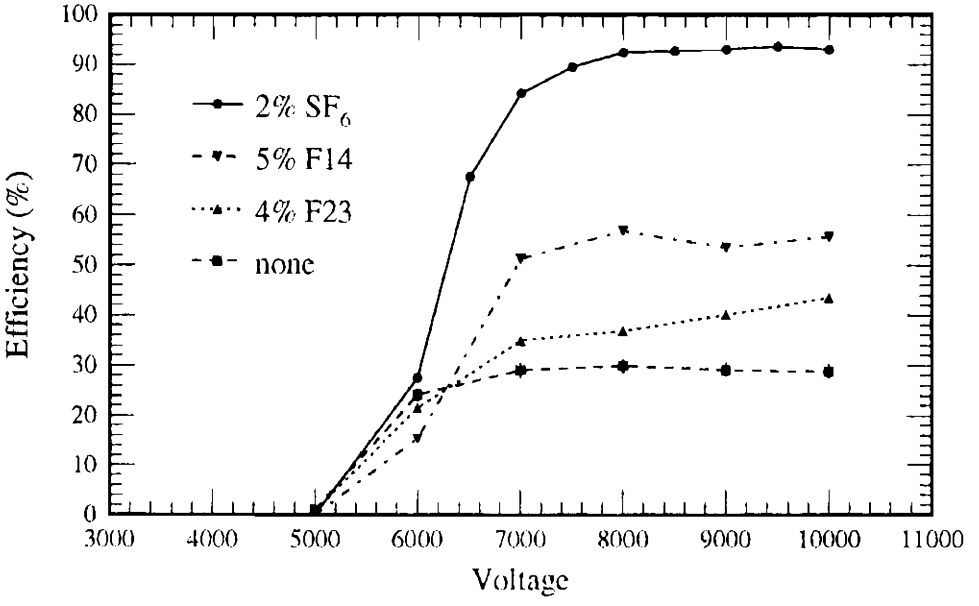

Fig. 8. Efficiency plateaus for gas mixtures with 20% isobutane, various F13B1 replacements and the balance argon.

using the electron beam at the SLAC Final Focus Test beam.

10. Summary

We have demonstrated that RPCs constructed from ABS M310 have nearly the same performance as the standard bakelite chambers. The ABS material has a number of advantages: the resistivity of the material is controlled by the manufacturer, it is inexpensive, does not require a surface treatment, and is easy to handle.

We have also demonstrated a successful gas mixture consisting of argon, isobutane and SF_6 that is free from ozone-depleting compounds and has reduced flammability compared to the standard streamer mode RPC gas. We are now investigating the long-term stability of ABS RPCs operated in this manner, as well as pursuing a number of new operating modes.

11. Acknowledgments

This work was performed under the auspices of the US Department

of Energy Contract W-7405-ENG-48.

12. References

1. R. Santonico and R. Cardarelli, Nucl. Instr. and Meth. 164 (1981) 377.
2. C. Wuest et al., High Rate Resistive Plate Chambers, Proceedings of the Fifth Annual 1993 International Industrial Symposium on the Supercollider, Plenum Press, San Francisco, California, May 1993.
3. N. Morgan et al., Nucl. Instr. and Meth. A 340 (1994) 341.
4. I. Crotty et al., Nucl. Instr. and Meth. A 360 (1995) 512.
5. BaBar Technical Design Report, SLAC-R-95-457, March 1995.

Performance and Simulation of Glass Spark Counter

M.De Deo, M.D'Incecco, C.Gustavino

INFN, Laboratori Nazionali del Gran Sasso, 67010 Assergi (AQ), Italy.

G.Bencivenni, G.Felici

INFN, Laboratori Nazionali di Frascati, 00044 Frascati, Italy.

ABSTRACT

In this paper the modular Glass Spark Counter is described. The detector performance as a function of the construction parameters is also discussed, making use of a simulation where the detector is treated as an electronic network.

INTRODUCTION

Besides the different design, the main difference between the modular Glass Spark Counter (GSC) and the standard RPC is the use of glass instead of bakelite as electrode material.

The advantage of glass is due to its homogeneity and to the excellent surface quality of this material; these allow the realization of noiseless devices without any surface treatment. Another advantage of glass is its stability with the detector operation, while with some other materials (i.e. bakelite, ABS), the resistivity increases with time due to their ionic conductivity. If the GSC is operated in the saturated mode, the inexpensive float glass ($\rho \sim 10^{12}\Omega$cm) is adequate for low rate applications, while the iron-oxide doped glass ($\rho \sim 10^{10}\Omega$cm) is suitable for particle rates up to about 100 particles/cm^2/s [1].

The good results obtained with the modular GSC prototypes, in terms of reliability and performance, encouraged us to start an R&D program to develope optimized new detectors in a fully engineered way.

In this paper we describe the present GSCs and we discuss the detector performance as a function of the detector parameters by means of a detector simulation.

STRUCTURE OF THE DEVICE

A sketch of the modular GSC is shown in fig.1. It consists of a pair of glass electrodes 2 m long, 8 cm wide and 2 mm thick. The 2 mm distance between the electrodes is ensured by precision Delrin spacers which clamp the edges of the plates. These "E" shaped spacers sustain both the electrodes, ensuring a gap tolerance at the level of a few microns. The high voltage is applied to the electrodes by means of a coating of water-based graphite, with a surface resistivity of about 200 kΩ/square. The gas containment is ensured by a PVC envelope which is the same used in the standard streamer tubes. The extrusion of opportune envelopes will permit the realization of larger detectors. The H.V. connections to the

graphite are located in one of the two end caps that close the GSC module. External pick-up electrodes (not shown in fig.1) are used to detect the induced pulses. All the materials used are commercially available, while the needed manpower is essentially due to the graphite coating and to the assembly. An estimate for large scale production is of the order of $\$100/m^2$ [2].

PERFORMANCE

A set of measurements has been performed with a telescope made up of 4 horizontal planes 20 cm apart; each of them is realized with 12 GSCs 1 m long and equipped with orthogonal X and Y pick-up strips 3 cm wide. Fig.2 shows the display of a muon event.

Fig.3 shows the single counting rate of a plane as a function of the high voltage. The gas mixture is Ar + $IsoC_4H_{10}$ + Freon 13B1 = 60% + 35% + 5%. A wide plateau is visible, the counting level being essentially due to the cosmic rays and to the ambient radioactivity.

The plane efficiency as a function of the high voltage is shown in fig.4. This measurement has been done selecting the muon events with a track around the vertical direction in both X and Y views. The 92% efficiency level is due to the geometrical dead area, the measured intrinsic device efficiency being more than 99%. The plane efficiency can be increased by about 3% by improving the contruction of the 8 cm wide GSCs. The contruction of 25 cm wide detectors is foreseen to obtain a 98% plane efficiency.

Cosmic ray muons, selected by using a scintillator telescope and a lead absorber 10 cm thick, have been used to measure the time resolution of GSCs. A fast scintillator, with a r.m.s. time resolution of about 150 ps has been used as reference detector. The time distribution of one GSC with respect to the reference scintillator is shown in fig.5. The supplied voltage is 8.6 kV; the measuring time is about 32 days. The distribution is fitted with 2 gaussians. The main one has a standard deviation of about 480 ps.

The tail of the distribution is due to sparks that develope where the electric field is lower than the nominal value. This tail can be strongly reduced by recording the first signal coming from 2 stacked detectors, as they are crossed by the same particle. Fig.6 shows the time distribution obtained by using 2 GSCs. For this configuration the resulting distribution is more symmetrical and the standard deviation of the fit is improved to 390 ps.

As for streamer tube based calorimeters, the energy measurement of a shower can be performed either by the digital hit counting of the fired pick-up or by measuring the total charge, that is proportional to the total number of streamers and thus to the shower energy. At low energy, the digital read-out gives better results than the total charge measurement. In fact, the digital read-out is almost independent of the single streamer charge fluctuaction. At high energy (more precisely at high track densities) the analog read-out is preferable to avoid saturation effects due to the non-negligible probability of having more than one track under the same pick-up.

For low energy e.m. showers, the digital read out gives good results also with the GSCs [4]. To assess the possibilities for using the GSC as a basic device in charge measuring sampling calorimeters, we have measured the charge response for vertical cosmic ray muons. Fig.7 shows the charge spectrum using a 120 ns integration time. The large time window used includes most of the afterpulses produced following the main spark, so that a secondary peak and a slightly long tail is visible in the spectrum. By using a 30 ns gate the afterpulses are cut off and the tail is strongly reduced (fig.8). The FWHM/peak of the distribution is about 20%, with very little high charge tail; only 12% of the pulses gives charge greater then 1.5 times the peak charge. As a comparison, the distribution for streamer tubes has a FWHM/peak of about 55%, with 15 - 20% of the pulses giving a charge 1.5 times the peak charge [5].

SIMULATION

To study the performance as a function of the detector parameters, we have carried out a detector simulation based on the SPICE program [6]. In this simulation, the GSC is treated as a lattice of proper resistors and capacitors. The spark is simulated with a short circuit between the electrodes, through a time variable resistor.

The essential input parameters are:

-Gap value;

-Electrode thickness,resistivity and dielectric constant;

-Graphite resistivity;

-Distance between the pick-up planes and the electrodes.

-Strip width.

-Lattice size and granularity.

In the following, if not otherwise specified, we will use these default parameters: gap=2 mm; electrode thickness=2 mm; $\rho = 10^{12}$ Ωcm; ϵ_r=5; σ=200 kΩ/square; distance between the pick-up planes and the electrodes=2 mm; strip width=10 mm.

A first result of the simulation is the confirmation of the well-known dependence of the induced charge with the pick-up plane distances respect to the electrodes. A uniform distance is essential to obtain a narrow distribution like the one shown in fig.8. In the case of a digital read-out, a disuniformity can give rise to inefficiency and/or high multiplicity problems. Fig.9a shows the signal on the strip facing the spark location (central strip); fig.9b shows the side strip signal, that is, the signal from the strip neighbouring the central one. Fig.10 shows the pulses in the real detector (the pulse signs are opposite to that of the simulation because the signals come from the strips faced to the anode, while in the simulation the signals are calculated for the strips close to the cathode). The central/side strip peak amplitude obtained with the simulation is about 3, in agreement with the measured one. The distortion of the induced pulses is due to the graphite resistivity value. Referring to fig.9a, the signal from the central strip has an exponential negative tail after the positive pulse. In

fact, the current due to the spark charges up the graphite-strip capacitance, giving a positive pulse. The capacitance discharges through the graphite in a time proportional to its resistivity, giving the exponential tail. On the side strip (fig.9b), the pulse shape is qualitatively different: the tail following the initial pulse starts positive before eventually going negative. In this case, the positive tail is due to the extra charge coming from the discharge of the central strip through the graphite. Therefore, a charge measurement is very sensitive to the graphite resistivity and depends on the integration time. In fig.11, the central/side strip integrated charge ratio is plotted as a function of the integration time window for 3 different resitivity values. We note that large integration times give rise to a broadening of the charge distribution on the strips even at relatively high resistivity values.

Fig.12 shows the electrode transparency as a function of the graphite resistivity. As a definition of the electrode transparency, the ratio between the central and the side strip peak amplitude, normalized to the limit for very high resistivity, is assumed. The simulation result is in good agreement with the experimental data, as shown in fig.12. For resistivities higher than a few hundred kΩ, a full transparency can be achieved.

Finally, the pulse rise time weakly depends on the detector parameters. In practice, the crucial parameter to obtain a good time resolution is the gap uniformity, which must be at least a few tens of microns to achieve a time resolution of one nanosecond.

CONCLUSION

The modular GSC is a noiseless detector with a time resolution of a few hundred picoseconds and interesting charge properties. Its design and the materials used permit a large production at low cost. The detector simulation will be used to contruct new detectors, to optimize detector parameters.

REFERENCES

[1] G.Bencivenni et al., Nucl. Instr.& Meth. A 332 (1993) 368.
[2] M.Meoni (POL.HI.TECH), private communication.
[3] M.G.Catanesi et al., Nucl. Instr.& Meth. A 247 (1986) 438.
[4] G.Bencivenni et al., Nucl. Instr.& Meth. A 315 (1992) 507.
[5] E.Iarocci, Nucl. Instr.& Meth. 217 (1983) 30.
[6] SPICE, E. Cohen, D.O. Pederson University of California, College of Engineerings, Dept. of Electrical Engineering and Computer Science.

FIGURE CAPTIONS

Fig. 1. Sketch of a GSC module.
Fig. 2. Display of a muon event (X and Y views).
Fig. 3. Single counting rate as a function of the high voltage for a 1 m^2 GSC plane.
Fig. 4. Detection efficiency as a function of the high voltage for a 1 m^2 GSC plane.
Fig. 5. Time distribution of one GSC with respect to a fast scintillator.
Fig. 6. Time distribution of 2 stacked GSCs with respect to a fast scintillator.
Fig. 7. Charge spectrum of a GSC (H.V.=7.4 kV, 120 ns gate).
Fig. 8. Charge spectrum of a GSC (H.V.=7.4 kV, 30 ns gate).
Fig. 9. Simulated pulses on 1 cm wide strips. a) Central strip; b) side strip.
Fig. 10. Induced pulse on strips in the modular GSC. Ch.1: Central strip; Ch.2,3: side strips. 50 Ω load.
Fig. 11. Central/side strip integrated charge ratio as a function of the integration time windows, for σ = 200 kΩ/square, σ = 1 MΩ/square, σ = 10 MΩ/square.
Fig. 12. Cathode transparency as a function of the graphite resistivity.

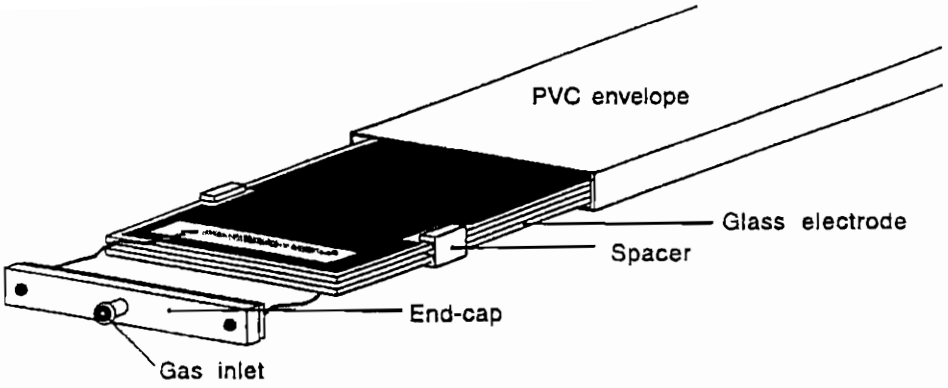
PVC envelope
Glass electrode
Spacer
End-cap
Gas inlet

fig. 1

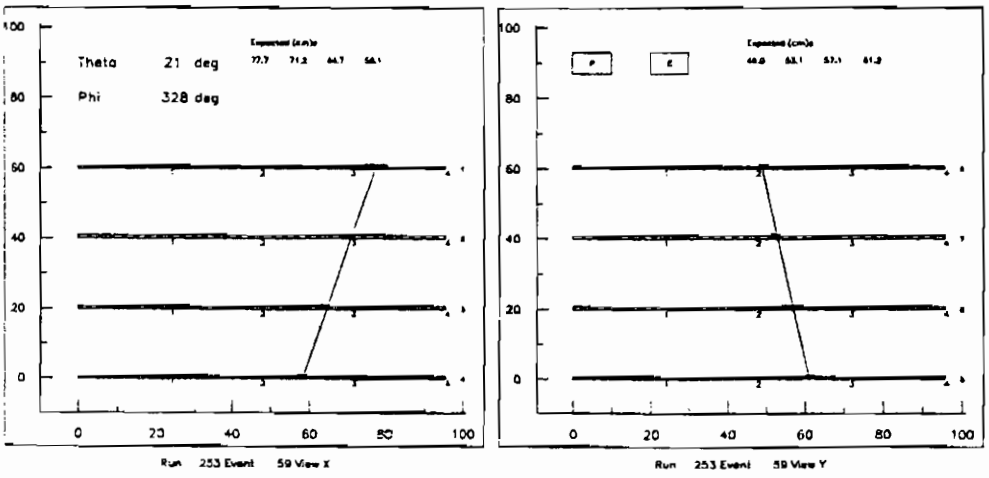
Theta 21 deg
Phi 328 deg
100
80
60
40
20
0
0 20 40 60 80 100
Run 253 Event 59 View X
Run 253 Event 59 View Y

fig. 2

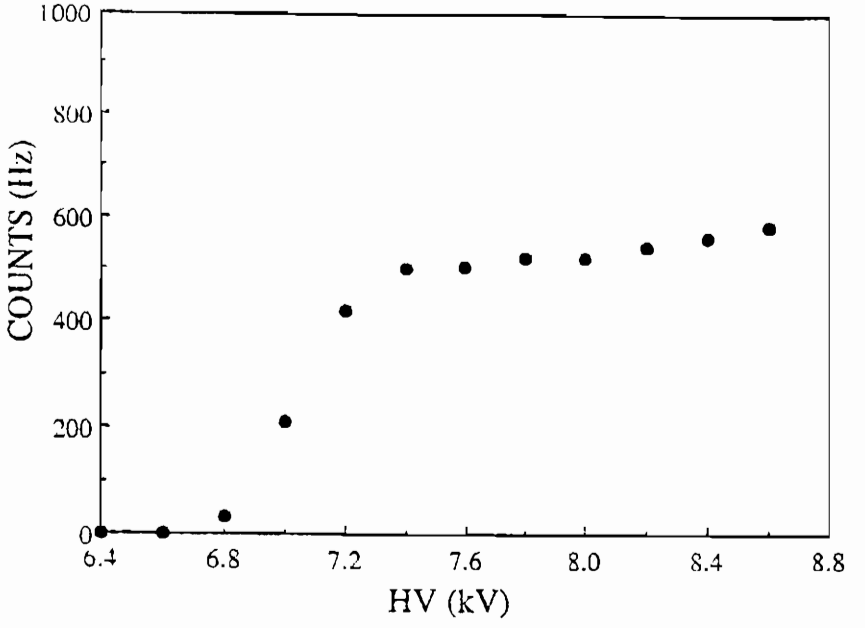
COUNTS (Hz)
1000
800
600
400
200
0
6.4
6.8
7.2
7.6
8.0
8.4
8.8
HV (kV)

fig. 3

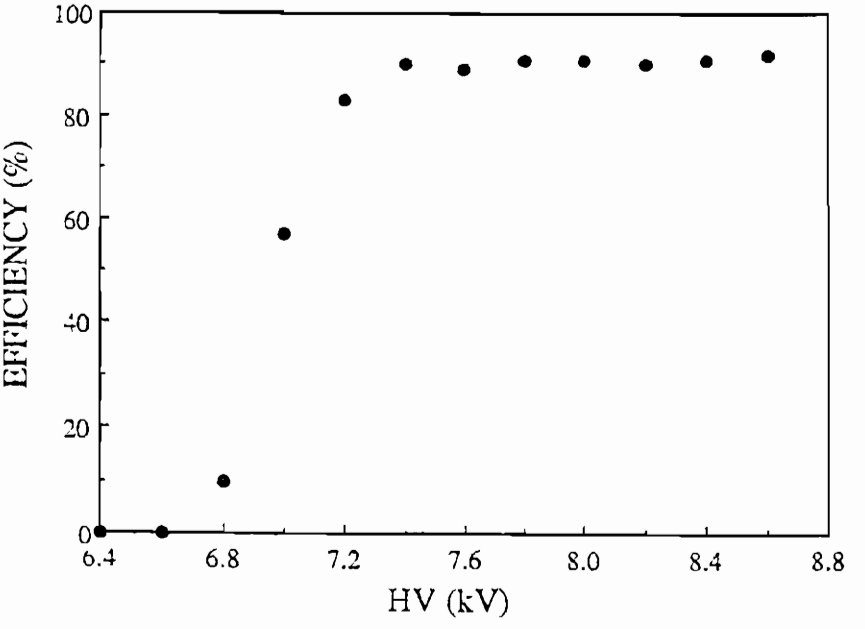
EFFICIENCY (%)
100
80
60
40
20
0
6.4
6.8
7.2
7.6
8.0
8.4
8.8
HV (kV)

fig. 4

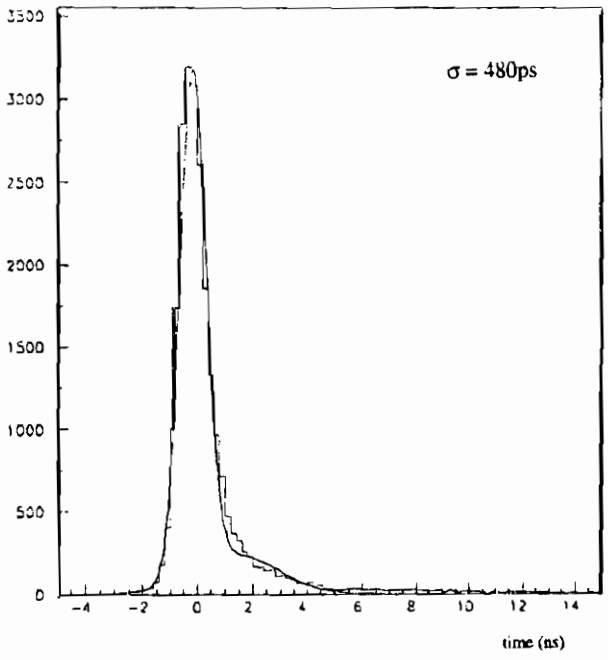
σ = 480ps
3500
3000
2500
2000
1500
1000
500
0
−4
−2
0
2
4
6
8
10
12
14
time (ns)

fig. 5

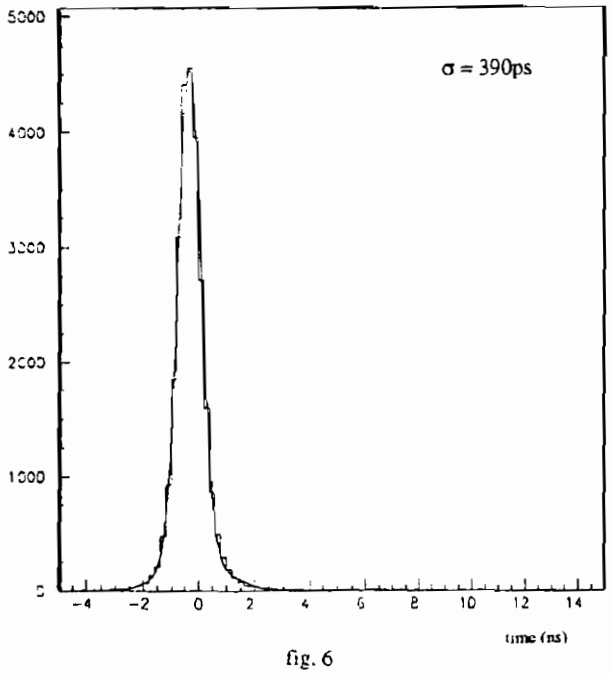
σ = 390ps
5000
4000
3000
2000
1000
0
−4
−2
0
2
4
6
8
10
12
14
time (ns)

fig. 6

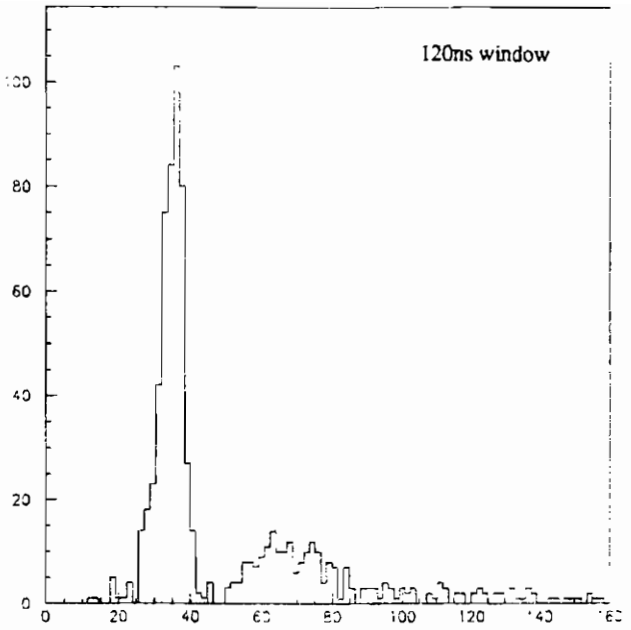
120ns window
100
80
60
40
20
0
0
20
40
60
80
100
120
140
160

fig. 7

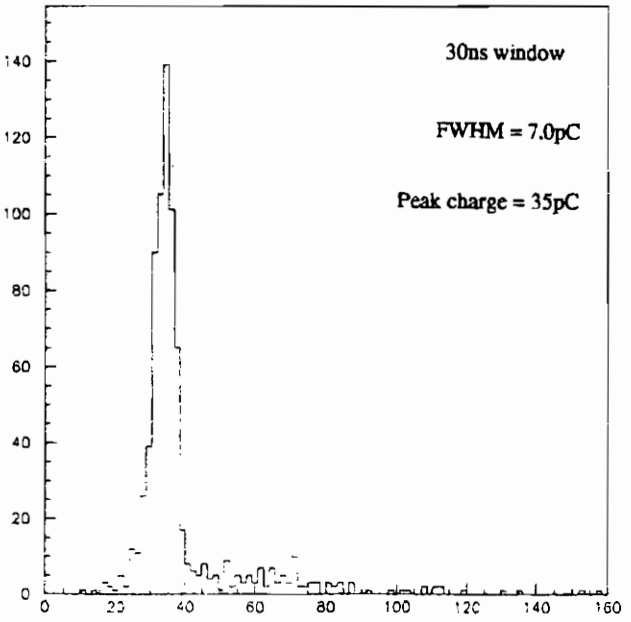
30ns window
FWHM = 7.0pC
Peak charge = 35pC
140
120
100
80
60
40
20
0
0
20
40
60
80
100
120
140
160

fig. 8

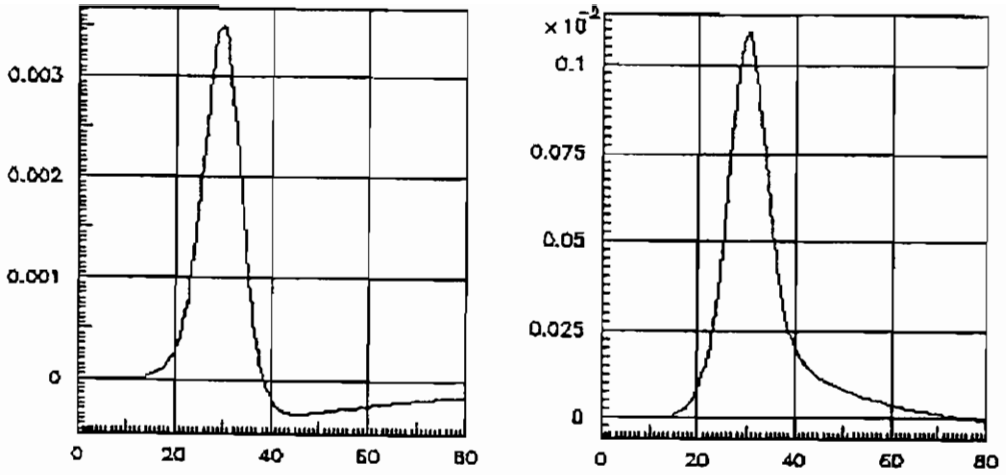

a) Central strip

b) Side strip

fig. 9

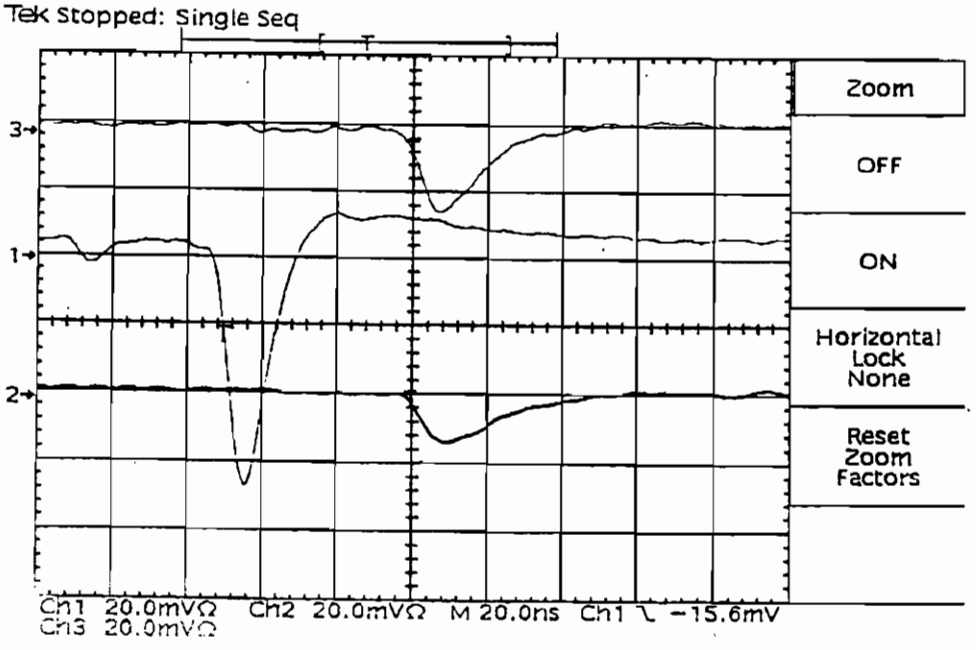

fig. 10

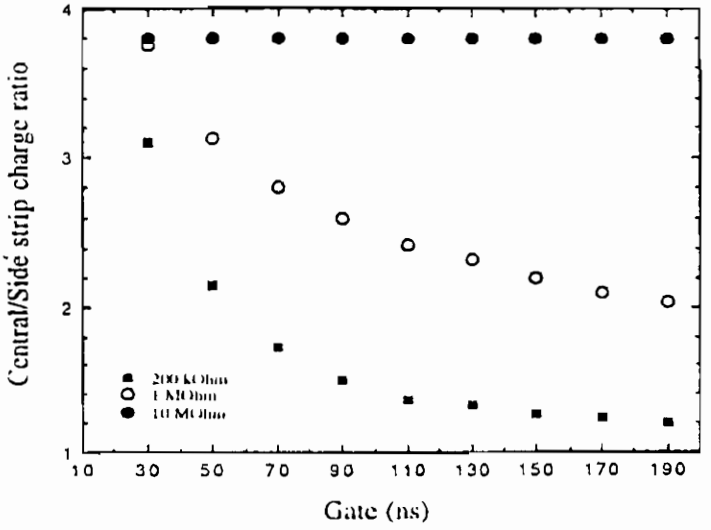
Central/Side strip charge ratio
Gate (ns)
200 kOhm
1 MOhm
10 MOhm

fig. 11

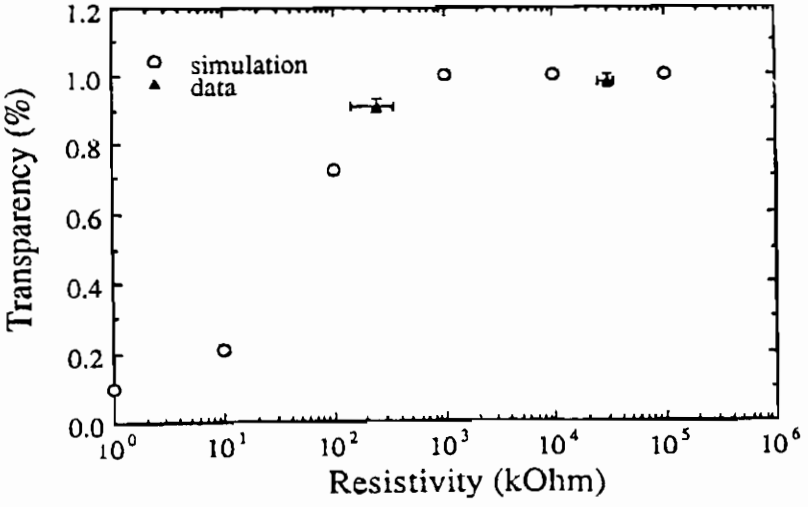
Transparency (%)
Resistivity (kOhm)
simulation
data

fig. 12

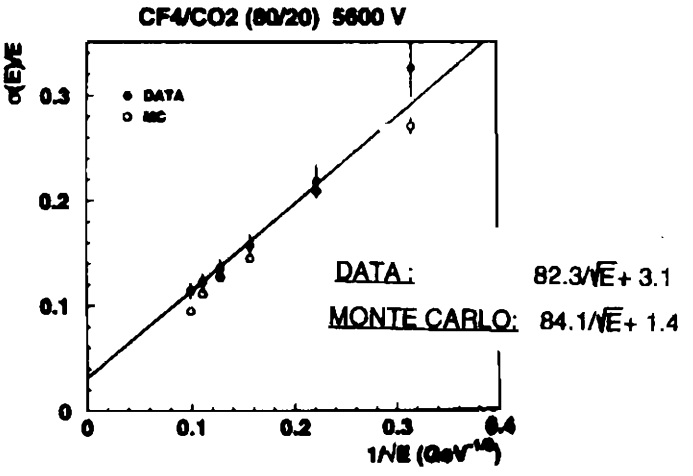

Fig. 13. Measured and calculated resolution of the calorimeter prototype.

6. Conclusions

Basic characteristics of PPCs have been investigated by the PPC Collaboration from the point of view of practical application. Efficiency, timing properties, spark probability, rate capability, spatial uniformity, spark resistance, radiation hardness for gammas and neutrons have been studied. Applicability of PPCs for triggering and calorimetry purposes have also been exerimentally investigated.

7. References

1. A. Arefiev et al., *A measurement of the first Townsend coefficient in CF_4, CO_2 and CF_4/CO_2 mixtures at high, uniform electric field.* **CMS-TN/93-82**(1993).
2. Yu. Galaktionov et al., *The parallel plate chamber as a detector for fast, radiation resistive calorimetry.* **NIM A317**(1993) 116.
3. A. Arefiev et al., *Measurement of the spark probability in single gap parallel plate chambers.* Accepted for publication in NIM A.
4. The CMS collaboration, *The Compact Muon Solenoid. Technical Proposal.* **CERN/LHCC/94-38**(1994).

R&D of Glass RPCs for the BELLE Detector

Y.Teramoto[a], A.Yamaguchi[b] and Y.Hoshi[c][1]

(a) Institute for Cosmic Ray Physics, Faculty of Science, Osaka City University, 3-3-138 Sugimoto, Sumiyoshi, Osaka 558, Japan.

(b) Department of Physics, Tohoku University, Aza Aoba, Aramaki, Aoba-ku, Sendai 980, Japan.

(c) Department of Physics, Faculty of Engineering, Tohoku Gakuin University, 1-13 Tagajo-shi, Miyagi 985, Japan.

ABSTRACT

Tests of glass RPCs for the KLM sub-detector of the BELLE detector are described. The tests include freon alternatives, Ar - CO_2 based non-flammable gas and the effects of water vapour in the RPC gas. Operations of the glass RPCs, with the existences of water vapour of 200 ppm or more, damaged the RPCs permanently. Calculations of the voltage distributions on the inner surfaces of electrodes are also described.

1. The BELLE Detector

1.1. Introduction

At KEK in Japan, the TRISTAN ring will be replaced by a pair of asymmetric $e^+(3.5GeV) \times e^-(8GeV)$ rings, KEKB, to study CP violations in B meson decays. In KEKB, the BELLE detector [2], shown in figure 1, is the only one detector that is approved for this one-intersection collider.

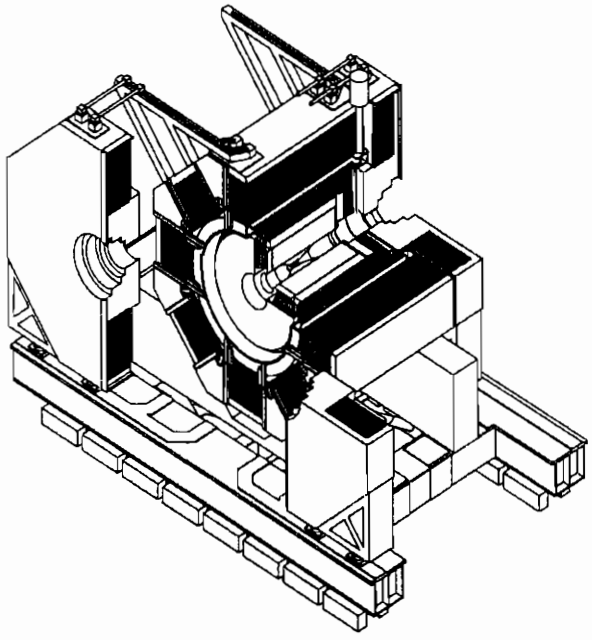

Fig. 1. The BELLE detector. KLM locates at the endcaps and at the outer layers in the barrel; seen as dark area in the figure.

In the BELLE detector, we plan to use glass RPCs for the K_L-catcher/μ(KLM) sub-detector. Glass was selected as the electrode material, because (1) bakelite RPCs require surface treatment with oil, which requires special techniques, (2) plastics, including PVC and ABS, seems to have problems in durability, (3) expected background's rate

is very low, i.e. the rate is in the same order of cosmic-rays, hence high resistivity materials, like glass($\rho_{\text{glass}} \approx 5 \times 10^{12}\Omega \cdot \text{cm}$), can be used. Glass RPCs do not require surface treatment and its durability is better than PVC and ABS in our tests. We plan to operate the RPCs in the streamer mode using Ar/iso-C_4H_{10}/(Freon 116) gas mixture. This report describes mainly the work done by the Japanese groups. The work done by the US groups is reported in an another talk in this workshop.

1.2. RPC Design

The endcap KLM consists of 14 layers of double-gap RPCs sandwiched with 5cm-thick iron plates. Those endcap RPCs are contained in the modules called quadrants. Figure 2 shows a schematics of one endcap quadrant.

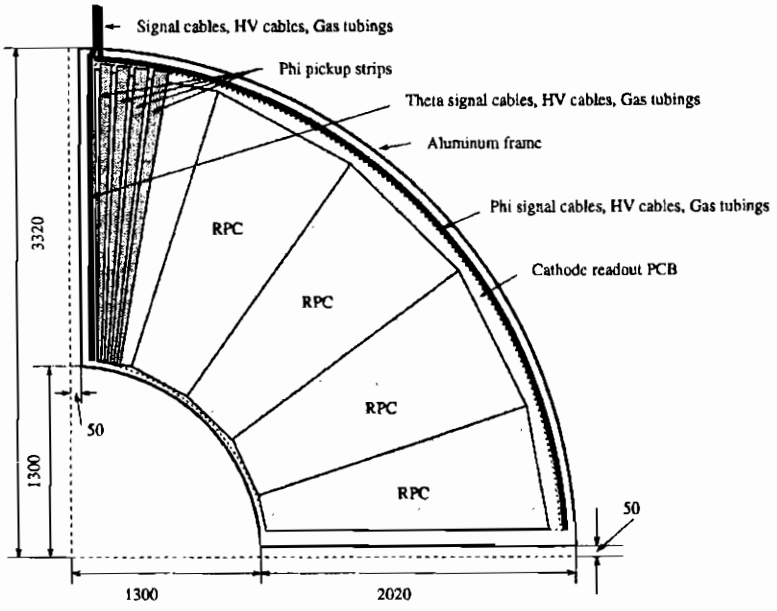

Fig. 2. Schematics of one endcap quadrant.

Each endcap quadrant consists of two layers of five RPCs, of which four are standard size(trapezoid: 98.4 cm for long side, 38.9 cm for short side, 183.3 cm height) and one is small size(trapezoid: 83.8 cm for long side, 31.6 cm for short side, 183.3 cm height), so that RPCs in each layer are staggered to the RPCs on the other layer. The total number of

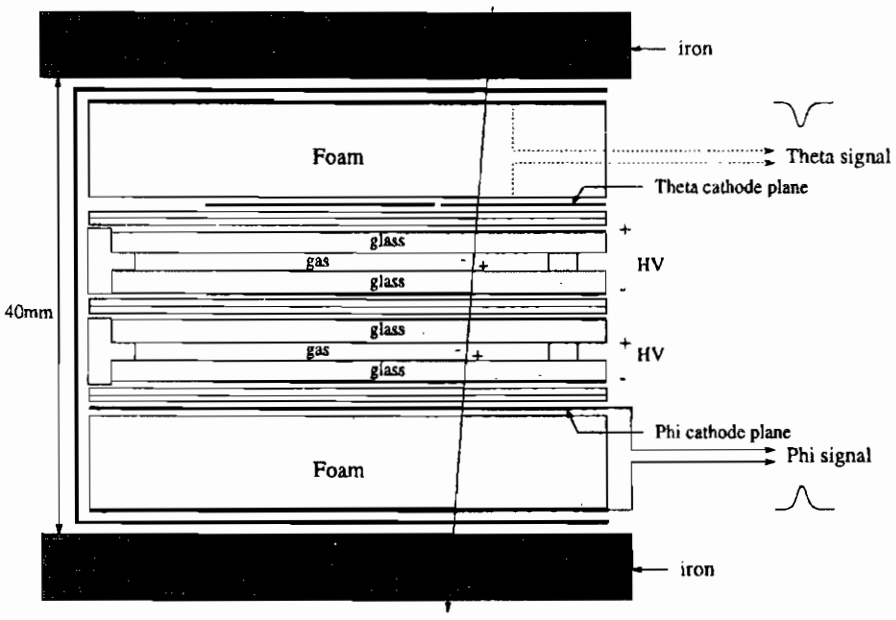

Fig. 3. Signal inductions in the module of double-gap RPCs.

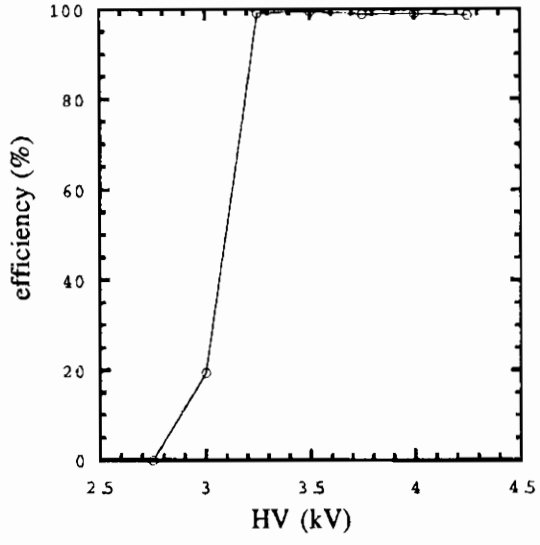

Fig. 4. Detection efficiency of the double-gap RPC.

RPCs for the endcaps is 10(RPCs in one quad) x 4(quad) x 14(layers) x 2(forward&backward) = 1120. Figure 3 shows a schematics of a double-gap RPC inserted into a 4cm gap of iron planes. The thickness of the glass electrodes is 2mm, the gas gap is 2mm. Two layers of 256μm Mylar sheets are used to insulate the graphite high-voltage-planes of the RPCs in the double-gap. One layer of 256μm Mylar is used for the insulation of high voltage of each RPC from the readout cathode plane. In addition, 125μm PET of the cathode-PCB plane itself works as an extra insulator. Theta and phi directional signals are independently picked-up from each side of the double-gap RPC. The widths of the pickup strips are 3.6 cm for θ and 1.89 cm - 4.76 cm for ϕ. Because only one signal from the double-gap RPC is enough to fire the discriminators, signals from the double-gap RPCs are OR'ed, and the efficiency in the plateau reaches approximately 100 %. The efficiency curve of the double-gap RPC is shown in figure 4. In operating RPCs, we use one positive and one negative high voltage power supplies of the same value. High voltage values, shown in the figures through out this report, are the values of the each power supply.

1.3. Readout Scheme

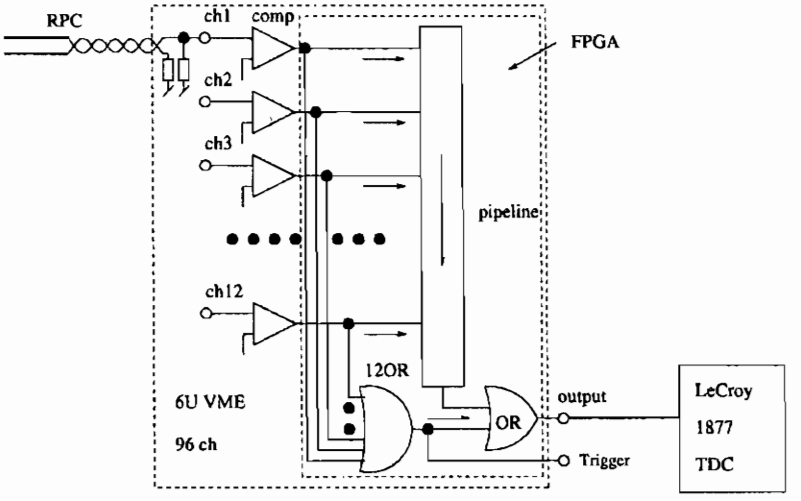

Fig. 5. Schematics of the time multiplexing circuit.

Since the expected rates in KLM is low, we plan to use time-multi-

plexing scheme to readout signals from RPCs to reduce the cost of readout electronics by taking the advantages of accurate timing of RPC signals. Figure 5 shows a schematics of the readout electronics. The readout board will be made on 6U VME modules, which will be located at the detector. Signals from the cathode pickup strips will be fed into the discriminators made of MAX908 comparators. Outputs of each 12 comparators are fed into a pipeline of shift-registers with continuous clocking of 25 MHz to multiplex signals in time series. These outputs are also tee'd to a 12-OR-gate to generate fiducial timing signals as well as to provide fast OR-signals for dimuon triggers. Then the outputs of the pipeline and the 12-OR-gate are OR-ed at the final output stage. The trains of signals from this final OR-gate are converted to ECL signals, then fed into LeCroy 1877 multi-hit TDCs. Hit channels will be obtained by decoding the time delays of the signals from the fiducial signal. All the logic are programmed in FPGA chips. Each VME board can accommodate four of these 12-channel multiplexing circuits. This multiplexing scheme reduces the required number of Fastbus TDCs by 1/12, hence reducing the total cost. The estimated cost is between $ 20 and $ 25 per channel for all the electronics of KLM, including readout electronics, cables, IIV, crates.

2. Tests Prier to the Prototypes

In prier to prototype RPC production, we did generic R&Ds: tests of freon alternatives, non-flammable gas mixtures, calculation of high voltage distributions on the inner surfaces of electrodes.

2.1. Freon Alternatives

Environmentally friendly kinds of freon 116(C_2F_6), 14(CF_4), 23(CHF_3) were tested to replace 13B1($CBrF_3$). Figure 6 shows the peaks of the charge distributions of signals as a function of high voltage for those kinds of freon[a] Among these four, 13B1 and 116 showed the similar charge suppression effects on signals. No significant charge suppression was seen for 14 and 23. Also, for the single's rate, 13B1 and 116 showed the similar behaviour. The plateau's efficiencies for all the mixtures exceeded 90 % and had no significant difference. As a conclusion, we

[a]A resistive PVC RPC was used for the freon gas test.

adopted 116 as our choice of alternative freon, judging from its charge suppression effects, and we used 116 in our following tests as default.

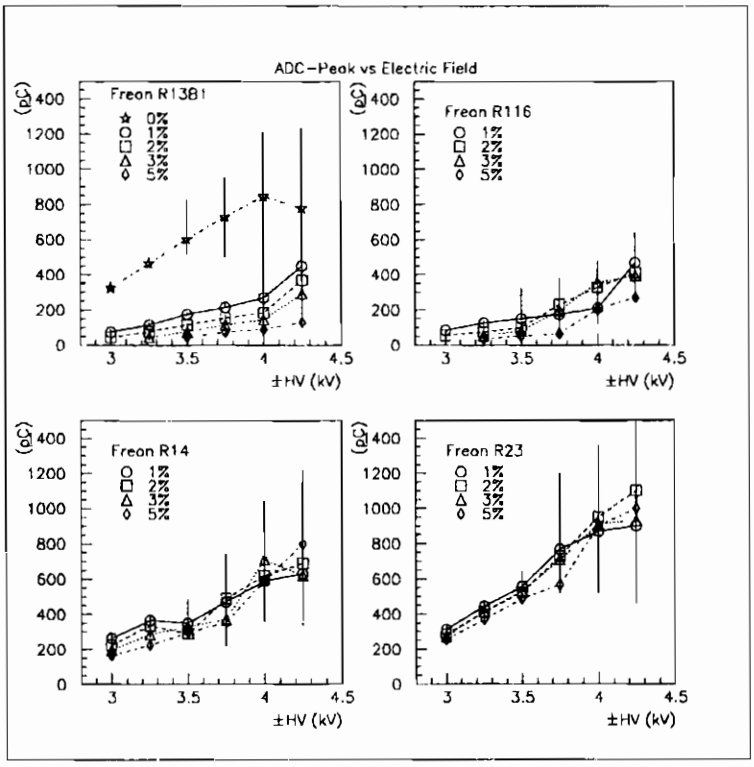

Fig. 6. Peak charge of signals for various kinds of freon as a function of high voltage.

2.2. Non-flammable Gas Mixtures

Mixtures of Ar-CO_2 based non-flammable gas were studied for a possible replacement of the standard gas [3]. Figure 7 shows the efficiency and the single's rates for the Ar-CO_2 mixtures with 1:1, 1:2 and 1:3 ratios, keeping the iso-C_4H_{10} concentrations in $4 \sim 6$ % level.[b] As for freon, 2, 4 and 6 % concentrations of 116 were tested. With higher the CO_2/Ar ratio, the operating voltage gets higher, but the detection efficiency at plateau remained approximately the same. An interesting behaviour of Ar-CO_2 based gas is its suppression effects on single's rates. In addition, this suppression effects are higher with higher CO_2/Ar ratios. One

[b] An ABS RPC was used in this test.

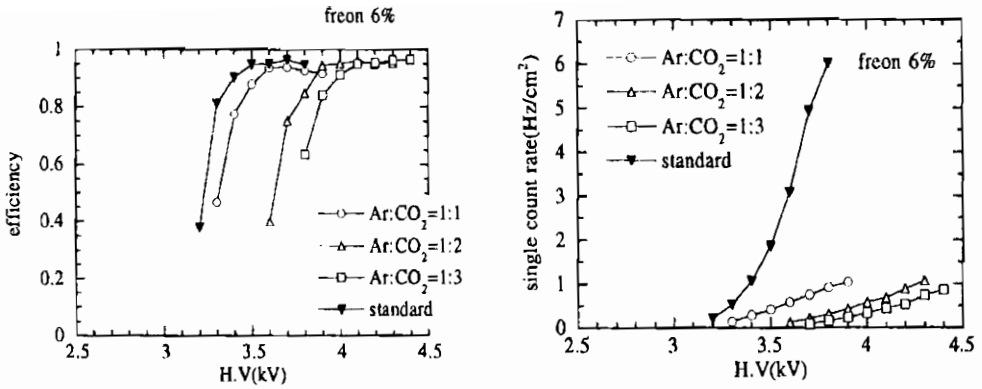

Fig. 7. Efficiency curves(left) and single's rates(right) for the Ar-CO_2 based gas.

drawback of using Ar-CO_2 based gas, however, is its existences of after-discharges. All the tested mixtures had after-discharges with 40 % $\sim$ 80 % probabilities, measured at the knees of the plateaus. Among the tested gas, mixtures with higher CO_2/Ar ratios had less after-discharges. As a conclusion, Ar/CO_2/iso-C_4H_{10}/(freon 116) = 22/66/6/6 was the best mixture among the tested gas.

2.3. Calculations of Voltage Distributions

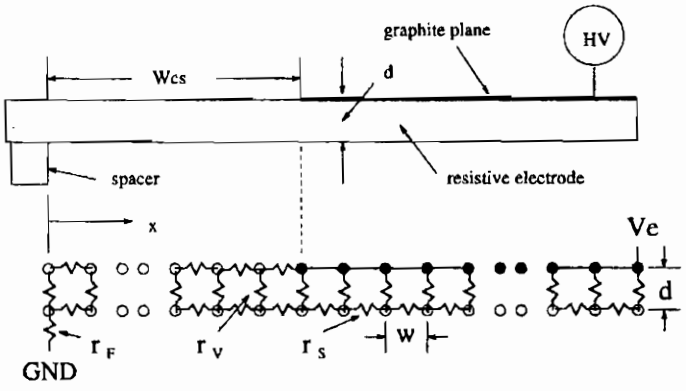

Fig. 8. Schematics of the one-dimensional model.

Calculations of the voltage distributions on the inner surfaces of the electrodes were done using a one-dimensional model to help understand

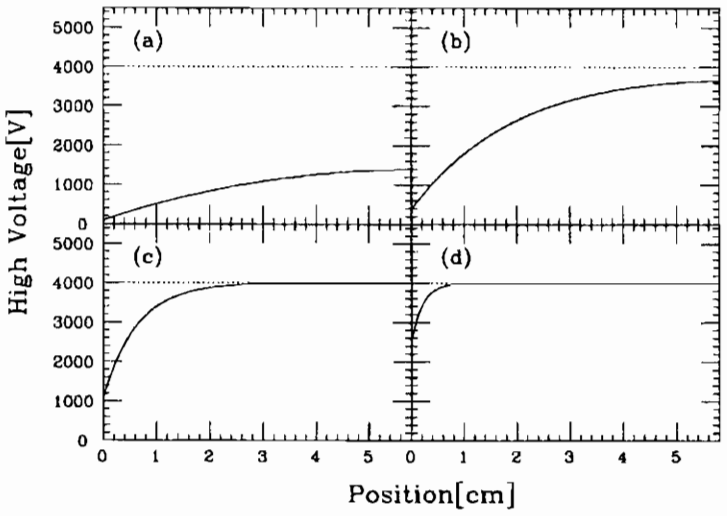

Fig. 9. Calculated voltage distributions on the inner surface of resistive electrodes as a function of distance from the spacer for various ρ/σ ratios with $d = 2$mm, $r_F = d \cdot \sigma$, $V_e = 4$ kV, $w_{cs} = 0$. (a) $\sigma = 2.5 \times 10^{-2}\rho d$, (b) $\sigma = 2.5 \times 10^{-1}\rho d$, (c) $\sigma = 2.5\rho d$, (d) $\sigma = 25\rho d$, in $\sigma[\Omega/\square]$ and $\rho[\Omega \cdot \mathrm{cm}]$ units.

glass as the electrode material [4]. Figure 8 shows a schematics of the one-dimensional model. Resistive electrodes are described as networks of resistances and graphite high-voltage-supplying-planes are treated as conductive planes. If there is no signal's current between the pair of the electrodes, biasing current will draw only through the spacers. In such a case, the current, $I(x)$, and the drop of voltage, $V(x)$ on the inner surface of the electrode, at distance, x, are expressed as,

$$I(x+dx) = I(x) - \frac{V(x)}{\rho d/w^2} \cdot \frac{dx}{w} \quad (1)$$

$$V(x+dx) = V(x) - \sigma \cdot I(x) \cdot \frac{dx}{w} \quad (2)$$

for $x > w_{cs}$, where w_{cs} is the space between the edge of the spacer and the edge of the graphite plane, w is the scale length of the resistivity measurement, ρ is the volume resistivity of the electrode, σ is the surface resistivity of the electrode. If ρ and σ are measured in Ω·cm and $\Omega/\square$ units, then $w = 1$cm. Eqs.(1), (2) can be written as differential equation's form as,

$$\frac{d^2I(x)}{dx^2} = \frac{1}{x_0^2} \cdot I(x) \tag{3}$$

$$\frac{d^2V(x)}{dx^2} = \frac{1}{x_0^2} \cdot V(x) \tag{4}$$

where x_0 is a characteristic length of the resistive electrode as defined by,

$$x_0 \equiv \sqrt{\frac{\rho d}{\sigma}} \tag{5}$$

For the case of no gap between the spacer and the edge of the graphite plane, i.e. $w_{cs} = 0$, solutions of Eq.(3), (4) are

$$I(x) = \frac{1}{1+\chi} \cdot \frac{V_e}{r_F} \cdot e^{-x/x_0} \tag{6}$$

$$V(x) = \frac{1}{1+1/\chi} \cdot V_e \cdot e^{-x/x_0} \tag{7}$$

where V_e is the externally applied high voltage, and χ determines the voltage's drop at the spacer, which is defined as the ratio of the resistivity to the spacer's resistance, r_F, as,

$$\chi \equiv \frac{\sqrt{\rho d \cdot \sigma}}{r_F} \cdot \frac{1}{w} \tag{8}$$

If $w_{cs} \neq 0$, numerical calculations with iterations have to be done to get $I(x)$, $V(x)$. Our calculations showed that there's no significant effects of $w_{cs} \neq 0$, if $w_{cs} \leq d$. If $w_{cs} \gg d$, the voltage drops approximately linearly in this gap region. The characteristic length of the electrode determines the size of the voltage-drop regions around the spacers. To sustain the biasing voltage on the inner surfaces of the electrodes, one should either, use (1) the electrode material with $x_0 <$ a few mm, or (2) the spacers with $\chi \ll 1$.

When this is extended to the signal's cases, streamers of signals are considered to behave as spacers with $\chi \gg 1$ of the static case. Then, the voltage-drop area around each signal is determined by x_0. It should

be noted that thinner the electrode, smaller the x_0, hence smaller the voltage-dip area.

3. 1st Round Tests of Glass RPCs

3.1. Prototype RPC's Deaths

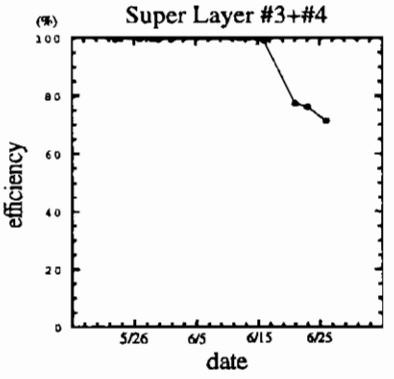

Fig. 10. Drop of detection efficiency of the prototype double-gap RPC.

Starting from early in this year, more than ten prototype glass RPCs for the endcap KLM were built and operated. During the rainy season in the June-July period, all 15 RPCs, operated at Tohoku Univ., lost their efficiency, dropping their efficiencies from 95 % to 40 % level in ten days. Figure 10 shows the efficiency's change in one of these double-gap RPCs during this period. A possible existence of water vapour in the gas, absorbed through the gas tubing made of polyurethane, was the prime suspect. In addition, spacers of those RPCs were made of acrylic, which is also known to absorb moisture. By absorbing moisture, their resistivity will be reduced. Those RPCs did not recover their efficiencies after the polyurethane tubing was replaced by a copper tubing and dry gas was supplied again. Autopsies of two of the RPCs revealed the existences of tiny dents on the inner glass surfaces, but with very low density — approximately a few in 10 cm^2 area. Those dents are crater-

like shape with 100 $\sim$ 150 μm diameters.

4. 2nd Round Tests of Glass RPCs

4.1. Water Vapour in RPC Gas

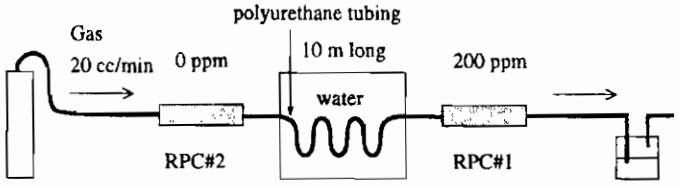

Fig. 11. Setup for the water vapour test.

To confirm the hypothesis of water vapour as the reason of the RPC's death, the Tohoku group made a setup shown in figure 11. For this test, two identical glass RPCs with acrylic spacers were made. Then, those two RPCs were put in the same gas line in series. In between the two RPCs, either a copper tubing or a polyurethane tubing of 10m long was connected, and the polyurethane tubing was dipped in the water. The gas, flown through the downstream RPC, had 200 ppm H_2O vapour, when the polyurethane tubing was connected, while dry gas was kept in the upstream RPC, which was used as a reference. In prier to this test, concentrations of water vapour, absorbed through the polyurethane tubing, was measured by using gas chromatography. Figure 12(top-left) shows the change of the plateau's efficiency of those two RPCs. Before September 9th, two RPCs were connected by a copper tubing, hence both RPCs had dry gas. On September 9th, the polyurethane tubing was connected in the middle. After a few days from this, the plateau's efficiency of the downstream RPC started to drop. On September 30th, the polyurethane tubing was replaced by a copper tubing and dry gas started to flow again in the downstream RPC. The efficiency of the downstream RPC dropped even further at this point. Then the drop of the efficiency stopped, but its efficiency did not recover even after the dry gas flowed again. Figure 12(top-right) shows the changes of plateau curves during this period. The efficiency increased slightly in the downstream RPC during the period of August 25th and 29th. This

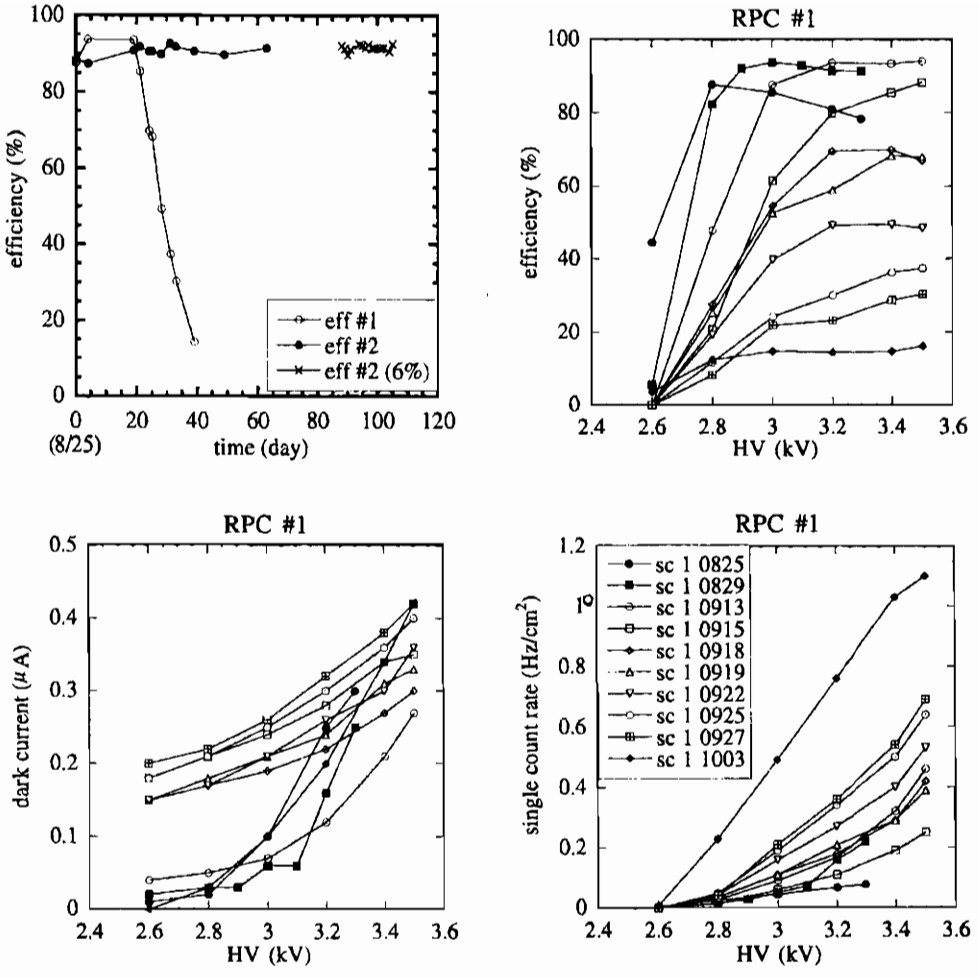

Fig. 12. Water vapour tests. Top-left: changes of efficiencies of the upstream RPC and the downstream RPC, top-right: changes of plateau curves, bottom-left: dark current, bottom-right: single's rate.

was either the initial training effect, or the effect of small amount of H_2O vapour in the chamber gas, which is known to improve the efficiency in our previous tests of glass RPCs. There was no such effect seen in the upstream RPC during the whole period of this test. After started flowing gas with water vapour, the plateau curve dropped continuously. As for the dark current of the downstream RPC, it was reduced during the initial training period of August 25th to 29th, as shown in figure 12(bottom-left). Then, after H_2O vapour was added in the gas, the dark current increased for the high voltage below the plateau. This is explained as the increase of dark current through the spacers. At the plateau region, however, the slope of the current v.s. high-voltage curve was reduced. This is explained by the effect that the total charge of each signal was reduced with the existence of water vapour. After started flowing dry gas again, the dark current's curve was immediately returned to the initial curve. The single's rates in the downstream RPC, shown in figure 12(bottom-right), jumped up, when the dry gas flowed again in the RPC. This is probably explained by the reason that, during the period when gas had high water vapour, there was high dark current across the spacer, and the surface resistivity of the glass electrodes was low, with the volume resistivity remaining the same. Hence, the voltage on the inner surfaces of the electrodes was not fully applied as expected by the calculation of the voltage on the inner surface of the electrodes. Therefore, the signal's charge was reduced. Also, the water vapour as gas itself seems to have an effect to suppress the signal's charge. After started flowing the dry gas again, however, those restrictions were removed. Then the RPC started to work with full-charge signals. Also, because of returning the high voltage on the damaged electrodes, signal's rates jumped up. Those two reduced the efficiency even further. During the whole test periods, reference RPC in the upstream showed no significant change, except the dark current. There was an initial training effect seen in the dark current of the reference RPC too. Since this test reproduced the behaviour of RPC's death during the rainy season, we concluded that the reason of the death was the contaminations of water vapour in the chamber gas.

4.2. High Current Operations

The existence of water vapour in the chamber gas was expected to make the following changes in the glass RPCs: (1) high drawing current,

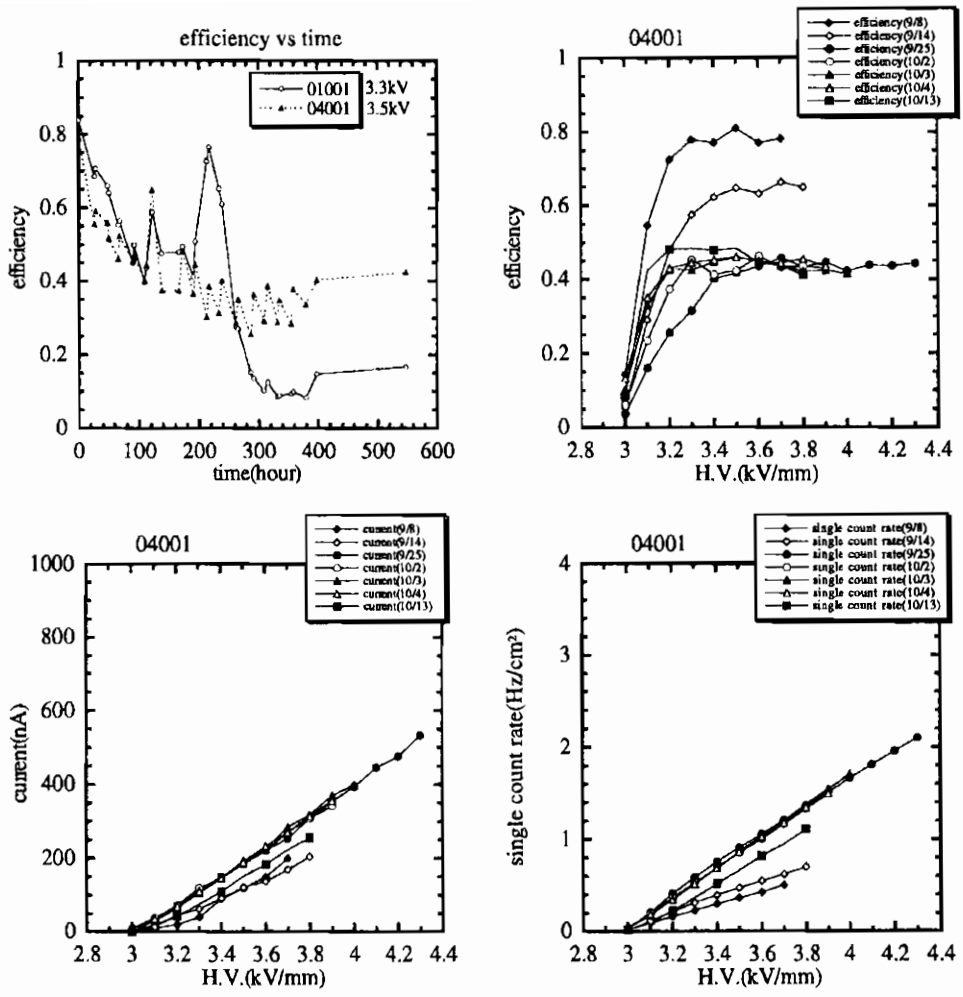

Fig. 13. High current tests. Top-left: changes of efficiencies, top-right: changes of plateau curves, bottom-left: dark current, bottom-right: single's rate

(2) change of the surface conditions of the glass electrodes including the reduction of their surface resistivity, (3) change of the characteristics of the chamber's gas. We speculated that the high drawing current may be the reason for the damage. To test this hypothesis, we operated one RPC with 10 $\mu A/m^2$ dark current, which is 10 times the standard dark current, 1 $\mu A/m^2$, for our glass RPCs. Figure 13(top-left) shows the change of the plateau's efficiency. The efficiency dropped immediately after operating the glass RPC with high current. Just after 100 hours from the beginning of the high current operation, the high voltage was stopped for a day to test a possible recovering. The efficiency recovered, but it did not recover to the initial level. And, when the high voltage was returned, the efficiency dropped again to the level, just before the high voltage was stopped. However, the drop of the efficiency ended and leveled off after 10 days of high current operation. Figure 13(top-right) shows the efficiency curves measured during this test. The efficiency curves, after they dropped, had long plateaus. The dark current and the single's rate also increased during the high current operation, as shown in figure 13(bottom-left and bottom-right, respectively). As a conclusion, high current operations could reproduce the common symptoms of the RPC's death: drops of efficiency, increases of dark current and single's rate, though the efficiency leveled off at higher level than the case of the high water vapour operation.

4.3. Possible Explanations for the RPC's Deaths

The explanation for the massive deaths of the glass RPC is as followed. First, the room's humidity jumped up, due to the onset of the rainy season at Tohoku in Japan. Since the polyurethane tubing was used to provide RPC gas, which absorbs water, water vapour was contaminated in the chamber gas. The estimated percentage of the water vapour was 200 ppm. In addition, the acrylic spacers, used in the RPC, absorbed water and their resistivity was reduced. This, together with reduced surface resistivity of the glass electrodes by water vapour, increased dark current and changed the electrical characteristics of the glass surface permanently. By flowing dry gas again to the damaged RPC, the single's rate increased further, and the efficiency was reduced even further. Operating the damaged RPC with the gas with $50 \sim 70$ % concentrations of freon 116 revived the efficiency to the 80 % level. Autopsies of two of the damaged RPCs showed that there were tiny,

$100 \sim 150\mu$m diameter, craters with low density, $\sim$ a few per 100cm^2, which could be related to the damage. By disassembling one of the damaged RPC, the Tohoku group made a small RPC using the same glass plates that was used in the damaged RPC. That small RPC worked with $\sim$ 80 % efficiency. At making the new RPC using the old glass, the glass surface was wiped by paper soaked with alcohol. Also, the edge region of the original electrodes was not used in the new RPC. Hence, either the damage was recovered by wiping the surface, or the damage was localized only near the edge of the electrodes.

Table 1. Operating conditions of glass RPCs.

	Normal operation	during high H_2O	after high H_2O	after high I
dark current[μA/m^2]	1	≥ 3	$1 \sim 2$	2
single's rate[Hz/cm^2]	0.05	0.5	1	0.5
efficiency[%]	95	$30 \sim 60$	$0 \sim 20$	$20 \sim 40$

The glass RPCs, in general, have low single's rate and dark current compared with plastic RPCs, because of the glass's high resistivity: 5 $\times$ $10^{12}\Omega$·cm. But, because of this high resistivity, the acceptable range of single's rate is narrow: < 0.3 Hz/cm^2, for our standard gas with streamer mode. Table 1 shows the typical operating values of glass RPCs for various operating conditions.

5. Summary

We built RPCs using 2mm thick window glass as their electrodes for the purpose of using glass RPCs for the detector that identify K_L^0s and muons in the BELLE detector of KEKB. The initial tests, before building the prototypes, showed, (1) freon R116 can be used as a replacement of 13B1, (2) a non-flammable mixture of $Ar/CO_2/C_4H_{10}$/(freon 116) = 22/66/6/6 is acceptable, (3) calculation of the voltage, on the inner surface of electrodes, showed that the characteristic length, $x_0 = \sqrt{\rho d/\sigma}$, determines the size of voltage-drop area near the spacers and near the signals. Prototype RPCs, operated at Tohoku, lost their efficiencies during the rainy season in Japan. Those deaths were caused by the contaminations of water vapour of 200 ppm level in the chamber gas, which increased the dark current of the chambers, and the elevated dark current damaged the inner surfaces of the glass electrodes. Hence, in operating glass RPCs, existence of water vapour in their chamber gas

is considered as fatal. In addition, dark current has to be kept below 2 $\mu A/m^2$, when operating glass RPCs.

6. Acknowledgements

This work is supported in part by a Grand in Aid of Scientific Research, Ministry of Education, Science and Culture, Japan.

7. References

1. E-mail addresses of authors: teramoto@ocux.hep.osaka-cu.ac.jp, thkepp::yamag, hoshi@tjcc.tohoku-gakuin.ac.jp. The authors are representing the KLM subgroup of the BELLE collaboration.
2. M.T.Cheng et al., *A Study of CP Violation in B Mesion Decays*, Technical Design Report for BELLE, KEK Report 95-1, April 1995.
3. H.Takamatsu et al., to be published in IEEE.
4. Y.Inoue et al., to be published in Nuclear Instruments and Methods in Physics Research A.

SOME RESULTS OF RESISTIVE PLATE COUNTER AND THE PROPOSAL TO TAU-CHARM FACTORY OF BEIJING

J.G.Bian Y.B.Chen H.G.Han K.L.He Y.Y.Jiang X.L.Wang Y.G.Xie
Y.L.Xu C.S.Yang G.A.Yang Y.Yang Z.T.Yu J.Q.Zhang Q.J.Zhang
submitted to 95RPC International Workshop, Pavia, Italy
Institute of High Energy Physics, Beijing, China
presented by J.Q.Zhang
October, 1995

ABSTRACT

Several prototypes with different sizes of resistive plate counters using glass, bakelite as resistive plate materials and high pressure gas have been tested. The streamer light output has been picked by PMT and better rise time output pulses have been obtained. It has been proposed that RPC-Fe system would be the first candidates for hadron/muon sub-detector system of the spectrometer in Beijing tau-charm factory proposal.

1. Prototypes and Results

In latest four years several prototypes with different resistive plate materials as well as the high pressure small gap chamber have been made and tested.

1) A small prototype of 20×20 cm^2 size shown in Fig.1 is composed by two glass plates with bulk resistivity coefficient about $\rho=3\times10^{10}$ Ωcm. The outer surface of two glass plates are painted by acquadac(liquid graphite) with surface resitivity $\sim$ 100k $\Omega/\Box$. The gap between two glass plates is 1.6 mm, filled by gas mixture of Ar(60%)+Isobutane(38%)+Freon(2%). High voltage acting on two graphite electrodes is about 7 kV. Plateau of 500 V and efficiency 95% are obtained by using two 10×10cm^2 scintillator counters telescope shown in Fig.2. The output positive signals picked from 4mm wide Al induced strips with the pitch of 10cm have the pulse amplitude 400mV (on 50Ω terminal), rise time 2ns and pulse width 10ns shown in Fig.3.

2) A large prototype with the dimension of 60×120cm^2 is also finished with its gap of 2mm. PVC frame with the tolerance of $\pm80\mu$m is

used to guarantee the precision of the gas gap homogenity. The induced output pulses with rise time 5ns, width ~10 ns, amplitude 500 mV (on 50Ω) and efficiency 90-95% have been obtained.

3) More than 10 kinds of domestic plate materials including different trade marks of glass and bakelite have been tested using same small size RPC chamber under same gas mixture shown in Tab.1. One may investigate from Tab.1 that the measured knee voltage varies the dielectric constant ε and bulk resistive coefficients. For PVC and epoxy only few signals may be observed occassionbly above 9 kV. At present, some ABS plastic plates are being prepared by collaborating with some chemical institutions.

4) Relationship between acting high voltage, gap electric field intensity and dielectric constant are calculated and discussed which are consistent with our experimental results. We derived a formulae by using the conditions of continuity of the electric displacement of the two resitive layers D_{r1}, D_{r2} with that of the gas gap D_g. From $D=\varepsilon E$ where E is the electric field intensity, one gets:

$$\varepsilon_r E_r = \varepsilon_g E_g \tag{1}$$

In general $\varepsilon_g=1$,

Thus, one has the acting voltage between two graphite electrodes V_0:

$$V_0 = 2E_r S + E_g L \tag{2}$$

where S is the thickness of the single resitive plate and L is the gap width, then:

$$E_g = \frac{V_0}{L + 2S/\varepsilon_r} = \frac{V_0}{L} \cdot \frac{1}{1 + 2S/\varepsilon_r L} \tag{3}$$

Here we choose S=2mm and L=1.5mm. Formulae 3) can be expressed by Fig.4a and Fig.4b. which describe gap electric field intensity E_g and V_0 versus ε_r respectively. One may see that:

- As V_0 is constant, E_g increases with increasing ε_r, but increases slowly when ε_r larger than 6.

- As E_g is constant, V_{knee} decreases with increasing ε_r.
- The results given in Tab.1 are consistent with that obtained from formulae 3) or Fig.4a,4b. For example, for PVC and epoxy, K_{knee} higher than 9 KV with lower ε_r.
- In general, the resistive plate materials with higher dielectric constants ε_r are preferable.

5) Observation with streamer light output has been done by using PMT. Signals with rather small resolution time ~0.4 nsec are picked directly from the lateral direction of the gas gap shown in Fig.5.

6) A small aluminium prototype with 10×10 cm^2 in dimension and 1mm gap width has been made and tested with gas pressure up to 2 atm . Very small rise time pulses ($\leq$ 1 ns) have been obtained.

2. RPC in Proposal of Beijing Tau-Charm Factory Spectrometer

From 1994 Beijing Tau Charm Factory (BTCF) has been proposed and the feasibility research budget has been given by the Chinese Government. The R&D step and further step of construction will depend on the approvement of the conceptual report in next October. In Hadron calorimeter/muon (HC/μ) subsystem RPC-Fe are selected as the first candidates and conceptual report including the sector strucrture, RPC configuration and Monte Carlo calculation using GEANT3 is now being prepared.

2.1. General Considerations

Hadron calorimeter/muon (HC/μ) subsystem is the outmost part of the BTCF spectrometer. The main functions are the following:

- Identify muons (0.5GeV-1.2GeV) from pion and other hadrons.
- measure the direction of pion and roughly estimate its energy.
- tag neutral hadrons K_L^0/n to complete hermiticity to measure missing energy brought by neutrino.

- provide the flux return for the solenoid magnet.

With above metioned features the most important interesting physics could be measured such as pure leptonic rare decay of τ and D charmed meson. For these purposes, by using the single lepton-missing energy trigger, cleaner events with high efficiency could be obtained. In these cases, K_L^0 should be rejected as a veto, but some times K_L^0 needs to be tagged specifically for some channels, for example, in final state of $\tau^{\pm}$ to $K_L^0\pi^{\pm}\nu$ in CP violation research.

2.2. General structure

The general structure and configuration follow the project proposed on Third TCF International Workshop with some further modifications and considerations are now being made.

The barrel part made of 16 sectors with 6m length shown in Fig.6a and rectangular and trapezoid cross sections shown in Fig.6b in order to avoid projective slots directing to the colliding points. The inner radius with 1.6m and outer radius 3.3m make the total thickness 1.7m.

Two endcap parts have the radius from 2.6m at the nearest edge to 3.3m at the farest edge and the thickness is also 1.7m

The total 1.7m thickness 3.7 λ_{int} stands for 52 layers sandwiched Fe-active detector configuration with 1cm thick Fe and about 2 cm active detector per layer with 10 cm Fe as the outmost layer to shield the radiation from outside. All the remain subdetectors inside HC/μ part have 1.1 λ_{int}. 26 layers with 2cm thickness Fe per layer or non-homogeneous layer thickness configuration are now being considered to reduce the active detector area from 7200 M^2 and about 50000 electronic channels down to half of those amounts. In addition, 1 cm thick Fe plate is difficult to manufacture.

For the moderate spatial resolution, X-Y strips with 3cm pitch are considered with the angular resolution about 10 mrad in HC/μ detector.

2.3. Choice of the active detector

Among the four kinds of detectors, resistive plate counter (RPC),

plastic streamer tube(PST) and drift chamber with 10-20 cm wire distance (DC) and scintillation counter (SC), for BTCF spectrometer RPC is selected as the first candidate. DC and SC have been canceled for the reason of the cost and difficulty for mass production and installation. Comparing with PST, we have four years experiences in RPC (fewer than ten years for PST), we choose RPC for its advantagess over PST in the following respects: smaller dead zone, fast trigger time, lower cost and no poisonous material emerging in flame. In particilar, in recent years the successful use of large area detector by L3 and no ageing problem as well as the safty gas (including the replacement of Freon) being resolved encouraged us to choose RPC as the prior candidate.

the baseline of the structure of the RPC is similar to that decided by IFR group of BARAR shown in Fig.7. For BTCF the single gap with X-Y direction with 3cm pitch Aluminium strips (with about 0.5 cm thick foam) sticked on two outer isolated film attached to the surface of the bare RPC.

All the RPC size for barrel part is rectangular, but for endcap the rectangular and trapezoid size continuously changed layer by layer with largest dimension at nearest edge to smallest dimension at farest edge shown in Fig.8.

2.4. Monte Carlo simulation and expected performance

A GEANT3 software pagckage describing BTCF spectrometer especially concentrated on the HC/μ detector has been compiled by our group, in which geometry and material refering RPC structure are now being implemented. The following results have been got:

- typical drawings for 1GeV/c μ, π and K_L^0, shown in Fig.9a,b.
- Observation of distributions of six parameters for μ, π and K_L^0 with 0.6 GeV/c to 1.2 GeV/c. Six parameters are TCTL (total charged track length) for EM calorimeter, time of flight detector and HITs in HC/μ, depth of the hits and hits per plane. The last four parameters are important to identify π/μ.
- Parameter distributions of μ, π and K_L^0 show that for 52 layer$\times$1cm Fe and 26 layer$\times$2cm Fe configurations the results for above men-

tioned six parameters are near the same shown in Fig.10a and Fig.10b. Yet the 26 layer configuration needs to be considered further claimed by special physics requirement.

- The higher efficiency of μ of 95% for 0.5 GeV with 2% π contamination and for 1.2 GeV with 0.6% are expected. Multi-layer RPC-Fe system to further reducing π contamination needs to be further investigated.

3. Conclusions and Prospect

RPC used in HC/μ subdetector system of the BTCF spectrometer is the first prior candidate and promising. Some preparation and experiences have already been got by Beijing IHEP and international high energy physics community has relatively sufficient experiences for large scale use up to date which is encouraging.

1. Y.B.Chen et al. Nuclear Electronics and Detection Technology, 12(1992)88
2. J.Kirby et al., Third Workshop on the Tau Charm factory, (Marbella) June,1993.
3. Letter of Intent of BABAR SLAC-4431994.
4. Technical Report of BABAR SLAC-R-94457.

Tab.1 V_{knee} vs. ε_r, ρ et. al.

investigated materials of resistive plate in China

material	ρ	E	Vkne kV (calculated)
glass			
ordinnary	3×10^{10}	5-10	6.9-5.7
YH-40 flat	2×10^{11}	5.95	6.5
YH-60	4×10^{10}	5.95	6.5
PS (Shanghai)	3×10^{12}		
bakelite			
ordinary	3×10^{10}	5.5-6.0	6.6-6.45
3021	1×10^{12}	6.0	6.45
PVC	10^{15}	2.55	9.3
epoxy	10^{14}	3.6	8.1

chosen $\rho=10^{11}-10^{12}$ ε= 5-7

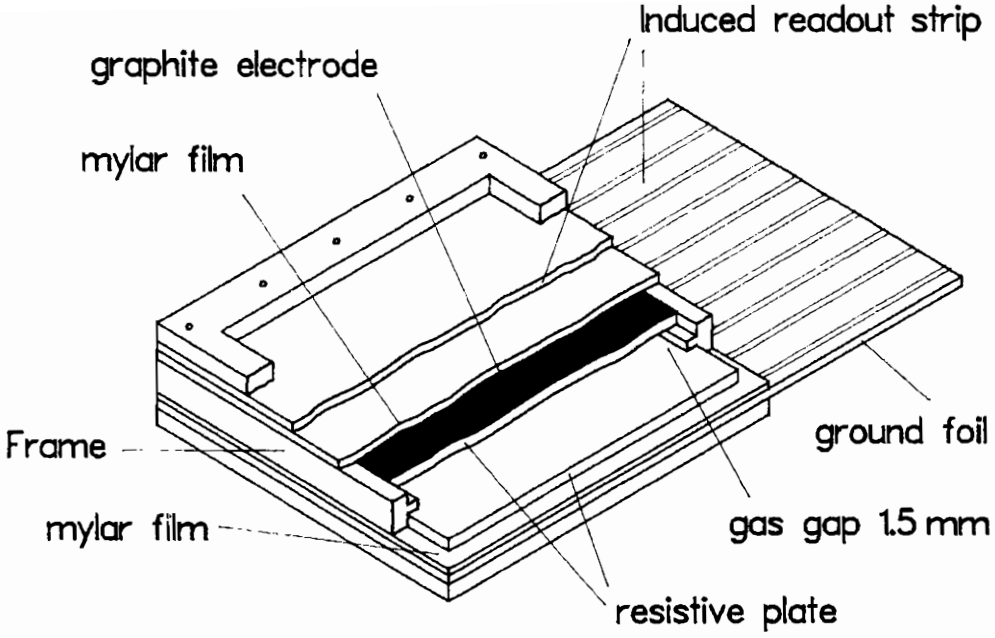

Fig.1 Schematic structure of small RPC prototype

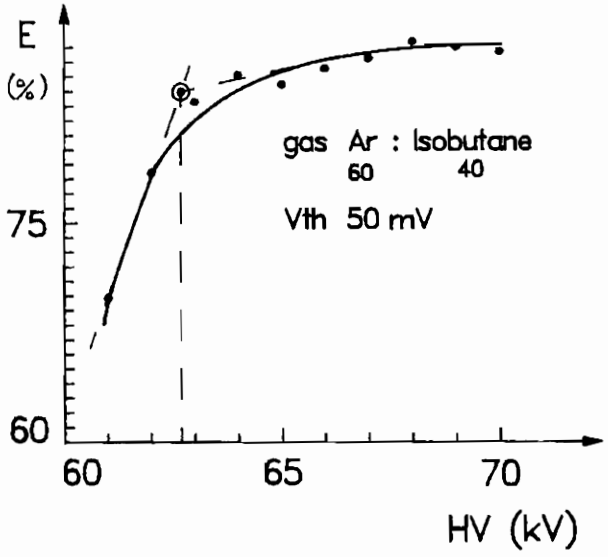

Fig.2 Efficiency plateau of RPC

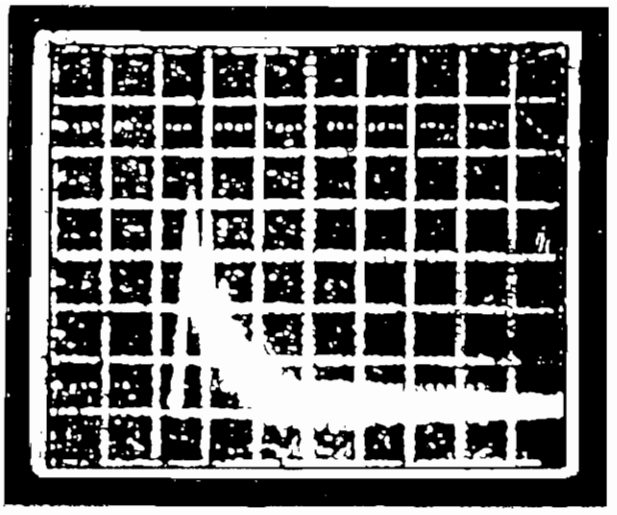

signal from induced strips
400 mV, rise time 3 ns

Fig.3 Output pulses of RPC

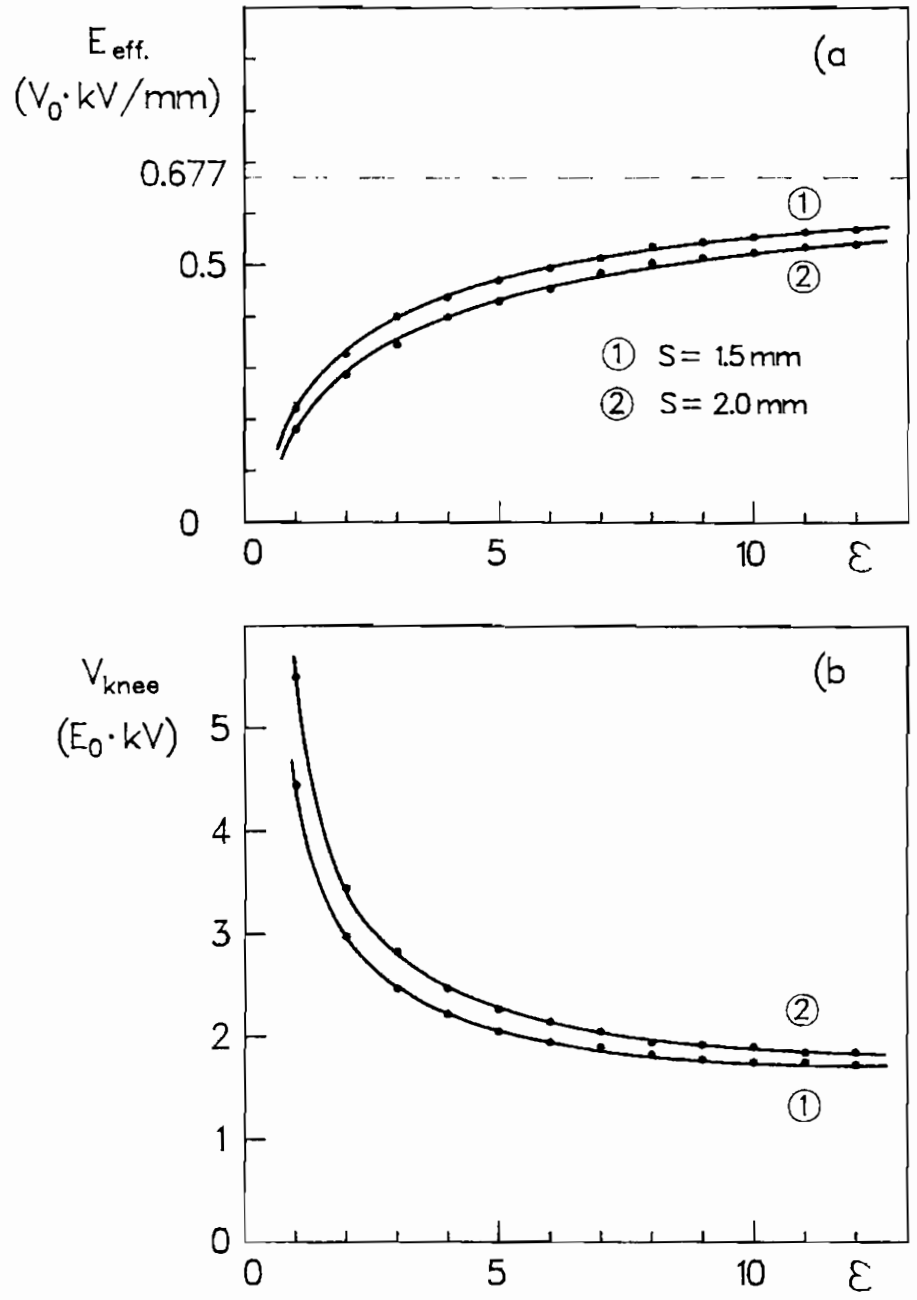

Fig.4(a) Effective electric field intensity vs. ε_r

(b) V_0 vs. ε_r

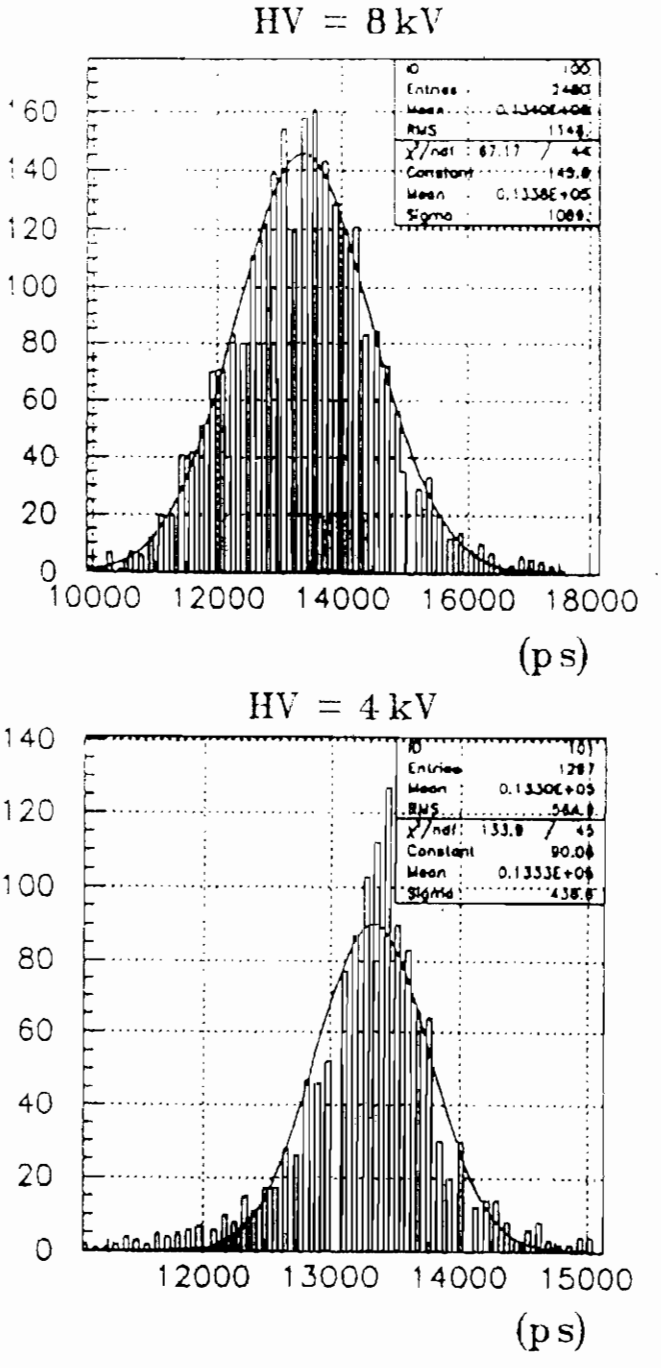

Fig.5 Time resolution of output pulse from streamer light

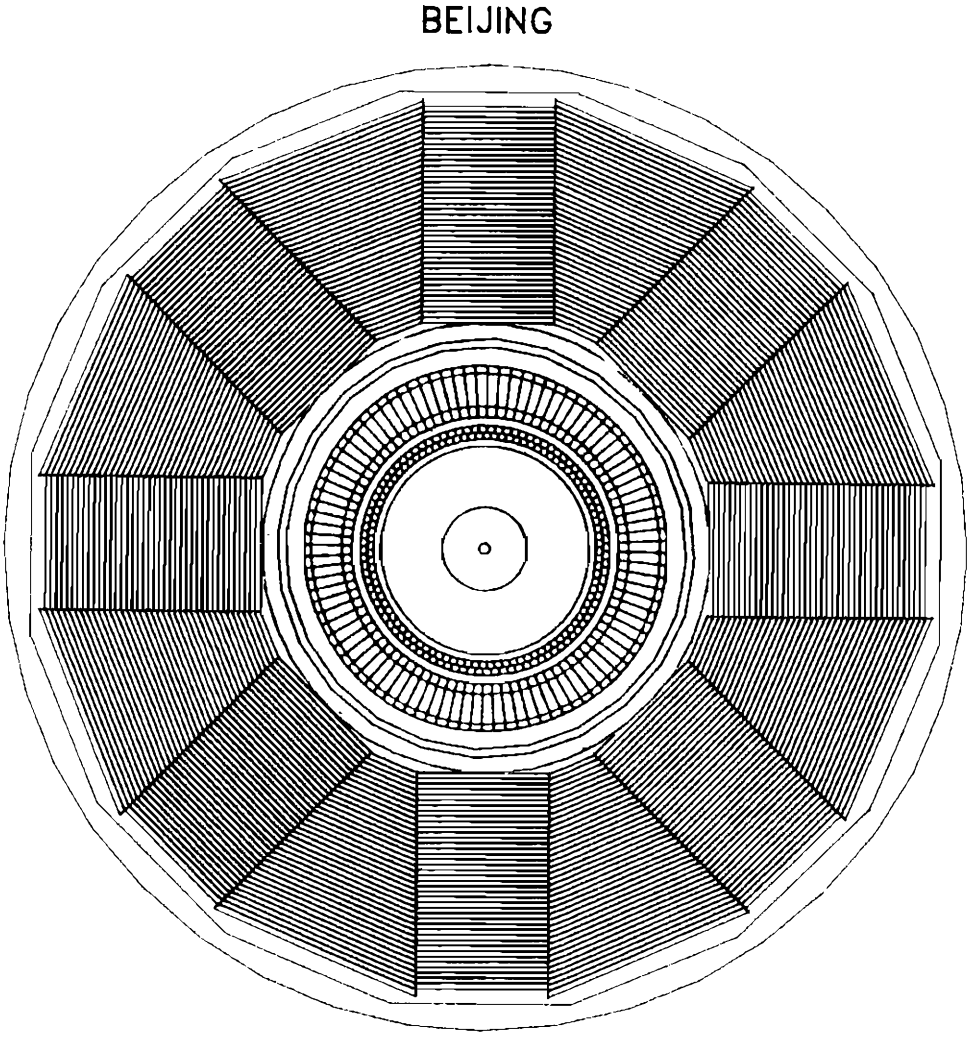

Fig. 6a End–view of HC/μ structure in BTCF

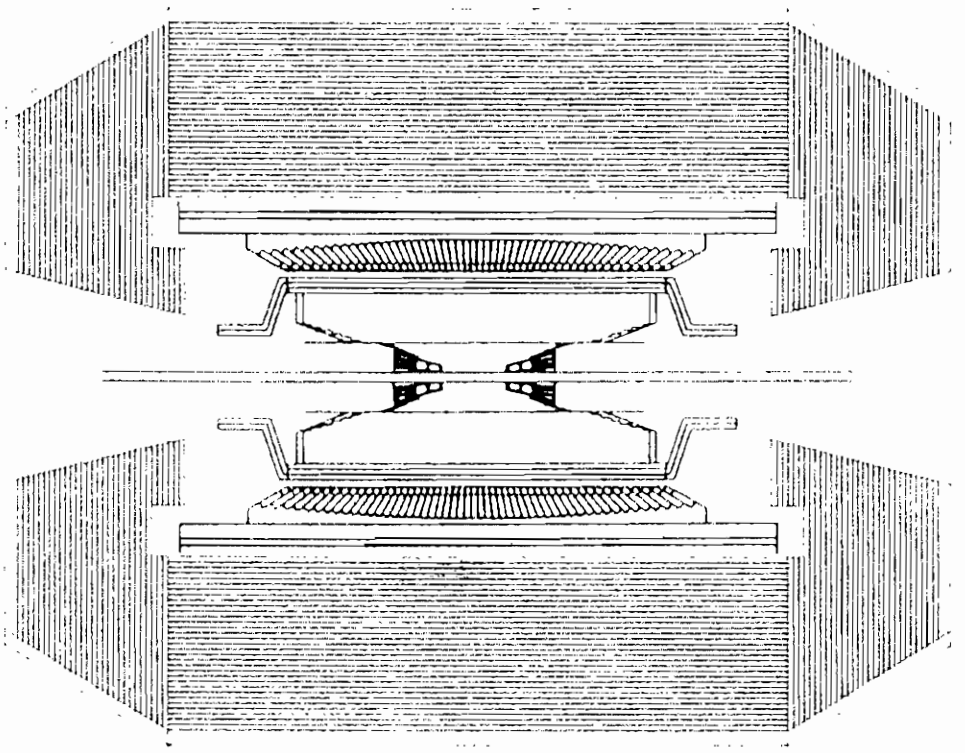

Fig. 6b Side–view of HC/μ structure in BTCF

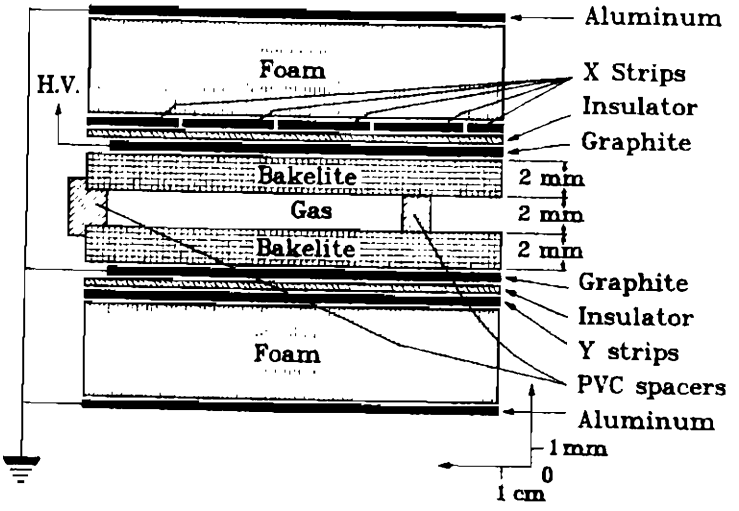

Fig.7 RPC strip structure configuration

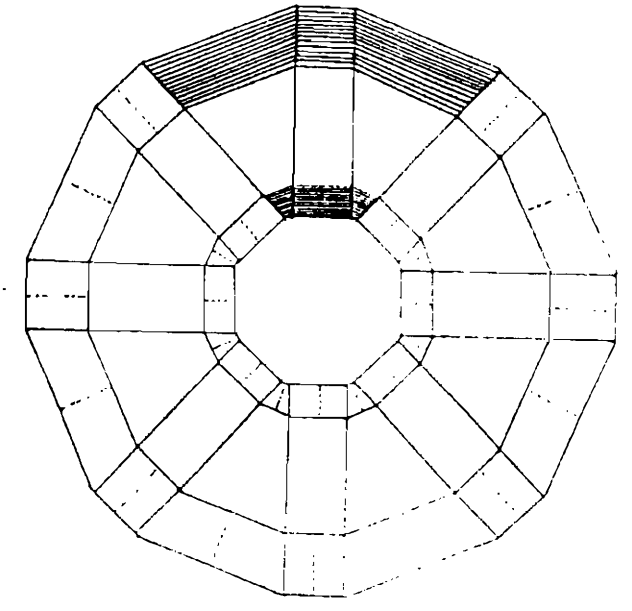

Fig.8 RPC configuration of Endcap part

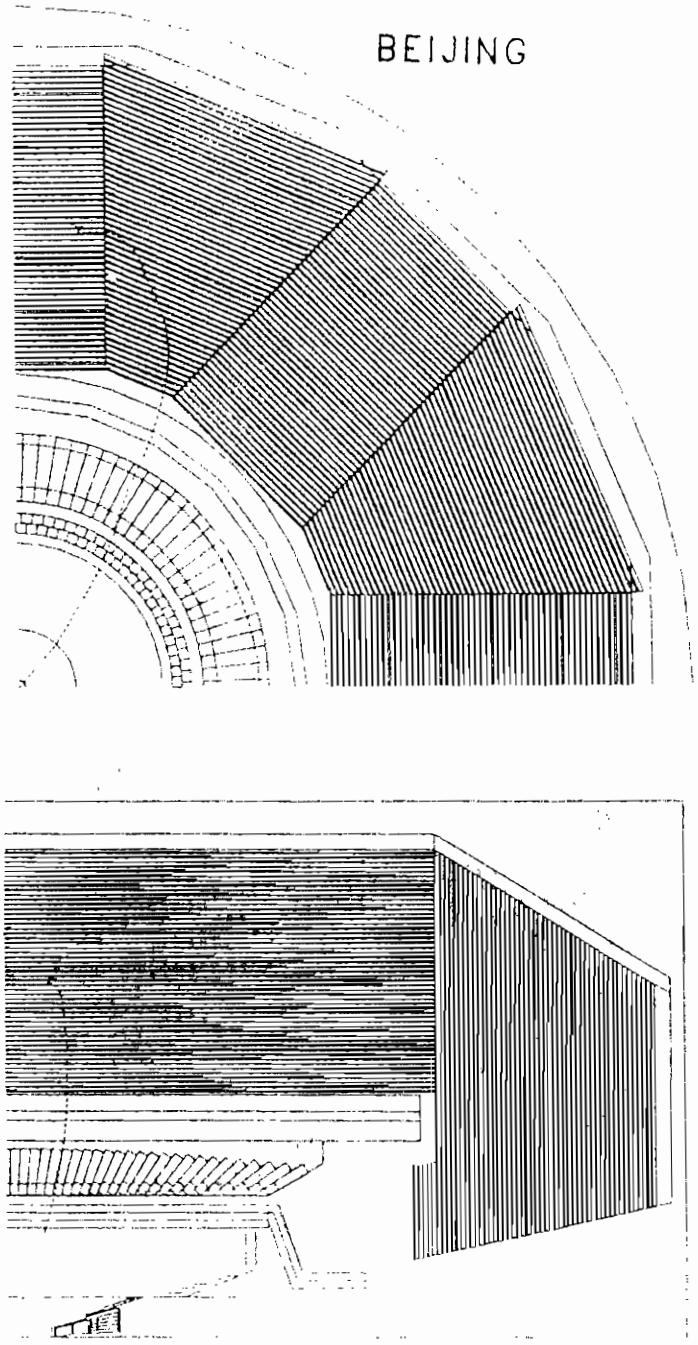

Fig.9a Typical μ track in HC/μ

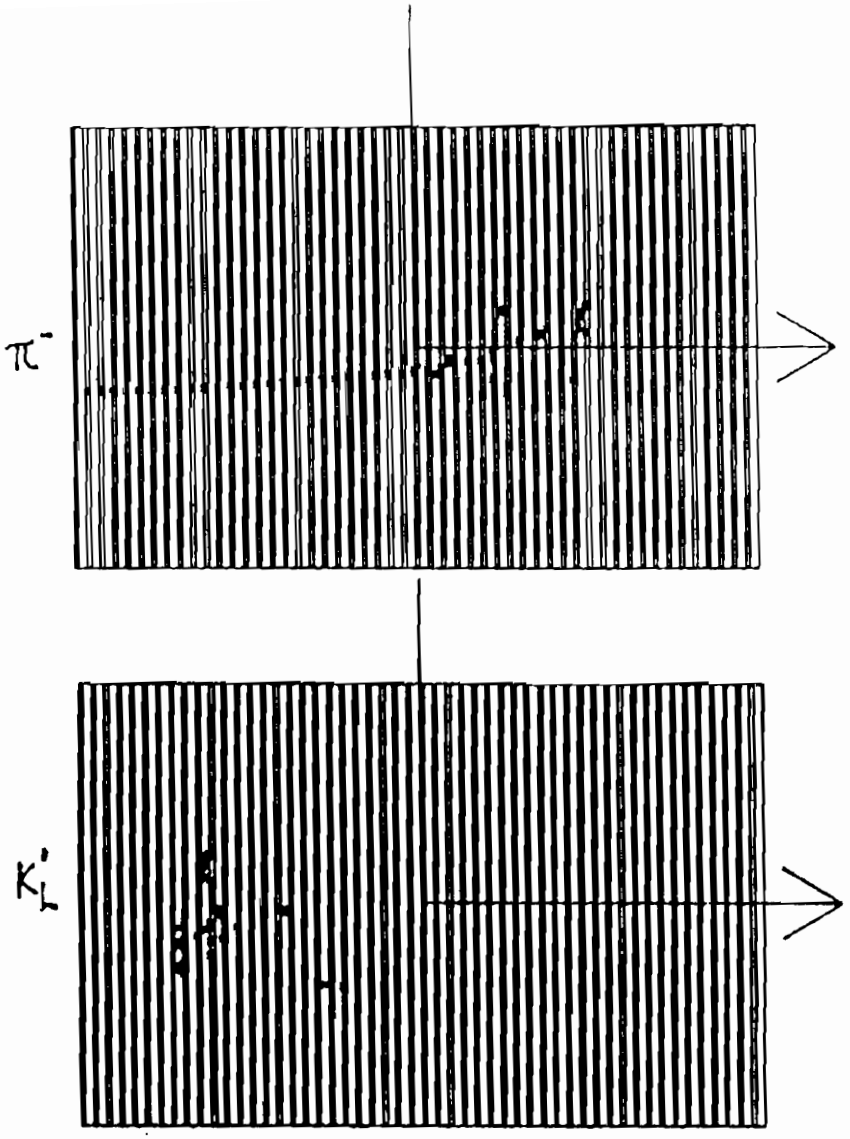

Fig.9b Typical π,K_L^0 track in HC/μ

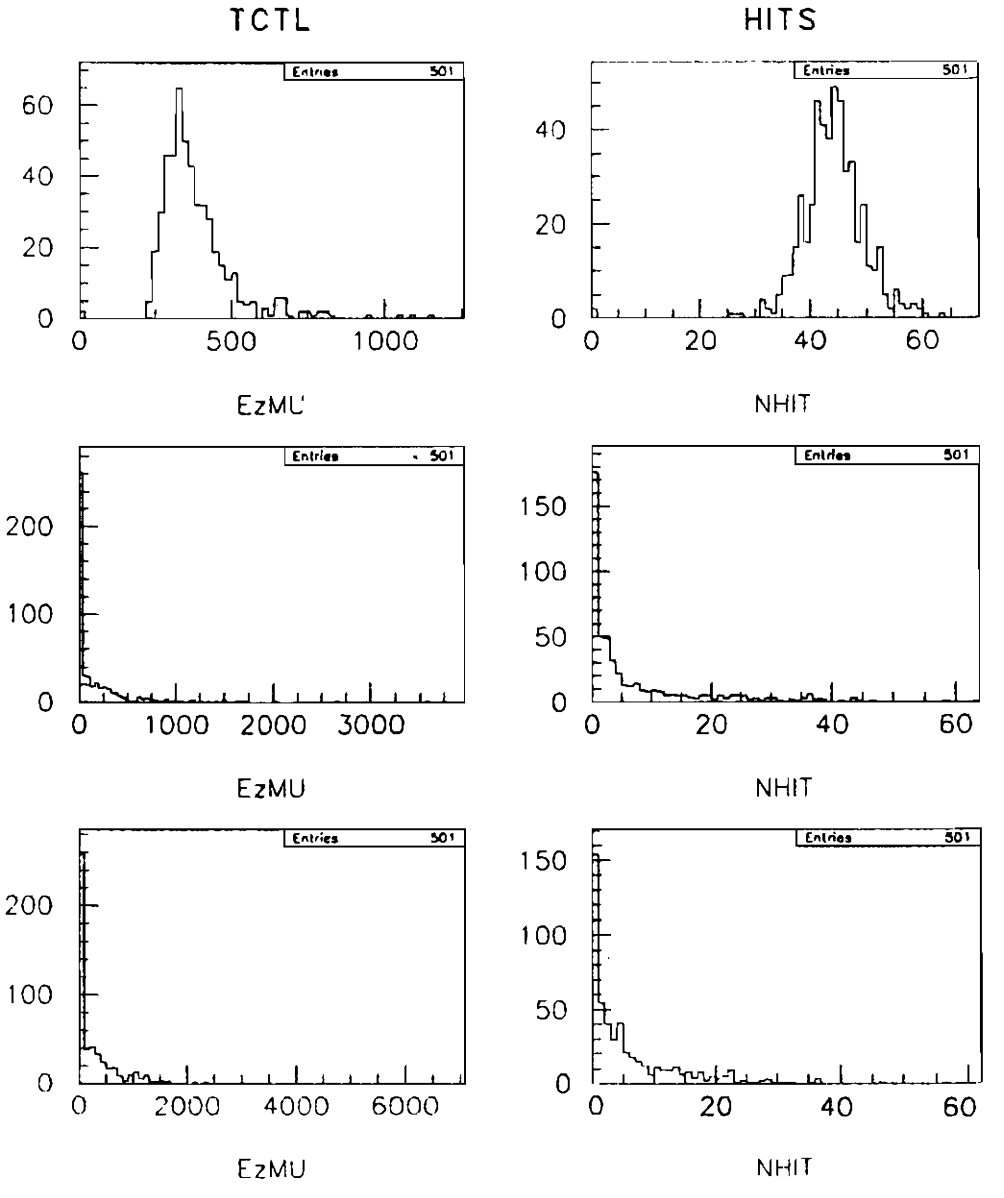

Fig.10a 1 Gev μ, π, K_L^0 in 52-Layer RPC-Fe

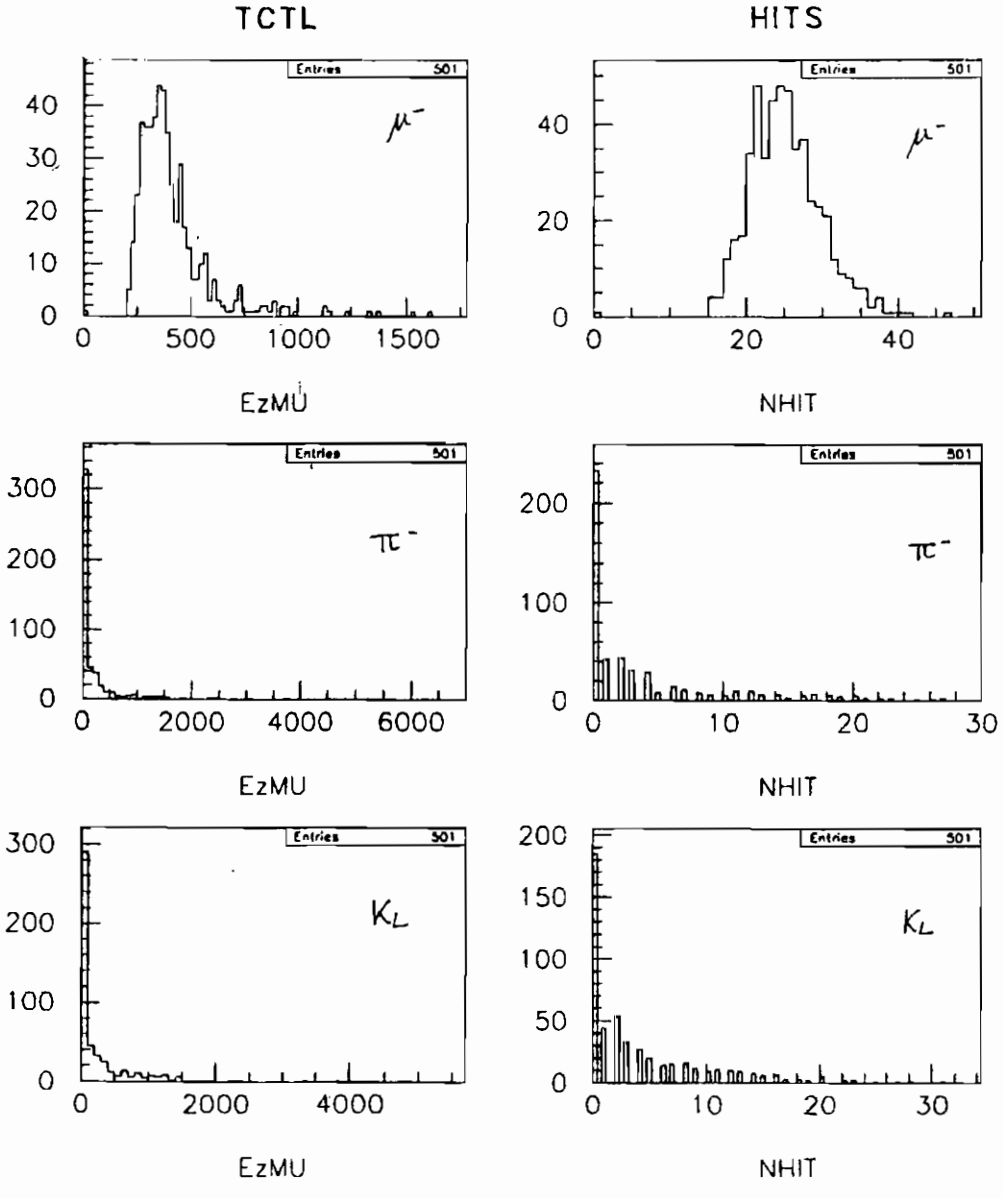

Fig.10b 1 Gev μ, π, K_L^0 in 26-Layer RPC-Fe

The FOCUS Experiment RPC Muon Identification Array

Paul D. Sheldon

Vanderbilt University, Nashville, TN 37235, USA

ABSTRACT

The heavy-flavor photoproduction experiment FOCUS (E831) will run in the 1996–97 fixed-target run at Fermilab. The experiment will accumulate a charm sample that is at least ten times larger than its predecessor E687. This paper describes one of the improvements made to the E687 spectrometer for FOCUS: a new outer muon system. This RPC system provides muon identification and trigger information for tracks at larger angles in the spectrometer's fiducial acceptance.

1. Introduction

FOCUS (E831) is a heavy-flavor photoproduction experiment located in the wideband photon area at Fermilab. FOCUS will collect data during the 1996–97 fixed target run, which will begin around the first of July, 1996.

FOCUS is an upgraded version of its predecessor, E687. E687 accumulated an effective charm sample that is among the largest in the world, and has made several recent contributions to our understanding of charm. FOCUS expects to accumulate a sample of charm decays that is ten times larger than that recorded by E687. A factor of five will come from improvements to the beam and a factor of two from improvements to the spectrometer. Most of the gain in this later category will come from improvements in the background rejection of the trigger and in the readout speed of the data acquisition electronics. The livetime of E687 was typically 50–60%, FOCUS is confident it can obtain livetimes of 85–90%.

To take maximum advantage of this increase in data, several improvements to the spectrometer are planned. For example, a new target silicon detector system will substantially improve the spectrometer's vertex resolution and background rejection. This paper describes a new "outer-muon" system, which provides muon identification and trigger information for tracks at larger angles in the fiducial acceptance of the spectrometer. This detector system will use resistive plate chambers (RPCs) as its active medium.

2. FOCUS Physics Goals Dependent on Muon Identification

Muon identification is vital to many of the physics goals of FOCUS. Semileptonic charm decays are currently of great interest. For example, because of the increased phase space available, the q^2 dependence of the form factors is much more evident in Cabibbo suppressed semileptonic decays. Such modes should therefore help to discriminate between form factor models and therefore shed light on the underlying physics. FOCUS will measure the form factors for Cabibbo suppressed as well as Cabibbo favored modes.

Rare charm decays such as the flavor changing neutral current decay

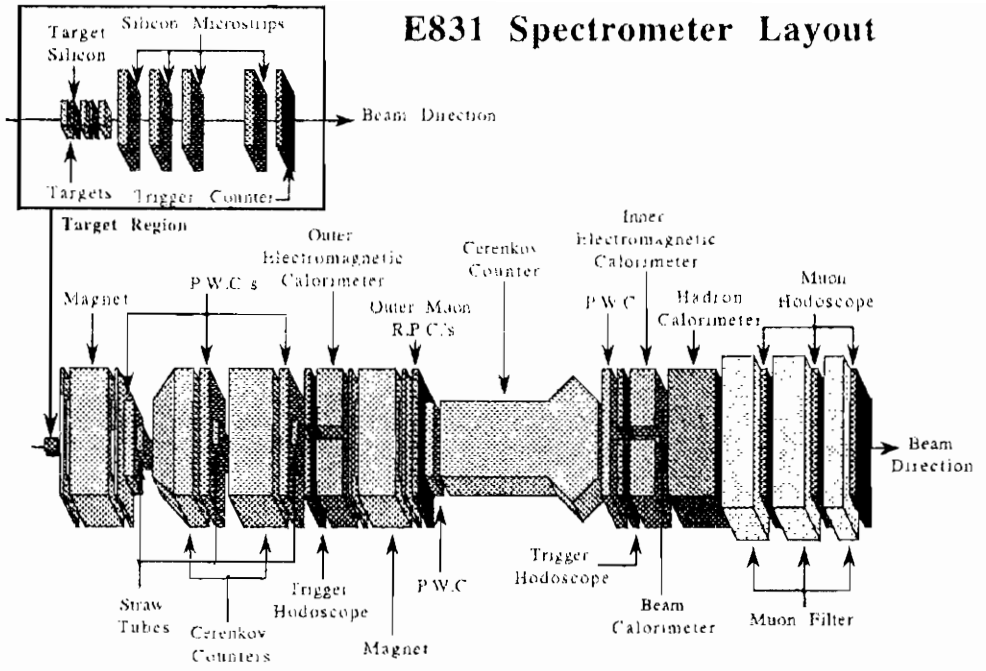

Fig. 1. Top view of the FOCUS Spectrometer.

$D^+ \to \pi^+\mu^-\mu^+$ are expected [1] to be extremely rare in the standard model (with branching fractions of 10^{-8} to 10^{-19}). Observation of such a decay or of a forbidden decay such as $D^+ \to \pi^+e^-\mu^+$ (lepton flavor number violating) or $D^+ \to \pi^-\mu^+\mu^+$ (lepton number violating) would be evidence for new physics beyond the standard model. If this new physics couples strongest (or solely) to the up-quark sector, charm may be our only hope of observing it.

Other goals include the observation of fully leptonic decays such as $D^+ \to \mu^+\nu_\mu$, and studies of J/ψ and Υ production.

3. Outer Muon System Requirements

The FOCUS spectrometer is depicted in Fig. 1. The fiducial volume of the outer muon system is a 16 cm deep region behind the magnet iron of the second analysis dipole magnet. Tracks passing through the aperture of this magnet pass through a square hole in the center of the

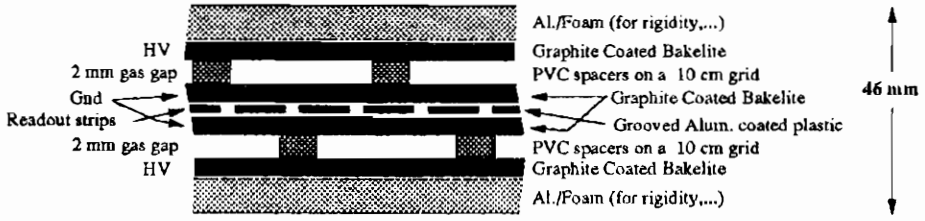

Fig. 2. Cross section of a FOCUS RPC module (not to scale).

outer muon system and into the downstream, or "inner" (small angle) portion of the spectrometer. The wider angle tracks that impinge on the iron of this second magnet are the responsibility of the outer muon system. Tracks reaching the outer muon system must first pass through the equivalent of 4 m of iron.

In E687, the outer muon system did not work adequately and was (for the most part) not used. A working outer muon system will improve the muon identification efficiency of the spectrometer by 50% (for single muons from semileptonic charm decay). The efficiency for modes with two muons (such as the rare and forbidden decays mentioned above) will more than double.

There were several criteria for the outer muon system that led to the selection of RPCs for the active part of the system. Approximately 1 kGauss fields exist in portions of the fiducial region near the magnet iron, so the detectors have to be insensitive to fields of this size. A muon trigger is required for the primary experiment trigger, so the detectors have to be fast and have good timing resolution. The detectors have to have high efficiency because there is not enough room for several layers of detector. Finally, the detectors have to be inexpensive and robust, and can't require expensive electronics. RPCs meet all these criteria. The rate limitation of RPCs run in streamer mode does not pose a problem since the occupancies in this region are expected to be much less than 50 Hz/cm^2. We therefore do not need to amplify the chamber signals before they are discriminated.

4. RPC Modules

The FOCUS RPCs are double-gap modules with a single, strip-geometry readout plane (see Fig. 2). The gaps are 2 mm thick. Spacers in each of the gaps result in dead regions. These spacers are staggered in

the two gaps to eliminate this source of inefficiency. The double gaps also provide some redundancy in the event one gap fails, and also increases the size of the chamber signals.

Because we do not need a large number of RPCs (tens instead of hundreds) we decided it would be most efficient to purchase our RPC modules from General Tecnica in Colli, Italy. General Tecnica makes bakelite RPCs. It fabricated RPCs for L3, and is making the RPCs for BaBar.

The modules are 1 m wide and are either 1.6 m or 1.8 m long. An aluminum/foam laminate covers the bakelite gaps and provides rigidity, as do stainless steel "u-channel" supports that run along the long sides of the modules. The u-channels extend 10 cm beyond the top and 5 cm beyond the bottom of the modules. These extensions support the gas and high voltage connections. The modules will be hung vertically, with the long axis vertical.

The readout strips are 2.9 cm wide, with a 2 mm gap in between. There are three different strip orientations. Modules with the strips parallel to the long axis will give the x position of muons in the spectrometer coordinate system. In these modules, the strips are cut at the center, so that each strip covers only half the height of the module. In y-view modules, the strips run perpendicular to the long axis and run the full width of the modules. In u-view modules the strips are at 45°. There is only room for three layers, and three views were chosen to provide correlated triplets for geometry and efficiency studies. Because the x-view strips are cut at the midpoint, they cannot be terminated. It was therefore decided not to terminate any of the strips.

The maximum number of strips in any one module is 64 (we will ignore the two "corner" strips in the 1.8 m u-view modules). The 1.6 m y-view modules will have only 52 channels.

Confusion radius studies using E687 data show that a 10–12 cm strip width would be sufficient. The 3.1 cm (effective) strip width was chosen because signal size decreases with increasing strip width (due to increased impedance) and there was insufficient experience with wider strips. We therefore decided to "OR" each set of four adjacent strips after the discriminators in the front-end electronics.

Currently we plan to use the "non-flammable" gas mixture tested by V. Arena it et al.[2]: 5% freon (F13b1), 8% isobutane, 16% CO_2, and 71% argon. Although it is not manufactured anymore, it is still possible to get recycled F13b1 in sufficient quantities for our use. Our own tests

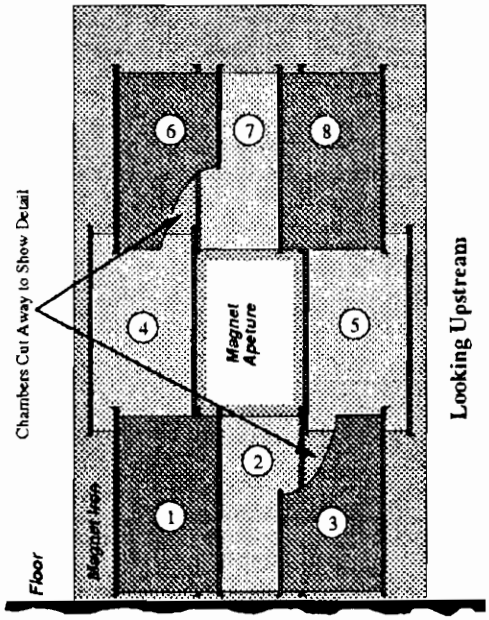

Fig. 3. View of one outer muon station, looking upstream along the beam axis The eight modules overlap and hence once station consists of two layers of modules.

with a prototype module (which we intend to use in the FOCUS system, so it is not really a prototype) indicate an operating voltage of roughly 5.8 kV with these modules and this gas. With high voltage on only one gap, a 50 mV discriminator threshold, and a 30 ns timing window, the efficiency of the prototype at 5.8 kV is better than 92%. With two gaps on high voltage the efficiency is better than 96–97%.

At 5.8 kV, each gap of the prototype draws roughly 10 microamps of current in our cosmic ray test stand. Singles rates on each strip were on the order of 0.1 Hz/cm^2.

5. Module Geometry in the Outer Muon System

The outer muon system must cover a square area perpendicular to the beam, with a square hole in the center to allow smaller angle tracks to pass through (these tracks are the responsibility of other systems in the spectrometer). To cover this area, each "station" consists of eight overlapping RPC modules (see Fig. 3) in two layers. There is just enough room for three stations. The stations look identical except for

the orientation of the readout strips. The x-view station is closest to the magnet (furthest upstream), and the u-view is the furthest downstream. In each station, the four corner modules (1, 3, 6, and 8 in Fig. 3) are farther downstream than the other four.

The modules in each station will be attached to a thin frame of 3/4" aluminum bar (four RPCs on each side of the frame). These frames will then be suspended from overhead rails, so that the frames can be slid out of the beam for servicing and installation. When in place, the three frames will be bolted together to form a rigid, reproducible structure.

Four VME-style crates will be hung on the sides of the system when it is in place in the beam. The crates will house and provide power for the front-end electronics. There will be two crates on each side: one approximately one-third of the way from the top and the other one-third of the way up from the bottom. These crates can be easily lifted off (after disconnecting the signal cables) so that the three stations can be unbolted in the event that an internal module needs to be serviced.

6. Electronics

The front-end electronics are being built by CAEN. Each front-end module recieves 64 inputs via four 34-pin "3M" type connectors on the front panel. There is one front-end module per RPC, 24 in all. The input signals are first discriminated. The threshold and output pulse width for this stage is common for each channel in a module, and is adjusted via an external VME module. After discrimination, each set of four adjacent channels is OR'ed together. The 16 output signals are presented in ECL at the back of the module on another 34-pin connector.

Trigger signals are also provided by the front-ends. Three ORs of the output signals are provided: all sixteen channels, the first eight channels, and the second eight.

Output signals (including the trigger signals) are ready 30 ns after the arrival of input signals. The ECL output signals will be sent via twisted flat "Spectra-strip" cables to LeCroy PCOS latches.

7. Outer Muon Primary Trigger

The muon trigger takes advantage of the 8-fold "tower" structure of the system. If two of the three modules in a tower have a hit, that tower is defined to have a muon candidate. The "16-fold OR" signal available

from the front-end electronics, which represents the OR of all the strips in an RPC module, will be used to determine if a module has a hit. The "single muon" trigger busline will be set if there is one or more muon candidates. The "di-muon" trigger busline will be set if two towers have muon candidates, but only if the towers are non-adjacent (because of the overlap, a single muon could trigger adjacent towers).

For the primary experimental trigger, we will be able to take all di-muon triggers. The single muon busline rate will be too high, however, and we will have to require energy in the hadronic calorimeter as part of the single muon trigger. The single muon trigger is primarily used to keep charm semileptonic decays, so a minimal hadronic energy requirement is acceptable.

8. Final Comments

The outer muon system is currently being installed at Fermilab.

Because FOCUS is an upgrade of a previous experiment, much of the analysis software already exists. The experiment expects to do concurrent data processing during the run, and physics results should begin to appear in 1997.

9. Acknowledgements

The author is grateful to the Vanderbilt University Research Council and the National Science Foundation for their generous support.

10. References

1. G. Burdman, E. Golowich, J. Hewett, and S. Pakvasa, *Phys. Rev.* **D52** (1995) 6383.
2. V. Arena *et al.*, *Nucl. Inst. and Meth.*, **A356** (1995) 264.

List of partecipants

Institution

ALVIGGI Mariagrazia	INFN e Università di Napoli
ARENA Vincenzo	INFN Sezione di Pavia
BARBERIO Elisabetta	Weizmann Institute of Science
BATURIN Vitaly	INFN Sezione di Napoli
BENCZE Gyorgy	CERN div. PPE
BOCA Gianluigi	INFN e Università di Pavia
CALLIGARICH Elio	INFN Sezione di Pavia
CAMARRI Paolo	INFN Sezione di Roma "La Sapienza"
CAMBIAGHI Mario	INFN e Università di Pavia
CARDARELLI Roberto	INFN e Univ. di Roma "Tor Vergata"
CAVALLO Nicola	INFN Sezione di Napoli
CERADINI Filippo	INFN e Terza Università di Roma
CERRON-ZEBALLOS Esteban	Blaise Pascal Univ.-World Laboratory
CHTCHETKOVSKI Alexandre	INFN Sezione di Napoli
CIAPETTI Guido	INFN e Univ. di Roma "La Sapienza"
COLALEO Anna	INFN e Università di Bari
COLESANTI Lorena	IFCAI CNR Palermo e INFN-Napoli
CROTTY Ian	CERN div. PPE
DE ASMUNDIS Riccardo	INFN Sezione di Napoli
DE GIORGI Marco	INFN e Università di Padova
D'ETTORRE PIAZZOLI Benedetto	INFN e Università di Napoli
DE VINCENZI Mario	INFN e Terza Università di Roma
DI CIACCIO Anna	INFN e Univ. di Roma "La Sapienza"
FABJAN Christian	CERN div. PPE
FLYAGIN Vladimir	JINR DUBNA
FONTE Paulo	LIP e University of Coimbra
GANTER Stefan	Forsch. Karlsruhe Inst.Kern Phys.
GAPIENKO Vladimir	IHEP Protvino
GIANNINI Gianrossano	INFN Sezione di Trieste
GASPARINI Fabrizio	INFN Sezione di Padova
GORSKI Maciej	Institute of Nuclear Studies Warsaw
GRANCAGNOLO Franco	INFN Sezione di Lecce

GRAYER Geoffrey	Rutherfors Appleton Laboratory
GUSTAVINO Carlo	Laboratori Nazionali del Gran Sasso
GUTAY Laszlo	Purdue University
HATZIFOTIADOU Despina	World Laboratory and CERN
HOSHI Yoshimoto	Tohoku Gakuin University
IASELLI Giuseppe	INFN Sezione di Bari
LACAVA Francesco	INFN e Univ. di Roma "La Sapienza"
LAMAS-VALVERDE Jose	Strasbourg Univ.-World Laboratory
LANZA Agostino	INFN Sezione di Pavia
LIGUORI Puccio	INFN e Università di Pavia
LIVAN Michele	INFN e Università di Pavia
MAGGI Marcello	INFN e Università di Bari
MAKEEV Valery	IHEP Protvino
MARCHESOTTI Marco	INFN e Università di Pavia
MAZUR Peter	FERMILAB
MORGAN Norman	Physics Department Virginia Tech
NAHNHAUER Rolf	DESY Zeuthen
NATALI Sergio	INFN e Università di Bari
NEUPANE Surya Kumar	CERN div. PPE
NISATI Aleandro	INFN e Univ. di Roma "La Sapienza"
NUZZO Salvatore	INFN e Università di Bari
ORESTANO Domizia	INFN e Univeristà di Pavia
PANTEA Dan	Institute of Atomic Physic
PAOLUCCI Pierluigi	INFN Sezione di Napoli
PIAZZOLI Adalberto	INFN e Università di Pavia
PATRICELLI Sergio	INFN e Università di Napoli
PICCOLO Davide	INFN Sezione di Napoli
PONTECORVO Ludovico	INFN Sezione di Roma "La Sapienza"
PRIMAVERA Margherita	INFN e Università di Lecce
RADERMACHER Ernst	CERN div. PPE
RAICS Peter	Kossuth University Debrecen
RANIERI Antonio	INFN e Università di Bari
RAPONI Teodorico	General Tecnica
RICCARDI Cristina	INFN e Università di Pavia
RIZZOTTO Vittorino	ANGI Srl
ROMANO Franco	INFN e Università di Bari

ROSENFELD Carl	University of South Carolina
SANTONICO Rinaldo	INFN e Univ. di Roma "Tor Vergata"
SCIACCA Crisostomo	INFN e Università di Napoli
SHELDON Paul	Vanderbilt University
TAMBURINI Giuseppe	ANGI srl
TERAMOTO Yoshiki	I. Cosmic Ray Phys. Osaka City U.
TORRE Paola	INFN e Università di Pavia
VENEZIANO Stefano	INFN e Univ. di Roma "La Sapienza"
VIOLA Laura	INFN e Università di Pavia
VIVALDI Franco	CAEN Spa
WILLIAMS Crispin	CERN div. PPE
WRIGHT Douglas	Lawrence Livermore National Lab.
WROCHNA Grzegorz	CERN div. PPE
WUEST Craig	Lawrence Livermore National Lab.
YAMAGUCHI Akira	Tohoku University
ZALLO Adriano	INFN Laboratori Naz. di Frascati

Local organizers

RATTI Sergio P.	INFN e Università di Pavia
ABBRESCIA Marcello	INFN e Università di Bari
BONOMI Germano	INFN e Università di Pavia
CALLIGHER Roberta	INFN Sezione di Pavia
GIANINI Gabriele	INFN e Università di Pavia
INTROZZI Gianluca	INFN e Università di Pavia
MANGIA Anna Rita	Università di Pavia
VITULO Paolo	INFN e Università di Pavia